



**The Synthesis and Characterisation of Photoresponsive  
Metal Organic Frameworks and the Implementation of  
Cavity Perturbation Theory in the study of Liquid  
Chromatography**

**Luke Frederick Incedon Kidwell**

Thesis submitted to Cardiff University for the degree of Doctor of Philosophy

December 2020



## Abstract

This thesis describes the process of designing a MOF that incorporates a spiropyran molecule as a linker, as well as the use of a dielectric measurement technique to measure separation in MOFs.

Chapter 1 covers the basics of MOF synthesis and techniques that facilitate the incorporation of functionalities into MOFs, as well as a small review of existing photoresponsive MOFs. This is followed by a brief summary of the challenges faced in xylene and styrene separation in industrial settings as well as some examples of MOFs used in these separations. Followed by some oversight into microwave studies on MOFs.

Chapter 2 describes the synthesis and characterisation of 10 novel organic compounds that have the spiropyran functionality that have potential as an organic linker in a MOF. First describing the minutiae of optimising the parameters sufficiently to progress to the synthesis of the MOFs, followed by a study that compares the NMR and UV-Vis spectra of the ligands and how slight variations in regiochemistry can affect the photoisomerization of the ligands synthesised.

Chapter 3 describes the combinatorial synthesis undergone which resulted in the synthesis of three novel materials that use some of the ligands, synthesised in chapter 2. This is then followed by a description of the characterisation of each of the frameworks, and in the case of LK-1 and LK-2 further reaction optimisation to obtain a phase-pure product.

Chapter 4 describes the work involved in designing an experimental set up that can analyse, *in-situ*, the chromatographic separation of analytes in MOFs. The chapter begins with a summary of the fundamentals of microwave cavity perturbation theory, sufficiently for the understanding of this work. The chapter then goes onto describe the details of the method development, eventually attempting chromatography with compounds typically found in industrial feedstocks for styrene and xylene production.

# Contents

Contents.....	i
List of Figures .....	iv
List of Equations .....	xi
List of tables .....	xi
List of abbreviations .....	xiv
Contributions .....	xviii
Acknowledgements.....	xviii
Chapter 1. Introduction .....	1
1.1 Metal Organic Frameworks .....	1
1.1.1 Synthetic strategies .....	2
1.1.2 Imparting functionality through ligand design.....	6
1.1.3 Photoresponsive materials .....	7
1.1.4 Spiropyran.....	9
1.2 Molecular separations.....	12
1.2.1 Xylene .....	12
1.2.2 Styrene.....	13
1.2.3 MOFs in separations.....	13
1.2.4 Microwave studies of MOFs .....	17
1.3 Scope of Thesis .....	19
1.4 References.....	19
Chapter 2. Synthesis of spiropyran ligands.....	23
2.1 Introduction.....	23
2.1.1 Spiropyran Synthesis .....	23
2.1.2 Spiropyran functionalisation.....	24
Spiropyran properties .....	27
2.2 Aims.....	28
2.3 Results and discussion.....	28
2.3.1 Electrophilic Aromatic Bromination of Spiropyran .....	29
2.3.2 Suzuki cross couplings .....	32
2.3.3 Ligand Properties.....	38
2.4 Summary and conclusions .....	56
2.5 Experimental.....	56
2.5.1 Characterisation techniques .....	56
2.5.2 Ligand synthesis .....	57

2.6	References.....	67
Chapter 3.	Synthesis and characterisation of Metal Organic Frameworks incorporating Spiropyran .....	70
3.1	Introduction.....	70
3.1.1	Designing a novel framework .....	70
3.1.2	Pillar-layer MOFs .....	71
3.1.3	Photoactive MOFs .....	72
3.2	Aim.....	79
3.3	Results and Discussion .....	81
3.3.1	Synthetic strategy “method development” .....	81
3.3.2	LK 1 and LK 2 .....	109
3.3.3	GG-1.....	130
3.3.4	GG-32.....	142
3.4	Summary and Conclusion .....	150
3.5	Experimental.....	151
Chapter 4.	Microwave dielectric studies of metal organic frameworks in chromatographic separation .....	158
4.1	Introduction.....	158
4.1.1	Separation in MOFs .....	158
4.1.2	Fundamentals of dielectric properties .....	159
4.1.3	Microwave Cavity Perturbation method .....	160
4.1.4	Temperature Correction .....	164
4.2	Aims.....	166
4.2.1	Frameworks of interest .....	167
4.3	Results and Discussion .....	168
4.3.1	Method Development part i) Static experiments .....	169
4.3.2	Method Development part ii) Flow experiments.....	174
4.3.3	Method Development part iii) Aliquot experiments.....	180
4.4	Summary and Conclusions.....	200
4.5	Experimental.....	201
4.5.1	Microwave Cavity measurements.....	201
4.5.2	<i>Static Experiments</i> .....	201
Appendix.....		209
S1.....		209
S2.....		236
S3.....		238

## List of Figures

- Figure 1 The  $Zn_4O(-COO)_6$  metal cluster that forms an octahedron metal SBU. When the metal SBU is combined with two different organic linkers, the octahedrons feature in the two different frameworks. Image reproduced from A. Schoedel.<sup>4</sup> 1
- Figure 2 Three examples of how equilibria shift upon addition of an acid with the active coordinating species (highlighted in green). In the cases of i) and ii) addition of acid shifts the equilibrium towards the protonated forms of the linkers which are unable to coordinate with the zinc metal ion. In the case of iii), it is showing how the addition of nitric acid reduces the dissociation of zinc nitrate. 2
- Figure 3 Three different possible cadmium frameworks determined by the structure-directing influences of the guest solvent molecules: dimethylformamide (DMF), diethylformamide (DEF) and isopropanol (IPA). Colour scheme is as follows: cadmium, yellow; carbon, grey; nitrogen, blue; oxygen, orange. Adapted from Ghosh et al.<sup>13</sup> 4
- Figure 4 Two different frameworks are synthesised by varying the stoichiometry of metals and ligands from 2:2:1 to 1:1:1 and also showing that a mixture of both frameworks is produced when a 5:2:2 ratio is used. The rest of the conditions were the same, 160°C, 72 hours, in an EtOH:H<sub>2</sub>O (1:1) solvent system. Adapted from Guo et al.<sup>15</sup> 5
- Figure 5 NTU-105 MOF (right) constructed using a triazole linker (left). Colour scheme is as follows: copper, green; nitrogen, blue; carbon, grey; oxygen, red. Image reproduced from X. Wang et al.<sup>18</sup> 6
- Figure 6 Fragment of the framework demonstrating the metal SBU (left). Views along a single channel to demonstrate how the serine and methionine moieties point towards the centre of the pore, the residues are present in a statistical disorder (1:1) and are superimposed for better visualisation. Copper (II) and calcium (II) ions from the network are represented as cyan and purple spheres, respectively. Oxygen and sulphur atoms from the residues are shown as red and yellow spheres, respectively. The organic ligands are represented as sticks with the following colour scheme: sulphur, yellow; oxygen, red; nitrogen, light blue; carbon, grey, with the exception of L-serine (-CH<sub>2</sub>OH) and L-methionine (-CH<sub>2</sub>CH<sub>2</sub>SCH<sub>3</sub>) residues, which are represented as red and yellow sticks, respectively. Reproduced from M. Mon et al.<sup>20</sup> 7
- Figure 7 Photoisomerism exhibited by azobenzene. 8
- Figure 8 illustrates a framework constructed from the photoresponsive linkers; azobenzene dicarboxylate (AzDC) and 1,2-bis(4-pyridyl)ethylene (4,4'-BPE) linker. 8
- Figure 9 Illustration of the photoisomerism exhibited by the dithienylethene molecule. 9

- Figure 10 Polarised light image of the DMOF-1@DTE single crystal before (a, c) and after (b, d) irradiation with 365 nm light. The plane of polarisation for each image is indicated by an arrow. Reproduced from I. Walton et al..<sup>26</sup> 9
- Figure 11 Photoisomerism exhibited by spiropyran and spirooxazine molecules. Upon irradiation with UV light, the closed spiropyran (SP) form breaks the C-O bond at the spiro centre and extends out to the open merocyanine (MC) form. The difference in properties of these two isomers are outlined beneath the scheme. Spiropyran, X = carbon; spirooxazine, X = nitrogen.<sup>28</sup> 10
- Figure 12 The MIL-53 framework, loaded with a spiropyran polymer, functions as a desalination material. Imaged taken from R. Ou et al..<sup>29</sup> 11
- Figure 13 ZIF-8 membrane encapsulating spiropyran acts as an active transport system for lithium ions. The inset shows the structure of the SSP@ZIF-8 composite in the merocyanine form. Colour scheme is as follows: lithium, purple; potassium, pink; sodium, green; magnesium, blue. Image taken from H. Liang et al..<sup>30</sup> 12
- Figure 14 (top) Chemical structures of the protonated forms of dobdc and *m*-dobdc. (bottom) Displays the interactions of each C<sub>8</sub> isomer with the open metal sites of the cobalt nodes in Co<sub>2</sub>(dobdc) with intermolecular distances highlighted for comparison. Purple, red, grey, and white spheres for cobalt, oxygen, carbon and hydrogen atoms, respectively. Reproduced from M. Gonzalez et al..<sup>39</sup> 15
- Figure 15 a) shows crystallographic data of how styrene packs inside a pore of MIL-47. b) illustrates how ethylbenzene packs inside the same pore, note only half of the positions displayed in the case of ethylbenzene are occupied. Dark grey, red, pink spheres for carbon, oxygen and vanadium atoms, hydrogen atoms omitted. Reproduced from M. Maes et al..<sup>40</sup> 16
- Figure 16 showing frequency and bandwidth over time. Frequency is proportional to the e' value of the system and bandwidth is proportional to the e'' value of the system. A is the initial filling of the CPO-27-Co framework with ND<sub>3</sub>. B is was then the ND<sub>3</sub> is displaced by a flow of argon. C is the refilling of the framework with ND<sub>3</sub> and D is the second displacing of ND<sub>3</sub> with argon. Reproduced from M. Barter et al..<sup>48</sup> 18
- Figure 17 Condensation of a salicyl aldehyde with Fischer's base to form spiropyran and by-product. 23
- Figure 18 Condensation of salicyl aldehyde with the conjugate acid of the Fischer's base. 23
- Figure 19 Cross-coupling employed by D. Williams et al. to functionalise two spiropyran molecules with pyridine rings. 25
- Figure 20 Suzuki cross coupling reaction by J. H. Lee et al. with associated yields. 25

Figure 21 Y. Cho et al. synthesising two iodinated spiropyran molecules in high yields. <sup>11</sup>	26
Figure 22 Synthetic scheme for bromination of indoline fragment with associated yields achieved (top). Phenanthridine derivative of spiropyran which restricts attack to the chromene fragment, only the dibrominated product was obtained, no mono-brominated species were identified (bottom). Reported by Zakhs et al.. <sup>12</sup>	27
Figure 23 Photoisomerism of spiropyran (left) ring opening to form the coloured merocyanine form (right). Reverse reaction typically occurs through thermal relaxation/visible light.	27
Figure 24 1,3,3-trimethylindolino- $\beta$ -naphthopyrylospiran molecule studied by M. Suzuki et al.. <sup>14</sup>	27
Figure 25 Schematic illustration of the cooperative photochemical reaction model adopted from Asahi et al.. <sup>16</sup> The open circles represent the ground-state spiro isomer, the filled ones represent the S1 states and/or the nonplanar open forms, and the filled rectangles represent the trans-planar photomerocyanines.	28
Figure 26 Scheme for synthesis for hetero/homoleptic spiropyrans.	29
Figure 27 Lowest energy conformations for the free ligands <b>3a</b> <b>3b</b> <b>6b</b> , calculated by the MM2 method on chem3D. Nitrogen (blue), oxygen (red), carbon (grey), hydrogen (white), lone pairs of electrons (pink).	30
Figure 28 Possible bromination sites. Br <sub>1</sub> is the primary bromination site with the nitrogen directing electrophilic attack to the para position. Br <sub>c</sub> and Br <sub>b</sub> are possible sites to which overbromination can occur.	31
Figure 29 TLC Left: Sample of starting material <b>2</b> . Right: Cross coupling reaction to form <b>3a</b> . Sample taken from crude product after following all purification steps before column chromatography.	33
Figure 30 Scheme demonstrating the possible intermediates when synthesising <b>3a</b> during the cross-coupling process.	38
Figure 31 The spiro-core relevant to study with the relevant protons highlighted.	38
Figure 32 Full <sup>1</sup> H spectra of <b>4a</b> , <b>4b</b> and <b>4c</b> in CDCl <sub>3</sub> .	39
Figure 33 Expansion of <sup>1</sup> H NMR spectra of <b>4a</b> , <b>4b</b> and <b>4c</b> in CDCl <sub>3</sub> . Dotted lines show peak centres for the appropriate peaks and are added to demonstrate the shift between NMR spectra <b>4a</b> , <b>4b</b> and <b>4c</b> .	40
Figure 34 Reproduced from Reddy et al.. <sup>39</sup> illustrating the electronic distribution around pyridine rings. Although there are two possible resonance pathways, the scheme depicting a negative charge on the nitrogen is more dominant therefore the overall effect is reduced electron density on the ortho and para positions in respect to the nitrogen.	41



Figure 35 Pyridine/pyrimidine moieties affect the electronic distribution around the rest of the spiropyran molecule. In the case of 4-pyridyl substitution ( <b>4a</b> , left) the mesomeric effects will extend to the adjacent benzene ring fused to the pyran. In the case of 3-pyridyl/5-pyrimdyl ( <b>4b/4c</b> , right), the mesomeric effects do not extend to the benzene ring.	41
Figure 36 Comparison of peak positions pre/post-bromination.	42
Figure 37 DFT of ligand <b>4a</b> displaying LUMO (top) and HOMO (bottom).	43
Figure 38 Expansion of <sup>1</sup> H NMR in CDCl <sub>3</sub> for <b>3a</b> , <b>3b</b> and <b>3c</b> . Dotted lines show peak centres for the appropriate peaks and are added to demonstrate the shift between NMR spectra.	44
Figure 39 Schematic to demonstrate how functionalisation of the indoline fragment would affect the electronics of the rest of the molecule. In the case of 4,4'-dipyridyl substitution ( <b>3a</b> , left) the mesomeric effects will extend to the nitrogen atom of the indoline. In the case of 3-pyridyl/5-pyrimdy ( <b>3b/3c</b> , right), like <b>4b/4c</b> the mesomeric effects do not extend beyond the pyridine/pyrmidine ring.	44
Figure 40 Solution state UV-vis spectra of molecule <b>4a</b> . Top: Before recording spectra, solutions left at room temperature in ambient light for 2 days. Bottom: Before recording spectra, solutions kept at -20°C in the dark for 2 days.	47
Figure 41 Outlining the equilibrium present when spiropyran is in solvent media. E.g. The polar solvent acetonitrile, would stabilise the polar MC form more than the non-polar SP form, in visible light however the MC form is being forced into the less suited SP form, thus the SP form begins aggregating to better suit the environment. <sup>45</sup>	48
Figure 42 Solution state spectra of molecules <b>4a</b> (blue), <b>4b</b> (green), <b>4c</b> (red) recorded in methanol (solid line) and in the solid state (dashed line). Solution was exposed to ambient conditions (incidental light and room temperature).	50
Figure 43 Solid state UV-Vis spectra zoomed in on the 400-550 nm region for ligands <b>4a</b> and <b>4b</b> .	51
Figure 44 Solution state spectrum of molecules <b>4a</b> (blue) and <b>5a</b> (red) recorded in MeOH (solid line) and the solid state (dashed line). Solution was exposed to ambient conditions (incidental light and room temperature).	52
Figure 45 Solution state spectrum of molecules <b>3a</b> (blue), <b>3b</b> (green), <b>3c</b> (red) recorded in MeOH (solid line) and the solid state (dashed line). Solution was exposed to ambient conditions (incidental light and room temperature).	54
Figure 46 Crystal Structure of spiropyran appended with two 4-pyridyl moieties ( <b>3a</b> ). Carbon (grey), oxygen (red), nitrogen (blue), hydrogen (white).	55
Figure 47 Ligand <b>3a</b> crystal structure with both parts overlaid, to demonstrate disorder. The red part is the dominant part shown in Figure 46.	55

Figure 48 Illustrating the principles of the one-pot synthesis compared with the layer-by-layer approach. Figure taken from Wang et al.. <sup>12</sup>	71
Figure 49 Nuances of how the different generations of azobenzene-based frameworks differ in their classification. Image taken directly from F. Coudert's review. <sup>16</sup>	72
Figure 50 MOF-5 encapsulating 1,3,3-trimethylindolino-6'-nitrobenzopyrlospiran as a guest molecule. (Image adapted from N. Rosi et al.. <sup>20</sup> )	73
Figure 51 Solid-State UV-vis profiles of frameworks encapsulating spiropyran before and after irradiation with 365 nm light for 1 minute. (a) = MOF-5, b) = MIL-68 (In), c) = MIL-68(Ga), and d) = MIL-53(Al))	74
Figure 52 Comparison of the PXRD obtained before and after loading MOF-5 with the spiropyran guest molecule (left). Comparison of PXRD patterns obtained before and after loading with MIL-53.	75
Figure 53 The photoresponsive materials synthesised by D. Williams et al.. <sup>23</sup> , outlining the composition of each framework. We will be focusing on frameworks <b>1</b> and <b>2</b> in this example.	76
Figure 54 Top: SCXRD of frameworks incorporating TNDS ( <b>1</b> ) and HDDB ( <b>2</b> ) linkers. Bottom: PXRD patterns comparing simulated patterns from the SCXRD data and the experimental patterns. The coloured numbers show the increase in interlay distance for each MOF which agree with the size of the spiropyran linkers.	77
Figure 55 UV-Vis data reported by D. Williams et al. comparing spiropyran linkers solution and solid state profiles to incorporation in a MOF. <sup>23</sup>	78
Figure 56 PXRD data obtained showing no discernible change with or without radiation (top left). Isotherm data obtained during cycling of radiation, showing uptake and release of gas coinciding with irradiation cycling (top right). CCC and CCN low-energy FTIR bending modes shows the linker excited by UV light in both the ligand (bottom left) and as a linker incorporated in the framework (bottom right).	79
Figure 57 Simple illustration of how a framework will behave upon photoconversion when all the linkers are photoresponsive (top) compared to a framework where only the pillaring linkers are photoresponsive. Image adapted from R. Lyndon et al.. <sup>27</sup>	80
Figure 58 The scope of spiropyran-based linkers used in synthetic attempts of a 3 <sup>rd</sup> generation metal organic framework.	81
Figure 59 The scope of non-photoactive co-linkers used in synthetic attempts of a 3 <sup>rd</sup> generation metal organic framework incorporating spiropyran linkers.	81
Figure 60 Copper paddlewheel (top). A variety of 1D frameworks synthesised by Hwang et al. utilising the copper paddlewheel and various N-heterocycle based pillar linkers <sup>30</sup> (bottom).	83

Figure 61 Image of IRMOF-10 (IRMOF-9 is the same but doubly interpenetrated) from M. Eddaoudi et al.. <sup>31</sup> They report interpenetration is more likely in higher concentrations of reagents (i.e. BPDC and Zn(NO <sub>3</sub> ) <sub>2</sub> ).	92
Figure 62 MFM-136 (top) synthesised by Benson et al.. <sup>39</sup> using the linker 5-[4-(pyrimidin-5-yl)benzamido]- isophthalic acid (bottom, left). The modified version of the <b>4c</b> linker that could potentially form a similar framework (bottom, right). The kink in the linker caused by the amide functionality has a passing similarity to the kink caused by a spiro-centre thus a framework isostructural to MFM-136 may be possible.	100
Figure 63 Large layer linkers DTD (4',5'-bis(4-carboxyphenyl)-[1,1':2',1''-terphenyl]-4,4''-dicarboxylic acid) and the brominated variant, DBTD (3',6'-dibromo-4',5'-bis(4-carboxyphenyl)-[1,1':2',1''-terphenyl]-4,4''-dicarboxylic acid)	101
Figure 64 Microscope picture of LK-1	109
Figure 65 Penta-coordinate zinc node of LK-1. Metal (colour): zinc (aqua), oxygen (red), carbon (grey), nitrogen (blue). Hydrogen atoms omitted for clarity.	111
Figure 66 Images obtained from single crystal X-Ray data of LK-1. View down the main channels (top left). View down the smaller channels (bottom left). View down the main channels with the BPDC linkers highlighted as red and the 3a linkers highlighted as blue (top right). Shortest distance from spiropyran linker to spiropyran linker measured to be 16.2 Å (bottom right).	112
Figure 67 Microscope picture of LK-2	113
Figure 68 Images obtained from SCXRD data of LK-2. Node (top left). Looking along the pillars (top right). Looking along the layers (bottom left). Looking along the layers that displays interpenetrated framework (bottom right).	113
Figure 69 View of LK-2 down b-axis (left) highlighting space between adjacent spiropyran linkers. View down c-axis right highlighting space between spiropyran linkers.	114
Figure 70 Powder X-Ray data of the bulk material of the LK mixture (experimental) with simulated powder patterns from the SCXRD data of LK-1 and LK-2 .	115
Figure 71 Solid state UV-vis of LK-1 and LK-2 mixture with solid state data of 3a and BPDC for comparison.	116
Figure 72 Thermogravimetric analysis of LK mixture, under N <sub>2</sub> at a ramp temperature of 10°C min <sup>-1</sup> .	118
Figure 73 Microscope picture of ellipsoid crystals of GG-1.	131

Figure 74 Picture of crystal structure GG-1, looking down the c axis (left). Picture of GG-1 looking down the b axis (right), the space between the layers is 17.435 Å. Zinc (cyan), oxygen (red), nitrogen (blue), bromine (brown), carbon (grey).	131
Figure 75 Linker <b>3a</b> showing distance between terminal N atoms for the closed form (left) and open form (right). Distances determined using the MM2 simulation from Chem3D.	132
Figure 76 NMR spectrum of ligand <b>3a</b> in d <sub>6</sub> -DMSO and DCl. Aromatic region (left) and approximate region of H <sub>k</sub> (right).	134
Figure 77 The spiropyran molecule that was analysed by Zhou et al., illustrating the equilibrium between the open and closed isomers and the protonated and non-protonated forms of each. Proton environments of interest are shown.	135
Figure 78 Spectrum of ligand <b>3a</b> in DCl and d <sub>6</sub> -DMSO, zoomed in on the 4.8-2.2 ppm region. Possible peak positions of H <sub>k</sub> highlighted with integrations. Peak position at 2.64 could possibly be the SP form however has not been integrated due to overlap with DMSO peak and satellites.	136
Figure 79 NMR spectrum obtained for LK mixture digested in DCl and DMSO-d <sub>6</sub> .	138
Figure 80 NMR spectrum obtained for GG-1 digested in DCl and DMSO-d <sub>6</sub> .	139
Figure 81 Powder X-ray data of the bulk material of the GG-1 synthesis (experimental) and the DBTD linker (DBTD) with the simulated powder pattern from the SCXRD data of GG-1.	140
Figure 82 Solid state UV-Vis spectrum of GG-1	141
Figure 83 Microscope picture of GG-32 in mother liquor (big orange/red cube).	143
Figure 84 Crystal structure pictures of GG-32. View down c-axis (left) with distance between nitrogen atoms highlighted to be 8.013 Å. View down a-axis (right).	143
Figure 85 NMR spectrum of ligand <b>6b</b> taken under digestion conditions	145
Figure 86 NMR spectrum of ligand <b>6b</b> , zoomed in on the 2.3-4.8 ppm region.	146
Figure 87 NMR spectrum of GG-32 digest.	147
Figure 88 Powder X-ray data of the bulk material of the GG-32 synthesis (experimental) and the DBTD linker (DBTD) with the simulated powder pattern from the SCXRD data of GG-32.	149
Figure 89 Solid state UV-Vis data of GG-32.	150
Figure 90 Dipoles (left) aligning when an electric field is applied (right). Image from "A guide to characterisation of dielectric materials at RF and microwave frequencies". <sup>20</sup>	159
Figure 91 A Debye relaxation response for deionised water. At low frequencies, the ε' is high and then begins to drop when it nears the relaxation frequency (f <sub>r</sub> ). The ε'' shows a Gaussian response, reaching a peak at f <sub>r</sub> .	160
Figure 92 TM010 mode cavity, image adapted from Cannel Youngs. <sup>20</sup> L represents the inductance of the magnetic field, E is the electric field and C is the capacitance of the sample being analysed.	

The cavities typically resonate between 1-10 GHz. For the cavity we use in our studies, the TM010 mode resonates at 2.5 GHz.	161
Figure 93 Electric field pattern (E) and magnetic field pattern (H) shown for TM010 mode. In this mode, maximal electric field strength can be seen at the centre while there is zero magnetic field strength at the same location. This location is where we would insert our sample. Reproduced from thesis of Mike Barter.	162
Figure 94 Resonant trace for an empty cavity (red) compared to when a sample is inserted (blue). Upon sample insertion the frequency is reduced due to polarisation ( $\epsilon'$ ) and the bandwidth increases due to dielectric loss ( $\epsilon''$ ). Figure provided by Professor Adrian Porch.	163
Figure 95 Worked examples of the data acquired and how we interpret it. Frequency over time (left) and Bandwidth over time (right).	164
Figure 96 Electronic field patterns of TM010 mode (left) and TM310 (right). Reproduced from thesis of Mike Barter.	165
Figure 97 Comparison of data with and without the temperature correction.	166
Figure 98 : MIL-53 (Al) secondary building unit (SBU) left, with octahedrally co-ordinated aluminium nodes with bridging oxygen atoms. Extended framework (right) shows how the SBUs are linked together, by the terephthalate linkers, to form a structure resembling a "wine rack". Image reproduced from Janiak et al. <sup>33</sup>	167
Figure 99 A demonstration of the "breathing" effect exhibited by MIL-53(Al) that can be triggered by guest adsorption, temperature or mechanical pressure. The arrow along the top demonstrates how pore volume is affected by this phenomenon. Figure reproduced from reference <sup>48</sup> .	171
Figure 100: Image of set up used to monitor the dielectric properties of UiO-66 under flow. (left) Diagram of the setup. (right) The quartz capillary is packed with the UiO-66 framework and inserted into the microwave cavity, the syringe pump then injects the analyte through the capillary at a steady rate which the VNA then records any change in the electric field being applied by the microwave cavity.	174
Figure 101 Top: Change of $\Delta f$ (left) and $\Delta BW$ (right) over time of UiO-66 preloaded with hexane being flushed out with a continuous flow of toluene at various rates. Bottom: Change of $\Delta f$ (left) and $\Delta BW$ (right) over time of UiO-66 loaded with toluene being flushed out with a continuous flow of hexane at various rates.	175
Figure 102 Top: Change of $\Delta f$ (left) and $\Delta BW$ (right) over time as a tube loaded with hexane (no MOF) is flushed out with toluene. Bottom: Change of $\Delta f$ (left) and $\Delta BW$ (right) over time as a tube loaded with toluene is flushed out with hexane.	176
Figure 103 Setup demonstrating the location of the "dwell tube"	177

- Figure 104 Left: Toluene displacing hexane from a quartz tube, with different sizes of dwell tube.  
 Right: Hexane displacing a quartz tube filled with toluene, with different sizes of dwell tube. 178
- Figure 105 Top Left: Toluene/toluene:chlorobenzene mixture displacing hexane from UiO-66 Top  
 Right: Hexane displacing toluene/toluene:chlorobenzene mixture from UiO-66. Bottom left:  
 Control experiment, toluene/toluene:chlorobenzene mixture displacing hexane from sample  
 tube. Bottom right: Control experiment, hexane displacing toluene/toluene:chlorobenzene  
 mixture from sample tube. 179
- Figure 106 Tracking  $\Delta F$  over time after injecting 0.1 mL of a specified aliquot into a continuous flow  
 of hexane passed through a column of UiO-66. 182
- Figure 107  $\Delta F$  over time as well as the % concentration determined by NMR for xylene isomers and  
 mixtures. Y axis is scaled individually to help show the information present. Analytes injected  
 were 33% concentration mixtures of 0.1 mL aliquots. a) o-xylene b) m/o-xylene c) m-xylene d)  
 o/p-xylene e) p-xylene f) m/p-xylene g) o/p/m-xylene. 183
- Figure 108  $\Delta F$  over time as well as the % concentration determined by NMR: h) Benzene i)  
 Ethylbenzene j) Toluene k) Chlorobenzene l) Styrene. Y axis is scaled individually to help show  
 the information present. Analytes injected were 33% concentration mixtures of 0.1 mL aliquots.  
 185
- Figure 109 Plot of the  $\Delta F_{\max}$  time against the permittivity ( $\epsilon'$ ) of each sample (top) and  $\text{NMR}_{\max}$  time  
 against  $\epsilon'$  of each sample (bottom). Insets have the chlorobenzene results removed and have  
 lines of best fit. 187
- Figure 110 Plot of the  $\Delta F_{\text{zero}}$  time against the  $\epsilon'$  of each sample.  $\text{NMR}_{\text{zero}}$  is not plotted as the NMR  
 plots never reach 0% concentration. Inset has the chlorobenzene result removed and has a line  
 of best fit. 188
- Figure 111 Plot of the  $\Delta F$  FWHM against the  $\epsilon'$  of each sample (top) and NMR FWHM against  $\epsilon'$  of  
 each sample (bottom). Insets have the chlorobenzene results removed and have lines of best  
 fit. 190
- Figure 112 Plot of the  $\Delta F$  asymmetry against the  $\epsilon'$  of each sample (top) and NMR asymmetry against  
 $\epsilon'$  of each sample (bottom). Insets have the chlorobenzene results removed and have lines of  
 best fit. 192
- Figure 113 Plot of the  $\Delta F$  mean against the  $\epsilon'$  of each sample (top) and NMR mean against  $\epsilon'$  of each  
 sample (bottom). Insets have the chlorobenzene results removed and have lines of best fit. 194
- Figure 114  $\Delta F$  over time as well as the % concentration determined by NMR: left) p-xylene right)  
 p/o-xylene mixture. Y axis is scaled individually to help show the information present. Analytes  
 injected were 3% concentration mixtures of 0.1 mL aliquots. 195

Figure 115  $\Delta F$  over time as well as the % concentration determined by NMR: o) p-xylene p) m-xylene q) o-xylene r) p/m-xylene s) p/o-xylene t) m/o-xylene u) p/m/o-xylene. Y axis is scaled individually to help show the information present. Analytes injected were 10% volume concentration mixtures of 0.1 mL aliquots. 198

Figure 116 Proton environments for each of the xylene isomers and hexane (top). Example of NMR peak integration, annotated with corresponding proton environments. (Taken from o/m/p-xylene mixture at 10% volume concentration, time = 240 seconds. 203

Figure 117 Worked example of calculating p-xylene %concentration from Figure 116. 203

## List of Equations

- Equation 1 for the complex relative permittivity of a material.  $\epsilon'$  is the real part of the equation that represents the dielectric constant.  $j$  represents the imaginary number of the square root of -1 and the  $\epsilon''$  represents the imaginary part of the equation, the dielectric loss. 17
- Equation 2 Kubelka-Munk function for converting the recorded R values into F(R). 152
- Equation 3 The absolute permittivity ( $\epsilon$ ) of a dielectric is found by multiplying the dimensionless quantity: relative permittivity ( $\epsilon_r$ ) by the vacuum permittivity:  $8.8541878128 \times 10^{-12} \text{ Fm}^{-1}$  ( $\epsilon_0$ ). 159
- Equation 4 The complex permittivity ( $\epsilon^*$ ) has two parts. The real part ( $\epsilon'$ ) and the imaginary part ( $\epsilon''$ ). Conventionally, in electrical engineering the imaginary number: square root of -1 is referred to as "j". 159
- Equation 5 Derivation of permittivity for the TM010 cavity.  $a$  is a constant that depends on the mode, for TM010 this is 0.539.  $f_r$  is the resonant frequency,  $\Delta f_r$  is the change in resonant frequency upon introduction of the sample.  $V_0$  is the volume of the cavity and  $V_s$  is the volume of the sample. 162
- Equation 6 Derivation of dielectric loss for the TM010 cavity. The constant  $b$  is calculated via:  $b = a/2$ .  $Q_0$  is the unloaded Q-factor and  $Q_l$  is the loaded Q-factor with the sample inserted.<sup>20</sup> 162
- Equation 7 Simplified relationship between quality factor (Q), frequency (f) and bandwidth (BW). 163
- Equation 8 describing the relationship between frequency shift and temperature.  $f_k$  is the fraction frequency shift caused by perturbation from the sample.  $k_{010}$  and  $k_{310}$  are the differences in gradient of the thermal expansion coefficient of the cavity material in the respective mode.  $k_{err}$  is the systematic thermal expansion error in the experiment. 165
- Equation 9 subtracts the 310 component from the 010 component of Equation 8 to remove the fractional frequency shift term caused by changes in temperature. 165
- Equation 10 is the equation used for temperature correction and is applied to all experimental data acquired using the microwave cavity perturbation method.  $u$  represents the unperturbed cavity and  $s$  is when the sample is present. 165
- Equation 11 showing how the mean is calculated for both the  $\Delta F$  and NMR data. 204



Equation 12 showing how the value is obtained for asymmetry. The right hand side (RHS) represents the peak maximum to the half maximum right of the peak. The left hand side (LHS) is the peak maximum to the half maximum, left of the peak maximum. 204

## List of tables

- Table 1 Bromination targets and their yields. **2** yield at ambient temperature (yield when under reflux) 31
- Table 2 Optimisation of **3a** and **3b** synthesis. Catalyst loading was 5 mol% per position (i.e. 10% for 2 positions), 2.4 mol phosphine ligand: 1 mol Pd catalyst, boronic acid added in excess. All solvents were mixed with H<sub>2</sub>O in a 4:1 ratio. Unless stated otherwise; temperature: 80°C, the limiting reagent (compound **2**) was 0.5 g. 35
- Table 3 Cross-coupling products and the respective yields 37
- Table 4 Comparison of peak positions of proton environments H<sub>a,b,c,d,k,g/h</sub> for molecules **4a**, **4b** and **4c**. \*Due to overlapping of peaks in 4c spectrum, there is reduced accuracy regarding these values. 40
- Table 5 Peak positions of proton environments H<sub>a,b,c,d,k,g/h</sub> of molecules **4a** and **5a** 42
- Table 6 Peak positions of proton environments H<sub>a,b,c,d,k,g/h</sub> of molecules **3a**, **3b** and **3c**. 44
- Table 7 Major peak positions recorded obtained from solution state UV-Vis spectra for ligand **3a**. Directly comparing peak positions recorded in the dark, at -20°C to ambient conditions. \*Due to scattering, the exact peak position is not known, the possible range of where it can be found is presented instead. 49
- Table 8 Comparison of peak positions observed in spectra regarding ligands **4a**, **4b** and **4c**. 51
- Table 9 Comparison of peak positions observed in spectra of ligands **4a** and **5a**. 52
- Table 10 Comparison of peak positions observed in spectra of ligands **3a**, **3b** and **3c**. 54
- Table 11 Outlines the conditions of each attempt at synthesising a 1D framework incorporating ligand **4a**. Vessel volumes: Wheaton Vial - 2.5 mL, Pressure Tube - 10 mL, Parr Bomb - 10 mL. \* denotes modulator. Outcomes: 1 = no reaction, 2 = amorphous/not crystalline enough for characterisation, 3a = novel crystalline and amorphous material, 3b = literature known crystalline and amorphous material, 4a = novel crystalline material, 4b = literature known crystalline material 85
- Table 12 Outlines the conditions of each attempt at synthesising a 2D framework incorporating ligand **4c**. Vessel volumes: Wheaton Vial - 2.5 mL, Pressure Tube - 10 mL, Parr Bomb - 10 mL. \* denotes modulator. Outcomes: 1 = no reaction, 2 = amorphous/not crystalline enough for characterisation, 3a = novel crystalline and amorphous material, 3b = literature known

crystalline and amorphous material, 4a = novel crystalline material, 4b = literature known crystalline material 91

Table 13 Outlines the conditions of each attempt at synthesising a 3D framework incorporating ligand **3c**. Vessel volumes: Wheaton Vial - 2.5 mL, Pressure Tube - 10 mL, Parr Bomb - 10 mL. \* denotes modulator. Outcomes: 1 = no reaction, 2 = amorphous/not crystalline enough for characterisation, 3a = novel crystalline and amorphous material, 3b = literature known crystalline and amorphous material, 4a = novel crystalline material, 4b = literature known crystalline material 93

Table 14 Outlines the conditions of each attempt at synthesising a 3D framework incorporating ligand **3a**. Vessel volumes: Wheaton Vial - 2.5 mL, Pressure Tube - 10 mL, Parr Bomb - 10 mL. \* denotes modulator. Outcomes: 1 = no reaction, 2 = amorphous/not crystalline enough for characterisation, 3a = novel crystalline and amorphous material, 3b = literature known crystalline and amorphous material, 4a = novel crystalline material, 4b = literature known crystalline material 98

Table 15 Outlines the conditions of each attempt at synthesising a 3D framework incorporating ligand **3c** and DBTD. Vessel volumes: Wheaton Vial - 2.5 mL, Pressure Tube - 10 mL, Parr Bomb - 10 mL. \* denotes modulator. Outcomes: 1 = no reaction, 2 = amorphous/not crystalline enough for characterisation, 3a = novel crystalline and amorphous material, 3b = literature known crystalline and amorphous material, 4a = novel crystalline material, 4b = literature known crystalline material 102

Table 16 Outlines the conditions of each attempt at synthesising a 3D framework incorporating ligand **3b** and DBTD. Vessel volumes: Wheaton Vial - 2.5 mL, Pressure Tube - 10 mL, Parr Bomb - 10 mL. \* denotes modulator. Outcomes: 1 = no reaction, 2 = amorphous/not crystalline enough for characterisation, 3a = novel crystalline and amorphous material, 3b = literature known crystalline and amorphous material, 4a = novel crystalline material, 4b = literature known crystalline material 103

Table 17 Outlines the conditions of each attempt at synthesising a 3D framework incorporating ligand **3a** and DBTD. Vessel volumes: Wheaton Vial - 2.5 mL, Pressure Tube - 10 mL, Parr Bomb - 10 mL. \* denotes modulator. Outcomes: 1 = no reaction, 2 = amorphous/not crystalline enough for characterisation, 3a = novel crystalline and amorphous material, 3b = literature known crystalline and amorphous material, 4a = novel crystalline material, 4b = literature known crystalline material 106

- Table 18 Outlines the conditions of each attempt at synthesising a 3D framework incorporating ligand **6b** and DBTD. Vessel volumes: Wheaton Vial - 2.5 mL, Pressure Tube - 10 mL, Parr Bomb - 10 mL. \* denotes modulator. Outcomes: 1 = no reaction, 2 = amorphous/not crystalline enough for characterisation, 3a = novel crystalline and amorphous material, 3b = literature known crystalline and amorphous material, 4a = novel crystalline material, 4b = literature known crystalline material 107
- Table 19 Showing calculations for molecular weight of frameworks and the theoretical residue ( $R_{\text{theo}}$ ) for each framework. If the mixture was solely these two samples then we would expect the experimental residue ( $R_{\text{exp}}$ ) to be a value between these two ratios. 118
- Table 20 Outlines the conditions of each attempt at optimising the synthesis of 3D frameworks LK-1 and LK-2. Vessel volumes: Wheaton Vial - 2.5 mL, Pressure Tube - 10 mL, Parr Bomb - 10 mL. \* denotes modulator. Outcomes: 1 = no reaction, 2 = amorphous/not crystalline enough for characterisation, 3a = novel crystalline and amorphous material, 3b = literature known crystalline and amorphous material, 4a = novel crystalline material, 4b = literature known crystalline material 125
- Table 21 Combinatorial assay, assessing the affect of varying the DMF:MeOH volume ratio. 129
- Table 22 NMR peaks recorded by Zhou et al. for the nitrobenzene functionalised spiropyran. 135
- Table 23 The difference between  $H_k'$  and  $H_k$  of the SP form is 0.53 ppm. By subtracting this value from the  $H_k'$  ppm values of the SPH+, MC and MCH+ forms we can roughly approximate the peak positions we expect for the forms SPH+, MC and MCH+ of **3a**. 136
- Table 24 Preliminary results from microwave resonance measurements of analytes loaded into MIL-53. Single components are outlined in bold. \* denotes the cases where the  $\Delta f$  lies outside the expected  $\Delta f$  range. † denotes experiments measured differently meaning the values are loosely comparable to the rest of the data, full explanation in experimental. 170
- Table 25 Preliminary results from microwave resonance measurements of analytes loaded into UiO-66. Single components are outlined in bold. \* denotes the cases where the  $\Delta f$  lies outside the expected  $\Delta f$  range. 172
- Table 26 Kinetic diameters of o, m, p-xylene isomers, hexane and toluene.<sup>44</sup> 181
- Table 27 Collated data from Figure 107 and Figure 108, comparing the features of each acquired chart.  $\epsilon'$  values obtained from UNITED STATES DEPARTMENT OF COMMERCE NATIONAL BUREAU OF STANDARDS.<sup>55</sup> 186

Table 28 Comparison of concentrations measured by NMR to the actual value. Mixtures of o-xylene made up using serial dilution and hamilton syringes. 191

Table 29 Displaying asymmetry values for the curves of data acquired when using 33% concentration of xylene isomers and mixtures. \*meta-xylene NMR is anomalous and is likely inaccurate. 193

Table 30 Displaying mean values calculated for the curves of data acquired when using 33% concentration of xylene isomers and mixtures. \*meta-xylene NMR is anomalous and is likely inaccurate. 194

Table 31 Displaying mean and asymmetry values for the curves of data acquired when using 3% concentration aliquots of p-xylene and p/o-xylene mixture. 196

Table 32 Displaying mean values calculated for the curves of data acquired when using 10% concentration of xylene isomers and mixtures. 199

Table 33 Displaying asymmetry values for the curves of data acquired when using 10% concentration of xylene isomers and mixtures. 199

## List of abbreviations

AcOH	Acetic Acid
AzDC	Azobenzene dicarboxylate
BDC	1,4-benzenedicarboxylate
BET	Brunauer-Emmett-Teller
4,4'-BPE	1,2-bis(4-pyridyl)ethylene
BPDC	4,4'-biphenyldicarboxylic acid
BW	Bandwidth
CCD	Charge Coupled Device
CPO	Coordination Polymer of Oslo MOF series
DBA	Dibenzylideneacetone
DBTD	3',6'-dibromo-4',5'-bis(4-carboxyphenyl)-[1,1':2',1''-terphenyl]-4,4''-dicarboxylic acid
DEF	Diethylformamide
DFT	Density Functional Theory
DCI	Deuterium Chloride
DCM	Dichloromethane
DME	1,2-Dimethoxyethane
DMF	Dimethylformamide
DMSO	Dimethyl sulfoxide
dobdc	2,5-dioxide-1,4-benzenedicarboxylate
<i>m</i> -dobdc	4,6-dioxide-1,3-benzenedicarboxylate
dppf	1,1'-Bis(diphenylphosphino)ferrocene
DTD	4',5'-bis(4-carboxyphenyl)-[1,1':2',1''-terphenyl]-4,4''-dicarboxylic acid
DTE	dithienylethene
EG	Ethylene glycol

ES	Electrospray
ESI	Electrospray ionisation
EtOH	Ethanol
FAU	Faujasite
FTIR	Fourier Transform Infrared
FWHM	Full-width Half maximum
H <sub>3</sub> BTB	1,3,5-Tris(4-carboxyphenyl)benzene
HCl	Hydrochloric Acid
HDDB	1',1'',3',3',3'',3'''-hexamethyl-6,6''-4,4'''di(pyridine-4-yl-7',7'''-bispiro[chromene-2,2'-indoline
HKUST	Hong Kong University of Science and Technology MOF series
HOMO	Highest Occupied Molecular Orbital
HPLC	High Performance Liquid Chromatography
GG	George Grove MOF series
ID	Internal Diameter
IPA	Iso-propanol
IRMOF	Isorecticular MOF series
LK	Luke Kidwell MOF series
LUMO	Lowest Unoccupied Molecular Orbital
MC	Merocyanine
MCH <sup>+</sup>	Protonated Merocyanine
MeOH	Methanol
MCR	Microwave Cavity Resonator
MFM	Manchester Framework Material MOF series
MIL	Matériaux de l'Institut Lavoisier MOF series

MOF	Metal-Organic Framework
MS	Mass Spectrometry
MTV	Multivariate MOF series
NBS	N-bromosuccinimide
NEt <sub>3</sub>	Triethylamine
NMP	N-Methyl-2-pyrrolidone
NMR	Nuclear Magnetic Resonance
NTU	Nanyang Technological University MOF series
NU	Northwestern University MOF series
OD	Outer Diameter
P(Cy) <sub>3</sub>	Tricyclohexylphospine
P(t-Bu) <sub>3</sub>	Tris-tert-butylphospine
PET	polyethyleneterephthalate
PFA	Perfluoroalkoxy alkane
PXRD	Powder X-Ray Diffraction
RT	Room Temperature
SBU	Secondary building unit
SCXRD	Single Crystal X-Ray Diffraction
SP	Spiropyran
SPH+	Protonated Spiropyran
SSP	Sulfonated Spiropyran
ssUV-Vis	Solid-State Ultra Violet-Visible
TGA	Thermogravimetric Analysis
TLC	Thin Layer Chromatography
TMA	Trimesic acid



TNDS	1',3',3'-trimethyl-6-nitro-4',7'-di(pyridine-4-yl)spiro[chromene-2,2'-indoline]
TPA	Terephthalic acid
UiO	Universitetet i Oslo MOF series
UV	Ultra-Violet
VNA	Vector Network Analyser
ZIF	Zeolitic Imidazole Framework MOF series

## Contributions

During this PhD I supervised a number of MChem, BSc and visiting project students, who worked alongside me on aspects of the work. I would like to thank the following people who assisted with and contributed to the work in this thesis:

### Synthesis and crystallography:

Dr Adam Nevin trained me on synthesis and crystallographic methods. MChem student Luke Joyner assisted with optimising Suzuki coupling reactions. Visiting student Pâmela Bernardini Dias trialled the first syntheses of 4a and 3c. BSc student Matthew Lomas-Hennessey trialled the first combinatorial syntheses of LK-1 and LK-2 using ligands I provided. MChem student George Grove synthesised frameworks GG-1 and GG-32 under my supervision during his project. Dr Benson Kariuki acquired and solved the structure of GG-1. Dr Stephen Argent assisted with the structure solution of LK-1. MChem student Joshua Morris performed DFT calculations on ligand 4a. Dr Yashar Soltani performed the first Grignard synthesis step in the synthesis of ligand 8a, training me to do so for all future cases.

### Microwave engineering:

Dr Daniel Slocombe and student/post-doc Dr Michael Barter set up, maintained and participated in the microwave experiment design and experimental data collection. The experimental setup and all data collection was performed jointly by Dr Barter and myself. Dr Samuel Partridge was responsible for the coding of the software that we used during the experiment. The microwave cavities, cabling and network analysers are the property of Prof. Adrian Porch, who kindly loaned them to us for the work in Chapter 4.

## Acknowledgements

Firstly, I would like to thank my supervisor Dr Timothy Easun for both training and moral support throughout the course of this PhD, as the projects all started ended with him and he played a pivotal role throughout.

I would also like to thank Dr Adam Nevin for his patient guidance and moral support that helped me get a running start on my PhD. I would also like to thank Dr Michael Barter and Dr Daniel Slocombe for their contributions to the microwave resonance project. I would like to thank the following MChem, BSc and visiting students that I had the pleasure of working with: Luke Joyner, Brandon Nigel Rhys Corbett, Dan Clements, Joshua Morris, Joseph Paul-Taylor, James Down, Matthew-Lomas Hennessey, Pâmela Bernardini Dias, George Grove, Joe Alemzadeh, Ross Sowden, Laura Deeming, Laura Gravener, Aisha Asghar and, especially, Joshua Morris who kept coming back to the Easun group every summer. I would also like to thank Dr Stephen Argent, Dr Benson Karuiki for their guidance on the art of crystallography. I would also like to thank Dr Robert Jenkins, Simon Waller, Robin Hicks and Dr Thomas Williams for the maintenance of the majority of the analytical equipment as well as acquiring the mass spectral data reported in this thesis, as well as Jamie Cross, James Griffiths, Shane Halton, Evelyn Blake, Simon James, George Summers, Steve Rogers, Paul Young for keeping the chemistry department running. I would like to thank Dr Michael Barter, Dr Daniel Slocombe and Dr Sam Partridge for being very friendly and cooperative throughout our collaboration. I would especially like to thank Steve Morris for teaching me the ways of Swagelok and Dr Christiane Schotten for showing me how to set up a flow system, without them chapter 4 would not exist.

I would also like to thank the following colleagues who played some significant part in the success of my PhD: Dom Ward, Jamie Hancock, Dan Ceresale, Dr Adam Day, Dr Sam Adams, Dr Joel-Cresser Brown, Dr Yasha Soltani, Lukas Gierlichs, Dr Lewis Wilkins, Dr Darren Ould, Theo Gazis, Jamie Carden, Dr Adam Ruddy, Katarina Stefkova, Dr Ayan Dasgupta, Dr Andy Wood, Dr Mauro Monti, Jacob Spencer, Dr Andrea Folli, Dr Riccardo Bonsignore, Sophie Thomas, Siôn Edwards, Bria Thomas, Ibrahim Shoetan, Ash Steer, Dr Benjamin Ward, Dr Mark Sullivan, Owaen Guppy, Robert Amesbury, Matt Shaw, Dr Robert Mart, Dr Nicolò Santi, Dr Paul “Woody” Newman, Vladimir Vladimirov, Chris Smalley and Roddy Stark. I would also like to thank everyone who was involved in the short-lived Chemistry PhD Football League. The Cardiff University Amateur Boxing Club, especially the coaches Jimmy, Shaine and Sunny. The delightful catering staff: Mark, Anne, Leanne and Sam who always made it a pleasure to come see them down in the canteen.

Finally, I would like to thank my partner Rachael and my family for the love and support that was instrumental in completing my PhD.

## Chapter 1. Introduction

This thesis investigates the design and characterisation of photoresponsive metal organic frameworks (MOFs) and also the design and implementation of an analytical technique using microwaves to monitor chromatographic separations in MOFs.

### 1.1 Metal Organic Frameworks

MOFs contain metal nodes linked together by polydentate organic ligands (linkers) to form microporous (pores with diameters < 2 nm) networks via self-assembly.<sup>1</sup> The vast majority are crystalline. These infinitely repeating arrays can be broken down into their secondary building units (SBUs). These SBUs can be broken down into two categories, the metal clusters that act as nodes and the organic ligands that link them together. The metal clusters are often linked together by oxo and/or carboxylate bonds to form a well-defined shape that feature points for extension (see Figure 1).<sup>2,3</sup> The polytopic organic ligands will feature two or more functional groups capable of coordinating to the metal nodes (e.g. carboxylates, pyridines)

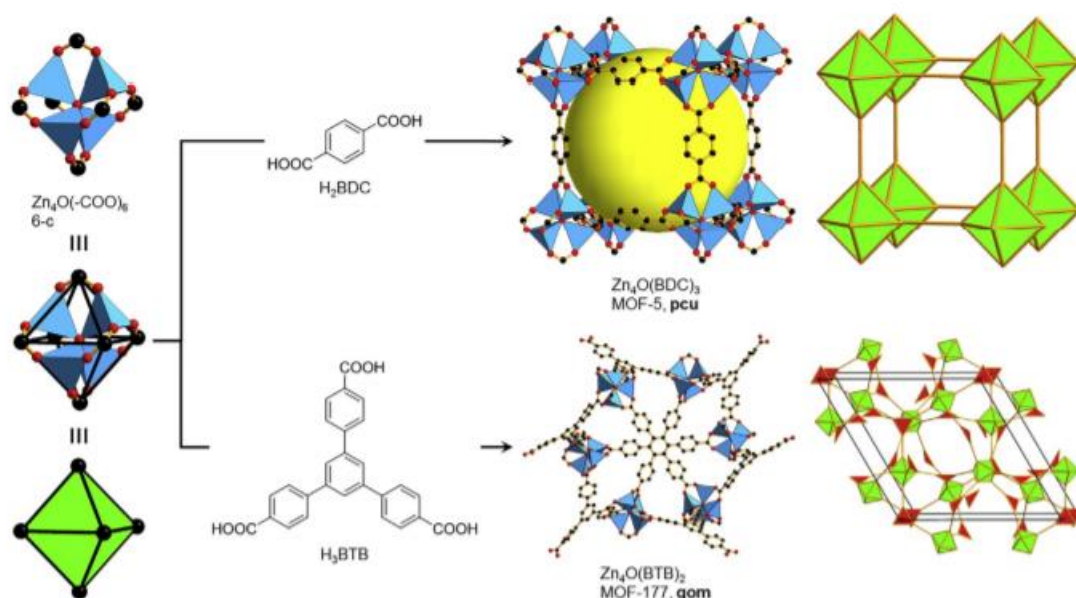


Figure 1 The  $Zn_4O(-COO)_6$  metal cluster that forms an octahedron metal SBU. When the metal SBU is combined with two different organic linkers, the octahedrons feature in the two different frameworks. Image reproduced from A. Schoedel.<sup>4</sup>

There are numerous ways to impart additional functionality to these frameworks such as open metal sites,<sup>5</sup> defect sites,<sup>6</sup> encapsulating an active guest species<sup>7</sup> but we will primarily be focusing on imparting functionality through organic linker design. A framework that is constructed with an organic linker with a specific property can inherit that property and combine it with the framework

environment to provide a material with capabilities which otherwise the framework and the organic linker would not have on their own.

### 1.1.1 Synthetic strategies

MOFs are typically synthesised through solvothermal or hydrothermal methods, often forming crystals under high temperatures and pressures. The ligands (linkers) will reversibly bind to the metal ions, this lability allows for bonds to break and reform to form the most energetically favourable product; being the highly ordered crystalline frameworks. The effectiveness of this self-corrective assembly varies from synthesis to synthesis and can purposefully be negated if a framework with lots of defects is desired. The typical method of producing new MOFs is a high throughput screening method that alters a number of conditions, including reaction temperature and time, solvent, reagent concentration, pH and the nature of the precursors used.<sup>8</sup>

#### 1.1.1.1 Modulators

There are two types of modulators: acidic modulators and coordination modulators. Acidic modulators indirectly slow the formation of the framework by shifting the position of equilibrium in the opposite direction to the active component, can be thought of as a non-competitive inhibitor (see Figure 2).<sup>9</sup> This concept extends to what choice of metal salts are included, e.g. using a  $MCl_x$  salt as a precursor will often produce a stoichiometric amount of HCl as a by-product, affecting crystal growth and in some cases dissolve the framework (depending on framework stability and the quantity of acid produced).<sup>8</sup>

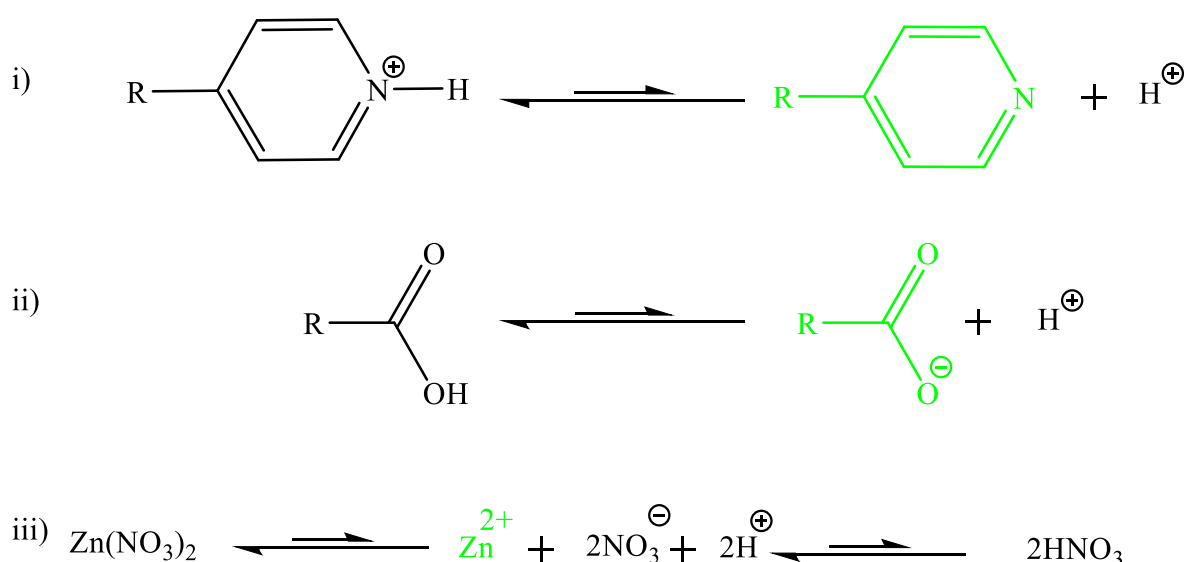


Figure 2 Three examples of how equilibria shift upon addition of an acid with the active coordinating species (highlighted in green). In the cases of i) and ii) addition of acid shifts the equilibrium towards the protonated forms of the linkers which are unable to coordinate with the zinc metal ion. In the case of iii), it is showing how the addition of nitric acid reduces the dissociation of zinc nitrate.

If acidic modulators are non-competitive inhibitors, then coordination modulators are like competitive inhibitors. These modulators are organic molecules which have the same binding functional groups as the organic linker and directly compete with the organic linkers for available coordination sites on the metal ion.<sup>10</sup> This capping effect tends to terminate the growth of framework crystals resulting in smaller particle sizes. In the case of carboxylic acid modulators, the modulator will also reduce the extent to which the linkers deprotonate which will lead to an increase in particle size. Therefore higher pKa values of modulators tends to reduce the particle sizes of MOFs.<sup>10</sup> Furthermore these types of coordination modulators can preform the metal SBUs which can lead to an increase in crystal growth along certain planes (e.g. 100, 111) while inhibiting the growth along others, leading to new crystal morphologies of the same framework.<sup>11</sup>

There are several reasons one would have for utilising a modulator in the synthesis, it can be used to slow the crystallisation process down to obtain better crystals for Single Crystal X-Ray diffraction (SCXRD) as typical methods of crystallisation do not apply (i.e. the framework cannot be recrystallised, as the framework is not soluble once formed). Another reason would be in the case where strong Metal-Ligand (M-L) bonds are formed, it can slow this process down and prevent the reaction from forming an amorphous, disordered material. This is the case for the zirconium-based framework series UiO, as the tetravalent zirconium ion forms strong coordination bonds with oxygen atoms.<sup>9</sup> More specific reasons for using modulators may be to induce defect sites into the framework for purposes such as catalysis or obtaining a specific topology or crystal morphology.<sup>12</sup>

#### *1.1.1.2 Solvent choice*

The effects of the solvent used in MOF synthesis is not fully understood but the consequences have been demonstrated in many instances, illustrating why it is an important factor. One of the key principles is ensuring that the reagents will be soluble at the reaction temperature but there are more criteria to consider beyond this.

There is a consensus that the solvent system will determine the coordination behaviour of the metal and ligands involved. Coordinating solvents can do this by directly coordinating with the metal ion or even feature as a capping molecule for an exposed metal site in the final structure, adding stability to the framework. This can also occur for solvents acting as guest molecules, by filling the pores reducing the likelihood of collapse of particularly large void-space frameworks. These guest molecules can also act as structure-directing agents, more so with flexible linkers as the guest molecules will restrict the movement of the flexible linkers to certain conformations which can result in completely different structures (see Figure 3).<sup>13</sup>

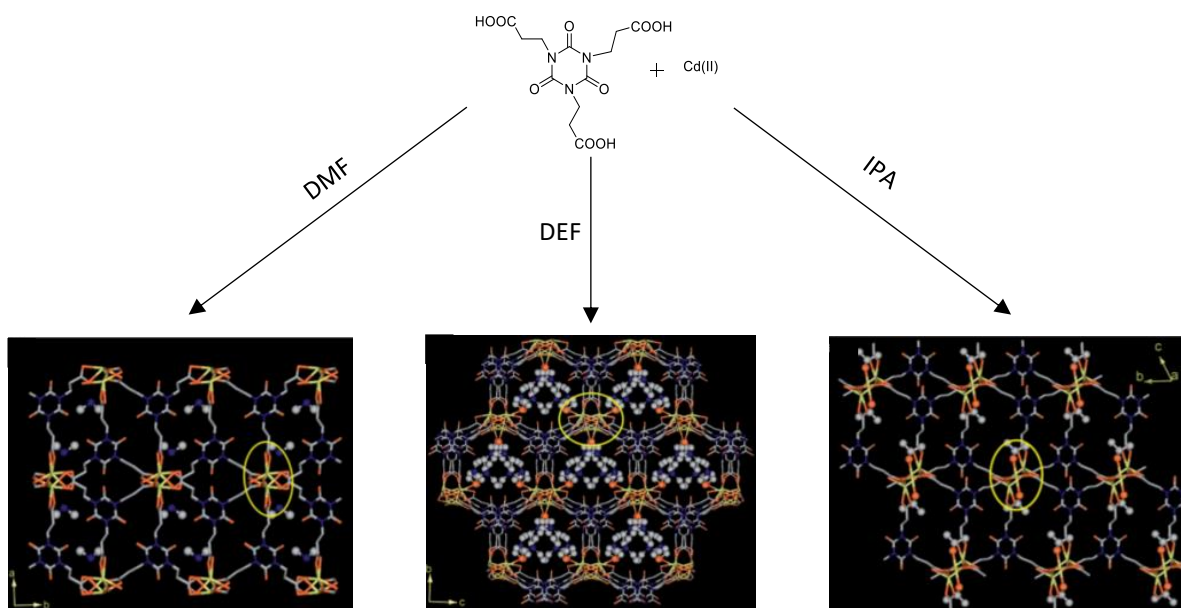


Figure 3 Three different possible cadmium frameworks determined by the structure-directing influences of the guest solvent molecules: dimethylformamide (DMF), diethylformamide (DEF) and isopropanol (IPA). Colour scheme is as follows: cadmium, yellow; carbon, grey; nitrogen, blue; oxygen, orange. Adapted from Ghosh et al..<sup>13</sup>

A solvent which also has a relatively strong basic character (e.g. DMF) could also have some modulating effects by encouraging the extent of ligand deprotonation (e.g. RCOOH  $\rightarrow$  RCOO<sup>-</sup>). Coordinating solvents can also act as modulators in the same way as the coordinating modulators, described previously.<sup>14</sup>

#### 1.1.1.3 Stoichiometry

In a typical MOF synthesis, there is often more than one coordination environment available (unless tightly controlled as we discussed earlier) thus the resulting framework will be closely linked to the stoichiometry of the reagents used. *X. Guo et al.* report an example with a cadmium-based framework.<sup>15</sup> They obtained two completely different frameworks in a one-pot synthesis and were able to obtain phase pure mixtures of both frameworks by varying the stoichiometry of the reagents (see Figure 4).

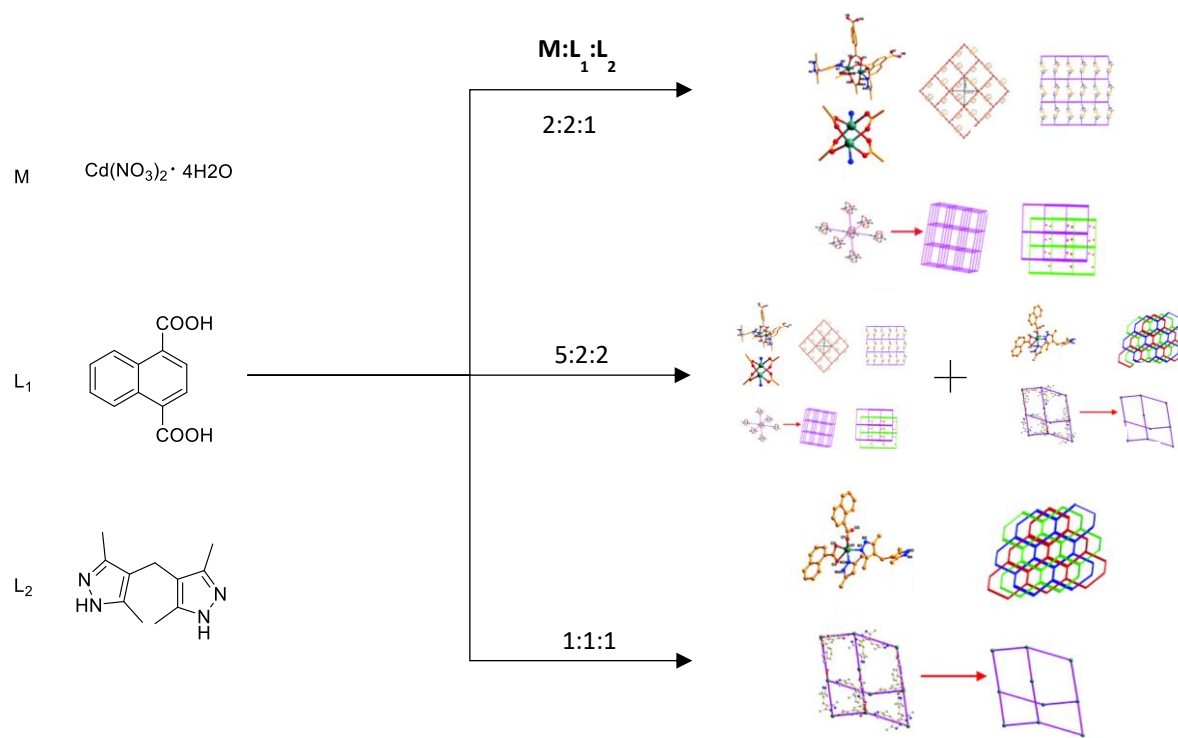


Figure 4 Two different frameworks are synthesised by varying the stoichiometry of metals and ligands from 2:2:1 to 1:1:1 and also showing that a mixture of both frameworks is produced when a 5:2:2 ratio is used. The rest of the conditions were the same, 160°C, 72 hours, in an EtOH:H<sub>2</sub>O (1:1) solvent system. Adapted from Guo et al.<sup>15</sup>

Framework **1**, which has more cadmium ions available, has a dicadmium paddlewheel with a square based pyramidal geometry with the equatorial positions occupied by four oxygen atoms belonging to the carboxylate linkers and the apical position bonding to the pyrazole linker. Framework **2**, which has more of the pyrazole ligand available, has a bent-trigonal bipyramidal geometry which is bound to three oxygen atoms and two nitrogen atoms. This perfectly illustrates a  $d^{10}$  transition metal which has access to multiple coordination geometries being directly affected by the stoichiometry of the reaction.

#### 1.1.1.4 Reaction Temperature

Like with any reaction, the temperature plays a big part in the synthesis of MOFs. The typical solvothermal method allows for higher solubility of reagents in a liquid media at temperatures far above the boiling point at normal atmospheric pressure, in this case the thermodynamic product is formed. These high temperatures are not always necessary for the formation of these materials, as there also frameworks which will form at much lower temperatures, the kinetic product.

The kinetic products observed in MOF synthesis tend to be low stability, low density and less symmetrical frameworks than the thermodynamic products (produced in solvothermal conditions).



The kinetic product can in some cases be the same framework with the same formula but crystallise in different space groups, often the thermodynamic product being the higher symmetry group.<sup>16</sup>

We have discussed the more subtle ways of designing and fine-tuning a MOF's properties, now we go on to discuss more drastic methods of encouraging change in the framework by designing the ligands themselves.

### 1.1.2 Imparting functionality through ligand design

There have been numerous examples in the literature of frameworks with clever linker design that give the MOF exciting properties. One such example is the design of frameworks with ligands that contain nitrogen, giving it enhanced capabilities in CO<sub>2</sub> adsorption through a combination of Lewis acid-base interactions and hydrogen bonds that depend on the nitrogen donor sites.<sup>17</sup> This allows this type of framework to selectively adsorb CO<sub>2</sub> from a gas mixture – an example is shown in Figure 5.

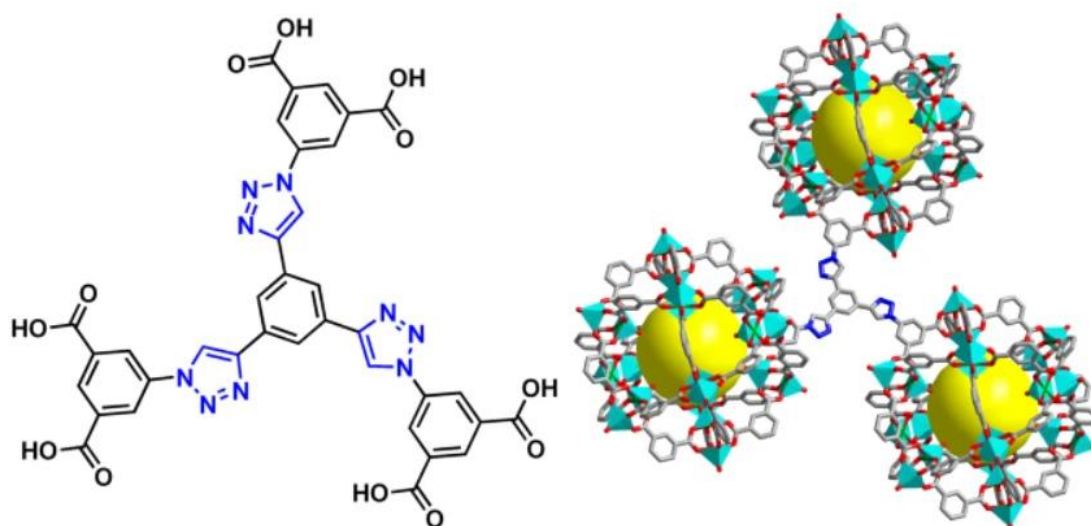


Figure 5 NTU-105 MOF (right) constructed using a triazole linker (left). Colour scheme is as follows: copper, green; nitrogen, blue; carbon, grey; oxygen, red. Image reproduced from X. Wang et al.<sup>18</sup>

The successful synthesis of this MOF relied on an understanding of isorecticular chemistry and basing it on previous amino-functionalised MOFs to design this new framework.<sup>18</sup> Although this framework was reported to have a BET surface area of 3543 m<sup>2</sup> g<sup>-1</sup>, which is on the lower end of what MOFs are capable of (maximum BET reported is 7140 m<sup>2</sup> g<sup>-1</sup> belonging to the NU-110 MOF),<sup>19</sup> it could store CO<sub>2</sub> up to 36.7% of its weight at 273K in 1 atm. This shows how the functionalities present in a framework can be more important than the overall porosity.

Another example is the MTV MOF series which use more than one type of organic linker to form a multi-functional framework. Figure 6 shows an example that incorporates amino acid residues serine

and methionine (featuring  $-\text{CH}_2\text{OH}$  and  $-\text{CH}_2\text{CH}_2\text{SCH}_3$  chains respectively) to allow for a framework that can purify water of both organic and inorganic contaminants.

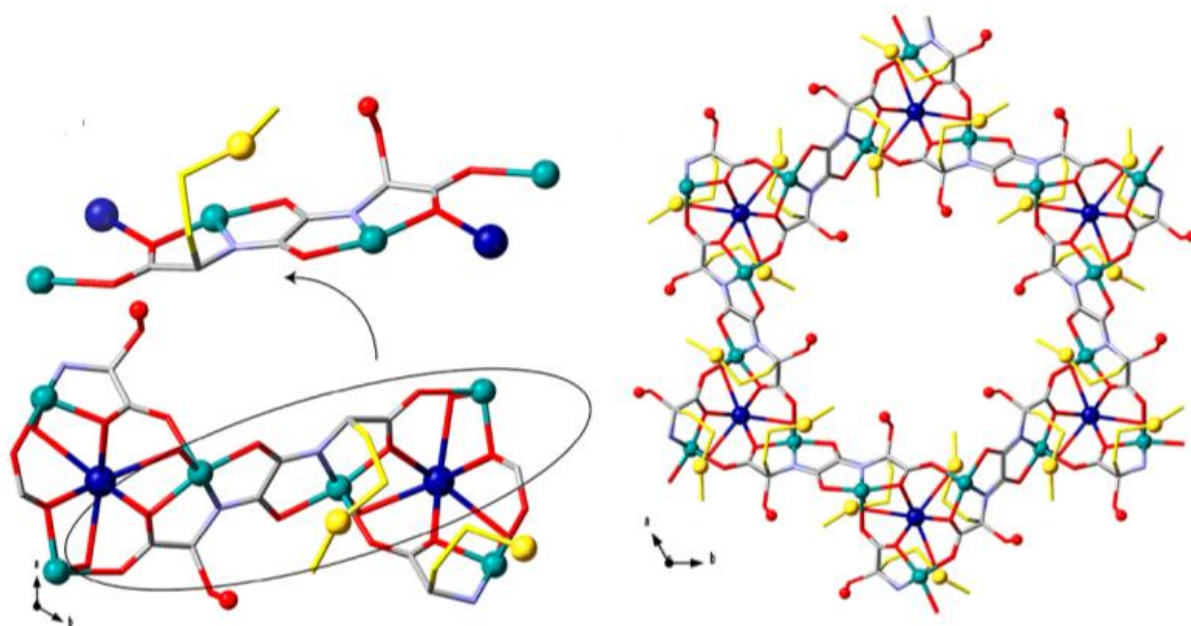


Figure 6 Fragment of the framework demonstrating the metal SBU (left). Views along a single channel to demonstrate how the serine and methionine moieties point towards the centre of the pore, the residues are present in a statistical disorder (1:1) and are superimposed for better visualisation. Copper (II) and calcium (II) ions from the network are represented as cyan and purple spheres, respectively. Oxygen and sulphur atoms from the residues are shown as red and yellow spheres, respectively. The organic ligands are represented as sticks with the following colour scheme: sulphur, yellow; oxygen, red; nitrogen, light blue; carbon, grey, with the exception of L-serine ( $-\text{CH}_2\text{OH}$ ) and L-methionine ( $-\text{CH}_2\text{CH}_2\text{SCH}_3$ ) residues, which are represented as red and yellow sticks, respectively. Reproduced from M. Mon et al.<sup>20</sup>

In this example the authors combined two different linkers with the same amino acid backbone so that the geometry and topology are unaffected by the incorporation of the two different moieties, shown by the 50:50 ratio of serine to methionine residues being incorporated. This is also an example of the functionality behaving as a pendant group rather than as an intrinsic part of the structure like the previous example. These two examples show the types of optimisation, the first example shows how the framework linker itself contains the functionality while the second framework shows the functionalisation occurring on a pendant into the pores. This thesis is concerned with photoactive functionalisation of frameworks, examples of both have been reported in the literature.

### 1.1.3 Photoresponsive materials

Frameworks that incorporate photoresponsive ligands are a specific subset of MOF chemistry that has received a lot of attention in the last decade.<sup>21,22</sup> Particular focus has been on the azobenzene, diarylethene and spiropyran/spirooxazine classes of photo-responsive molecules. These materials are

particularly interesting, as the ability to directly control the structure of a framework with the ease of flipping a light switch is a very attractive concept.<sup>23</sup>

Previously we discussed the NTU-105 MOF being designed for a high uptake of CO<sub>2</sub> due to its non-covalent interactions with carbon dioxide, but the issue with these kinds of materials is that to release the guest molecules (the carbon dioxide in this case) they must be put under heat and/or vacuum which are energy intensive processes.<sup>24</sup> R. Lyndon *et al.* reported a MOF that uses an azobenzene linker which allows for the reversible uptake of CO<sub>2</sub> which can be controlled with ultra-violet (UV) and visible light (see Figure 7, Figure 8).<sup>25</sup>

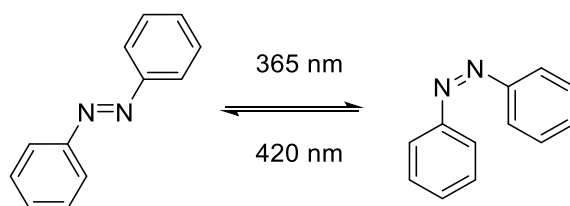


Figure 7 Photoisomerism exhibited by azobenzene.

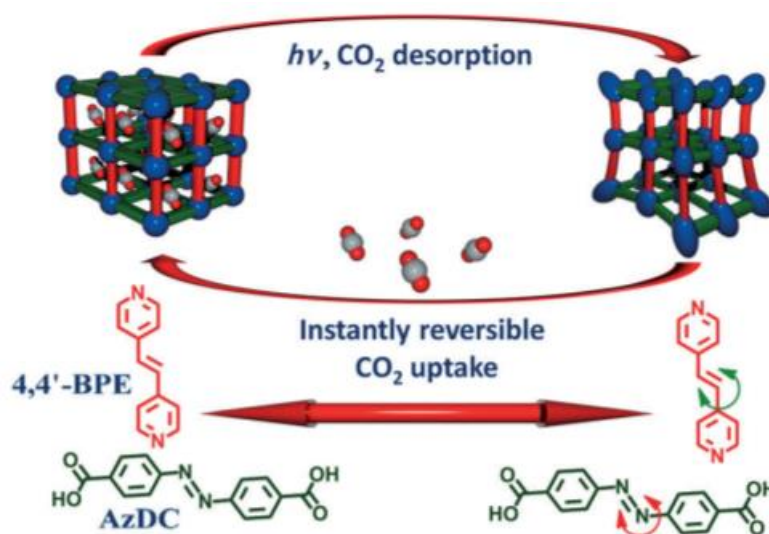


Figure 8 illustrates a framework constructed from the photoresponsive linkers; azobenzene dicarboxylate (AzDC) and 1,2-bis(4-pyridyl)ethylene (4,4'-BPE) linker.

They successfully synthesised a triply interpenetrated framework utilising only photoresponsive linkers. Therefore each structural support had the potential for isomerisation while also having little space to manoeuvre, as such the photoresponse did not occur in a uniform manner, but rather produced a localised structural change. The framework would adsorb carbon dioxide then upon irradiation would “squeeze” the carbon dioxide molecules out of the pores. Although the effectiveness of this MOF’s desorption was better when irradiated with a 365 nm wavelength, it still had a significant response using unfiltered sunlight therefore could be used as a solar powered, carbon-capture device.

An example of a photodynamic material with a long-range response, *I. Walton et al.* use the photochromic moiety diarylethylene as a guest molecule in DMOF-1. The dithienylethene (DTE) molecule has a very subtle structural change but has an easily observable spectroscopic change from colourless to red (see Figure 9, Figure 10).<sup>26</sup> By mixing evacuated DMOF-1 crystals with molten DTE, the DMOF-1@DTE composite material was created.

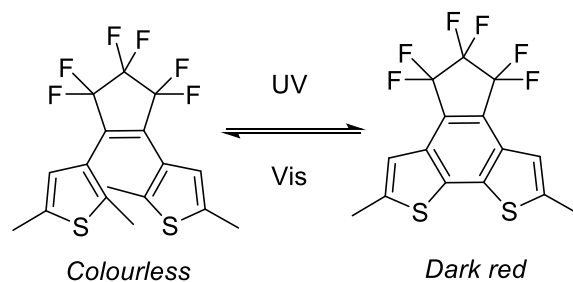


Figure 9 Illustration of the photoisomerism exhibited by the dithienylethene molecule.

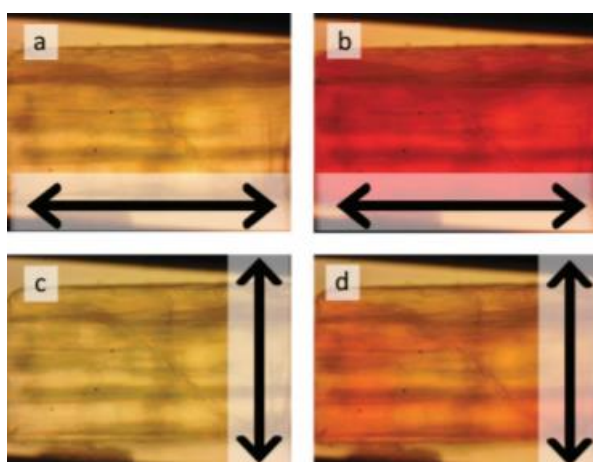


Figure 10 Polarised light image of the DMOF-1@DTE single crystal before (a, c) and after (b, d) irradiation with 365 nm light. The plane of polarisation for each image is indicated by an arrow. Reproduced from *I. Walton et al.*<sup>26</sup>

*I. Walton et al.* demonstrated that the framework assimilates the photoresponsive property of DTE and the MOF crystals also convert to a dark red colour upon irradiation with UV light, reversed by irradiation with visible light. The unique property provided by using the framework as the host material was that the DTE molecules were preferentially aligned with the pores of the host, exhibiting as linear dichroism (see Figure 10).

The two examples presented here demonstrate that photoresponsive moieties have potential applications in situations where there is significant structural change on a short-range scale (Figure 8) or a subtle photoresponse on a long-range scale (Figure 10).

### 1.1.4 Spiropyran

Spiropyran is the photoresponsive core this thesis will be focusing on. The design and syntheses of materials incorporating these moieties are discussed in chapter 3.

Spiropyran and spirooxazines share the same opening and closing mechanism: the breaking of the C-O bond to form the open structure (see Figure 11). The difference is that spirooxazine has an extra nitrogen atom in place of a carbon atom on the double bond of the chromene fragment. Spiropyran and spirooxazine are structurally very similar and therefore their syntheses are also quite similar. The key difference is that spirooxazines possess a higher photofatigue resistance than spiropyran, improving the overall longevity of the material in photoswitching applications.<sup>27</sup>

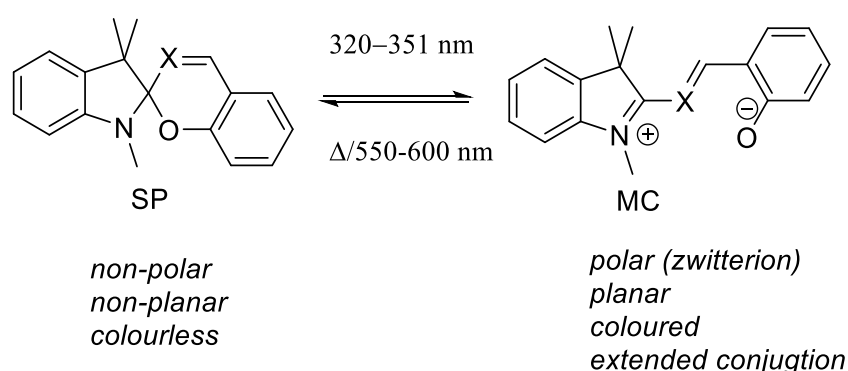


Figure 11 Photoisomerism exhibited by spiropyran and spirooxazine molecules. Upon irradiation with UV light, the closed spiropyran (SP) form breaks the C-O bond at the spiro centre and extends out to the open merocyanine (MC) form. The difference in properties of these two isomers are outlined beneath the scheme. Spiropyran, X = carbon; spirooxazine, X = nitrogen.<sup>28</sup>

This class of molecules has drawn a lot of attention as the closed spiropyran (SP) form and the open merocyanine (MC) form have vastly different properties. The zwitterionic MC form can bind to monovalent and divalent metal ions which can then be released when irradiated with the wavelength of light that triggers the back conversion. However merocyanine molecules tend to aggregate, reducing their efficacy in any kind of metal-extracting application.<sup>28</sup> R. Ou *et al.* resolved this issue by incorporating these molecules as guests in the MIL-53 framework, the framework acting as a buffer between the photoresponsive molecules preventing self-aggregation.<sup>29</sup> The spiropyran was incorporated as a precursor to a polymer, the polymerisation performed once the spiro molecules were encapsulated in the framework. The polymer prevented leaching of the spiropyran moiety. The spiropyran-loaded MIL-53 was then tested for its ability to adsorb NaCl from water, demonstrating its potential as an energy efficient and renewable means of desalination (see Figure 12).

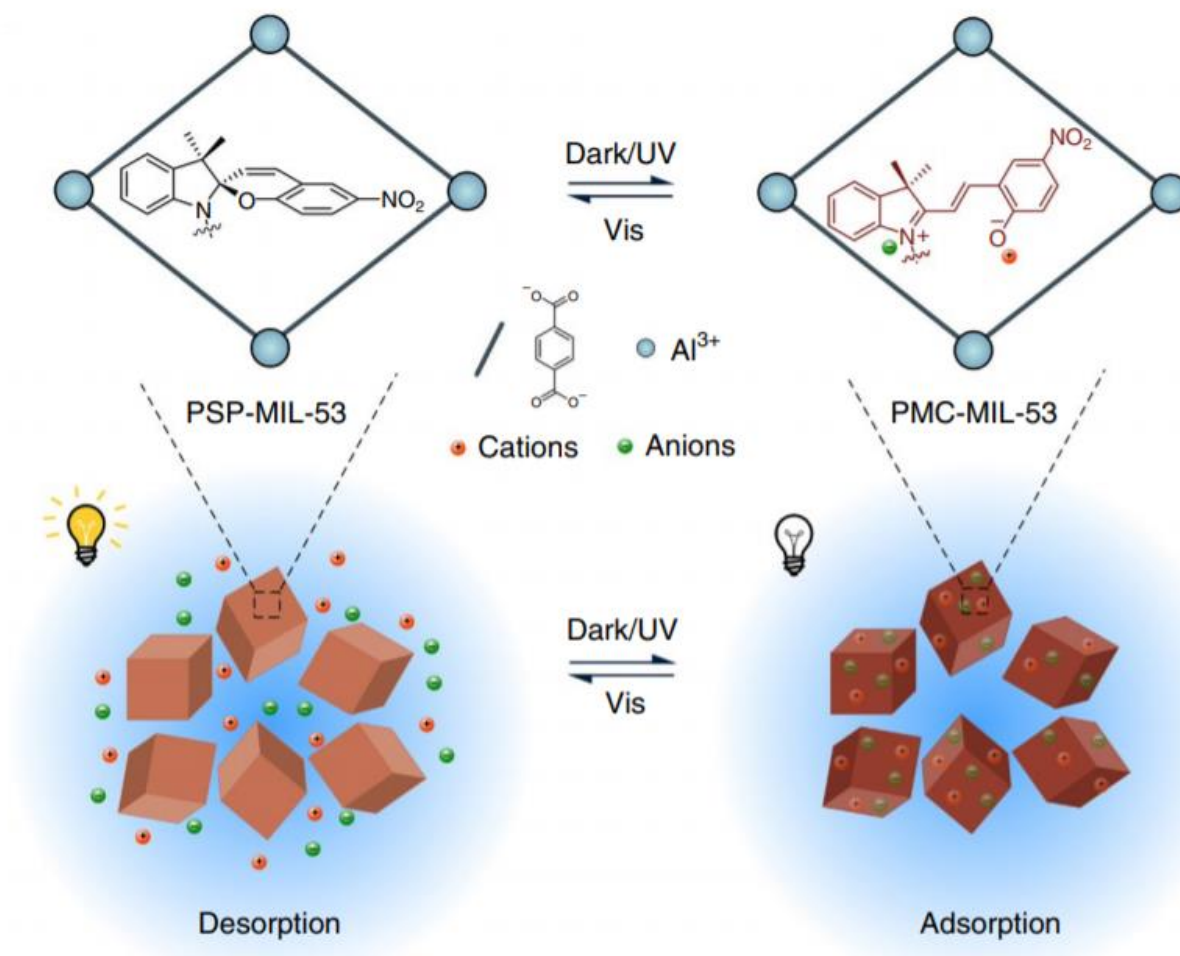


Figure 12 The MIL-53 framework, loaded with a spiropyran polymer, functions as a desalination material. Imaged taken from R. Ou et al.<sup>29</sup>

H. Liang et al. further demonstrated the potential of materials utilising the spiropyran class of molecules. They encapsulated the spiropyran molecule inside of a ZIF-8 membrane, to provide a means of selective  $\text{Li}^+$  ion transport, ideal for applications in batteries and lithium enrichment. The narrow channel sizes associated with ZIF-8 restrict the diffusion of  $\text{K}^+$ ,  $\text{Na}^+$  and  $\text{Mg}^{2+}$  while allowing the smaller  $\text{Li}^+$  ions to move freely (see Figure 13). This movement is then accelerated by the spiropyran molecules reducing the impedance of the material dramatically (by two orders of magnitude).<sup>30</sup>

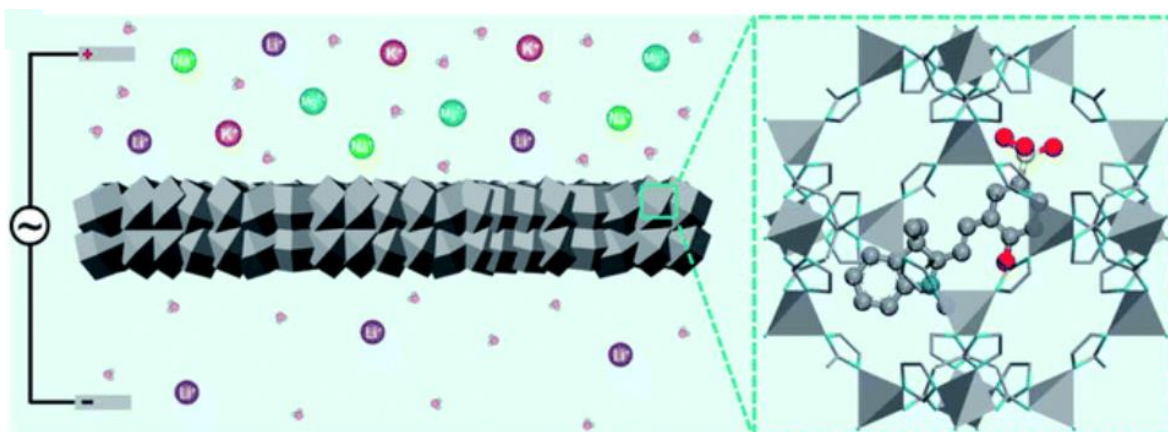


Figure 13 ZIF-8 membrane encapsulating spiropyran acts as an active transport system for lithium ions. The inset shows the structure of the SSP@ZIF-8 composite in the merocyanine form. Colour scheme is as follows: lithium, purple; potassium, pink; sodium, green; magnesium, blue. Image taken from H. Liang et al.<sup>30</sup>

The two examples presented in this section, demonstrate the extra functionality that is provided by spiropyran over other photoresponsive moieties (e.g. azobenzene, diarylethylene) due to the significant difference in properties between the SP and MC forms. The long term goal of this thesis, is to analyse a light-controlled molecular separation (similar to the SSP@ZIF-8 example) using a material we designed via an *in-situ* analytical technique.

## 1.2 Molecular separations

The typical method for molecular separation of liquids is often fractional distillation which is very energy intensive. Distillation processes currently account for 10-15% of the worlds energy consumption.<sup>31,32</sup> As such there is a big interest in finding more nuanced and energy conservative methods of separations. One such nuanced method is the design of porous materials like MOFs to selectively separate and extract desirable products in ambient conditions. As such there are a few separations which researchers have attempted to fine-tune existing MOFs or design entirely new frameworks for.

### 1.2.1 Xylene

The regioisomers *p*-xylene, *o*-xylene and *m*-xylene are chiefly produced in catalytic reforming of crude oil. The *p*-xylene isomer is the most valuable product although there is a commercial demand for *o*-xylene.<sup>33</sup> *p*-xylene is a key intermediate in the production of polyethyleneterephthalate (PET) which currently accounts for 18% of the worlds polymer production.<sup>34</sup> The old method of practice for the industrial production of *p*-xylene involved catalytic cracking (which has very little selectivity) which also produced toluene, benzene and ethylbenzene as by-products. The isomers were then separated via fractional distillation. This method of separation is expensive due to the sheer amount of energy

required, further exacerbated by the fact some of these regioisomers have similar boiling points (*p*-xylene 138.5°C, *m*-xylene 139.3°C, *o*-xylene 144.6°C, ethylbenzene 136.3°C)<sup>35</sup>.

Processes have moved on since then, fractional crystallisation and adsorptive materials (simulated moving beds) are now the chief method of separation since the 1960s.<sup>34–36</sup> The latter is the focus of much research application of membrane and sorbent materials to aid separation, other chemical processes that may improve the yield are treated with much caution as the building of a chemical plant can cost up to 1 billion dollars and so it is a big risk to take without existing proof that it already works on a large scale. Although this is unfortunate it also presents opportunity for porous materials such as MOFs, as they are comparatively cheaper to implement and can improve the sustainability of the process. The current industrial method is the use of cation-exchanged faujasite (FAU)-type zeolites X and Y, these materials are more efficient than the fractional distillation method, but considerable energy is wasted on the desorption process and therefore more appropriate materials are still highly sought after. The criteria for these improved materials are high selectivity, high capacity, high diffusivity and must have sufficient chemical, thermal and mechanical stability. A number of MOFs have already been reported to have higher capacities and selectivities than the current industrial standard adsorbents and it would seem it is only a matter of time before materials such as these become the new industrial standard.<sup>35</sup>

### 1.2.2 Styrene

Styrene is another important intermediate in the polymer industry. 25 million tonnes are produced annually, of which, 80% is used in polymerisation reactions for various plastics and rubbers. The standard industry strategy for styrene production is the dehydrogenation of ethylbenzene which only reaches 20-40% completion and therefore a significant amount of the ethylbenzene needs to be removed from the final product as well as impurities commonly found in the feedstock: toluene and *o*-xylene. Like the xylene separation, the boiling point of styrene (145°C) is quite similar to the boiling points of the by-products, with the added difficulty of self-polymerisation due to the reactive vinyl group. As such, vacuum distillation and extractive distillation must be employed in the presence of inhibitors to prevent self-polymerisation. Once again this presents an opportunity for porous media as being able to purify mixtures at room temperature would be ideal for this process, saving on both inhibitors and energy. As such researchers have sought to use MOFs in this separative process.

### 1.2.3 MOFs in separations

The attractiveness of MOFs as separative media is the ability to precisely design the apertures and therefore the selectivity of the material; other porous materials tend to have a limited range of pore sizes or a nonuniform pore size.<sup>37</sup> This tunability is further exemplified by the ease to which additional



functional groups can be added to a framework to improve binding affinities, as discussed previously (Figure 5, Figure 6).

#### 1.2.3.1 MOFs in separation xylene isomers

Many research scientists are looking to replace zeolites with a metal organic framework in xylene separation. The goal is a material that can selectively purify the whole mixture in one step, in the liquid phase. As of yet, there has not been a porous material capable of achieving this. Often a material is able to separate out one isomer (that is not *p*-xylene) but unable to purify the rest or struggles to do so in the liquid phase.

*D. Peralta et al.* demonstrated that a well-known and synthetically easily accessible framework, ZIF-8, was capable of separating *p*-xylene from isomers *o*- and *m*-xylene quite well in the gas phase, reporting separation factors 3.9 for *p*-xylene/*o*-xylene and 1.6 for *p*-xylene/*m*-xylene.<sup>38</sup> This selectivity was achieved due to *p*-xylene's significantly smaller kinetic diameter (6.7 Å) than the other isomers (*m*-xylene 7.4 Å and *o*-xylene 7.5 Å). The kinetic diameter of *p*-xylene is twice the size of the ZIF-8 apertures (3.4 Å), but the framework undergoes a transitory structural deformation in the presence of the xylene (which has been estimated to increase the pore diameter to 6.4 Å) followed by a reformation of the previous form allowing the *p*-xylene to diffuse through. This transformation is driven by the adsorption of the *p*-xylene molecule to the ZIF-8 framework which is energetically favourable, but the deformation is an unfavourable conformation, which is why it returns to the original shape once the *p*-xylene has passed through the aperture. Unfortunately, ZIF-8 performed poorly in the separation of *p*-xylene from ethylbenzene, as they have similar kinetic diameters (ethylbenzene 6.7 Å). This is an example of a MOF employed to separate the isomers driven by molecular sieving rather than selective site interactions.

*M. Gonzalez et al.* designed two cobalt-based frameworks, one using the 2,5-dioxido-1,4-benzenedicarboxylate (dobdc) molecule as a linker and the other using 4,6-dioxide-1,3-benzenedicarboxylate (*m*-dobdc), to form Co<sub>2</sub>(dobdc) and Co<sub>2</sub>(*m*-dobdc) respectively.<sup>39</sup> The Co<sub>2</sub>(dobdc) framework reported affinities in the order of *o*-xylene > ethylbenzene > *m*-xylene > *p*-xylene, observed for both liquid and gas phase experiments, suggesting that this framework could potentially do the separation in one continuous process. While the Co<sub>2</sub>(*m*-dobdc) framework reported affinities *o*-xylene > ethylbenzene ≈ *m*-xylene > *p*-xylene, the lack of selectivity between ethylbenzene and *m*-xylene was unexpected as this framework is structurally very similar to the Co<sub>2</sub>(dobdc) framework. The affinity these frameworks have for C<sub>8</sub> aromatic molecules is due to the nature of the interactions between the C<sub>8</sub> aromatics and the open metal sites of the cobalt nodes in the frameworks. In the cases of *o*-xylene, *m*-xylene and ethylbenzene the arrangement of the

cobalt nodes allows for interaction between two metal sites while in the case of *p*-xylene, only one of the sites interacts with the guest molecule (See Figure 14).

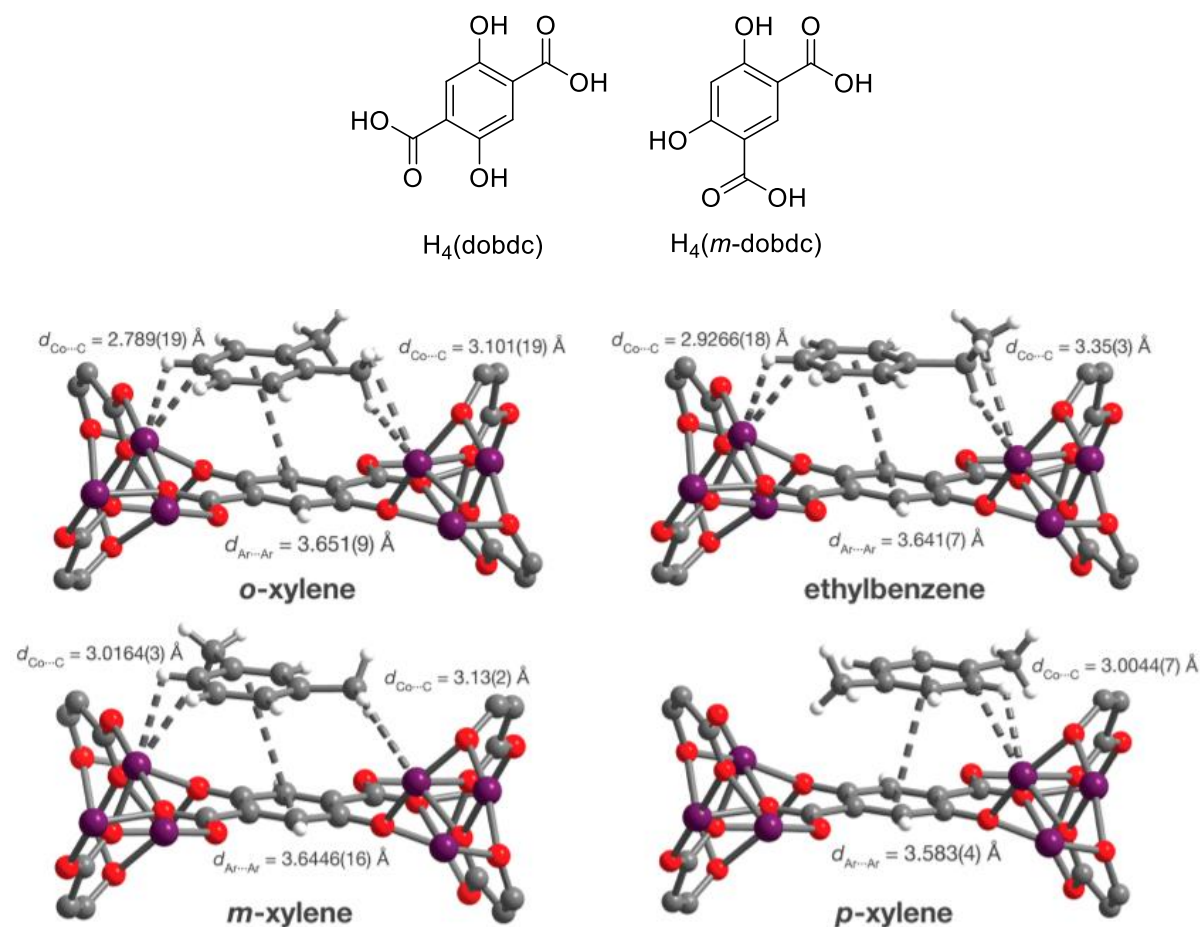


Figure 14 (top) Chemical structures of the protonated forms of *dobdc* and *m-dobdc* (bottom) Displays the interactions of each *C<sub>8</sub>* isomer with the open metal sites of the cobalt nodes in *Co<sub>2</sub>(dobdc)* with intermolecular distances highlighted for comparison. Purple, red, grey, and white spheres for cobalt, oxygen, carbon and hydrogen atoms, respectively. Reproduced from M. Gonzalez et al.<sup>39</sup>

In the case of *Co<sub>2</sub>(dobdc)*, a structural deformation was observed when adsorbing *o*-xylene and ethylbenzene, as the structure would distort to accommodate an extra aromatic molecule in three out of every four pores. This MOF demonstrates a separation that is driven by intermolecular interactions with the framework rather than size exclusivity, as we saw previously with ZIF-8. In both cases there was a structural deformation in order to accommodate specific molecules, which demonstrates the complexity of the mechanisms involved for each framework and that each separation has the potential to be unique.

### 1.2.3.2 MOFs in separation of styrene

The styrene separation is not as commercially attractive as the xylene separation, although still significant, it has attracted a lot less attention by material chemists. Therefore, there is less literature

on the topic, but the separation still focuses on C<sub>8</sub> aromatics and therefore some of the knowledge from the xylene separation can be used as a basis for the styrene separation.

M. Maes *et al.* demonstrate the capabilities of MIL-47 and MIL-53 (Al) for separating ethylbenzene and styrene mixtures.<sup>40</sup> MIL-53 (Al) was found to be capable of also purifying small amounts of *o*-xylene and toluene (2% wt) which are typically present in the feedstock for this industrial process. The framework had a higher affinity for these two molecules over ethylbenzene and styrene and would be able to tolerate these contaminants in small quantities as they would be retained in the pores of the framework while ethylbenzene and styrene pass through.

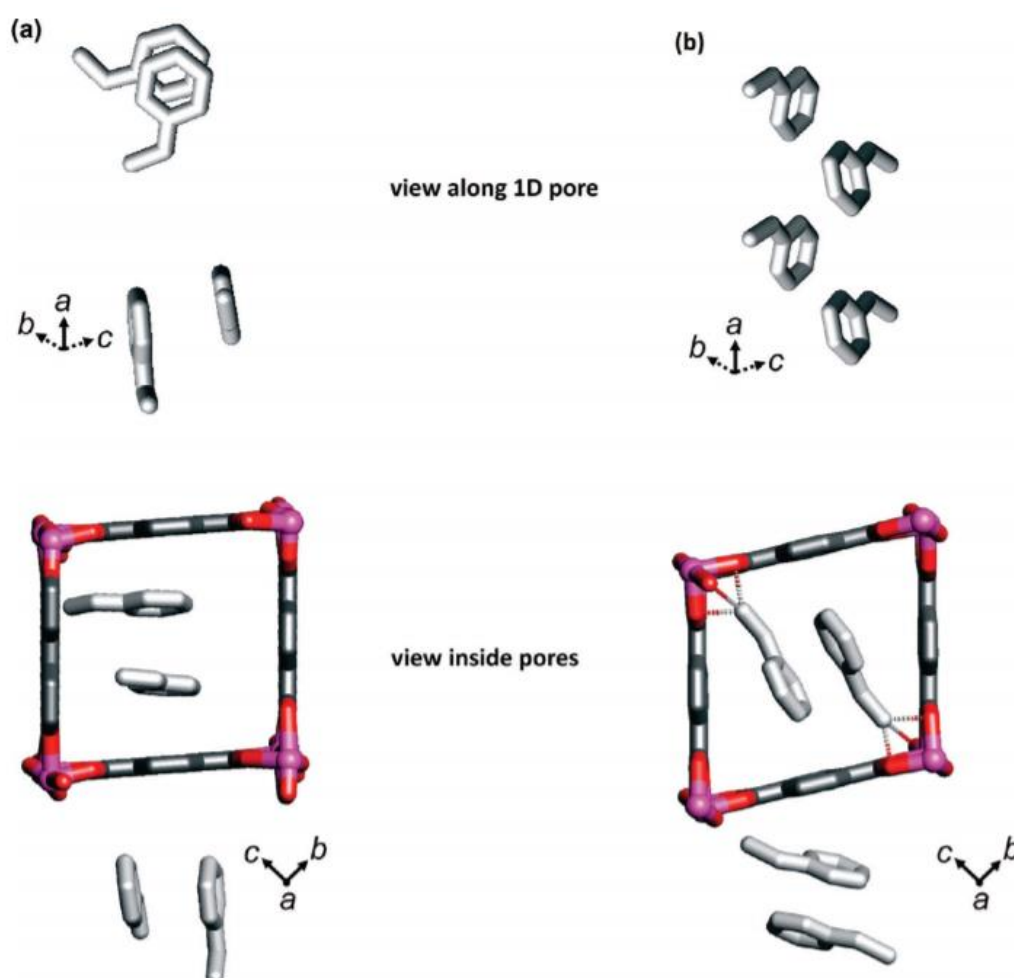


Figure 15 a) shows crystallographic data of how styrene packs inside a pore of MIL-47. b) illustrates how ethylbenzene packs inside the same pore, note only half of the positions displayed in the case of ethylbenzene are occupied. Dark grey, red, pink spheres for carbon, oxygen and vanadium atoms, hydrogen atoms omitted. Reproduced from M. Maes *et al.*<sup>40</sup>

There is significantly more attention paid to gas phase separations than liquid phase separations in the field of MOFs, which could be due to the additional challenge presented in designing a material that is both selective and stable to the solvent media used.<sup>41,42</sup> As such the separative mechanisms that exist in a liquid phase separation are not as well understood as they are in the gas phase,

furthermore modelling stationary phases is even harder if the particles are non-uniform, which typical MOFs generally are.<sup>43</sup> It is therefore of value to add data of experiments in the liquid phase to the literature for future computational modelling to benchmark against.

There are numerous potential stationary phases and an infinite number of possible separations. An analytical technique that can be used as a standard to compare all these materials in separative processes is needed, and one that could also provide analysis *in-situ* to understand the separative mechanisms in play would be ideal. In this thesis we investigate non-invasive microwave methods to monitor *in-situ* separation processes.

#### 1.2.4 Microwave studies of MOFs

Microwave-assisted synthesis of MOFs is grown in popularity over the last decade, providing advantages such as short reaction times, phase selectivity and control over crystal morphology.<sup>44</sup> The popularity of this method has in turn sparked an interest in understanding the specific interactions of the microwaves with these frameworks. There are several analytical methods that implement microwaves to characterise dielectric properties, the suitability of each technique dependent on the nature of the material, the frequency range you wish to measure in, accuracy and ease of use. All of the techniques, however, are derived from the same fundamental principles of permittivity.<sup>45</sup> The principles of dielectric measurements are discussed in detail in chapter 4. Briefly, there are two values that dielectric measurements are concerned with when an electric field is applied (see Equation 1).  $\epsilon'$ , the dielectric constant, describes the energy that is stored in a material due to polarisation and  $\epsilon''$ , the dielectric loss, describes the energy lost in a system (typically as heat).<sup>46</sup>

$$\epsilon^* = \epsilon' - j\epsilon''$$

*Equation 1 for the complex relative permittivity of a material.  $\epsilon'$  is the real part of the equation that represents the dielectric constant.  $j$  represents the imaginary number of the square root of -1 and the  $\epsilon''$  represents the imaginary part of the equation, the dielectric loss.*

A. Laybourn *et al.* studied the dielectric properties of the reagents used to synthesise the MIL-53 and MIL-47 frameworks.<sup>47</sup> They investigated the linker 1,4-benzenedicarboxylate (BDC) and the metal salts with various counter anions. They determined that the M(III) salt solutions at concentrations above 5 mM had larger  $\epsilon''$  values than the BDC<sup>2-</sup> solutions, suggesting that the heat generated will be primarily through the metal salts interacting with the electric field rather than the organic linker. The BDC<sup>2-</sup> solutions did however demonstrate higher  $\epsilon'$  values than the metal salts, meaning the non-coordinated ligands were able to interact with the electric field in phase better than the metal salts, this distinction is important as it means that these linkers still interact with the field, but the heat generated during the synthesis is primarily through the metal salts.

The investigation of the adsorption of analytes in MOFs via these dielectric measurements is still in its infancy and have only dealt with gas phase adsorption to date. *M. Barter et al.* used the microwave cavity perturbation method in tandem with *in-situ* neutron powder diffraction to study ammonia adsorption in frameworks: HKUST-1, UiO-67 and CPO-27-Co.<sup>48</sup> Upon exposure of HKUST-1 to ammonia there was structural deformation which was observed by both analytical methods. In the cases of CPO-27-Co and UiO-67, however, there were effective demonstrations of the information that the dielectric measurements can collect that the neutron powder diffraction method could not.

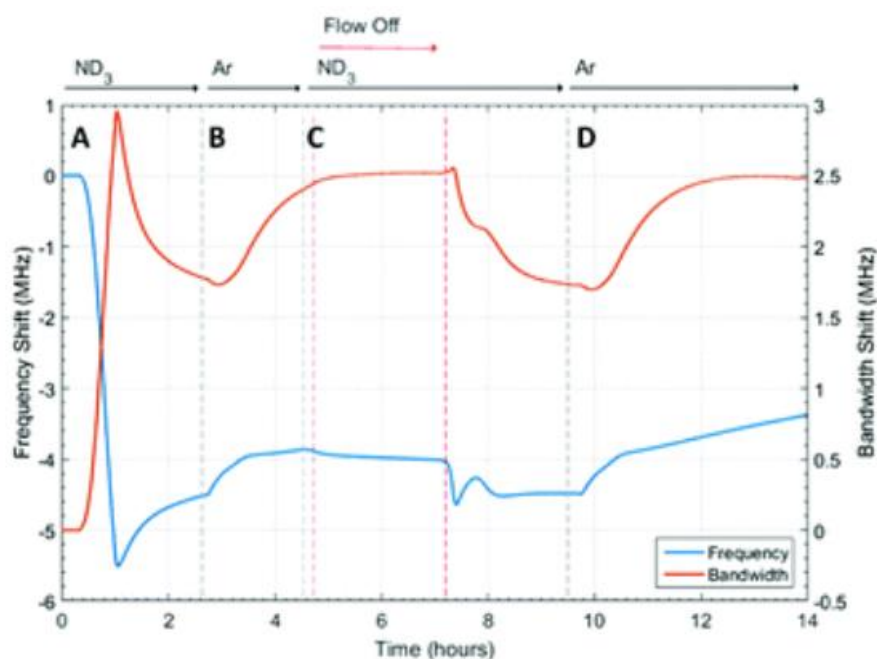


Figure 16 showing frequency and bandwidth over time. Frequency is proportional to the  $\epsilon'$  value of the system and bandwidth is proportional to the  $\epsilon''$  value of the system. A is the initial filling of the CPO-27-Co framework with  $\text{ND}_3$ . B is when the  $\text{ND}_3$  is displaced by a flow of argon. C is the refilling of the framework with  $\text{ND}_3$  and D is the second displacing of  $\text{ND}_3$  with argon. Reproduced from *M. Barter et al.*<sup>48</sup>

An example of the information provided from the dielectric measurements is shown by period A on Figure 16. Upon exposure to ammonia, a peak was observed for the frequency and bandwidth, but the powder diffraction Bragg peaks remained unchanged. The powder pattern suggested there was no structural change, meaning that what the dielectric measurement was observing a process specific to the ammonia gas molecules. They proposed that as the ammonia content was increasing in the framework the dielectric loss was increasing (the bandwidth), as expected. At a certain point, the ammonia molecules began making hydrogen bonds with each other inside the framework forming a network of ammonia molecules. The hydrogen bonded ammonia molecules loss of freedom resulted in a smaller contribution to the dielectric loss, observed as the fall in the peak.

In the case of UiO-67, no complex mechanism was observed. However, upon flushing with argon, the frequency failed to return to the original value before being exposed a second time with ammonia. This is indicative that ammonia was strongly bound to the framework in some way (either coordinated to metals at defect sites or hydrogen bound at metal clusters) and was unable to be removed via flushing with argon.

In summary, the nature of the data provided by these dielectric measurements do not provide crystal-clear conclusions (unlike a SCXRD experiment), but rather provide subtle bits of information that would have been otherwise missed and allow for the beginning of new investigations.

### 1.3 Scope of Thesis

This thesis details the pursuit of two separate research aims. The primary goal was to synthesise a spiropyran-based framework that responds to light stimulus (which is discussed in chapters 2 and 3). The second goal was to design and test an *in-situ* analytical technique capable of studying the separation mechanisms of metal-organic frameworks (which is discussed in chapter 4). The two goals are linked by the desire to monitor the photoswitching of the metal organic frameworks with this analytical technique, but this was ultimately beyond the scope of the project.

Chapter 2 focuses on the design and implementation of synthetic routes for the spiropyran ligands themselves. There are 10 novel ligands in total which were successfully synthesised, chiefly utilising N-bromosuccinimide and Suzuki-Miyaura cross-couplings to functionalise spiropyran molecules with N-heterocyclic moieties. This chapter also discusses the characterisation of the photoisomerism of these ligands studied via UV-Vis absorption spectroscopy, and the effects of the type of N-heterocyclic functionalisation upon the electronics of the molecules studied via  $^1\text{H}$  NMR.

Chapter 3 focuses on the synthesis of the metal organic frameworks utilising the spiropyran ligands synthesised in chapter 2 and a co-linker. It discusses the synthetic attempts and the factors affecting the success rate of synthesising such a material, of which three different frameworks were successfully synthesised incorporating the spiropyran moiety and a fourth novel framework which does not incorporate a spiropyran moiety was produced serendipitously. This chapter also discusses the challenges of characterising these spiropyran-based frameworks.

Chapter 4 details the utilisation of microwave cavity perturbation theory to provide *in-situ* analytical data of MOFs as stationary phases in molecular separations. It begins with studies of MIL-53(Al) and UiO-66 loaded with several different compounds, varying in electronics and sterics. The chapter continues by describing the implementation of a flow system that studies the ability of UiO-66 to perform in the industrial separative processes involved in xylene and styrene production.

## 1.4 References

- 1 S. Castellanos, F. Kapteijn and J. Gascon, *CrystEngComm*, 2016, **18**, 4006–4012.
- 2 J. Ha, J. H. Lee and H. R. Moon, *Inorg. Chem. Front.*, 2020, **7**, 12–27.
- 3 A. Schoedel, M. Li, D. Li, M. O’Keeffe and O. M. Yaghi, *Chem. Rev.*, 2016, **116**, 12466–12535.
- 4 A. Schoedel, ed. M. B. T.-M.-O. F. for B. A. Mozafari, Woodhead Publishing, 2020, pp. 11–44.
- 5 Ü. Kökçam-Demir, A. Goldman, L. Esrafilı, M. Gharib, A. Morsali, O. Weingart and C. Janiak, *Chem. Soc. Rev.*, 2020, **49**, 2751–2798.
- 6 D. S. Sholl and R. P. Lively, *J. Phys. Chem. Lett.*, 2015, **6**, 3437–3444.
- 7 J. Juan-Alcañiz, J. Gascon and F. Kapteijn, *J. Mater. Chem.*, 2012, **22**, 10102–10118.
- 8 A. J. Howarth, A. W. Peters, N. A. Vermeulen, T. C. Wang, J. T. Hupp and O. K. Farha, *Chem. Mater.*, 2017, **29**, 26–39.
- 9 R. J. Marshall, C. L. Hobday, C. F. Murphie, S. L. Griffin, C. A. Morrison, S. A. Moggach and R. S. Forgan, *J. Mater. Chem. A*, 2016, **4**, 6955–6963.
- 10 C. R. Marshall, S. A. Staudhammer and C. K. Brozek, *Chem. Sci.*, 2019, **10**, 9396–9408.
- 11 R. S. Forgan, *Chem. Sci.*, 2020, **11**, 4546–4562.
- 12 M. R. DeStefano, T. Islamoglu, S. J. Garibay, J. T. Hupp and O. K. Farha, *Chem. Mater.*, 2017, **29**, 1357–1361.
- 13 S. Ghosh and S. Kitagawa, *CrystEngComm*, 2008, **10**, 1739–1742.
- 14 S. Benmansour, I. Pérez-Herráez, C. Cerezo-Navarrete, G. López-Martínez, C. Martínez Hernández and C. J. Gómez-García, *Dalt. Trans.*, 2018, **47**, 6729–6741.
- 15 X.-G. Guo, W.-B. Yang, X.-Y. Wu, Q.-K. Zhang, L. Lin, R. Yu and C.-Z. Lu, *CrystEngComm*, 2013, **15**, 3654–3663.
- 16 R. Seetharaj, P. V Vandana, P. Arya and S. Mathew, *Arab. J. Chem.*, 2019, **12**, 295–315.
- 17 K. D. Vogiatzis, A. Mavrandonakis, W. Klopper and G. E. Froudakis, *ChemPhysChem*, 2009, **10**, 374–383.
- 18 X.-J. Wang, P.-Z. Li, Y. Chen, Q. Zhang, H. Zhang, X. X. Chan, R. Ganguly, Y. Li, J. Jiang and Y. Zhao, *Sci. Rep.*, 2013, **3**, 1149.

- 19 O. K. Farha, I. Eryazici, N. C. Jeong, B. G. Hauser, C. E. Wilmer, A. A. Sarjeant, R. Q. Snurr, S. T. Nguyen, A. Ö. Yazaydın and J. T. Hupp, *J. Am. Chem. Soc.*, 2012, **134**, 15016–15021.
- 20 M. Mon, R. Bruno, E. Tiburcio, M. Viciano-Chumillas, L. H. G. Kalinke, J. Ferrando-Soria, D. Armentano and E. Pardo, *J. Am. Chem. Soc.*, 2019, **141**, 13601–13609.
- 21 A. Schneemann, V. Bon, I. Schwedler, I. Senkovska, S. Kaskel and R. A. Fischer, *Chem. Soc. Rev.*, 2014, **43**, 6062–6096.
- 22 A. Modrow, D. Zargarani, R. Herges and N. Stock, *Dalt. Trans.*, 2011, **40**, 4217–4222.
- 23 F.-X. Coudert, *Chem. Mater.*, 2015, **27**, 1905–1916.
- 24 D. M. D’Alessandro, B. Smit and J. R. Long, *Angew. Chemie Int. Ed.*, 2010, **49**, 6058–6082.
- 25 R. Lyndon, K. Konstas, B. P. Ladewig, P. D. Southon, P. C. J. Kepert and M. R. Hill, *Angew. Chemie Int. Ed.*, 2013, **52**, 3695–3698.
- 26 I. M. Walton, J. M. Cox, J. A. Coppin, C. M. Linderman, D. G. (Dan) Patel and J. B. Benedict, *Chem. Commun.*, 2013, **49**, 8012–8014.
- 27 H. Xia, K. Xie and G. Zou, *Molecules*, 2017, **22**, 2236.
- 28 R. Klajn, *Chem. Soc. Rev.*, 2014, **43**, 148–184.
- 29 R. Ou, H. Zhang, V. X. Truong, L. Zhang, H. M. Hegab, L. Han, J. Hou, X. Zhang, A. Deletic, L. Jiang, G. P. Simon and H. Wang, *Nat. Sustain.*, 2020, **3**, 1052–1058.
- 30 H.-Q. Liang, Y. Guo, X. Peng and B. Chen, *J. Mater. Chem. A*, 2020, **8**, 11399–11405.
- 31 D. S. Sholl and R. P. Lively, *Nature*, 2016, **532**, 435+.
- 32 *Materials for Separation Technologies. Energy and Emission Reduction Opportunities*, United States, 2005.
- 33 J. L. [Energetics Pellegrino Inc., Columbia, MD (United States)], *Energy and Environmental Profile of the Chemicals Industry*, United States, 2000.
- 34 L. Ji, *Appl. Mech. Mater.*, 2013, **312**, 406–410.
- 35 Y. Yang, P. Bai and X. Guo, *Ind. Eng. Chem. Res.*, 2017, **56**, 14725–14753.
- 36 US Patent, US2985589A, 1961.
- 37 X. Zhao, Y. Wang, D.-S. Li, X. Bu and P. Feng, *Adv. Mater.*, 2018, **30**, 1705189.



- 38 D. Peralta, G. Chaplais, J.-L. Paillaud, A. Simon-Masseron, K. Barthelet and G. D. Pirngruber, *Microporous Mesoporous Mater.*, 2013, **173**, 1–5.
- 39 M. I. Gonzalez, M. T. Kapelewski, E. D. Bloch, P. J. Milner, D. A. Reed, M. R. Hudson, J. A. Mason, G. Barin, C. M. Brown and J. R. Long, *J. Am. Chem. Soc.*, 2018, **140**, 3412–3422.
- 40 M. Maes, F. Vermoortele, L. Alaerts, S. Couck, C. E. A. Kirschhock, J. F. M. Denayer and D. E. De Vos, *J. Am. Chem. Soc.*, 2010, **132**, 15277–15285.
- 41 B. Van de Voorde, B. Bueken, J. Denayer and D. De Vos, *Chem. Soc. Rev.*, 2014, **43**, 5766–5788.
- 42 Z.-Y. Gu, C.-X. Yang, N. Chang and X.-P. Yan, *Acc. Chem. Res.*, 2012, **45**, 734–745.
- 43 W. Qin, M. E. Silvestre, Y. Li and M. Franzreb, *J. Chromatogr. A*, 2016, **1432**, 84–91.
- 44 J. Klinowski, F. A. Almeida Paz, P. Silva and J. Rocha, *Dalt. Trans.*, 2011, **40**, 321–330.
- 45 M. S. Venkatesh and V. Raghavan, *Can. Biosyst. Eng. / Le Genie des Biosyst. au Canada*, 2005, **47**, 15–30.
- 46 R. Clarke, A. Gregory, D. Cannell, M. Patrick, S. Wylie, I. Youngs and G. Hill, 2003.
- 47 A. Laybourn, J. Katrib, P. A. Palade, T. L. Easun, N. R. Champness, M. Schröder and S. W. Kingman, *Phys. Chem. Chem. Phys.*, 2016, **18**, 5419–5431.
- 48 M. Barter, J. Hartley, F.-J. Yazigi, R. J. Marshall, R. S. Forgan, A. Porch and M. O. Jones, *Phys. Chem. Chem. Phys.*, 2018, **20**, 10460–10469.

## Chapter 2. Synthesis of spiropyran ligands

### 2.1 Introduction

Before we can begin to design the metal organic framework, we must first design a suitable linker. We aimed to design a pillar-layer MOF (discussed further in chapter 3), typically the layer linker is functionalised with carboxylate groups and the pillaring linkers are functionalised with N-heterocycles.<sup>1</sup> We desire to use a spiropyran ligand as a pillaring linker therefore the first step is to design a spiropyran linker with N-heterocycles attached. This chapter will discuss the obstacles in synthesising these ligands followed by characterisation of these ligands which will not only benefit the further work involved in designing the MOF but also have wider contributions to the research community concerning these photoactive molecules.

#### 2.1.1 Spiropyran Synthesis

There are two common methods of synthesising the spiro-centre in molecules. The simpler of the two is to condense a methylene base with an *o*-hydroxy aromatic aldehyde. There is the risk of a side product in which the desired product condenses with the indoline again (See Figure 17).

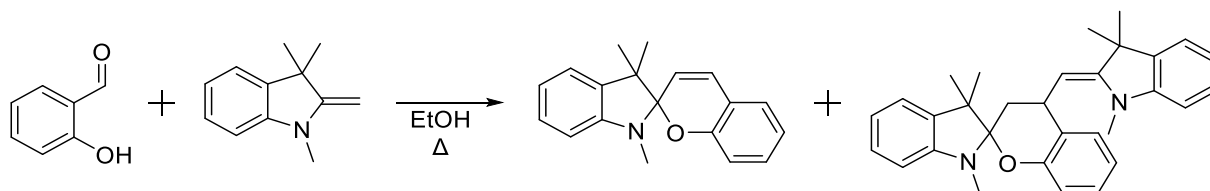


Figure 17 Condensation of a salicyl aldehyde with Fischer's base to form spiropyran and by-product.

Formation of the side product can be reduced by reacting the quaternary indolenylium salt with the salicyl aldehyde with the addition of an organic base (typically piperidine).<sup>2</sup> The second way is to condense the *o*-hydroxy aromatic aldehyde with the salt of the heterocyclic cation which contains active methylene groups and isolation of the intermediate styryl salts followed by an acidic work up (typically perchloric acid) with organic bases (often dry ammonia in solution of benzene or ether).<sup>2</sup>

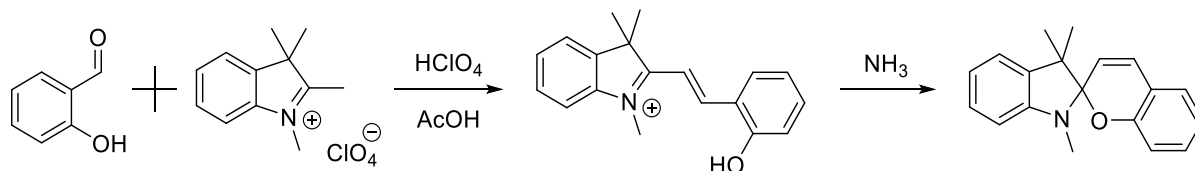


Figure 18 Condensation of salicyl aldehyde with the conjugate acid of the Fischer's base.

As the use of perchlorates and ammonia require more care and precaution, this method is less preferable.<sup>2</sup>

### 2.1.2 Spiropyran functionalisation

The main concern when functionalising spiropyran molecules is the spiro-centre. There is a chance that each time the spiropyran isomerises to the open form, it may cleave at the spiro centre into its indoline and chromene fragments.<sup>3,4</sup> This issue is compounded by the fact that the isomerisation does not only occur through photolysis, but can also be triggered by the solvent polarity, pH and mechanical stimulus.<sup>5</sup> As we discussed earlier, the relaxation of the merocyanine back to the closed form is encouraged by thermal stimulus. Most reactions require heating to progress, therefore when a spiropyran is used as a reagent, it is exposed to constant heat and any other stimuli present in the reaction mixture, encouraging rapid cycling through the open and closed isomers and reaching fatigue much quicker.

*D. Williams et al.* coupled pyridine functionalities to a brominated dimer and a monomer of the spiropyran using a Castro-Stephens/Sonogoshira protocol (see Figure 19).<sup>6,7</sup> They were quite low yielding, interestingly the dimer did not have a significantly lower yield than the monomer. The authors do not go into any great detail as to what causes the low yield as it was not the focus of the publication. Key details of the reaction that may have negatively impacted the yield is that the reaction was done at 120°C which may have caused the spiro-centre to fatigue rapidly. DMF is a very polar solvent and would encourage the open merocyanine isomer to form during the reaction. The use of copper chloride may have also sequestered some of the reagent, as the merocyanine is well documented to have a strong binding affinity with bivalent transition metal cations. Cu<sup>2+</sup> specifically can cause homocoupling between spiropyrans though its precise mechanism remains unclear.<sup>8</sup>

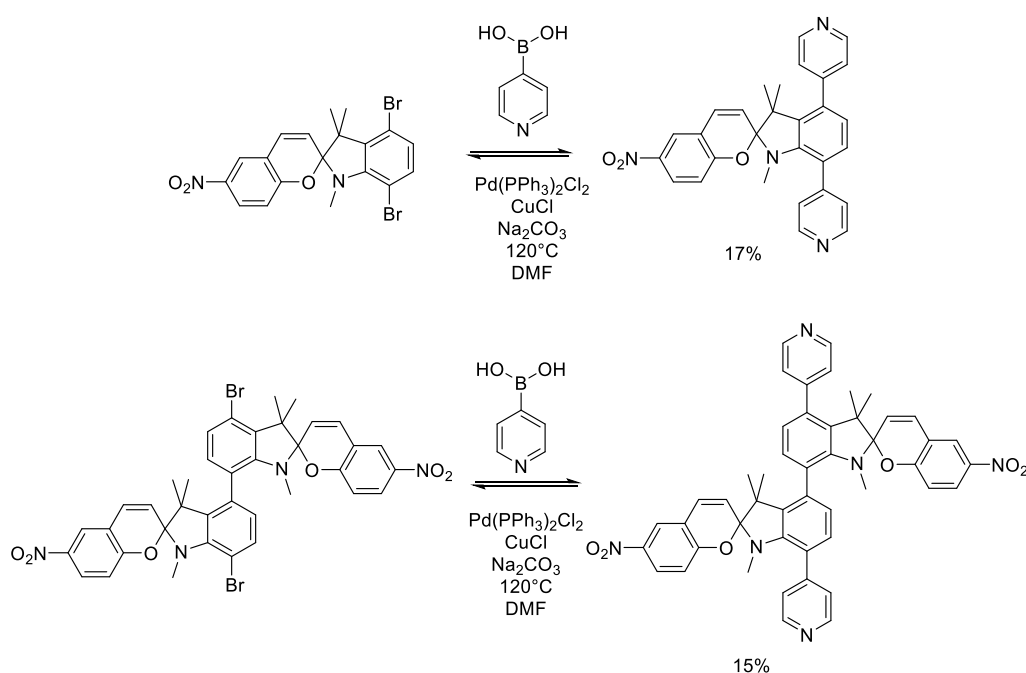


Figure 19 Cross-coupling employed by *D. Williams et al.* to functionalise two spiropyran molecules with pyridine rings.

*J. H. Lee et al.* demonstrated a Suzuki cross-coupling method for iodinated forms of spiropyran. Initially they aimed to cross couple with the iodinated salicylaldehyde and perform condensation afterwards as this avoids the complications of designing reaction conditions suitable for spiropyran, but the yield was too low due to an unidentified side product that kept forming as the major product. Both mono- and di-substitutions using phenylboronic acid were performed with decent yields. They applied this method to a wider scope of substrates which had adequate yields (see Figure 20).

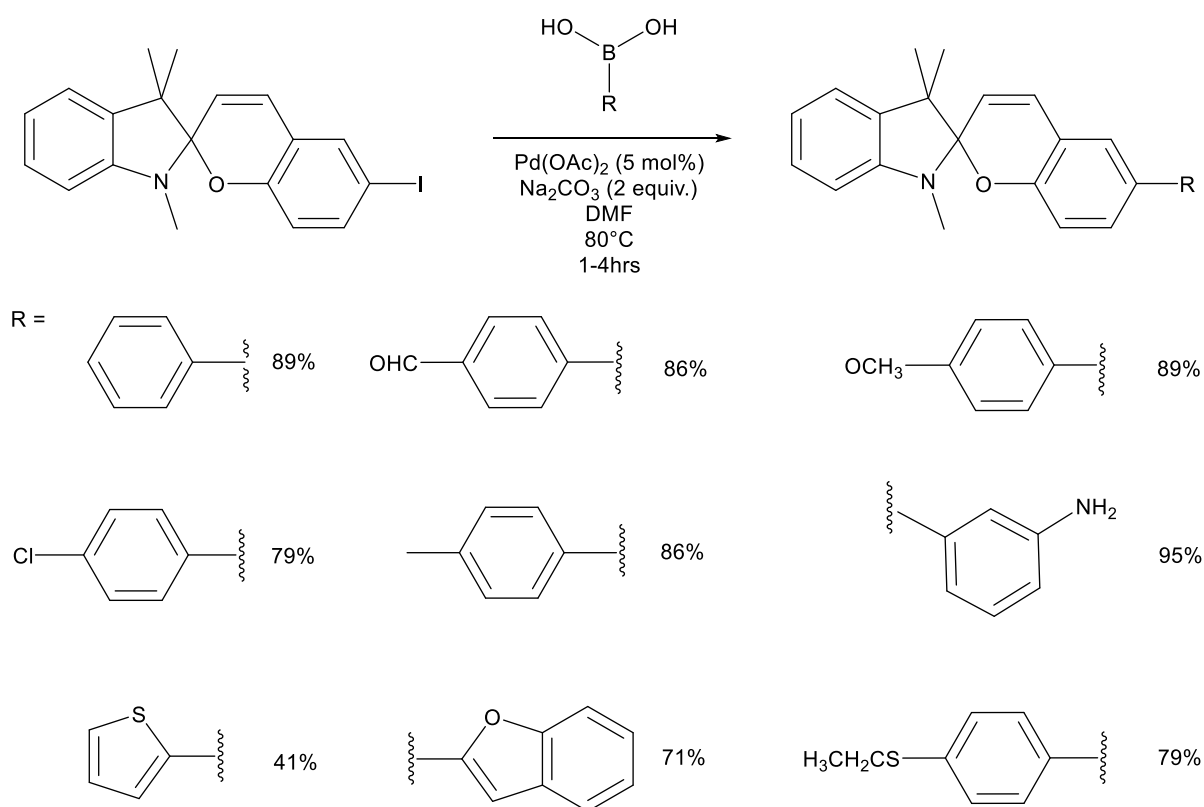


Figure 20 Suzuki cross coupling reaction by *J. H. Lee et al.* with associated yields.

The reaction was performed at  $80^\circ\text{C}$  which may be more accommodating for the spiro-centre than the conditions used by *D. Williams et al.*. As previous, DMF was also used here, perhaps demonstrating that the solvent polarity does not have a significant effect on the yield.

The coupling seems more successful through iodine than bromine, as expected with Suzuki couplings due to the extra lability of the iodine atom. We must also consider the ease with which these halogenated spiropyran are obtained. There are plenty of high yielding examples of spiropyran molecules functionalised with iodine on the chromene fragment.<sup>9-11</sup>

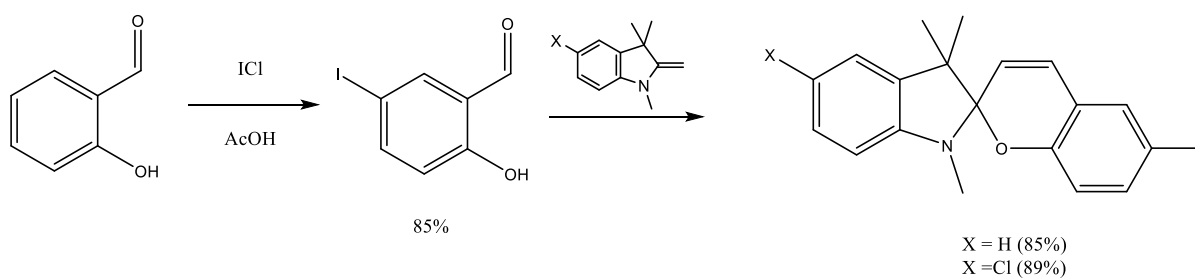


Figure 21 Y. Cho et al. synthesising two iodinated spiroopyran molecules in high yields.<sup>11</sup>

Typically, functionalisation on the chromene fragment occurs before the condensation reaction that forms the spiro centre, as it is easier to prepare the salicylaldehyde with the desired functional group rather than specifically target the site on a spiroopyran molecule. The indoline fragment is quite susceptible to electrophilic attack (particularly at position X in Figure 21). As far as we know, there are no examples in the literature of a spiroopyran molecule functionalised on the para-position to the indoline with an iodine atom. Conversely, there are plenty of target-specific bromination examples using spiroopyrans.<sup>9,12,13</sup> There may not be any good reason for this, it is quite possible that its simply down to cost effectiveness (brominating agents are typically cheaper than iodinating agents).

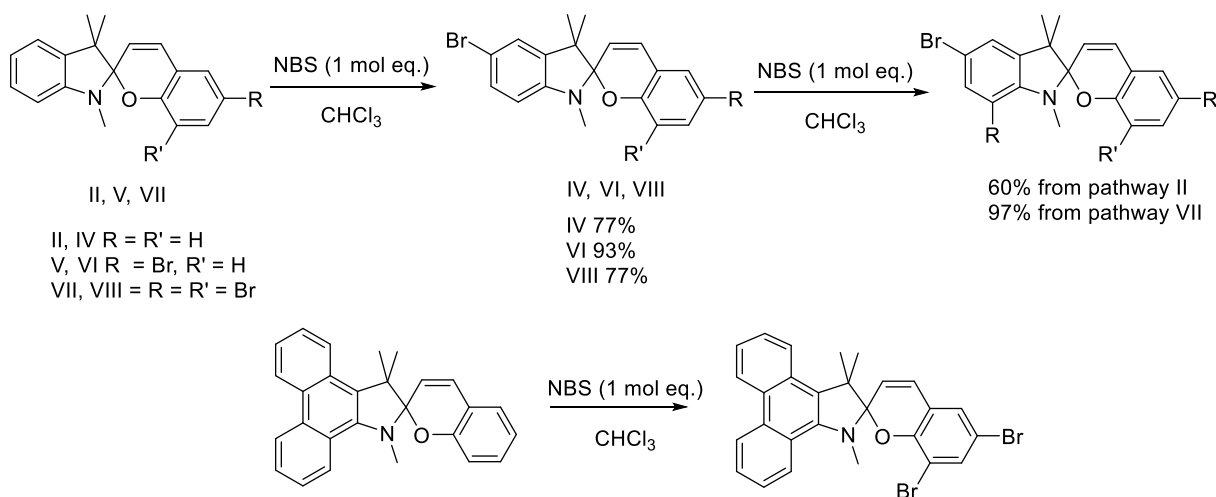


Figure 22 Synthetic scheme for bromination of indoline fragment with associated yields achieved (top). Phenanthridine derivative of spiroopyran which restricts attack to the chromene fragment, only the dibrominated product was obtained, no mono-brominated species were identified (bottom). Reported by Zakhs et al..<sup>12</sup>

In summary, the optimal synthetic strategy that takes into account difficulty of synthesis and cost-effectiveness is to brominate the salicyl aldehyde, then perform the condensation that forms the spiroopyran which will then direct electrophilic attack to the indoline ring, from here we can selectively build a variety of regioisomers utilising Suzuki cross-couplings.

### Spiroopyran properties

As discussed earlier in chapter 1, spiropyran is an interesting photoactive molecule due to its two isomers having vastly different properties.

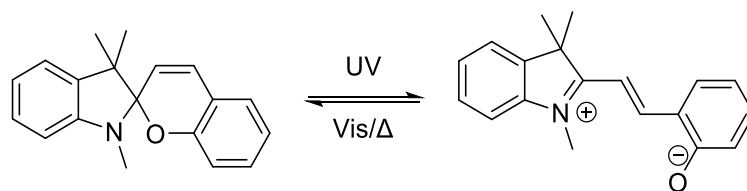


Figure 23 Photoisomerism of spiropyran (left) ring opening to form the coloured merocyanine form (right). Reverse reaction typically occurs through thermal relaxation/visible light.

The wavelengths at which the forward and reverse reactions occur can be tuned by several modifications of the molecule. Commonly, the position *para* to the C-O spiro bond is modified with nitrobenzene which gives the open form more stability and results in a bathochromic shift for the chromene fragment absorption band.<sup>5</sup>

Crystals of spiropyran are typically resistant to photoisomerism due to the crystal lattice restricting the movement of the photomolecules. *M. Suzuki et al.*<sup>14</sup> demonstrated how the physical state of a spiropyran molecule (see Figure 24) affected its photoresponsivity. The lifetime of the open form was reported to be 90 seconds in the solid state as opposed to 50 milliseconds when dissolved in ethanol as a solution.<sup>15</sup>

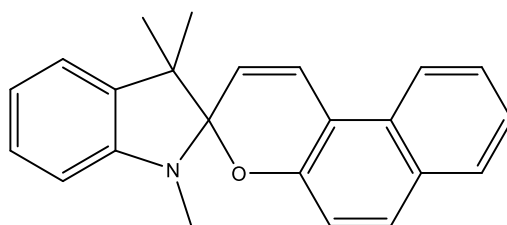


Figure 24 1,3,3-trimethylindolino-6-naphthopyrlospiran molecule studied by *M. Suzuki et al.*<sup>14</sup>

Although it is difficult, it is not impossible for the photoisomerism to take place when the spiropyran is in a solid lattice. *Asahi et al.* demonstrated that with a strong enough light source (sufficient fluence), in their case a pulsed laser, they can force individual molecules in the lattice to isomerise.<sup>16</sup> The interesting part of their findings was that by isomerising one molecule, there is a coupling effect where molecules adjacent to the isomerised molecule are more likely to isomerise. The localised ablation with a laser increases absorbance and the isomerism creates some extra space round adjacent molecules encouraging further isomerism to occur (See Figure 25).

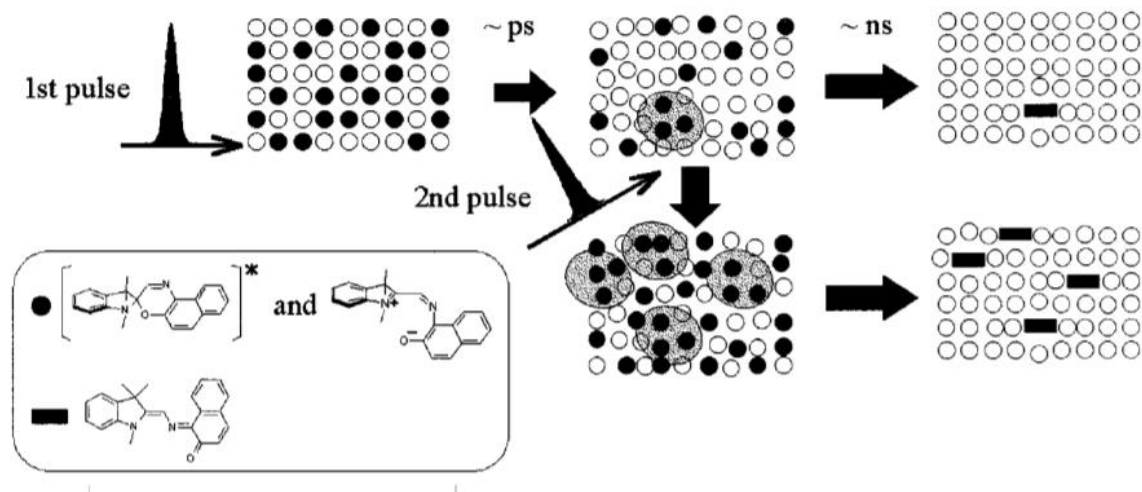


Figure 25 Schematic illustration of the cooperative photochemical reaction model adopted from Asahi et al.<sup>16</sup> The open circles represent the ground-state spiro isomer, the filled ones represent the  $S_1$  states and/or the nonplanar open forms, and the filled rectangles represent the trans-planar photomerocyanines.

## 2.2 Aims

To synthesise a library of ligands containing the spiropyran moiety, functionalised with N-heterocycles to be effective MOF linkers. The photoactivity of the spiropyran ligands will also be characterised to allow for comparison and observe how minor changes can affect this property.

## 2.3 Results and discussion

The general syntheses of the heteroleptic and homoleptic, N-heterocycle substituted spiropyrans are shown in Figure 26. **3a**, **3b**, **3c** are the homoleptic di-substituted spiropyrans and **6a** and **6b** are the heteroleptic spiropyrans. While the synthesis of **6a** was attempted from precursor **5b**, unfortunately no successful outcome was achieved. The successful syntheses of the rest of these molecules are discussed in this section.

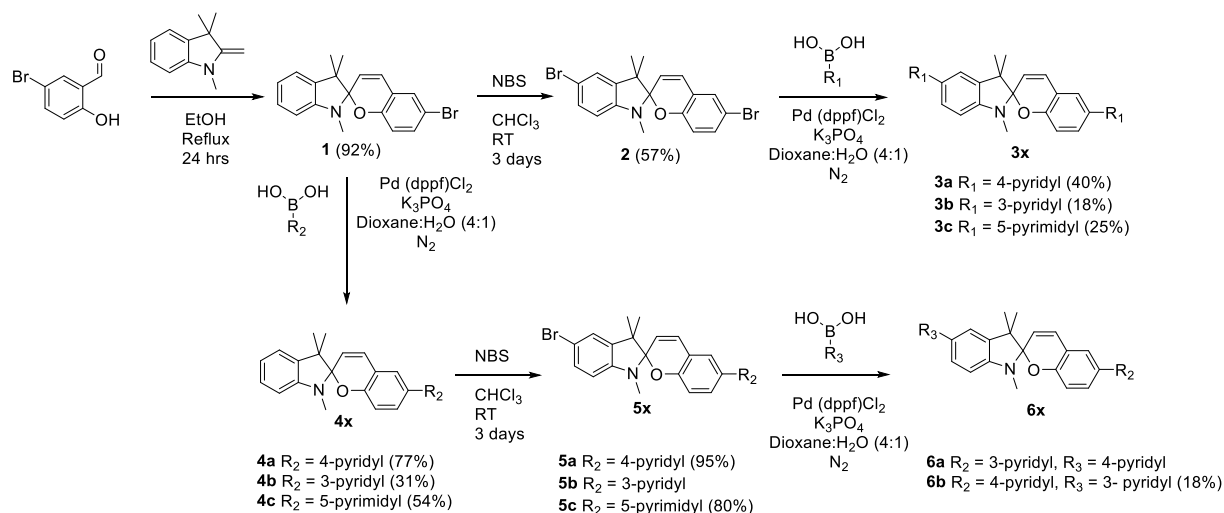


Figure 26 Scheme for synthesis for hetero/homoleptic spiropyrans.

6-bromo-1',3',3'-trimethylspiro[chromene-2,2'-indoline] (**1**) was formed by the Fischer's base condensation (see Figure 17). As this reaction was high yielding (92%), we believed this method to be sufficient and saw no reason to investigate the other synthetic routes (see Figure 18).

### 2.3.1 Electrophilic Aromatic Bromination of Spiropyran

Molecule **2** is well established in the literature<sup>12</sup> and, when used in a cross-coupling reaction, could lead to suitable pillaring linkers for our frameworks. The simplest and most common pillaring linkers tend to be linear, rigid and symmetrical. Having said that, there are many examples of asymmetric and flexible pillaring linkers being used in metal-organic frameworks, however they tend to lead to interesting and, often, unpredictable topologies.<sup>17</sup> Spiropyran is both asymmetric and bent; the angles between the points of extension of the phenyl rings of the photoactive cores (see Figure 27) and the spiro centres typically range from 129 to 141°.<sup>18</sup> This kink in the spiro core means homoleptic functionality (e.g. compounds **3a-3c**) of spiropyran will usually result in non-linear directionality of the consequential metal-linker bonding. Heteroleptic functionalisation (e.g. compounds **6a** and **6b**) may provide a more linear pillar and therefore be a more successful pillaring agent with a more consistent topology.



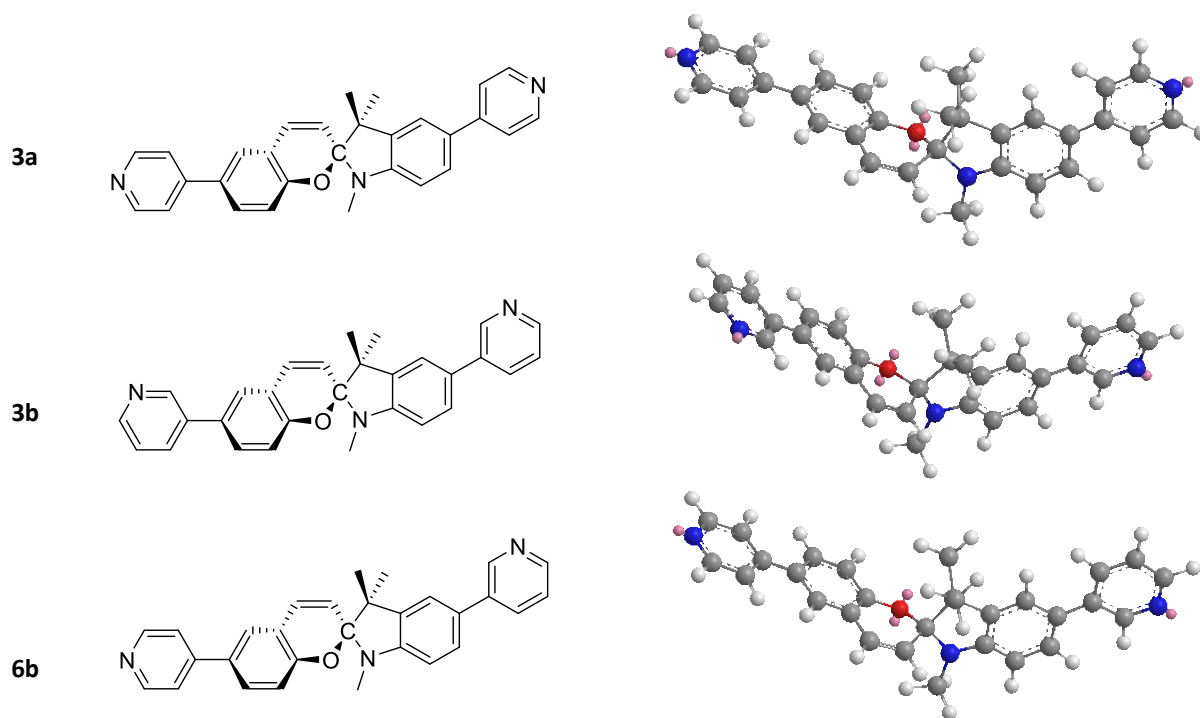


Figure 27 Lowest energy conformations for the free ligands **3a** **3b** **6b**, calculated by the MM2 method on chem3D. Nitrogen (blue), oxygen (red), carbon (grey), hydrogen (white), lone pairs of electrons (pink).

Performing a cross coupling reaction using **2** and two different boronic acids would produce our desired targets however it would also result in 3 other possible stereoisomers which would be very difficult to purify and provide very little control over the stereospecificity of the products. The logical solution is to brominate a spiropyran that has already been functionalised on the chromene side. The nitrogen on the pyran fragment of **2** directs electrophilic attack to the para position providing regioselectivity,<sup>12</sup> we see no presence of any other regioisomers in the NMR data (see **S1** for raw data). The molecules we wish to brominate contain N-heterocycles. Electrophilic attack on N-heterocycles tend to have reduced activity due to the electron-withdrawing effect of the nitrogen as well the ease to which N can gain a positive charge.<sup>19</sup> There are still other sites on the spiropyran molecule where bromination can occur. *Zakhs et al.* reported the likelihood of bromination is as follows:  $Br_I > Br_c = Br_b$  for molecule **2**.<sup>12</sup> (See Figure 28.) Steric hindrance could reduce the likelihood of bromination to occur at the  $Br_c$  position for molecules **4a**, **4b**, **4c** but  $Br_I$  should still be the preferred bromination site.

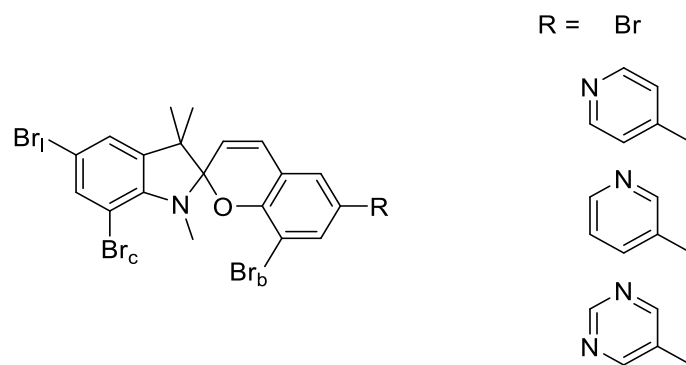


Figure 28 Possible bromination sites.  $Br_I$  is the primary bromination site with the nitrogen directing electrophilic attack to the *para* position.  $Br_C$  and  $Br_b$  are possible sites to which overbromination can occur.

NBS is an ideal bromination agent as it can work at room temperature and therefore the rate of reaction can be more easily controlled, also due to the insoluble nature of NBS it provides a low active concentration of the brominating agent at a time, further reducing the chance of over-bromination. Our initial approach was to mix mono-brominated **1** with an excess of NBS at room temperature in  $CHCl_3$  for 3 days. In the synthesis of **2** this results in a 57% yield (Table 1) but heating to reflux increased the yield of this dibrominated product to 81%.

	Target Molecule	Yield
<b>2</b>		57% (81%)
<b>5a</b>		95%
<b>5b</b>		47%
<b>5c</b>		80%
-		-

Table 1 Bromination targets and their yields. **2** yield at ambient temperature (yield when under reflux)

Heating the reaction would encourage over-bromination, but in cases where bromination would not take place at room temperature, this could provide just enough activation energy for the reaction to occur. For all bromination experiments, after 3 days an NMR and an MS sample would be taken to see

if any bromination had taken place. Initially if only the starting material was present, to try and force the reaction, it was put under reflux. This was often a last resort, as over-bromination was a major risk. Even if there was still the desired product in the reaction, purifying the mixture was too difficult. An effective eluent system was not found that could separate the brominated products by chromatography; bromine is a very weak electron withdrawing group therefore the overall polarity was not significantly affected. This also made finding a suitable set of recrystallization conditions also too difficult.

The only case where heating the reaction improved the yield was synthesis of **2**. In all other cases there was significant over-bromination, making the product unrecoverable. In the cases of **5a** and **5c**, the reaction took longer: 5 and 7 days, respectively. Unexpectedly the presence of pyridine and pyrimidine seemed to enhance the overall yield. There should be minimal effects to the electronics of the molecule, as the chromene fragment's  $\pi$ -system is not conjugated on the pyran fragment's  $\pi$ -system, ruling out any mesomeric effects. The inductive effect would be reduced by at least 10 chemical bonds of separation. There was no sign of over-brominated products when synthesising **2**, thus the sterics of the N-heterocycle does not seem to matter when it comes preventing attack on the chromene fragment and if anything should have reduced the overall activity very slightly. This reactivity difference is not yet explained; all molecules displayed similar solubilities and there was no clear evidence of merocyanine being formed during the reaction (i.e. no apparent colour changes during the reaction and nothing indicative in the NMR spectra).

Bromination of the Fischer's base was also investigated, as performing the cross-coupling before the spiro-center had formed may improve the overall yield, removing the risk of spiro-center cleavage during the coupling process and allowing for harsher coupling conditions to be used. This method would also avoid any of the zwitterionic MC form being sequestered from the reaction by binding with any metal salts present in the reaction. Unfortunately, the bromination reaction would not go forward at room temperature or under reflux.

### 2.3.2 Suzuki cross couplings

The cross-coupling reactions of N-heterocycle boronic acids and brominated spiropyran were performed using Suzuki-Miyaura methods. This section first discusses finding the optimal Suzuki conditions for coupling 4-pyridyl boronic acid with **2** over 2 positions. Then using this method, discusses the nuances of applying this method to synthesising the other Suzuki products. During the optimisation of synthesis of **3a** a big issue was the work up and purification rather than the reaction conditions tested, so the purification process will be discussed first.

### 2.3.2.1 Method Development: Work up and purification

The N-heterocyclic products can cause challenges in purification as pyridine is typically soluble in most solvents, which presented challenges in finding suitable recrystallisation conditions. Column chromatography is often the preferred alternative; however the spiro-containing compounds can interact with the acidic silica. We established that the addition of triethylamine significantly improved the transit of products through the column and hence the final recovered yield (Table 2, first three entries). Triethylamine is added to neutralise the plate, to stop the pyridine moieties from adhering to the silica, but there is still a peculiar separative effect observed by TLC which suggests multiple different compounds present (Figure 29). The separation was also attempted using Alumina TLC plates, unfortunately no separation occurred.

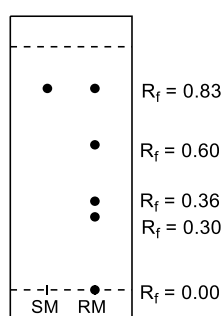


Figure 29 TLC Left: Sample of starting material **2**. Right: Cross coupling reaction to form **3a**. Sample taken from crude product after following all purification steps before column chromatography.

The presence of several spots could be explained by spiropyran opening and closing while travelling through the silica, which causes varied separation. When removed from the acidic environment and put in  $\text{CDCl}_3$  (neutral, organic media) the ring closes to form the common compound. Due to this interaction, monitoring the reaction progression via TLC was challenging as the only compounds that could be monitored effectively by chromatography were starting materials **1** and **2**.

The severe drop in yield for **3a**, **3b** and **3c** could be explained by being unable to track the second coupling and therefore these reactions may have not reached completion. Separating the starting material **1** (which has no N-heterocycle functionality) from products **4a**, **4b** and **4c** is relatively trivial. In the case of **6b** it is difficult to separate the starting material (**4a**) from the product and in the cases of **3a**, **3b** and **3c** the difficulty is the products being separated from the intermediates (**5a**, **5b** and **5c** respectively).

Fractions:  $R_f = 0.30, 0.36, 0.60$  all produce the same NMR spectrum suggesting the target product **3a**.  $R_f = 0.6$  was a brown/yellow solution while  $R_f = 0.36, 0.30$  produced a bright pink colour. The MS of all three samples had a peak at 676.26 which has an isotope distribution that suggests it contains iron in

some form. An iron species would explain the pink solution as opposed to the yellow/brown we would expect. We can assume that since nothing was observed in the NMR spectrum, the iron species is either paramagnetic (high spin) or simply not present in a significant enough quantity to be observable. As the NMR could not observe the iron species and the MS is neither quantitative nor able to distinguish between regioisomers, we can only speculate as to what extent the contamination is and the nature of the complex. Iron contamination could act as a poison for the ligands or affect the MOF synthesis in some unforeseen way, therefore we sought to remove it. The water solubility of  $\text{Fe}^{2+}$  complexes and the water insolubility of spiropyran made an ethanol-water recrystallisation an ideal choice.<sup>5,20</sup> It would also remove any pyridine that was present as a by-product of using 4-pyridyl boronic acid. Confirmation of the removal of the iron species was afforded via the absence of the peak in the mass spectrum.

#### 2.3.2.2 Method Development: Synthesising 3a

The usual difficulties of cross-couplings involving N-heterocycles are also combined with the challenges of working with spiropyrans. The reaction conditions can trigger isomerisation of the spiropyran to form the merocyanine form and possibly complex with any metal salts present, with a particular preference for metals with 2+ oxidation states.<sup>21</sup> A further challenge is the fatigue associated with spiropyrans, discussed earlier. By being exposed to any conditions that would trigger the opening of spiropyran (e.g. light, solvent polarity, pH, metal ions) as well as the closing of merocyanine (i.e. heat), the molecule will continuously cycle through the open and closed form. By repeatedly opening and closing, the likelihood that the molecule cleaves is increased and hence the rate of degradation of the spiro-core increases.<sup>22</sup> This phenomenon adds a limitation on the reaction temperature and time. The experiments were done at 80°C and usually for a maximum of 24 hours (or 48 hours if done on a 5 g scale to ensure completion). The first three entries in Table 2 show examples of syntheses without triethylamine in the workup (see above) and hence do not represent fairly the efficacy of the Suzuki-coupling conditions trialled. The rest of Table 2 describes the reactions in which triethylamine was employed in the purification and compares different combinations of the type of base used, the solvent media and the palladium catalyst. All solvents were mixed with water (solvent:H<sub>2</sub>O 4:1) as it has been reported that anhydrous conditions can cause poisoning of the palladium catalyst.<sup>23</sup>

Sample	Catalyst [phosphine ligand]	Base	Solvent	Yield	Notes
<b>3a</b>	$\text{Pd}(\text{P}(\text{Ph})_3)_4$	$\text{K}_2\text{CO}_3$	DME	-	No $\text{NEt}_3$
<b>3a</b>	$\text{Pd}_2(\text{DBA})_3$	$\text{K}_2\text{CO}_3$	Toluene	4%	No $\text{NEt}_3$

	[P(t-Bu) <sub>3</sub> ]				
<b>3a</b>	Pd <sub>2</sub> (DBA) <sub>3</sub> [P(t-Bu) <sub>3</sub> ]	Na <sub>2</sub> CO <sub>3</sub>	Toluene	10%	No NEt <sub>3</sub>
<b>3a</b>	Pd(dppf)Cl <sub>2</sub>	Na <sub>2</sub> CO <sub>3</sub>	DME	38%	
<b>3a</b>	Pd <sub>2</sub> (DBA) <sub>3</sub> [P(t-Bu) <sub>3</sub> ]	K <sub>2</sub> CO <sub>3</sub>	Toluene	43%	
<b>3a</b>	Pd <sub>2</sub> (DBA) <sub>3</sub> [P(t-Bu) <sub>3</sub> ]	NaOH	Toluene	-	
<b>3a</b>	Pd <sub>2</sub> (DBA) <sub>3</sub> [P(Cy) <sub>3</sub> ]	K <sub>3</sub> PO <sub>4</sub>	Toluene	-	2.5 g
<b>3a</b>	Pd(dppf)Cl <sub>2</sub>	K <sub>3</sub> PO <sub>4</sub>	Dioxane	40%	5g scale
<b>3a</b>	Pd <sub>2</sub> (DBA) <sub>3</sub> [P(t-Bu) <sub>3</sub> ]	K <sub>2</sub> CO <sub>3</sub>	Toluene	-	5g scale
<b>3b</b>	Pd(dppf)Cl <sub>2</sub>	K <sub>2</sub> CO <sub>3</sub>	DME	5%	
<b>3b</b>	Pd <sub>2</sub> (DBA) <sub>3</sub> [P(t-Bu) <sub>3</sub> ]	K <sub>2</sub> CO <sub>3</sub>	DME	27%	
<b>3b</b>	Pd <sub>2</sub> (DBA) <sub>3</sub> [P(Cy) <sub>3</sub> ]	K <sub>3</sub> PO <sub>4</sub>	Dioxane	-	100°C
<b>3b</b>	Pd <sub>2</sub> (DBA) <sub>3</sub> [P(Cy) <sub>3</sub> ]	K <sub>3</sub> PO <sub>4</sub>	Toluene	-	2.5g scale
<b>3b</b>	Pd(dppf)Cl <sub>2</sub>	K <sub>3</sub> PO <sub>4</sub>	Dioxane	18%	5g scale

Table 2 Optimisation of **3a** and **3b** synthesis. Catalyst loading was 5 mol% per position (i.e. 10% for 2 positions), 2.4 mol phosphine ligand: 1 mol Pd catalyst, boronic acid added in excess. All solvents were mixed with H<sub>2</sub>O in a 4:1 ratio. Unless stated otherwise; temperature: 80°C, the limiting reagent (compound **2**) was 0.5 g.

The 3/4-pyridyl and 5-pyrimidyl boronic acids are typically unreactive in Suzuki conditions and they fall into a research area receiving a lot of recent attention due to the prevalence of N-heterocyclic moieties in target drugs for the pharmaceutical industry.<sup>24</sup> One issue is the stability of the N-heterocyclic boronic acid. During cross coupling the boronic reagents can undergo protodeboronation while also exhibiting low reactivities.<sup>25,26</sup> Another issue is the potential binding of the N-atom on the heterocycle to the palladium catalyst, which can poison the catalyst and render the substrate inactive.<sup>27,28</sup> There are various methods of circumventing this issue, such as functionalising with sulfonates or cross-coupling with the N-oxide instead of the pyridine.<sup>29,30</sup> The main issue with most Suzuki couplings is that the optimal conditions vary from substrate to substrate and therefore have to be dealt with on a case-by-case basis. A common strategy for optimising synthetic routes in industry

is to screen a variety of different catalysts, as the bite angle of the phosphine ligands is a key determining factor in how well the substrate binds to the palladium.<sup>31</sup> So this simple strategy was applied to our issue and a range of different phosphine ligands were tested. The typical choice of catalyst for Suzuki cross couplings is Pd(PPh<sub>3</sub>)<sub>4</sub>,<sup>32</sup> however it is reported to be a poor catalyst for N-heterocyclic boronic acids.<sup>33</sup> As expected, when we tested it in the synthesis for **3a** it failed to react. P(Cy)<sub>3</sub> when combined with Pd<sub>2</sub>(DBA)<sub>3</sub> has also been reported to be successful when coupling N-heterocycles.<sup>26</sup> Another popular phosphine ligand is P(t-Bu)<sub>3</sub>,<sup>34</sup> which we combined with Pd<sub>2</sub>(DBA)<sub>3</sub>. This catalyst achieved our highest recorded yield, 43%. The downside was that when scaled up by a factor of 10 (5 g) there was no reaction. Pd(dppf)Cl<sub>2</sub> was shown to work almost as well as P(t-Bu)<sub>3</sub> (40% yield), which was consistent on scale up with no appreciable loss in yield. On a larger scale keeping an inert atmosphere was more difficult to maintain. The better scale up outcome of the Pd(dppf)Cl<sub>2</sub> complex is most likely due to the ferrocene ligand being more robust to the effects of oxygen than the more labile Pd<sub>2</sub>(DBA)<sub>3</sub> /P(t-Bu)<sub>3</sub> system.<sup>35</sup> With a more rigorously controlled air-sensitive environment, Pd<sub>2</sub>(DBA)<sub>3</sub> with P(t-Bu)<sub>3</sub> would probably be the ideal catalyst-ligand pairing as it is quicker and higher yielding, although the more robust Pd(dppf)Cl<sub>2</sub> conditions were only 3% lower yielding. In order to achieve consistent results, Pd(dppf)Cl<sub>2</sub> was chosen as the catalyst going forward.

Selecting the appropriate base can make a big difference to the yield, depending on how it influences the boronic acid–borate equilibria (which is dependent on the boronic acid's pKa) and therefore how much of the active reagent (borate) is present.<sup>36</sup> The strongest base attempted, NaOH, caused the spiropyran to cleave before the coupling could take place. The significantly weaker bases, K<sub>2</sub>CO<sub>3</sub> and Na<sub>2</sub>CO<sub>3</sub>, were able to perform in the reaction however highest yields were recorded with K<sub>3</sub>PO<sub>4</sub>.

The standard solvent system used throughout industry is toluene:H<sub>2</sub>O, however in an attempt to improve the reaction rate without altering the temperature, coordinating solvents such as dimethoxyethane (DME) and 1,4-dioxane were used, since they have been reported to increase stability at cost of reactivity.<sup>23</sup> The cost to reactivity can be solved by adding more catalyst; the 5-10 mol% is already more than enough to mitigate the loss in reactivity from use of coordinating solvents. The trial experiments in Table 2 didn't show a clear improvement of yield when using either dioxane or DME, but neither did they show significant negative impact. Therefore, given the potential benefits of using either of these solvents in other cases, they were used for all subsequent syntheses in conjunction with water (4:1).

### 2.3.2.3 Cross couplings of N-heterocyclic

Although optimisation of the synthesis of **3a** and **3b** may not be the optimal conditions for the rest of the target molecules, they are conditions that have been able to accommodate for the fragility of

spiropyran while also still providing an environment where N-heterocyclic boronic acids can react. Table 3 shows the respective yields for each target molecule using the conditions described previously.

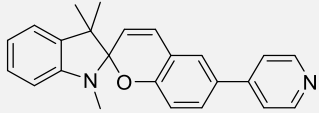
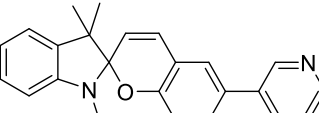
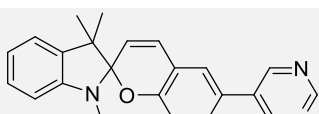
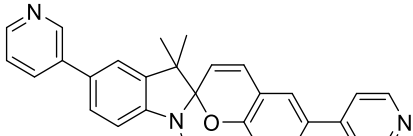
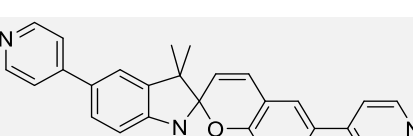
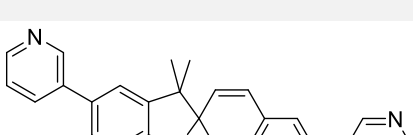
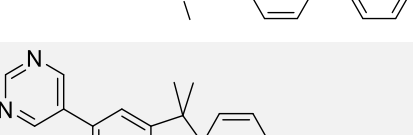
	No. of positions coupled	Target Molecule	Yield
<b>4a</b>	1		77%
<b>4b</b>	1		31%
<b>4c</b>	1		54%
<b>6b</b>	1		18%
<b>3a</b>	2		40%
<b>3b</b>	2		18%
<b>3c</b>	2		25%

Table 3 Cross-coupling products and the respective yields

We would expect that coupling one position will produce a higher yield than coupling two positions. Suzuki couplings using **1** and **2** as starting materials follow this trend, however **6b** was among the lowest yielding. The second factor to consider is the reactivities of the different boronic acids. 4-pyridyl boronic acid, possessing the most nucleophilic character, should be the most reactive and should provide higher yields while 3-pyridyl boronic acid, having the least nucleophilic character is the least reactive and provide the lowest yields.<sup>37</sup> **3a**, **3b**, **3c** do follow this trend and **4b** was far lower yielding than **4a** and **4c**. 3-pyridyl boronic acid is significantly less reactive than the other boronic acids. It may



be possible to improve the yield with further optimisations but the established unreactivity of 3-pyridyl boronic acids suggested the potential yield gained from doing so would not be enough to justify pursuing this further. These factors do not account for why **3b** and **6b** have the same yield, substitution of the 3-pyridyl boronic acid at two positions should be lower yielding than one position. It is established in the literature that Suzuki couplings are lower yielding when halogenated substrates also contain N-heterocycles.<sup>38</sup> We could speculate that when coupling over two positions, the actual loss of yield is due to the mono-coupled intermediate hindering the reaction, rather than it simply being a case of the reaction had not reached completion and unable to track the product and intermediates separately (see Figure 30).

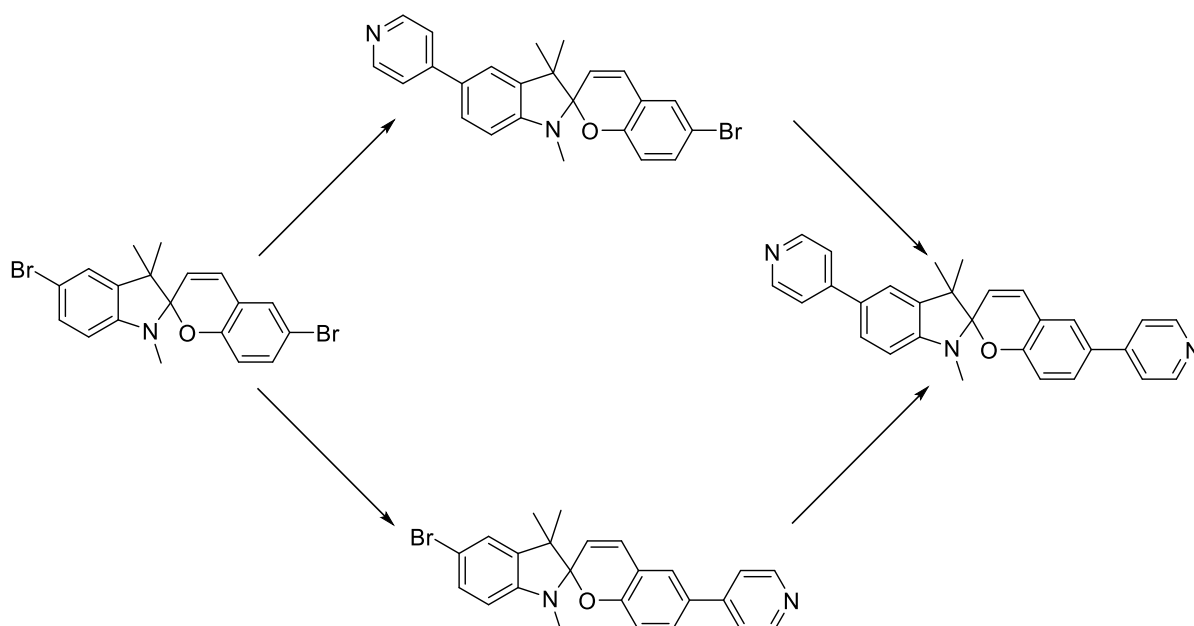


Figure 30 Scheme demonstrating the possible intermediates when synthesising **3a** during the cross-coupling process.

### 2.3.3 Ligand Properties

#### 2.3.3.1 Study of proton environments using NMR

This section looks at the substituent effects on the proton environments in the spirocyclic molecule via <sup>1</sup>H NMR spectroscopy. First, we make a direct comparison of N-heterocycle substituent effects on the chromene fragment. This is followed by comparing the effects of brominating the indoline fragment. Finally, we compare the N-heterocyclic substituent effects on both fragments.

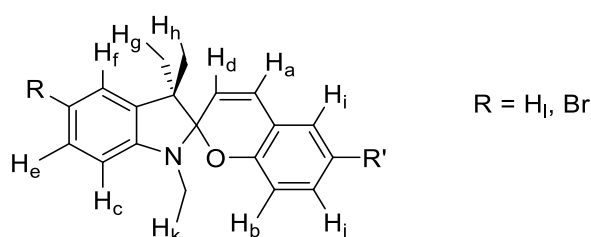


Figure 31 The spiro-core relevant to study with the relevant protons highlighted.

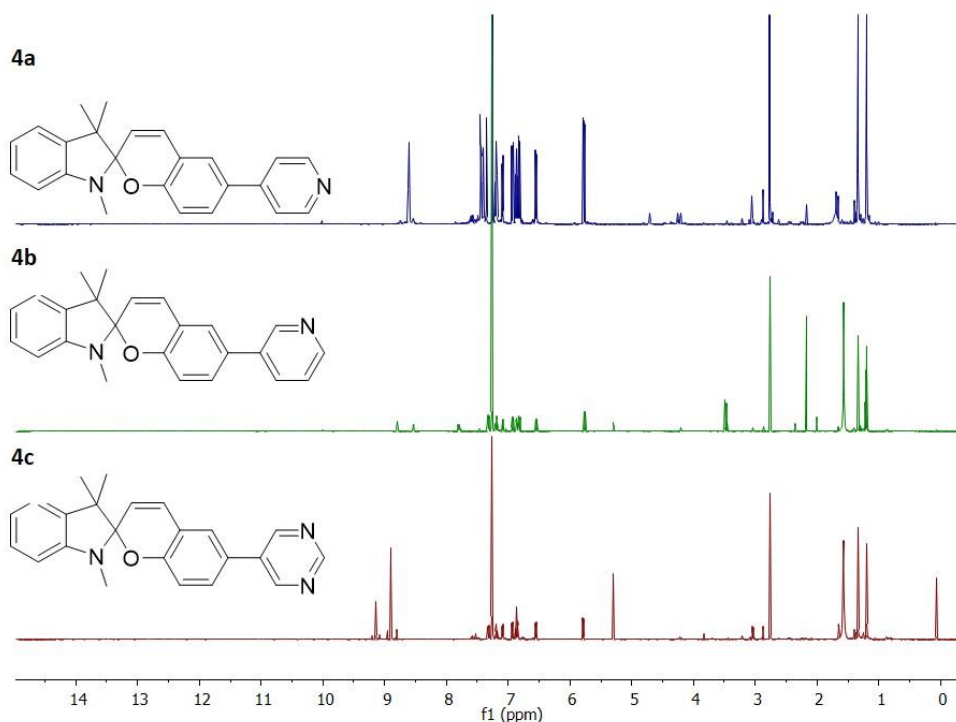


Figure 32 Full  $^1\text{H}$  spectra of **4a**, **4b** and **4c** in  $\text{CDCl}_3$ .

Figure 32 shows the full spectrum of **4a**, **4b** and **4c**. Protons in the 7-8 ppm region overlap and are not readily differentiated. Thus, for a comparative study of proton environments we shall focus on the regions 7.0-5.5 ppm and 3.0-1.0 ppm. (Trace amounts of solvent (acetone and water) are visible in this region but do not significantly affect the analysis herein)

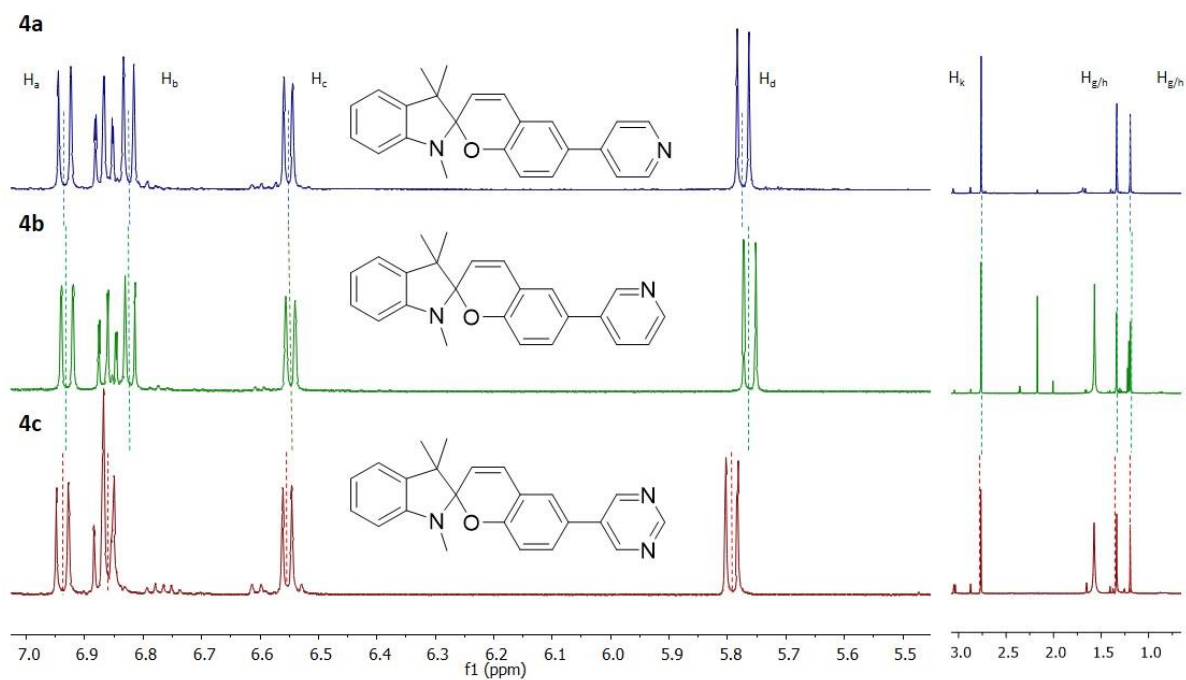


Figure 33 Expansion of  $^1\text{H}$  NMR spectra of **4a**, **4b** and **4c** in  $\text{CDCl}_3$ . Dotted lines show peak centres for the appropriate peaks and are added to demonstrate the shift between NMR spectra **4a**, **4b** and **4c**.

Molecule	H <sub>a</sub> $\delta$ (ppm)	H <sub>b</sub> $\delta$ (ppm)	H <sub>c</sub> $\delta$ (ppm)	H <sub>d</sub> $\delta$ (ppm)	H <sub>k</sub> $\delta$ (ppm)	H <sub>g/h</sub> $\delta$ (ppm)
<b>4a</b>	6.935	6.825	6.552	5.774	2.762	1.335/1.194
<b>4b</b>	6.930	6.823	6.548	5.763	2.765	1.339/1.192
<b>4c</b>	6.938	6.859*	6.554	5.793	2.765	1.336/1.195

Table 4 Comparison of peak positions of proton environments H<sub>a,b,c,d,k,g/h</sub> for molecules **4a**, **4b** and **4c**. \*Due to overlapping of peaks in **4c** spectrum, there is reduced accuracy regarding these values.

The effects of the position of the nitrogen on the electronic distribution around each molecule can be considered in terms of mesomeric and inductive effects (Figure 34, Figure 35). Experimentally these can be observed by directly comparing **4a** and **4b**. The details for selected protons are shown in Table 4. In the case of **4b**, we assume the selected protons will not be affected by any mesomeric effects relating to the pyridine moiety since they are not conjugated to that group. Conversely, for molecule **4a**, we anticipate mesomeric effects on the adjoining benzene ring, causing shifts for protons H<sub>i</sub> and H<sub>j</sub> (not distinguishable in the spectra due to peak overlap) and smaller effects on protons H<sub>a</sub>, H<sub>b</sub> and H<sub>d</sub> by proximity. H<sub>b</sub> is located in the *meta* position to the pyridine moiety and experiences negligible shift when compared with its equivalent proton in **4b**, which is also expected as the resonance forms do not apply/take away any electron density to this position (Figure 35). H<sub>a</sub> and H<sub>d</sub> see a measurable shift upfield (0.005 ppm and 0.01 ppm respectively) when comparing **4a** to **4b**. This is a surprising shift as the mesomeric effects from the pyridyl molecule should not extend to the double bond where the proton environments H<sub>d</sub> and H<sub>a</sub> are found. Protons found on the indoline fragment (H<sub>c</sub>, H<sub>g/h</sub>, H<sub>k</sub>) have negligible peak shifts (<0.005 ppm) between these two molecules and are relatively unaffected by the position of the nitrogen on the heterocyclic fragment. This is to be expected as the inductive effect is going to be negligibly small when the atom is 10+ bonds away, and since there is no conjugation between the chromene and indoline fragments the mesomeric effect does not extend to the indoline fragment.

Comparing **4b** and **4c** (3-pyridyl and 5-pyrimidyl respectively), allows us to observe the changes directly caused by the inductive effects of the additional nitrogen atom, as mesomeric effects will not extend beyond the N-heterocycle. The methyl proton environments located on the indoline fragment (H<sub>g/h</sub> and H<sub>k</sub>) were largely unaffected, as we would expect from an environment 10+ bonds away. Unexpectedly H<sub>c</sub> saw a shift of 0.008 ppm downfield in **4c**, which is even further away from the pyrimidine moiety than H<sub>k</sub> and H<sub>g/h</sub>. H<sub>b</sub> on the chromene fragment exhibits a shift of 0.036 ppm; even when accounting for the lack of accuracy due to peak overlap, this is a significant shift in the context of this study, although within our expectations due to its proximity to the pyrimidine moiety. As we

saw when comparing **4a** and **4b**, H<sub>a</sub> and H<sub>d</sub> in **4c** show some unexpected shifts downfield (0.008 ppm and 0.03 ppm with respect to **4b**), and the protons located on the double bond seem to be very sensitive to any functionality on the substituent position we are varying.

H<sub>i</sub> is observed as a ddd peak and seems relatively unaffected by the substituent present on the chromene fragment. We concluded from this, electronically speaking, the bromination probability at this position should be the same for molecules **4a**, **4b** and **4c** in the subsequent bromination reactions discussed above.

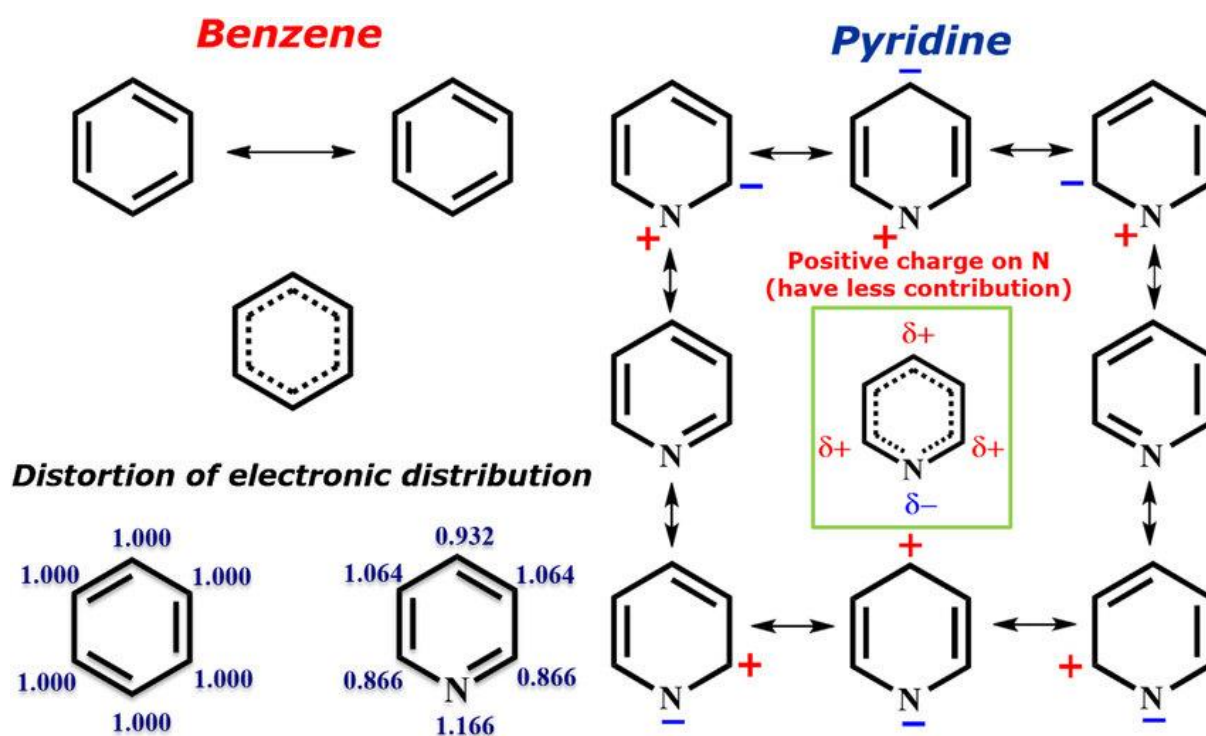


Figure 34 Reproduced from Reddy et al.<sup>39</sup> illustrating the electronic distribution around pyridine rings. Although there are two possible resonance pathways, the scheme depicting a negative charge on the nitrogen is more dominant therefore the overall effect is reduced electron density on the ortho and para positions in respect to the nitrogen.

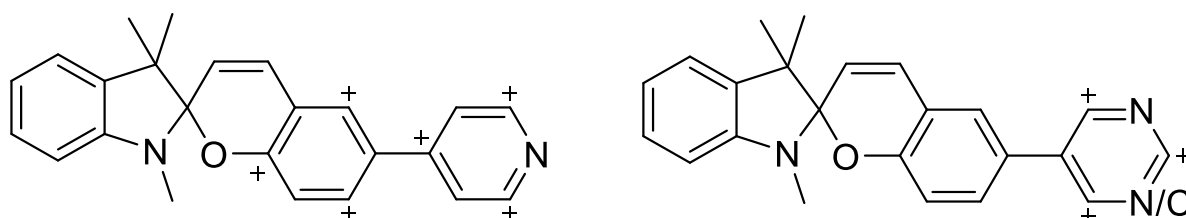


Figure 35 Pyridine/pyrimidine moieties affect the electronic distribution around the rest of the spiropyran molecule. In the case of 4-pyridyl substitution (**4a**, left) the mesomeric effects will extend to the adjacent benzene ring fused to the pyran. In the case of 3-pyridyl/5-pyrimidyl (**4b/4c**, right), the mesomeric effects do not extend to the benzene ring.

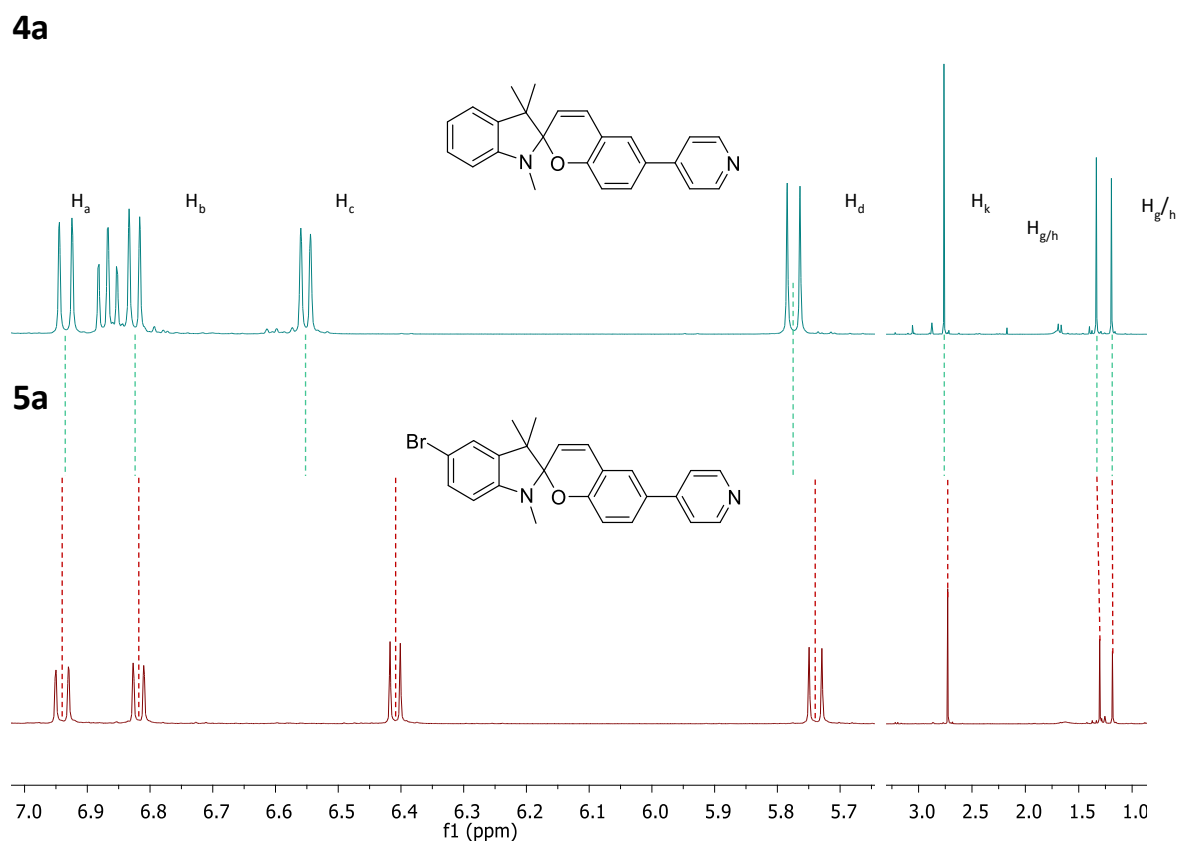


Figure 36 Comparison of peak positions pre/post-bromination.

Molecule	H <sub>a</sub> δ (ppm)	H <sub>b</sub> δ (ppm)	H <sub>c</sub> δ (ppm)	H <sub>d</sub> δ (ppm)	H <sub>k</sub> δ (ppm)	H <sub>g/h</sub> δ (ppm)
<b>4a</b>	6.935	6.825	6.552	5.774	2.762	1.335/1.194
<b>5a</b>	6.940	6.819	6.409	5.739	2.727	1.304/1.184

Table 5 Peak positions of proton environments H<sub>a,b,c,d,k,g/h</sub> of molecules **4a** and **5a**

The most obvious difference between the two spectra is that the ddd peak observed at 6.87 ppm (**4a**) is not present on the brominated molecule (**5a**). As the substitution takes place on the indoline fragment, we would expect the proton environments located on this fragment to be most affected by bromination. *Zakhs et al.* stated they found bromination at the H<sub>l</sub> position (Br<sub>l</sub>) or the addition of any substituents on the chromene ring did not affect the chemical shift of H<sub>k</sub>. Comparison of **4a** and **5a** shows a shift of 0.04 ppm upfield. *Zakhs et al.* used a 60 MHz spectrometer for their measurements and therefore would not be able to resolve this shift clearly to the same precision. Other proton environments located on the indoline fragment also see shifts upfield upon bromination: H<sub>c</sub> shifts 0.15 ppm upfield and H<sub>g/h</sub> also shifts 0.03/0.01 ppm upfield.

On the chromene fragment, the H<sub>b</sub> has a small shift upfield (0.006 ppm). The proton environments around the double bond are again peculiar. H<sub>a</sub> is the one proton environment that we observe to have

a small shift downfield as a result of the bromination but we see quite a large shift upfield for H<sub>d</sub> of 0.04 ppm. H<sub>d</sub> seems to be an environment that is quite sensitive to functionalisation of the spiroopyran molecule. The shifts in opposite directions for H<sub>a</sub> and H<sub>d</sub> are indicative of a mesomeric effect influencing their behaviour, which is also peculiar as the indoline fragment and chromene fragment being orthogonal ought to significantly hinder orbital overlap therefore any mesomeric effects resulting from the bromination were not expected to extend over the spiro centre. Another student in the group calculated the electronic orbitals of **4a** by DFT and found that i) the oxygen lone pair on the chromene is involved in the  $\pi$ -system of the indoline and ii) the  $\pi$  orbitals adjacent to H<sub>d</sub> and H<sub>a</sub> are involved in the  $\pi$ -system of the chromene and the rest of the chromene fragment. Selected orbitals are shown in Figure 37.

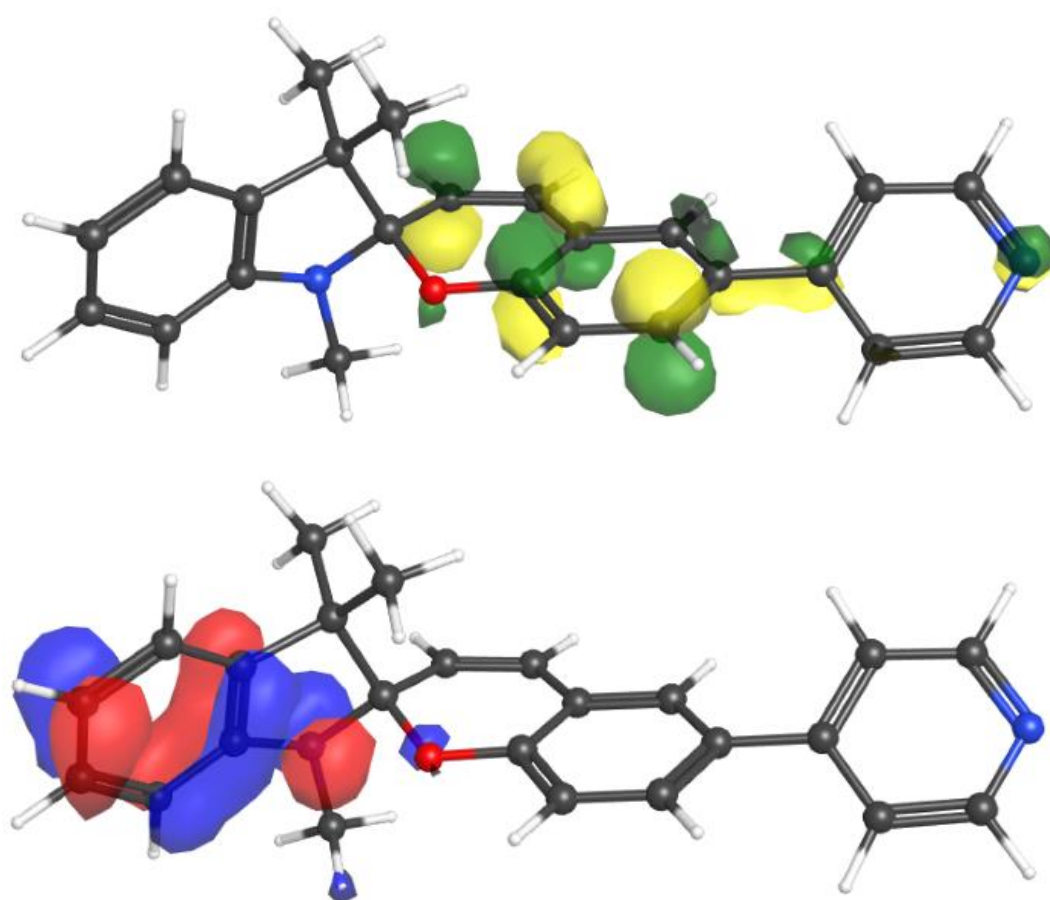


Figure 37 DFT of ligand **4a** displaying LUMO (top) and HOMO (bottom).

On the basis of these calculations, it is perhaps less surprising that H<sub>a</sub> and H<sub>d</sub> can be visibly affected by changes on the indoline side of the molecule.

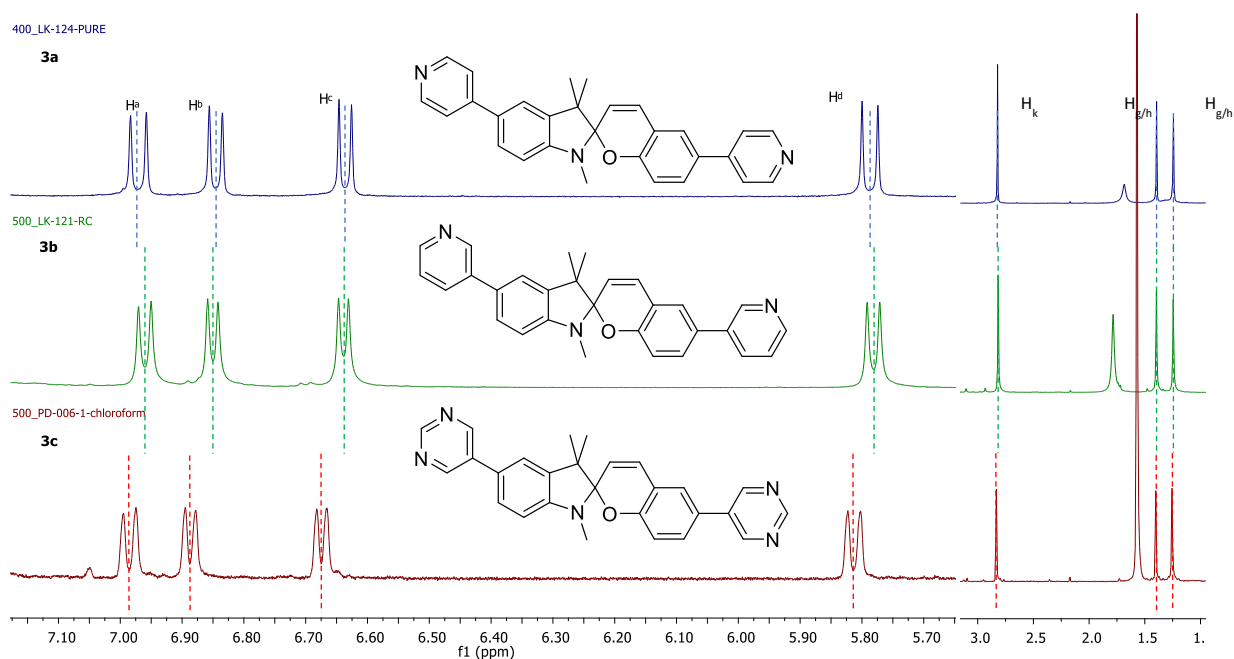


Figure 38 Expansion of  $^1\text{H}$  NMR in  $\text{CDCl}_3$  for **3a**, **3b** and **3c**. Dotted lines show peak centres for the appropriate peaks and are added to demonstrate the shift between NMR spectra.

Molecule	$\text{H}_a$ $\delta$ (ppm)	$\text{H}_b$ $\delta$ (ppm)	$\text{H}_c$ $\delta$ (ppm)	$\text{H}_d$ $\delta$ (ppm)	$\text{H}_k$ $\delta$ (ppm)	$\text{H}_{g/h}$ $\delta$ (ppm)
<b>3a</b>	6.971	6.846	6.636	5.787	2.822	1.394/1.243
<b>3b</b>	6.961	6.868	6.639	5.782	2.817	1.396/1.245
<b>3c</b>	6.984	6.887	6.675	5.813	2.833	1.401/1.256

Table 6 Peak positions of proton environments  $\text{H}_{a,b,c,d,k,g/h}$  of molecules **3a**, **3b** and **3c**.

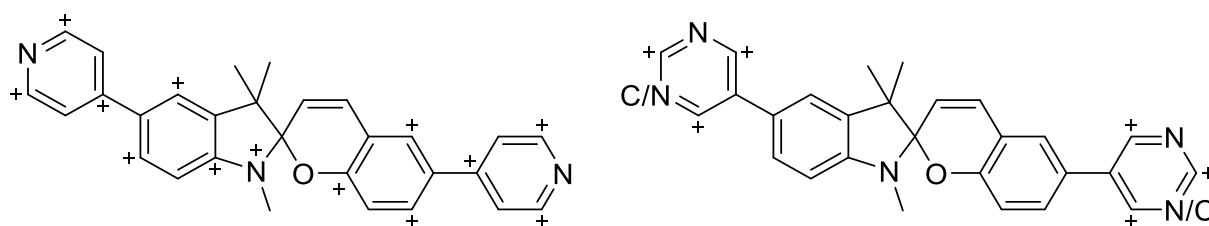


Figure 39 Schematic to demonstrate how functionalisation of the indoline fragment would affect the electronics of the rest of the molecule. In the case of 4,4'-dipyridyl substitution (**3a**, left) the mesomeric effects will extend to the nitrogen atom of the indoline. In the case of 3-pyridyl/5-pyrimidyl (**3b/3c**, right), like **4b/4c** the mesomeric effects do not extend beyond the pyridine/pyrimidine ring.

Comparing **3a** and **3b**, we expect the mesomeric effect of the additional N-heterocycle to extend to the nitrogen atom of the indoline fragment and cause a shift downfield in the case of **3a** of the protons of the adjacent ring (See Figure 39). In the case of  $\text{H}_k$  (located on the N-methyl), **3a** is 0.005 ppm downfield from **3b**, which is what we would expect from the mesomeric effects predicted.

The chemical shift for H<sub>c</sub> is quite negligible when comparing **3a** and **3b** which is in line with what we have observed so far as there is a slight shielding effect (Figure 34) on this position from the mesomeric effect of **3a**. The impact of substitution will be further diluted by the reduced inductive effect by the nitrogen atom being one more bond further away in **3a** versus **3b**. H<sub>g/h</sub> seem to be insensitive to which stereoisomer of pyridine is present, as we saw in the case of **4a** and **4b** earlier. H<sub>b</sub> has a relatively significant shift of 0.022 ppm from **3a** to **3b**, which is peculiar as the position of H<sub>b</sub> hardly changed between **4a** and **4b**, therefore this shift can be attributed to the functionalisation of the indoline fragment. Furthermore, we have typically seen a downfield shift because of the 4-pyridyl moieties when compared with 3-pyridyl however in the case of H<sub>b</sub> the shift is upfield, raising further questions.

Surprisingly, H<sub>d</sub> had a small upfield shift (0.005 ppm) when 4-pyridyl (**3a**) was replaced with 3-pyridyl (**3b**). So far, we have observed H<sub>d</sub> to be quite sensitive to functionalisation of spiropyran. When comparing **4a** and **4b** and also in the case of **4a** and **5a**, in both cases this caused a significant chemical shift. H<sub>a</sub> is also located on the double bond but has been less sensitive to change compared to H<sub>d</sub> in previous examples, but in this case, there is a shift of 0.01 ppm; the first and only instance where the position of the <sup>1</sup>H NMR peak of H<sub>a</sub> has been more affected than H<sub>d</sub>. The electronics around the double bond have been quite difficult to predict with basic fundamental knowledge but play an important part in the ring opening and closing mechanism.

Looking at molecule **3c**, we can see whether the enhanced inductive effects of the additional nitrogens have more of an influence than the mesomeric effects on the selected proton environments. For H<sub>k</sub> the shift when compared to **3b** is even further downfield than that of **3a**, suggesting the inductive effects from the two extra nitrogen atoms from the pyrimidyl moieties have a bigger influence on the electronics of H<sub>k</sub> than the mesomeric effect of **3a**. The H<sub>g/h</sub> has a bigger than usual shift downfield in the case of **3c** compared to **3a** and **3b**; so far we have typically observed this region to be quite insensitive to changes in the electronic environment, with the exception of the brominated molecule **5a**. The position of H<sub>b</sub> in **3c** has shifted further downfield in response to the enhanced electron withdrawing effect of pyrimidine, with the trend of **3c>3b>3a** (in terms of H<sub>b</sub> chemical shift) further demonstrating that inductive effects are the major electronic influencer in this position. Counter-intuitively, when comparing the functionalisation of just the chromene fragment, **4c>4b=4a** which is peculiar as inductive effects work better with proximity, yet functionalisation of the indoline fragment seemed to have a stronger effect. H<sub>c</sub> has behaved in a similar fashion to H<sub>b</sub>, though this is less surprising as H<sub>c</sub> is found on the indoline fragment.



Finally, the alkenyl protons H<sub>a</sub> and H<sub>d</sub> prove to be most sensitive to the change from pyridyl to pyrimidyl functionality. It would be interesting to see whether the electronic effects of these proton environments relate to the photophysical behaviour of the spiropyran molecules.

Although these shifts are discussed at length in this section it should be noted none of them are greater than 0.2 ppm. We might therefore expect any differences in photophysical behaviour to be on a scale that reflects these relatively small differences. Ideally, we would repeat the collection of NMR spectra several times to have a better indicator of whether the observed shifts are genuine, unfortunately this was not possible due to COVID-19. We would encourage the reader to treat this section with a modicum of scepticism and anyone seeking to replicate the experiment to perform repeat measurements.

#### *2.3.3.2 Study of conjugated $\pi$ -systems using UV-Vis spectroscopy*

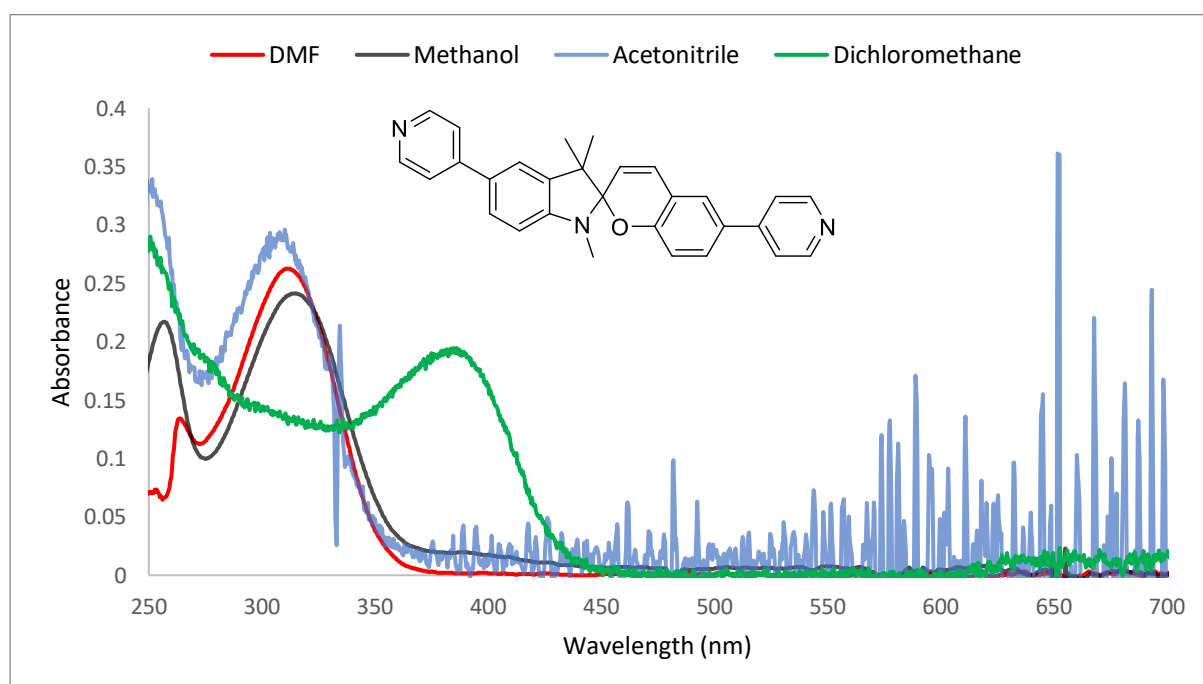
The ultimate aim for synthesising all of these spiropyran molecules is to be incorporated into a metal organic framework, in the hope of synthesising a photodynamic material. To better understand such photodynamic materials, it is important to study the ligands before being incorporated into the framework, as it will help with the characterisation of any materials that may result from this. As such we have studied each of the synthesised ligands using UV-Vis spectroscopy. A secondary aim of this study will be to compare and contrast the different ligands and see how the energy requirements for the photoconversion change according to the type of N-heterocycle substituent that is present.

One of the main absorption profiles under investigation relates to the chromene fragment's  $\pi$ - $\pi^*$  transitions, typically manifesting as an absorption in the 323-351 nm range.<sup>40</sup> Excitation of this wavelength ultimately results in the breaking of the C-O bond and the formation of the merocyanine form. It is well documented that extending the conjugated  $\pi$ -system of the chromene fragment allows longer wavelengths of light to cause photoconversion.<sup>41</sup>

The other peak that is key to understanding a ligand's photophysical profile is the peak typically found around 500-700 nm, which corresponds to the  $\pi$ - $\pi^*$  transition of the conjugated merocyanine molecule. Excitation at this wavelength often triggers the ring closing and reformation of spiropyran.<sup>42</sup> Spiropyran typically does not show significant photoconversion at ambient conditions and the open form is typically short lived (microsecond scale).<sup>43</sup> Studies of the merocyanine form are typically done at or below 77 K to prevent the thermal back conversion.<sup>44</sup> In this work we are interested in the absorption bands directly related to the opening and closing of the spiropyran isomer. We will be ignoring the  $\pi$ - $\pi^*$  electronic transition of the indoline moiety (usually found between 272-296 nm) as it has been reported to have a negligible effect on the ring opening/closing photophysics of the molecule.<sup>5</sup>

### 2.3.3.2.1 Studying the effects of solvatochromism in ligand **3a**

The well-documented solvatochromism of spiropyran led us to choose a selection of solvents to be tested. We used our ligand **3a**, which is exploited in multiple sections in this thesis, to determine what solvent we should use for the rest of the study. We expect any functionality dependent bathochromic or hypsochromic shifts to be on a small scale. To help with this characterisation we have also obtained a UV-Vis absorption spectrum for when the sample has been kept in the dark at  $-20^{\circ}\text{C}$ . The dark should allow each solution to establish a new equilibrium between SP and MC without visible light forcing it back to the SP form; the drop in temperature should also help reduce thermal back conversion. This should allow us to identify the peak relating to the open form, if it is present at all (see Figure 40).<sup>44</sup>



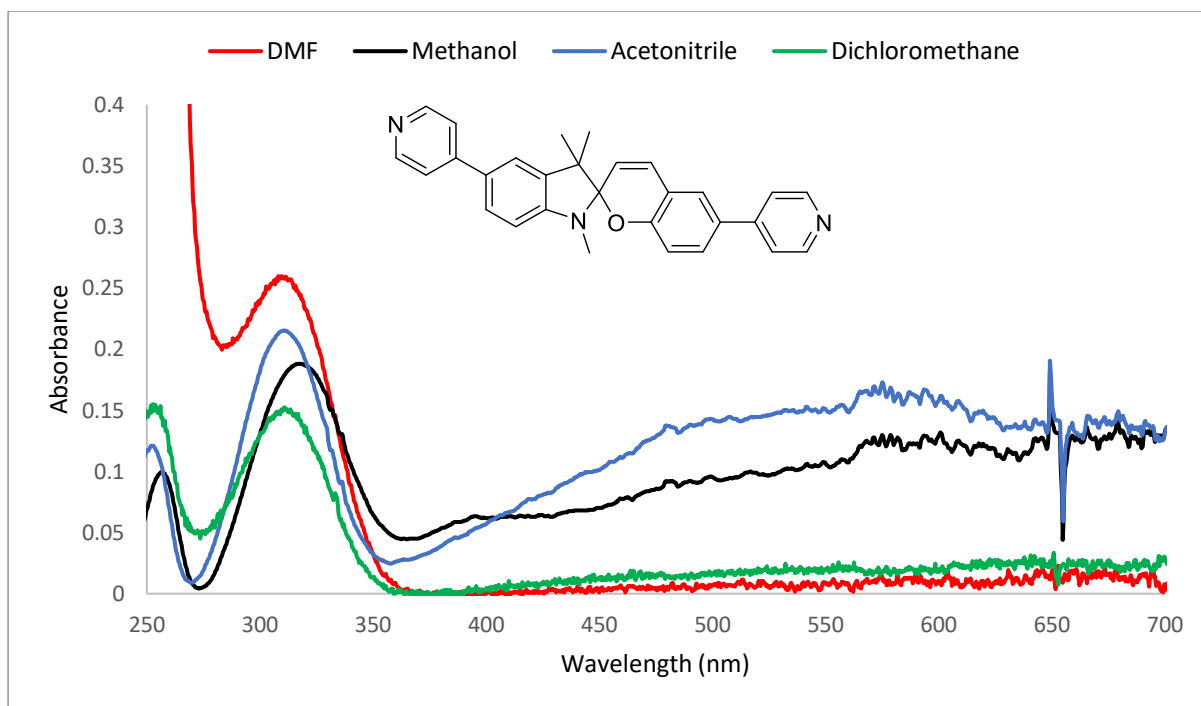
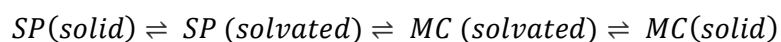


Figure 40 Solution state UV-vis spectra of molecule **4a**. Top: Before recording spectra, solutions left at room temperature in ambient light for 2 days. Bottom: Before recording spectra, solutions kept at  $-20^{\circ}\text{C}$  in the dark for 2 days.

We chose dichloromethane, methanol, acetonitrile and DMF as the solvents to test our ligands in. DMF was chosen because most of our MOF syntheses use DMF and therefore this gives us insight into what state the ligand will be in during framework assembly. Methanol is also used in MOF synthesis and is a good example of a polar, protic solvent. Acetonitrile was included because it is an example of a relatively polar, aprotic solvent. Finally, dichloromethane was included as an example of an aprotic and relatively non-polar solvent.

When the methanol and acetonitrile solutions are kept in the dark, the spectra change. Absorption at longer wavelength ( $> 400$  nm) appears to rise significantly although the band for the  $\pi$ - $\pi^*$  transition of the spiropyran form remains prominent (ca. 315 nm). The spectral profile in the visible region in methanol looks like a rising sloped baseline. In acetonitrile, however, this rising spectrum looks more like an absorption band. A rising baseline can be caused by the presence of particulates in solution or condensation on the cold cuvette (however if it was condensation, we would likely see this rising baseline for the spectra collected using DMF and DCM). There are therefore two possible reasons for the changes observed. Firstly, chilling these solutions has caused the spiropyran molecules to precipitate into a fine suspension. This is unlikely as the solutions were  $0.01 \text{ mmol dm}^{-3}$  which were made up by serial dilution of an unsaturated  $1.0 \text{ mmol dm}^{-3}$  solution. Alternatively, the scattering is representative of merocyanine formation which then forms aggregates causing significant scattering (noisy data) and a rising baseline. The spectra recorded in acetonitrile display scattering in both

ambient and dark conditions, causing a lot of noise in the lower energy region of the spectrum. This is most likely a manifestation of the complex aggregation phenomena exhibited by these molecules (see Figure 41).



*Figure 41 Outlining the equilibrium present when spiropyran is in solvent media. E.g. The polar solvent acetonitrile, would stabilise the polar MC form more than the non-polar SP form, in visible light however the MC form is being forced into the less suited SP form, thus the SP form begins aggregating to better suit the environment.<sup>45</sup>*

This unusual equilibrium (Figure 41) can be observed in the synthesis of ligand **2**, as the recrystallisation using ethanol displays a slight delay upon dissolution of the crude material before the white solid product precipitates. The second possible reason for the rise in visible absorption for methanol and acetonitrile solutions kept in the dark is simply under those conditions a proportion of the spiropyran converts in the polar solvent to the merocyanine form. It is perhaps therefore surprising in DMF the same outcome is not strongly observed.

The spectrum acquired in DCM at ambient conditions is different to the others. The primary peak maximum is observed at 387 nm, significantly lower energy compared with the spectra obtained in the other solvents. This peak is observed in the non-polar aprotic solvent at ambient conditions, but it is not present in the cold, dark conditions. We would not expect to see either the MC form or the protonated MC form in this solvent. Although a protonated form of spiropyran exists, it is typically observed to absorb near 220 nm.<sup>46</sup> Furthermore, *Kortekaas et al.* report that the protonated SP form (SPH<sup>+</sup>) is not observed in aqueous media when the pH is greater than 0.5.<sup>47</sup> The small amounts of HCl that can form due to hydrolysis of dichloromethane (approximately 5-10 mg HCl per 1 kg DCM) is unlikely to lower the pH enough to see the SPH<sup>+</sup> form. Therefore, by process of elimination, this has to be the protonated MCH<sup>+</sup> species. However, why this is observed in DCM in ambient conditions but not the dark is unclear and requires further investigation. In the cold dark solution, the primary absorption peak is at 312 nm, consistent with the spiropyran form as observed in the other solvents.

Solvent	Peak positions recorded in ambient conditions (nm)	Peak positions recorded in the dark at -20°C (nm)	Relative Peak Shifts (nm)
CH <sub>3</sub> CN	309	312, 359-484*	+3, N/A
MeOH	311, 395	320, 365-428*	+9, -30 - +33
DMF	316	312	-4
DCM	280 (shoulder), 387	312	N/A, N/A

*Table 7 Major peak positions recorded obtained from solution state UV-Vis spectra for ligand 3a. Directly comparing peak positions recorded in the dark, at -20°C to ambient conditions. \*Due to scattering, the exact peak position is not known, the possible range of where it can be found is presented instead.*

A closer look at the  $\pi$ - $\pi^*$  transition pertaining to the chromene fragment of the closed form shows how the peak shifts in response to the environment (see Table 7). It has been shown that molecules with a larger conjugated  $\pi$ -electron system like merocyanine can exhibit solvatochromism.<sup>48</sup> The conjugated open form exhibits solvatochromism, therefore only this absorption band should show significant shifts based on polarity and the  $\pi$ - $\pi^*$  transition of the SP form should be relatively unaffected. In order of increasing polarity, the solvents are as follows: DCM < MeOH < CH<sub>3</sub>CN < DMF.<sup>49</sup> Our recorded peak positions show a small bathochromic shift in the SP chromene fragment's absorption band upon increasing solvent polarity (with the exception DCM) under ambient conditions. In the dark this trend is not observed.

In summary, ligand **3a** in acetonitrile aggregated significantly in ambient conditions and in dichloromethane displayed unexpected behaviour. Methanol presented the clearest opportunity to possibly identify multiple species (including the open form) and was chosen to test the rest of the ligands for this reason. Substituent effects based on the functionalisation with 4-pyridyl/3-pyridyl/5-pyrimidyl are anticipated in two ways: electronic impact on the  $\pi$ - $\pi^*$  transition on the chromene fragment, and possible direct hydrogen bonding of the N-heterocyclic nitrogen.

The next logical step is to compare the ligands **4a**, **4b** and **4c**, as these ligands serve as a good comparison of substituent.

#### 2.3.3.2.2 Comparison of stabilising effects of N-heterocycles substituted on the chromene fragment

In a similar format to the NMR study discussed earlier, we compare the UV-vis spectra acquired for ligands **4a**, **4b** and **4c** to investigate how the substituent affects the absorption profile and by extension the ability for the spiro- compounds to open and close (see Figure 47).

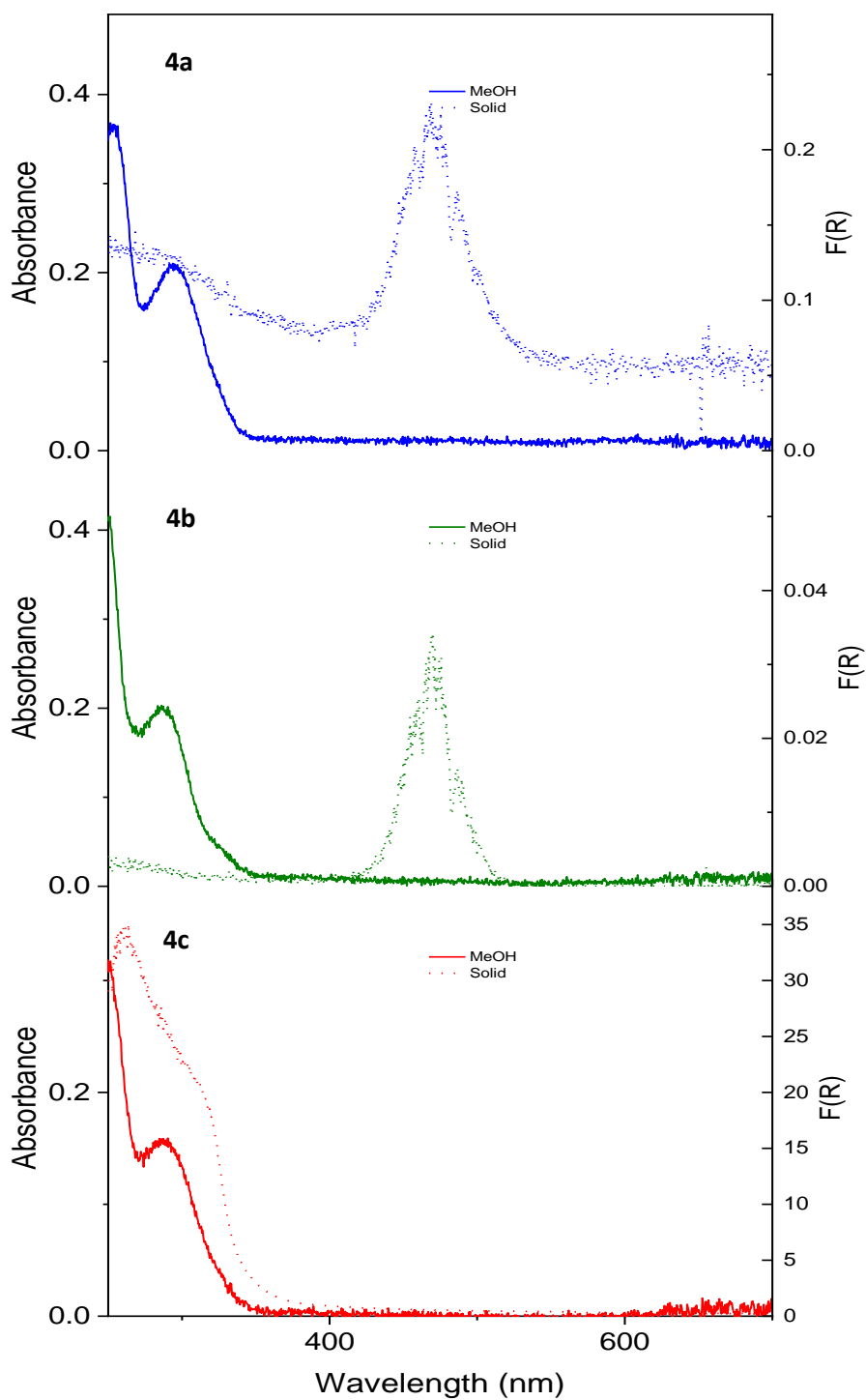


Figure 42 Solution state spectra of molecules 4a (blue), 4b (green), 4c (red) recorded in methanol (solid line) and in the solid state (dashed line). Solution was exposed to ambient conditions (incidental light and room temperature).

Ligand	Peak positions solvent (nm)	Peak positions solid (nm)
<b>4a</b>	296	470
<b>4b</b>	288	468
<b>4c</b>	286	308 (shoulder)

Table 8 Comparison of peak positions observed in spectra regarding ligands **4a**, **4b** and **4c**.

Comparing ligand **4a** to ligands **4b** and **4c** in the solution state, we can clearly observe a hypsochromic shift of 8-10 nm for the latter. Based on the NMR analyses, we would anticipate the **4a** ligand has the greatest electronic conjugation between the 4-pyridyl and the chromene fragment, which is consistent with the lower energy  $\pi$ - $\pi^*$  absorption band observed in the UV-Vis absorption spectrum. The solid-state spectrum acquired for **4c** seems quite informative and, despite the overlap of the indoline and chromene  $\pi$ - $\pi^*$  bands, the presence of primarily the spiro form is still evident. **4a** and **4b** solid state spectra exhibited extremely weak absorption, and very similar spectral profiles, with a band present at 470 nm. On closer inspection, and by comparison of the FWHM we believe these absorption bands to be real and not an artifact of the spectrometer as the FWHM are different (see Figure 43). Having established that these are real absorption bands, it is clear that in the solid state, **4a** and **4b** are in the open merocyanine form. The solid products are formed by recrystallisation with polar solvents, which we have observed can stabilise the merocyanine form and it appears that this is what precipitates for **4a** and **4b**. Considering that **4c** precipitates as the SP form and could be considered structurally very similar, this shows how fine the balance between these states can be.

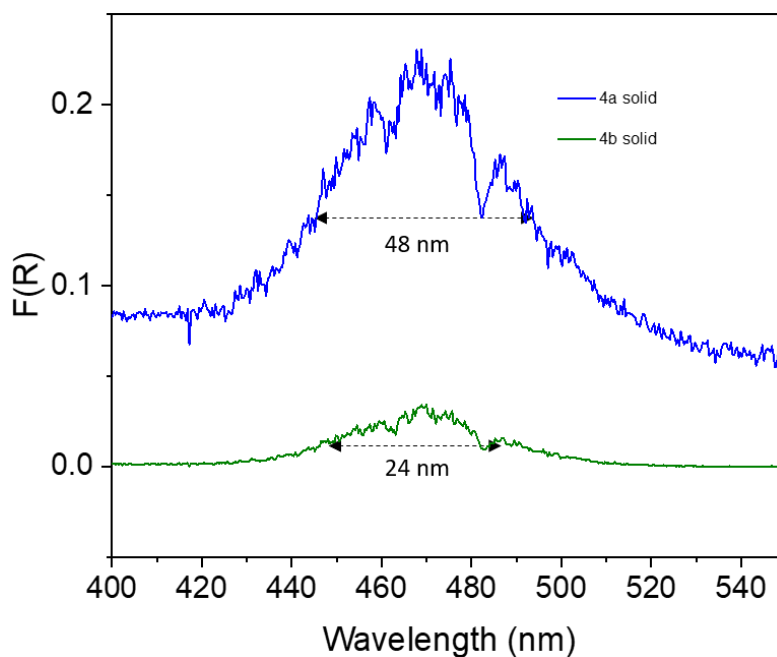


Figure 43 Solid state UV-Vis spectra zoomed in on the 400-550 nm region for ligands **4a** and **4b**.

### 2.3.3.2.3 Effects of bromination

Zakhs *et al.* reported that bromination of the chromene fragment lead to stabilisation of the merocyanine form. Conversely, bromination of the indoline fragment stabilised the spiropyran form.<sup>12</sup> With this in mind we compared the UV-vis spectra of **4a** and **5a** (Figure 44).

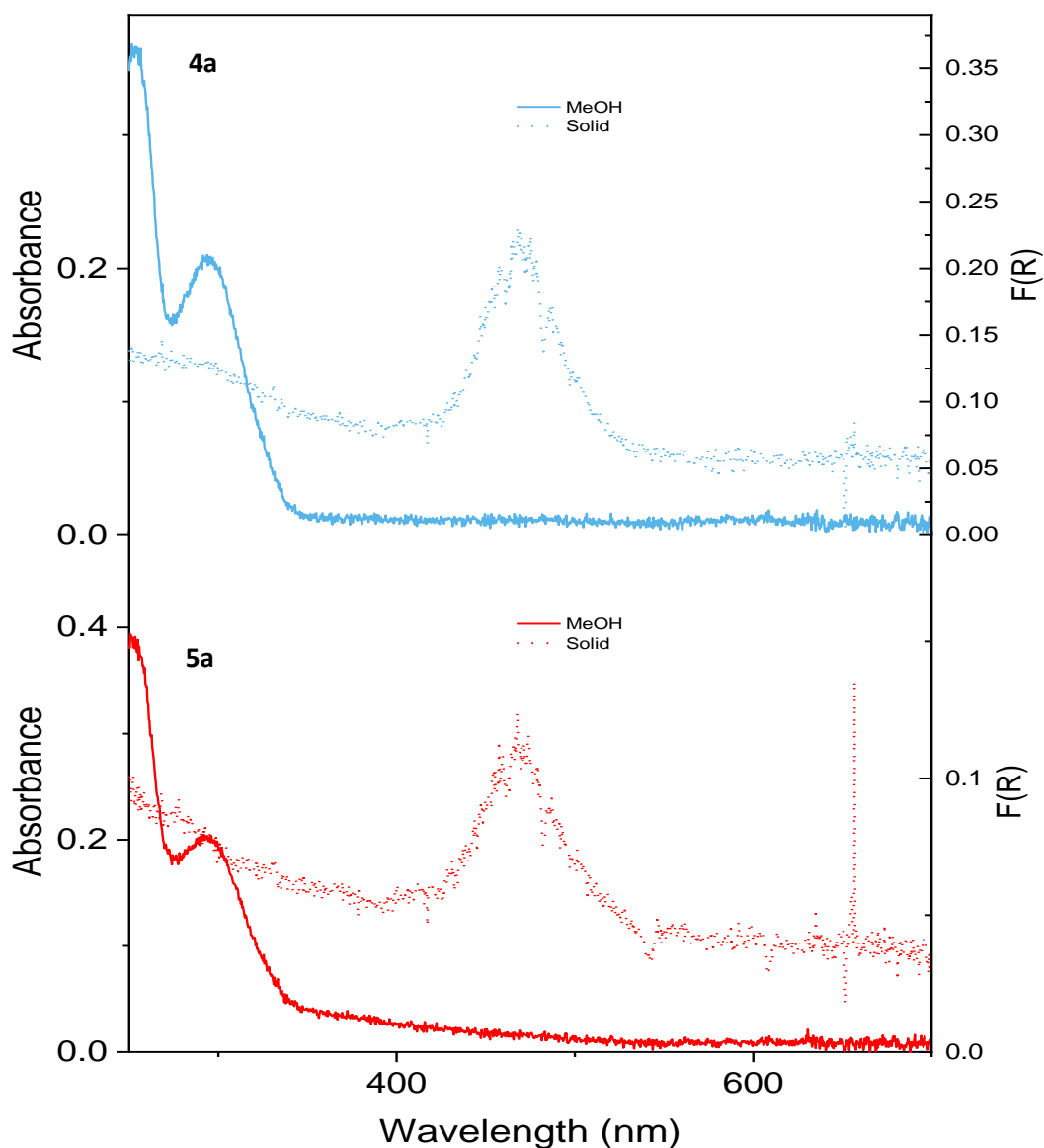


Figure 44 Solution state spectrum of molecules **4a** (blue) and **5a** (red) recorded in MeOH (solid line) and the solid state (dashed line). Solution was exposed to ambient conditions (incidental light and room temperature).

Ligand	Peak positions in solvent (nm)	Peak positions in solid (nm)
<b>4a</b>	296	470
<b>5a</b>	294	468

Table 9 Comparison of peak positions observed in spectra of ligands **4a** and **5a**.



Our NMR study showed that bromination affects the electronics of the ring systems of these molecules, as observed by changes in the proton environments on the indoline fragment but not the chromene fragment. This is consistent with the observation of only very small changes in peak position of the  $\pi$ - $\pi^*$  transition of the chromene fragment (Table 9). As in the case of **4a** and **4b**, the solid-state UV-Vis spectrum of **5a** again primarily shows MC form, with a peak position very close to that of **4a**.

#### 2.3.3.2.4 Comparison of N-heterocycle functionalisation of the indoline fragment on UV-Vis profile.

Continuing with the hypothesis that stabilising the indoline fragment will stabilise the spiropyran form, we would expect that whatever N-heterocycle substituent is present on the indoline fragment to have a greater overall effect on the absorption band observed. We compared the spectral profiles of ligands **3a**, **3b** and **3c** to see how modifying the indoline fragment affects the photophysics of the spiropyran molecule.

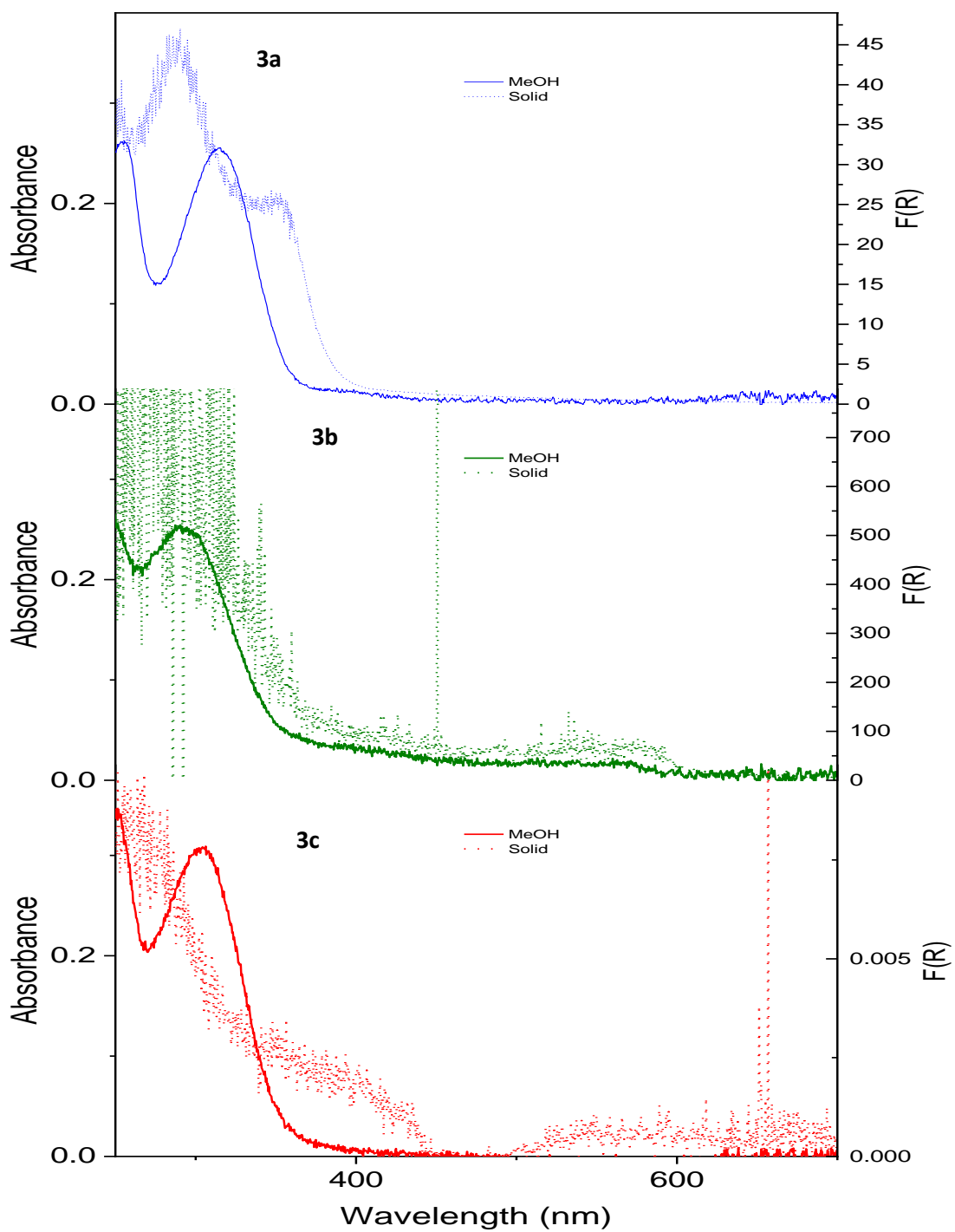


Figure 45 Solution state spectrum of molecules 3a (blue), 3b (green), 3c (red) recorded in MeOH (solid line) and the solid state (dashed line). Solution was exposed to ambient conditions (incidental light and room temperature).

Ligand	Peak positions solvent (nm)	Peak positions solid (nm)
<b>3a</b>	311, 395	289, 357
<b>3b</b>	293, 381	249-325, 499-595
<b>3c</b>	303	304 (shoulder), 393 (shoulder), 494-700

Table 10 Comparison of peak positions observed in spectra of ligands **3a**, **3b** and **3c**.

As before there was very little change observed when comparing **4b** and **4c**. However their counterparts **3b** and **3c** show a significant shift of 10 nm. Furthermore there is a subtle expression of the protonated MC form at 381 nm present in **3b** that is not at all present in **3c**. This suggests that the pyrimidine has a greater stabilising effect on the spiropyran form than the 3-pyridine substituent. Somewhat expectedly, **3a** demonstrates the greatest stabilisation of the spiropyran form and quite a significant bathochromic shift of 15 nm compared to **4a**.

Solid state data of **3a** shows a peak at 357 nm and this could also be a sign of the protonated form of spiropyran. The crystallisation method was a two-solvent system, ethanol and water (both protic solvents), which could explain the protonated form. Neither **3b** or **3c** show this band, though **3c** does show a band at 393 nm which could be the protonated merocyanine form. The presence of SPH<sup>+</sup> and lack of MCH<sup>+</sup> observed in the ssUV-Vis spectrum of **3a** would suggest ligand **3a** shows a higher affinity for the closed form than ligand **3c**. This conclusion however does not corroborate with what is observed in the solution state data.

In conclusion, there is an overall dominance of spiropyran with little contribution of merocyanine at room temperature and at -20 °C. Had there been more time, we would have done a variable temperature UV-Vis study imitating the conditions for a MOF synthesis. There have been instances where the merocyanine form is favoured by high temperatures, where intermolecular interactions with the solvent (e.g. hydrogen bonding) lowers the ground state energy of the MC form to be favourable.<sup>50</sup> If this was the case, then there would be a significant amount of merocyanine present during solvothermal conditions and could affect the outcome of MOF synthesis in some way. We would assume due to the ability for the MC form to bind to bivalent cations, it would have a negative effect, but it is possible that the merocyanine geometry is more favourable for the formation of a MOF.

### 2.3.3.3 Crystal Data

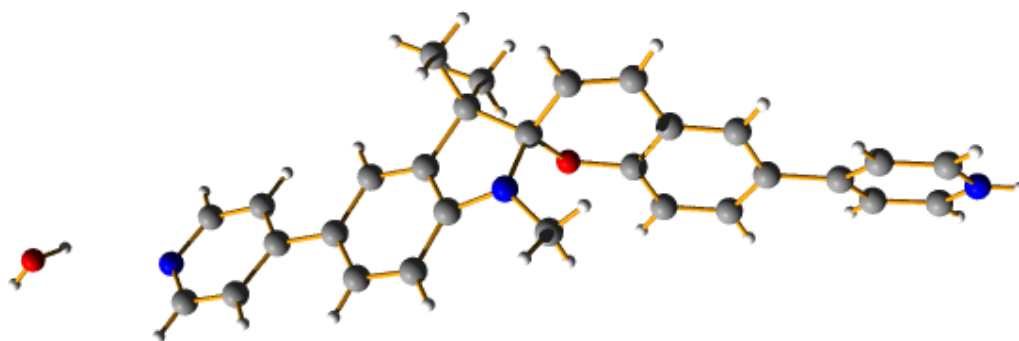


Figure 46 Crystal Structure of spiro[chromene-indole] appended with two 4-pyridyl moieties (**3a**). Carbon (grey), oxygen (red), nitrogen (blue), hydrogen (white).

Obtaining Single Crystal X-Ray Diffraction (SCXRD) data was difficult for these compounds. The usual difficulties of obtaining a good quality crystal are further complicated by the complex equilibrium in play (Figure 41) and combined with the solvatochromism usually result in amorphous/small crystalline materials. This issue is further complicated by these molecules typically displaying disorder, although the solid state spiro[chromene-indole] should not be able to photosynthesise due to close packing effects, there is some flexibility around the spiro-core which can be a source of disorder throughout the crystal. This flexibility is observed in the crystal data for the only spiro[chromene-indole] molecule that was able to provide sufficiently adequate crystal data for, ligand **3a**.

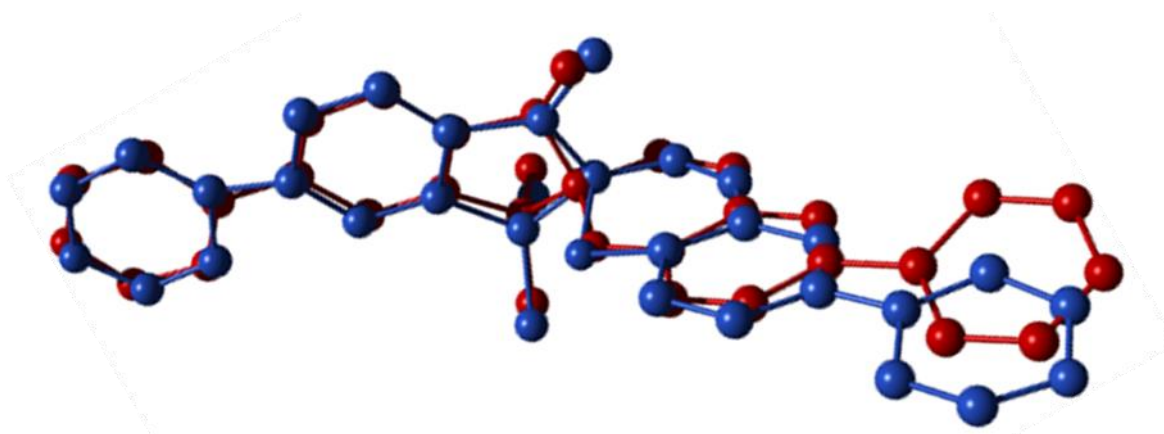


Figure 47 Ligand **3a** crystal structure with both parts overlaid, to demonstrate disorder. The red part is the dominant part shown in Figure 46.

Figure 47 illustrates the disorder present in the **3a** crystal, the indole fragments (including the pyridyl ring) of both forms are mostly overlapping (i.e. same position) however the chromene fragment is in a distinctly different position, further demonstrating the flexibility around the spiro-core. Typically, the disorder in photoactive molecules is resolved by ablating the crystal with a sufficiently powerful

light source, to force it all into one form however what we are observing is not a direct result of the photoisomerism and therefore this tactic will not work. All of the novel ligands we have synthesised feature largely similar structures at the chromene fragment and therefore it is likely that this type of disorder is present for all crystals of these ligands.

## 2.4 Summary and conclusions

We have synthesised nine novel spiropyran molecules featuring N-heterocycles. We have established a general method to couple N-heterocycles to spiropyran molecules that used the Pd(dppf) catalyst. Suzuki cycles and brominations involving the 3-pyridyl moiety saw significant reductions in yield, which can be a problem in Suzuki cross couplings, it is less obvious as to why this is the case for the bromination step. The NMR study on how different N-heterocycles affected the electronics of the indoline and chromene fragments shown that the 4-pyridine moiety had the greatest influence, as we expected due to its enhanced conjugation. It also revealed to what extent functionalising the chromene fragment affected the proton environments on the indoline fragment and vice versa. This corroborated the results from the UV-vis study as the **3a** ligand had the longest wavelength for absorption and therefore the lowest energy  $\pi$ - $\pi^*$  transition state. The solid-state UV-vis was not as conclusive as we would have liked, it is very possible that the less conclusive spectra (**4a**, **4b**, **5a**) were more a result of the method of crystallisation rather than the different functionalities present. However the solution-state behaviour of **3a** was peculiar as the MC form seem to be more expressed in the non-polar solvent DCM than the others. Typically, the MC form is only favoured if it has the ability to form hydrogen bonds in the solvent, therefore it is unclear as to what interactions are present that are causing these results although we have tried to explain possible causes, it is not yet conclusive.

We have achieved our primary objective of successfully synthesising a sizeable library of spiropyran ligands that would be suitable for the synthesis of a MOF and we shall discuss the outcomes of those attempts in the next chapter.

## 2.5 Experimental

### 2.5.1 Characterisation techniques

#### 2.5.1.1 NMR

$^1\text{H}$  and  $^{13}\text{C}$  nuclear magnetic resonance (NMR) spectra were recorded on either a Bruker 400 MHz UltraShield<sup>TM</sup> or a Bruker 500 MHz Avance NMR spectrometer. The obtained chemical shifts ( $\delta$ ) are reported in ppm and are referenced to the residual solvent signal. Spin-spin coupling constants (J) are given in Hz.

#### 2.5.1.2 Mass spectrometry

Mass spectra were obtained by Analytical Services using a Xevo G2-XS QToF Quadrupole Time-of-Flight Mass Spectrometer.

#### 2.5.1.3 Infra-red spectroscopy

A SHIMADZU IRAffinitt-1S spectrometer was used to collect IR data, scanning between 500 – 4000  $\text{cm}^{-1}$  and averaging 16 scans.

#### 2.5.1.4 SCXRD

This is discussed in the experimental section of chapter 3.

#### 2.5.1.5 Solution state UV-Vis spectroscopy

Spectra were recorded with Optics USB2000+UV-VISES spectrometer using a DT-MINI-2-GS light source; solution state UV-vis spectra were obtained in a quartz cuvette (path length 1.0 cm) placed in a CUV 1 cm cuvette holder with P200-2 transmission fibre optic and recorded in absorbance (A) mode.

For a low temperature ( $-20^{\circ}\text{C}$ ) spectral acquisition, the solution was kept in a 10 mL volumetric flask wrapped in tin foil and left in the freezer for two days. The solution was then transferred quickly to a cuvette and the spectrum was recorded. The spectrometer equipment was at room temperature and therefore there will be small variations in temperature between the events of leaving the freezer and recording the spectrum.

#### 2.5.1.6 Solid state UV-Vis spectroscopy

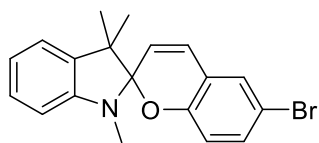
Discussed in the experimental section of chapter 3.

### 2.5.2 Ligand synthesis

All chemicals were of reagent-grade quality and used as received. 1,1'-Bis(diphenylphosphino)ferrocene palladium (II) dichloride ( $\text{Pd}(\text{dppf})\text{Cl}_2$ ), trisdibenzylideneacetone)dipalladium(0) ( $\text{Pd}_2\text{DBA}_3$ ), the boronic acid reagents, potassium triphosphate, 1,4 Dioxane and tricyclohexylphosphine ( $\text{PCy}_3$ ) were bought from Fluorochem.

N-bromosuccinimide, dimethoxyethane, tri-tert-butylphosphine ( $\text{P}(\text{t-Bu})_3$ ) in toluene (1.0M) and 1,3,3-trimethyl-2-methyleneindoline were purchased from Sigma Aldrich. 5-bromosalicylaldehyde was purchased from Acros Organics. All other metal salts that have not been specifically mentioned were bought from Alfa Aesar. Chloroform, ethanol and toluene were obtained from Fisher Scientific.

### 6-Bromo-1',3',3'-trimethylspiro[chromene-2,2'-indoline] (**1**)

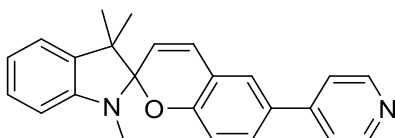


To a solution of 5-bromosalicylaldehyde (17.04 g, 85 mmol) in EtOH (250 mL), 1,3,3-trimethyl-2-methyleneindoline (15 mL, 85 mmol) was added. The purple solution was heated to reflux for 16 hours. The reaction was allowed to cool and then left in a freezer (-20°C) overnight and the precipitate collected by filtration and washed with ethanol to yield **1** as a pale pink solid (27.85 g, 78.2 mmol, 92%).

<sup>1</sup>H NMR (400 MHz, CDCl<sub>3</sub>) 1.16 (3H, s, CH<sub>3</sub>), 1.29 (3H, s, CH<sub>3</sub>), 2.72 (3H, s, CH<sub>3</sub>), 5.72 (1H, d, J = 10.0, CH), 6.54 (1H, d, J = 7.6, CH), 6.60 (1H, d, J = 9.2, CH), 6.78 (1H, d, J = 10.4, CH), 6.86 (1H, dd, J = 7.6, 7.2, CH), 7.07 (1H, d, J = 7.2, CH), 7.18 (3H, m, CH)

HRMS (ES): m/z 356.0635, calculated 355.0572

### 1',3',3'-trimethyl-6-(pyridin-4-yl)spiro[chromene-2,2'-indoline] (**4a**)



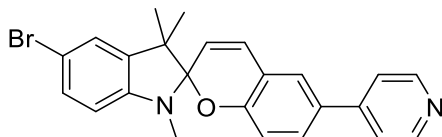
A solution of **1** (5.00 g, 14.0 mmol), 4-pyridinylboronic acid (1.8 g, 14.6 mmol), K<sub>3</sub>PO<sub>4</sub> (4.49 g, 21.2 mmol) dissolved in a mixture of 1,4-dioxane (200 mL) and H<sub>2</sub>O (50 mL) was sparged with nitrogen for 30 mins at 60°C. To this stirring degassed solution was added [1,1'-bis(diphenylphosphino)ferrocene]palladium(II) dichloride (0.5g, 0.68 mmol) and the resulting mixture was heated to reflux at 80 °C for 21 hours under nitrogen. After 21 hours the reaction mixture was filtered whilst hot before the solvent was removed *in vacuo* to yield a brown precipitate. The precipitate was extracted with DCM. The solvent was removed *in vacuo* and the resulting brown precipitate was purified *via* column chromatography (98% DCM: MeOH 1%: Et<sub>3</sub>N 1%) followed by recrystallization from acetone and H<sub>2</sub>O to yield the product as a pale brown powder. (3.82 g, 10.8 mmol, 77%)

<sup>1</sup>H NMR (500 MHz, CDCl<sub>3</sub>) 1.19 (3H, s, CH<sub>3</sub>), 1.33 (3H, s, CH<sub>3</sub>), 2.79 (3H, s, CH<sub>3</sub>), 5.76 (1H, d, J = 10.0, CH), 6.56 (1H, d, J = 8.0, CH), 6.83 (1H, d, J = 8.0, CH), 6.87 (1H, ddd, J = 7.5, 7.5, 0.5, CH), 6.93 (1H, d, J = 10.0, CH), 7.09 (1H, ddd, J = 7.0, 1.0, 0.5, CH), 7.20 (1H, ddd, J = 8.0, 8.0, 1.5, CH), 7.35 (1H, d, J = 2.0, CH), 7.41 (1H, dd, J = 8.0, 2.0, CH), 7.50 (2H, dd, J = 4.5, 1.5, CH), 8.61 (2H, J = 5, 1.5, CH)

<sup>13</sup>C NMR (126 MHz, CDCl<sub>3</sub>) 20.26, 26.02, 29.07, 52.06, 104.94, 107.03, 115.91, 119.44, 119.46, 120.50, 121.05, 121.67, 125.33, 127.82, 128.45, 129.24, 147.84, 148.22, 150.34, 155.71

MS (ES): m/z 355.1813, calculated 354.1732

#### 5'-bromo-1',3',3'-trimethyl-6-(pyridin-4-yl)spiro[chromene-2,2'-indoline] (**5a**)



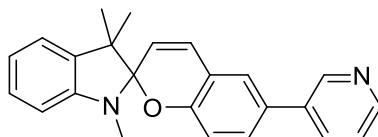
To a stirring solution of **4a** (0.8 g, 2.26 mmol) dissolved in CHCl<sub>3</sub> (100 mL) was added N-bromosuccinimide (NBS) (0.4 g, 2.25 mmol) and the solution stirred under ambient conditions for 6 days. Once reaction had gone to completion (monitored via NMR), the solution was extracted with water. The CHCl<sub>3</sub> was then removed in vacuo to yield a red-brown oil. This oil was then recrystallised via slow evaporation using diethyl ether to yield **5a** as a pale brown-red powder. (0.93g, 2.15 mmol, 95%)

<sup>1</sup>H NMR (500 MHz, CDCl<sub>3</sub>) 1.18 (3H, s, CH<sub>3</sub>), 1.30 (3H, s, CH<sub>3</sub>), 2.73 (3H, s, CH<sub>3</sub>), 5.74 (1H, d, J = 10.5, CH), 6.41 (1H, d, J = 8.5, CH), 6.82 (1H, d, J = 8.5, CH), 6.94 (1H, d, J = 10.0, CH), 7.16 (1H, d, J = 2.0, CH), 7.27 (1H, dd, J = 8.0, 2.0, CH), 7.35 (1H, d, J = 2.5, CH), 7.42 (1H, dd, J = 8.5, 2.5, CH) 7.45 (2H, d, J = 4.5, CH) 8.62 (2H, s, CH)

<sup>13</sup>C NMR (126 MHz, CDCl<sub>3</sub>) 20.09, 25.85, 29.11, 52.12, 104.93, 108.54, 111.18, 115.88, 119.29, 119.88, 121.10, 124.99, 125.43, 128.62, 129.55, 130.20, 130.42, 139.13, 147.34, 147.80, 150.30, 155.36

MS (ES): m/z 433.0917, calculated 432.0837

#### 1',3',3'-trimethyl-6-(pyridin-3-yl)spiro[chromene-2,2'-indoline] (**4b**)



A solution of **1** (2.50 g, 7.0 mmol), 3-pyridinylboronic acid (1.8 g, 14.6 mmol), K<sub>3</sub>PO<sub>4</sub> (4.49 g, 21.2 mmol) dissolved in a mixture of 1,4-dioxane (200 mL) and H<sub>2</sub>O (50 mL) was sparged with nitrogen for 30 mins at 60°C. [1,1'-Bis(diphenylphosphino)ferrocene]palladium(II) dichloride (0.5g, 0.68 mmol) was then added and the resulting mixture was heated to reflux at 80 °C for 21 hours under nitrogen. The reaction mixture was filtered whilst hot before the solvent was removed *in vacuo* to yield a brown precipitate. The precipitate was then extracted with DCM. The solvent was removed *in vacuo* and the resulting brown precipitate was purified *via* column chromatography (98% DCM: MeOH 1%: Et<sub>3</sub>N



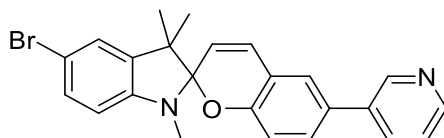
1%). The product was then recrystallised with EtOH and H<sub>2</sub>O to yield the product as a pale brown powder. (0.77 g, 2.2 mmol, 31%)

<sup>1</sup>H NMR (500 MHz, CDCl<sub>3</sub>) 1.19 (3H, s, CH<sub>3</sub>), 1.34 (3H, s, CH<sub>3</sub>), 2.75 (3H, s, CH<sub>3</sub>), 5.76 (1H, d, J = 10.5, CH), 6.55 (1H, d, J = 8.0, CH), 6.82 (1H, d, J = 8.5, CH), 6.86 (1H, ddd, J = 8.0, 8.0, 1.0, CH), 6.93 (1H, d, J = 10.0, CH), 7.09 (1H, ddd, J = 7.0, 1.5, 0.5, CH), 7.19 (1H, ddd, J = 7.5, 7.5, 1.0, CH), 7.27 (2H, dd, J = 7.0, 2.5, CH), 7.32 (2H, m, CH), 7.81 (2H, ddd, J = 8.0, 2.0, 2.0, CH), 8.80 (1H, d, J = 2.0, CH)

<sup>13</sup>C NMR (126 MHz, CDCl<sub>3</sub>) 20.26, 25.99, 29.07, 51.99, 104.77, 106.98, 115.85, 119.37, 119.41, 120.36, 121.65, 125.38, 127.77, 128.34, 128.54, 129.15, 129.29, 129.78, 133.87, 136.74, 147.94, 148.23, 154.86

MS (ES): m/z 355.1813, calculated 354.1732

#### 5'-bromo-1',3',3'-trimethyl-6-(pyridin-3-yl)spiro[chromene-2,2'-indoline] (**5b**)



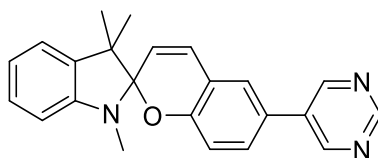
To a stirring solution of **4b** (0.7 g, 1.97 mmol) dissolved in CHCl<sub>3</sub> (50 mL) was added N-bromosuccinimide (NBS) (0.35 g, 1.97 mmol) and the solution stirred under ambient conditions for 6 days. Once reaction had gone to completion (monitored via NMR), the solution was extracted with water. The CHCl<sub>3</sub> was then removed in vacuo to yield a brown oil. This oil was then recrystallised via good-bad solvent, DCM and hexane to yield **5b** as a dark red powder. (0.40g, 0.92 mmol, 47%)

<sup>1</sup>H NMR (500 MHz, (CD<sub>3</sub>)<sub>2</sub>SO) 1.12 (3H, s, CH<sub>3</sub>), 1.24 (3H, s, CH<sub>3</sub>), 2.67 (3H, s, CH<sub>3</sub>), 5.84 (1H, d, J = 10.5, CH), 6.56 (1H, d, J = 8.0, CH), 6.82 (1H, d, J = 8.5, CH), 7.11 (1H, d, J = 10.5, CH), 7.27 (1H, dd, J = 8.0, 2.0, CH), 7.29 (1H, dd, J = 2.0, 2.0, CH), 7.44 (1H, dd, J = 7.5, 4.5, CH), 7.48 (1H, dd, J = 8.5, 2.0, CH), 7.61 (1H, d, J = 2.5, CH), 8.01 (1H, dt, J = 8.0, 2.0, CH), 8.51 (1H, d, J = 5.0), 8.84 (1H, d, J = 1.5, CH)

<sup>13</sup>C NMR (126 MHz, CDCl<sub>3</sub>) 19.57, 25.35, 28.62, 51.71, 100.36, 104.32, 108.83, 110.08, 115.13, 119.04, 123.80, 124.65, 125.51, 128.33, 128.94, 129.27, 129.51, 130.06, 133.47, 139.11, 147.14, 147.19, 147.86, 153.94

MS (ES): m/z 433.0908, calculated 432.0837

### 1',3',3'-trimethyl-6-(pyrimidin-5-yl)spiro[chromene-2,2'-indoline] (4c)



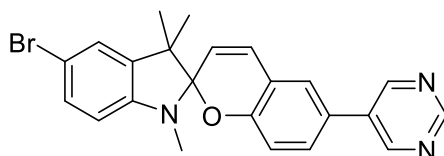
A solution of **1** (0.50 g, 1.4 mmol), 4-pyridinylboronic acid (0.2 g, 1.61 mmol),  $K_3PO_4$  (0.90 g, 4.24 mmol) dissolved in a mixture of 1,4-dioxane (40 mL) and  $H_2O$  (10 mL) was sparged for 20 minutes at 60°C. [1,1'-Bis(diphenylphosphino)ferrocene]palladium(II) dichloride (0.05g, 0.07 mmol) was added and the resulting mixture was heated to reflux at 80 °C for 24 hours under nitrogen (monitored by TLC). Once the reaction had gone to completion, the mixture was filtered whilst hot before the solvent was removed by rotary evaporation to yield a green precipitate. The precipitate was dissolved in DCM and extracted with  $H_2O$  (3X200 mL). The solvent was removed from the organic layer by rotary evaporation and the resulting brown precipitate was purified *via* column chromatography (97% DCM: MeOH 2%:  $Et_3N$  1%) followed by recrystallisation from the minimum amount of ethanol and using  $H_2O$  as an antisolvent to yield the product as a pale brown powder. (0.27 g, 0.76 mmol, 54%)

$^1H$  NMR (500 MHz,  $CDCl_3$ ) 1.19 (3H, s,  $CH_3$ ), 1.33 (3H, s,  $CH_3$ ), 2.76 (3H, s,  $CH_3$ ), 5.79 (1H, d,  $J = 10.5$ , CH), 6.55 (1H, d,  $J = 7.5$ , CH), 6.87 (2H, m), 6.94 (1H, d,  $J = 10.5$ , CH), 7.09 (1H, d,  $J = 7.0$ , CH), 7.20 (1H, ddd,  $J = 8.0, 8.0, 1.0$ , CH), 7.26 (1H, m, CH), 7.32 (1H, dd,  $J = 8.5, 1.5$ , CH), 8.90 (2H, s, CH), 9.15 (1H, s, CH)

$^{13}C$  NMR (126 MHz,  $CDCl_3$ ) 20.06, 25.85, 29.12, 52.15, 104.98, 105.29, 108.57, 108.62, 111.24, 116.26, 116.67, 119.67, 120.21, 125.01, 125.36, 126.40, 128.57, 129.32, 130.45, 139.07, 154.51, 155.32, 157.11

MS (ES):  $m/z$  356.1765, calculated 355.4410

### 5'-bromo-1',3',3'-trimethyl-6-(pyrimidin-5-yl)spiro[chromene-2,2'-indoline] (5c)



To a stirring solution of **4c** (1.0 g, 2.8 mmol) dissolved in  $CHCl_3$  (50 mL), NBS (0.5 g, 2.8 mmol) was added and the solution was stirred at room temperature for 5 days. The reaction was monitored by  $^1H$  NMR to determine when the reaction had reached completion. The solution was extracted with  $H_2O$ . The solvent was then removed from the organic layer *in vacuo* to yield a red solid. Followed by

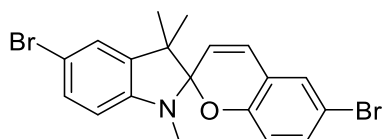
recrystallisation from the minimum amount of ethanol and using H<sub>2</sub>O as an antisolvent to yield a red solid. (1.0 g, 2.30 mmol, 80%)

<sup>1</sup>H NMR (500 MHz, CDCl<sub>3</sub>) 1.19 (3H, s, CH<sub>3</sub>), 1.31 (3H, s, CH<sub>3</sub>), 2.73 (3H, s, CH<sub>3</sub>), 5.76 (1H, d, J = 10.5, CH), 6.40 (1H, d, J = 8.0, CH), 6.84 (1H, d, J = 8.5, CH), 6.94 (1H, d, J = 8.5, CH), 7.16 (1H, d, J = 2.0, CH), 7.28 (1H, dd, J = 8.5, 2.0, CH), 7.33 (1H, dd, J = 8.0, 2.0, CH), 8.89 (2H, s, CH), 9.15 (1H, s, CH)

<sup>13</sup>C NMR (126 MHz, CDCl<sub>3</sub>) 20.08, 25.84, 29.11, 52.17, 104.98, 108.56, 111.24, 116.26, 119.67, 120.21, 125.00, 125.35, 126.39, 128.56, 129.35, 130.44, 133.98, 139.07, 147.31, 154.51, 155.32, 157.10

MS (ES): m/z 434.0869, calculated 433.0790

### 5',6-dibromo-1',3',3'-trimethylspiro[chromene-2,2'-indoline] (**2**)



#### Room Temperature Method:

**1** (19.62 g, 55.1 mmol) was dissolved in chloroform (400 mL) to form a dark red solution. N-bromosuccinimide (9.789 g, 55.0 mmol) was then added to the solution, forming a suspension. The mixture was left to stir at RT for 12 hours. The mixture was filtered, an orange precipitate was removed, and a brown filtrate obtained. The brown filtrate was then washed twice with water followed by brine, the solvent was then removed from the organic layer, leaving a brown residue. The residue is then dissolved in ethanol, additional ethanol is added while the solution is agitated till **2** crashed out as a white precipitate. (13.67 g, 31.4 mmol, 57 %)

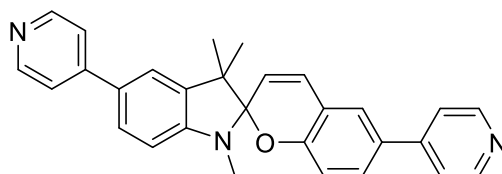
#### Heated Method:

**1** (7.84 g, 22.02 mmol) was dissolved in chloroform (60 mL) to form a dark red solution and heated to 60°C. N-bromosuccinimide (3.84 g, 21.58 mmol) was dispersed in chloroform (400 mL) and added dropwise over 1 hour and heated for a further 30 minutes. The mixture was filtered, an orange precipitate was removed and a brown filtrate obtained. The brown filtrate was then washed twice with water followed by brine, the solvent was then removed from the organic layer, leaving a brown residue. The residue is then dissolved in ethanol, additional ethanol is added while the solution is agitated till **2** crashed out as a white precipitate. (7.755 g, 17.83 mmol, 81%)

<sup>1</sup>H NMR (400 MHz, CDCl<sub>3</sub>) δ 1.15 (3H, s, CH<sub>3</sub>), 1.26 (3H, s, CH<sub>3</sub>), 2.69 (3H, s, CH<sub>3</sub>), 5.69 (1H, d, CH<sub>2</sub>, 10.4), 6.39 (1H, d, J = 8.4, CH<sub>2</sub>), 6.59 (1H, d, J = 9.2, CH<sub>2</sub>), 6.79 (1H, d, J = 10.0), 7.16 (3H, m, CH), 7.26 (1H, dd, CH, J = 8, 1.6)

MS (ESI): m/z 435.9739, calculated 432.9677

**1',3',3'-trimethyl-5',6-di(pyridin-4-yl)spiro[chromene-2,2'-indoline] (3a)**



**2** (5 g, 11.5 mmol), tripotassium phosphate (9 g, 42.4 mmol) and 4-pyridyl-boronic acid (4 g, 32.5 mmol) was dissolved in 1,4-dioxane (200 mL) and deionised water (50 mL). Reaction is sparged with N<sub>2</sub> for 30 mins at 60°C. [1,1'-Bis(diphenylphosphino)ferrocene]palladium(II) dichloride (1 g, 1.37 mmol) was then added and the reaction was heated to 80°C for 24 hours under an N<sub>2</sub> atmosphere. The mixture is then filtered while hot and the solid is washed with dichloromethane. The brown filtrate is then reduced to dryness, to remove the 1,4-dioxane, leaving a brown residue. The residue is then dissolved in dichloromethane and washed with water twice, followed by brine. The organic layer is reduced and product purified by column chromatography (95% DCM: 4% MeOH: 1% NEt<sub>3</sub>). The crude product is then recrystallised from ethanol and water to give **3a** as pale brown crystals. (2.00 g, 4.63 mmol, 40%)

<sup>1</sup>H NMR (400 MHz, CDCl<sub>3</sub>) δ 1.24 (3H, s, CH<sub>3</sub>), 1.39 (3H, s, CH<sub>3</sub>), 2.82 (3H, s, CH<sub>3</sub>), 5.77 (1H, d, J = 10.4, CH), 6.64 (1H, d, J = 8.0, CH), 6.85 (1H, d, J = 8.4, CH), 6.97 (1H, d, J = 10.0, CH), 7.38 (2H, m, CH), 7.43 (1H, dd, J = 8.8, 2.4, CH), 7.45 (2H, m, CH), 7.50 (2H, m, CH), 7.53 (1H, dd, J = 8, 1.6, CH), 8.61 (4H, m, CH)

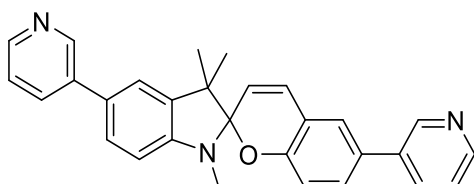
<sup>13</sup>C NMR (101 MHz, CDCl<sub>3</sub>) δ 20.27, 26.12, 29.09, 52.08, 104.99, 107.32, 115.90, 119.30, 119.92, 120.99, 121.07, 124.46, 125.45, 125.82, 127.13, 128.62, 129.18, 129.56, 130.25, 137.86, 148.78, 149.31, 150.21, 150.35, 155.42

MS (ESI): m/z 432.2076, calculated 431.1998

Single crystals of **3a** were recrystallised by slow evaporation in ethanol. A colourless crystal was selected, mounted in fomblin on a micromount and flash frozen under a cold nitrogen stream on an Agilent SuperNova Dual Atlas four-circle diffractometer using Mo-K $\alpha$  radiation and a CCD detector. Measurements were taken at 150 K with temperatures maintained using an Oxford cryostream. Solved by direct methods using Olex2 [30], with the ShelXT and ShelXS structure solution program, refined with the ShelXL refinement package using least-squares minimization. Bond lengths on the pyridine rings were restrained using the SAME command for each pyridine, e.g. for the pyridine ring on the indoline fragment in part 1 "SAME 0.02 0.04 N31A C36A C35A C34A C33A C32A SAME 0.02 0.04

N31A > C36A". Disorder was modelled for the whole molecule in a slightly different conformation isotropically (part 2). Part 1 used the RIGU command on the atoms in the pyridine ring on the indoline fragment. Part 2 used RIGU on geminal methyl groups on the indoline fragment and AFIX 66 commands to constrain each phenyl ring and restrained with a FLAT command. Further details can be found in the appendix.

**1',3',3'-trimethyl-5',6-di(pyridin-3-yl)spiro[chromene-2,2'-indoline] (3b)**



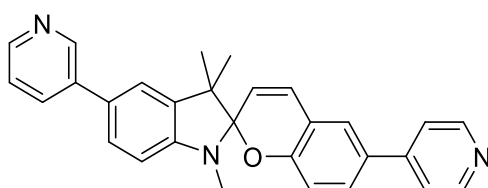
**2** (5g, 11.5 mmol), tripotassium phosphate (9 g, 42.4 mmol) and 3-pyridyl boronic acid (4 g, 32.5 mmol) was dissolved in 1,4-dioxane and sparged with N<sub>2</sub> for 30 mins at 60°C. [1,1'-Bis(diphenylphosphino)ferrocene]palladium(II) dichloride (1 g, 1.37 mmol) was then added and the reaction was heated to 80°C for 24 hours under an N<sub>2</sub> atmosphere. The mixture is then filtered while hot and the solid is washed with dichloromethane. The brown filtrate is then reduced to dryness, to remove the 1,4-dioxane, leaving a brown residue. The residue is then dissolved in dichloromethane and washed with water twice, followed by brine. The organic layer is reduced and separated by column chromatography (DCM 96%: MeOH 3%: NEt<sub>3</sub> 1%). The crude product is then recrystallised with ethanol and water to give **3b** as a red solid. (0.89 g, 2.06 mmol, 18%)

<sup>1</sup>H NMR (400 MHz, CDCl<sub>3</sub>) δ 1.25 (3H, s, CH<sub>3</sub>), 1.40 (3H, s, CH<sub>3</sub>), 2.82 (3H, s, CH<sub>3</sub>), 5.78 (1H, d, J = 10.5, CH), 6.64 (1H, d, J = 8.0, CH), 6.85 (1H, d, J = 8.5, CH), 6.96 (1H, d, J = 10.5, CH), 7.32 (5H, m, CH), 7.43 (1H, d, J = 8.0, CH), 7.81 (1H, d, J = 8.0, CH), 7.86 (1H, d, J = 8.0, CH), 8.51 (1H, d, J = 4.0, CH), 8.54 (1H, d, J = 4.0, CH) 8.80 (1H, s, CH), 8.84 (1H, s, CH)

<sup>13</sup>C NMR (101 MHz, CDCl<sub>3</sub>) δ 20.30, 26.12, 29.14, 52.10, 104.88, 107.39, 115.88, 119.35, 119.97, 120.62, 123.61, 123.67, 125.50, 127.00, 128.69, 129.09, 129.56, 133.87, 133.93, 135.80, 136.27, 136.31 137.34, 137.94, 147.45, 147.99, 148.04, 148.50, 154.71

MS (ESI): m/z: 432.2076, calculated 431.1998

**1',3',3'-trimethyl-5'-(pyridin-3-yl)-6-(pyridin-4-yl)spiro[chromene-2,2'-indoline] (6b)**



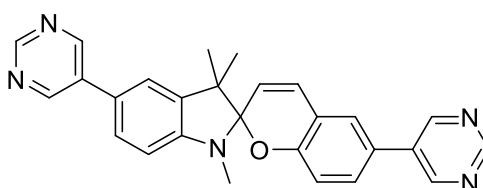
**5a** (0.5 g, 1.15 mmol), tripotassium phosphate (0.9 g, 4.24 mmol) and 3-pyridyl boronic acid (0.17 g, mmol) was dissolved in 1,4-dioxane and sparged with N<sub>2</sub> for 30 mins at 60°C. [1,1'-Bis(diphenylphosphino)ferrocene]palladium(II) dichloride (0.05 g, 0.06 mmol) was then added and the reaction was heated to 80°C for 24 hours under an N<sub>2</sub> atmosphere. The mixture is then filtered while hot and the solid is washed with dichloromethane. The brown filtrate is then reduced to dryness to remove the 1,4-dioxane, leaving a brown residue. The residue is then dissolved in dichloromethane and washed with water twice, followed by brine. The organic layer is reduced and separated by column chromatography (97% DCM: 2% MeOH: 1% NEt<sub>3</sub>). The crude product is then recrystallised with ethanol and water to give **6b** as yellow/brown precipitate (0.09 g, 0.20 mmol, 18%)

<sup>1</sup>H NMR (500 MHz, CDCl<sub>3</sub>) δ 1.19 (3H, s, CH<sub>3</sub>), 1.33 (3H, s, CH<sub>3</sub>), 2.76 (3H, s, CH<sub>3</sub>), 5.77 (1H, d, J = 10.0, CH), 6.55 (1H, d, J = 7.5, CH), 6.64 (1H, d, J = 8.0, CH), 6.81 (1H, d, J = 8.5, CH), 6.93 (1H, d, J = 10.0, CH), 7.11 (1H, d, J = 7.0, 1.0, CH), 7.19 (1H, ddd, J = 8.0, 8.0, CH), 7.35 (1H, d, J = 2.5 CH) 7.40 (1H, d, J = 2.5, CH), 7.44 (2H, m, CH), 7.85 (1H, m, CH), 8.61 (3H, m, CH), 8.85 (1H, m, CH)

<sup>13</sup>C NMR (126 MHz, CDCl<sub>3</sub>) δ 20.26, 26.12, 29.09, 52.16, 105.02, 107.45, 115.90, 120.08, 120.51, 120.63, 121.10, 123.63, 125.44, 127.00, 128.37, 128.46, 128.59, 129.18, 129.49, 130.12, 133.86, 137.37, 137.87, 147.97, 148.47, 150.19, 150.29

MS (ESI): m/z: 432.2068, calculated 431.1998

### 1',3',3'-trimethyl-5',6-di(pyrimidin-5-yl)spiro[chromene-2,2'-indoline] (**3c**)



**2** (0.5 g, 1.15 mmol), tripotassium phosphate (0.9 g, 4.24 mmol) and 5-pyrimidyl boronic acid (4 g, 3.25 mmol) was dissolved in 1,4-dioxane and sparged with N<sub>2</sub> for 30 mins at 60°C. [1,1'-Bis(diphenylphosphino)ferrocene]palladium(II) dichloride (0.1 g, 0.12 mmol) was then added and the reaction was heated to 80°C for 24 hours under an N<sub>2</sub> atmosphere. The mixture is then filtered while hot and the solid is washed with dichloromethane. The brown filtrate is then reduced to dryness, to remove the 1,4-dioxane, leaving a brown residue. The residue is then dissolved in dichloromethane and washed with water twice, followed by brine. The organic layer is reduced and separated by column

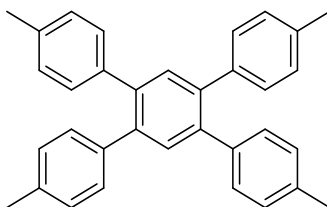
chromatography (97% DCM: 2% MeOH: 1% NEt<sub>3</sub>). The crude product is then recrystallised from ethanol and water to give **3c** as pale pink solid. (0.12 g, 0.29 mmol, 25%)

<sup>1</sup>H NMR (500 MHz, CDCl<sub>3</sub>) δ 1.18 (3H, s, CH<sub>3</sub>), 1.33 (3H, s, CH<sub>3</sub>), 2.76 (3H, s, CH<sub>3</sub>), 5.74 (1H, d, J = 10.0, CH), 6.60 (1H, d, J = 10.0, CH), 6.82 (1H, d, J = 8.0, CH), 6.91 (1H, d, J = 10.0, CH), 7.22 (2H, s, CH), 7.27 (1H, d, J = 8.0, CH), 7.36 (1H, d, J = 8.0, CH), 8.83 (2H, s, CH), 8.87 (2H, s, CH), 9.06 (1H, s, CH), 9.09 (1H, s, CH)

<sup>13</sup>C NMR (126 MHz, CDCl<sub>3</sub>) δ 20.22, 26.09, 29.11, 52.17, 105.00, 107.69, 116.29, 119.66, 120.17, 120.36, 125.35, 125.41, 126.49, 127.09, 128.61, 129.46, 133.96, 134.94, 138.28, 149.11, 154.42, 154.52, 155.28, 156.59, 157.13

MS (ESI): m/z: 434.1985, calculated 433.1903

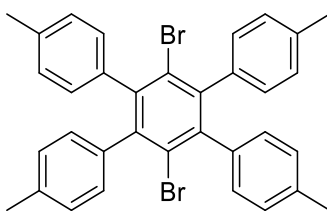
#### **4,4''-dimethyl-4',5'-di-p-tolyl-1,1':2',1''-terphenyl (7a)**



<sup>1</sup>H NMR (500 MHz, (CD<sub>3</sub>)<sub>2</sub>SO) δ 7.14 (8H, d, J = 8.0 Hz, CH), 7.44 (8H, d, J = 8.0 Hz, CH), 7.52 (2H, s, CH)

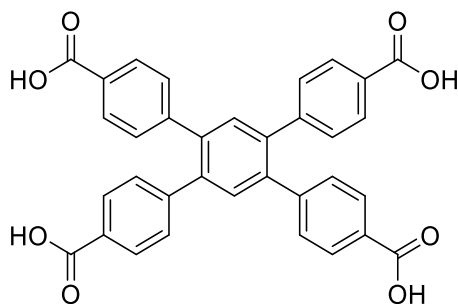
MS (ESI): m/z 438.2358, calculated 438.2348

#### **3',6'-dibromo-4,4''-dimethyl-4',5'-di-p-tolyl-1,1':2',1''-terphenyl (7b)**



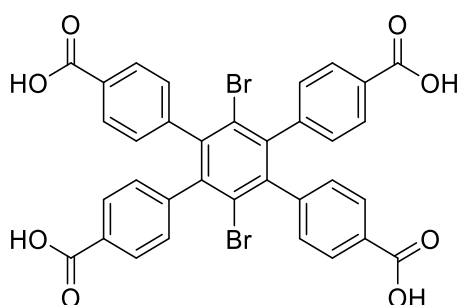
<sup>1</sup>H NMR (400 MHz, CDCl<sub>3</sub>) δ 2.26 (12H, s, CH<sub>3</sub>), 6.97 (16H, m, CH)

#### **4',5'-bis(4-carboxyphenyl)-[1,1':2',1''-terphenyl]-4,4''-dicarboxylic acid (8a)**



$^1\text{H NMR}$  (500 MHz,  $(\text{CD}_3)_2\text{SO}$ )  $\delta$  7.37 (8H, d,  $J = 8.0$ , CH), 7.83 (8H, d,  $J = 8.5$ , CH), 8.04 (2H, s, CH), 13.04 (4H, sb, COOH)

**3',6'-dibromo-4',5'-bis(4-carboxyphenyl)-[1,1':2',1''-terphenyl]-4,4''-dicarboxylic acid (8b)**



$^1\text{H NMR}$  (400 MHz,  $(\text{CD}_3)_2\text{SO}$ )  $\delta$  7.30 (8H, d,  $J = 8.4$ , CH), 7.78 (8H, d,  $J = 8.0$ , CH), 13.00 (4H, sb, COOH)

## 2.6 References

- 1 F. ZareKarizi, M. Joharian and A. Morsali, *J. Mater. Chem. A*, 2018, **6**, 19288–19329.
- 2 B. S. Lukyanov and M. B. Lukyanova, *Chem. Heterocycl. Compd.*, 2005, **41**, 281–311.
- 3 G. Baillet, G. Giusti and R. Guglielmetti, *J. Photochem. Photobiol. A Chem.*, 1993, **70**, 157–161.
- 4 M. Hammarson, J. R. Nilsson, S. Li, T. Beke-Somfai and J. Andréasson, *J. Phys. Chem. B*, 2013, **117**, 13561–13571.
- 5 R. Klajn, *Chem. Soc. Rev.*, 2014, **43**, 148–184.
- 6 F. Maya and J. M. Tour, *Tetrahedron*, 2004, **60**, 81–92.
- 7 D. E. Williams, C. R. Martin, E. A. Dolgoplova, A. Swifton, D. C. Godfrey, O. A. Ejegbavwo, P. J. Pellechia, M. D. Smith and N. B. Shustova, *J. Am. Chem. Soc.*, 2018, **140**, 7611–7622.
- 8 M. Natali and S. Giordani, *Org. Biomol. Chem.*, 2012, **10**, 1162–1171.
- 9 T. R. Silvia, V. S. L. Ana and E. A. S. González, *Synth. Commun.*, 1995, **25**, 105–110.
- 10 S.-R. Keum, S.-M. Ahn, S.-J. Roh, S.-J. Park, S.-H. Kim and K. Koh, *Magn. Reson. Chem.*, 2006,



- 44**, 90–94.
- 11 Y. J. Cho, K. Y. Rho, S. Rok Keum, S. H. Kim and C. M. Yoon, *Synth. Commun.*, 1999, **29**, 2061–2068.
- 12 É. R. Zakhs, L. A. Zvenigorodskaya, N. G. Leshenyuk and V. P. Martynova, *Chem. Heterocycl. Compd.*, 1977, **13**, 1055–1061.
- 13 L. Qu, X. Xu, J. Song, D. Wu, L. Wang, W. Zhou, X. Zhou and H. Xiang, *Dye. Pigment.*, 2020, **181**, 108597.
- 14 M. Suzuki, T. Asahi and H. Masuhara, *Phys. Chem. Chem. Phys.*, 2002, **4**, 185–192.
- 15 E. Pottier, R. Dubest, R. Guglielmetti, P. Tardieu, A. Kellmann, F. Tfibel, P. Levoir and J. Aubard, *Helv. Chim. Acta*, 1990, **73**, 303–315.
- 16 T. Asahi, M. Suzuki and H. Masuhara, *J. Phys. Chem. A*, 2002, **106**, 2335–2340.
- 17 A. Karmakar, C. L. Oliver, S. Roy and L. Öhrström, *Dalt. Trans.*, 2015, **44**, 10156–10165.
- 18 M. Chong, University of Nottingham, 2016.
- 19 R. A. Abramovitch, *Pyridine and its Derivatives, Supplemental ed.*, Wiley-Interscience, New York, 1974.
- 20 J. Shapiro, *Limnol. Oceanogr.*, 1966, **11**, 293–298.
- 21 A. Perry and C. J. Kousseff, *Beilstein J. Org. Chem.*, 2017, **13**, 1542–1550.
- 22 T. Stafforst and D. Hilvert, *Chem. Commun.*, 2009, 287–288.
- 23 P. J. Dyson and P. G. Jessop, *Catal. Sci. Technol.*, 2016, **6**, 3302–3316.
- 24 T. Eicher, *J. für Prakt. Chemie/Chemiker-Zeitung*, 1998, **340**, 487–488.
- 25 P. A. Cox, A. G. Leach, A. D. Campbell and G. C. Lloyd-Jones, *J. Am. Chem. Soc.*, 2016, **138**, 9145–9157.
- 26 N. Kudo, M. Perseghini and G. C. Fu, *Angew. Chemie Int. Ed.*, 2006, **45**, 1282–1284.
- 27 N. Yanai, T. Uemura, M. Inoue, R. Matsuda, T. Fukushima, M. Tsujimoto, S. Isoda and S. Kitagawa, *J. Am. Chem. Soc.*, 2012, **134**, 4501–4504.
- 28 M. Feuerstein, H. Doucet and M. Santelli, *Tetrahedron Lett.*, 2005, **46**, 1717–1720.
- 29 T. Markovic, B. N. Rocke, D. C. Blakemore, V. Mascitti and M. C. Willis, *Chem. Sci.*, 2017, **8**,

- 4437–4442.
- 30 C. Liu, J. Luo, L. Xu and Z. Huo, *ARKIVOC*, 2013, **2013**, 154–174.
- 31 M.-N. Birkholz (née Gensow), Z. Freixa and P. W. N. M. van Leeuwen, *Chem. Soc. Rev.*, 2009, **38**, 1099–1118.
- 32 N. Miyaura and A. Suzuki, *Chem. Rev.*, 1995, **95**, 2457–2483.
- 33 A. Migliorini, C. Oliviero, T. Gasperi and M. A. Loreto, *Molecules*, 2012, **17**, 4508–4521.
- 34 S. R. Dubbaka, *Synlett*, 2005, **4**, 709–710.
- 35 C. Adamo, C. Amatore, I. Ciofini, A. Jutand and H. Lakmini, *J. Am. Chem. Soc.*, 2006, **128**, 6829–6836.
- 36 C. F. R. A. C. Lima, A. S. M. C. Rodrigues, V. L. M. Silva, A. M. S. Silva and L. M. N. B. F. Santos, *ChemCatChem*, 2014, **6**, 1291–1302.
- 37 T. E. Barder, S. D. Walker, J. R. Martinelli and S. L. Buchwald, *J. Am. Chem. Soc.*, 2005, **127**, 4685–4696.
- 38 A. S. Guram, X. Wang, E. E. Bunel, M. M. Faul, R. D. Larsen and M. J. Martinelli, *J. Org. Chem.*, 2007, **72**, 5104–5112.
- 39 M. L. P. Reddy, *JPhCPhB C Photochemistry Review*, 2018.
- 40 N. W. Tyler and R. S. Becker, *J. Am. Chem. Soc.*, 1970, **92**, 1289–1294.
- 41 C. Beyer and H.-A. Wagenknecht, *J. Org. Chem.*, 2010, **75**, 2752–2755.
- 42 M. Sanchez-Lozano, C. M. Estévez, J. Hermida-Ramón and L. Serrano-Andres, *J. Phys. Chem. A*, 2011, **115**, 9128–9138.
- 43 Y. Sheng, J. Leszczynski, A. A. Garcia, R. Rosario, D. Gust and J. Springer, *J. Phys. Chem. B*, 2004, **108**, 16233–16243.
- 44 R. S. Becker and J. Michl, *J. Am. Chem. Soc.*, 1966, **88**, 5931–5933.
- 45 W. Tian and J. Tian, *Dye. Pigment.*, 2014, **105**, 66–74.
- 46 P. B. Markworth, B. D. Adamson, N. J. A. Coughlan, L. Goerigk and E. J. Bieske, *Phys. Chem. Chem. Phys.*, 2015, **17**, 25676–25688.
- 47 L. Kortekaas, J. Chen, D. Jacquemin and W. R. Browne, *J. Phys. Chem. B*, 2018, **122**, 6423–

- 6430.
- 48 C. Reichardt and T. Welton, *Solvents and solvent effects in organic chemistry*, John Wiley & Sons, Inc., 2011.
- 49 D. Harris, *Quantitative Chemical Analysis*, WH Freeman, 9th edn., 2015.
- 50 Y. Shiraishi, M. Itoh and T. Hirai, *Phys. Chem. Chem. Phys.*, 2010, **12**, 13737–13745.

## Chapter 3. Synthesis and characterisation of Metal Organic Frameworks incorporating Spiropyran

### 3.1 Introduction

In this chapter we discuss the synthetic attempts that incorporate a spiropyran into a MOF, followed by the characterisation of these materials. The strategy was to use the N-heterocyclic spiropyran ligands, which were discussed in chapter 2, as pillaring linkers with a suitable co-linker acting as the layering linker.

#### 3.1.1 Designing a novel framework

The requirements for a framework can be any organic ligand functionalised with the appropriate functional groups capable of binding to a metal (e.g. carboxylates, pyridines etc.) and any metal source which has access to the appropriate coordination geometries. Initially, when MOFs were discovered over 30 years ago, researchers were combining easily accessible linkers (e.g. terephthalic acid, trimesic acid) with transition metals and creating quite simple frameworks, these frameworks are quite forgiving in the variety of conditions that can be employed to design the materials (e.g. HKUST-1, MOF-5).<sup>1,2</sup> Since then researchers have moved on to incorporating much more complex molecules into their frameworks, such as porphyrins, amino acids or cyclodextrins.<sup>3-5</sup> These complex molecules are typically much harder to incorporate into a framework and are less forgiving in the variation of conditions that will synthesise these materials successfully. These complex molecules can present extra challenge due to their sheer size, irregular geometry or instability under solvothermal conditions.

The most common method for designing a novel framework is trial and error, commonly varying parameters such as temperature, reaction time, solvents, modulators, stoichiometry in solvothermal conditions. Less orthodox methods can include mechanochemistry, microwaves and sonochemistry.<sup>6-8</sup> There are methods of narrowing down the possible conditions to try that use computational simulation packages but we did not have access to these resources so will not be discussing them further.<sup>9</sup> Isoreticular chemistry is also a widely accepted method of designing new frameworks. Organic ligands of different sizes but with similar geometries/symmetries can create new frameworks with the same topology but expanded pore sizes.<sup>10</sup> This does not strictly apply to our work because there are no existing frameworks with the spiropyran ligand incorporated into a 3<sup>rd</sup> generation photoactive MOF (generations are discussed below) and therefore we do not have a framework that incorporates a linker with similar geometries to compare to. We can, however, base our synthetic

strategies on linkers which also adopt a pillar-layer motif which will bear a passing resemblance to our spiropyran linkers, but we would not expect the same topologies.

### 3.1.2 Pillar-layer MOFs

Pillar-layer frameworks are a well-studied mixed linker group of structures, typically using pyridyl derivatives to link together 2D sheets into pillar-layered structures.<sup>11</sup> The formation of these frameworks is not fully understood. Intuitively one would expect the 2D layers to form before being linked together by the pillaring agents. There have been examples of these 2D layer intermediates being isolated and there have also been examples of frameworks being built on a layer-by-layer approach (see Figure 48). Typically, they are synthesised via a one-pot synthesis which offers little control over the variables effecting what sequence these frameworks are formed.<sup>12</sup>

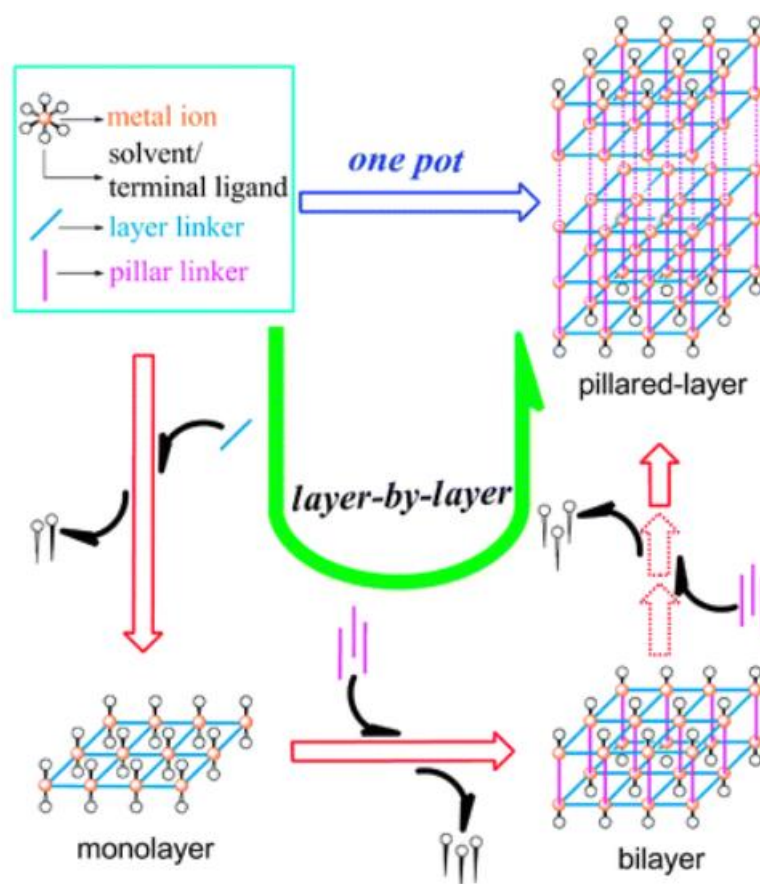


Figure 48 Illustrating the principles of the one-pot synthesis compared with the layer-by-layer approach. Figure taken from Wang et al.<sup>12</sup>

Initially, these designs are sought after to finely tune the pore channels (isoreticular chemistry), but these frameworks have been noted to provide materials that can respond to external stimuli such as electric fields, a specific guest or light.<sup>13,14</sup> This potential for dynamic materials, is due to the pillars providing flexibility through layer sliding, pillar rotation, pillar stretching and framework

expansion/contraction. Furthermore these types of frameworks have an affinity for interpenetration which often adds to the stability and enhancements to gas adsorption, and in some cases can improve the flexibility of a framework improving its performance as a dynamic material.<sup>15</sup> The interpenetration can still be prevented by several strategies such as adding steric bulk to a linker as a pendant group, or replacing either the layer or pillar linker with a smaller isostructural substitute.<sup>11</sup> Thus the interpenetration should be viewed as another avenue for further customisation of our desired MOF.

### 3.1.3 Photoactive MOFs

In chapter 1 we discussed the potential applications of photoactive frameworks, in this section we will be focusing on the techniques used for characterising photoresponsive MOFs and what behaviours we can use to identify the successful synthesis of these smart materials and what language we can use to describe them.

The field of photoactive MOFs, although relatively new, is a hot topic and has made some seemingly rapid progress over recent years. There are several methods of inducing the property of photoresponsiveness in a material and as such we need a way to describe and categorise these materials effectively. In a review by *F. Coudert*, the terms 1<sup>st</sup>, 2<sup>nd</sup> and 3<sup>rd</sup> generation metal organic frameworks are used<sup>16</sup> (see Figure 49).

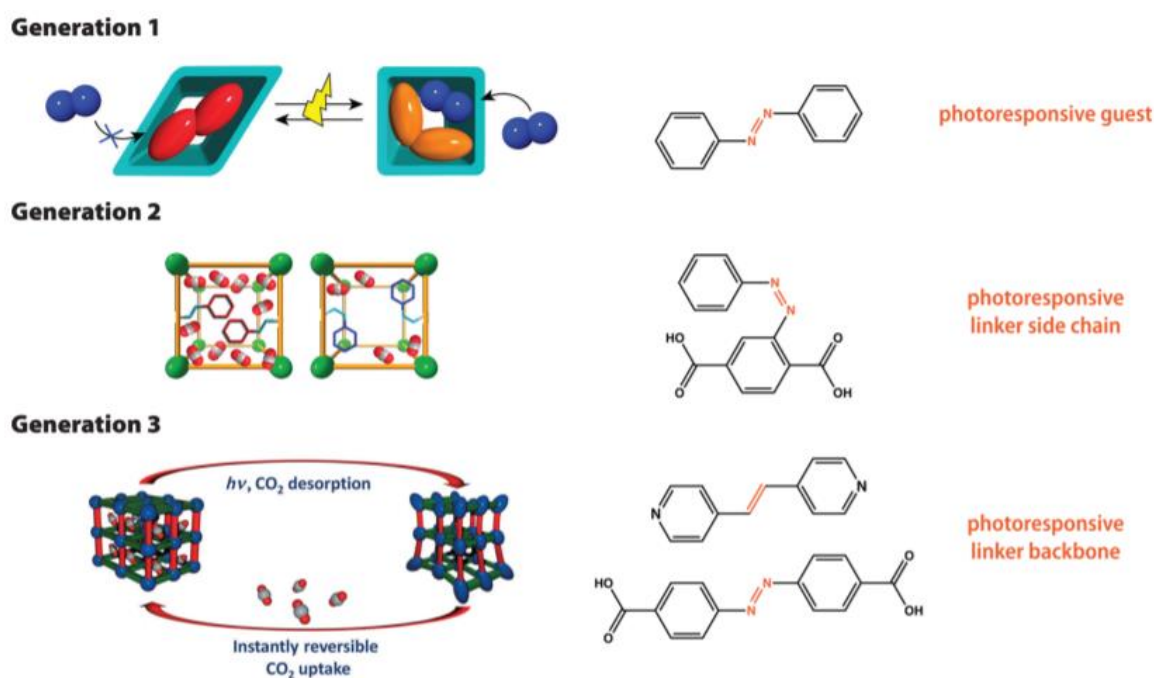


Figure 49 Nuances of how the different generations of azobenzene-based frameworks differ in their classification. Image taken directly from *F. Coudert's* review.<sup>16</sup>

1<sup>st</sup> generation photoactive MOFs refer to photoactive molecules encapsulated within the MOF but is not chemically bonded to the framework in any way. As a guest molecule they can photoswitch within

the pore and can induce some structural change due to flexibility of the metal organic framework. 2<sup>nd</sup> generation photoactive MOFs refer to photoactive moieties grafted onto the linker. This is the generation which has produced the most examples reported in the literature. The linker photoisomerising does not affect the overall structure of the framework but is able to expand into the pore, often causing significant pore volume changes. Finally, 3<sup>rd</sup> generation photoactive frameworks refer to metal organic frameworks which have the photoactive moiety intrinsic to the overall structure and do cause an overall change in the framework structure. This generation is both the most difficult to achieve and most highly sought after, and is what we aimed to design. These terms serve as a useful classification to put our work into perspective and we shall be using these terms throughout the chapter.

### 3.1.3.1 Behaviour of photoactive 1<sup>st</sup> generation MOFs

A common method of imparting functionality on a metal organic framework is to encapsulate the active species which already has the property that you wish to design the framework with.<sup>17,18</sup> This technique also includes photoactive molecules such as spiropyran. As we have discussed earlier in Chapter 2, these photoactive molecules are typically only responsive in the solution state. The confines of a solid-packing structure usually restrict the movement of the photoactive molecule, rendering it inactive. The reason these 1<sup>st</sup> generation frameworks are so interesting is that when encapsulated inside the framework, they can exhibit solution-state behaviour.<sup>19</sup>

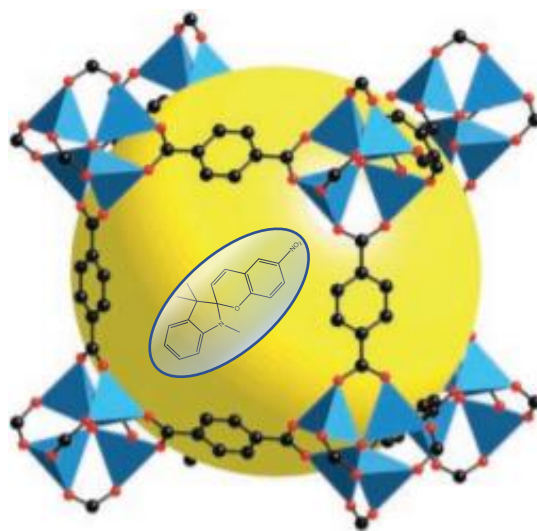


Figure 50 MOF-5 encapsulating 1,3,3-trimethylindolino-6'-nitrobenzopyrrolospiran as a guest molecule. (Image adapted from N. Rosi et al..<sup>20</sup>)

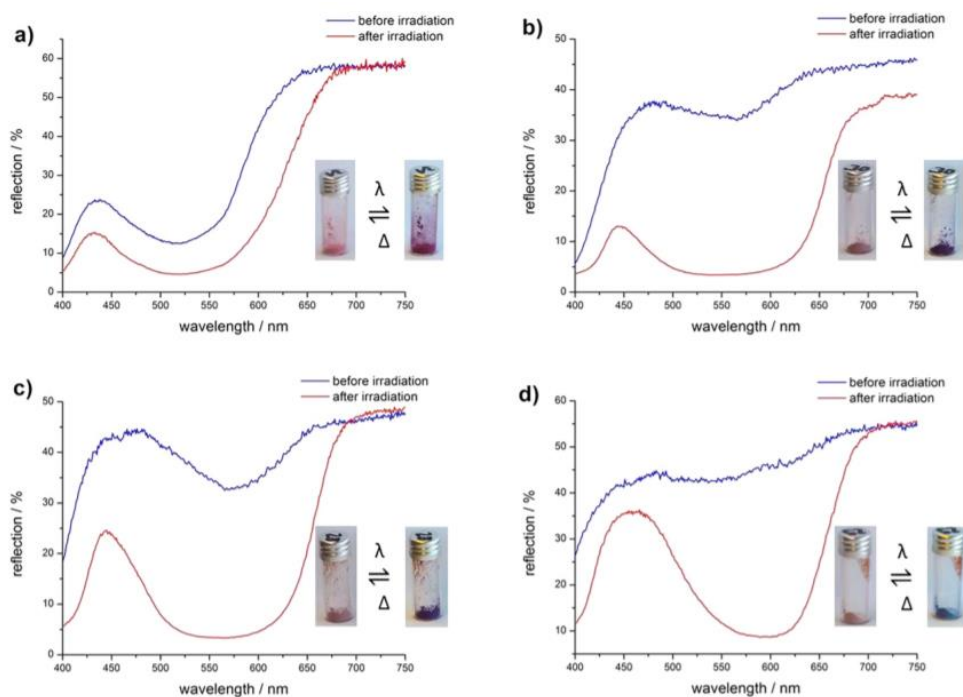


Figure 51 Solid-State UV-vis profiles of frameworks encapsulating spiropyran before and after irradiation with 365 nm light for 1 minute. (a) = MOF-5, b) = MIL-68 (In), c) = MIL-68(Ga), and d) = MIL-53(Al))

H. Schwartz *et al.* investigated the behaviour of nitrated spiropyran as a guest in the pores of four different frameworks, MOF-5 (depicted in Figure 50), MIL-68(In), MIL-68(Ga) and MIL-53(Al).<sup>21</sup> H. Schwarz *et al.* conclude that the metal nodes of each framework determine the polarity of the environment which affects the equilibrium between the open and closed form of the spiropyran. The MOF-5 framework provides a more polar environment (contains  $[\text{ZnO}_4]^{6+}$  nodes) and the spiropyran molecule prefers to be in the open form signified by a hypsochromic shift. Both MIL-68 frameworks provide non-polar environments (contains  $[\text{Ga}(\text{OH})]^{2+}$  and  $[\text{In}(\text{OH})]^{2+}$  nodes) making the closed form preferred which is signified by a bathochromic shift. They liken this behaviour to the phenomenon of the equilibrium's dependence on the polarity of the solvent.<sup>22</sup> In the case of MIL-53(Al), the spiropyran is embedded on the surface of the framework and therefore the least polar environment (despite the  $[\text{Al}(\text{OH})]^{2+}$  nodes).



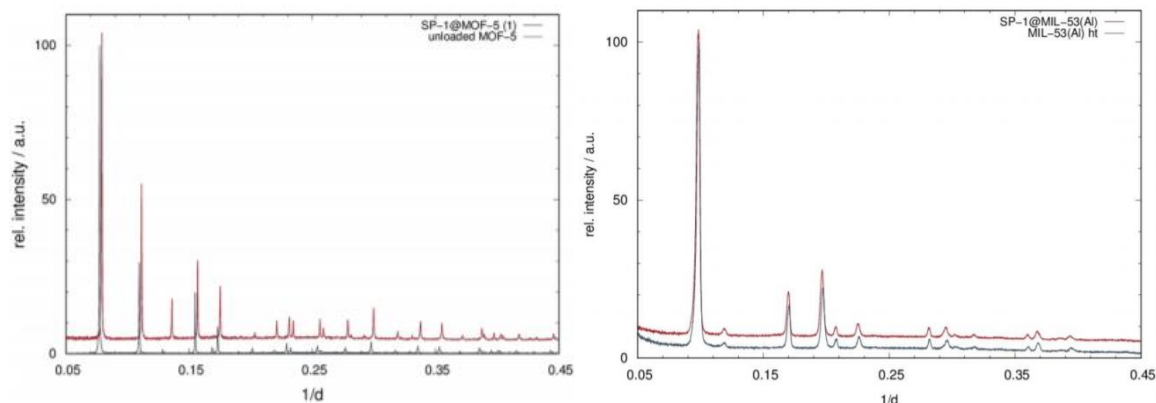


Figure 52 Comparison of the PXRD obtained before and after loading MOF-5 with the spiropyran guest molecule (left). Comparison of PXRD patterns obtained before and after loading with MIL-53.

Another technique they used to identify successful loading of spiropyran into the pores was PXRD (see Figure 52). By comparing peak positions and intensities before and after loading. The positions should be almost the same (depending on the flexibility of the framework and how it changes upon guest incorporation), the relative peak intensities increase however which is how the extra electron density inside the pores of the MOF manifests. For comparison, the MIL-53 example shows negligible change in both position and intensity of the peaks. Producing a first-generation MOF is one of the possible outcomes during our synthetic attempts at a third generation MOF, thus being able to identify such a material will be useful during our synthetic screenings.

### 3.1.3.2 Behaviour of photoactive 2<sup>nd</sup> generation MOFs

To our knowledge there has only been one publication that showcases examples of a 2<sup>nd</sup> generation framework incorporating spiropyran; *D. Williams et al.* report two metal organic frameworks that incorporate spiropyran as an intrinsic part of the structural support for the framework but still functions as a pendant group as the photoresponse does not cause a change in the overall topology of the framework. They confirm the successful synthesis of their materials via SCXRD and PXRD (see Figure 54). The SCXRD data was only able to model half of the photoactive linker incorporated in the framework, the indoline fragment functionalised with the nitrobenzene was found to be disordered in both the TNDS and HDDB examples and were not able to be assigned but their contribution were accounted for with the SQUEEZE option of the PLATON program. The simulated PXRD patterns derived from the SCXRD data agree with the PXRD patterns and the calculated interspatial difference corroborates with the size of the linkers. It is clear that the disordered nature of these spiropyran-based materials present significant problems in crystallographic characterisation and therefore must rely on less direct methods of confirming the presence of spiropyran.

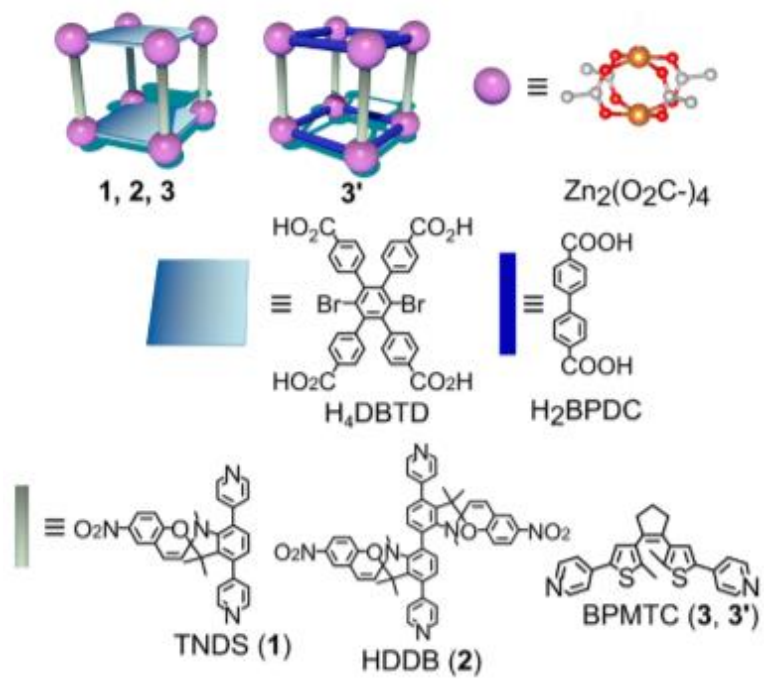


Figure 53 The photoresponsive materials synthesised by D. Williams et al.<sup>23</sup>, outlining the composition of each framework. We will be focusing on frameworks **1** and **2** in this example.

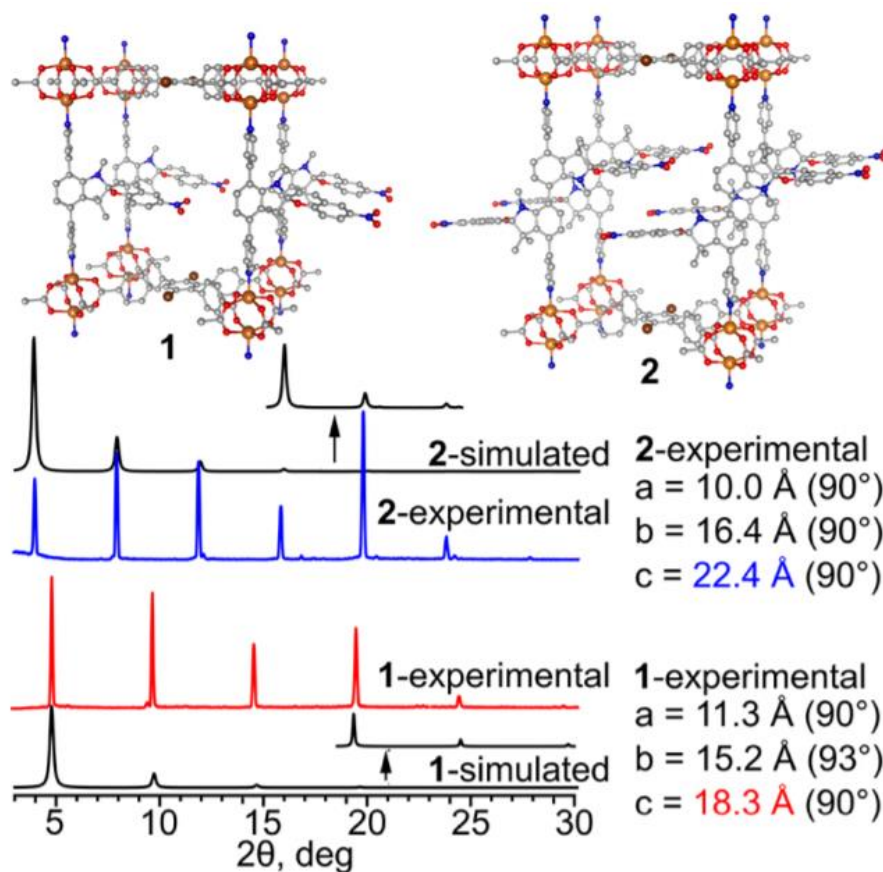


Figure 54 Top: SCXRD of frameworks incorporating TNDS (1) and HDDB (2) linkers. Bottom: PXRD patterns comparing simulated patterns from the SCXRD data and the experimental patterns. The coloured numbers show the increase in interlayer distance for each MOF which agree with the size of the spiropyran linkers.<sup>23</sup>

They further evidence the incorporation of spiropyran into their material (framework 1, Figure 53) using photoluminescence. By bubbling 6M HCl vapour through the TNDS framework they observe a significant hypsochromic shift in the emission profile more than 100 nm, this post degradation emission profile matched that of the control experiment where just the TNDS linker was used. This is a clever indirect way of confirming the successful incorporation of their spiropyran linker that uses the framework's ability to change the photophysics of the spiro linkers.

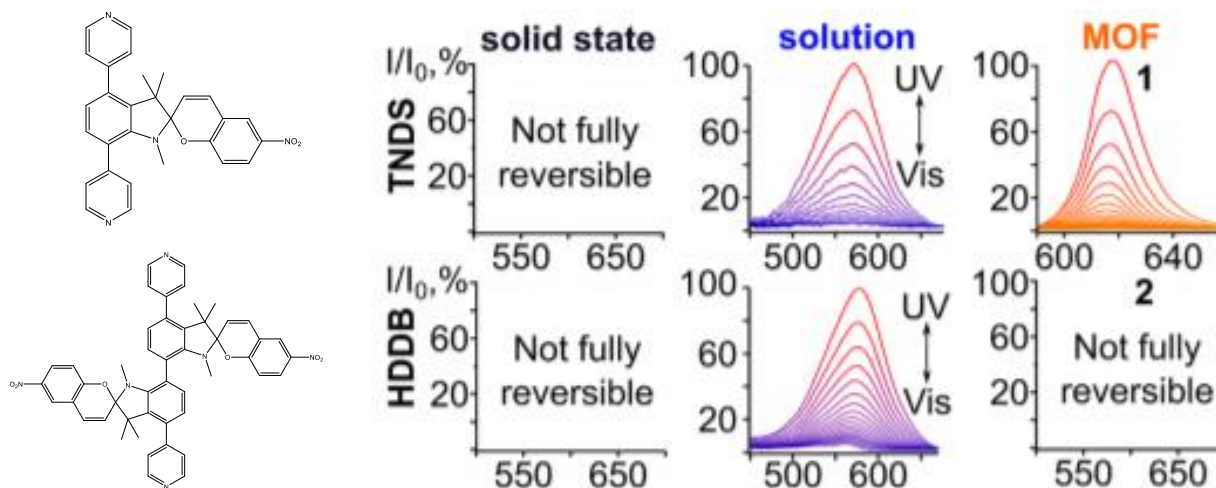


Figure 55 UV-Vis data reported by D. Williams *et al.* comparing spiropyran linkers solution and solid state profiles to incorporation in a MOF.<sup>23</sup>

D. Williams *et al.* effectively demonstrate that in some cases a spiropyran molecule not capable of reversible photoconversion on its own can have that property induced in a metal organic framework (Figure 55). The group also report that extra spatial separation provided by the MOF compared to the close solid packing of the ligand on its own is enough to give it the property of a fully reversible photoactive material. The HDDB linker, an example of a more sterically congested linker, demonstrates a situation where a MOF environment is not guaranteed to induce fully reversible photoactive change and further demonstrates that the steric environment of the linker inside the framework must be taken into consideration.

### 3.1.3.3 Behaviour of photoactive 3<sup>rd</sup> generation MOFs

There are no examples of third generation frameworks for spiropyran to date, therefore we must look to examples of other third generation photoactive MOFs to form our expectations of how a spiropyran framework would behave.

R. Lyndon *et al.* reports the first example of a third generation photoresponsive MOF, an azobenzene based framework (the example of a third generation MOF used in Figure 49).<sup>27</sup> Their experiments in the synchrotron facility in Sydney shown that instead of a uniform change across the crystal, instead they observed localised non-periodic change throughout the structure which the X-Ray diffraction technique was poorly suited to define (see Figure 56).

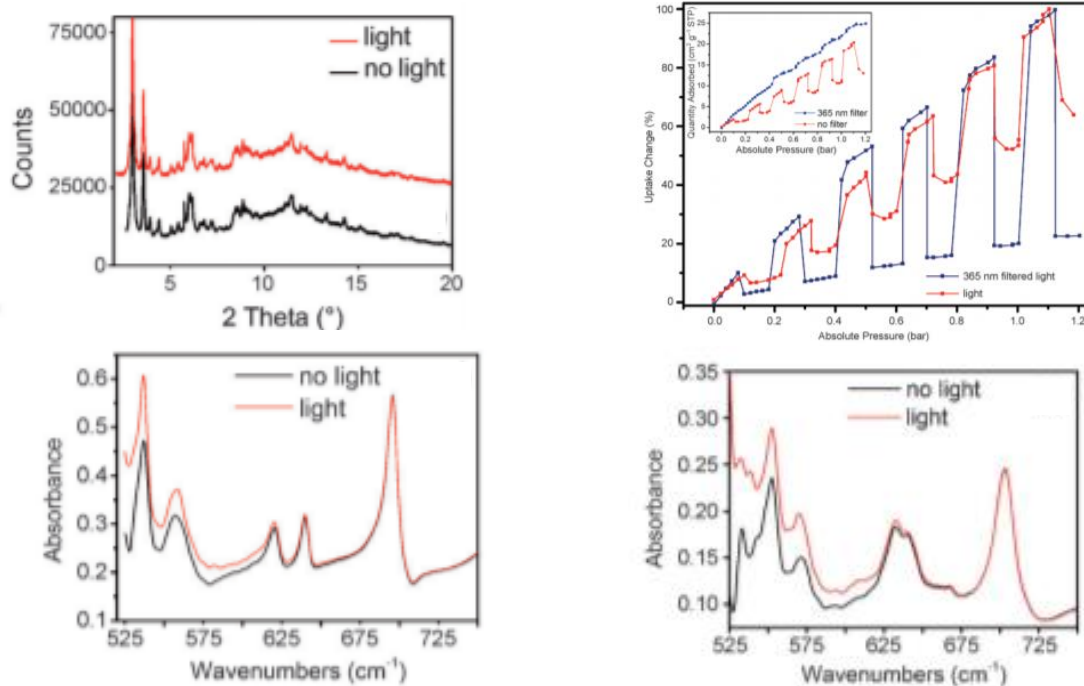


Figure 56 PXRD data obtained showing no discernible change with or without radiation (top left). Isotherm data obtained during cycling of radiation, showing uptake and release of gas coinciding with irradiation cycling (top right). CCC and CCN low-energy FTIR bending modes shows the linker excited by UV light in both the ligand (bottom left) and as a linker incorporated in the framework (bottom right).<sup>27</sup>

Their work demonstrates the difficulty of working with these third-generation materials, as it required a combination of analytical techniques to determine whether the material is photoresponsive or not. X-Ray diffraction is one of the staples of MOF characterisation and is typically the go-to method even when studying dynamic materials such as these but often supplemented by other techniques to study the dynamic aspect specifically.<sup>24–26</sup>

In summary, in all cases determining the successful incorporation of the linker into the framework is determined by X-Ray diffraction (both powder and single crystal methods). Determining the photophysics of the framework is a bit more complex, as consistent and uniform radiation of the whole crystal is not feasible (the surface of the framework will receive more irradiation than the core of the framework) and therefore the photoconversion will not be uniform throughout. This makes the crystallographic techniques ill-suited to study the photophysics as the models require an ordered system. Therefore, more indirect means of analysis are used, such as monitoring the C-O spiro stretch with IR spectroscopy or comparing the emission profiles of the framework to the free ligand.

### 3.2 Aim

Our goal can be divided into two objectives: First we need to synthesise a 3<sup>rd</sup> generation photoactive MOF incorporating the spiro pyran moiety, secondly we need to characterise the photoactivity these

materials display. To accomplish the first step, we shall be using co-linkers with our spiropyran linker in order to encourage pillar-layer frameworks to form.

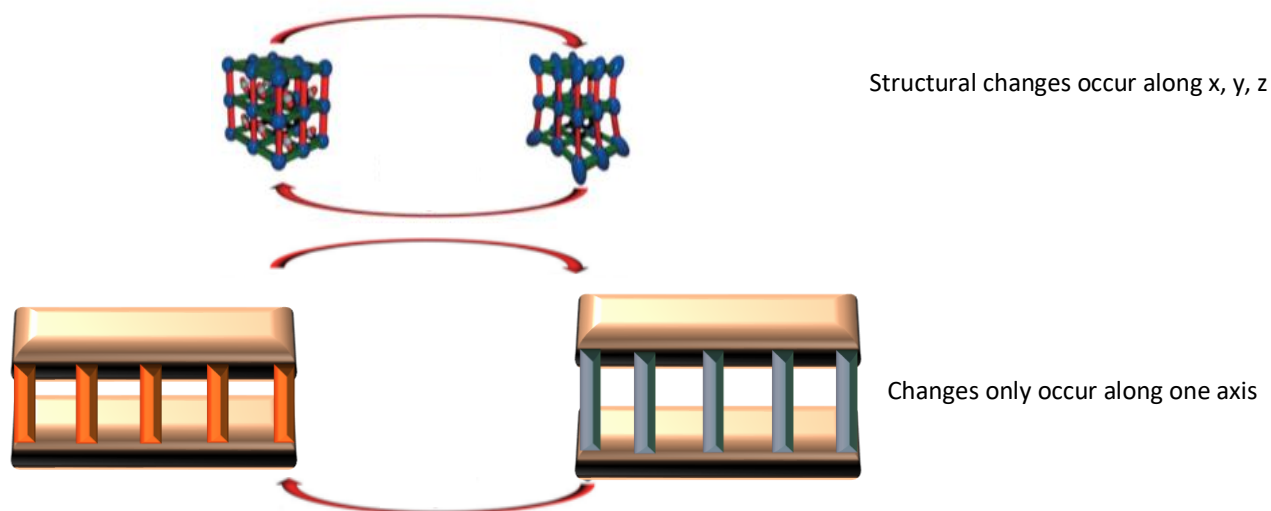


Figure 57 Simple illustration of how a framework will behave upon photoconversion when all the linkers are photoresponsive (top) compared to a framework where only the pillaring linkers are photoresponsive. Image adapted from R. Lyndon et al.<sup>27</sup>

The majority of second and third generation examples described in the previous section used this technique and demonstrates a successful record. The second reason we are adopting this strategy is to accommodate for the challenge faced by most frameworks of restricting the movement of the photoresponsive linkers, by only allowing photoisomerization to occur along one axis we can reduce the overall strain photoisomerization puts on the framework which will both encourage the photoresponsiveness of the material and reduce the chances of framework collapse upon conversion (see Figure 57). Some of the photoactive linkers that were discussed in detail in chapter 2 are used here in our synthetic attempts at creating 3<sup>rd</sup> generation photoactive MOF (see Figure 58). The rigorousness of the testing of each ligand will depend on how accessible the material was (higher yielding ligands will be tested more, e.g. **3a**) and when the synthesis was established (i.e. more recently synthesised ligands had less time to be tested).

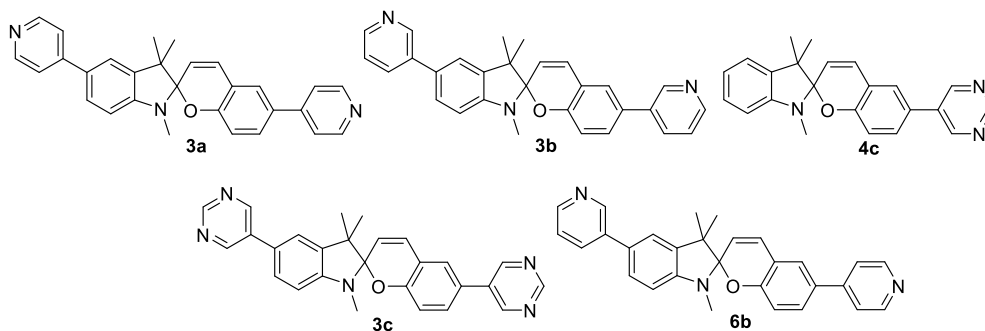


Figure 58 The scope of spiropyran-based linkers used in synthetic attempts of a 3<sup>rd</sup> generation metal organic framework.

The co-linkers we will employ with our spiropyran linkers are literature known and easily accessible linkers that vary in length, connectivity, and shape to ensure a wide scope to begin with. After initial testing we began eliminating and adapting our selection as we progressed (see Figure 59). Once we confirmed our material incorporated the desired spiropyran linker, we then investigated the photoresponsiveness of the material.

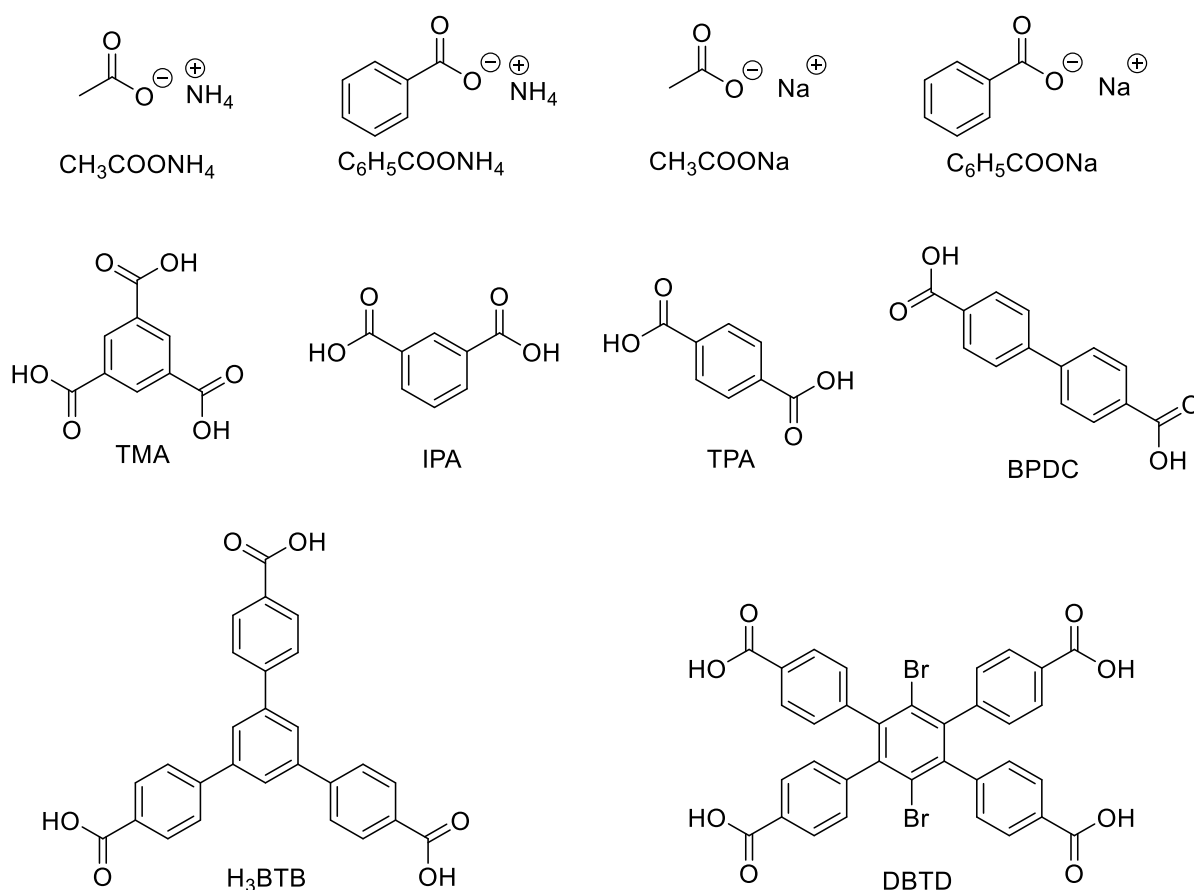


Figure 59 The scope of non-photoactive co-linkers used in synthetic attempts of a 3<sup>rd</sup> generation metal organic framework incorporating spiropyran linkers.

### 3.3 Results and Discussion

#### 3.3.1 Synthetic strategy “method development”

Our primary goal with this work is to not just incorporate the spiropyran linker but to also ensure it is photoactive and characterise that photoactivity. As such, the metal choices will primarily focus on non-photoactive metals (e.g. group II,  $d^{10}$  metals etc.). By choosing non-photoactive metals, any photoactivity can be attributed solely to the spiropyran linker thus avoiding the need to deconvolute any data obtained. Metals with a full outer shell (i.e.  $d^{10}$ ), often form high symmetry complexes which are preferred for metal organic frameworks.<sup>28</sup> Most of the focus will be on zinc, it is photo-inert and allows for a wide variety of possible coordination geometries (4, 5, 6, 7 co-ordinate)<sup>29</sup> which will increase the likelihood of one being suitable for incorporating the spiropyran linker into an extended framework.

As discussed in the introduction of this chapter, our MOF synthesis attempts will focus on designing pillar-layer type frameworks as N-heterocycles typically perform well as a pillaring linker and also reducing the amount of structural strain upon photoswitching as the structural change occurs along only one axis. A starting point is to look at pillar-layer frameworks reported in the literature. Most pillar-layer frameworks tend to combine linkers containing carboxylic acid functionalities with linkers containing pyridyl functionalities, with the pyridyl linkers acting as pillars while carboxylic acid linkers act as layer linkers. Although there are examples of pyridyl-only frameworks, they tend to be extremely unstable which would make the characterisation process particularly challenging.

Due to the kink at the spiro-core and the size ( $\approx 16 \text{ \AA}$ ), they differ quite significantly from typical, more-linear pillar linkers. Therefore the scope of possible pillar layer strategies is quite broad. Our strategy began with a trial and error approach, depending on the errors or successes, we outline key factors that contribute to the successful incorporation of the spiropyran linker. The analyses used to determine the relative success of these trials are primarily: i) inspection under microscope ii) PXRD iii) SCXRD (although ii) and iii) will depend on suitable crystalline material being present).

##### 3.3.1.1 1-D/2-D Metal Organic Frameworks

Due to the peculiar shape of the spiropyran molecule, utilising these ligands as a pillaring linker to connect between layers will be difficult. One strategy that could circumvent the challenge presented by the awkward shape of spiropyran would be to synthesise a 1-D/2-D framework. By doing so the geometry restrictions that the spiro-linker impose will be reduced as these frameworks tend to be more forgiving. We tried synthesising a 1D framework (**3a-01**) using copper paddlewheel units formed by capped carboxylate groups leaving the axial positions free to connect via pillaring spiropyran linkers to form 1-D chains. This strategy was based on work by *Hwang et al.*<sup>30</sup> which clearly demonstrates



that a wide variety of pillaring N-heterocycles of various sizes and flexibilities can be incorporated into frameworks utilising these paddlewheels (see Figure 60).

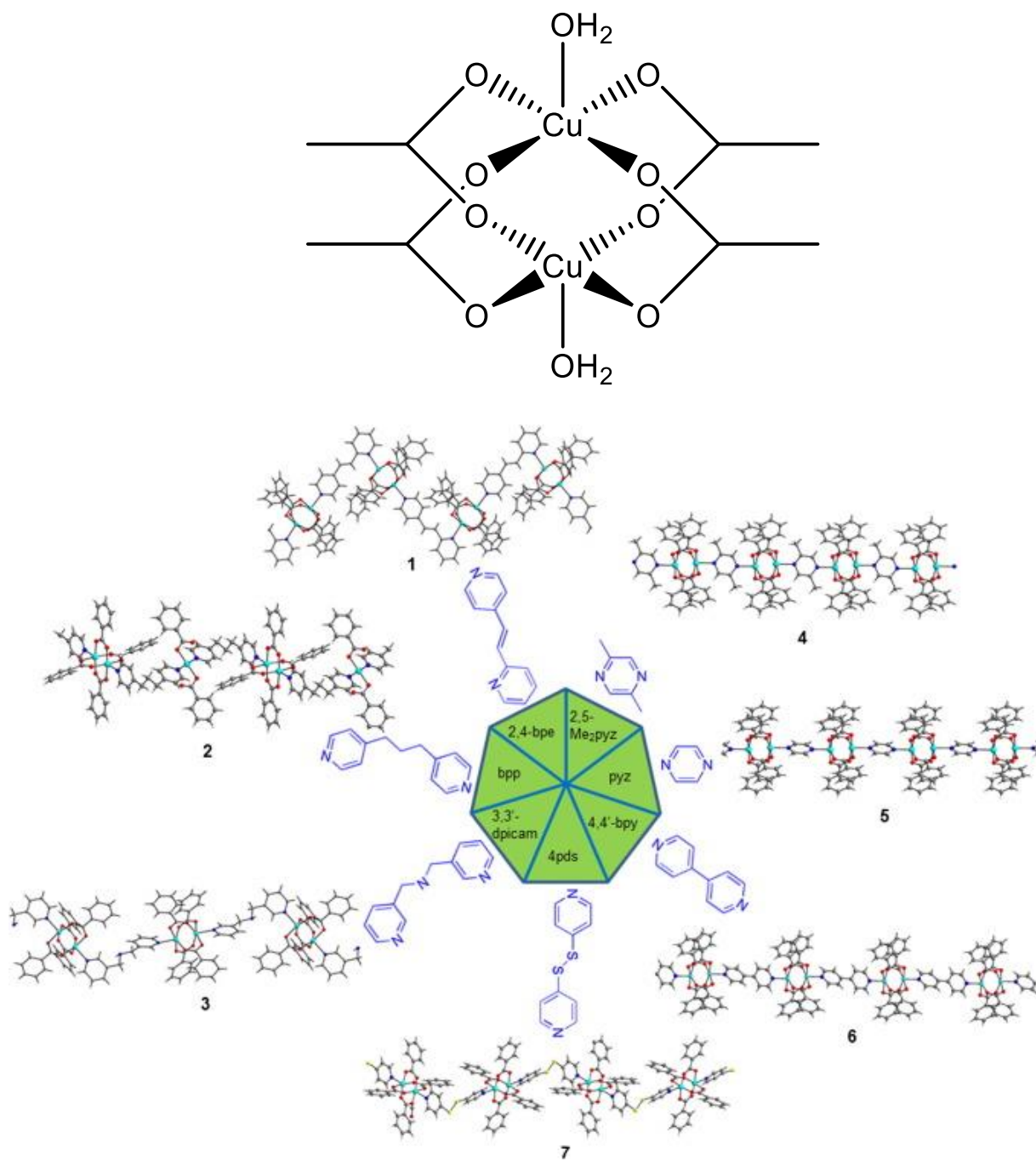
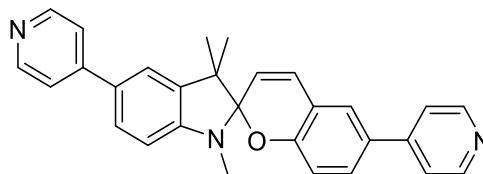


Figure 60 Copper paddlewheel (top). A variety of 1D frameworks synthesised by Hwang et al. utilising the copper paddlewheel and various N-heterocycle based pillar linkers<sup>30</sup> (bottom).

### 3.3.1.1.1 Linker 3a

Outlined below is a list of all the synthetic attempts at incorporating ligand **3a** into a 1D framework. In Table 11, the measure of success is given by a numbering system which shall be used through this chapter. After each attempt the reaction mixture would be checked under an optical microscope for any resulting material or change, any resulting material was analysed by PXRD/SCXRD when possible. Outcome 1 indicates that no observable change had occurred. Outcome 2 indicates that some change had been observed however the resulting material did not produce any usable data via PXRD or SCXRD. Outcome 3a indicates that a novel crystalline material incorporating of the spiropyran linker (outcome 3b indicates a literature known framework that does not incorporate spiropyran linker) was produced which could be characterised via SCXRD and/or PXRD but that also a lot of other uncharacterizable amorphous material was present. Outcome 4a indicates a novel crystalline material incorporating the spiropyran linker (outcome 4b indicates a literature known material that does not incorporate a spiropyran linker), in this case the crystalline material forms the bulk of the mixture.



Experiment <sup>(ref.)</sup>	Pillaring linker (P) (mmol)	Layering linker (L)	Metal Salt (M)	Molar ratio P:L:M	Solvent(s) (v:v)	Vessel	Temperature (°C)	Time	Notes	Result
<b>3a-01-a</b> <sup>30</sup>	0.025	CH <sub>3</sub> COO	Cu(NO <sub>3</sub> ) <sub>2</sub>	2:2:1	DCM:MeOH (1:1)	Wheaton vial	60	48h	-	1
CIJTAS		NH <sub>4</sub>	3H <sub>2</sub> O							
<b>3a-01-b</b> <sup>30</sup>	0.025	CH <sub>3</sub> COO	Cu(NO <sub>3</sub> ) <sub>2</sub>	2:1:1	DCM:MeOH (1:1)	Wheaton vial	60	48h	-	1
CIJTAS		NH <sub>4</sub>	3H <sub>2</sub> O							

<b>3a-01-c<sup>30</sup></b>	0.025	CH <sub>3</sub> COO	Cu(NO <sub>3</sub> ) <sub>2</sub>	4:2:1	DCM:MeOH (1:1)	Wheaton vial	60	48h	-	1
CIJTAS		NH <sub>4</sub>	3H <sub>2</sub> O							
<b>3a-01-d<sup>30</sup></b>	0.025	CH <sub>3</sub> COO	Cu(NO <sub>3</sub> ) <sub>2</sub>	4:4:1	DCM:MeOH (1:1)	Wheaton vial	60	48h	-	1
CIJTAS		NH <sub>4</sub>	3H <sub>2</sub> O							
<b>3a-01-e<sup>30</sup></b>	0.025	C <sub>6</sub> H <sub>5</sub> COO	Cu(NO <sub>3</sub> ) <sub>2</sub>	2:2:1	DCM:DMF (1:1)	Wheaton vial	60	48h	-	1
CIJTAS		NH <sub>4</sub>	3H <sub>2</sub> O							
<b>3a-01-f<sup>30</sup></b>	0.025	C <sub>6</sub> H <sub>5</sub> COO	Cu(NO <sub>3</sub> ) <sub>2</sub>	2:1:1	DCM:DMF (1:1)	Wheaton vial	60	48h	-	1
CIJTAS		NH <sub>4</sub>	3H <sub>2</sub> O							
<b>3a-01-g<sup>30</sup></b>	0.025	C <sub>6</sub> H <sub>5</sub> COO	Cu(NO <sub>3</sub> ) <sub>2</sub>	4:2:1	DCM:DMF (1:1)	Wheaton vial	60	48h	-	1
CIJTAS		NH <sub>4</sub>	3H <sub>2</sub> O							
<b>3a-01-h<sup>30</sup></b>	0.025	C <sub>6</sub> H <sub>5</sub> COO	Cu(NO <sub>3</sub> ) <sub>2</sub>	4:4:1	DCM:DMF (1:1)	Wheaton vial	60	48h	-	1
CIJTAS		NH <sub>4</sub>	3H <sub>2</sub> O							
<b>3a-01-i<sup>30</sup></b>	0.025	C <sub>6</sub> H <sub>5</sub> COO Na	Cu(NO <sub>3</sub> ) <sub>2</sub>	2:2:1	DCM:MeOH (1:1)	Wheaton vial	60	48h	-	1
CIJTAS			3H <sub>2</sub> O							
<b>3a-01-j<sup>30</sup></b>	0.025	C <sub>6</sub> H <sub>5</sub> COO Na	Cu(NO <sub>3</sub> ) <sub>2</sub>	2:1:1	DCM:MeOH (1:1)	Wheaton vial	60	48h	-	1
CIJTAS			3H <sub>2</sub> O							
<b>3a-01-k<sup>30</sup></b>	0.025	C <sub>6</sub> H <sub>5</sub> COO Na	Cu(NO <sub>3</sub> ) <sub>2</sub>	4:2:1	DCM:MeOH (1:1)	Wheaton vial	60	48h	-	1
CIJTAS			3H <sub>2</sub> O							
<b>3a-01-l<sup>30</sup></b>	0.025	C <sub>6</sub> H <sub>5</sub> COO Na	Cu(NO <sub>3</sub> ) <sub>2</sub>	4:4:1	DCM:MeOH (1:1)	Wheaton vial	60	48h	-	1
CIJTAS			3H <sub>2</sub> O							
<b>3a-01-m<sup>30</sup></b>	0.025	CH <sub>3</sub> COO Na	Cu(NO <sub>3</sub> ) <sub>2</sub>	2:2:1	DCM:DMF (1:1)	Wheaton vial	60	48h	-	1
CIJTAS			3H <sub>2</sub> O							

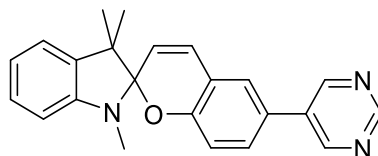
<b>3a-01-n</b> <sup>30</sup>	0.025	CH <sub>3</sub> COO Na	Cu(NO <sub>3</sub> ) <sub>2</sub>	2:1:1	DCM:DMF (1:1)	Wheaton vial	60	48h	-	1
CIJTAS			3H <sub>2</sub> O							
<b>3a-01-o</b> <sup>30</sup>	0.025	CH <sub>3</sub> COO Na	Cu(NO <sub>3</sub> ) <sub>2</sub>	4:2:1	DCM:DMF (1:1)	Wheaton vial	60	48h	-	1
CIJTAS			3H <sub>2</sub> O							
<b>3a-01-p</b> <sup>30</sup>	0.025	CH <sub>3</sub> COO Na	Cu(NO <sub>3</sub> ) <sub>2</sub>	4:4:1	DCM:DMF (1:1)	Wheaton vial	60	48h	-	1
CIJTAS			3H <sub>2</sub> O							

Table 11 Outlines the conditions of each attempt at synthesising a 1D framework incorporating ligand **4a**. Vessel volumes: Wheaton Vial - 2.5 mL, Pressure Tube - 10 mL, Parr Bomb - 10 mL. \* denotes modulator. Outcomes: 1 = no reaction, 2 = amorphous/not crystalline enough for characterisation, 3a = novel crystalline and amorphous material, 3b = literature known crystalline and amorphous material, 4a = novel crystalline material, 4b = literature known crystalline material

The 1-D framework attempts were unsuccessful using benzoate and acetate linkers. Ammonium and sodium-based carboxylates were used to see if there was any significant modulating effect from the counter ion that could improve the synthesis. Copper was used as the metal source despite its photoactive tendencies. The reasoning was that, due to the work by *Hwang et al.*,<sup>30</sup> succeeding with copper would be more representative. If a positive result was achieved then we would have focused our efforts on optimising synthetic conditions for zinc, as there are examples of zinc also forming these paddlewheels. As these efforts were unsuccessful, we moved onto other strategies.

2-D frameworks often include N-heterocyclic ligands, often acting as excellent capping agents allowing the carboxylate linkers to expand along the other two axes. Our efforts primarily focused on 4,4'-biphenyldicarboxylic acid as the layer linker, due to a lot of examples of 2-D frameworks using this linker and also because we had some success with this layer linker in other attempts, discussed further on. The 5-pyrimidyl spiropyran ligand (**4c**) was used. The obvious advantages of a pyrimidyl linker are as follows; one extra possible coordination site, an increase in the effectiveness of intermolecular forces that are intrinsic to keeping 2-D framework layers together, and the increased electron density on the ring will allow for potentially stronger M-N bonds to form.

### 3.3.1.1.2 Linker 4c



Experiment <sup>(ref.)</sup>	Pillaring linker (P) (mmol)	Layering linker (L)	Metal Salt (M)	Molar ratio P:L:M	Solvent(s) (v:v)	Vessel	Temperature (°C)	Time	Notes	Result
4c-02-a	0.03	BPDC	Zn(NO <sub>3</sub> ) <sub>2</sub> 6H <sub>2</sub> O	1:1:1	DMF:H <sub>2</sub> O (2:3)	Wheaton vial	100	96h	-	2
4c-02-b	0.03	BPDC	Zn(NO <sub>3</sub> ) <sub>2</sub> 6H <sub>2</sub> O	1:4:8	DMF:H <sub>2</sub> O (2:3)	Wheaton vial	100	96h	-	2
4c-02-c	0.03	BPDC	Zn(NO <sub>3</sub> ) <sub>2</sub> 6H <sub>2</sub> O	1:4:8	DMF	Wheaton vial	100	96h	-	1
4c-02-d	0.03	BPDC	Zn(NO <sub>3</sub> ) <sub>2</sub> 6H <sub>2</sub> O	1:4:4	DMF:H <sub>2</sub> O (2:3)	Wheaton vial	100	96h	-	1
4c-02-e	0.03	BPDC	Zn(NO <sub>3</sub> ) <sub>2</sub> 6H <sub>2</sub> O	1:4:4	DMF:MeOH (3:2)	Wheaton vial	100	96h	-	3b
4c-02-f	0.03	BPDC	Zn(NO <sub>3</sub> ) <sub>2</sub> 6H <sub>2</sub> O	1:4:4	DEF	Wheaton vial	100	96h	-	2

4c-02-g	0.03	TPA	Zn(NO <sub>3</sub> ) <sub>2</sub> 6H <sub>2</sub> O	1:4:8	DMF	Wheaton vial	100	96h	-	4b
4c-02-h	0.06	TPA	Zn(NO <sub>3</sub> ) <sub>2</sub> 6H <sub>2</sub> O	1:1:4	DMF	Wheaton vial	100	96h	-	4b
4c-03-a	0.03	BPDC	Zn(NO <sub>3</sub> ) <sub>2</sub> 6H <sub>2</sub> O	1:4:4	DEF	Wheaton vial	100	96h	0.2 uL HCl*	2
4c-03-b	0.03	BPDC	Zn(NO <sub>3</sub> ) <sub>2</sub> 6H <sub>2</sub> O	1:4:4	DEF	Wheaton vial	100	96h	0.4 uL HCl*	2
4c-03-c	0.03	BPDC	Zn(NO <sub>3</sub> ) <sub>2</sub> 6H <sub>2</sub> O	1:4:4	DEF	Wheaton vial	100	96h	0.8 uL HCl*	2
4c-03-d	0.03	BPDC	Zn(NO <sub>3</sub> ) <sub>2</sub> 6H <sub>2</sub> O	1:4:4	DEF	Wheaton vial	100	96h	1.6 uL HCl*	2
4c-03-e	0.03	BPDC	Zn(NO <sub>3</sub> ) <sub>2</sub> 6H <sub>2</sub> O	1:2:4	DEF	Wheaton vial	100	96h	0.2 uL HCl*	2
4c-03-f	0.03	BPDC	Zn(NO <sub>3</sub> ) <sub>2</sub> 6H <sub>2</sub> O	1:2:4	DEF	Wheaton vial	100	96h	0.4 uL HCl*	2
4c-03-g	0.03	BPDC	Zn(NO <sub>3</sub> ) <sub>2</sub> 6H <sub>2</sub> O	1:2:4	DEF	Wheaton vial	100	96h	0.8 uL HCl*	2
4c-03-h	0.03	BPDC	Zn(NO <sub>3</sub> ) <sub>2</sub> 6H <sub>2</sub> O	1:2:4	DEF	Wheaton vial	100	96h	1.6 uL HCl*	2
4c-04-a	0.03	BPDC	Zn(NO <sub>3</sub> ) <sub>2</sub> 6H <sub>2</sub> O	1:4:4	DMF	Wheaton vial	100	96h	-	3b

4c-04-b	0.03	BPDC	Zn(NO <sub>3</sub> ) <sub>2</sub> 6H <sub>2</sub> O	1:8:8	DMF	Wheaton vial	100	96h	20 uL HCl*	2
4c-04-c	0.03	BPDC	Zn(NO <sub>3</sub> ) <sub>2</sub> 6H <sub>2</sub> O	2:2:9	DMF	Wheaton vial	100	24h	20uL HCl*	1
4c-04-d	0.03	BPDC	Zn(NO <sub>3</sub> ) <sub>2</sub> 6H <sub>2</sub> O	1:8:8	DMF	Wheaton vial	80	24h	-	1
4c-04-e	0.03	BPDC	Zn(NO <sub>3</sub> ) <sub>2</sub> 6H <sub>2</sub> O	1:8:1	DMF	Wheaton vial	60	60h	20 uL HCl*	1
4c-04-f	0.03	BPDC	Zn(NO <sub>3</sub> ) <sub>2</sub> 6H <sub>2</sub> O	1:1:8	DMF	Wheaton vial	60	96h	10uL HCl*	1
4c-04-g	0.03	BPDC	Zn(NO <sub>3</sub> ) <sub>2</sub> 6H <sub>2</sub> O	2:9:2	DMF	Wheaton vial	100	96h	-	3b
4c-04-h	0.06	BPDC	Zn(NO <sub>3</sub> ) <sub>2</sub> 6H <sub>2</sub> O	2:9:16	DMF	Wheaton vial	60	24h	20 uL HCl*	1
4c-04-i	0.03	BPDC	Zn(NO <sub>3</sub> ) <sub>2</sub> 6H <sub>2</sub> O	1:8:1	DMF	Wheaton vial	100	24h	10 uL HCl*	1
4c-04-j	0.03	BPDC	Zn(NO <sub>3</sub> ) <sub>2</sub> 6H <sub>2</sub> O	1:1:8	DMF	Wheaton vial	100	60h	-	3b
4c-04-k	0.03	BPDC	Zn(NO <sub>3</sub> ) <sub>2</sub> 6H <sub>2</sub> O	1:1:1	DMF	Wheaton vial	80	96h	20 uL HCl*	1
4c-04-l	0.03	BPDC	Zn(NO <sub>3</sub> ) <sub>2</sub> 6H <sub>2</sub> O	2:16:9	DMF	Wheaton vial	60	96h	-	1

4c-04-m	0.03	BPDC	Zn(NO <sub>3</sub> ) <sub>2</sub> 6H <sub>2</sub> O	1:1:1	DMF	Wheaton vial	100	24h	-	1
4c-04-n	0.03	BPDC	Zn(NO <sub>3</sub> ) <sub>2</sub> 6H <sub>2</sub> O	1:1:1	DMF	Wheaton vial	60	24h	20 uL HCl*	1
4c-04-o	0.03	BPDC	Zn(NO <sub>3</sub> ) <sub>2</sub> 6H <sub>2</sub> O	1:8:8	DMF	Wheaton vial	60	24h	-	1
4c-04-p	0.03	BPDC	Zn(NO <sub>3</sub> ) <sub>2</sub> 6H <sub>2</sub> O	1:8:1	DMF	Wheaton vial	60	24h	-	1
4c-05-a	0.03	BPDC	Zn(NO <sub>3</sub> ) <sub>2</sub> 6H <sub>2</sub> O	1:4:4	DEF	Wheaton Vial	100	24h	-	4b
4c-05-b	0.03	BPDC	Zn(NO <sub>3</sub> ) <sub>2</sub> 6H <sub>2</sub> O	1:4:4	DMF	Wheaton vial	100	72h	-	4b
4c-05-c	0.03	BPDC	Zn(NO <sub>3</sub> ) <sub>2</sub> 6H <sub>2</sub> O	1:4:4	DMF	Wheaton vial	100	72h	0.3 uL HCl*	4b
4c-05-d	0.03	BPDC	Zn(NO <sub>3</sub> ) <sub>2</sub> 6H <sub>2</sub> O	1:4:4	DMF	Wheaton vial	100	72h	1 uL HCl*	4b
4c-05-e	0.03	BPDC	Zn(NO <sub>3</sub> ) <sub>2</sub> 6H <sub>2</sub> O	1:4:4	DMF	Wheaton Vial	100	72h	5 uL HCl*	4b
4c-05-f	0.03	BPDC	Zn(NO <sub>3</sub> ) <sub>2</sub> 6H <sub>2</sub> O	1:4:4	DMF	Wheaton vial	100	72h	10 uL HCl*	4b
4c-05-g	0.03	BPDC	Zn(NO <sub>3</sub> ) <sub>2</sub> 6H <sub>2</sub> O	1:4:4	DMF	Wheaton vial	100	72h	0.3 uL HNO <sub>3</sub> *	4b



<b>4c-05-h</b>	0.03	BPDC	Zn(NO <sub>3</sub> ) <sub>2</sub> 6H <sub>2</sub> O	1:4:4	DMF	Wheaton vial	100	72h	1 uL HNO <sub>3</sub> *	4b
<b>4c-05-i</b>	0.03	BPDC	Zn(NO <sub>3</sub> ) <sub>2</sub> 6H <sub>2</sub> O	1:4:4	DMF	Wheaton Vial	100	72h	5 uL HNO <sub>3</sub> *	4b
<b>4c-05-j</b>	0.03	BPDC	Zn(NO <sub>3</sub> ) <sub>2</sub> 6H <sub>2</sub> O	1:4:4	DMF	Wheaton vial	100	72h	10 uL HNO <sub>3</sub> *	4b
<b>4c-05-k</b>	0.03	BPDC	Zn(NO <sub>3</sub> ) <sub>2</sub> 6H <sub>2</sub> O	1:4:4	DEF	Wheaton vial	100	72h	1 uL HCl*	1
<b>4c-05-l</b>	0.03	BPDC	Zn(NO <sub>3</sub> ) <sub>2</sub> 6H <sub>2</sub> O	1:4:4	DEF	Wheaton Vial	100	72h	1 uL HNO <sub>3</sub> *	1
<b>4c-06-a</b>	0.03	DBTD	Zn(NO <sub>3</sub> ) <sub>2</sub> ·6H <sub>2</sub> O	4:3:15	DMF	Wheaton vial	80	72h	0.3 uL HCl*	1
<b>4c-06-b</b>	0.03	DBTD	Zn(NO <sub>3</sub> ) <sub>2</sub> ·6H <sub>2</sub> O	4:3:15	DMF	Wheaton vial	80	72h		1

Table 12 Outlines the conditions of each attempt at synthesising a 2D framework incorporating ligand **4c**. Vessel volumes: Wheaton Vial - 2.5 mL, Pressure Tube - 10 mL, Parr Bomb - 10 mL. \* denotes modulator. Outcomes: 1 = no reaction, 2 = amorphous/not crystalline enough for characterisation, 3a = novel crystalline and amorphous material, 3b = literature known crystalline and amorphous material, 4a = novel crystalline material, 4b = literature known crystalline material

Using **4c** and bpdc, many attempts were made at optimising the synthesis by varying solvents, temperature, concentration, time, and modulators. The reason was that crystalline material did form in some cases however it was too poor a quality to establish its identity via PXRD or SCXRD. Further attempts did manage to create crystals of sufficient quality for SCXRD. These crystalline materials shown no incorporation of the spiro linker and were simply an IRMOF-9/10 framework (see Figure 61, Figure 49) . Although this may not necessarily be the case for all the reactions where crystals were not suitable for characterisation, enough attempts were made to determine that either we were obtaining a material with no spiro pyran incorporated or a material that could not be made

reliably enough to be characterised. With such little success designing 1D/2D-frameworks, as well as not being as desirable as a 3D photoactive framework, the rest of our efforts focused on 3D frameworks.

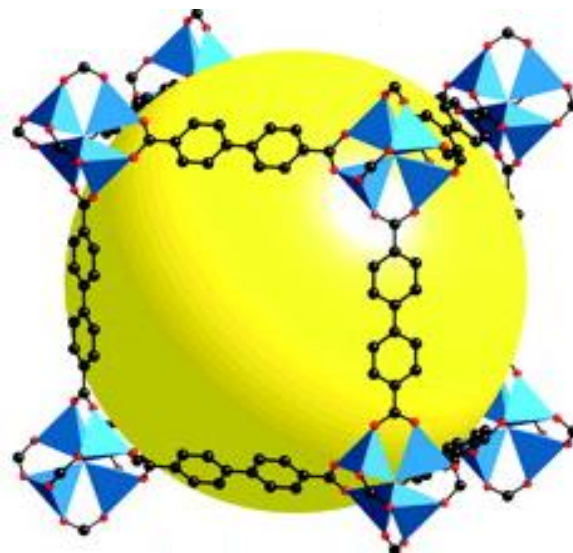
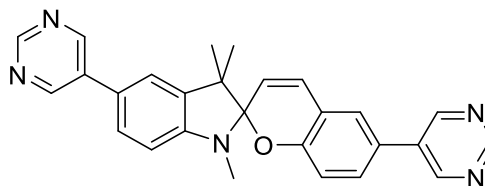


Figure 61 Image of IRMOF-10 (IRMOF-9 is the same but doubly interpenetrated) from M. Eddaoudi et al. who report interpenetration is more likely in higher concentrations of reagents (i.e. BPDC and  $Zn(NO_3)_2$ ).<sup>31</sup>

### 3.3.1.2 3D-Frameworks

#### 3.3.1.2.1 Linker 3c

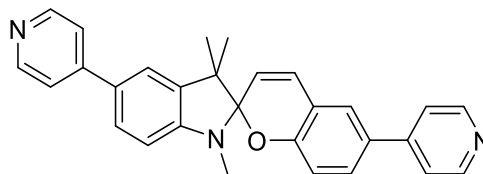


Experiment <sup>(ref.)</sup>	Pillaring linker (P) (mmol)	Layering linker (L)	Metal Salt (M)	Molar ratio P:L:M	Solvent(s) (v:v)	Vessel	Temperature (°C)	Time	Notes	Result
<b>3c-07-a</b>	0.02	BPDC	Zn(NO <sub>3</sub> ) <sub>2</sub> 6H <sub>2</sub> O	1:1:2	DMF:MeOH (1:1)	Wheaton vial	100	96h	-	3b
<b>3c-07-b</b>	0.02	BPDC	Zn(NO <sub>3</sub> ) <sub>2</sub> 6H <sub>2</sub> O	1:1:2	DMF	Wheaton vial	100	96h	-	3b
<b>3c-07-c</b>	0.02	BPDC	Zn(NO <sub>3</sub> ) <sub>2</sub> 6H <sub>2</sub> O	1:4:8	DMF	Wheaton vial	100	96h	-	3b
<b>3c-07-d</b>	0.02	BPDC	Zn(NO <sub>3</sub> ) <sub>2</sub> 6H <sub>2</sub> O	1:4:8	DEF	Wheaton vial	100	96h	-	1
<b>3c-07-e</b>	0.06	BPDC	Zn(NO <sub>3</sub> ) <sub>2</sub> 6H <sub>2</sub> O	3:1:8	DMF	Wheaton vial	100	96h	-	3b
<b>3c-07-f</b>	0.02	BPDC	Zn(NO <sub>3</sub> ) <sub>2</sub> 6H <sub>2</sub> O	1:4:6	DMF	Wheaton vial	100	96h	-	3b
<b>3c-07-g</b>	0.02	TPA	Zn(NO <sub>3</sub> ) <sub>2</sub> 6H <sub>2</sub> O	1:1:4	DMF	Wheaton vial	100	96h	-	3b
<b>3c-07-h</b>	0.04	TPA	Zn(NO <sub>3</sub> ) <sub>2</sub> 6H <sub>2</sub> O	2:1:8	DEF	Wheaton vial	100	96h	-	3b

Table 13 Outlines the conditions of each attempt at synthesising a 3D framework incorporating ligand **3c**. Vessel volumes: Wheaton Vial - 2.5 mL, Pressure Tube - 10 mL, Parr Bomb - 10 mL. \* denotes modulator. Outcomes: 1 = no reaction, 2 = amorphous/not crystalline enough for characterisation, 3a = novel crystalline and amorphous material, 3b = literature known crystalline and amorphous material, 4a = novel crystalline material, 4b = literature known crystalline material

Much like our efforts with **4c**, attempts at a framework using **3c** also failed to incorporate the spiropyran linker. Instead, the result was a formation of IRMOF-9 or IRMOF-10 (or in the cases of **3c-07-e/f**, MOF-5 was produced). The pyrimidyl functionality is seemingly not binding, or at least without sufficient strength to encourage a framework.

### 3.3.1.2.2 Linker **3a**



Experiment (ref.)	Pillaring linker (P) (mmol)	Layering linker (L)	Metal Salt (M)	Molar Ratio P:L:M	Solvent(s) (v:v)	Vessels	Temperature (°C)	Time	Notes	Result
<b>3a-08-a</b> <sup>32</sup>	0.01	H <sub>3</sub> BTB	Zn(NO <sub>3</sub> ) <sub>2</sub> 6H <sub>2</sub> O	3:4:6	DMF	Wheaton vial	85	48h	-	1
<b>3a-08-b</b> <sup>33</sup>	0.01	H <sub>3</sub> BTB	Zn(NO <sub>3</sub> ) <sub>2</sub> 6H <sub>2</sub> O	1.05:1:4	DEF	Wheaton vial	100	24h	-	1
<b>3a-08-c</b> <sup>34</sup>	1	IPA	Zn(NO <sub>3</sub> ) <sub>2</sub> 6H <sub>2</sub> O	1:1:1	H <sub>2</sub> O	Parr bomb	170	72h	-	1
<b>3a-08-d</b> <sup>35</sup>	0.1	TPA	ZnCl <sub>2</sub>	1:1:1	H <sub>2</sub> O	Wheaton vial	100	18h	-	1
<b>3a-08-e</b> <sup>35</sup>	0.05	IPA	Zn(CH <sub>3</sub> CO <sub>2</sub> ) 2H <sub>2</sub> O	1:1:1	H <sub>2</sub> O	Wheaton vial	100	18h	-	1

<b>3a-08-f</b> <sup>35</sup>	0.05	IPA	Co(CH <sub>3</sub> CO <sub>2</sub> ) 4H <sub>2</sub> O	1:1:1	H <sub>2</sub> O	Wheaton vial	100	24h	-	1
<b>3a-08-g</b> <sup>35</sup>	0.1	TPA	Co(CH <sub>3</sub> CO <sub>2</sub> ) 4H <sub>2</sub> O	1:1:1	H <sub>2</sub> O	Wheaton vial	100	18h	-	1
<b>3a-08-h</b> <sup>35</sup>	0.05	IPA	Ni(CH <sub>3</sub> CO <sub>2</sub> )	1:1:1	H <sub>2</sub> O:DMF (4:1)	Wheaton vial	100	18h	-	1
<b>3a-08-i</b> <sup>35</sup>	0.2	TPA	Ni(CH <sub>3</sub> CO <sub>2</sub> ) <sub>2</sub> 4H <sub>2</sub> O	1:1:1	H <sub>2</sub> O	Wheaton vial	100	24h	-	1
<b>3a-08-j</b> <sup>35</sup>	0.1	IPA	Cu(CH <sub>3</sub> CO <sub>2</sub> ) <sub>2</sub> H <sub>2</sub> O	1:1:1	H <sub>2</sub> O	Wheaton vial	100	18h	-	1
<b>3a-08-k</b> <sup>33</sup>	0.27	TMA	Cu(NO <sub>3</sub> ) <sub>2</sub> 3H <sub>2</sub> O	1.05:1:4	DMF:EtOH 1:1	Pressure tube	80	20h	TFA (2 drops)	1
<b>3a-08-l</b> <sup>33</sup>	0.27	TMA	Co(NO <sub>3</sub> ) <sub>2</sub> 6H <sub>2</sub> O	1.05:1:4	DEF	Pressure tube	80	48h	-	1
<b>3a-08-m</b>	0.54	TMA	Ni(NO <sub>3</sub> ) <sub>2</sub> 6H <sub>2</sub> O	2.7:2.5:1	DMF	Wheaton vial	120	48h	-	1
<b>3a-09-a</b> <sup>32</sup>	0.02	H <sub>3</sub> BTB	Zn(NO <sub>3</sub> ) <sub>2</sub> 6H <sub>2</sub> O	4:3:6	DMF	Wheaton vial	85	72h	-	1
<b>3a-09-b</b> <sup>32</sup>	0.02	H <sub>3</sub> BTB	Zn(NO <sub>3</sub> ) <sub>2</sub> 6H <sub>2</sub> O	8:3:6	DMF	Wheaton vial	85	72h	-	1
<b>3a-09-c</b> <sup>32</sup>	0.02	H <sub>3</sub> BTB	Co(NO <sub>3</sub> ) <sub>2</sub> 6H <sub>2</sub> O	4:3:6	DMF	Wheaton vial	85	72h	-	1

<b>3a-09-d</b> <sup>32</sup>	0.02	H <sub>3</sub> BTB	Co(NO <sub>3</sub> ) <sub>2</sub> 6H <sub>2</sub> O	8:3:6	DMF	Wheaton vial	85	72h	-	1
<b>3a-10-a</b> <sup>33</sup>	0.02	H <sub>3</sub> BTB	Cu(NO <sub>3</sub> ) <sub>2</sub> 3H <sub>2</sub> O	1.05:1:4	DMF:EtOH (1:1)	Wheaton Vial	85	72h	TFA (2 drops)	1
<b>3a-10-b</b> <sup>33</sup>	0.02	H <sub>3</sub> BTB	Cu(NO <sub>3</sub> ) <sub>2</sub> 3H <sub>2</sub> O	1.05:1:4	DMF:EtOH (1:1)	Wheaton Vial	85	72h		1
<b>3a-10-c</b> <sup>33</sup>	0.02	H <sub>3</sub> BTB	Co(NO <sub>3</sub> ) <sub>2</sub> 6H <sub>2</sub> O	1.05:1:4	DEF	Wheaton Vial	85	72h	-	1
<b>3a-10-d</b> <sup>33</sup>	0.02	H <sub>3</sub> BTB	Co(NO <sub>3</sub> ) <sub>2</sub> 6H <sub>2</sub> O	1.05:1:4	DEF	Wheaton Vial	85	72h	-	1
<b>3a-11-a</b> <sup>32</sup> VEDWUY	0.02	H <sub>3</sub> BTB	Zn(NO <sub>3</sub> ) <sub>2</sub> 6H <sub>2</sub> O	3:4:60	DMF	Wheaton Vial	85	72h	-	1
<b>3a-11-b</b> <sup>32</sup> VEDWUY	0.02	H <sub>3</sub> BTB	Zn(NO <sub>3</sub> ) <sub>2</sub> 6H <sub>2</sub> O	4:1:20	DMF	Wheaton Vial	85	72h	-	1
<b>3a-12-a</b>	0.02	BPDC	Zn(NO <sub>3</sub> ) <sub>2</sub> 6H <sub>2</sub> O	1:1:2	DMF:MeOH (1:1)	Wheaton vial	100	240h	-	2
<b>3a-12-b</b>	0.02	BPDC	Zn(NO <sub>3</sub> ) <sub>2</sub> 6H <sub>2</sub> O	1:2:2	DMF	Wheaton vial	100	240h	-	2
<b>3a-12-c</b>	0.02	BPDC	Zn(NO <sub>3</sub> ) <sub>2</sub> 6H <sub>2</sub> O	1:1:2	MeOH:DEF (1:1)	Wheaton vial	100	240h	-	2
<b>3a-12-d</b>	0.02	BPDC	Zn(NO <sub>3</sub> ) <sub>2</sub> 6H <sub>2</sub> O	1:2:2	DEF	Wheaton vial	100	240h	-	1

<b>3a-12-e</b>	0.02	BPDC	Zn(NO <sub>3</sub> ) <sub>2</sub> 6H <sub>2</sub> O	1:1:2	EtOH:DMF (1:1)	Wheaton vial	100	240h	-	2
<b>3a-12-f</b>	0.02	BPDC	Zn(NO <sub>3</sub> ) <sub>2</sub> 6H <sub>2</sub> O	1:2:2	DMF	Wheaton vial	100	240h	HNO <sub>3</sub> (2 drops)	1
<b>3a-12-g</b>	0.02	BPDC	Zn(NO <sub>3</sub> ) <sub>2</sub> 6H <sub>2</sub> O	1:1:2	EtOH:DMF (1:1)	Wheaton vial	100	240h		2
<b>3a-12-h</b>	0.02	BPDC	Zn(NO <sub>3</sub> ) <sub>2</sub> 6H <sub>2</sub> O	1:2:2	DEF	Wheaton vial	100	240h	HNO <sub>3</sub> (2 drops)	1
<b>3a-12-i</b>	0.02	BPDC	In(NO <sub>3</sub> ) <sub>2</sub> H <sub>2</sub> O	1:2:2	DMF	Wheaton vial	100	240h	-	1
<b>3a-12-j</b>	0.02	BPDC	In(NO <sub>3</sub> ) <sub>2</sub> H <sub>2</sub> O	1:1:2	DMF:MeOH (1:1)	Wheaton vial	100	240h	-	1
<b>3a-12-k</b>	0.02	BPDC	In(NO <sub>3</sub> ) <sub>2</sub> H <sub>2</sub> O	1:2:2	DEF	Wheaton vial	100	240h	-	1
<b>3a-12-l</b>	0.02	BPDC	In(NO <sub>3</sub> ) <sub>2</sub> H <sub>2</sub> O	1:1:2	DEF:MeOH (1:1)	Wheaton vial	100	240h	-	1
<b>3a-13-a</b>	0.001	BPDC	Zn(NO <sub>3</sub> ) <sub>2</sub> 6H <sub>2</sub> O	1:1:2	DMF:MeOH (1:1)	Pressure tube	100	96h	-	4a (LK-1/2)
<b>3a-13-b</b>	0.001	BPDC	Zn(NO <sub>3</sub> ) <sub>2</sub> 6H <sub>2</sub> O	1:2:2	DMF	Pressure tube	100	96h	-	4b
<b>3a-13-c</b>	0.001	BPDC	Zn(NO <sub>3</sub> ) <sub>2</sub> 6H <sub>2</sub> O	1:1.4:1.5	DEF	Pressure tube	100	96h	-	4b
<b>3a-13-d</b>	0.001	BPDC	Zn(NO <sub>3</sub> ) <sub>2</sub> 6H <sub>2</sub> O	1:1.17:1.8	DEF:MeOH (1:1)	Pressure tube	100	96h	-	4a (LK-1/2)

<b>3a-14-a</b>	BPDC	In(NO <sub>3</sub> ) <sub>2</sub> 3H <sub>2</sub> O	DMF	Pressure tube	100	168h	-	2
<b>3a-14-b</b>	BPDC	Zn(NO <sub>3</sub> ) <sub>2</sub> 6H <sub>2</sub> O	DMF:MeOH (1:1)	Pressure tube	100	168h	-	1
<b>3a-14-c</b>	BPDC	Zn(NO <sub>3</sub> ) <sub>2</sub> 6H <sub>2</sub> O	DMF	Pressure tube	100	168h	-	2
<b>3a-14-d</b>	BPDC	Zn(NO <sub>3</sub> ) <sub>2</sub> 6H <sub>2</sub> O	DEF	Pressure tube	100	168h	-	2
<b>3a-14-e</b>	BPDC	Zn(NO <sub>3</sub> ) <sub>2</sub> 6H <sub>2</sub> O	DEF:MeOH (1:1)	Pressure tube	100	168h	-	1

Table 14 Outlines the conditions of each attempt at synthesising a 3D framework incorporating ligand **3a**. Vessel volumes: Wheaton Vial - 2.5 mL, Pressure Tube - 10 mL, Parr Bomb - 10 mL. \* denotes modulator. Outcomes: 1 = no reaction, 2 = amorphous/not crystalline enough for characterisation, 3a = novel crystalline and amorphous material, 3b = literature known crystalline and amorphous material, 4a = novel crystalline material, 4b = literature known crystalline material



Positive results were achieved when using BPDC as the layer linker (**3a-13-a**) and these experiments produced two novel frameworks: LK-1 and LK-2. These new frameworks are discussed later. The common reasons for negative results were either no characterizable material was synthesised (i.e. amorphous products or crystals were too small to be analysed) or a framework formed without incorporating the spiro pyran linker (as observed in the 2D-framework synthesis attempts). It is well-established in the literature that simpler, symmetrical, and rigid linkers tend to provide better quality crystals.<sup>36,37</sup> Conversely, incorporation of the spiro pyran linker (an asymmetric, flexible linker) as a pillar requires a layer linker that would not simply form a framework on its own that isn't significantly more stable without the spiro pyran linker; typically these are simple, highly symmetrical molecules such as TPA.

Successful results were achieved with zinc nitrate. No such success was observed in the cases of copper, cobalt or nickel nitrates. As mentioned earlier zinc has a much wider scope of accessible geometries due to its full 3d shell<sup>29</sup> therefore it is expected that this would have a distinct advantage over the other metals we tried. Although it is quite common to substitute zinc for copper in metal organic frameworks that have paddlewheels (e.g. HKUST-1, Zn-HKUST-1). We did not attempt to substitute the zinc metal as the frameworks LK-1 and LK-2 did not have paddlewheels but instead a rare penta-coordinate zinc cluster and a tri-nuclear co-linear cluster, respectively. In the case of LK-2, the co-linear structure includes tetrahedrally co-ordinated zinc as well as octahedrally co-ordinated zinc, tetrahedrally coordinated copper is not so easily accessible due to it being much more energetically favourable in the square planar arrangement. In the case of LK-1, there is not enough data as to why such penta-coordinate clusters form in the first place to make an assumption about whether the copper would effectively substitute into this type of framework. However, the coordination of the zinc nodes are trigonal bipyramidal and octahedral geometries (which are both readily accessible for copper) so it could be possible based solely on this factor.<sup>38</sup> There were some results using indium as a metal source which could not be characterised as the small yellow crystals produced were simply too small for crystallographic analysis. We could have pursued these crystals further, however thus far attempts at producing bigger crystals had not improved crystal quality discernibly and there was no guarantee the potential framework incorporated **3a** and so was not investigated further in favour of more promising avenues of research.

The mono-pyrimidyl linker **4c** did not form a MOF structure with BPDC, which is unsurprising as it only binds at one end of the spiro molecule. The intermolecular forces that would act between the molecules are simply not enough to drive the formation of a framework incorporating this linker. If we were to functionalise the other end of the spiro molecule with an isophthalic acid, then we may be able to produce a framework similar to MFM-136 (see Figure 62)

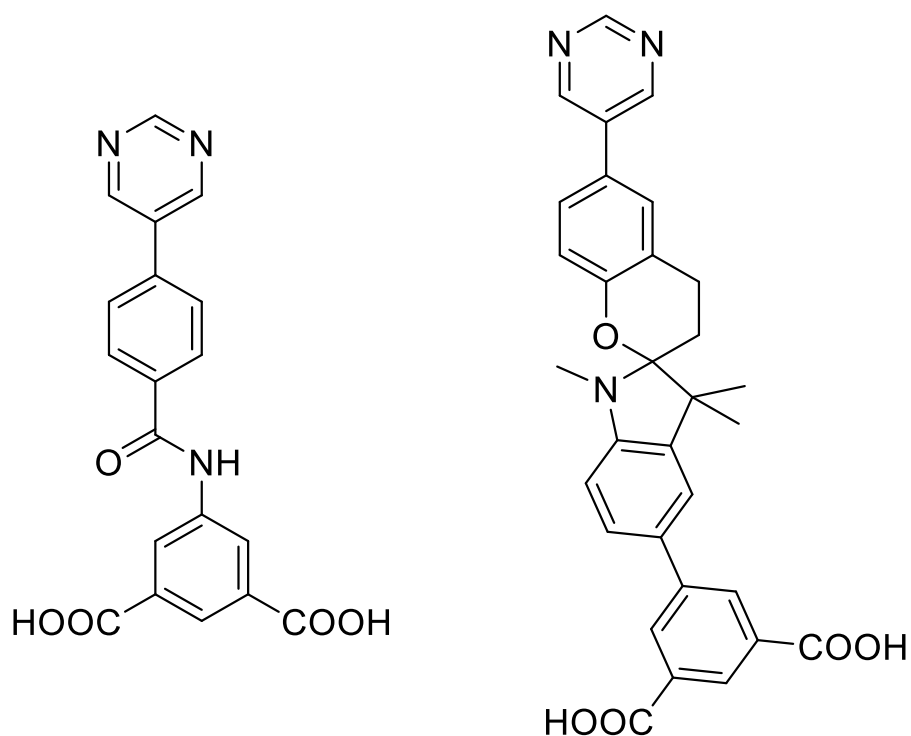
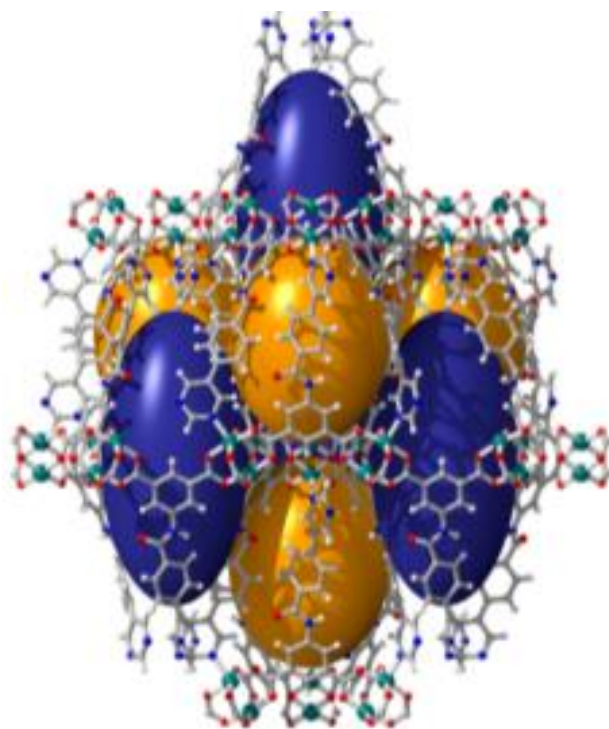


Figure 62 MFM-136 (top) synthesised by Benson et al.<sup>39</sup> using the linker 5-[4-(pyrimidin-5-yl)benzamido]-isophthalic acid (bottom, left). The modified version of the **4c** linker that could potentially form a similar framework (bottom, right). The kink in the linker caused by the amide functionality has a passing similarity to the kink caused by a spiro-centre thus a framework isostructural to MFM-136 may be possible.

The addition of two carboxylic acid moieties would lead to stronger binding forces, also there would not be any potential competition from a co-linker and the impressively sized pores could

accommodate some structural change upon photoconversion. The result would most likely be similar to R. Lyndon et al.'s azobenzene MOF that only succeeded in localised structural change<sup>27</sup>, discussed earlier.

Unlike **4c**, the bipyridyl linker **3a** can bind at both ends and is much more likely to act as a linker in a crystalline framework. Another helpful comparison is that attempts with TPA were unsuccessful in all cases. TPA is a well-studied MOF linker and there are numerous frameworks throughout the literature with a variety of metals that incorporate it in the structure. Therefore, an ideal layer linker for our purposes is one that is symmetrical and rigid while being energetically unfavourable to form a framework with the metal of interest by itself.

### 3.3.1.3 Frameworks incorporating 4',5'-bis(4-carboxyphenyl)-[1,1':2',1''-terphenyl]-4,4''-dicarboxylic acid (DTD) and 3',6'-dibromo-4',5'-bis(4-carboxyphenyl)-[1,1':2',1''-terphenyl]-4,4''-dicarboxylic acid (DBTD)

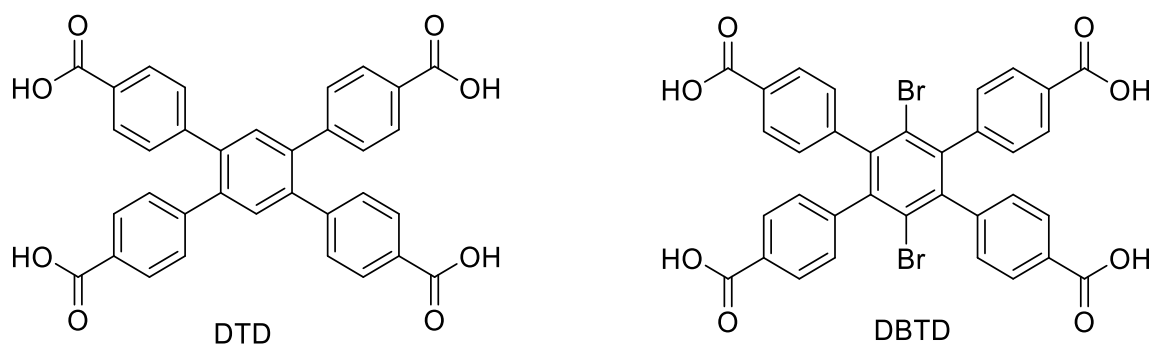
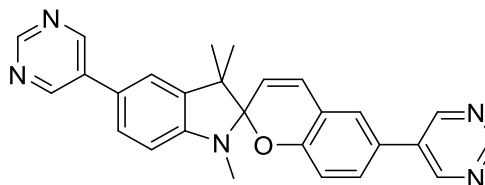


Figure 63 Large layer linkers DTD (4',5'-bis(4-carboxyphenyl)-[1,1':2',1''-terphenyl]-4,4''-dicarboxylic acid) and the brominated variant, DBTD (3',6'-dibromo-4',5'-bis(4-carboxyphenyl)-[1,1':2',1''-terphenyl]-4,4''-dicarboxylic acid)

DBTD (Figure 63) is an excellent candidate as a layer linker, since it is quite large and the bromine atoms provide additional steric hindrance preventing a stable framework forming with just the linker.<sup>40</sup> Having decided to try using the DBTD linker in our syntheses and having synthesised it to use in MOF syntheses, this choice of layer linker was further supported when *D. Williams et al.* reported successful synthesis of a framework using DBTD with a co-linker consisting of spiropyran scaffolded onto the side of a 1,4-di(pyridin-4-yl)benzene molecule.<sup>23</sup> We decided to begin trials using their successful synthetic conditions.

### 3.3.1.3.1 Linker **3c**

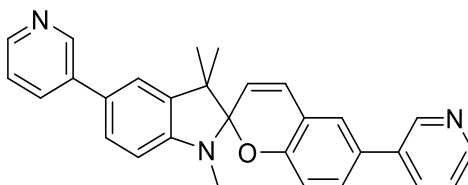


Experiment <sup>(ref.)</sup>	Pillaring linker (P) (mmol)	Layering linker (L)	Metal Salt (M)	Molar ratio P:L:M	Solvent(s) (v:v)	Vessel	Temperature (°C)	Time	Notes	Result
<b>3c-14-a</b>	0.03	DBTD	Zn(NO <sub>3</sub> ) <sub>2</sub> ·6H <sub>2</sub> O	4:3:15	DMF	Wheaton vial	80	72h	0.3 uL HCl*	1
<b>3c-14-b</b>	0.03	DBTD	Zn(NO <sub>3</sub> ) <sub>2</sub> ·6H <sub>2</sub> O	4:3:15	DMF	Wheaton vial	80	72h	-	1

Table 15 Outlines the conditions of each attempt at synthesising a 3D framework incorporating ligand **3c** and DBTD. Vessel volumes: Wheaton Vial - 2.5 mL, Pressure Tube - 10 mL, Parr Bomb - 10 mL. \* denotes modulator. Outcomes: 1 = no reaction, 2 = amorphous/not crystalline enough for characterisation, 3a = novel crystalline and amorphous material, 3b = literature known crystalline and amorphous material, 4a = novel crystalline material, 4b = literature known crystalline material

Though not rigorously tested, no success was observed when these conditions were tested with **3c**; no solid products were formed.

### 3.3.1.3.2 Linker **3b**

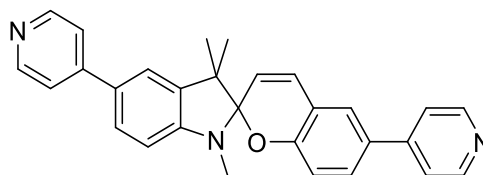


Experiment <sup>(ref.)</sup>	Pillaring linker (P) (mmol)	Layering linker (L)	Metal Salt (M)	Molar ratio P:L:M	Solvent(s) (v:v)	Vessel	Temperature (°C)	Time	Notes	Result
<b>3b-15-a</b>	0.03	DBTD	Zn(NO <sub>3</sub> ) <sub>2</sub> ·6H <sub>2</sub> O	4:3:15	DMF	Wheaton vial	80	72h	0.3 uL HCl*	1
<b>3b-15-b</b>	0.03	DBTD	Zn(NO <sub>3</sub> ) <sub>2</sub> ·6H <sub>2</sub> O	4:3:15	DMF	Wheaton vial	80	72h	-	2

Table 16 Outlines the conditions of each attempt at synthesising a 3D framework incorporating ligand **3b** and DBTD. Vessel volumes: Wheaton Vial - 2.5 mL, Pressure Tube - 10 mL, Parr Bomb - 10 mL. \* denotes modulator. Outcomes: 1 = no reaction, 2 = amorphous/not crystalline enough for characterisation, 3a = novel crystalline and amorphous material, 3b = literature known crystalline and amorphous material, 4a = novel crystalline material, 4b = literature known crystalline material

Like our tests with **3c**, **3b** showed little success in these non-exhaustive trials. Only amorphous solids were obtained. Strictly speaking, **3c** has access to similar geometries as ligand **3b** with the added option of being able to bind to both nitrogen atom sites<sup>41</sup>, but differ quite significantly electronically due to the additional nitrogen atom.<sup>42,43</sup> When taking into account the lack of success achieved in previous synthetic attempts with **3c** and **4c**, we could hypothesise that these ligands have unfavourable geometry for the formation of these frameworks and that the 4-pyridyl functionality (**3a**) is preferred for that reason.

## 3.3.1.3.3 Linker 3a



Experiment <sup>(ref.)</sup>	Pillaring linker (P) (mmol)	Layering linker (L)	Metal Salt (M)	Molar ratio P:L:M	Solvent(s) (v:v)	Vessel	Temperature (°C)	Time	Notes	Result
<b>3a-16-a</b>	0.03	DBTD	Zn(NO <sub>3</sub> ) <sub>2</sub> 6H <sub>2</sub> O	4:3:15	DMF	Wheaton Vial	80	72h	0.3 uL HCl*	4a (GG-1)
<b>3a-17-a</b>	0.03	DBTD	Zn(NO <sub>3</sub> ) <sub>2</sub> 6H <sub>2</sub> O	4:3:15	DMF	Wheaton vial	80	24h	0.2 uL HCl*	4a (GG-1)
<b>3a-17-b</b>	0.03	DBTD	Zn(NO <sub>3</sub> ) <sub>2</sub> 6H <sub>2</sub> O	4:3:15	DMF	Wheaton vial	80	24h	0.3 uL HCl*	4a (GG-1)
<b>3a-17-c</b>	0.03	DBTD	Zn(NO <sub>3</sub> ) <sub>2</sub> 6H <sub>2</sub> O	4:3:15	DMF	Wheaton vial	80	24h	0.4 uL HCl*	3a (GG-1)
<b>3a-18-a</b>	0.03	DBTD	In (NO <sub>3</sub> ) <sub>2</sub> H <sub>2</sub> O	4:3:15	DMF	Wheaton Vial	80	72h	0.3 uL	1
<b>3a-18-b</b>	0.03	DBTD	Mn (NO <sub>3</sub> ) <sub>2</sub> 4H <sub>2</sub> O	4:3:15	DMF	Wheaton Vial	80	72h	0.3 uL	4b
<b>3a-18-c</b>	0.03	DBTD	Co (NO <sub>3</sub> ) <sub>2</sub> 6H <sub>2</sub> O	4:3:15	DMF	Wheaton Vial	80	72h	0.3 uL	2

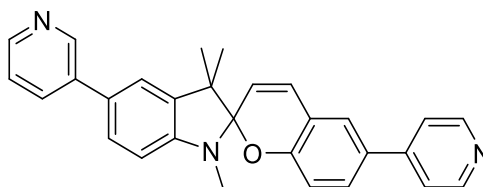
<b>3a-18-d</b>	0.03	DBTD	Ca (NO <sub>3</sub> ) <sub>2</sub> ·4H <sub>2</sub> O	4:3:15	DMF	Wheaton Vial	80	72h	0.3 uL	2
<b>3a-18-e</b>	0.03	DBTD	Ba (NO <sub>3</sub> ) <sub>2</sub>	4:3:15	DMF	Wheaton Vial	80	72h	0.3 uL	1
<b>3a-18-f</b>	0.03	DBTD	Sr (NO <sub>3</sub> ) <sub>2</sub>	4:3:15	DMF	Wheaton Vial	80	72h	0.3 uL	1
<b>3a-18-g</b>	0.03	DBTD	Zn (NO <sub>3</sub> ) <sub>2</sub> ·6H <sub>2</sub> O	4:3:15	DMF	Wheaton Vial	80	72h	0.3 uL	4a (GG-1)
<b>3a-18-h</b>	0.03	DBTD	Mg (NO <sub>3</sub> ) <sub>2</sub> ·6H <sub>2</sub> O	4:3:15	DMF	Wheaton Vial	80	72h	0.3 uL	2
<b>3a-19-a</b>	0.12	DBTD	Zn(NO <sub>3</sub> ) <sub>2</sub> ·6H <sub>2</sub> O	4:3:15	DMF	Pressure Tube	80	24h	1.2 uL	1
<b>3a-20-a</b>	-	DBTD	Zn(NO <sub>3</sub> ) <sub>2</sub> ·6H <sub>2</sub> O	0:1:5	DMF	Wheaton Vial	80	24h	0.3 uL	1
<b>3a-20-b</b>	0.03	DBTD	Zn(NO <sub>3</sub> ) <sub>2</sub> ·6H <sub>2</sub> O	4:3:15	DMF	Wheaton Vial	80	24h	10 uL	4a (GG-1)
<b>3a-20-c</b>	0.03	DBTD	Zn(NO <sub>3</sub> ) <sub>2</sub> ·6H <sub>2</sub> O	4:3:15	DMF	Wheaton Vial	80	24h	15 uL	4a (GG-1)
<b>3a-20-d</b>	0.03	DTD	Zn(NO <sub>3</sub> ) <sub>2</sub> ·6H <sub>2</sub> O	4:3:15	DMF	Wheaton Vial	80	24h	0.3 uL	2
<b>3a-20-e</b>	0.03	DTD	Zn(NO <sub>3</sub> ) <sub>2</sub> ·6H <sub>2</sub> O	4:3:15	DMF	Wheaton Vial	80	24h	10 uL	1

<b>3a-21-a</b>	0.1	DBTD	Zn(NO <sub>3</sub> ) <sub>2</sub> ·6H <sub>2</sub> O	1:1:2	DMF	Pressure tube	60	72h	12 uL	2
<b>3a-21-b</b>	0.1	DBTD	Zn(NO <sub>3</sub> ) <sub>2</sub> ·6H <sub>2</sub> O	1:1:2	DMF	Pressure tube	100	72h	12 uL	3a (GG-1)

Table 17 Outlines the conditions of each attempt at synthesising a 3D framework incorporating ligand **3a** and DBTD. Vessel volumes: Wheaton Vial - 2.5 mL, Pressure Tube - 10 mL, Parr Bomb - 10 mL. \* denotes modulator. Outcomes: 1 = no reaction, 2 = amorphous/not crystalline enough for characterisation, 3a = novel crystalline and amorphous material, 3b = literature known crystalline and amorphous material, 4a = novel crystalline material, 4b = literature known crystalline material

Trials with DBTD and **3a** provided crystals of a new framework. It is believed to be a single polymorph as no other material was immediately identifiable. Similar to the issues with LK-1/2, (discussed further below) characterisation of this framework was difficult due to its disordered nature and poor stability. The details of the characterisation are discussed later: briefly, a variety of conditions were attempted to achieve bigger crystals to improve the quality of SCXRD data but none of these trials show a discernible improvement over the original method. The synthesis of the framework also did not scale up successfully for reasons that are not immediately clear and hence the material had to be made in multiple small batches rather than one big batch.<sup>44,45</sup>

#### 3.3.1.3.4 Linker **6b**



Ex. No. Based off	Pillaring linker (P) (mmol)	Layering linker (L)	Metal Salt (M)	Molar ratio P:L:M	Solvent(s) (v:v)	Vessel	Temperature (°C)	Time	Notes	Result
----------------------	-----------------------------------	------------------------	-------------------	-------------------------	---------------------	--------	---------------------	------	-------	--------



<b>6b-21-a</b>	0.03	DBTD	Zn(NO <sub>3</sub> ) <sub>2</sub> ·6H <sub>2</sub> O	4:3:15	DMF	Wheaton vial	80	72h	0.5 uL HCl*	4a (GG-32)
<b>6b-21-b</b>	0.03	DBTD	Zn(NO <sub>3</sub> ) <sub>2</sub> ·6H <sub>2</sub> O	4:3:15	DMF	Wheaton vial	80	72h	10 uL HCl*	3a (GG-32)
<b>6b-22-a</b>	-	DBTD	Zn(NO <sub>3</sub> ) <sub>2</sub> ·6H <sub>2</sub> O	0:3:15	DMF	Wheaton vial	80	72h	10 uL HCl* G-32 seed	2
<b>6b-23-a</b>	0.03	DTD	Zn(NO <sub>3</sub> ) <sub>2</sub> ·6H <sub>2</sub> O	4:3:15	DMF	Wheaton Vial	80	72h	0.5 uL	1
<b>6b-23-b</b>	0.03	DTD	Zn(NO <sub>3</sub> ) <sub>2</sub> ·6H <sub>2</sub> O	4:3:15	DMF	Wheaton Vial	80	72h	-	1

Table 18 Outlines the conditions of each attempt at synthesising a 3D framework incorporating ligand **6b** and DBTD. Vessel volumes: Wheaton Vial - 2.5 mL, Pressure Tube - 10 mL, Parr Bomb - 10 mL. \* denotes modulator. Outcomes: 1 = no reaction, 2 = amorphous/not crystalline enough for characterisation, 3a = novel crystalline and amorphous material, 3b = literature known crystalline and amorphous material, 4a = novel crystalline material, 4b = literature known crystalline material

Despite not being able to fully purify ligand **6b**, we still used the impure product in the synthesis of DBTD. The best-case scenario, it would form a framework with the spiropyran and be purified that way or in the less ideal scenario, it could form a framework with the impurity, which could lead to the determination of its identity which would make it easier to remove from the final product.

By adapting the synthesis of *D. Williams et al.*, we were able to produce a crystalline material with **6b** that is almost definitely a metal organic framework (**6b-21-a/b**). The details of characterisation are discussed later. To determine whether spiropyran was incorporated into the framework, a control synthesis without the spiropyran linker present was performed. This produced many small white crystals too small for characterisation by PXRD/SCXRD with the

equipment available. These crystals remain unidentified, but as they look nothing like the crystals produced in the synthesis utilising **6b**, it is quite possible that the linker (or a derivative of **6b**) is incorporated in the framework.

#### 3.3.1.4 Synthetic Summary

Two 3-D frameworks were successfully synthesised using BPDC and ligand **3a**. The chief factor that seems to dictate the success of these pillar layering attempts is whether the pillaring linker can compete effectively with the layering linker. In cases where small linkers were used (TPA, IPA, TMA) the framework simply formed with the layering linker exclusively, likely due to being significantly more thermodynamically favourable to form without the spiropyran linker. Simply extending the TPA linker by one benzene ring (BPDC) was able to reduce the availability of the layer linker allowing for effective competition of ligand **3a**. Further discussion on how to encourage the competitive aspects of ligand **3a** is discussed later.

It would appear BPDC had the right kind of symmetry to complement ligand **3a**, for other linkers such as linkers **3b** and **3c** it is possible that an extended version of IPA or TMA would lead to a framework or perhaps further increasing the size of BPDC, further reducing its competitiveness, would be enough to allow for incorporation of these linkers. The trials using linkers **3b** and **3c** with DBTD linker although unsuccessful, would need more rigorous testing before we can draw a clear conclusion about the effectiveness of these ligands as a MOF linker. The frameworks GG-1 and GG-32 are discussed later.

The LK-1 and LK-2 frameworks were produced as a mix, which is most likely a manifestation of the zinc's flexibility in coordination due to the lack of ligand field stabilisation.<sup>29</sup> Although useful for increasing the likelihood of a framework forming, unfortunately the drawback is a lack of selectiveness. We did not observe any significant successes with other metals, but it is quite likely that more rigorous testing with other metals and conditions similar to what produced LK-1 and LK-2 may produce a derivative of one of the two and could lead to a singular product and improve the stability of the framework.

### 3.3.2 LK-1 and LK-2

The mixture of frameworks LK-1 and LK-2 was both a blessing and a curse. As where there were zero examples of third generation frameworks incorporating spiropyran in the literature, we have made two. The drawback is that as a mixture we cannot characterise each of the frameworks specifically, preventing the acquisition of an adsorption isotherm. Adsorption isothermal data is one of the most important characterisations a metal organic framework could have. By determining surface area and pore volume, you can determine how effective the framework will be in its possible functionalities, such as gas storage, molecular sieves etc.

In the first instance we obtained specific characterisation data for each framework where possible, any data collected for the bulk material was collated and characterised to the best of our ability.

#### 3.3.2.1 LK-1 Properties

LK-1 forms well defined pink cuboid crystals (Figure 64), that are extremely fragile to crystal manipulation techniques often resulting in shattering and rapidly degrade upon leaving the mother liquor.



Figure 64 Microscope picture of LK-1

Obtaining crystallographic data proved especially difficult, as the mother liquor would interfere with data collection but completely removing the mother liquor caused complete loss of crystallinity. The crude solution to this problem was to leave the crystal in as small amount of mother liquor as possible and then rapidly transfer for data acquisition.

#### 3.3.2.1.1 Single Crystal X-Ray Diffraction Data

Acquisition of single crystal data for this framework was made difficult for a multitude of reasons. The issues commonly associated with metal organic frameworks (in particular frameworks with large pore sizes), have a large amount of disorder due to all the freely moving guest molecules within the pores resulting in lots of areas of electron density that simply cannot be assigned and reducing the effectiveness of the overall model. The second issue is the potential for photoisomerism of the framework, as we mentioned before photoisomerism in the solid form is quite difficult and typically requires a lot of energy, however metal organic frameworks behave differently as the large pore sizes allow space for structural changes to be made therefore not behaving as a typical solid. This lack of control over the photoactivity of the framework can lead to further disorder over the spiro- molecules as it could be in the open, closed or any transition state in between. Finally the instability of the framework outside the mother liquor causes a rapid loss in crystallinity, meaning you have to have a small amount of the mother liquor present in order to preserve the crystal while obtaining data which will further obscure any data obtained.

The SCXRD data that was obtained, although not complete (90% completeness), was sufficient to elucidate the spiro- molecule that was incorporated into the structure, providing conclusive proof that this was a third-generation metal organic framework with spiro-.

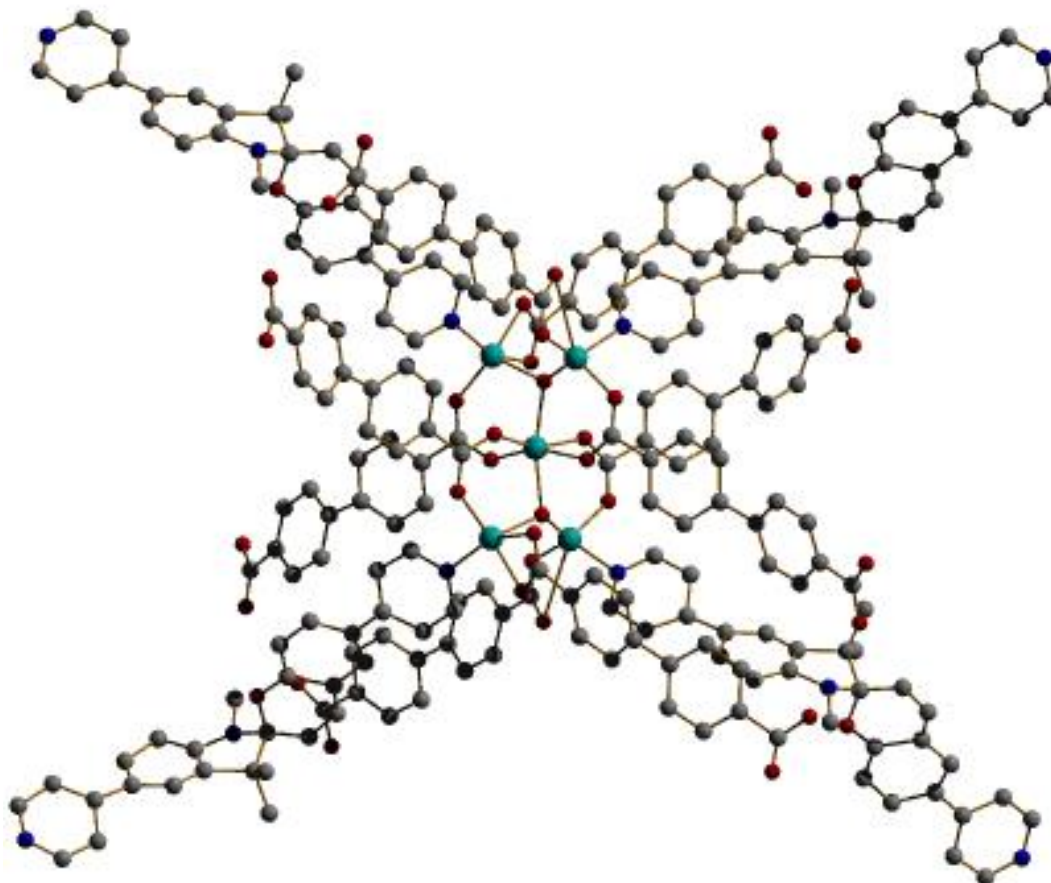


Figure 65 Penta-coordinate zinc node of LK-1. Metal (colour): zinc (aqua), oxygen (red), carbon (grey), nitrogen (blue). Hydrogen atoms omitted for clarity.

LK-1 has a distinctive structure since it has a penta-coordinate zinc metal node that has only been observed in two frameworks so far in the literature (see Figure 65).<sup>46,47</sup> The structure is not a typical pillar layer structure as instead the skeleton of the framework seems to be provided entirely by the BPDC linkers and the spiropyran forms an inlay inside each of the pores (see Figure 66). The spiropyran is still an integral part of the framework and the framework has not been seen to form without it being there, so it certainly is not a pendant group. The inlay that the spiropyran forms looks like it could accommodate the structural change upon photoisomerism as it would potentially expand into the pore (see Figure 66).

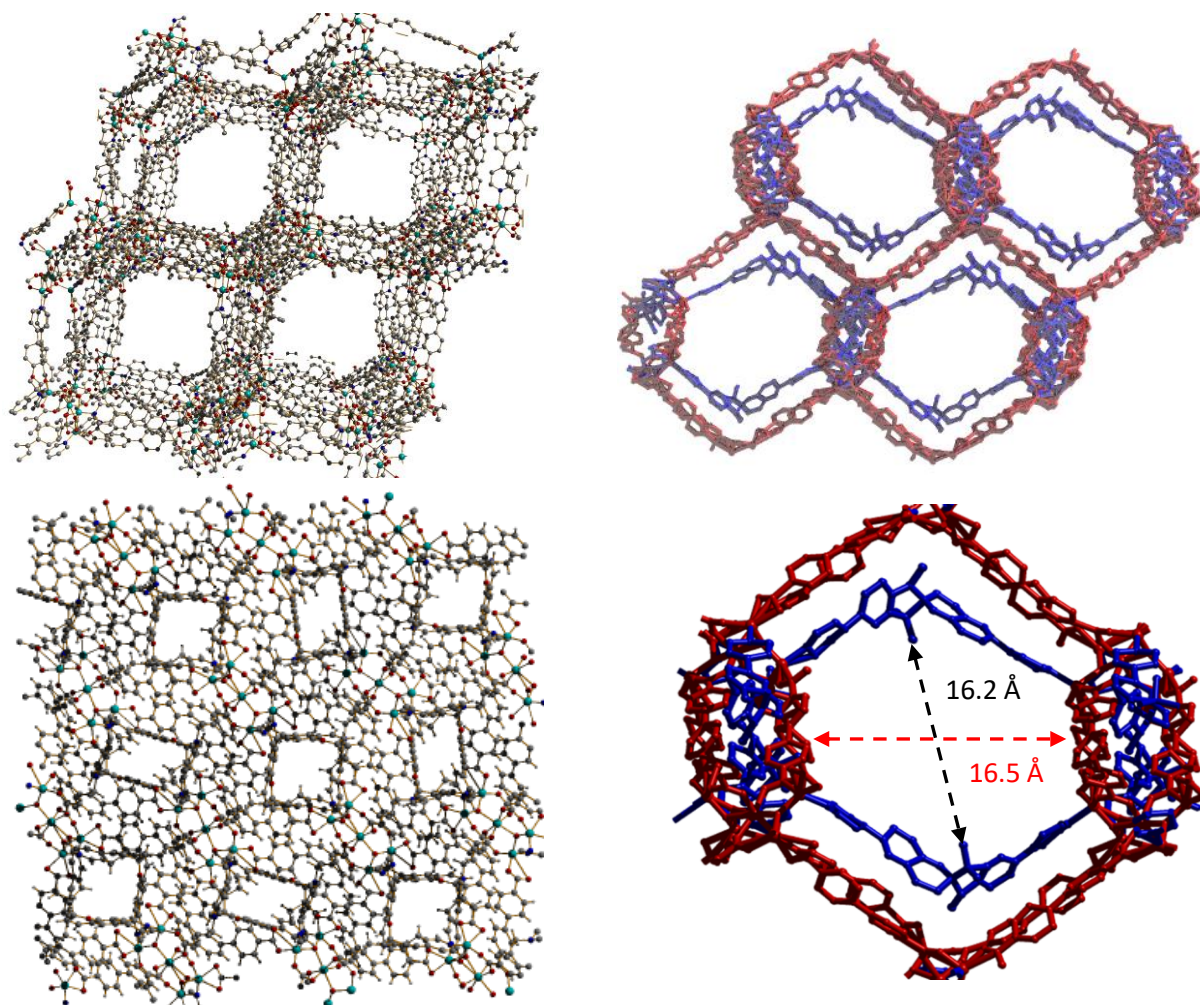


Figure 66 Images obtained from single crystal X-Ray data of LK-1. View down the main channels (top left). View down the smaller channels (bottom left). View down the main channels with the BPDC linkers highlighted as red and the **3a** linkers highlighted as blue (top right). Shortest distance from spiropyran linker to spiropyran linker measured to be 16.2 Å (bottom right).

There was no conclusive proof of the merocyanine form being present in the crystal structure but we would not expect to see it using the in-house SCXRD equipment and it could quite easily be hidden among all the unassigned electron density in the pores.

### 3.3.2.1.2 LK-1 Diamond experiment

### 3.3.2.2 LK-2 Properties

LK-2 formed as dark red ill-defined structures (Figure 67), not as easily identified as the pink cuboids of LK-1. LK-2 did seem less fragile to crystal manipulation techniques but was still quite unstable outside of the mother liquor and required the same treatment as LK-1 described earlier.



Figure 67 Microscope picture of LK-2

All the challenges associated with collecting crystallographic data for LK-1 applied to LK-2. Surprisingly, a collection with 100% completeness was obtained allowing us to clearly characterise the ligand **3a** in the framework.

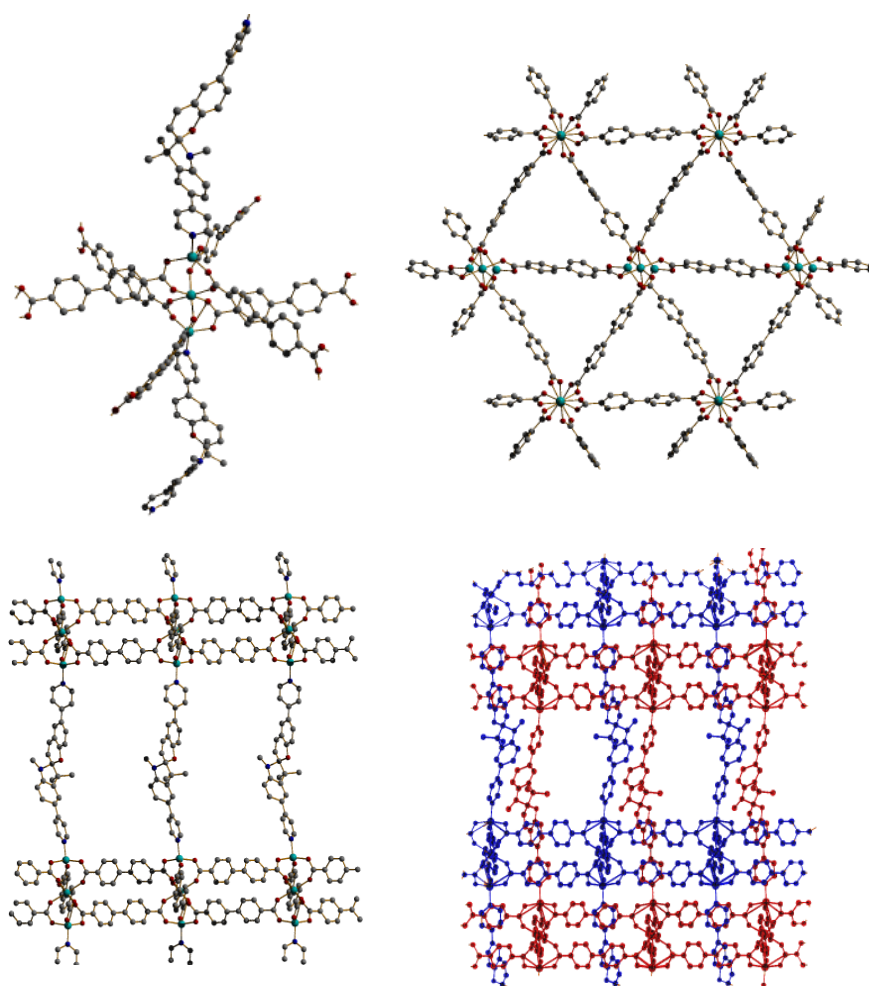


Figure 68 Images obtained from SCXRD data of LK-2. Node (top left). Looking along the pillars (top right). Looking along the layers (bottom left). Looking along the layers that displays interpenetrated framework (bottom right).

LK-2 has a more familiar tri-nuclear zinc node<sup>48</sup> with the three metal ions co-linear, tetrahedral coordination at the terminal ions and octahedral coordination for the central zinc ion. The layers are formed by the BPDC linkers joining the zinc node together and forming bridges to the adjacent nodes to form a bilayer. These layers are then pillared by the **3a** linkers coordinating to the tetrahedral zinc atoms at the terminals of the nodes to form a 3D structure. The perceived stability that it has compared to LK-1 could be explained by the interpenetration of the framework. Interpenetration would also reduce the available pore space and reduce the freedom of movement for guest molecules, reducing the overall disorder present in the data (see Figure 69).

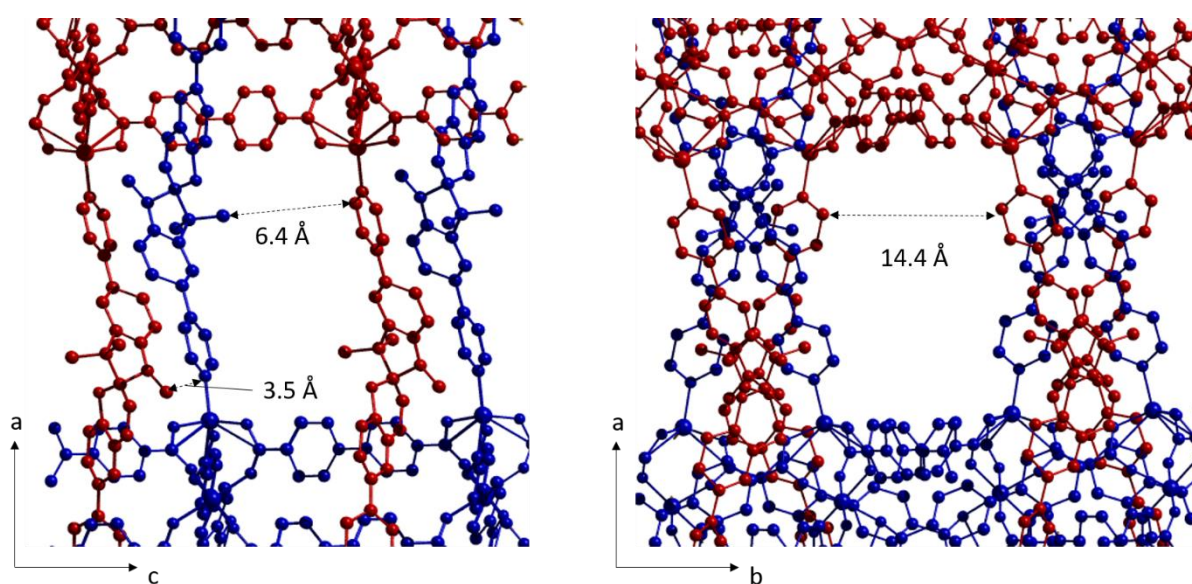


Figure 69 View of LK-2 down *b*-axis (left) highlighting space between adjacent spirocyan linkers. View down *c*-axis right highlighting space between spirocyan linkers.

There is space available along the *c*-axis to expand, although quite restricted in other directions. This could mean that the framework can photoisomerise and restrict the expansion to one direction. Although there is a reduction in the overall mobility of the spirocyan linkers, the photoisomerism is more likely to be uniform throughout the structure.

No open form species were identified in the crystal data, the crystal data is considerably better than LK-1 but there is still a lot of disorder throughout the structure. This should not be used as conclusive evidence of its ability to photoisomerise, as the crystal could simply be at rest and still be able to photoisomerise with the appropriate stimulus. As discussed in chapter 2, solid state photoisomerism is still possible with crystals of just spirocyan molecules. There is considerably more space for the spirocyan molecules to photoisomerise in the LK-2 structure compared to the solid crystals of spirocyan, therefore we would still expect a significant reduction in the energy required to stimulate photoisomerism in the LK-2 structure.



### 3.3.2.3 LK-1/2 PXRD

Figure 70 shows the experimental powder X-ray diffraction pattern for the bulk solid formed from the LK-1 and LK-2 synthesis. Crystalline material is clearly present. The sample was left with a small amount of solvent present in order to prevent degradation on drying and hence there is a small amorphous background in the observed pattern. If the sample is allowed to fully dry before collection no diffraction peaks are observed. Also shown in Figure 70 is powder X-ray data of the bulk material of the LK mixture (experimental) with simulated powder patterns from the SCXRD data of LK-1 and LK-2 (from the crystal structures collected at 150 K). Ideally, we would be able to quantify the amount of each phase present in the experimental pattern but unfortunately there are too few diffraction peaks to do so.<sup>49</sup> However some observations on the experimental data can be made.

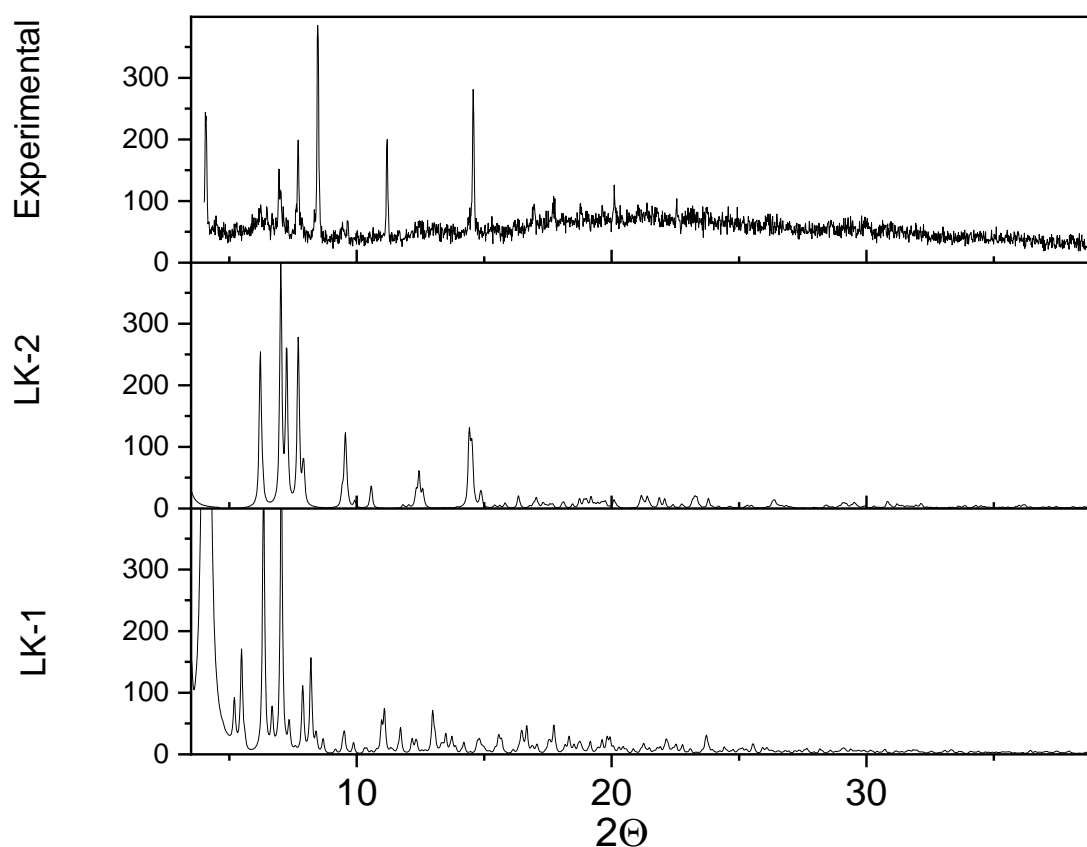


Figure 70 Powder X-Ray data of the bulk material of the LK mixture (experimental) with simulated powder patterns from the SCXRD data of LK-1 and LK-2 .

The simulated powder pattern for LK-1 has some key identifying peaks at 6.18, 6.98, 7.68, 7.74  $2\theta$ . The simulated powder pattern for LK-2 has key peaks at 4.08, 6.38 and 7.08  $2\theta$ . In the experimental pattern we are collecting X-ray data for these two different phases, but also for each crystal across the sample at different states of degradation (due to solvent loss) and photoactivation (different crystals

will most likely have different amounts of the open and closed form of the spiropyran linkers). This results in identifiable peaks at 4.07, 6.96, 7.71, 8.43, 11.16, 14.60  $2\theta$ . These peaks are consistent with the presence of both LK-1 and LK-2 (accounting for small shifts due to difference in collection temperatures). No other crystalline species appear to be present, and there is no evidence for the presence of the precursor metal salt (simulated PXRD pattern of zinc nitrate hexahydrate shows a peak at an angle of 15.98  $2\theta$ ). Given these observations, the pink material that surrounds the crystals produced in this synthesis is either composed of microcrystalline LK-1 and/or LK-2 or is amorphous and contributes to the weak amorphous background.

#### 3.3.2.4 LK-1/2- Solid State UV vis

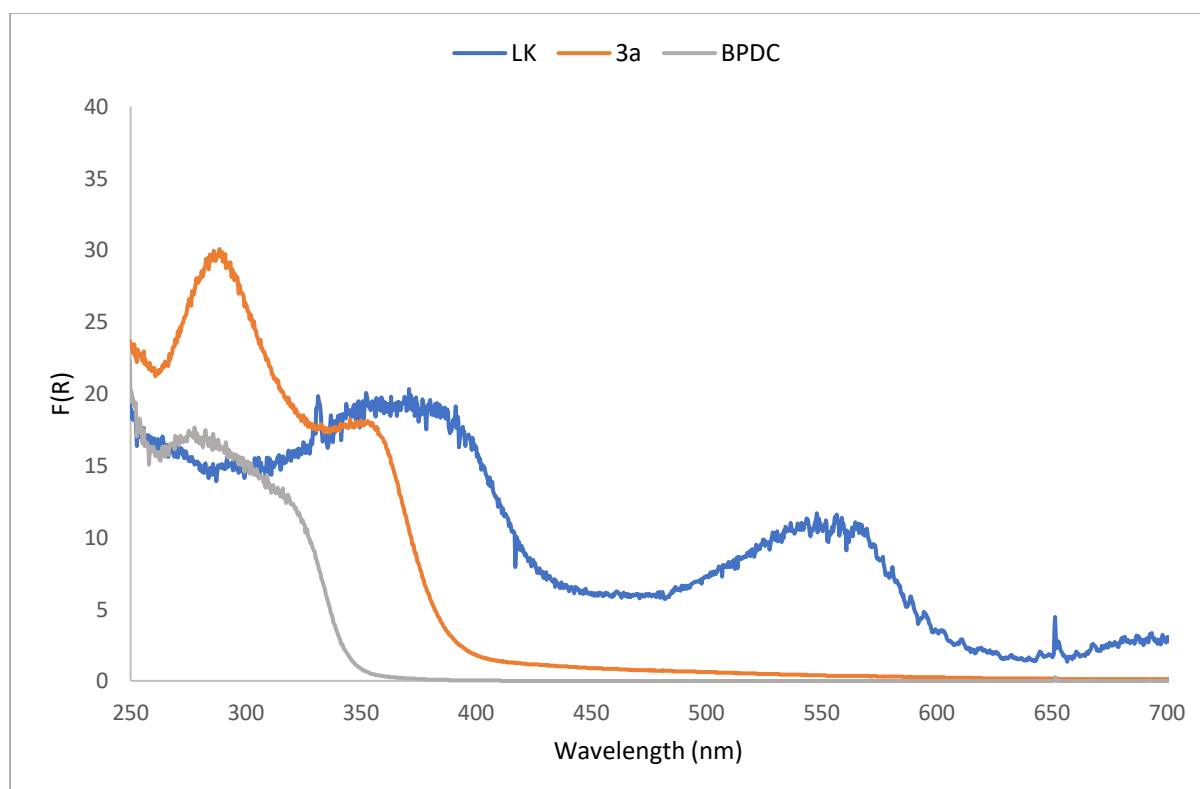


Figure 71 Solid state UV-vis of LK-1 and LK-2 mixture with solid state data of 3a and BPDC for comparison.

The profile for **3a** and the bulk material for the LK mixture looks very different. The merocyanine form is very pronounced in the LK sample, signified with a peak at 554 nm. Although we cannot determine how much merocyanine there is compared to spiropyran, as merocyanine is consistently reported to have a much higher molar extinction coefficient than spiropyran, we can however say its present in significantly higher amounts than the **3a** ligand sample.

The second caveat is that the open form may not be present at all in either of the frameworks and simply be guests in the pores of the frameworks or some other artifact of the mixture. If we attribute these peaks to a result of the LK materials, we can draw two conclusions. As we only see two broad

peaks for the LK material, we could conclude that both LK materials have similar photoactivation parameters with a high degree of overlap in the peak regions or if the case that either LK-1 or LK-2 is present in a significantly larger quantity than the other species, then the dominant species could have a signal that is too strong for the signal pertaining to the other species to be reliably identified.

The peak representing the  $\pi$ - $\pi^*$  transition of the chromene fragment at 354 nm has shifted to 374 nm. As we saw from our UV-Vis studies on the ligands in chapter 2, we saw shifts as big as 18 nm depending on whether it was functionalised with a 3-pyridyl or 4-pyridyl upon functionalisation with pyridine molecules, therefore the framework must be also lowering the energy of this transition further. More importantly this shifts the absorption into the visible light region, meaning that normal room lights could potentially cause photoisomerization. This would support the claim that the disorder observed in the crystallographic data for LK-1 and LK-2, in some part, is caused by photoisomerization of the linker.

### 3.3.2.5 Thermogravimetric analysis

So far, the SCXRD data revealed there are two different frameworks present in the MOF mixture, the PXRD also corroborates the presence of the two frameworks in the mixture. These two techniques rely on the crystallinity of the sample which is disadvantaged by the general instability of both frameworks, furthermore there is an unidentified pink amorphous material present which we have not discussed yet. Thermogravimetric analysis was also performed on a dried sample of the LK mixture to quantify the stability of the frameworks and an idea of what ratio they exist in. The MOF's thermal stability is largely dictated by the nature of the ligand and the stability of the inorganic node. In our case the ligands are the same for both frameworks however the inorganic nodes are very different, therefore if the decomposition mechanism of one of these two materials is dependent on the stability of the inorganic node we should see a clear difference in thermal stability. The material was washed and dried to try and remove any excess linker, working on the assumption that the loss of crystallinity does not necessarily mean the complete collapse of the framework but if that were the case then we would expect a loss in thermal stability and should see it in the TGA profile. We have no modulators and no coordinated solvent molecules to be concerned with as the metal nodes are solely coordinated to the linkers, therefore the significant decomposition steps should only correspond with the two frameworks and the amorphous material if we assume that there are also no defect sites in the frameworks.<sup>50</sup>

Framework	Mol of Zn (ZnO)	Mol of <b>3a</b>	Mol of BPDC	Mol of $\mu$ -O atoms	MOF Mw	R <sub>theo</sub>

LK-1	5*65.38 (81.38)	2*431.54	4*242.23	2*16.00	2190.9	0.19
LK-2	3*65.38 (81.38)	1*431.54	3*242.23	N/A	1354.37	0.18

Table 19 Showing calculations for molecular weight of frameworks and the theoretical residue ( $R_{theo}$ ) for each framework. If the mixture was solely these two samples then we would expect the experimental residue ( $R_{exp}$ ) to be a value between these two ratios.

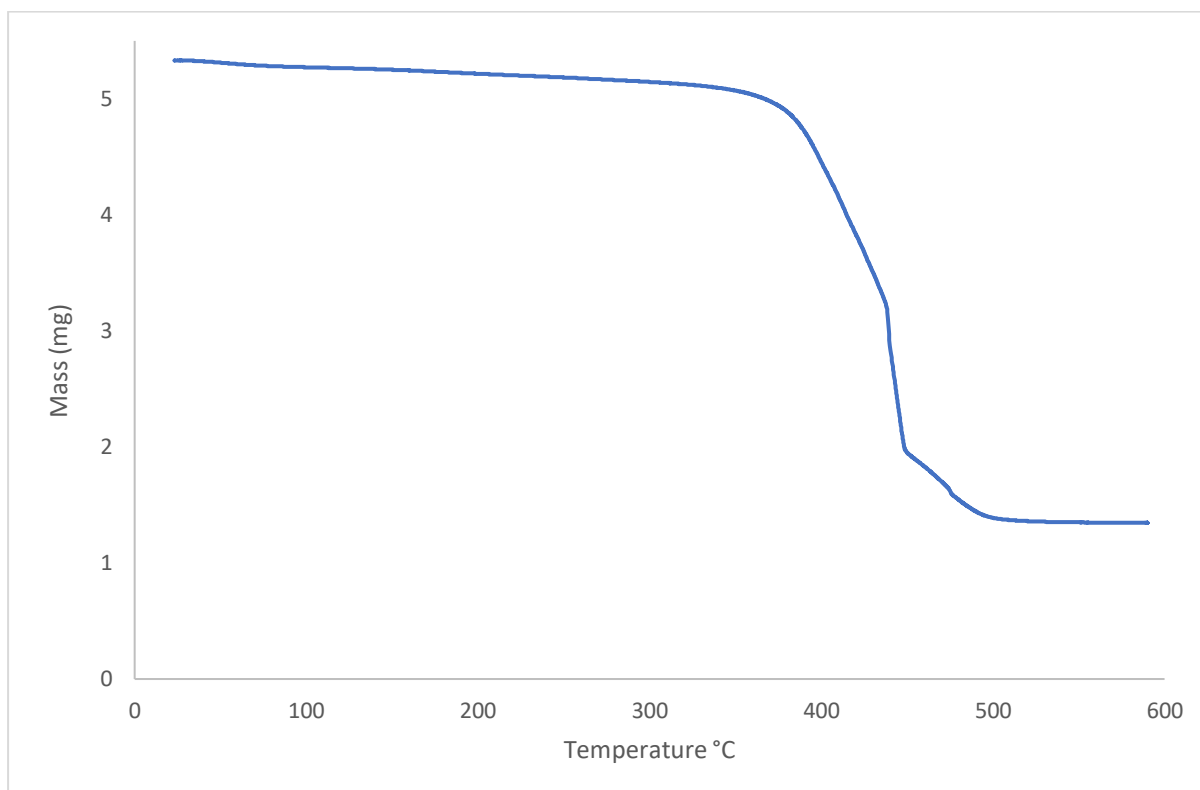


Figure 72 Thermogravimetric analysis of LK mixture, under  $N_2$  at a ramp temperature of  $10^\circ C \text{ min}^{-1}$ .

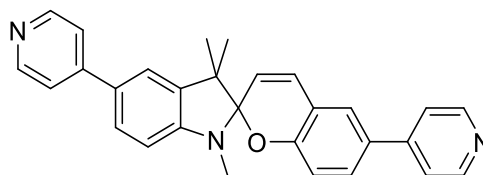
The TGA shows solvent loss up to  $367^\circ C$  which is in the range of what we would expect for a zinc-based MOF ( $300\text{--}450^\circ C$ <sup>46,48,51</sup>). There is another step in the curve at  $438^\circ C$  and a final step at  $451^\circ C$ . Based on the fact that there are three steps after solvent loss, this could suggest the presence of three species although multi-step decomposition mechanisms have been observed for single frameworks.<sup>52</sup> We cannot assign each step to the relevant species, but we could estimate that the amorphous material would be the species that decomposes at  $367^\circ C$  as crystalline materials tend to be more robust than amorphous materials. Furthermore, we would expect that the two frameworks to have somewhat similar stabilities due to having the same ligand and same choice of metal (i.e. zinc).

The dehydrated mass of the material is the mass just before the first decomposition step ( $367^\circ C$ ) which is 5.03 mg. The weight of the final residue is 1.35 mg, therefore the  $R_{exp}$  is 0.27. Assuming full

decomposition of the frameworks, this would suggest that the amorphous material contains a higher ratio of metal to organic material. The material is most likely the majority of the overall yield and it indicates that the amorphous material is not a derivative of either of the LK frameworks but a different species altogether. If the amorphous material were the degraded frameworks from the drying treatment before the analysis, the stoichiometry of the metals and ligands would be unaffected and therefore we would expect a similar  $R_{\text{exp}}$  value.

It is clear that the attempts at bulk characterisations have too many variables in order for a decisive conclusion to be drawn. We required specific bulk data for one of the frameworks, which would in turn allow for the deconvolution of the data we already gathered to characterise the other framework. Thus our efforts focused on improving the selectivity for one of the desired frameworks, with a secondary goal of improving the stability of either framework.

### 3.3.2.6 LK-1/2 Synthesis Optimisation



<i>Experiment (ref.)</i>	<b>Pillaring liner (P) (mmol)</b>	<b>Layering linker (L)</b>	<b>Metal Salt (M)</b>	<b>Molar Ratio P:L:M</b>	<b>Solvent(s) (v:v)</b>	<b>Vessels</b>	<b>Temperature (°C)</b>	<b>Time</b>	<b>Notes</b>	<b>Result</b>
<b>3a-24-a</b>	0.03	BPDC	Zn(NO <sub>3</sub> ) <sub>2</sub> 6H <sub>2</sub> O	2:1:4	DMF:MeOH (1:1)	Wheaton vial	60	144h	-	2
<b>3a-24-b</b>	0.03	BPDC	Zn(NO <sub>3</sub> ) <sub>2</sub> 6H <sub>2</sub> O	2:1:4	DMF	Wheaton vial	60	144h	-	3b
<b>3a-24-c</b>	0.03	BPDC	Zn(NO <sub>3</sub> ) <sub>2</sub> 6H <sub>2</sub> O	2:1:4	DMF:MeOH (1:1)	Wheaton vial	60	144h	Seed with LK-1	2
<b>3a-24-d</b>	0.03	BPDC	Zn(NO <sub>3</sub> ) <sub>2</sub> 6H <sub>2</sub> O	2:1:4	DMF	Wheaton vial	60	144h	Seed with LK-2	3b
<b>3a-24-e</b>	0.03	BPDC	Zn(NO <sub>3</sub> ) <sub>2</sub> 6H <sub>2</sub> O	1:1:2	DMF:MeOH (1:1)	Wheaton vial	60	144h	-	2
<b>3a-24-f</b>	0.03	BPDC	Zn(NO <sub>3</sub> ) <sub>2</sub> 6H <sub>2</sub> O	1:1:2	DMF	Wheaton vial	60	144h	-	3b
<b>3a-24-g</b>	0.03	BPDC	Zn(NO <sub>3</sub> ) <sub>2</sub> 6H <sub>2</sub> O	1:1:2	DMF:MeOH (1:1)	Wheaton vial	60	144h	Seed with LK-1	2
<b>3a-234g</b>	0.03	BPDC	Zn(NO <sub>3</sub> ) <sub>2</sub> 6H <sub>2</sub> O	1:1:2	DMF	Wheaton vial	60	144h	Seed with LK-2	3b
<b>3a-25-a</b>	0.10	BPDC	Zn(NO <sub>3</sub> ) <sub>2</sub> 6H <sub>2</sub> O	2:1:2	DMF:MeOH (1:1)	Pressure tube	60	72h	Seed LK-1 scale up	2
<b>3a-25-b</b>	0.21	BPDC	Zn(NO <sub>3</sub> ) <sub>2</sub> 6H <sub>2</sub> O	1:1:1	DMF:MeOH (1:1)	Pressure tube	60	72h	Seed LK-1 scale up	2
<b>3a-25-c</b>	0.10	BPDC	Zn(NO <sub>3</sub> ) <sub>2</sub> 6H <sub>2</sub> O	1:2:2	DMF:MeOH (1:1)	Pressure tube	60	72h	Seed LK-1 scale up	1

<b>3a-25-d</b>	0.10	BPDC	Zn(NO <sub>3</sub> ) <sub>2</sub> 6H <sub>2</sub> O	1:3:2	DMF:MeOH (1:1)	Pressure tube	60	72h	Seed LK-1 scale up	1
<b>3a-25-e</b>	0.10	BPDC	Zn(NO <sub>3</sub> ) <sub>2</sub> 6H <sub>2</sub> O	2:1:2	DMF:MeOH (1:1)	Pressure tube	60	72h	Seed LK-2 scale up	4a (LK-1/2)
<b>3a-25-f</b>	0.10	BPDC	Zn(NO <sub>3</sub> ) <sub>2</sub> 6H <sub>2</sub> O	1:1:1	DMF:MeOH (1:1)	Pressure tube	60	72h	Seed LK-2 scale up	1
<b>3a-25-g</b>	0.10	BPDC	Zn(NO <sub>3</sub> ) <sub>2</sub> 6H <sub>2</sub> O	1:2:2	DMF:MeOH (1:1)	Pressure tube	60	72h	Seed LK-2 scale up	2
<b>3a-26-a</b>	0.10	BPDC	Zn(NO <sub>3</sub> ) <sub>2</sub> 6H <sub>2</sub> O	1:2:4	MeOH	Parr bomb	180	72h	-	1
<b>3a-26-b</b>	0.10	BPDC	Zn(NO <sub>3</sub> ) <sub>2</sub> 6H <sub>2</sub> O	1:2:2	MeOH	Parr bomb	180	72h	-	1
<b>3a-26-c</b>	0.05	BPDC	Zn(NO <sub>3</sub> ) <sub>2</sub> 6H <sub>2</sub> O	1:2:4	MeOH	Parr bomb	180	72h	-	1
<b>3a-26-d</b>	0.05	BPDC	Zn(NO <sub>3</sub> ) <sub>2</sub> 6H <sub>2</sub> O	1:2:2	MeOH	Parr bomb	180	72h	-	1
<b>3a-27-a</b>	0.02	BPDC	Zn(NO <sub>3</sub> ) <sub>2</sub> 6H <sub>2</sub> O	2:4:5	Ethylene glycol (EG)	Wheaton vial	100	120h	-	1
<b>3a-27-b</b>	0.02	BPDC	Zn(NO <sub>3</sub> ) <sub>2</sub> 6H <sub>2</sub> O	2:4:5	EG:H <sub>2</sub> O (1:1)	Wheaton vial	100	120h	-	1
<b>3a-27-c</b>	0.02	BPDC	Zn(NO <sub>3</sub> ) <sub>2</sub> 6H <sub>2</sub> O	2:4:5	EG:DMF (1:1)	Wheaton vial	100	120h	-	2
<b>3a-27-d</b>	0.02	BPDC	Zn(NO <sub>3</sub> ) <sub>2</sub> 6H <sub>2</sub> O	2:4:5	EG:DMF:H <sub>2</sub> O (1:1:1)	Wheaton vial	100	120h	-	1
<b>3a-27-e</b>	0.02	BPDC	Zn(NO <sub>3</sub> ) <sub>2</sub> 6H <sub>2</sub> O	2:4:5	NMP	Wheaton vial	100	120h	-	3b
<b>3a-27-f</b>	0.02	BPDC	Zn(NO <sub>3</sub> ) <sub>2</sub> 6H <sub>2</sub> O	2:4:5	NMP:H <sub>2</sub> O (1:1)	Wheaton vial	100	120h	-	1
<b>3a-27-g</b>	0.02	BPDC	Zn(NO <sub>3</sub> ) <sub>2</sub> 6H <sub>2</sub> O	2:4:5	NMP:DMF (1:1)	Wheaton vial	100	120h	-	2

<b>3a-27-h</b>	0.02	BPDC	Zn(NO <sub>3</sub> ) <sub>2</sub> 6H <sub>2</sub> O	2:4:5	NMP:DMF:H <sub>2</sub> O (1:1:1)	Wheaton vial	100	120h	-	1
<b>3a-27-i</b>	0.02	BPDC	Zn(NO <sub>3</sub> ) <sub>2</sub> 6H <sub>2</sub> O	2:4:5	DMF	Wheaton vial	100	120h	-	2
<b>3a-27-j</b>	0.02	BPDC	Zn(NO <sub>3</sub> ) <sub>2</sub> 6H <sub>2</sub> O	2:4:5	DMF:H <sub>2</sub> O (1:1)	Wheaton vial	100	120h	-	1
<b>3a-27-k</b>	0.02	BPDC	Zn(NO <sub>3</sub> ) <sub>2</sub> 6H <sub>2</sub> O	2:4:5	DMF:MeOH(1:1)	Wheaton vial	100	120h	-	3a (LK-1/2)
<b>3a-28-a</b>	0.02	BPDC	Zn(NO <sub>3</sub> ) <sub>2</sub> 6H <sub>2</sub> O	2:4:5	DMF:MeOH (1:1)	Wheaton vial	100	72h	0.1 uL HCl	3a (LK-1/2)
<b>3a-28-b</b>	0.02	BPDC	Zn(NO <sub>3</sub> ) <sub>2</sub> 6H <sub>2</sub> O	2:4:5	DMF:MeOH (1:1)	Wheaton vial	100	72h	0.3 uL HCl	3a (LK-1/2)
<b>3a-28-c</b>	0.02	BPDC	Zn(NO <sub>3</sub> ) <sub>2</sub> 6H <sub>2</sub> O	2:4:5	DMF:MeOH (1:1)	Wheaton vial	100	72h	0.5 uL HCl	3a (LK-1/2)
<b>3a-28-d</b>	0.02	BPDC	Zn(NO <sub>3</sub> ) <sub>2</sub> 6H <sub>2</sub> O	2:4:5	DMF:MeOH (1:1)	Wheaton vial	100	72h	1.0 uL HCl	3a (LK-1/2)
<b>3a-28-e</b>	0.02	BPDC	Zn(NO <sub>3</sub> ) <sub>2</sub> 6H <sub>2</sub> O	1:2:3	DMF:MeOH (1:1)	Wheaton vial	100	72h	0.1 uL HCl	3a (LK-1/2)
<b>3a-28-f</b>	0.02	BPDC	Zn(NO <sub>3</sub> ) <sub>2</sub> 6H <sub>2</sub> O	1:2:3	DMF:MeOH (1:1)	Wheaton vial	100	72h	0.3 uL HCl	3a (LK-1/2)
<b>3a-28-g</b>	0.02	BPDC	Zn(NO <sub>3</sub> ) <sub>2</sub> 6H <sub>2</sub> O	1:2:3	DMF:MeOH (1:1)	Wheaton vial	100	72h	0.5 uL HCl	3a (LK-1/2)
<b>3a-28-h</b>	0.02	BPDC	Zn(NO <sub>3</sub> ) <sub>2</sub> 6H <sub>2</sub> O	1:2:3	DMF:MeOH (1:1)	Wheaton vial	100	72h	1.0 uL HCl	3a (LK-1/2)
<b>3a-28-i</b>	0.02	BPDC	Zn(NO <sub>3</sub> ) <sub>2</sub> 6H <sub>2</sub> O	2:4:5	DMF:MeOH (1:1)	Wheaton Vial	100	72h	-	3a (LK-1/2)
<b>3a-28-j</b>	0.02	BPDC	Zn(NO <sub>3</sub> ) <sub>2</sub> 6H <sub>2</sub> O	1:2:3	DMF:MeOH (1:1)	Wheaton Vial	100	72h	-	3a (LK-1/2)
<b>3a-29-a</b>	0.02	BPDC	Zn(NO <sub>3</sub> ) <sub>2</sub> 6H <sub>2</sub> O	2:4:5	DMF:MeOH (1:1)	Wheaton vial	100	48h	-	1
<b>3a-29-b</b>	0.02	BPDC	Zn(NO <sub>3</sub> ) <sub>2</sub> 6H <sub>2</sub> O	2:2:5	DMF:MeOH (1:1)	Wheaton vial	100	48h	-	1
<b>3a-29-c</b>	0.02	BPDC	Zn(NO <sub>3</sub> ) <sub>2</sub> 6H <sub>2</sub> O	2:6:5	DMF:MeOH (1:1)	Wheaton Vial	100	48h	-	1
<b>3a-29-d</b>	0.02	BPDC	Zn(NO <sub>3</sub> ) <sub>2</sub> 6H <sub>2</sub> O	2:8:5	DMF:MeOH (1:1)	Wheaton Vial	100	48h	-	1
<b>3a-29-e</b>	0.01	BPDC	Zn(NO <sub>3</sub> ) <sub>2</sub> 6H <sub>2</sub> O	2:4:5	DMF:MeOH (1:1)	Wheaton vial	100	48h	-	1
<b>3a-29-f</b>	0.005	BPDC	Zn(NO <sub>3</sub> ) <sub>2</sub> 6H <sub>2</sub> O	2:4:5	DMF:MeOH (1:1)	Wheaton vial	100	48h	-	1
<b>3a-29-g</b>	0.025	BPDC	Zn(NO <sub>3</sub> ) <sub>2</sub> 6H <sub>2</sub> O	2:4:5	DMF:MeOH (1:1)	Wheaton Vial	100	48h	-	1



<b>3a-29-h</b>	0.03	BPDC	Zn(NO <sub>3</sub> ) <sub>2</sub> 6H <sub>2</sub> O	2:4:5	DMF:MeOH (1:1)	Wheaton Vial	100	48h	-	1
<b>3a-30-a</b>	0.03	BPDC	Zn(NO <sub>3</sub> ) <sub>2</sub> 6H <sub>2</sub> O	1:1:3	DMF:MeOH (1:1)	Wheaton Vial	60	4h	-	1
<b>3a-30-b</b>	0.03	BPDC	Zn(NO <sub>3</sub> ) <sub>2</sub> 6H <sub>2</sub> O	1:1:3	DMF:MeOH (1:1)	Wheaton Vial	60	20h	-	2
<b>3a-30-c</b>	0.03	BPDC	Zn(NO <sub>3</sub> ) <sub>2</sub> 6H <sub>2</sub> O	1:1:3	DMF:MeOH (1:1)	Wheaton Vial	60	28h	-	2
<b>3a-30-d</b>	0.03	BPDC	Zn(NO <sub>3</sub> ) <sub>2</sub> 6H <sub>2</sub> O	1:1:3	DMF:MeOH (1:1)	Wheaton Vial	60	44h	-	2
<b>3a-30-e</b>	0.03	BPDC	Zn(NO <sub>3</sub> ) <sub>2</sub> 6H <sub>2</sub> O	1:1:3	DMF:MeOH (1:1)	Wheaton Vial	60	52h	-	3a (LK-1/2)
<b>3a-30-f</b>	0.03	BPDC	Zn(NO <sub>3</sub> ) <sub>2</sub> 6H <sub>2</sub> O	1:1:3	DMF:MeOH (1:1)	Wheaton Vial	60	68h	-	3a (LK-1/2)
<b>3a-30-g</b>	0.03	BPDC	Zn(NO <sub>3</sub> ) <sub>2</sub> 6H <sub>2</sub> O	1:1:3	DMF:MeOH (1:1)	Wheaton Vial	60	76h	-	3a (LK-1/2)
<b>3a-30-h</b>	0.03	BPDC	Zn(NO <sub>3</sub> ) <sub>2</sub> 6H <sub>2</sub> O	1:1:3	DMF:MeOH (1:1)	Wheaton Vial	60	92h	-	3a (LK-1/2)
<b>3a-30-i</b>	0.03	BPDC	Zn(NO <sub>3</sub> ) <sub>2</sub> 6H <sub>2</sub> O	1:1:3	DMF:MeOH (1:1)	Wheaton Vial	60	100h	-	3a (LK-1/2)
<b>3a-31-a</b>	0.02	BPDC	Zn(NO <sub>3</sub> ) <sub>2</sub> 6H <sub>2</sub> O	1:10:1 0	DMF:MeOH (1:1)	Wheaton vial	100	104h	50 uL HCl	3a (LK-1/2)
<b>3a-31-b</b>	0.02	BPDC	Zn(NO <sub>3</sub> ) <sub>2</sub> 6H <sub>2</sub> O	1:5:10	DMF:MeOH (1:1)	Wheaton Vial	60	104h	50 uL HCl	2
<b>3a-31-c</b>	0.02	BPDC	Zn(NO <sub>3</sub> ) <sub>2</sub> 6H <sub>2</sub> O	1:10:1 0	DMF:MeOH (1:1)	Wheaton Vial	60	8h	25 uL HCl	2
<b>3a-31-d</b>	0.02	BPDC	Zn(NO <sub>3</sub> ) <sub>2</sub> 6H <sub>2</sub> O	2:1:20	DMF:MeOH (1:1)	Wheaton vial	80	104h	-	2
<b>3a-31-e</b>	0.02	BPDC	Zn(NO <sub>3</sub> ) <sub>2</sub> 6H <sub>2</sub> O	2:20:1	DMF:MeOH (1:1)	Wheaton Vial	100	56h	-	2
<b>3a-31-f</b>	0.02	BPDC	Zn(NO <sub>3</sub> ) <sub>2</sub> 6H <sub>2</sub> O	2:1:10	DMF:MeOH (1:1)	Wheaton Vial	100	104h	50 hcl ul	2
<b>3a-31-g</b>	0.02	BPDC	Zn(NO <sub>3</sub> ) <sub>2</sub> 6H <sub>2</sub> O	1:10:5	DMF:MeOH (1:1)	Wheaton vial	60	104h	-	3a (LK-1/2)
<b>3a-31-h</b>	0.02	BPDC	Zn(NO <sub>3</sub> ) <sub>2</sub> 6H <sub>2</sub> O	2:1:20	DMF:MeOH (1:1)	Wheaton Vial	60	56h	50 uL HCl	1
<b>3a-31-i</b>	0.02	BPDC	Zn(NO <sub>3</sub> ) <sub>2</sub> 6H <sub>2</sub> O	2:20:1	DMF:MeOH (1:1)	Wheaton Vial	80	8h	50 uL HCl	2
<b>3a-31-j</b>	0.02	BPDC	Zn(NO <sub>3</sub> ) <sub>2</sub> 6H <sub>2</sub> O	2:1:1	DMF:MeOH (1:1)	Wheaton vial	100	104h	25 uL HCl	1

<b>3a-31-k</b>	0.02	BPDC	Zn(NO <sub>3</sub> ) <sub>2</sub> 6H <sub>2</sub> O	1:5:10	DMF:MeOH (1:1)	Wheaton Vial	100	104h	-	2
<b>3a-31-l</b>	0.02	BPDC	Zn(NO <sub>3</sub> ) <sub>2</sub> 6H <sub>2</sub> O	2:1:1	DMF:MeOH (1:1)	Wheaton Vial	60	8h	50 uL HCl	1
<b>3a-31-m</b>	0.02	BPDC	Zn(NO <sub>3</sub> ) <sub>2</sub> 6H <sub>2</sub> O	2:1:1	DMF:MeOH (1:1)	Wheaton vial	60	104h	-	1
<b>3a-31-n</b>	0.02	BPDC	Zn(NO <sub>3</sub> ) <sub>2</sub> 6H <sub>2</sub> O	2:20:1	DMF:MeOH (1:1)	Wheaton Vial	60	8h	-	2
<b>3a-31-o</b>	0.02	BPDC	Zn(NO <sub>3</sub> ) <sub>2</sub> 6H <sub>2</sub> O	2:1:20	DMF:MeOH (1:1)	Wheaton Vial	60	8h	-	1
<b>3a-31-p</b>	0.02	BPDC	Zn(NO <sub>3</sub> ) <sub>2</sub> 6H <sub>2</sub> O	1:10:1	DMF:MeOH (1:1)	Wheaton vial	60	104h	50 uL HCl	2
				0						
<b>3a-32-a</b>	-	BPDC	Zn(NO <sub>3</sub> ) <sub>2</sub> 6H <sub>2</sub> O	0:1:1	DMF:MeOH (1:1)	Wheaton vial	100	104h	50 uL HCl	3b
<b>3a-32-b</b>	-	BPDC	Zn(NO <sub>3</sub> ) <sub>2</sub> 6H <sub>2</sub> O	0:10:1	DMF:MeOH (1:1)	Wheaton Vial	60	104h	50 uL HCl	3b
<b>3a-32-c</b>	-	BPDC	Zn(NO <sub>3</sub> ) <sub>2</sub> 6H <sub>2</sub> O	0:1:1	DMF:MeOH (1:1)	Wheaton Vial	60	8h	25 uL HCl	4b
<b>3a-32-d</b>	-	BPDC	Zn(NO <sub>3</sub> ) <sub>2</sub> 6H <sub>2</sub> O	0:1:10	DMF:MeOH (1:1)	Wheaton vial	80	104h	-	3b
<b>3a-32-e</b>	-	BPDC	Zn(NO <sub>3</sub> ) <sub>2</sub> 6H <sub>2</sub> O	0:20:1	DMF:MeOH (1:1)	Wheaton vial	100	56h	-	3b
<b>3a-32-f</b>	-	BPDC	Zn(NO <sub>3</sub> ) <sub>2</sub> 6H <sub>2</sub> O	0:1:10	DMF:MeOH (1:1)	Wheaton Vial	100	8h	50uL HCl	4b
<b>3a-32-g</b>	-	BPDC	Zn(NO <sub>3</sub> ) <sub>2</sub> 6H <sub>2</sub> O	0:2:1	DMF:MeOH (1:1)	Wheaton Vial	60	104h	-	1
<b>3a-32-h</b>	-	BPDC	Zn(NO <sub>3</sub> ) <sub>2</sub> 6H <sub>2</sub> O	0:10:1	DMF:MeOH (1:1)	Wheaton vial	80	8h	50 uL HCl	4b
<b>3a-32-i</b>	-	BPDC	Zn(NO <sub>3</sub> ) <sub>2</sub> 6H <sub>2</sub> O	0:1:2	DMF:MeOH (1:1)	Wheaton Vial	100	8h	-	1
<b>3a-32-j</b>	-	BPDC	Zn(NO <sub>3</sub> ) <sub>2</sub> 6H <sub>2</sub> O	0:1:20	DMF:MeOH (1:1)	Wheaton Vial	60	8h	-	1
<b>3a-32-k</b>	-	BPDC	Zn(NO <sub>3</sub> ) <sub>2</sub> 6H <sub>2</sub> O	0:1:1	DMF:MeOH (1:1)	Wheaton Vial	60	104h	50 uL HCl	4b
<b>3a-33-a</b>	0.1	BPDC	Zn(NO <sub>3</sub> ) <sub>2</sub> 6H <sub>2</sub> O	1:1:2	DMF:MeOH (1:1)	Pressure tube	60	72h	-	1
<b>3a-33-b</b>	0.1	BPDC	Zn(NO <sub>3</sub> ) <sub>2</sub> 6H <sub>2</sub> O	1:1:2	DMF:MeOH (1:1)	Pressure tube	100	72h	-	3a (LK-1/2)
<b>3a-34-a</b>	0.05	BPDC	Zn(NO <sub>3</sub> ) <sub>2</sub> 6H <sub>2</sub> O	1:1:1	DMF:MeOH (1:1)	Wheaton vial	80	72h	-	2
<b>3a-34-b</b>	0.025	BPDC	Zn(NO <sub>3</sub> ) <sub>2</sub> 6H <sub>2</sub> O	1:1:1	DMF:MeOH (1:1)	Wheaton vial	80	72h	-	2

<b>3a-34-c</b>	0.05	BPDC	Zn(NO <sub>3</sub> ) <sub>2</sub> 6H <sub>2</sub> O	2:2:1	DMF:MeOH (1:1)	Wheaton vial	80	72h	-	2
<b>3a-34-d</b>	0.05	BPDC	Zn(NO <sub>3</sub> ) <sub>2</sub> 6H <sub>2</sub> O	1:1:1	DMF	Wheaton vial	80	72h	-	2
<b>3a-34-e</b>	0.025	BPDC	Zn(NO <sub>3</sub> ) <sub>2</sub> 6H <sub>2</sub> O	1:3:2	DMF:MeOH (1:1)	Wheaton Vial	80	72h	-	3a (LK-1/2)
<b>3a-34-f</b>	0.025	BPDC	Zn(NO <sub>3</sub> ) <sub>2</sub> 6H <sub>2</sub> O	1:3:2	DMF	Wheaton Vial	80	72h	-	3b
<b>3a-34-g</b>	0.025	BPDC	Zn(NO <sub>3</sub> ) <sub>2</sub> 6H <sub>2</sub> O	2:3:2	DMF	Wheaton Vial	80	72h	-	1
<b>3a-34-h</b>	0.025	BPDC	Zn(NO <sub>3</sub> ) <sub>2</sub> 6H <sub>2</sub> O	2:3:2	DMF	Wheaton vial	80	72h	-	4a (LK-1/2)
<b>3a-34-i</b>	0.025	BPDC	Zn(NO <sub>3</sub> ) <sub>2</sub> 6H <sub>2</sub> O	1:2:2	DMF:MeOH (1:1)	Wheaton vial	80	72h	-	4a (LK-1/2)
<b>3a-34-j</b>	0.025	BPDC	Zn(NO <sub>3</sub> ) <sub>2</sub> 6H <sub>2</sub> O	1:2:2	DMF	Wheaton vial	80	72h	-	3b
<b>3a-34-k</b>	0.013	BPDC	Zn(NO <sub>3</sub> ) <sub>2</sub> 6H <sub>2</sub> O	1:2:2	DMF:MeOH (1:1)	Wheaton vial	80	72h	-	3a (LK-1/2)
<b>3a-34-l</b>	0.013	BPDC	Zn(NO <sub>3</sub> ) <sub>2</sub> 6H <sub>2</sub> O	1:2:2	DMF	Wheaton vial	80	72h	-	1
<b>3a-34-m</b>	0.025	BPDC	Zn(NO <sub>3</sub> ) <sub>2</sub> 6H <sub>2</sub> O	1:1:2	DMF:MeOH (1:1)	Wheaton vial	80	72h	-	3a (LK-1/2)
<b>3a-34-n</b>	0.025	BPDC	Zn(NO <sub>3</sub> ) <sub>2</sub> 6H <sub>2</sub> O	2:1:2	DMF:MeOH (1:1)	Wheaton vial	80	72h	-	3a (LK-1/2)
<b>3a-34-o</b>	0.025	BPDC	Zn(NO <sub>3</sub> ) <sub>2</sub> 6H <sub>2</sub> O	2:1:2	DMF	Wheaton vial	80	72h	-	1
<b>3a-34-p</b>	0.013	BPDC	Zn(NO <sub>3</sub> ) <sub>2</sub> 6H <sub>2</sub> O	1:2:4	DMF	Wheaton vial	80	72h	-	1
<b>3a-35-a</b>	0.10	BPDC	Zn(NO <sub>3</sub> ) <sub>2</sub> 6H <sub>2</sub> O	1:2:2	DMF:MeOH (1:1)	Pressure tube	100	72h	-	4b
<b>3a-35-b</b>	0.10	BPDC	Zn(NO <sub>3</sub> ) <sub>2</sub> 6H <sub>2</sub> O	1:3:2	DMF:MeOH (1:1)	Pressure tube	100	72h	-	4b
<b>3a-35-c</b>	0.10	BPDC	Zn(NO <sub>3</sub> ) <sub>2</sub>	1:1:2	DMF:MeOH (1:1)	Pressure tube	100	72h	-	4b

Table 20 Outlines the conditions of each attempt at optimising the synthesis of 3D frameworks LK-1 and LK-2. Vessel volumes: Wheaton Vial - 2.5 mL, Pressure Tube - 10 mL, Parr Bomb - 10 mL. \* denotes modulator. Outcomes: 1 = no reaction, 2 = amorphous/not crystalline enough for characterisation, 3a = novel crystalline and amorphous material, 3b = literature known crystalline and amorphous material, 4a = novel crystalline material, 4b = literature known crystalline material

LK-1 and LK-2 are produced in the same reaction with no clear preference (**3a-13-a**). To characterise either of these frameworks effectively (e.g. BET, PXRD, solid state UV-Vis) we require a means by which we can obtain a phase-pure sample. These frameworks seem to exhibit little stability outside the mother liquor, perishing even when the mother liquor is replaced with fresh solvent of the same composition as the original reaction mixture. Strategies for separating the two frameworks that involved manipulating the solvent media (density flotation, selective degradation) have had little success, as the result was always the framework crystallites collapsing. The frameworks however have shown good stability in the mother liquor and have shown a shelf-life of 6+ months. It is unclear what it is about the mother liquor that provides an environment in which the frameworks can maintain their integrity, but this does suggest that the best strategy for obtaining one of these frameworks independent of the other is to manipulate the reaction conditions to engender selectivity for one framework over the other, rather attempting to separate them post-hoc.

We trialled reactions with a variety of different reagent stoichiometries, however the stoichiometries (Zn:BPDC:SP) of the frameworks LK-1 and LK-2 are quite similar, 5:4:2 and 3:3:1 respectively. This is further complicated by the fact the other possible framework is IRMOF-9(10), a framework consisting entirely of zinc and BPDC linkers (and the non-interpenetrated version), and as such the pillar linker is usually used in excess with respect to the BPDC linker to discourage the formation of the IRMOF. No selectivity was achieved in any of these trials.

Next, we tried to encourage selective formation of LK-1 or LK-2 by seeding fresh reaction mixtures with crystals of only one of the frameworks, in the hope that crystal growth would out-compete nucleation and therefore provide selectivity that way. Again there was not much success with this method, and it is quite possible the crystals fell apart when they entered the fresh reaction mixture before they could act as a nucleation device, as we had seen previously when investigating the solvent stability of both frameworks.

An alternative possibility for the instability of the framework could be the presence of the volatile solvent methanol causing framework collapse upon evaporation. Solvents capable of hydrogen bonding have been known to encourage capillary-force-driven channel collapse in MOFs.<sup>53</sup> We did observe that LK-1 and LK-2 were synthesised in both DMF:MeOH (1:1) (Experiment **3a-13-a**) and DEF:MeOH (1:1) mixtures (Experiment **3a-13-d**), suggesting there could be some variation in the overall polarity of the solvent. We attempted the synthesis of the frameworks in solvents with higher boiling points in an attempt to reduce evaporative solvent loss and hence improve stability post-synthesis, but unfortunately neither of the frameworks were successfully synthesised in these experiments. (**3a-27-a-j**) This suggests that the methanol plays a key role in the synthesis of LK-1 and

LK-2. In all cases without methanol the reaction either did not produce anything or a framework that did not include the spiropyran linker was synthesised. One observation is that the BPDC linker is poorly soluble in methanol and when the synthesis begins it is not fully dissolved. It is possible that the presence of methanol causes a low steady-state concentration of BPDC being available at all times and therefore allowing the **3a** linker to compete effectively with the BPDC linker to be incorporated into the framework which may be why reaction mixtures that do not include methanol never successfully synthesise LK-1/2.

We also tried varying reaction times, to see one of the frameworks was more significantly favoured either kinetically or thermodynamically. These experiments were ran at 60°C to slow the reaction down and increase the likelihood of observing any meaningful changes. **3a-30-a** (4 hours) showed no significant change. **3a-30-b** (20 hours) showed some dark red crystalline material had begun to form, reminiscent of LK-2 but was too small/poor a quality to provide any crystallographic data that could confirm this. **3a-30-e** (52 hours) showed evidence of both LK frameworks being present in a significant enough quality and quantity. **3a-30-f** (68 hours) big amorphous spheres had formed; the LK framework crystals were still present. There were no significant changes to be seen from **3a-30-g** (68 hours) **3a-30-i** (100 hours). Although there is some indication that LK-2 may be kinetically favoured over LK-1 it is not conclusive. Furthermore, the LK-2 was not present in any significant way until LK-1 had formed. It is even possible that due to the pale pink typical of LK-1, that it would be less easily observed as smaller crystals and may have just gone unnoticed when observing **3a-30-b**.

Another strategy was to try and modulate the reaction, in the hope that one framework may form quicker than the other or is slightly higher energy. Due to the nature of spiropyran, the addition of modulators could cause the spiro- centre to break or cause some unwanted opening or closing of the framework. As we had seen that spiropyran frameworks had successfully formed in the case of **3a-16-a** with HCl added in amounts of  $\mu\text{L}$ , our efforts were focused on tests that added various micro-volumes of HCl. **3a-28** tested volumes of HCl ranging from 0.1 – 1.0  $\mu\text{L}$ , all produced similar results with no discernible improvement with or without HCl. **3a-31** and **3a-32** tested 25 and 50  $\mu\text{L}$  of HCl with various conditions. In all 3 sets of experiments, no clear benefit was seen by including HCl. **3a-31-a** was able to synthesise the LK frameworks with 50  $\mu\text{L}$  HCl present, suggesting that both frameworks are stable to acid concentrations of this magnitude.

From these data the instability of these frameworks outside of the mother liquor remains a challenge to be overcome. It is obvious that methanol plays a key role in this synthesis, though it is not immediately obvious what that is. If it was simply acting to provide a low steady-state concentration of the BPDC linker, then we would surely observe some success with our attempts at modifying the

stoichiometry in pure DMF. Neither of the crystal structures show the methanol playing any key structural role, although it is possible that the data was simply not good enough to identify the methanol present. The fact that both frameworks require methanol to be present suggests that whatever role it is playing, it is likely playing the same role for both. In an attempt to further investigate the role of methanol, the synthesis for LK-1/2 was attempted with varying ratios of MeOH:DMF (see Table 21).

<b>Experiment</b> <i>(ref.)</i>	<b>Pillaring</b> <b>liner (P)</b> <b>(mmol)</b>	<b>Layering</b> <b>linker (L)</b>	<b>Metal Salt</b> <b>(M)</b>	<b>Molar</b> <b>Ratio</b> <b>P:L:M</b>	<b>Solvent(s) (v:v)</b>	<b>Vessels</b>	<b>Temperature (°C)</b>	<b>Time</b>	<b>Notes</b>	<b>Result</b>
<b>3a-35-a</b>	0.025	BPDC	Zn(NO <sub>3</sub> ) <sub>2</sub>	1:1:2	DMF	Wheaton Vial	80	72h	-	3b
<b>3a-35-b</b>	0.025	BPDC	Zn(NO <sub>3</sub> ) <sub>2</sub>	1:1:2	MeOH:DMF (1:4)	Wheaton Vial	80	72h	-	3b
<b>3a-35-c</b>	0.025	BPDC	Zn(NO <sub>3</sub> ) <sub>2</sub>	1:1:2	MeOH:DMF (2:3)	Wheaton Vial	80	72h	-	4a (LK-1/2)
<b>3a-35-d</b>	0.025	BPDC	Zn(NO <sub>3</sub> ) <sub>2</sub>	1:1:2	MeOH:DMF (1:1)	Wheaton Vial	80	72h	-	3a (LK-1/2)
<b>3a-35-e</b>	0.025	BPDC	Zn(NO <sub>3</sub> ) <sub>2</sub>	1:1:2	MeOH:DMF (3:2)	Wheaton Vial	80	72h	-	2
<b>3a-35-f</b>	0.025	BPDC	Zn(NO <sub>3</sub> ) <sub>2</sub>	1:1:2	MeOH:DMF (4:1)	Wheaton Vial	80	72h	-	2
<b>3a-35-g</b>	0.025	BPDC	Zn(NO <sub>3</sub> ) <sub>2</sub>	1:1:2	MeOH	Wheaton Vial	80	72h	-	1

Table 21 Combinatorial assay, assessing the affect of varying the DMF:MeOH volume ratio.

From experiment **3a-35**, we can see a rough trend. When DMF was  $\geq 75\%$  of the total reaction volume, the frameworks synthesised did not include the spiro-*pyran* ligand. When the DMF was  $< 50\%$  the material was too amorphous to analyse. The DMF solubilised all the reagents while the MeOH desolvates the BPDC and the  $\text{Zn}(\text{NO}_3)_2$ , but the **3a** linker remains soluble in both. In doing so the steady state concentration of **3a** is much higher in relation to the other reagents therefore yielding the LK frameworks over the frameworks not incorporating the **3a** ligand. Typically, longer crystallisation times should result in higher quality crystals if given enough time. However, the integrity of the spiro-*pyran* must also be accounted for. The longer the reaction time, the more likely the spiro- centre is to cleave and therefore no longer able to act as a linker. Although it is unclear as to whether the spiro- centre is more stable to cleavage upon incorporation into the framework, the lack stability of the framework as a whole suggests that either this is not the case or that the framework is too unstable for it to matter. Also experiment **3a-30** ran at  $60^\circ\text{C}$  for 100 hours (with no further changes occurring after 68 hours) shown a loss in a crystal quality compared to when the reaction is running at  $80^\circ\text{C}$  for 72 hours.

As discussed earlier (**3a-27**), a possible source of instability is the volatility of the MeOH. We may be able to preserve the frameworks more successfully if we replaced methanol for longer chain alcohols which will have roughly the same solubilities for the reagents but reduced volatility, therefore reducing the likelihood of framework collapse upon solvent leaving the framework and also the increased size of the molecule should better fill the pores of the framework providing further stabilisation.

### 3.3.3 GG-1

The GG-1 framework forms as orange ellipsoid crystals (see Figure 73). Interestingly, under polarised light the colours vary from orange to blue depending on orientation which is indicative already of open and closed forms of spiro-*pyran* being present, although the orange colour seemed to dominate throughout the sample. In this case, this framework seems to be the only crystalline material present in this mixture. There is some unidentified amorphous material which could be the GG-1 framework or some other impurity. Like the LK frameworks, this framework is also quite unstable outside the mother liquor and is fragile to crystal manipulation techniques. This instability outside the mother liquor prevents adsorption isothermal data being acquired and so we must look to other forms of characterisation.



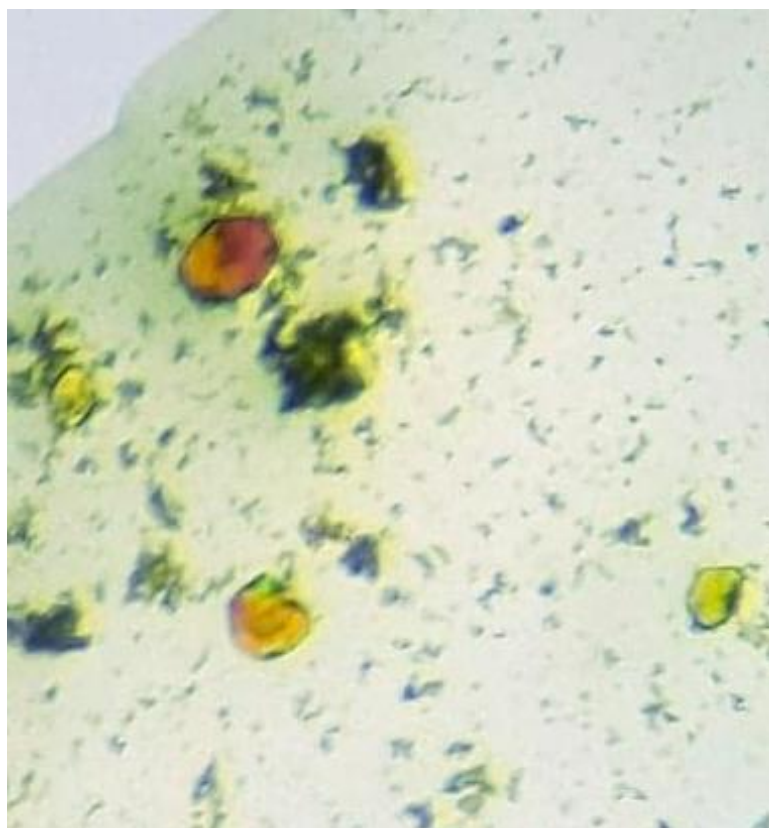


Figure 73 Microscope picture of elipsoid crystals of GG-1.

### 3.3.3.1.1 Single Crystal X-Ray Diffraction

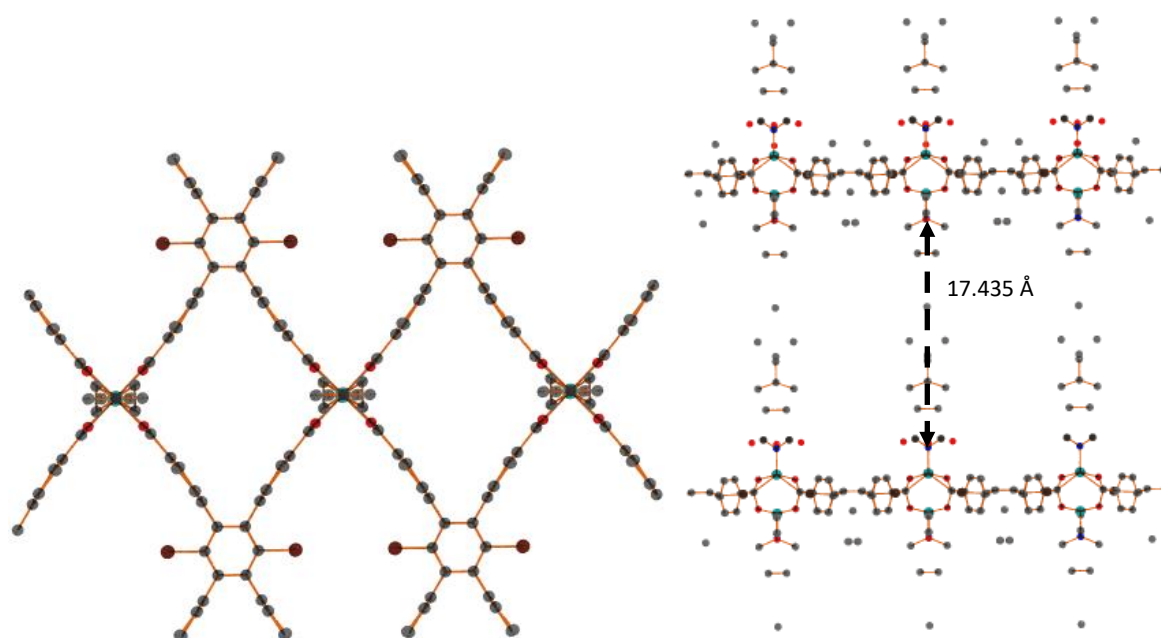


Figure 74 Picture of crystal structure GG-1, looking down the *c* axis (left). Picture of GG-1 looking down the *b* axis (right), the space between the layers is 17.435 Å. Zinc (cyan), oxygen (red), nitrogen (blue), bromine (brown), carbon (grey).

The GG-1 framework seems to be a pillar layer framework as we can clearly identify the layers of DBTD linker with the zinc paddlewheels (see Figure 74). There is, however, significant disorder in the structure located in the gaps between the layers which simply cannot be modelled. Judging from the size and quality of the crystal we would expect a reasonable data set. The disorder that was observed in the LK frameworks is an order of magnitude less than this framework and bears a similarity to the disorder in the frameworks published by *D. Williams et al.*, although in this case the whole spiropyran molecule is unassigned rather than just the indoline fragment. Modelling of the **3a** ligand in its lowest energy state suggests the distance between both terminal nitrogen atoms is 15.2 Å in the closed form and 18.4 Å in the open form (see Figure 75). The gap between the layers is approximately 17-18 Å, which could potentially be either the closed or open form. We also identified both blue and orange crystals under the microscope, which as we know from chapter 2, the blue is indicative of the open form as it is typically absorbing in the 500-700 nm region.<sup>54</sup>

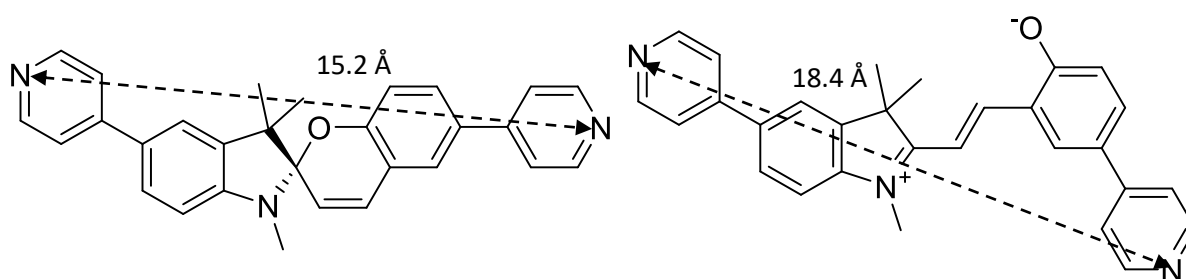


Figure 75 Linker **3a** showing distance between terminal N atoms for the closed form (left) and open form (right). Distances determined using the MM2 simulation from Chem3D.

We know there is some degree of flexibility around the spiropyran core which will already cause some disorder, combine this with the fact that the open form is present which also has multiple forms (discussed earlier), then we have strong indicators that this pillar linker is the ligand **3a** and secondly that this framework is capable of photoisomerization. As seems to be the case with these photoactive materials, characterisation proves to be a constant challenge. Before we can draw any more conclusions about the photophysics of GG-1, we must confirm that the pillaring linker is **3a**.

### 3.3.3.2 NMR Digest

A typical method of confirming the presence of a desired ligand in a framework, is to digest the material in deuterated acid and confirm the presence of the ligand via NMR. The standard method is to take 2 mg of washed and dried material, sonicate it in a few drops of the deuterated acid. Then dissolve the resultant mixture in deuterated DMSO and analyse the sample.<sup>55</sup>

In the case of GG-1, there are several factors that adds to the complexity of this work. Firstly, the spiropyran is acidochromic and will open and close based on relative pH, furthermore, not only will

the open form be present but also both the open and closed forms have protonated forms as well. This means that there will be at least 4 different possible conformations that could be seen in the NMR spectrum, this will make the NMR spectrum particularly difficult to resolve, especially around the aromatic region (7-9 ppm) as there are 12 different proton environments in the aromatic region for ligand **3a** which will lead to a possible 48 different environments which is guaranteed to have some overlap and be extremely difficult to resolve. The second issue is that because these frameworks are unstable, we are not able to wash the frameworks of residual ligand as the frameworks will most likely break down and wash away the ligand that was incorporated in the framework. This also presents issues with drying the framework as without the washes, drying the framework will leave the residual ligand which could give a false positive. The best we could do to accommodate for this was to try and remove excess mother liquor from the framework with absorbent material and remove the majority of residual linker, although there will likely still be some unreacted ligand present and so we should prepare to accommodate for some inaccuracy in our final results. The first issue is significantly more difficult to account for. We do not know the kinetic behaviour of ligand **3a** and therefore cannot predict how the equilibrium will change depending on pH. As we have crystallographic evidence that LK-1 and LK-2 has successfully incorporated ligand **3a** and we know the stoichiometry of the pillaring and layering ligands (2 moles BPDC:1 mole **3a** for both frameworks), its logical to establish an effective method with these frameworks.

#### 3.3.3.2.1 Ligand **3a** control

First and foremost we sought to investigate how **3a** behaves in the conditions used for digestion, so we applied the digestion method to a sample of **3a** and obtained a spectrum (see Figure 76).

500\_LK-3A-DIGEST

Proton.icon DMSO {C:\Bruker\TopSpin3.2.7} TE 29

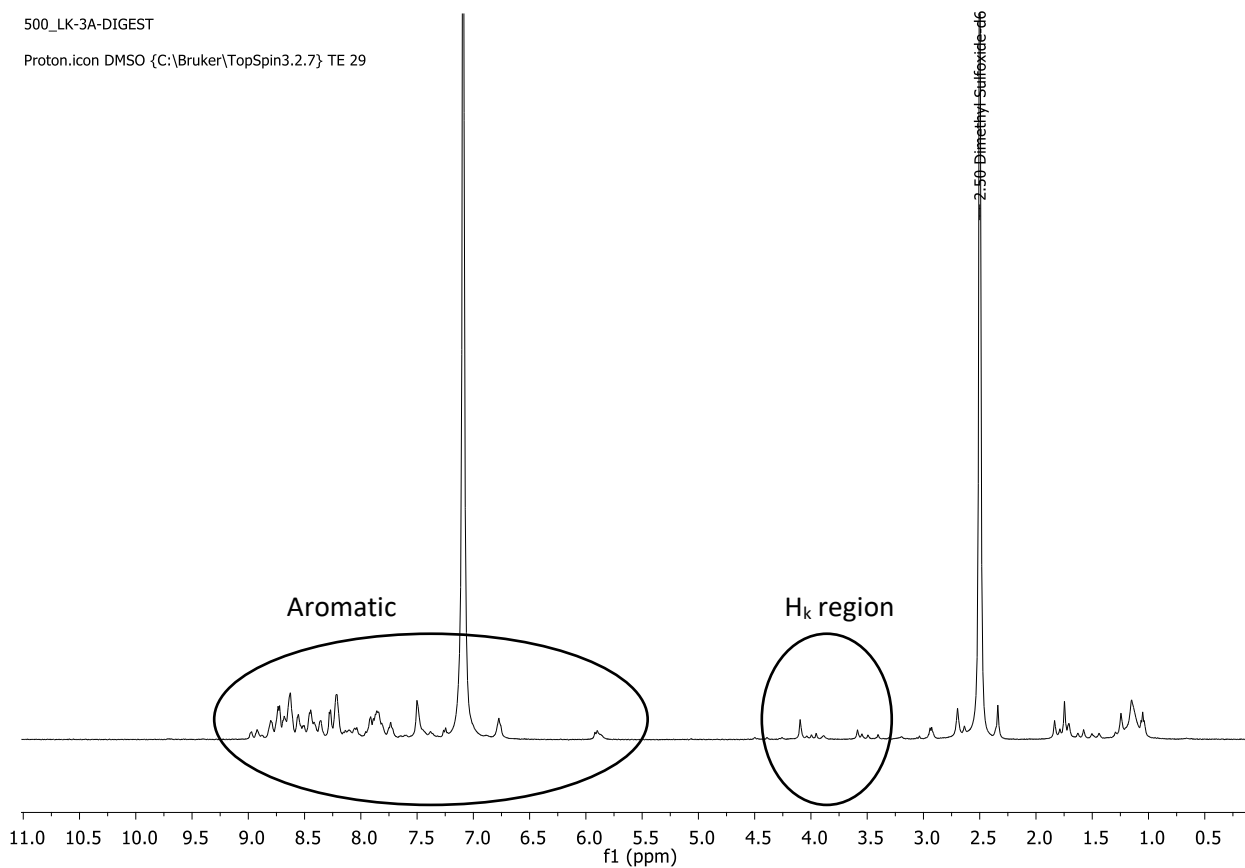


Figure 76 NMR spectrum of ligand **3a** in  $d_6$ -DMSO and DCl. Aromatic region (left) and approximate region of  $H_k$  (right).

It is clear that there has been significant shifts in peaks due to the presence of the acid, with little semblance to the spectrum acquired in  $CDCl_3$  (see Chapter 2 experimental section for spectrum obtained in  $CDCl_3$ ). *Zhou et al.* studied the spiro molecule functionalised with nitrobenzene with via NMR and were able to characterise the open form (MC), closed form (SP) and their protonated counter parts (MCH<sup>+</sup> and SPH<sup>+</sup> respectively, see Figure 77).<sup>56</sup>

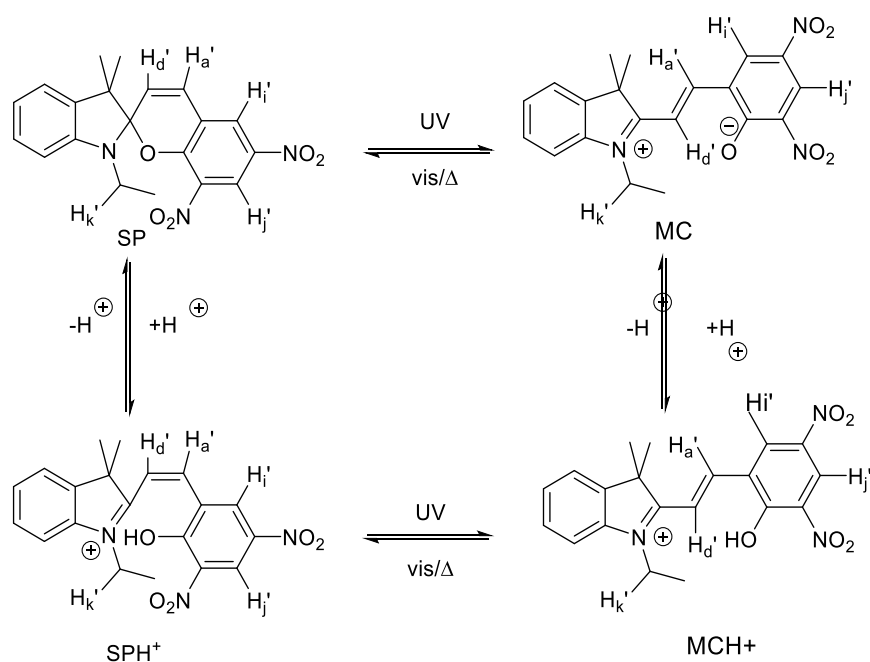


Figure 77 The spiropyran molecule that was analysed by Zhou *et al.*, illustrating the equilibrium between the open and closed isomers and the protonated and non-protonated forms of each. Proton environments of interest are shown.<sup>56</sup>

Although the molecule is electronically quite different, these data should provide some approximation of the relative peak positions as it shifts through the various forms (see Table 11).

Molecule	H <sub>a</sub> ' (ppm)	H <sub>d</sub> ' (ppm)	H <sub>i</sub> ' (ppm)	H <sub>j</sub> ' (ppm)	H <sub>k</sub> ' (ppm)
SP	7.38	6.27	8.44	8.60	3.29
SPH <sup>+</sup>	7.71	7.37	8.62	9.02	4.30
MC	8.95	8.56	8.59	8.59	4.60
MCH <sup>+</sup>	8.70	8.25	9.08	9.08	4.85

Table 22 NMR peaks recorded by Zhou *et al.* for the nitrobenzene functionalised spiropyran.

The spectrum we obtained had very poor resolution of the peaks in the aromatic region (5.0-9.0 ppm) making it difficult to draw comparisons between proton environments H<sub>a</sub>, H<sub>d</sub>, H<sub>i</sub> and H<sub>j</sub>. The region pertaining to the N-alkyl region (2.5-5.0 ppm), has significantly better resolution. Thus, it makes logical sense to focus on this region to determine how many of the forms are present and in what stoichiometry. Using the detailed NMR study of proton environments in Chapter 2, in all the ligands studied the H<sub>k</sub> environment was 2.7-2.9 ppm. Zhou *et al.* found that although the merocyanine (open form) is conjugated across the central double bond, the nitrobenzene does not have any mesomeric effects on the indole ring, due to the double bond being in the *meta* position in regard to the nitrobenzene functionalities. Therefore we can assume that the only electronic effects on the proton

environments on the indole ring are inductive, so we could approximate peak positions for the proton environment  $H_k$  for the forms SPH+, MC and MCH+ of ligand **3a** (Table 23).

Molecule	Zhou et al. $H_k'$ (ppm)	<b>3a</b> $H_k$ (ppm)
SP	3.29	2.82
SPH+	4.30	<b>~3.83</b>
MC	4.60	<b>~4.13</b>
MCH+	4.85	<b>~4.38</b>

Table 23 The difference between  $H_k'$  and  $H_k$  of the SP form is 0.53 ppm. By subtracting this value from the  $H_k'$  ppm values of the SPH+, MC and MCH+ forms we can roughly approximate the peak positions we expect for the forms SPH+, MC and MCH+ of **3a**.

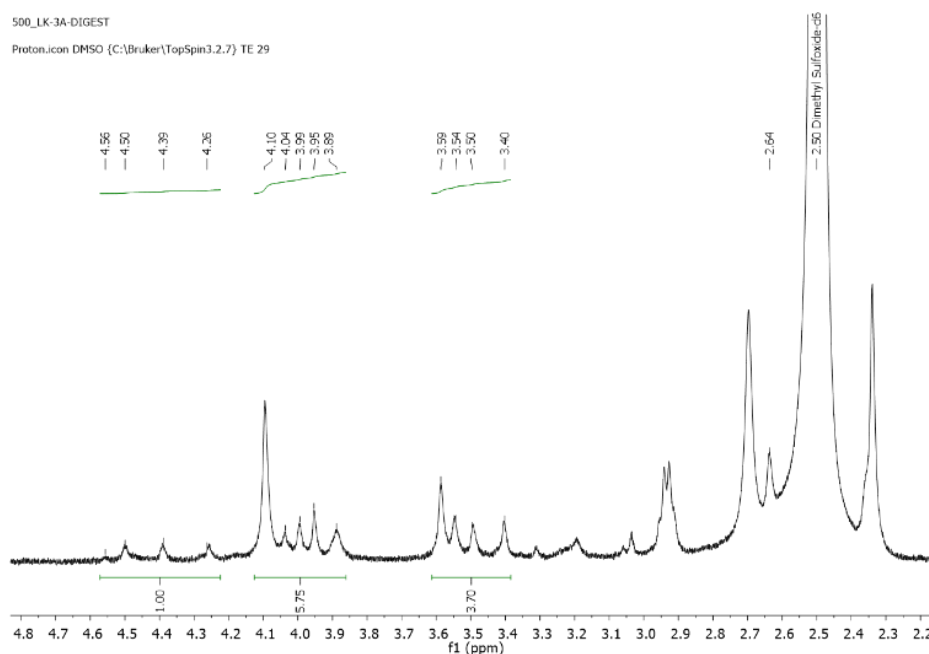


Figure 78 Spectrum of ligand **3a** in DCl and  $d_6$ -DMSO, zoomed in on the 4.8-2.2 ppm region. Possible peak positions of  $H_k$  highlighted with integrations. Peak position at 2.64 could possibly be the SP form however has not been integrated due to overlap with DMSO peak and satellites.

When analysing the NMR spectrum for ligand **3a** (Figure 78) we would expect to find a maximum of four peaks in the region of 2.7-4.8 ppm, for each of the possible forms of **3a** (SP, SPH+, MC and MCH+). In each of the regions we predicted finding one singlet peak for each form, we instead find that there are four to five singlet peaks. These clusters of singlet peaks could be due to there being slightly different variants of each of the four forms outlined earlier, therefore appearing as significantly more than the four peaks we were expecting.<sup>57</sup> These forms could be a manifestation of the various forms of MC discussed in Chapter 1.

If each cluster represents one of the SP, SPH+, MC and MCH+ forms, then comparing the integrals of the whole clusters could provide some insight into the equilibria present. There seem to be three significant clusters present: 3.40-3.59, 3.89-4.10 and 4.26-4.56 ppm. Although we originally expected four different identifiable environments, our previous experiments shown the H<sub>k</sub> peak position of the SP form to be 2.82 ppm in CDCl<sub>3</sub>. This region is however overlapping with the DMSO solvent peak and the associated satellites, therefore we are unlikely to be able to observe it. We would assume that due to the strong concentration of DCI present that the equilibrium would shift towards the protonated forms SPH+ and MCH+, furthermore the open form would be heavily favoured over the closed form due to the acidochromicity, thus we would expect very little of the SP form to be present and therefore have a negligible presence.

According to the study by *Zhou et al.*, we expect the peak positions to shift upfield from SPH+ to MC to MCH+. Combining this pattern with our rough predictions suggests the 4.26-4.56 ppm cluster represents MCH+ (predicted 4.38 ppm), the 3.89-4.10 ppm cluster represents the MC form (predicted 4.13 ppm) and finally the 3.40-3.59 ppm cluster must belong to the SPH+ form (predicted 3.83 ppm). Going by the integrals it would appear that the equilibrium is in a 1:6:4 ratio (MCH+:MC:SPH+), which is slightly surprising as in an acidic solution we would expect MCH+ to be a bigger contributor than the MC. We do not know the pK<sub>a</sub> of the MCH+ molecule so it may be a stronger acid than expected or it may be possible that the 4.26-4.56 ppm cluster actually belongs to MC and the 3.89-4.10 ppm cluster represents MCH+. Our goal is to determine the amount of **3a** present in the LK frameworks therefore determining which of the two aforementioned clusters belong to MC and MCH+ is not necessary. This control is not a perfect replication of the conditions of the MOF, as any Zn<sup>2+</sup> ions released into solution can potentially bind to the MC form which is another species that we do not have data for. The differences in pH is less of a concern as the DCI was used in an excess which will render any differences, caused by the presence of the dicarboxylic acid linker, BPDC, and any trace amounts of nitric acid left over as a by-product, negligible.

### 3.3.3.2.2 LK NMR digest

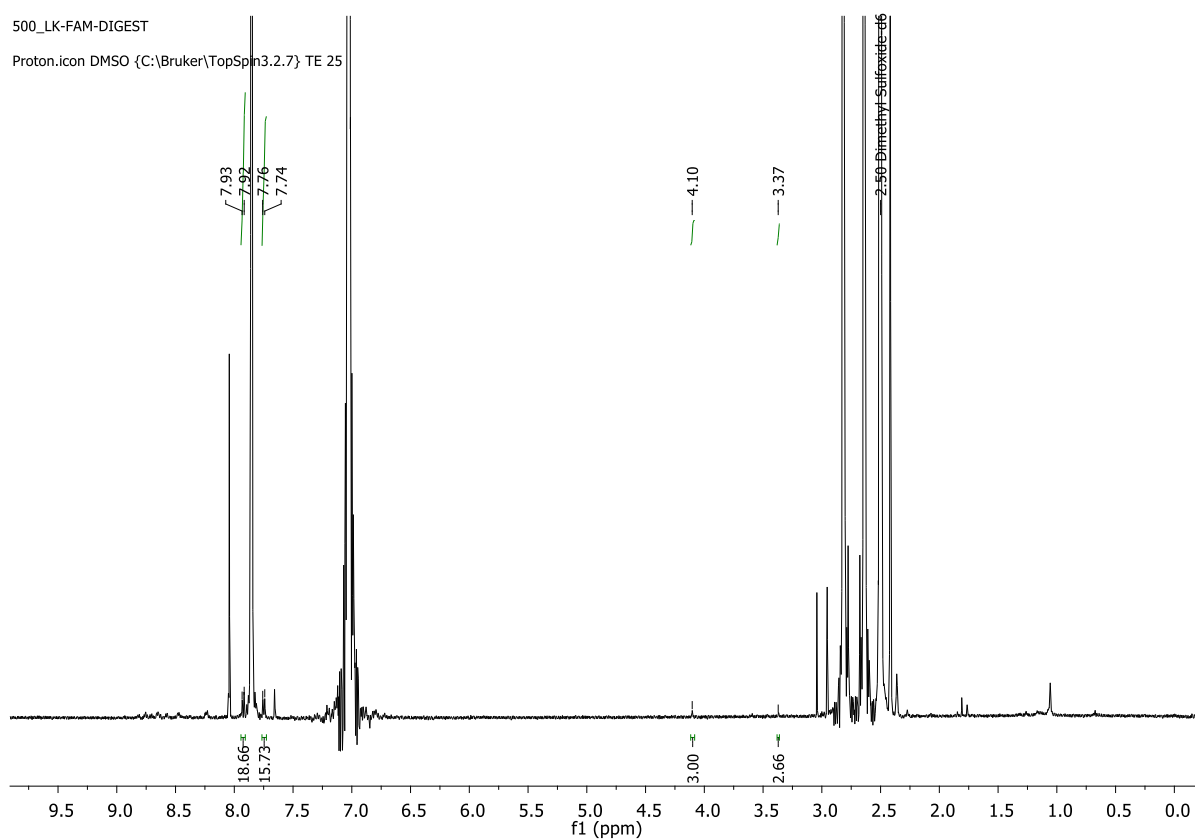


Figure 79 NMR spectrum obtained for LK mixture digested in DCl and DMSO- $d_6$ .

The control spectrum acquired for BPDC shown two doublets: 7.92 ppm (4H) and 7.75 ppm (4H), which are easily observed in this spectrum (See Appendix S2 NMR digest section). Unfortunately, the peak at 7.92 ppm has some overlap with the large peak 7.85 ppm, therefore the peak at 7.75 ppm was used to gauge the BPDC content.

Due to the presence of DMF solvent, the signals pertaining to ligand **3a** are quite weak however we can see some small peaks in the  $H_k$  region at 4.10 and 3.37 ppm (which we assigned as MC and SPH+ respectively), the peak at 4.26-4.56 ppm is not observed, however it had a minor contribution in the spectrum acquired for **3a** (Figure 78) and therefore the signal is quite possibly too weak to be observed on this spectrum. Although we would expect the ratio of the spiropyran forms to change to some degree as the presence of BPDC and  $Zn^{2+}$  ions will affect the overall pH of the solution and the  $Zn^{2+}$  could potentially complex with the MC form, the ratio of SPH+ to MC remains relatively similar (previously 2:3, now 5:6). We calculate the relative ratios of BPDC to SP to be the following: BPDC is 15.73/4 protons per molecule  $\approx$  4 molecules, **3a** (SPH+ and MC) 3.00+2.66/3 protons per molecule  $\approx$  2 molecules. The SCXRD data shows the ratio of ligands BPDC:**3a** to be 2:1 (for both LK-1 and LK-2) but



the stoichiometry of the reaction was 1:1 (**3a-13-a**), so this suggests that our rough approximations have worked in this case and should allow us to gauge the SP content in GG-1.

### 3.3.3.2.3 GG-1 NMR Digest

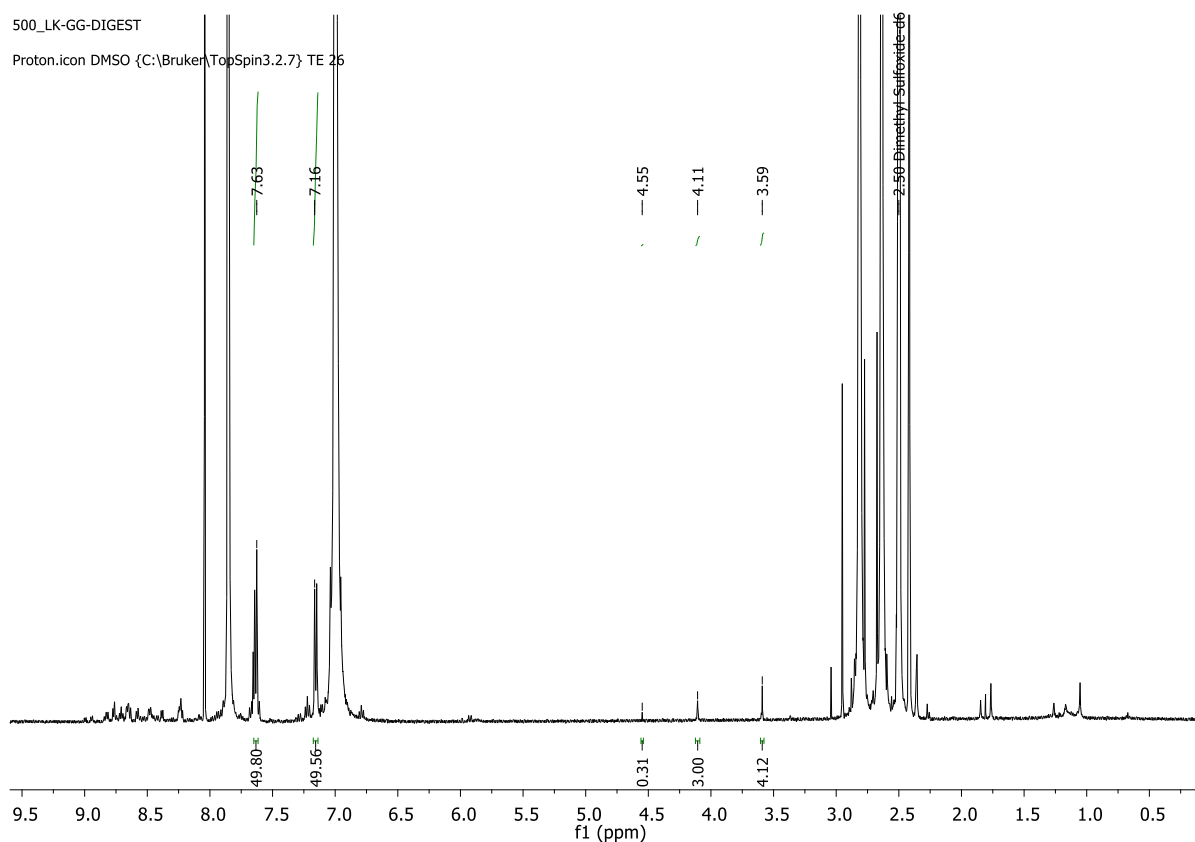


Figure 80 NMR spectrum obtained for GG-1 digested in DCl and DMSO- $d_6$ .

The control spectrum acquired for DBTD shown two doublets: 7.76 ppm (8H) and 7.24 ppm (8H), which are easily observed in this spectrum (See Appendix S2 NMR digest section). In this case we can see the peak representing MCH+ at 4.55 ppm in characteristically small amount. We calculate the relative ratios of DBTD to SP to be the following: DBTD is 49.56/8 protons per molecule  $\approx$  6 molecules, **3a** (MCH+, MC and SPH+) 0.31+3.00+4.12/3 protons per molecule  $\approx$  2-3 molecules. The ratio is approximately 2:1 (DBTD:SP). The stoichiometry of the original reaction (**3a-16-a**) was 4:3 (SP:DBTD) and the crystal data suggests a 1:1 ratio. Although the spiropyran is roughly half the concentration we were expecting, we still believe that the ligand has been incorporated as there are no other peaks present in the NMR that would be indicative of another species acting as the linker.

There are some possible explanations for why the observed ligand ratio does not match what we expect from the crystallographic data. The unidentified amorphous material produced as a by-product could consist of DBTD which would lead to an overestimate of the amount of DBTD present. Another explanation due to the disorder, there is an overestimation in the amount of SP present in the crystal

structure. It is entirely possible that spiropyran is missing from certain nodes throughout the crystal structure.

### 3.3.3.3 Powder X-Ray Diffraction

As the ratio of ligand **3a** to DBTD is lower in the digested sample than that observed in the SCXRD structure, we need to look at bulk characterisation techniques to determine whether GG-1 is the only species present. Under the optical microscope only one type of crystal suitable for SCXRD is observed, but there are some smaller crystals and also an unidentifiable, potentially amorphous material neither of which could be characterised by SCXRD.

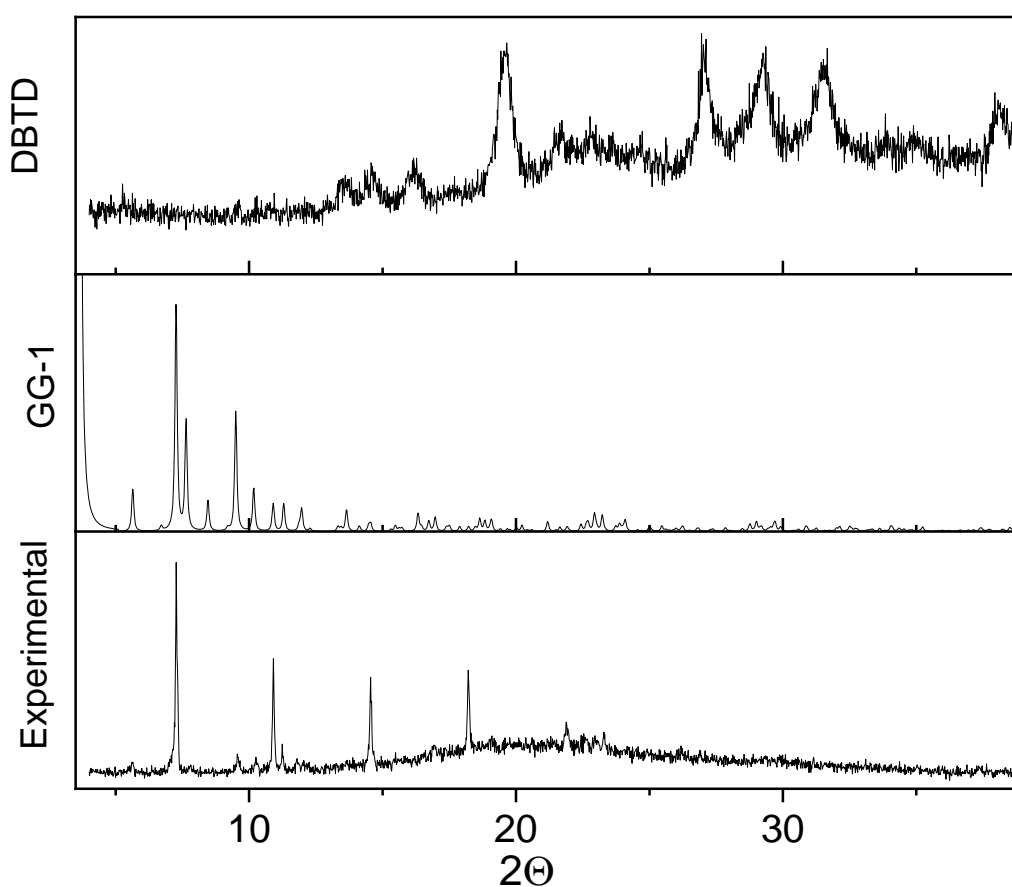


Figure 81 Powder X-ray data of the bulk material of the GG-1 synthesis (experimental) and the DBTD linker (DBTD) with the simulated powder pattern from the SCXRD data of GG-1.

The same issues that were present for the PXRD analysis of the LK frameworks are still present here; solvent evaporation, crystal degradation and potential photoactivation. The PXRD pattern shows diffraction peaks that mostly align with the peaks in the simulated pattern. There are peaks at 18.26 and 21.93  $2\theta$  which do not appear to fit with the simulated data. This is potentially indicative of a second species that is present that we have not been able to identify. The presence of a second species

is consistent with the result of the NMR experiment in which a 2:1 DBTD:**3a** ratio was observed, in contrast to the 1:1 ratio of the SCXRD structure. The DBTD powder pattern suggests that it is not purely crystallised DBTD, we can hypothesise the additional peaks may be due to some crystallised coordination compound of DBTD.

#### 3.3.3.4 Solid State UV-Vis

Further characterisation data of the bulk is required to confirm whether there is a significant second species present. The NMR spectrum would suggest the second species has the DBTD ligand present in some form while the PXRD suggests that it is not simply just the DBTD linker. Figure 82 shows the solid-state UV-Vis spectrum.

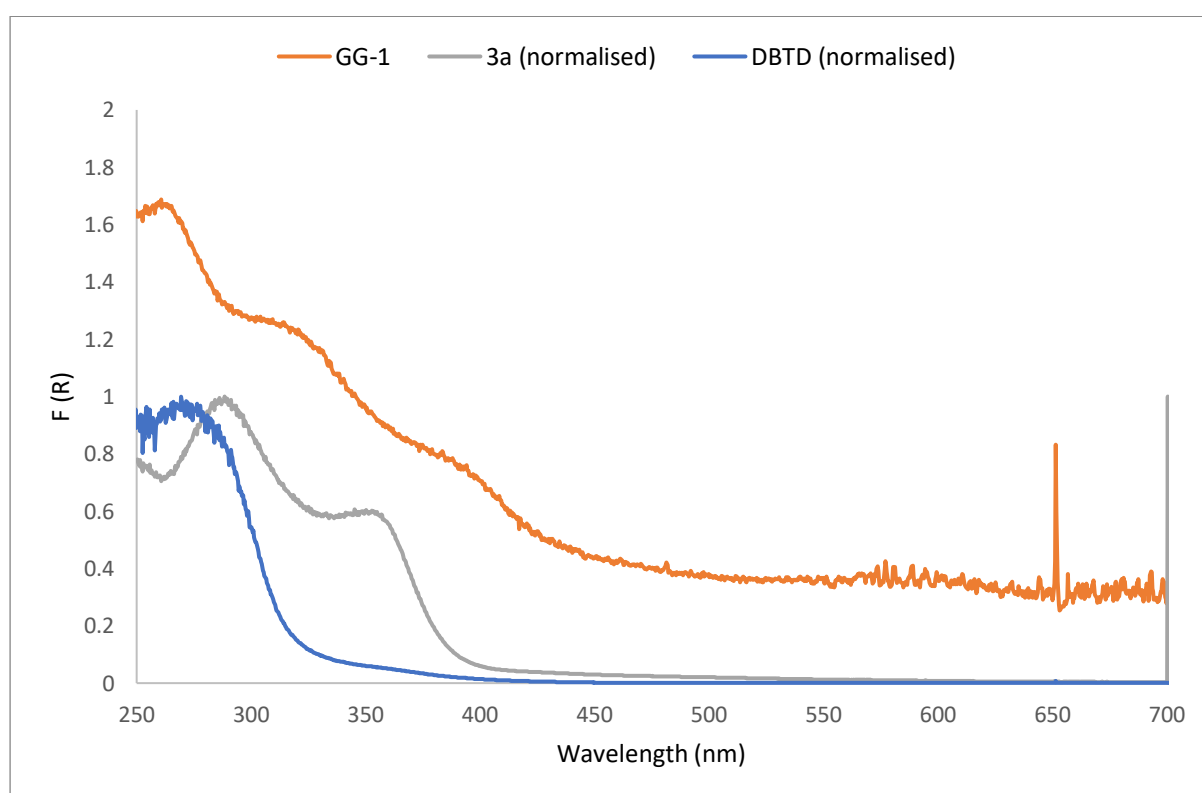


Figure 82 Solid state UV-Vis spectrum of GG-1

We can see three significant peaks in the spectrum acquired for the GG-1 sample: 265 nm, 317 nm and 395 nm. It is likely the 264 nm peak corresponds to the  $\pi$ - $\pi^*$  transition of the DBTD absorption (272 nm) while the 318 nm and 387 nm peaks correspond to the  $\pi$ - $\pi^*$  transitions associated with ligand **3a** (291 nm and 354 nm). The peak that corresponds to the DBTD seems to have a significantly stronger reflectance compared to the two assigned to spiropyran, we do not know the specific molar extinction coefficients but this could indicate a higher concentration of DBTD compared to **3a** like we observed in the NMR data. Like we saw with LK, we see a bathochromic shift of peaks corresponding to the spiropyran species. We can also clearly see both transitions for spiropyran unlike the case with

LK where it was just one broad absorption. There are two possible explanations here, it could be because there was more than one species containing the ligand **3a** in the LK mixture and therefore the broad peaks were caused by overlap, however in GG-1 there seems to be only one species that possesses the ligand **3a**. The other and more likely explanation is that the transition at 395 nm belongs to one of the protonated forms (MCH<sup>+</sup> or SPH<sup>+</sup>) which is plausible as the GG-1 synthesis uses HCl as a modulator. Furthermore, there also seems to be no significant reflection in the 550 nm region which we did see in the LK sample. Earlier we spotted some blue crystals in our sample, which we would expect to see manifest in this spectrum. It seems the reflectance is almost silent in the 500-700 nm region, therefore we could theorise that only the SPH<sup>+</sup>/MCH<sup>+</sup> forms are present in any significant capacity and the blue crystals are anomalous. This would suggest the disorder is caused by a mixture of the SPH<sup>+</sup>, MCH<sup>+</sup> and SP forms in the framework.

In summary, we have a pillar layer framework GG-1 that consists of DBTD and some form of ligand **3a** (open or closed). Based on the colours and the UV-vis data this framework is likely a mixture of the closed form and one of the protonated forms. The small concentration of HCl and the high polarity of solvent are conditions that would favour the MCH<sup>+</sup> form. There is an unknown by-product that we believe to contain DBTD in some form as there is a significant amount of it present in the NMR digest that is otherwise unaccounted for. The PXRD pattern suggests that the unknown species is not simply just DBTD but must be complexed with something else. The solid state uv-vis suggests that the form of ligand **3a** is primarily in the protonated form, the SCXRD data shows the distance between zinc paddlewheels where the pillar linker should be is 17.435 Å, which can potentially be either the open MC form (18.4 Å as a free ligand) or the closed SP form (15.2 Å as a free ligand).

#### 3.3.4 GG-32

Our final framework presents itself as a square orange crystal (see Figure 83). Like the previous frameworks, this framework is also unstable outside the mother liquor and like the other frameworks cannot be purified effectively, and we can see a familiar amorphous material present. We can also clearly see a second crystalline species in the form of little ill-defined pink crystals that we were unable to collect a decent dataset for SCXRD analysis.

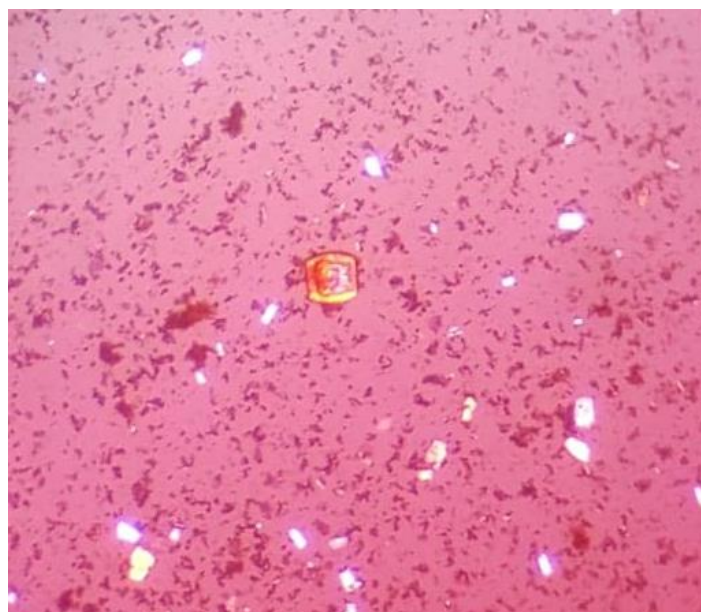


Figure 83 Microscope picture of GG-32 in mother liquor (big orange/red cube).

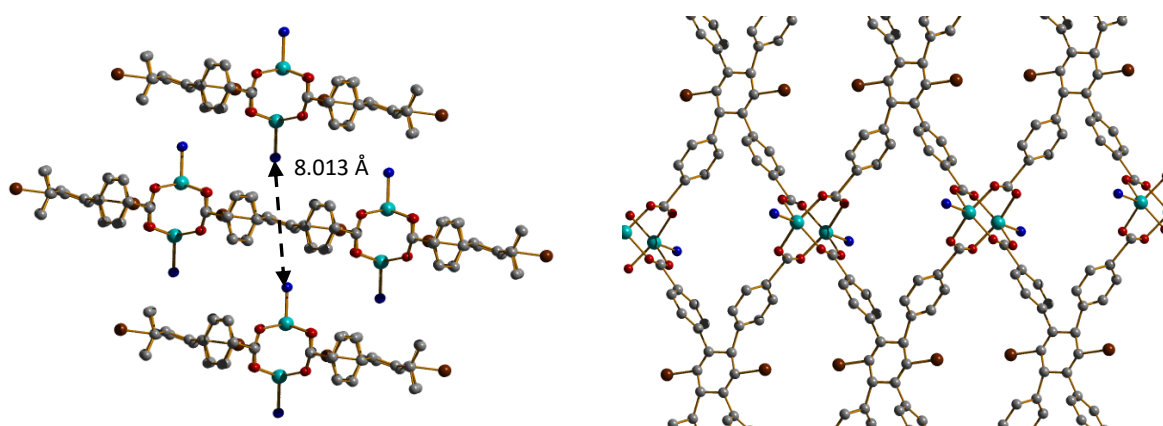


Figure 84 Crystal structure pictures of GG-32. View down *c*-axis (left) with distance between nitrogen atoms highlighted to be 8.013 Å. View down *a*-axis (right).

GG-32 is almost certainly an interpenetrated metal organic framework as we can identify zinc paddlewheels connected by DBTD linkers to form an infinite 2D layer (See Figure 84). The 8 Å gap between the 2D layers was not able to be fully resolved, therefore the nature of the pillar linker is unknown. It is unlikely to be the **6b** linker as it is half the size (see Figure 75) but it is unclear as to what else it could be. It is possible that there is no pillaring linker and it is simply capped by another species, either a product of degradation of the spiropyran linker or a solvent. Similar to GG-1 we were only able to identify one of the crystal types present. Also, like GG-1, the stability of the material upon leaving the mother liquor was also quite poor. One subtle difference between the GG series and the

LK series is that the source of characterisation issues for LK was the lack of stability however the GG series seems to be more robust than the LK series, but disorder is present in a greater extent.

#### 3.3.4.1 NMR Digest

The identity of the pillaring linker is the most elusive of the 4 frameworks discussed in this chapter. The single crystal data suggests a linker which has a size of 8 Å, although it is unlikely to be a spiropyran linker, a digestion experiment similar to what was discussed earlier for the LK frameworks and the GG-1 framework could confirm if this is the case and provide some insight on what the linker is.

##### 3.3.4.1.1 Ligand **6b** control

As was the case with the **3a** ligand, we need to establish a control spectrum with ligand **6b**. There is added difficulty as the NMR spectrum obtained for **6b** has some unassigned peaks belonging to unidentified impurities.

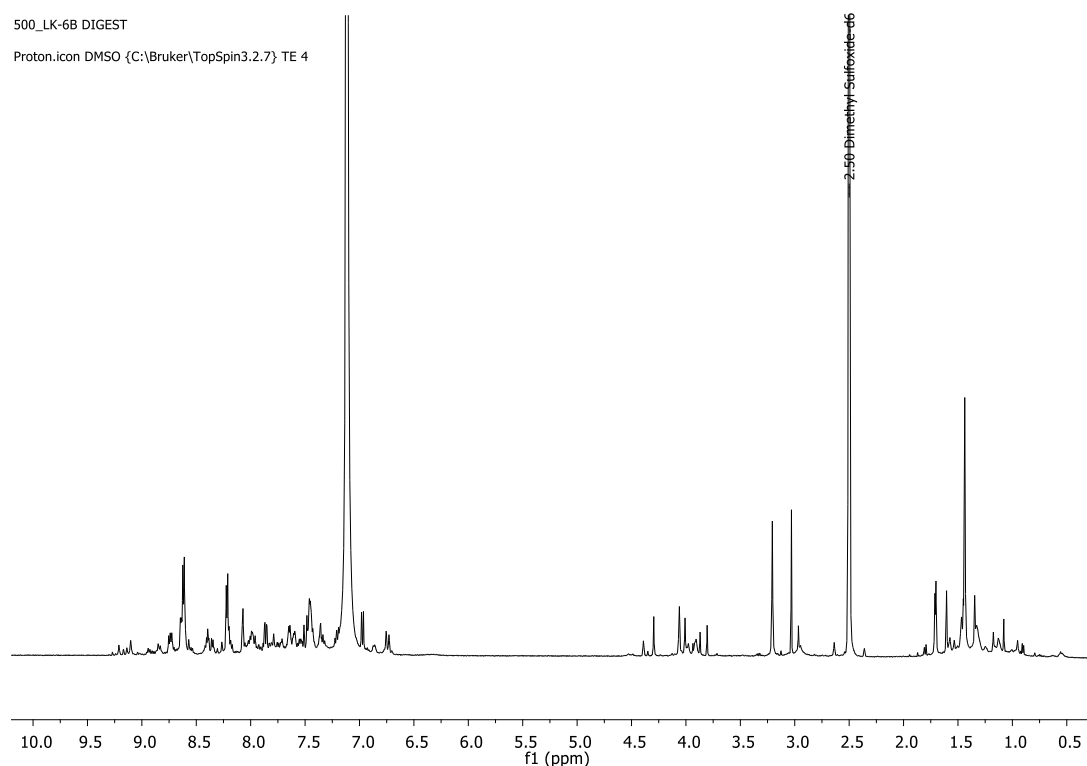


Figure 85 NMR spectrum of ligand **6b** taken under digestion conditions

As we saw earlier with the spectrum of ligand **3a** in digestion conditions (Figure 76), the aromatic region has significant overlap with other peaks therefore integrating these peaks will provide little insight, this is made worse by the fact there are unidentified species in this spectrum.

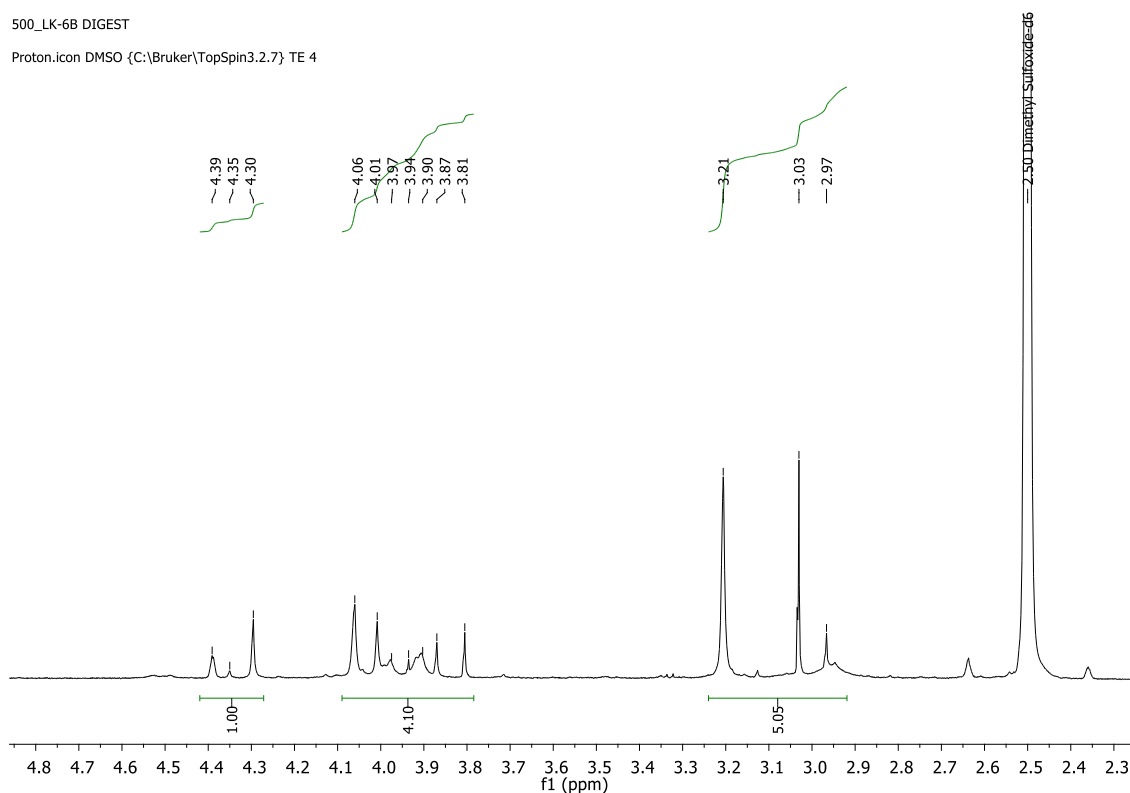


Figure 86 NMR spectrum of ligand **6b**, zoomed in on the 2.3-4.8 ppm region.

A closer look at the ppm region where we would expect to find the H<sub>k</sub> environment (Figure 86) shows multiple peaks. The spectrum obtained for **6b** in CDCl<sub>3</sub> suggested peaks at 2.69 and 2.75 could be H<sub>k</sub> for the SP form, this strongly suggests the presence of two different species that have an N-methyl group which would logically manifest here. The two signals at 3.21 and 3.03 ppm is indicative of two separate species due to the strength of the signals. Although the spectrum of **3a** also shown clusters of peaks, there was usually a dominant peak in the cluster that could act as the identifier. This also seems the case for the cluster of peaks at 4.06-3.81 ppm, which appears to have two sets of clusters with similar patterns overlapping each other signified by the two strong signals at 4.06 and 4.01 ppm. Like **3a** we can approximate the forms of spiropyran to each cluster: SPH+ 2.97-3.21 ppm, MC 3.81-4.06 ppm, MCH+ 4.30-4.39 ppm. The integrals of the peak clusters show a similar trend to what we observed with ligand **3a**, significant contributions by the SPH+ and MC forms with a small contribution by the MCH+ form, which further suggests the assignments are approximately correct.

### 3.3.4.1.2 GG-32 Digest

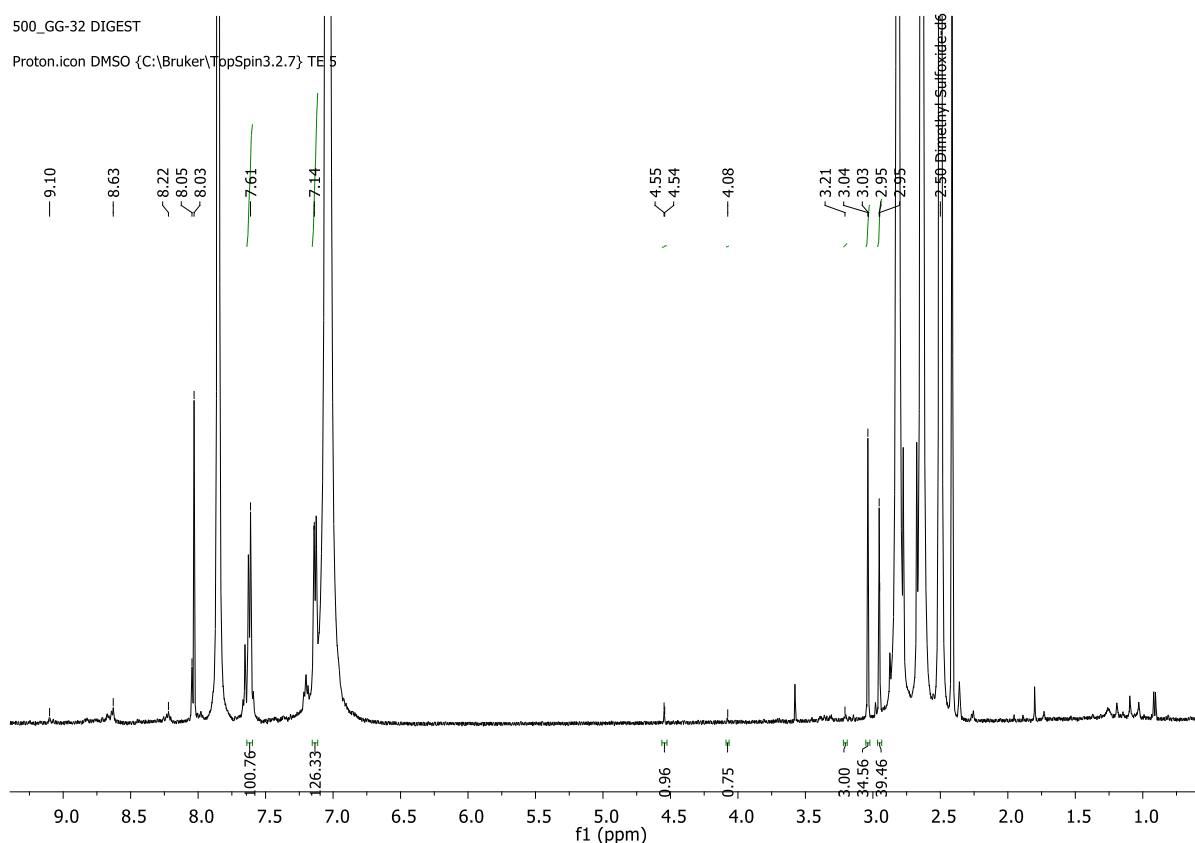


Figure 87 NMR spectrum of GG-32 digest.

The spectrum appears to be cleaner than the spectrum we obtained for the ligand **6b** (Figure 87). This would be indicative of purification by MOF synthesis, as the framework will only use one of the species and leave behind the other if incorporated into the structure. Of the two most prominent peaks at 3.21 and 3.04, only the 3.04 peak has remained and the peak at 2.97 has increased in intensity. Of the two prominent peaks in the MC cluster, 4.06 and 4.01 it would seem the peak at 4.06 has remained. The peak cluster at 4.30-4.39 ppm has not appeared at all on this spectrum but the peaks found at 4.53 have become more prominent. This indicates that whatever species has been purified out, it was most of the sample that was analysed in the **6b** spectrum and the ligand that has been incorporated was a minor product. As discussed earlier in the analysis of GG-1, the peaks representing the DBTD molecule are observed as doublets at 7.14 ppm and 7.61 ppm, the peak at 7.14 ppm has significant overlap with the solvent peak, thus the 7.61 ppm peak was used to determine the content of DBTD. 4.71H/3 protons per molecule  $\approx$  1-2 spiro molecules, 100.76H/8 protons per molecule  $\approx$  12-13 DBTD molecules. The SCXRD data suggests a 2:1 ratio (layering linker:pillaring linker) but the NMR data show our supposed spiro pyran species to be a ratio of 6:1. This means although the spiro species is likely present in the solution it would be as residual linker or spiro trapped inside the pores of the framework



and not as part of the structure. Identifying peaks at 8.22 8.63 and 9.10 ppm which we saw in the spectrum for **6b**, further suggest that the pillaring linker identity is not a spiro molecule.

As for what the identity of the pillaring linker is, there are peaks at 8.05, 8.03, 3.04 and 3.03 that could belong to the pillaring linker that have integrals that seem more related to the DBTD peaks. Assuming the peak at 3.03 is still an N-methyl group, the molecular ratio works out to be:  $34.96/3$  protons per molecule  $\approx$  11-12 pillaring molecule,  $100.76/8$  protons per molecule  $\approx$  12-13 layering molecule, so approximately a 1:1 ratio. Accounting for inaccuracies in the integrations due to overlapping peaks, it would be plausible that is the unknown pillaring species (present in a 2:1 ratio according to the SCXRD data). These peaks were present in the **6b** spectrum therefore the framework must have incorporated the unknown impurity as the pillaring linker instead of ligand **6b**. As we do not see any evidence of peaks that could belong to an open form species of this unknown impurity. The evidence would indicate this framework does not incorporate the **6b** linker or any ligand with the spiropyran functionality. Another possibility is that the pillaring site is capped with solvent (DMF) or a pyridine derivative.<sup>58</sup>

#### 3.3.4.2 PXR

Figure X shows a PXR pattern of experimentally synthesised GG-32 and the simulated pattern generated from the SCXRD structure.

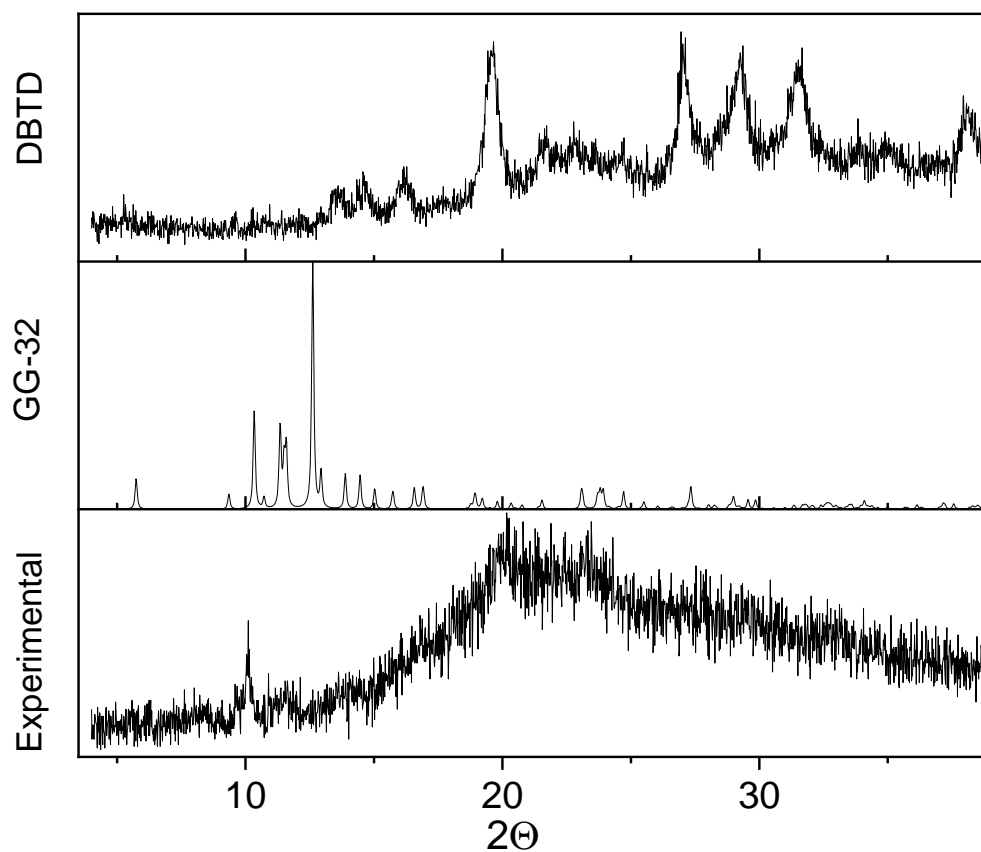


Figure 88 Powder X-ray data of the bulk material of the GG-32 synthesis (experimental) and the DBTD linker (DBTD) with the simulated powder pattern from the SCXRD data of GG-32.

Unfortunately, only weak diffraction is observed against the amorphous background (probably due to DMF solvent). One of the peaks obtained for the PXRD pattern of GG-32 did match with the simulated pattern from the SCXRD data at 10.36  $2\theta$ , but no other substantive conclusions can be made.

#### 3.3.4.3 Solid State UV-Vis

Our analysis of the NMR spectra of GG-32 suggests although the ligand **6b** was not incorporated into the framework, there was still some indicator that it was present. **6b** recorded peaks at 418 nm and 518 nm and the GG-32 sample recorded peaks at 396 nm and 549 nm.

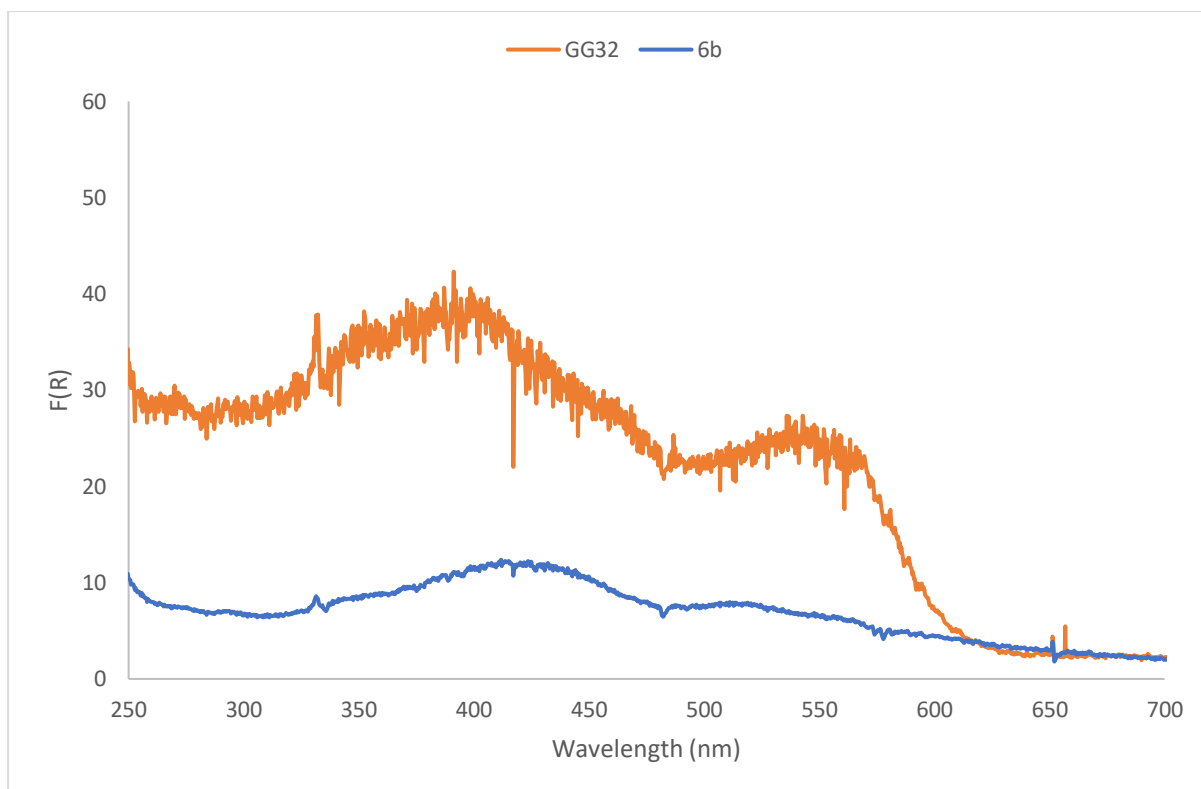


Figure 89 Solid state UV-Vis data of GG-32.

Although we have some unknown impurity, it would seem highly unlikely that this impurity would have a stronger absorption profile than the spiropyran moieties or that it could possess low energy transitions in the region of 400-650 nm. In the region of 400-650 nm we would expect to find the MC form and possibly the MCH<sup>+</sup> form. It is likely that the peaks we observe are in fact belonging to ligand **6b**, likely in the pores or on the surface of the framework. From the solid state and PXRD we cannot draw any concrete conclusions about the nature of the incorporation of the spiropyran (encapsulated, embedded etc) or to what extent it has been incorporated.

### 3.4 Summary and Conclusion

We have successfully synthesised three 3<sup>rd</sup> generation frameworks utilising ligand **3a** and possibly a 1<sup>st</sup> generation framework utilising ligand **6b**. Frameworks LK-1 and LK-2 utilising the BPDC layering linker were always produced in the same reaction and could not be separated by purification or modifying the synthetic procedure to favour one of the frameworks. We believe the volatility of the methanol solvent could be causing issues in framework stability but determined that it plays an important role in the formation of LK-1 and LK-2 and therefore have not found a suitable substitute.

For all of the frameworks, the stability outside of the mother liquor prevented typical characterisation data being gathered, such as gas adsorption isotherms. The presence of ligand **3a** was characterised directly by SCXRD for LK-1 and LK-2, in the case of GG-1 we indirectly confirmed the presence of ligand

**3a** through comparison of the size of the disordered region between the 2D layers of DBTD in the crystal structure and the ligand size which was corroborated by the NMR digestion experiments. The identity of the pillaring linker in framework GG-32 is unknown, but we can be quite certain that it is not a spiropyran linker due to the size of the disordered region between the 2D layers and the ligand **6b** also corroborated by the NMR digest experiments. The ssUV-vis shown that the spiropyran was present, possibly on the surface or included in the pores. Repeating the synthesis of GG-32, in the presence of a pyridine modulator rather than the ligand **6b** could help determine the nature of GG-32.

The main obstacle in this research was the nature of the spiropyran ligands, causing issues in both synthesis and analysis. The isomerisation occurring through multiple stimuli such as a change in solvent, it is most likely the cause for framework decomposition outside the mother liquor as changes in polarity or pH could cause photoisomerism to occur too quickly and the crystals were unable to withstand the stress caused by such drastic structural change. It may improve the stability if we could improve the strength of the metal-ligand coordination bonds, such as replacing the zinc metal node with elements with higher valent metals and larger charge densities (e.g. Zr<sup>4+</sup>, Cr<sup>3+</sup> etc).<sup>59</sup>

## 3.5 Experimental

### 3.5.1.1 Single Crystal X-Ray Diffraction

*GG-1 was collected and solved by Dr Benson Kariuki. I collected and solved the data for LK-2 and GG-32 crystals. I collected the LK-1 data myself but it was solved with the help of Dr Stephen Argent.*

Single crystals were mounted in paratone and studied on an Agilent SuperNova Dual Atlas three-circle diffractometer using Mo- or Cu-K<sub>α</sub> radiation and a CCD detector. Measurements were taken at 150(2) K with temperatures maintained using an Oxford Cryostream. Data were collected and integrated and data corrected for absorption using a numerical absorption correction based on Gaussian integration over a multifaceted crystal model within CrysAlisPro.<sup>60</sup> All structures were solved by direct methods using Olex2,<sup>61</sup> with the ShelXT<sup>62</sup>int and ShelXS<sup>63</sup> structure solution program, refined with the ShelXL<sup>64</sup> refinement package using least squares minimisation. The unit cells contain a large region of disordered solvent due to the high porosity of the frameworks, which could not be modelled as discrete molecules. For crystals LK-1, LK-2 and GG-32 the PLATON SQUEEZE<sup>65</sup> function was used to calculate the diffraction contribution of these molecules, and mask them to produce a new set of solvent-free diffraction intensities which were used in the final refinement.

### 3.5.1.2 Powder X-Ray Diffraction

PXRD patterns of all synthesised materials were obtained using a PANalytical X'Pert PRO Chiller 59 using a Ni-filtered CuK<sub>α</sub> radiation source ( $\lambda = 1.5419 \text{ \AA}$ ) scanning a range of  $2\theta = 4^\circ - 50^\circ$ . Samples were loaded onto zero-background silicon wafers directly from the reaction solution.

### 3.5.1.3 Solid state UV-VIS

Solid-state UV-Vis-NIR spectroscopy was conducted using an Ocean Optics FLAME-S-UV-VIS-ES portable miniature spectrophotometer, with an Ocean Optics DH-mini UV-Vis-NIR Lightsource. The solid-state samples were deposited onto a silicon zero background holder, excess liquid (in the case of MOFs) would be soaked up by tissue paper and a diffuse reflectance spectrum recorded in reflectance mode (R). Light and dark background spectra were recorded, the latter was to account for the electrical interference within the spectrophotometer. Reflectance spectra obtained were converted to F(R) using the Kubelka-Munk function.<sup>66</sup>

$$F(R) = \frac{(1 - R)^2}{2R}$$

Equation 2 Kubelka-Munk function for converting the recorded R values into F(R).

### 3.5.1.4 NMR MOF Digest experiments

The methodology of these experiments was adapted from A. Howarth *et al.*<sup>55</sup> The frameworks were pipetted into a vial and the excess mother liquor was wicked away with tissue to try and remove any residual non-coordinated linker present in the mother liquor. The “dry” framework weighed approximately 2 mg in the vial. 10 drops of DCI (20% w/w in D<sub>2</sub>O, 99.5%, purchased from Alfa Aesar) was added to the vial and sonicated for 10 minutes. An ampule of d6-DMSO is then added to the vial and sonicated further to dissolve any linker present. The mixture was then analysed by <sup>1</sup>H NMR.

### 3.5.1.5 Thermogravimetric analysis

Samples were washed with fresh DMF 3 times and dried overnight under vacuum at 150°C the previous day. TGA was performed using a PerkinElmer Pyris 1 thermogravimetric analyser. The samples were heated from 25°C to 600°C under a flow of air (20 ml min<sup>-1</sup>), using a heating rate of 10°C min<sup>-1</sup>.

### 3.5.1.6 Example of LK-1 and LK-2 synthesis (based on experiment 3a-13-a)

In a 20 mL pressure tube, 45 mg of linker **3a** was dissolved in 10 mL of a DMF:MeOH (1:1) mixture. 60 mg of Zn(NO<sub>3</sub>)<sub>2</sub>•6H<sub>2</sub>O was then fully dissolved into the mixture. 25 mg of 4,4'- biphenyl dicarboxylic acid was then dispersed throughout the solution by sonicating for 2 mins. The mixture was then heated to 100°C for 96 hours in an oil bath. LK-1 crystals appeared as square and pink, LK-2 crystals appeared as dark red with an ill-defined shape. Crystals were obtained for SCXRD analysis directly from the mother liquor after the mixture had cooled. Once the crystal has been acquired it was swiftly immersed in fomblin and put under a cool stream of N<sub>2</sub> (150K) before the crystals degraded.

### 3.5.1.7 Example of GG-1 synthesis (based on experiment 3a-16-a)

In a 5 mL Wheaton vial, 15 mg of linker **3a** was dissolved in 2.5 mL of DMF. 54 mg of  $\text{Zn}(\text{NO}_3)_2 \cdot 6\text{H}_2\text{O}$  was then dissolved in the mixture followed by 16 mg of DBTD. 0.3  $\mu\text{L}$  of HCl is then added to the solution and sonicated for 2 minutes. The solution is then heated to 80°C for 72 hours. The product formed as orange ellipsoid crystals.

### 3.5.1.8 Example of GG-32 synthesis (based on experiment 6b-21-a)

In a 5 mL Wheaton vial, 15 mg of linker **6b** was dissolved in 2.5 mL of DMF. 54 mg of  $\text{Zn}(\text{NO}_3)_2 \cdot 6\text{H}_2\text{O}$  was then dissolved in the mixture followed by 16 mg of DBTD. 0.5  $\mu\text{L}$  of HCl is then added to the solution and sonicated for 2 minutes. The solution is then heated to 80°C for 72 hours. The product formed as small, square, and pink crystals.

- 1 S. M. Moosavi, A. Chidambaram, L. Talirz, M. Haranczyk, K. C. Stylianou and B. Smit, *Nat. Commun.*, 2019, **10**, 539.
- 2 H. Li, M. Eddaoudi, M. O’Keeffe and O. M. Yaghi, *Nature*, 1999, **402**, 276–279.
- 3 S. Wang, Y. Chen, S. Wang, P. Li, C. A. Mirkin and O. K. Farha, *J. Am. Chem. Soc.*, 2019, **141**, 2215–2219.
- 4 S. Wang, M. Wahiduzzaman, L. Davis, A. Tissot, W. Shepard, J. Marrot, C. Martineau-Corcoss, D. Hamdane, G. Maurin, S. Devautour-Vinot and C. Serre, *Nat. Commun.*, 2018, **9**, 4937.
- 5 R. S. Forgan, R. A. Smaldone, J. J. Gassensmith, H. Furukawa, D. B. Cordes, Q. Li, C. E. Wilmer, Y. Y. Botros, R. Q. Snurr, A. M. Z. Slawin and J. F. Stoddart, *J. Am. Chem. Soc.*, 2012, **134**, 406–417.
- 6 T. Stolar and K. Užarević, *CrystEngComm*, 2020, **22**, 4511–4525.
- 7 J. Klinowski, F. A. Almeida Paz, P. Silva and J. Rocha, *Dalt. Trans.*, 2011, **40**, 321–330.
- 8 C. Vaitsis, G. Sourkouni and C. Argirusis, *Ultrason. Sonochem.*, 2019, **52**, 106–119.
- 9 J. Park, B. L. Suh and J. Kim, *J. Phys. Chem. C*, 2020, **124**, 13162–13167.
- 10 M. Bosch, S. Yuan, W. Rutledge and H.-C. Zhou, *Acc. Chem. Res.*, 2017, **50**, 857–865.
- 11 W. Lu, Z. Wei, Z.-Y. Gu, T.-F. Liu, J. Park, J. Park, J. Tian, M. Zhang, Q. Zhang, T. Gentle III, M. Bosch and H.-C. Zhou, *Chem. Soc. Rev.*, 2014, **43**, 5561–5593.
- 12 X.-F. Wang, Y. Wang, Y.-B. Zhang, W. Xue, J.-P. Zhang and X.-M. Chen, *Chem. Commun.*, 2012, **48**, 133–135.

- 13 X.-L. Luo, Z. Yin, M.-H. Zeng and M. Kurmoo, *Inorg. Chem. Front.*, 2016, **3**, 1208–1226.
- 14 S. Horike, S. Shimomura and S. Kitagawa, *Nat. Chem.*, 2009, **1**, 695–704.
- 15 Y.-N. Gong, D.-C. Zhong and T.-B. Lu, *CrystEngComm*, 2016, **18**, 2596–2606.
- 16 F.-X. Coudert, *Chem. Mater.*, 2015, **27**, 1905–1916.
- 17 A. M. Ullman, J. W. Brown, M. E. Foster, F. Léonard, K. Leong, V. Stavila and M. D. Allendorf, *Inorg. Chem.*, 2016, **55**, 7233–7249.
- 18 M. Allendorf, R. Medishetty and R. Fischer, *MRS Bull.*, 2016, **41**, 865–869.
- 19 L. Kortekaas and W. R. Browne, *Chem. Soc. Rev.*, 2019, **48**, 3406–3424.
- 20 N. L. Rosi, J. Eckert, M. Eddaoudi, D. T. Vodak, J. Kim, M. O’Keeffe and O. M. Yaghi, *Science (80-. )*, 2003, **300**, 1127 LP – 1129.
- 21 H. A. Schwartz, S. Olthof, D. Schaniel, K. Meerholz and U. Ruschewitz, *Inorg. Chem.*, 2017, **56**, 13100–13110.
- 22 W. Tian and J. Tian, *Dye. Pigment.*, 2014, **105**, 66–74.
- 23 D. E. Williams, C. R. Martin, E. A. Dolgoplova, A. Swifton, D. C. Godfrey, O. A. Ejegbavwo, P. J. Pellechia, M. D. Smith and N. B. Shustova, *J. Am. Chem. Soc.*, 2018, **140**, 7611–7622.
- 24 M. Shivanna, Q.-Y. Yang, A. Bajpai, E. Patyk-Kazmierczak and M. J. Zaworotko, *Nat. Commun.*, 2018, **9**, 3080.
- 25 L. R. Redfern and O. K. Farha, *Chem. Sci.*, 2019, **10**, 10666–10679.
- 26 S. Øien-Ødegaard, G. C. Shearer, D. S. Wragg and K. P. Lillerud, *Chem. Soc. Rev.*, 2017, **46**, 4867–4876.
- 27 R. Lyndon, K. Konstas, B. P. Ladewig, P. D. Southon, P. C. J. Kepert and M. R. Hill, *Angew. Chemie Int. Ed.*, 2013, **52**, 3695–3698.
- 28 H. L. Nguyen, T. T. Vu, D.-K. Nguyen, C. A. Trickett, T. L. H. Doan, C. S. Diercks, V. Q. Nguyen and K. E. Cordova, *Commun. Chem.*, 2018, **1**, 70.
- 29 A. Krężel and W. Maret, *Arch. Biochem. Biophys.*, 2016, **611**, 3–19.
- 30 I. H. Hwang, Y. D. Jo, H. Kim, K. B. Kim, K.-D. Jung, C. Kim, Y. Kim and S.-J. Kim, *Inorganica Chim. Acta*, 2013, **402**, 39–45.

- 31 M. Eddaoudi, J. Kim, N. Rosi, D. Vodak, J. Wachter, M. O’Keeffe and O. M. Yaghi, *Science* (80-), 2002, **295**, 469 LP – 472.
- 32 Q. Yao, J. Sun, K. Li, J. Su, M. V Peskov and X. Zou, *Dalt. Trans.*, 2012, **41**, 3953–3955.
- 33 N. Klein, I. Senkovska, I. A. Baburin, R. Grünker, U. Stoeck, M. Schlichtenmayer, B. Streppel, U. Mueller, S. Leoni, M. Hirscher and S. Kaskel, *Chem. – A Eur. J.*, 2011, **17**, 13007–13016.
- 34 D.-S. Zhou, F.-K. Wang, S.-Y. Yang, Z.-X. Xie and R.-B. Huang, *CrystEngComm*, 2009, **11**, 2548–2554.
- 35 Z. Hulvey, J. D. Furman, S. A. Turner, M. Tang and A. K. Cheetham, *Cryst. Growth Des.*, 2010, **10**, 2041–2043.
- 36 Z.-J. Lin, J. Lü, M. Hong and R. Cao, *Chem. Soc. Rev.*, 2014, **43**, 5867–5895.
- 37 S. Yuan, L. Feng, K. Wang, J. Pang, M. Bosch, C. Lollar, Y. Sun, J. Qin, X. Yang, P. Zhang, Q. Wang, L. Zou, Y. Zhang, L. Zhang, Y. Fang, J. Li and H.-C. Zhou, *Adv. Mater.*, 2018, **30**, 1704303.
- 38 I. Shimizu, Y. Morimoto, D. Faltermeier, M. Kerscher, S. Paria, T. Abe, H. Sugimoto, N. Fujieda, K. Asano, T. Suzuki, P. Comba and S. Itoh, *Inorg. Chem.*, 2017, **56**, 9634–9645.
- 39 O. Benson, I. da Silva, S. P. Argent, R. Cabot, M. Savage, H. G. W. Godfrey, Y. Yan, S. F. Parker, P. Manuel, M. J. Lennox, T. Mitra, T. L. Easun, W. Lewis, A. J. Blake, E. Besley, S. Yang and M. Schröder, *J. Am. Chem. Soc.*, 2016, **138**, 14828–14831.
- 40 O. K. Farha, C. D. Malliakas, M. G. Kanatzidis and J. T. Hupp, *J. Am. Chem. Soc.*, 2010, **132**, 950–952.
- 41 G. Beobide, O. Castillo, A. Luque, U. García-Couceiro, J. P. García-Terán and P. Román, *Dalt. Trans.*, 2007, 2669–2680.
- 42 J. D. Humby, O. Benson, G. L. Smith, S. P. Argent, I. da Silva, Y. Cheng, S. Rudić, P. Manuel, M. D. Frogley, G. Cinque, L. K. Saunders, I. J. Vitorica-Yrezabal, G. F. S. Whitehead, T. L. Easun, W. Lewis, A. J. Blake, A. J. Ramirez-Cuesta, S. Yang and M. Schröder, *Chem. Sci.*, 2019, **10**, 1098–1106.
- 43 J. Ye, H. Xu, X. Li and Z. Xu, *Inorg. Chem. Commun.*, 2016, **66**, 36–40.
- 44 I. Thomas-Hillman, A. Laybourn, C. Dodds and S. W. Kingman, *J. Mater. Chem. A*, 2018, **6**, 11564–11581.
- 45 A. Laybourn, J. Katrib, R. S. Ferrari-John, C. G. Morris, S. Yang, O. Udoudo, T. L. Easun, C.



- Dodds, N. R. Champness, S. W. Kingman and M. Schröder, *J. Mater. Chem. A*, 2017, **5**, 7333–7338.
- 46 G. Yuan, K.-Z. Shao, X.-L. Wang, Y.-Q. Lan, Y.-H. Zhao and Z.-M. Su, *Inorg. Chem. Commun.*, 2008, **11**, 1246–1249.
- 47 J. Ding, C. Yin, K. Li, B. Li and B. Wu, *Chinese J. Chem.*, 2014, **32**, 626–630.
- 48 A.-L. Cheng, Y. Ma, Q. Sun and E.-Q. Gao, *CrystEngComm*, 2011, **13**, 2721–2726.
- 49 C. T. Kniess, ed. J. C. de Lima, IntechOpen, Rijeka, 2012, p. Ch. 14.
- 50 I. A. Lázaro, *Eur. J. Inorg. Chem.*, 2020, **2020**, 4284–4294.
- 51 S. Mendiratta, M. Usman, C.-C. Chang, Y.-C. Lee, J.-W. Chen, M.-K. Wu, Y.-C. Lin, C.-P. Hsu and K.-L. Lu, *J. Mater. Chem. C*, 2017, **5**, 1508–1513.
- 52 K. A. McDonald, N. Ko, K. Noh, J. C. Bennion, J. Kim and A. J. Matzger, *Chem. Commun.*, 2017, **53**, 7808–7811.
- 53 J. E. Mondloch, M. J. Katz, N. Planas, D. Semrouni, L. Gagliardi, J. T. Hupp and O. K. Farha, *Chem. Commun.*, 2014, **50**, 8944–8946.
- 54 M. Sanchez-Lozano, C. M. Estévez, J. Hermida-Ramón and L. Serrano-Andres, *J. Phys. Chem. A*, 2011, **115**, 9128–9138.
- 55 A. J. Howarth, A. W. Peters, N. A. Vermeulen, T. C. Wang, J. T. Hupp and O. K. Farha, *Chem. Mater.*, 2017, **29**, 26–39.
- 56 J. Zhou, Y. Li, Y. Tang, F. Zhao, X. Song and E. Li, *J. Photochem. Photobiol. A Chem.*, 1995, **90**, 117–123.
- 57 C. J. Wohl and D. Kuciauskas, *J. Phys. Chem. B*, 2005, **109**, 22186–22191.
- 58 O. K. Farha, K. L. Mulfort and J. T. Hupp, *Inorg. Chem.*, 2008, **47**, 10223–10225.
- 59 M. Ding, X. Cai and H.-L. Jiang, *Chem. Sci.*, 2019, **10**, 10209–10230.
- 60 CrysAlisPro, Agilent Technologies, Version 1.171.37.33 (release 27-03-2014 CrysAlis171 .NET).
- 61 O. V Dolomanov, L. J. Bourhis, R. J. Gildea, J. A. K. Howard and H. Puschmann, *J. Appl. Crystallogr.*, 2009, **42**, 339–341.
- 62 G. M. Sheldrick, *Acta Crystallogr. Sect. A*, 2015, **71**, 3–8.

- 63 G. M. Sheldrick, *Acta Crystallogr. Sect. A*, 2008, **64**, 112–122.
- 64 G. M. Sheldrick, *Acta Crystallogr. Sect. C*, 2015, **71**, 3–8.
- 65 P. Van Der Sluis and A. L. Spek, *Acta Crystallogr. Sect. A*, 1990, **46**, 194–201.
- 66 P. Kubelka and F. Munk, *Zeitschrift für Tech. Phys.*, 1931, **12**, 593–601.

## Chapter 4. Microwave dielectric studies of metal organic frameworks in chromatographic separation

### 4.1 Introduction

#### 4.1.1 Separation in MOFs

In industry, molecular separations occur through the design of materials with specifically sized windows and channels that allow only appropriately sized/shaped molecules to pass through. The effectiveness of these materials is heavily dependent on the ability to tune and customise these materials.

The current industry standard for most separative processes are zeolites.<sup>1</sup> There are currently 232 reported zeolite structures (2020).<sup>2</sup> This is quite a small number when compared to the 70,000 MOF structures deposited in the Cambridge Structural Database (2017).<sup>3</sup> Demonstrating the vastly greater potential for customisability of MOFs compared to zeolites, it stands to reason that they will one day replace a lot of zeolite processes as the materials can be more specifically designed. For MOFs can not only tune the pore windows/channel sizes more precisely, but they can also be customised with some extra-functionality such as photoactivity which we have discussed in the previous chapters in great detail. High profile separations<sup>4</sup> that MOFs have potential to be used include the following: hydrocarbons<sup>5</sup>, uranium extraction<sup>6</sup>, water purification<sup>7</sup>, flue gas<sup>8</sup> and xylenes<sup>9</sup>.

These separations can occur through more than just simple size exclusion, analytes can preferentially bind to the framework through interactions such as Lewis acid-base pairs (open metal sites<sup>10</sup>), Brønsted acid sites<sup>11</sup>, hydrogen bonding<sup>12</sup>, dipole-quadrupole<sup>13</sup> or  $\pi$ - $\pi$  stacking<sup>14</sup>. There are a number of ways to characterise these interactions in the MOFs, which have varying levels of success and difficulty. If a certain interaction is already theorised to present during a separation, then techniques such as titration or gas sorption can be used.<sup>11</sup> If you are lucky enough to have access to resources such as a Single Crystal X-Ray Diffractometer<sup>15</sup> or an NMR spectrometer capable of solid state analysis<sup>16</sup>, then you can get in-depth information of the interactions present this way. Fewer still are the techniques that allow for real-time analysis of what goes on in a MOF during the separation process (gas adsorption crystallography<sup>17</sup>, synchrotron infra-red spectroscopy<sup>18</sup>, nuclear magnetic resonance pulse-field gradient diffusion<sup>19</sup>). It is apparent that there is a need for a cheap, non-invasive analytical technique that can provide detailed, real-time data.

We have developed a new measurement approach using microwave cavity perturbation, yielding an *in-situ* non-invasive method of analysis. The development of this new approach is described in this chapter.

#### 4.1.2 Fundamentals of dielectric properties

$$\epsilon = \epsilon_r \epsilon_0$$

*Equation 3 The absolute permittivity ( $\epsilon$ ) of a dielectric is found by multiplying the dimensionless quantity: relative permittivity ( $\epsilon_r$ ) by the vacuum permittivity:  $8.8541878128 \times 10^{-12} \text{ Fm}^{-1}$  ( $\epsilon_0$ ).*

The absolute permittivity of a substance is its ability to store and dissipate electrical energy when in an applied electric field. It is conventional to describe dielectric studies using the relative permittivity and ignore the absolute permittivity, and as such we shall simply be referring to  $\epsilon_r$  as  $\epsilon$  henceforth.<sup>20</sup> The relative permittivity is a complex quantity that refers to the ability for the material to store and dissipate electrical energy in an applied electric field (see Equation 4). When a dielectric material is placed in an applied electric field, the molecules will align to form a dipole that opposes the applied field. This polarisation effect is described by the real term  $\epsilon'$  and refers to the materials ability to store electromagnetic energy. The energy lost during this process is referred to as  $\epsilon''$ , also known as the “dielectric loss” of a material.<sup>21</sup> The simplest example of a contributor to  $\epsilon''$  is energy lost as heat.

$$\epsilon^* = \epsilon' - j\epsilon''$$

*Equation 4 The complex permittivity ( $\epsilon^*$ ) has two parts. The real part ( $\epsilon'$ ) and the imaginary part ( $\epsilon''$ ). Conventionally, in electrical engineering the imaginary number: square root of -1 is referred to as “j”.*



*Figure 90 Dipoles (left) aligning when an electric field is applied (right). Image from “A guide to characterisation of dielectric materials at RF and microwave frequencies”.*<sup>20</sup>

There are four possible mechanisms that can generate dielectric loss; electrical conduction (free movement of charge carriers (electrons, holes and ions) under the influence of an electric field typical of conductive materials), dielectric relaxation (this is the main source of loss that will apply to our materials, discussed further below), dielectric resonance (an umbrella term that describes phenomena specific to low pressure gases, composite materials and pure inorganic crystals), and loss from non-linear processes (e.g. ferromagnetic and ferroelectric hysteresis loops when varying frequency). As we are focusing on the passage of liquids through metal organic frameworks, the main mechanism of loss is dielectric relaxation.<sup>20</sup>

#### 4.1.2.1.1 Dielectric relaxation

At frequencies far below the relaxation frequency, molecular dipoles will respond to an applied field almost entirely in phase and very little energy is lost, giving a situation similar to that illustrated in Figure 90. At frequencies much higher than the relaxation frequency, the dipoles are unable to respond to the rapidly alternating field at all, thus  $\epsilon'$  and  $\epsilon''$  drop to almost zero. When the applied frequency is close to the relaxation frequency of the material, the dipoles struggle to keep up with the field thus the polarisation aspect is reduced and the lag produces thermal vibrations (e.g. friction) that manifest as a high  $\epsilon''$ . The effects of dielectric relaxation on the  $\epsilon'$  and  $\epsilon''$  is illustrated in Figure 91.

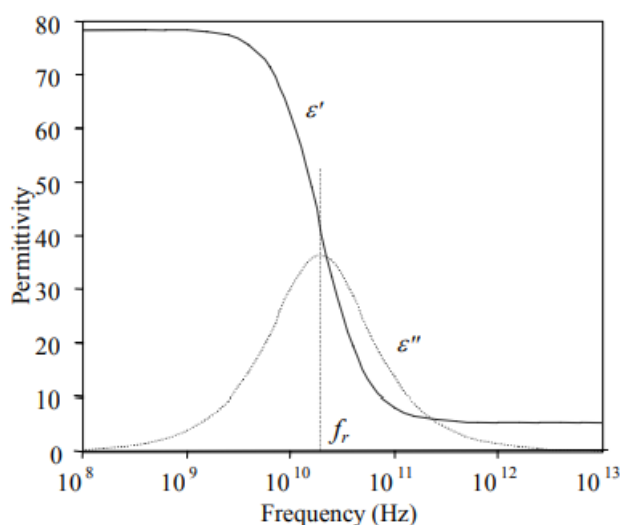


Figure 91 A Debye relaxation response for deionised water. At low frequencies, the  $\epsilon'$  is high and then begins to drop when it nears the relaxation frequency ( $f_r$ ). The  $\epsilon''$  shows a Gaussian response, reaching a peak at  $f_r$ .

#### 4.1.3 Microwave Cavity Perturbation method

The cavity perturbation method was first established by Bethe and Schwinger in 1943 by deriving the solutions of some of Maxwell's equations.<sup>22</sup> Since then, it has been used to study the properties of carbon nanotubes<sup>23</sup>, nanodiamonds<sup>24</sup>, plastics<sup>25</sup> and explosives<sup>26</sup>. More advanced studies have studied the in-depth interactions involved in gas storage in various materials.<sup>27,28</sup> It is quite common knowledge that MOFs have a huge potential when it comes to storage, hence our interest in this method.

A resonant cavity is a volume enclosed by metal walls that supports an electromagnetic oscillation. The microwave cavity perturbation method is a non-invasive technique that can measure the dielectric properties of a material. A sample with a small volume, such that the overall change in geometrical configuration of the electromagnetic field is small, is inserted into a microwave cavity and the small changes in the electromagnetic field (resonant frequency and bandwidth) are measured.<sup>29</sup>

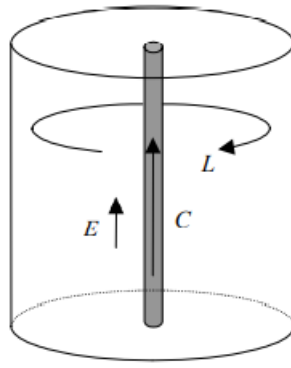


Figure 92 TM010 mode cavity, image adapted from Cannel Youngs.<sup>20</sup>  $L$  represents the inductance of the magnetic field,  $E$  is the electric field and  $C$  is the capacitance of the sample being analysed. The cavities typically resonate between 1-10 GHz. For the cavity we use in our studies, the TM010 mode resonates at 2.5 GHz.

At different resonant frequencies in a cavity, different field patterns are produced which manifest as certain areas of the cavity having zero magnetic and/or electrical contributions. These field patterns are referred to as “modes” and we will be exploiting only two of these modes for our purposes. The TM<sub>m</sub>10 mode series, represent a number of modes where there is maximal electric field contribution but zero magnetic contribution, the TM010 mode has the lowest frequency and is the mode used in this study. We have not discussed the magnetic parameter ( $\mu$ ) that corresponds to the dielectric parameter ( $\epsilon$ ) as we will be using modes which exert a negligible magnetic field on the samples and therefore  $\mu$  can be disregarded entirely.<sup>30</sup> (See Figure 93)

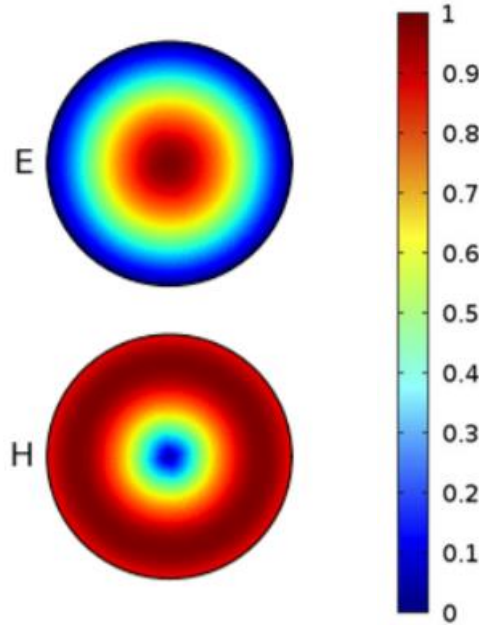


Figure 93 Electric field pattern (E) and magnetic field pattern (H) shown for TM<sub>010</sub> mode. In this mode, maximal electric field strength can be seen at the centre while there is zero magnetic field strength at the same location. This location is where we would insert our sample. Reproduced from thesis of Mike Barter.

A further advantage of the TM<sub>010</sub> mode is that the measurement equation is relatively simple.

$$\epsilon' = 1 - a \frac{\Delta f_r}{f} \cdot \frac{V_0}{V_s}$$

Equation 5 Derivation of permittivity for the TM<sub>010</sub> cavity.  $a$  is a constant that depends on the mode, for TM<sub>010</sub> this is 0.539.  $f_r$  is the resonant frequency,  $\Delta f_r$  is the change in resonant frequency upon introduction of the sample.  $V_0$  is the volume of the cavity and  $V_s$  is the volume of the sample.

$$\epsilon'' = b \cdot \frac{V_0}{V_s} \cdot \left( \frac{1}{Q_l} - \frac{1}{Q_0} \right)$$

Equation 6 Derivation of dielectric loss for the TM<sub>010</sub> cavity. The constant  $b$  is calculated via:  $b = a/2$ .  $Q_0$  is the unloaded Q-factor and  $Q_l$  is the loaded Q-factor with the sample inserted.<sup>20</sup>

The  $\epsilon'$  is computed from the change in resonant frequency. The Q-factor is a term that quantifies the rate of electromagnetic energy lost from the cavity which is design to store that energy.

#### 4.1.3.1 Microwave cavity perturbation in practice

The cavity has a span of frequencies swept at 1 mW, the transmitted power is then measured by the VNA and is expressed as insertion loss. Upon insertion of a sample into this cavity we observe a shift in both the resonant frequency and power transmission coefficient (see Figure 94).

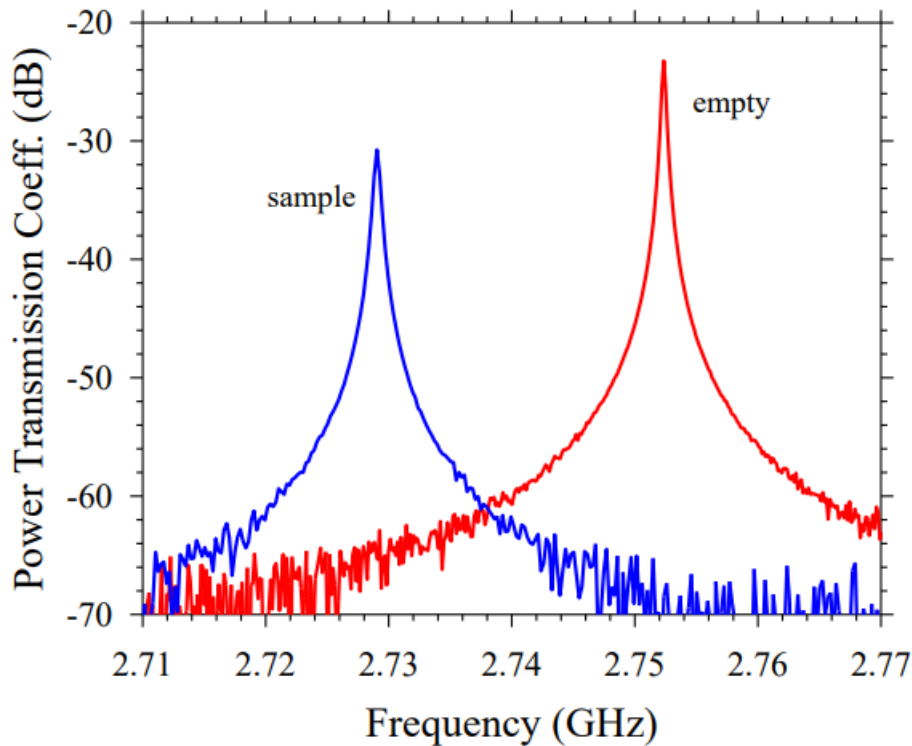


Figure 94 Resonant trace for an empty cavity (red) compared to when a sample is inserted (blue). Upon sample insertion the frequency is reduced due to polarisation ( $\epsilon'$ ) and the bandwidth increases due to dielectric loss ( $\epsilon''$ ). Figure provided by Professor Adrian Porch.

The change in frequency is relatively simple to calculate as we can see the peak maximum shift towards a lower frequency upon sample insertion, in this example its  $\approx 0.02$  GHz. We know from Equation 5 this is enough to determine the  $\epsilon'$  of the sample. We can obtain the Q factor from the Lorentzian fit of the resonant peak, providing the FWHM of the peak or 3-dB (bandwidth). The Q factor is then calculated via Equation 7. The VNA will compute the value via a more complex and precise method for calculating this value (the insertion loss method)<sup>20</sup>, but for this example this approximation will suffice. Both the Q factor and the bandwidth can be used to describe the  $\epsilon''$  parameter (according to Equation 6), in this work we will be using the bandwidth parameter.

$$Q = \frac{f}{BW}$$

Equation 7 Simplified relationship between quality factor (Q), frequency (f) and bandwidth (BW).

A simplified way of interpreting the data is to work on the basis that  $F \propto \epsilon'$  and  $BW \propto \epsilon''$ . All of our interpretations will focus on frequency or bandwidth over time (see Figure 95),  $\Delta F$  and  $\Delta BW$  will be referring to the initial frequency minus the frequency recorded at the end of the measurement. We



will therefore not be directly calculating the  $\epsilon'$  and  $\epsilon''$  for each sample, instead comparison of the shifts in frequency and bandwidth are sufficient to effectively describe the contents of each sample.

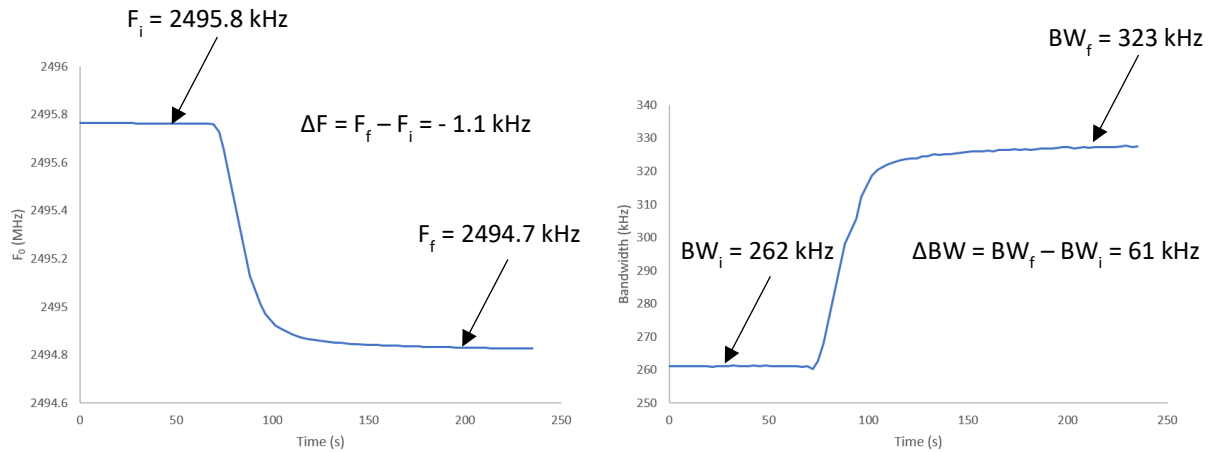


Figure 95 Worked examples of the data acquired and how we interpret it. Frequency over time (left) and Bandwidth over time (right).

#### 4.1.4 Temperature Correction

Temperature changes in the environment are an issue for microwave cavity perturbation. The resonant frequency will change due to thermal expansion and the temperature-dependent conductivity of the metal cavity, and the sample can also affect this through radiative heat transfer to the cavity.<sup>31</sup> If we do not account for changes in ambient temperature then it will directly affect the accuracy of our measurements. As we discussed above, we perform all our measurements with the TM010 mode as it just measures the sample region, but in order to monitor temperature effects we need a mode that is completely unaffected by the sample and only interacts with the changes in the resonant frequency caused by fluctuations in the environmental temperature. TM310 is such a mode, as it measures in the periphery of the cavity (see Figure 96) allowing for the *in-situ* monitoring and correction for temperature effects.

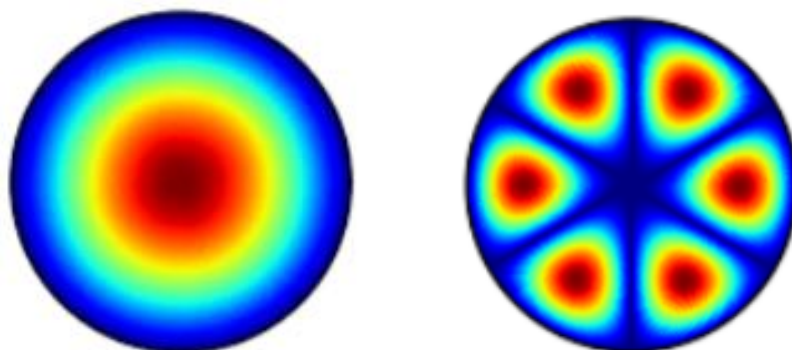


Figure 96 Electronic field patterns of TM010 mode (left) and TM310 (right). Reproduced from thesis of Mike Barter.

Using TM010 as the measurement mode and TM310 as the reference mode, the frequency shift with temperature can be defined as seen in Equation 8

$$\frac{\Delta f_{010}(T)}{f_{010}(0)} \approx \frac{\Delta f_k(T)}{f_k(0)} - (a_c + k_{010})\Delta T + k_{err}(T)$$

$$\frac{\Delta f_{310}(T)}{f_{310}(0)} \approx -(a_c + k_{310})\Delta T + k_{err}(T)$$

Equation 8 describing the relationship between frequency shift and temperature.  $f_k$  is the fraction frequency shift caused by perturbation from the sample.  $k_{010}$  and  $k_{310}$  are the differences in gradient of the thermal expansion coefficient of the cavity material in the respective mode.  $k_{err}$  is the systematic thermal expansion error in the experiment.

We remove the fractional frequency shift caused by changes in temperature by applying Equation 8 as we do in Equation 9.

$$\frac{\Delta f_{010}(T)}{f_{010}(0)} - \frac{\Delta f_{310}(T)}{f_{310}(0)} \approx \frac{\Delta f_k(T)}{f_k(0)} - (k_{010} - k_{310})\Delta T$$

Equation 9 subtracts the 310 component from the 010 component of Equation 8 to remove the fractional frequency shift term caused by changes in temperature.

Finally to account for the errors in the gradient we subtract the unperturbed state of the system over the same temperature range, as shown in Equation 10.<sup>31</sup>

$$\frac{\Delta f_s(T)}{f_s(0)} \approx \left[ \frac{\Delta f_{010,s}(T)}{f_{310,s}(0)} - \frac{\Delta f_{310,s}(T)}{f_{310,s}(0)} \right] - \left[ \frac{\Delta f_{010,u}(T)}{f_{310,u}(0)} - \frac{\Delta f_{310,u}(T)}{f_{310,u}(0)} \right]$$

Equation 10 is the equation used for temperature correction and is applied to all experimental data acquired using the microwave cavity perturbation method.  $u$  represents the unperturbed cavity and  $s$  is when the sample is present.

The necessity of this correction is demonstrated in Figure 97.

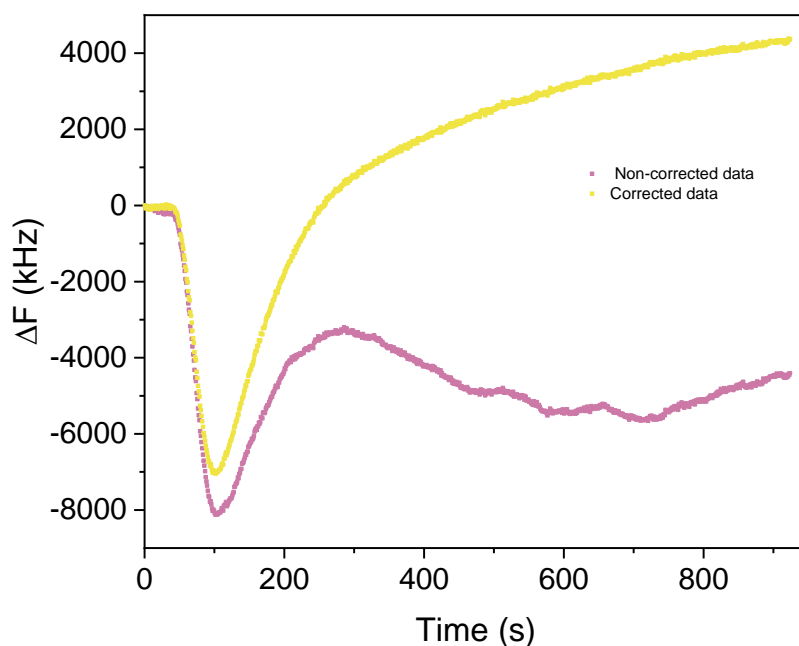


Figure 97 Comparison of data with and without the temperature correction.

Without the correction, the curve is not as smooth and shows the  $\Delta F_{\max}$  to be 1000 kHz greater than it should be. Without the knowledge that the effects are due to temperature, this data has seemingly random fluctuations.

In this work the series of control experiments were performed on all materials of interest, measuring each sample and its effect on the cavity. These data are included later, and they pertain to frameworks, solvents and analytes.

The first phase of our experiments were “static” measurements, where the analytes and materials were at rest and some values were obtained for comparison. The next phase introduces “dynamic” measurements, where the system is under a continuous flow of analyte, to see how the response under flow and to identify and solve any additional challenges provided by a flow system. The final phase involves the injection of small aliquots of analyte in a framework and tracking its progression through the material in real-time.

## 4.2 Aims

First, we implement a series of experiments that uses the microwave cavity perturbation technique to understand its scope and limitations. We then apply the microwave cavity perturbation technique to a flow system and optimise specific parameters that will allow for accurate and reliable data to be obtained regarding the separative capabilities of a MOF. Finally, we will be exploring the ability for this analytical technique to effectively characterise interactions between analytes and the

frameworks, to better understand the key factors which determine the successfulness of a molecular separation.

#### 4.2.1 Frameworks of interest

MIL-53(Al) and UiO-66 are both extensively reported in the literature, are both water stable frameworks and have both demonstrated the capacities for molecular separation under specific conditions. They are also both commercially available and hence can be produced at scale. For these reasons they make excellent test subjects for the method development in this chapter. The MIL-53 (Al) used in this chapter was commercially sourced and the UiO-66 was synthesised in house (Full details of synthesis are in the experimental section)

##### 4.2.1.1 MIL-53 (Al)

The MIL (Materials Institute of Lavoisier) series involve the binding of trivalent cations ( $\text{Fe}^{3+}$ ,  $\text{V}^{3+}$ ,  $\text{Cr}^{3+}$ ) and some the P-block elements ( $\text{Al}^{3+}$ ,  $\text{Ga}^{3+}$ ,  $\text{In}^{3+}$ ) with carboxylate linkers. The MIL-53 frameworks in particular have been heavily studied with over a thousand reported publications within the last decade.<sup>32</sup> It is highly flexible and can change shape depending on the host-guest interaction, thus should heave easily observable changes by analysis.<sup>33</sup>

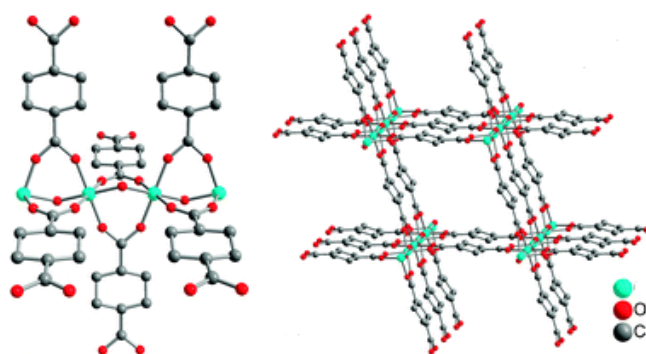


Figure 98 : MIL-53 (Al) secondary building unit (SBU) left, with octahedrally co-ordinated aluminium nodes with bridging oxygen atoms. Extended framework (right) shows how the SBUs are linked together, by the terephthalate linkers, to form a structure resembling a “wine rack”. Image reproduced from Janiak et al.<sup>33</sup>

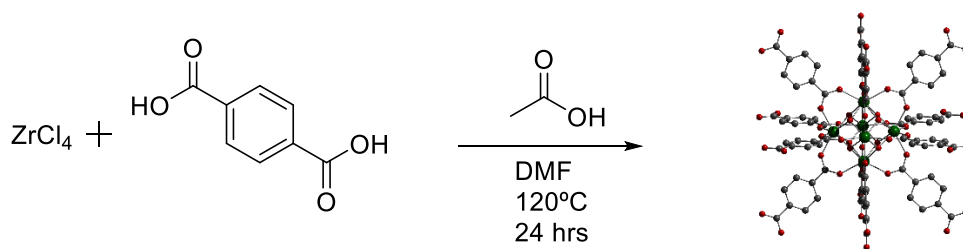
MIL-53 (Al) is a framework that is well studied in the scientific community and has a strong scientific knowledge base for separations which we can use in our studies. Nitrobenzene and its interactions with frameworks are currently being investigated by the wider research community to find the best material for extracting nitrobenzene out of aqueous media, due to its nature as a very toxic pollutant. MIL-53(Al) has an affinity for nitrobenzene due to charge transfer and  $\pi$ - $\pi$  stacking interactions with

the terephthalate linkers.<sup>34</sup> These  $\pi$ - $\pi$  stacking interactions also provide it with some affinity for other aromatics like toluene.<sup>35</sup> With a focus on molecules that have this aromatic functionality we can design an experiment that investigates the dielectric effects of these interactions on the material as a whole.

#### 4.2.1.2 UiO-66

The UiO (Universitetet i Oslo) series famed for its chemical and thermal stability in comparison with other MOFs, in particular the zirconium MOFs in this series.<sup>36</sup> UiO-66 is the archetypal framework of this series and has been heavily studied over the last decade, well-over a thousand papers have been published on this framework as the main topic.<sup>32</sup>

The SBUs consist of 6 zirconium ions in an octahedral arrangement, connected by four 3-fold bridging hydroxyl groups and four 3-fold bridging oxide groups which occupy alternating faces of the octahedron respectively to achieve the minimum repulsion between each other.<sup>37</sup>



*Scheme 1: Synthesis of UiO-66, reproduced from Schaate et al. The SBU is consists of six zirconium metal cations, linked together by bridging oxygen and hydroxy groups, which form an octahedron. Each octahedral node is linked together by the terephthalic acid linker.*

Studies involving this zirconium framework have been investigated in numerous separations<sup>38-40</sup>, typically applications regarding water purification, to take advantage of its water stability which is quite uncommon for a MOF.<sup>41</sup> As we are investigating analytes with aromatic features in MIL-53, it seemed suitable to also investigate processes involving aromatic analytes with this framework, fortunately studies utilising UiO-66 as the stationary phase in regarding key separations in the manufacture of xylene and styrene have been reported which will provide insight into our own studies.<sup>42,43</sup>

### 4.3 Results and Discussion

This chapter discusses the process of development of the analytical method. We started with experiments that tested the permittivity properties of the MOF and analytes as well as framework selection and moved onto doing experiments under flow conditions. The flow experiments enabled us to see how the dielectric properties were affected and establish certain experimental parameters

(e.g. flow rate, tube length etc). Finally testing the MOF under separation conditions allowed us to determine some physical properties and separation capabilities of the framework in question, developing a method of deconvoluting the raw data into a meaningful output. Full experimental details are in the Experimental section.

#### 4.3.1 Method Development part i) Static experiments

These experiments were done in the engineering department. This department was not equipped to handle the toxic fumes given off by the majority of our chosen analytes (especially nitrobenzene), therefore we ensured all samples were sealed completely. The methodology was to pack aluminium framework MIL-53 (Basolite® A100) into a quartz capillary tube, which was then loaded with the target analyte and sealed with either epoxy resin or nylon depending on the chosen analyte. The changes in frequency ( $\Delta f$ ) and bandwidth ( $\Delta BW$ ) of the packed tube in the microwave cavity compared with those of an empty quartz tube were then recorded. The selection of analytes were chosen to provide variation in polarity (e.g. nitrobenzene is very polar, toluene is considerably less polar but a similar shape) and sterics (e.g. hexane and biphenyl have similar polarities but very different shapes). Hexane also doubled as an excellent carrier solvent since it is not going to react with the frameworks or the analytes, is cheap and readily available and has a relatively weak interaction with microwaves. (See Table 24)

A key question in this analysis is the nature of the interactions between analytes and frameworks. Clearly it is important to understand if these interactions are host-guest or surface-only with respect to uptake of the analyte into the framework. In other words, does the analyte enter the pores of the chosen framework?

The kinetic diameter of hexane is reported as 4.3 Å and toluene is 5.85 Å. There is no reported data purporting to the kinetic diameter of biphenyl, 2,2' bipyridine or nitrobenzene, however we estimate their kinetic diameters to be similar to toluene, just as the kinetic diameter of *p*-xylene and toluene are reported to be identical.<sup>44,45</sup> The pore diameter of MIL-53 (Al) is 8.5 Å markedly bigger than the kinetic diameters of our analytes, and on that basis the analytes selected can physically enter the pores of the framework.<sup>46</sup> Nitrobenzene was chosen specifically as it has a reported affinity with the aromatic rings present on linkers such as terephthalic acid. The  $\pi$ - $\pi$  stacking interaction between the linkers and the nitrobenzene which is reported to be the cause of this affinity, is an ideal interaction to look for with this investigation.

Sample	$\Delta f$ (kHz)	$\Delta BW$ (kHz)	Anticipated $\Delta f$ range (kHz)
MIL-53	-2483.0	683.8	-
Hexane	-2015.0	5.3	-

Hexane MIL-53	-3994.7	445.7	-4498.0 – -2483.0
<b>2,2'-bipyridine</b>	-1804.4	5.4	-
2,2'-bipyridine in Hexane (0.1M)	-2975.1	1.7	-
2,2'-bipyridine MIL-53	-1368.6*	18.3	-4287.4 – -2483.0
2,2'-bipyridine in Hexane (0.1M) MIL-53	-3856.7	390.3	-5458.1 – -2483.0
<b>Biphenyl</b>	-1880.0	1.1	-
Biphenyl in Hexane (0.1M)	-2060.4	1.2	-
Biphenyl MIL-53	-1341.2*	15.7	-4363.0 – -2483.0
Biphenyl in Hexane (0.1M) MIL-53	-4003.5	392.2	-4543.4 – -2483.0
<b>Toluene</b>	-2662.1	68.8	-
Toluene in Hexane (0.1M) <sup>†</sup>	-2093.3	0.8	-
Toluene MIL-53 <sup>†</sup>	-3747.5	-83.7	-5145.1 – -2483.0
Toluene in Hexane (0.1M) MIL-53 <sup>†</sup>	-3256.2	14.1	-4576.3 – -2483.0
<b>Nitrobenzene</b>	-52314.4	75841.4	-
Nitrobenzene in Hexane (0.1M)	-2320.3	80.1	-
Nitrobenzene MIL-53 <sup>†</sup>	-23611.8	22490.5	-54797.4 – -2483.0
Nitrobenzene in Hexane (0.1M) MIL-53	-2619.6	149.8	-4803.3 – -2483.0

Table 24 Preliminary results from microwave resonance measurements of analytes loaded into MIL-53. Single components are outlined in bold. \* denotes the cases where the  $\Delta f$  lies outside the expected  $\Delta f$  range. † denotes experiments measured differently meaning the values are loosely comparable to the rest of the data, full explanation in experimental.

The preliminary results in Table 24 showed that in all cases on adding an additional component to any given system (e.g. adding MOF into the empty quartz capillary) there are changes in  $F_0$  and BW that were measurable. The analytes could therefore be detected in the cavity, the MOF and the MOF loaded with said analyte.

To address the question of host-guest interactions, we can consider how the analytes being taken up into a MOF change the measured dielectric properties. In the simplest case, with no strong interactions, we would anticipate that changes in  $F_0$  would simply be an additive combination of the individual component shifts from the empty tube values (BW is more complicated and cannot be predicted in this manner). Making the assumption that the maximum amount of analyte is the same as the control experiment without the MOF present and the minimum amount is zero (i.e. just the MOF). As it was not possible to determine precisely how much analyte is present in a sample filled with MIL-53, we can safely assume that it is between zero and the full amount. Therefore we set the limits of our range between MIL-53 by itself and the sum of MIL-53 and the component being tested. E.g. MIL-53 in hexane expected  $\Delta f$  range = -2483.0 (MIL-53) – -2483.0 -2015.0 (MIL-53  $\Delta f$  + Hexane  $\Delta f$ ) = -2483.0 – -4498.0 After taking into account these hypothetical extremes of minimum and maximum

filling, any values lying outside the range may indicate some kind of interaction between the framework and the analyte as there are no other immediately obvious contributing factors. There are two results that lie outside the expected  $\Delta f$  range (indicated by \* in Table 24), the biphenyl in MIL-53 and the 2,2' bipyridine in MIL-53, suggesting both the bipyridine and the biphenyl interact with the framework in some way to reduce the overall polarizability of the sample. The  $\Delta BW$  of 2,2'-bipyridine/biphenyl in hexane (0.1M) loaded into the MIL-53 were significantly larger than the individual parts, likely showing that the hexane helps facilitate the interaction of these analytes with the framework.

Although this was a positive sign that interactions between the analytes and the MIL-53 framework could be qualitatively observed, no further information could be easily derived such as how these interactions affected the guest selectivity of the framework or the order of magnitude of such interactions and how they compete with each other. In order to begin deconvoluting this data we needed to reduce any and all external factors as much as possible, such as the way we account for the influence of temperature (TM310 correction). A factor that is not so easily accounted for is a property inherent to certain frameworks, such as MIL-53: framework flexibility. The “breathing” behaviour that MIL-53 exhibits is well documented; the coordination of carboxylate molecules to the metal centres is not necessarily fixed and behaves more like a hinge. The framework can be envisaged as a “wine-rack” which collapses/ extends depending on the properties of the media it is present in, particularly if there is potential for hydrogen bonding between host and guest.<sup>47</sup>

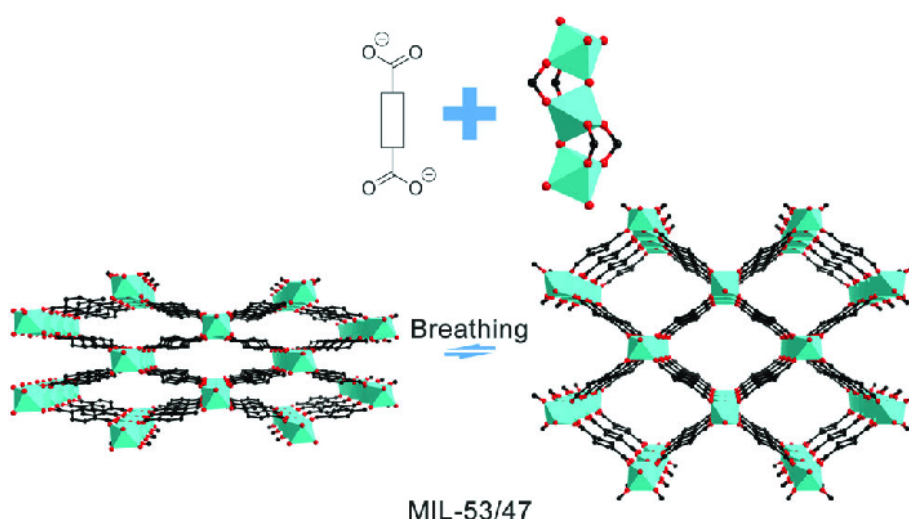


Figure 99 A demonstration of the “breathing” effect exhibited by MIL-53(Al) that can be triggered by guest adsorption, temperature or mechanical pressure. The arrow along the top demonstrates how pore volume is affected by this phenomenon. Figure reproduced from reference<sup>48</sup>.



Although we previously thought this would make the framework an ideal candidate, as we would see some very obvious changes. The dynamic properties of the framework thus naturally cause the polarity distribution in the bulk of the MOF to be variable under different environmental and chemical conditions (e.g. see Figure 99), which significantly complicates data interpretation since changes observed upon analyte loading cannot readily be deconvoluted from consequential framework structure changes. Therefore we changed our target framework to something more inflexible and structurally constant, the zirconium-based MOF, UiO-66.

The UiO-66 framework is not just unreactive to our analytes, it is renowned for showing extreme thermal, mechanical and chemical stability.<sup>37</sup> We have demonstrated with MIL-53(Al) that the static microwave method can distinguish between loaded and unloaded MOF/analyte mixtures and can provide some indicative discrimination between analytes. On changing the target framework to UiO-66 we decided to change analytes, as each MOF has unique separation capabilities for different species. The styrene separation is typically carried out in steam if using the method of dehydrogenating ethylbenzene. With our set up we thought it would be prudent to try something considerably less polar than water to see if our equipment could still obtain reasonable data, therefore we tried methanol.

Sample	$\Delta f$ (kHz)	$\Delta BW$ (kHz)	Expected $\Delta f$ range (kHz)
<b>UiO-66</b>	-1482.6	4.8	-
<b>Hexane</b>	-2015.0	5.3	-
Hexane UiO-66	-1540.4	12.0	-3497.6 – -1482.6
<b>Methanol</b>	-37773.4	79070.7	-
Methanol UiO-66	-5099.7	1986.8	-39256.0 – -1482.6
<b>Toluene</b>	-2662.1	68.8	-
Toluene UiO-66	-8084.6*	2756.2	-4144.7 – -1482.6
<b><i>o</i>-Xylene</b>	-3391.1	189.4	-
<i>o</i> -Xylene UiO-66	-9274.9*	3482.6	-4873.7 – -1482.6
<b><i>m</i>-Xylene</b>	-3075.5	63.3	-
<i>m</i> -Xylene UiO-66	-9114.7*	3251.5	-4558.1 – -1482.6
<b><i>p</i>-Xylene</b>	-2874.0	13.6	-
<i>p</i> -Xylene UiO-66	-6726.3*	2435.8	-4356.6 – -1482.6
<b>Ethylbenzene</b>	-2954.6	122.9	-
Ethylbenzene UiO-66	-8376.1*	2981.0	-4437.2 – -1482.6
<b>Styrene</b>	-3074.8	21.6	-

Styrene UiO-66	-8126.1*	2657.6	-4557.4 – -1482.6
----------------	----------	--------	-------------------

Table 25 Preliminary results from microwave resonance measurements of analytes loaded into UiO-66. Single components are outlined in bold. \* denotes the cases where the  $\Delta f$  lies outside the expected  $\Delta f$  range.

A comparison of UiO-66 and MIL-53(Al) shows immediately that the  $\Delta f$  and  $\Delta BW$  for UiO-66 versus the empty tube are both significantly smaller than the same values for MIL-53(Al). This has the added advantages that smaller changes to these values on addition of analytes will be more readily observed. Table 25 shows  $\Delta f$  and  $\Delta BW$  for UiO-66 with a range of analytes. Target molecules with an aryl functionality provide  $\Delta f$  values consistently outside the expected ranges. This may be an indication of the  $\pi$ - $\pi$  stacking interaction discussed earlier. Our findings with MIL-53 only demonstrated biphenyl and 2,2 bipyridine demonstrating this phenomenon. As we mentioned earlier, the literature reports MIL-53 has these interactions with all sorts of aromatic moieties such as toluene and therefore the MIL-53 framework's dynamic motion must be masking these interactions in the data. As these interactions are of a key interest, this demonstrates that UiO-66 is a more suitable framework for this experiment.

Methanol was too polar for our equipment to provide reasonable results, causing significantly higher values for  $\Delta f$  and  $\Delta BW$ , similar to that of nitrobenzene. Another issue is that the data suggests a significant interaction between UiO-66 and methanol, of a similar magnitude to those observed with our target analytes (xylenes, styrene etc.). This potential interaction between methanol and UiO-66 indicates that methanol may outcompete some of the analytes or make the interactions between the analytes and the framework harder to detect. These factors all suggest methanol would function very poorly as a carrier solvent and water is likely to be far worse. Hexane, however, has a far weaker interaction with the framework and therefore would be a much more suited to this purpose. In previous work done by Zhiming Yan *et al.*<sup>49</sup> hexane is used as the mobile phase successfully.

The static experiments were a good starting point, however there are several factors affecting the reliability of these results. An important factor was that each of the samples that involved being packed with MOF powder could not be packed the same. The particles synthesised do not have a uniform size distribution and we simply do not have the means to pack every tube exactly the same. Each sample will vary in the gaps between particles due to different sizes and orientations, this is further complicated by the fact different shapes will have different depolarisation factors. Two samples that we prepare with the same material and analyte will still produce different absolute F and BW signals.<sup>50</sup> Another issue is that our goal of achieving an *in-situ* method of analysis could not be met with simply measuring a framework loaded with solvent. An *in-situ* representation of molecular separation required the system to resemble a set-up you would find in the field of chromatography. Both these issues can be solved by designing the equipment to allow for readings to be taken under

flow. Packing is less of an issue in flow with multiple experiments and flow is better as analogue of chromatography and real-world usage

#### 4.3.2 Method Development part ii) Flow experiments

To have a system under flow, it had to be set up in a fumehood equipped to deal with the hazards that it presented. The VNA model used so far (ref static experiments) although extremely accurate, was not a viable option in a chemistry lab, so we had to use a more portable VNA and accept a trade off in accuracy. (See Figure 100 for set up)

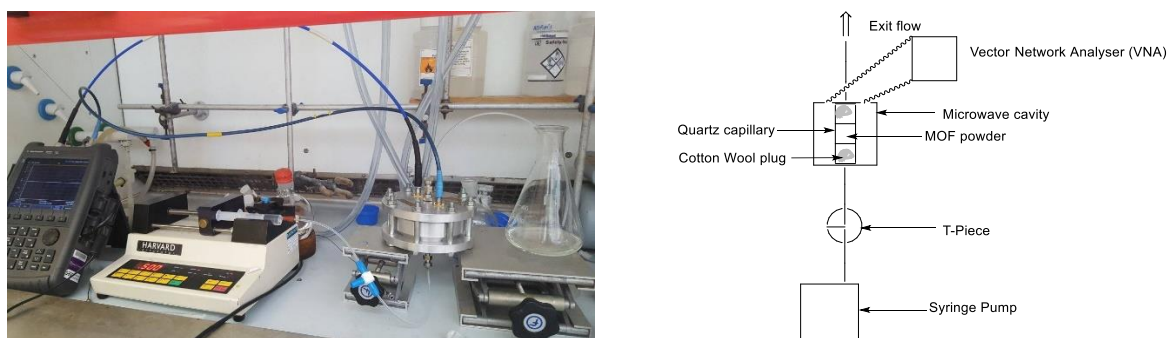


Figure 100: Image of set up used to monitor the dielectric properties of UiO-66 under flow. (left) Diagram of the setup. (right) The quartz capillary is packed with the UiO-66 framework and inserted into the microwave cavity, the syringe pump then injects the analyte through the capillary at a steady rate which the VNA then records any change in the electric field being applied by the microwave cavity.

The new set up had a T-piece to allow for the release of air bubbles which would surely interfere with the packing of the MOF powder, although the continuous flow of analytes through the MOF bed will cause some disturbance which is unavoidable, the disparity in density between liquid and air would cause much greater disruption. The flow system was set so that the solvent would travel up the column to help push out any residual air that was not removed by the T-piece. By using the same microwave cavity that was used in the static experiments, the previous results will still be comparable to the readings obtained in this set up.

The static experiments helped determine factors such as analyte and framework choice and provided familiarity with the limitations of the microwave perturbation technique. There are however a few more variables to be accounted for by changing our static system to a flow system. Thus the next step was to run some preliminary testing in order to ascertain what information we could obtain from monitoring *in-situ* and also uncover any experimental issues.

One such parameter that needed to be determined was the appropriate flow rate. According to Peristyy *et al.*, UiO-66 has improved separation with slower flow rates as this gives the analytes more time to enter the pores and therefore increases retention time. Faster flow rates result in the analytes

just passing by the MOFs and travelling through the extrinsic void space left between particles.<sup>51</sup> In order to explore this we measured the flow-rate dependent changes over time in  $\Delta F$  and  $\Delta BW$  when flowing toluene through a capillary containing UiO-66 pre-loaded with hexane; the freshly toluene loaded capillary was then flushed with hexane to measure the reverse process. Figure 101 shows these changes at four separate flow rates. Both the data for  $\Delta F$  and  $\Delta BW$  have been included, however the  $\Delta BW$  data seems to just mirror the  $\Delta F$  data and no extra information can be ascertained. With this being the case, further discussion will focus on the  $\Delta F$  data.

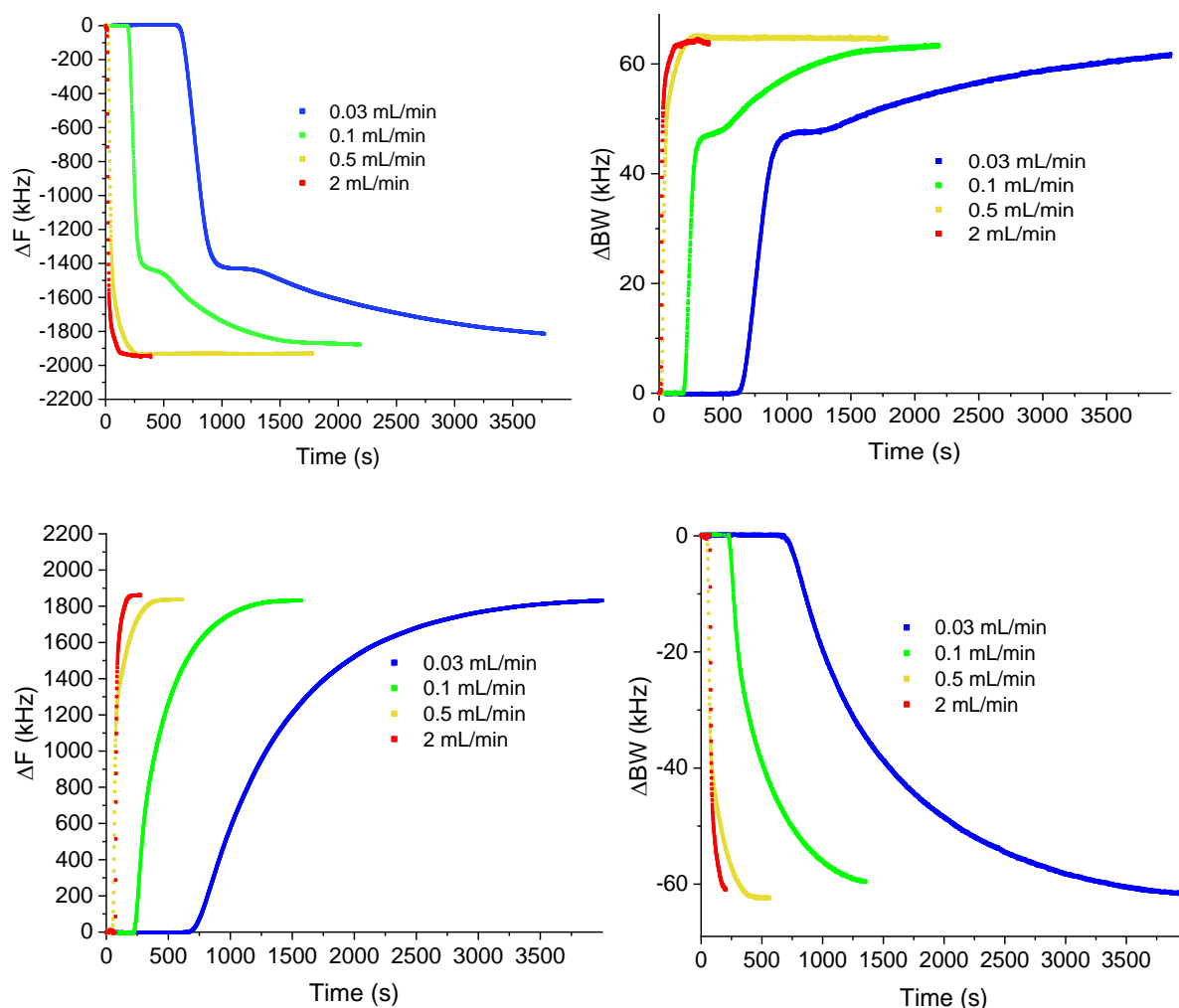


Figure 101 Top: Change of  $\Delta f$  (left) and  $\Delta BW$  (right) over time of UiO-66 preloaded with hexane being flushed out with a continuous flow of toluene at various rates. Bottom: Change of  $\Delta f$  (left) and  $\Delta BW$  (right) over time of UiO-66 loaded with toluene being flushed out with a continuous flow of hexane at various rates.

It is immediately obvious that at all flow rates that toluene displaces hexane from UiO-66 faster than hexane displaces toluene. Two other features of note; there is a small step in the curve present only for when toluene is displacing hexane from the framework but not for the reverse process; some of the runs do not have the same end point. With respect to the end points, *Peristyy's* paper suggested

that lower flow rates result in greater exposure time for the analytes to the pore windows therefore increasing the likelihood of analyte entering the pores of the framework. On that basis, we would expect that the lower flow rates would reach the end point sooner but with a shallow and unstepped curve, while higher flow rates would show fast initial change representing extrinsic solvent change and then a second shallower gradient to a later end point as solvent within the framework exchanges. We do not see this behaviour as the flow rate changes.

However, these changes in curve shape are observed when comparing the lower flow rates for hexane displacing toluene versus toluene displacing hexane. There are 2 possible reasons for this. Firstly the MOF may have a strong preference for hexane over toluene, or secondly there is some mixing effect based on the order of displacement. To investigate this we performed the experiment with an empty tube. (Figure 102)

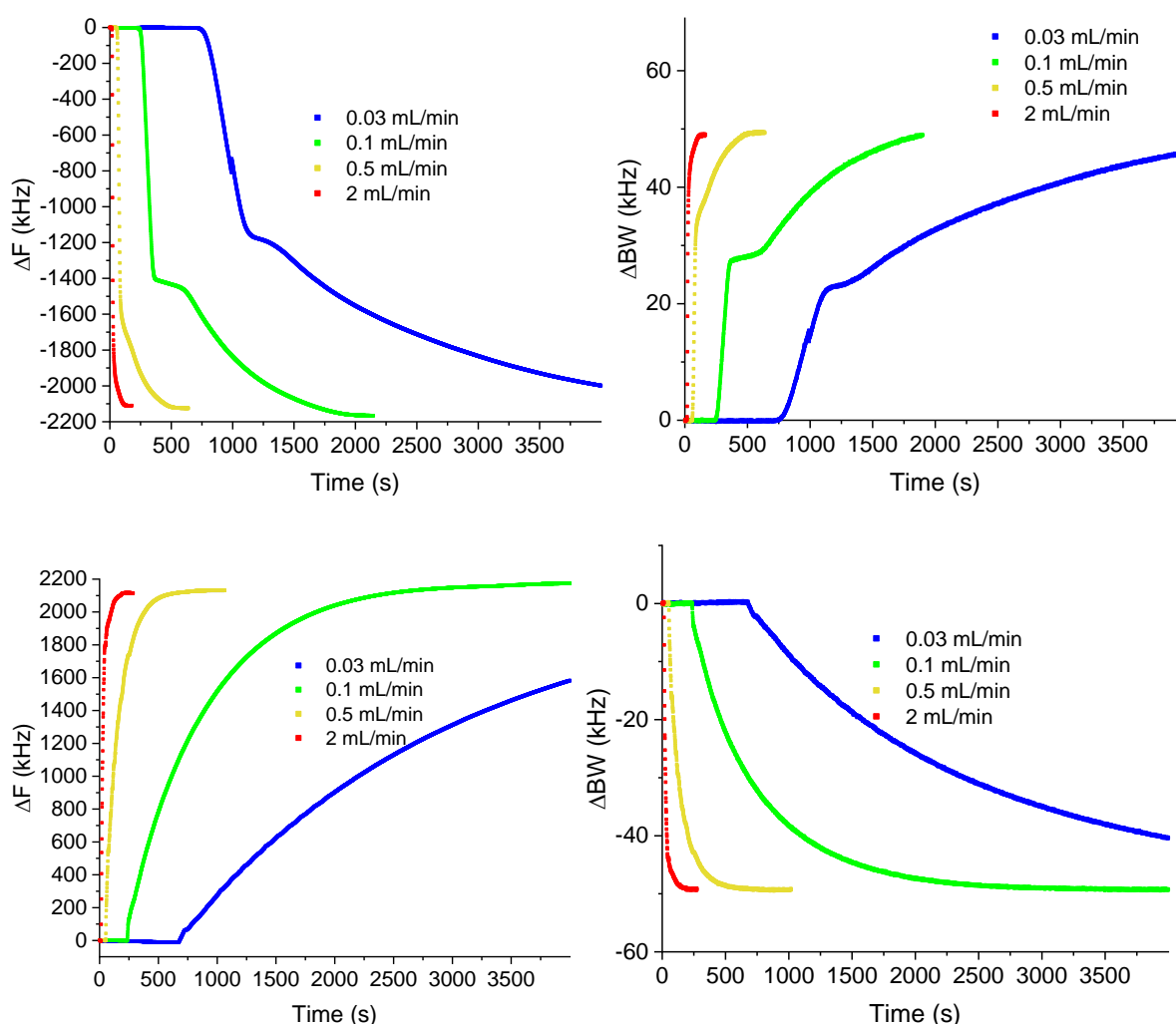


Figure 102 Top: Change of  $\Delta f$  (left) and  $\Delta BW$  (right) over time as a tube loaded with hexane (no MOF) is flushed out with toluene. Bottom: Change of  $\Delta f$  (left) and  $\Delta BW$  (right) over time as a tube loaded with toluene is flushed out with hexane.

Notably, the MOF experiments were all done on the same sample and the control experiments were all done on a single empty tube so in each case we would expect (within reason) the same available volume for analytes to fill which should be illustrated by the same final  $\Delta F$  and  $\Delta BW$ . The final  $\Delta F$  and  $\Delta BW$  values are not all the same, with the slower flow rates clearly not reaching their final points.

With the empty tube control experiments the same curve shape phenomena occurred as in the UiO-66 experiment therefore indicating the cause is something more fundamental to flow chemistry (See Figure 102) rather than a feature of the framework. As we saw earlier from our static experiments (see Table 25), toluene is more polarising and has higher values for  $\epsilon'$  and  $\epsilon''$ . Therefore the first step could be the introduction of toluene, polarising the hexane and hence having an initially greater effect at a small concentration. The second step is simply the rest of the hexane being replaced by toluene. This effect is negligible at flow rates  $\geq 0.5$  mL/min therefore suggesting 0.5 mL/min is an appropriate flow rate for future experiments.

Furthermore, these experiments show that the gradient delay time ( $t_D = V_D$  (dwell volume)/ $F$  (flow rate)), is much greater at lower flow rates, which gives greater time for the analytes to mix with each other before reaching the framework. Gradient delay time can be defined as a time period between the moment when the gradient is formed and the moment when it reaches the column.<sup>52</sup> To confirm that the dwell volume is the cause, further experiments were done where the "dwell tube" was varied from its original length (237 mm) and the flow rate was fixed at 0.5 mL/min.

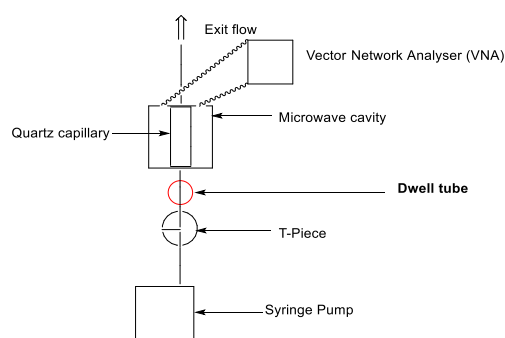


Figure 103 Setup demonstrating the location of the "dwell tube"

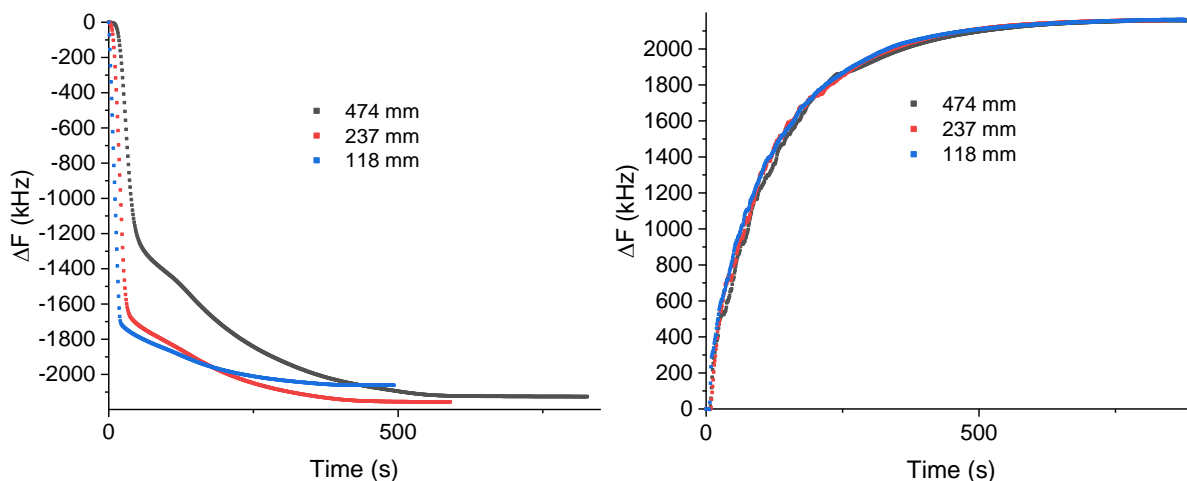


Figure 104 Left: Toluene displacing hexane from a quartz tube, with different sizes of dwell tube. Right: Hexane displacing a quartz tube filled with toluene, with different sizes of dwell tube.

Figure 104 shows that when toluene is displacing hexane from a quartz tube, the “step” in the curve is much reduced when the dwell tube is halved to 118 mm. Interestingly, when doubling the size of the dwell tube (474 mm) the step is exaggerated which further indicates that this step is caused by solvent mixing in the dwell volume. When hexane is displacing toluene, we can clearly see this solvent mixing effect is not present regardless of dwell volume. There is a slight discrepancy when toluene is displacing hexane, as the  $\Delta F$  value is different for 118 mm compared to the other lengths. Due to the sensitive nature of the cavity perturbation technique, this is most likely caused by a slight displacement of the tube within the cavity. In subsequent experiments we used plastic spacers to minimise these effects. We can conclude that reducing the tube length is a solution to the hexane/toluene mixing problem. 118 mm is the minimum dwell tube length that is achievable, so all further experiments were done with this tube length. As the dwell “volume” issue is solved, for all further data in this chapter we have removed the data corresponding to the time taken for the analyte to reach the cavity, the zero time value is set to when the analyte is first detected to enter the sample.

The next experiment was to investigate the effect of using a significantly more polar analyte. We therefore compared the displacement of hexane by toluene with displacement of hexane by mixtures of chlorobenzene and toluene. Figure 105 shows  $\Delta F$  for UiO-66 preloaded with hexane when the solvent is changed to either toluene or a 1:1 or 1:9 mixture of chlorobenzene:toluene. (Pure chlorobenzene had large  $\epsilon'$  and  $\epsilon''$  values causing the overall permittivity to be reduced too much to provide any meaningful data, see Figure 91)

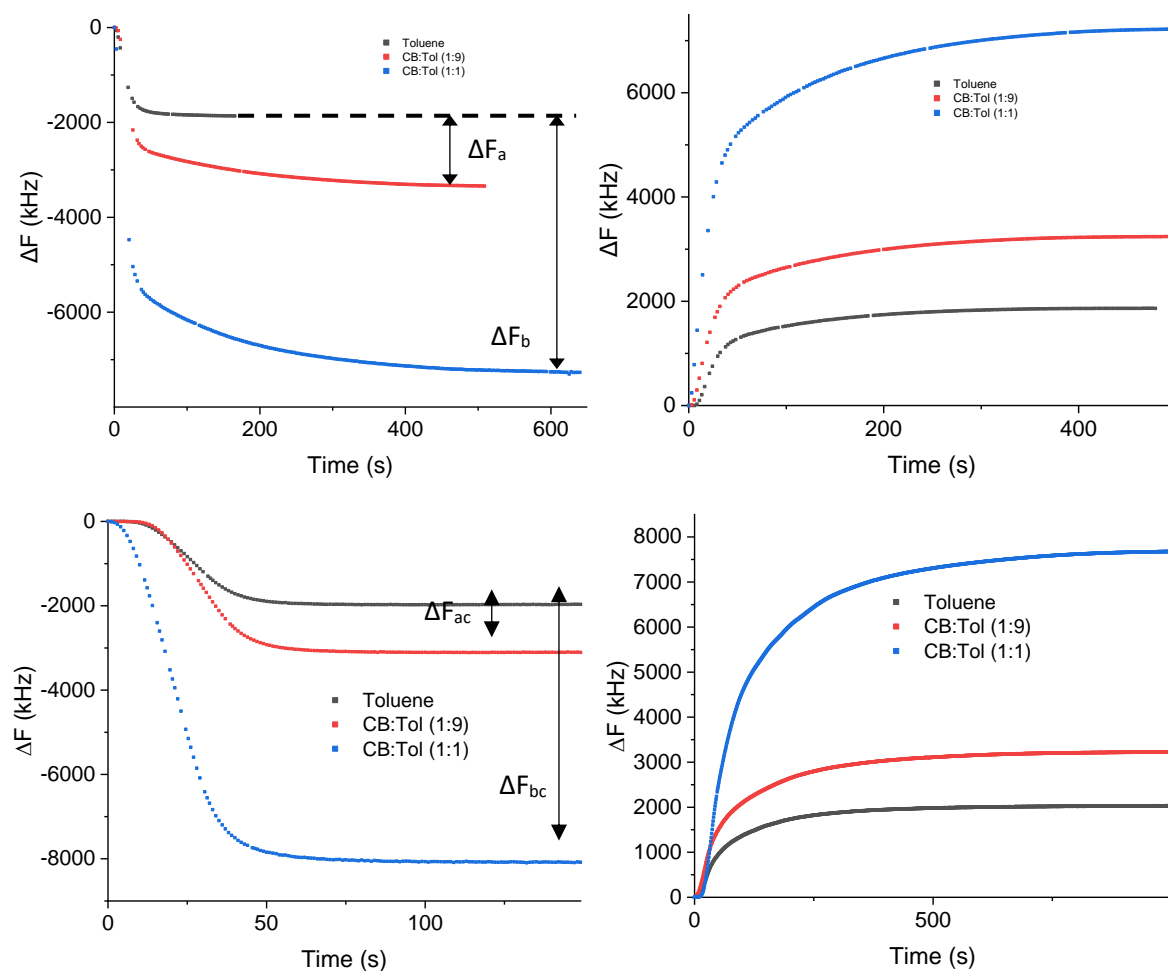


Figure 105 Top Left: Toluene/toluene:chlorobenzene mixture displacing hexane from UiO-66 Top Right: Hexane displacing toluene/toluene:chlorobenzene mixture from UiO-66. Bottom left: Control experiment, toluene/toluene:chlorobenzene mixture displacing hexane from sample tube. Bottom right: Control experiment, hexane displacing toluene/toluene:chlorobenzene mixture from sample tube.

Figure 105 shows that the curves are not stepped and therefore there is no indication of a solvent mixing problem. As chlorobenzene is the most polar analyte we use in this setup and no solvent polarisation effect is observed the experimental changes in previous experiments have successfully removed this issue for this and subsequent experiments. We observed that flushing the hexane loaded sample tube reached completion (curve reached a plateau) for the control experiment ( $\approx 50$  s) faster, than the experiments with UiO-66 (200+ s) this is a good sign that the analytes are being absorbed into the framework and not simply flowing through the interstitial voids. When the toluene/toluene:CB mixture loaded sample is flushed with hexane, the control experiment and the UiO-66 experiment are quite similar. Its possible that the density of the toluene and chlorobenzene (0.87 g mL and 1.11 g mL, respectively) made it more difficult for hexane (0.66 g mL) to flush the column. This is further supported by the fact the amount of chlorobenzene present in the mixture, directly correlated to how long the sample took to flush in the control experiment.



In this experiment, we would expect that on reducing the concentration of chlorobenzene by a fifth  $\Delta F$  would also reduce by a fifth. The control experiment demonstrates the validity of this expectation,  $\Delta F_{ac} / \Delta F_{bc} = 0.18$  (see Figure 105). What we observe when these mixtures are flown through the UiO-66 powder is  $\Delta F_a / \Delta F_b = 0.27$ . There are two possible phenomena this could be an indicator of. There is a significant selectivity preference for chlorobenzene over toluene in this framework or there is a significantly more polarising interaction between chlorobenzene and the framework compared to toluene, these possibilities are not mutually exclusive. *Yan et al.* observed that there was a selectivity preference for chlorobenzene over the xylenes due to chlorobenzene's potential for hydrogen bonding.<sup>49</sup>

In summary; we have designed a flow system that can monitor separative capabilities of UiO-66 *in-situ*. We have minimised the solvent mixing effect via appropriate choice of flow rate and reducing the dwell volume. We have also tested the limits of cavity and determined the set up should be suitable to test all the components of the styrene separation as chlorobenzene is far more polar than any of the components involved in the styrene separation.

The equipment's capabilities in a flow set up was proven, the next step was to create an experiment that allowed to determine, quantitatively, the separability of the target MOF. The absolute  $\Delta F$  does provide a rough approximation of how much of the analyte has been taken up by the MOF, but other factors such as the polarity of the analyte. Also it was not possible to tell how much of the analyte was entering the pores of the MOF and how much was simply travelling between the MOF particles, through the interstitial voids.<sup>51</sup>

#### 4.3.3 Method Development part iii) Aliquot experiments

In order to make our system more representative of a chromatographic separation we made an important modification to our approach: we injected a known, small quantity of analyte into a continuously flowed hexane carrier solvent and tracked its progress through the apparatus. By keeping the quantity small, we were increasing the chance of being taken up by the pores, as we have already established that UiO-66 has a preference for aromatic solvents instead of hexane, therefore the analyte has significantly less competition for occupying pore space.

Molecule	Kinetic Diameter (Å)
<i>o</i> -xylene	6.80
<i>m</i> -xylene	6.80
<i>p</i> -xylene	5.85
Hexane	4.30

Toluene	5.85
---------	------

Table 26 Kinetic diameters of *o*, *m*, *p*-xylene isomers, hexane and toluene.<sup>44</sup>

There are two types of pore windows in UiO-66, sized at 6 Å and 4 Å. The kinetic diameter is used to describe the chances of a gas molecule to collide with another gas molecule, therefore it is not ideally suited to describing the ability of the molecules to enter through the pores of a framework and does not account for the general flexibility in MOFs that accommodate adsorbates. For example, *H. Hu et al.* demonstrate that the larger acetone molecule (4.6 Å) is preferentially adsorbed into their etb-type framework over the smaller, more polar methanol molecule (3.6 Å). They concluded that the polarity of the analyte dictated the conformation of the MOF where the pore aperture could vary between 2.5-5.2 Å.<sup>53</sup> We use it as a rough approximation and there is precedent to do so based on the research of other groups.<sup>49,54</sup>

Based on the findings of previous research groups, UiO-66 is supposed to affect the retention times of *o*-xylene significantly while the separation between *m*-xylene and *p*-xylene is poor. During this analysis, we will first check to see if our analysis corroborates with what has already established in the literature, we shall then look at any new information that this analysis may provide.

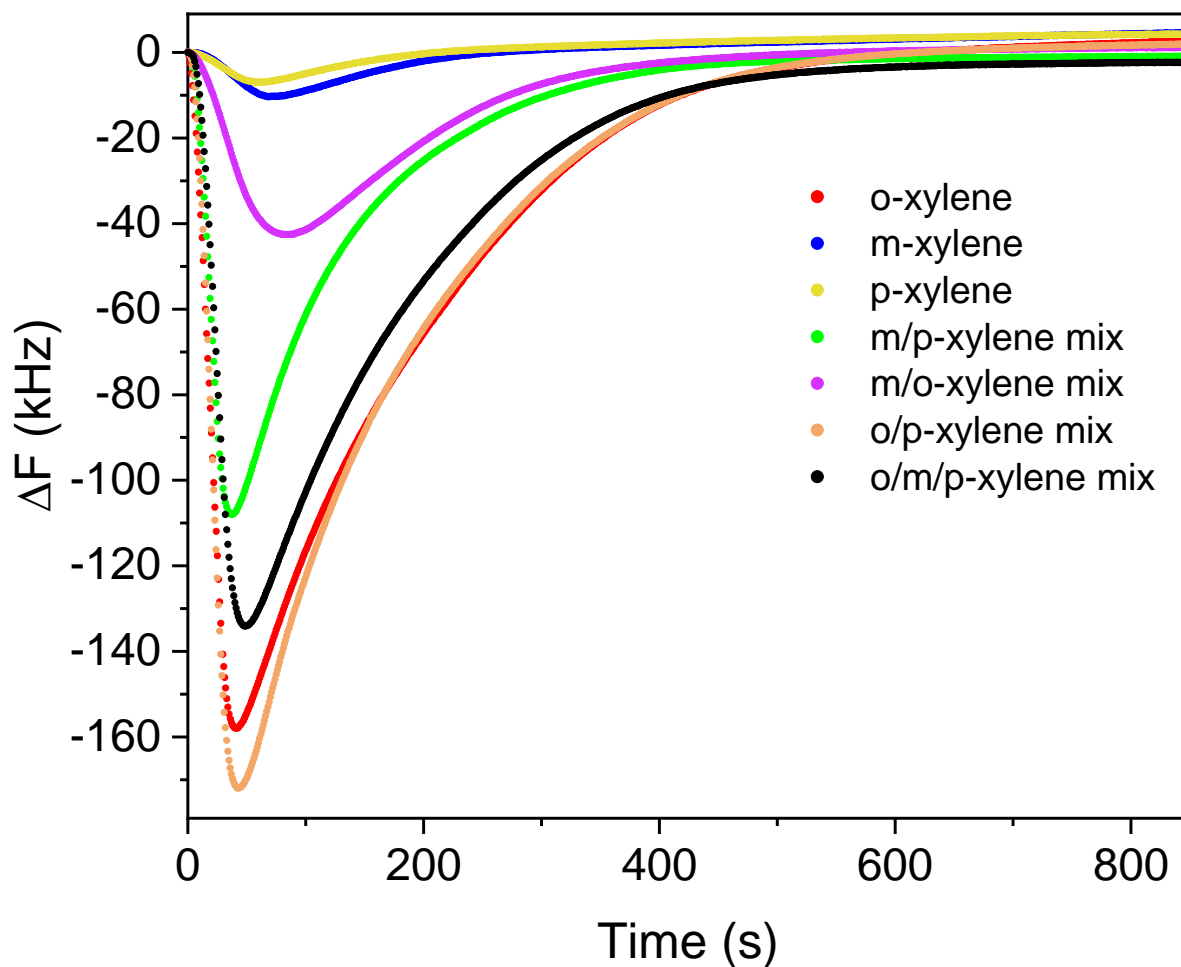


Figure 106 Tracking  $\Delta F$  over time after injecting 0.1 mL of a specified aliquot into a continuous flow of hexane passed through a column of UiO-66.

We can see immediately that the mixtures including *o*-xylene take longer to reach the end point. We can see that *m*-xylene's retention time is slightly longer than *p*-xylene. These findings correlate with the respective retention times reported by Yan *et al.*<sup>49</sup> The *m/p*-xylene mixture also had a longer retention time than its individual components. This suggests that in the case of *o*-xylene mixtures the rate limiting step is the *o*-xylene passing through the framework while in the case of the *p/m*-xylene mixture the rate limiting factor is the competition for passing through the pore windows. The maximum  $\Delta F$  values ( $\Delta F_{\max}$ ) for the individual components are as we would expect:  $o > m > p$  as it correlates to the relative strength of the dipoles. The  $\Delta F_{\max}$  values for the mixtures however are less intuitive, as the mixture of *m/p*-xylene has a greater  $\Delta F_{\max}$  value than *o*-xylene and the *o/m*-xylene mixture. As we do not fully understand what dictates the magnitude of  $\Delta F_{\max}$  we are instead looking at what time this occurs and also the end point of the separation (when the curve reaches a plateau). Also due to the amount of uncertainty in this measurement, it required another, more well-known and established technique to help with the interpretation of our results. In this case we also collected

fractions from the runoff of each experiment to be analysed via NMR to monitor the relative concentrations of the analytes.

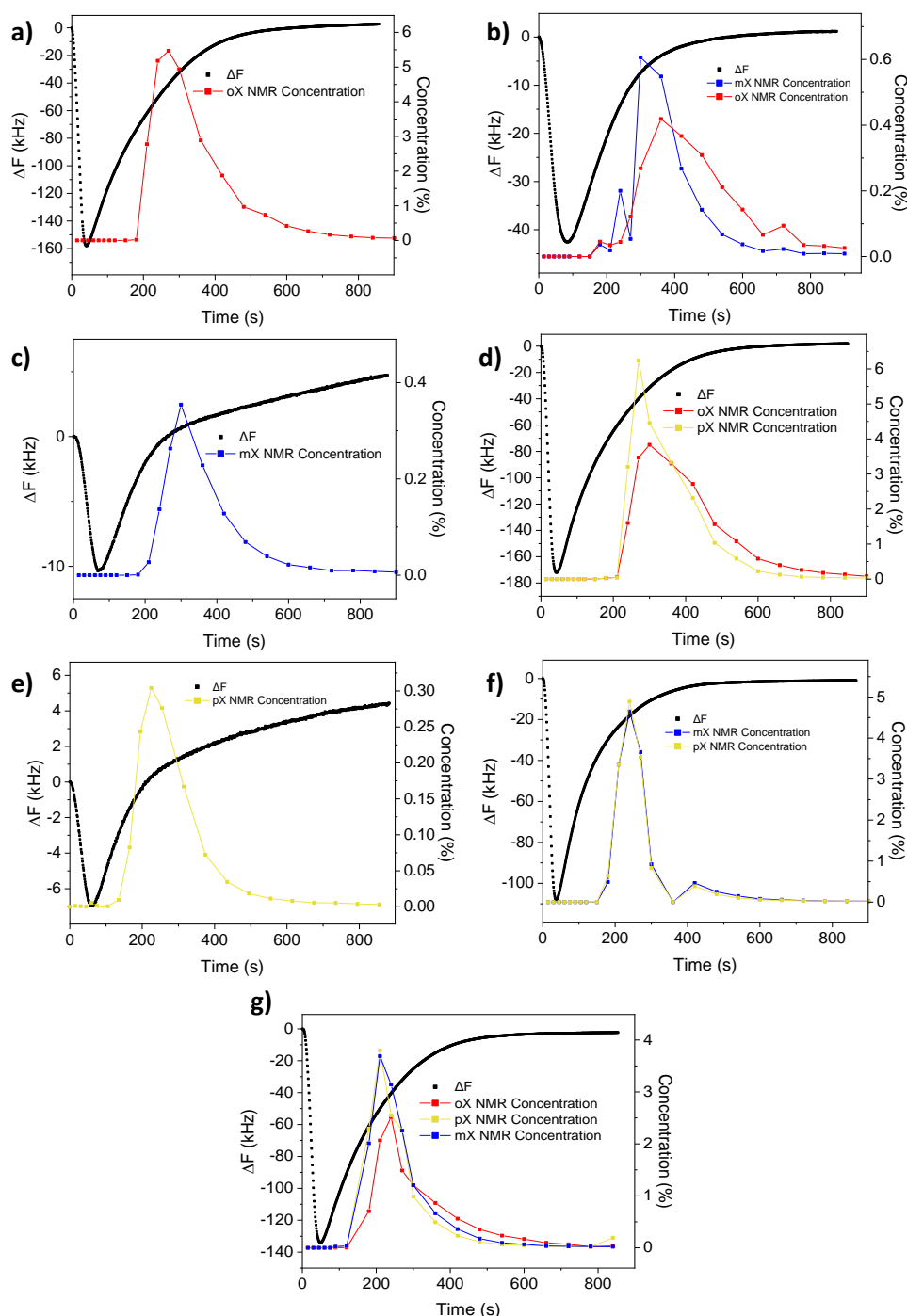


Figure 107  $\Delta F$  over time as well as the % concentration determined by NMR for xylene isomers and mixtures. Y axis is scaled individually to help show the information present. Analytes injected were 33% concentration mixtures of 0.1 mL aliquots. a) o-xylene b) m/o-xylene c) m-xylene d) o/p-xylene e) p-xylene f) m/p-xylene g) o/p/m-xylene.

Figure 107 shows a direct comparison of the time-dependent microwave and NMR measurements of the xylene isomers and various mixtures as they flow through and out of the column (respectively).

One immediate issue presented by NMR analysis is the values of concentration from experiment to experiment, despite all samples having the same amount of analyte injected, the recorded maximum concentration varies from 0.3-6%. The error seems to be systematic as the NMR curve shapes look genuine, starts at zero, reaches a maximal peak and then reduces. Although we are not sure what is the cause of this issue, we trust the curve shapes and shall base our conclusions on the shapes of the curves rather than the magnitudes for now.

The shapes of the curves shown by NMR are mostly what we would expect. As we mentioned earlier, we have set time zero to be when the analyte is first detected in the microwave cavity, the NMR samples are collected in the run off after it has travelled through the column of UiO-66, this creates a time lag of  $\approx 200$  seconds between the microwave cavity and the NMR timings. The *o*-xylene's rate of transport seems to be slowed by travelling through the UiO-66, demonstrated by broader and shallower peaks compared to that of *m*-xylene and *p*-xylene. The NMR technique fails to identify some subtleties that the microwave perturbation analysis was able to provide indicators for. According to NMR, the UiO-66 does not seem to show any preference for *m*-xylene or *p*-xylene (**f**) and **g**) according to the NMR experiment but as we identified earlier, the microwave experiment shown that *p*-xylene passed through slightly quicker than *m*-xylene which corroborates with the literature. The lack of microwave sensitivity of *m/p*-xylene is demonstrated with smaller  $\Delta F_{\max}$  values ( $< 10\text{kHz}$ ) and the baseline drift makes determining end points more difficult. The other (non-xylene) components involved in the styrene separation as well as chlorobenzene were also ran through the equipment (see Figure 108).

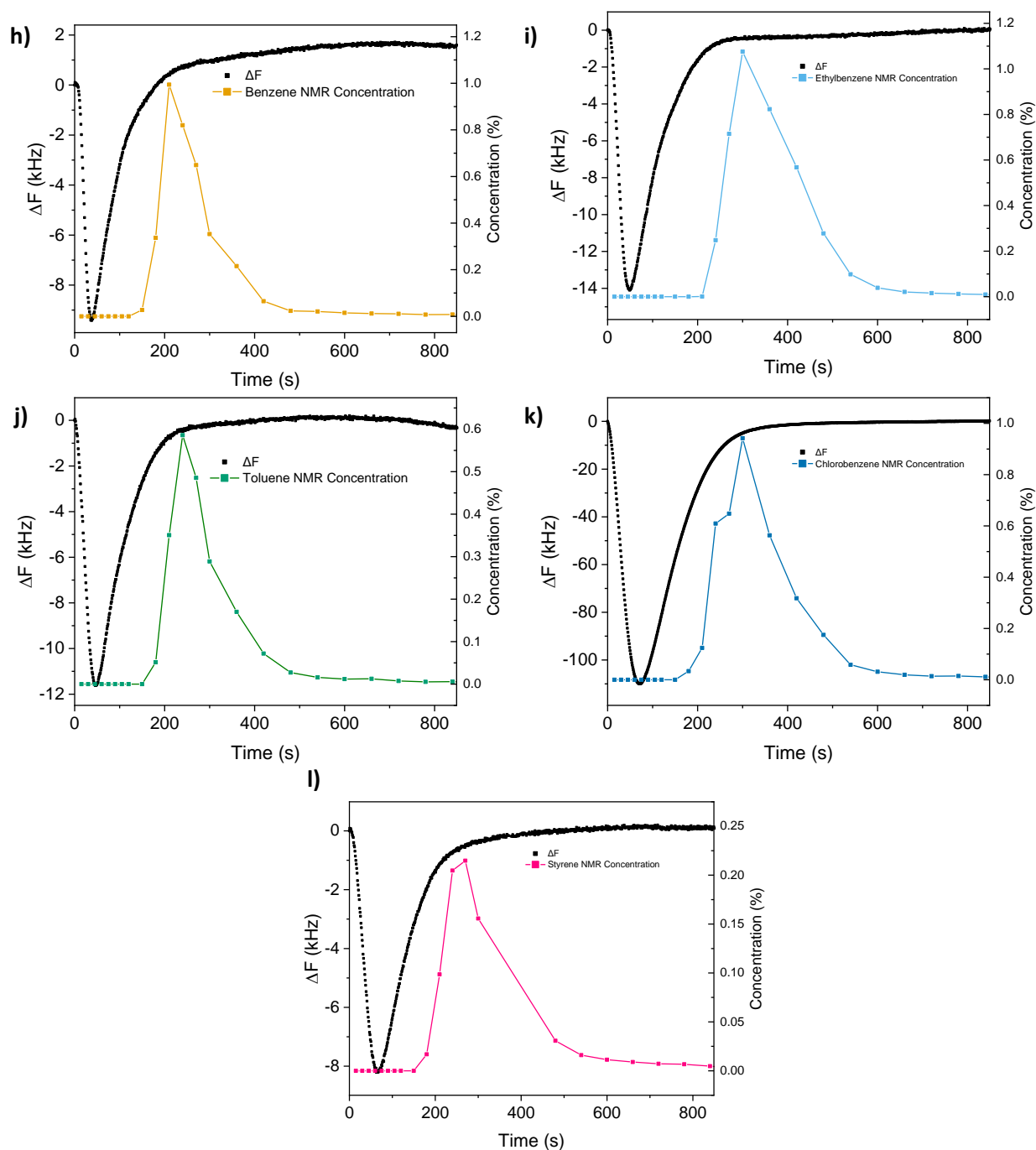


Figure 108  $\Delta F$  over time as well as the % concentration determined by NMR: h) Benzene i) Ethylbenzene j) Toluene k) Chlorobenzene l) Styrene. Y axis is scaled individually to help show the information present. Analytes injected were 33% concentration mixtures of 0.1 mL aliquots.

These experiments were run on the same column of UiO-66 therefore allow for direct comparison with the xylene samples, therefore we have tabulated our results. In all cases, we were unable to determine an end point with NMR as trace amounts of the analyte were still able to be analysed after 840 seconds. Though we continued to flush the sample with hexane for a further 15 minutes per sample (flow rate = 0.5 mL/min), the NMR samples were not collected for this time period.

Analyte(s)	$\Delta F_{\text{Max}}$ (kHz)	$\Delta F_{\text{Max}}$ time (s)	$\Delta F_{\text{zero}}$ time (s)	$\Delta F$ FWHM	$\epsilon'$ (temp. taken)
<i>o</i> -xylene	-158.0	41	621	128.0	2.568 (20°C)
<i>m</i> -xylene	-10.4	72	262	109.6	2.374 (20°C)
<i>p</i> -xylene	-7.0	57	213	93.6	2.270 (20°C)
Benzene	-9.4	38	183	62.6	2.284 (20°C)
Ethylbenzene	-14.1	49	700	86.5	2.412 (20°C)
Toluene	-11.5	44	390	83.0	2.379 (25°C)
Chlorobenzene	-110.0	72	738	120.9	5.621 (25°C)
Styrene	-8.2	64	443	102.0	2.43 (25°C)

Table 27 Collated data from Figure 107 and Figure 108, comparing the features of each acquired chart.  $\epsilon'$  values obtained from UNITED STATES DEPARTMENT OF COMMERCE NATIONAL BUREAU OF STANDARDS.<sup>55</sup>

In HPLC and GC, retention time ( $t_R$ ) is typically used to describe the transportation of compounds through a column. The  $t_R$  being defined as: “the time elapsed between sample introduction and the maximum signal of the given compound at the sample detector.”<sup>56</sup> In our case the comparable equivalent would be time from when the sample is detected to have reached the cavity (sample introduction) and the  $\Delta F_{\text{max}}$  time (maximum signal of the given compound at the sample detector). The trend displayed by comparing  $\Delta F_{\text{max}}$  times of each component (see Table 27) is as follows: benzene < *o*-xylene < toluene < ethylbenzene < *p*-xylene < styrene < *m*-xylene = chlorobenzene. We know from the NMR curves and also the reported findings of other research groups that *o*-xylene is retained significantly more than *p*-xylene and *m*-xylene, which does not agree with our  $\Delta F_{\text{max}}$  findings.<sup>49</sup> Typically, in GC/HPLC, the detector is solely at the end of the column, while we are measuring over the central portion of the column during the separation itself. According to Figure 109, there is no correlation between the permittivity and the  $\Delta F_{\text{max}}$  time. Secondly, the  $\Delta F$  is proportional to the  $\epsilon'$  value, but we also know that there is a solvent polarisation effect from our previous experiments; analytes with higher  $\epsilon'$  values will have a greater polarisation effect and therefore may reach  $\Delta F_{\text{max}}$  quicker than analytes with smaller  $\epsilon'$  values, which would explain why *o*-xylene reaches  $\Delta F_{\text{max}}$  quicker than *m/p*-xylene. This parameter could be used if we only measured the end of the column, but then we would only obtain the same information as a standard HPLC detector.

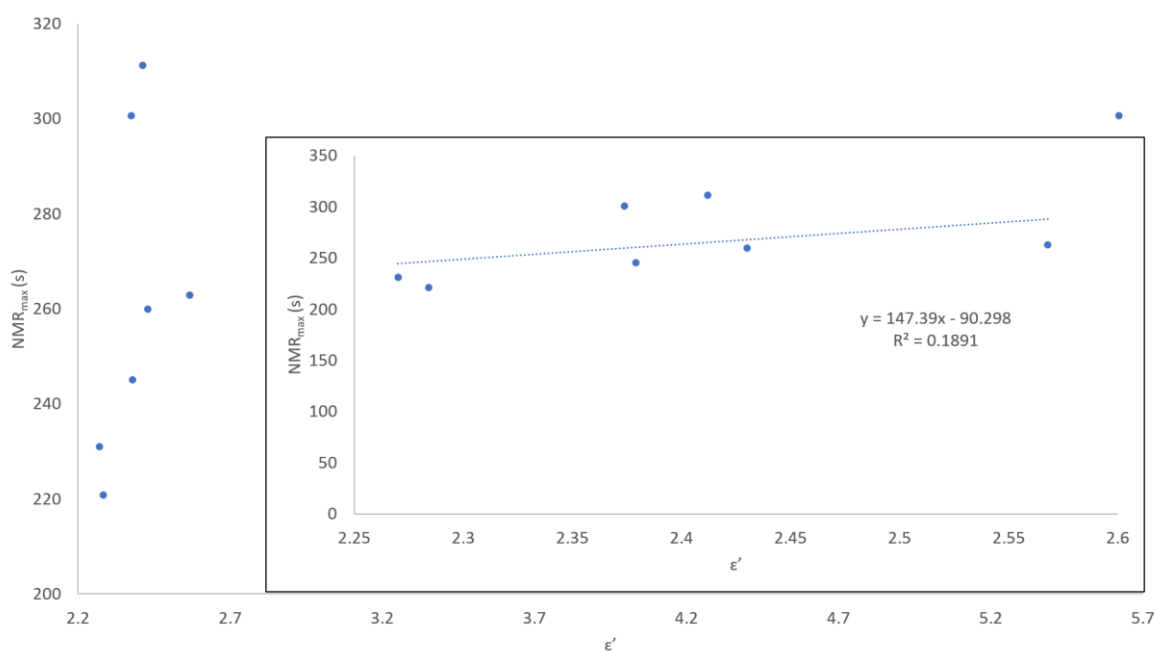
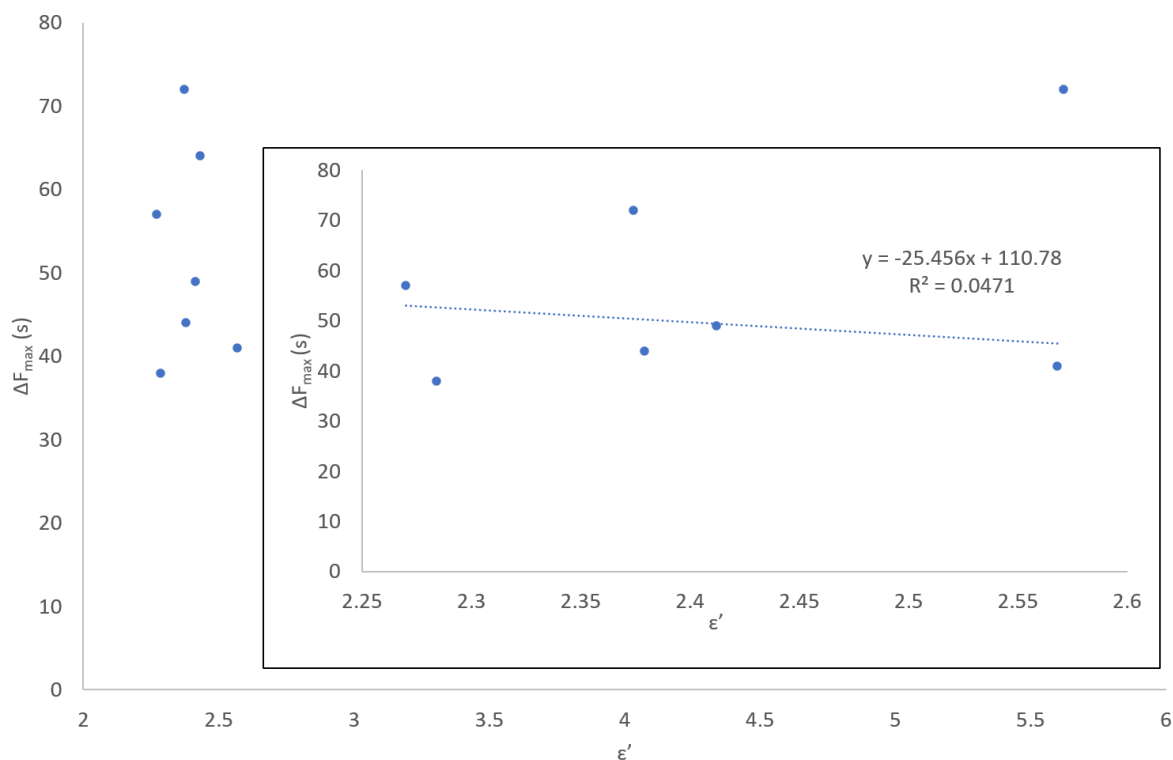


Figure 109 Plot of the  $\Delta F_{\max}$  time against the permittivity ( $\epsilon'$ ) of each sample (top) and  $NMR_{\max}$  time against  $\epsilon'$  of each sample (bottom). Insets have the chlorobenzene results removed and have lines of best fit.

$\Delta F_{\text{zero}}$  is the term we use to describe the time when  $\Delta F$  returns to zero.  $\Delta F_{\text{zero}}$  provides the time when it is believed that all of the analyte material has left the column (i.e. been displaced by hexane). We know that this value has two factors affecting the accuracy of this measurement: firstly, the baseline drift present may affect the  $\Delta F_{\text{zero}}$  time recorded, hence the effect will cause more inaccuracy in



analytes with smaller  $\epsilon'$  values. Secondly, the NMR analysis was able to record trace amounts of the analyte in all cases, which were not detected by the microwave cavity, thus we know there are limits to the concentration the microwave cavity can feasibly detect. With that in mind the trend observed for  $\Delta F_{\text{zero}}$  is: benzene < *p*-xylene < *m*-xylene < toluene < styrene < *o*-xylene < ethylbenzene < chlorobenzene. This trend broadly resembles the trends reported in the literature. Furthermore, we have a much stronger correlation between the  $\Delta F_{\text{zero}}$  time and the permittivity than we did with the  $\Delta F_{\text{max}}$  time (see Figure 110). Styrene and ethylbenzene are suspicious, as styrene is reported to be strongly retained in the UiO-66 framework. It has been reported that the unsaturated double bond of styrene binds to open metal sites in frameworks.<sup>42,57,58</sup> Such active metal sites are present as defects in the formation of UiO-66. It is possible that this batch of UiO-66 is lacking in defect sites and therefore is failing to retain the styrene.<sup>59</sup> Ethylbenzene is also reported to elute faster than the *m*- and *o*-xylene isomers, while here it has significant retention.<sup>60</sup> The NMR suggests that this retention is genuine, but it is unclear as to why this is the case. Unfortunately, as the NMR data never reaches a zero point, we cannot make a direct comparison. It would seem that the NMR method is more sensitive to the lower concentrations, however if we corrected for the baseline drift, we may see a dramatic increase in the precision of the microwave method.

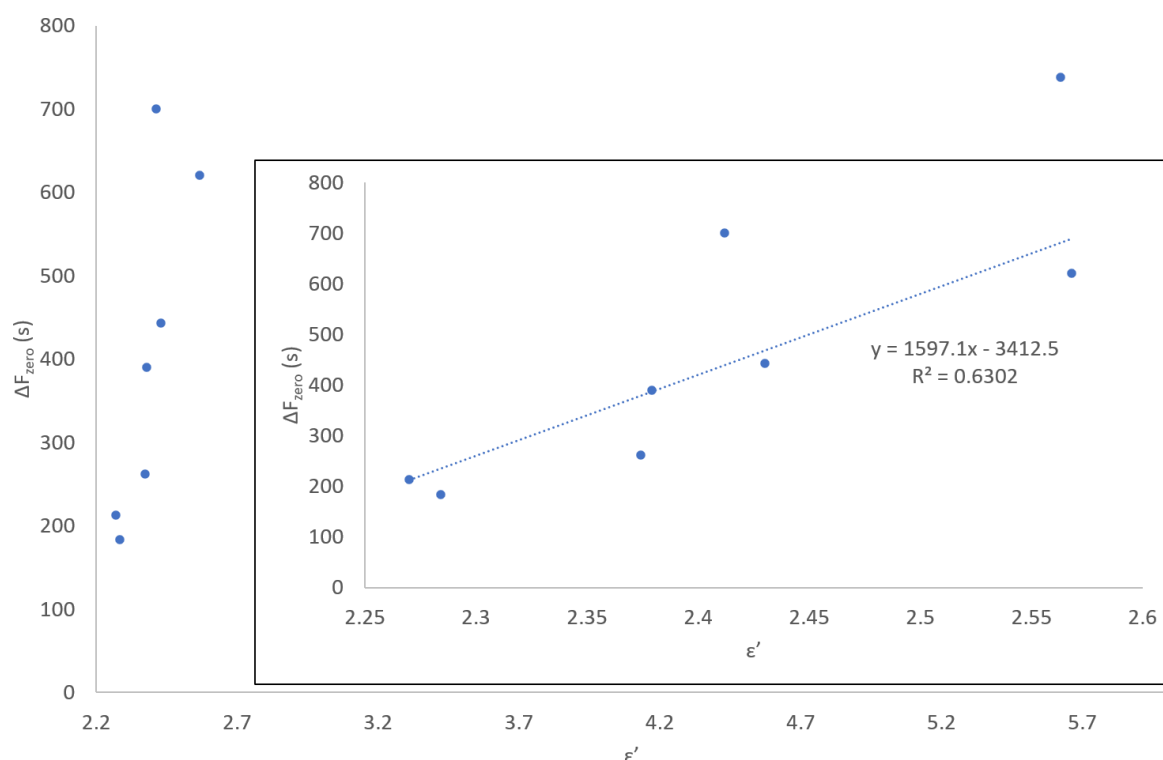
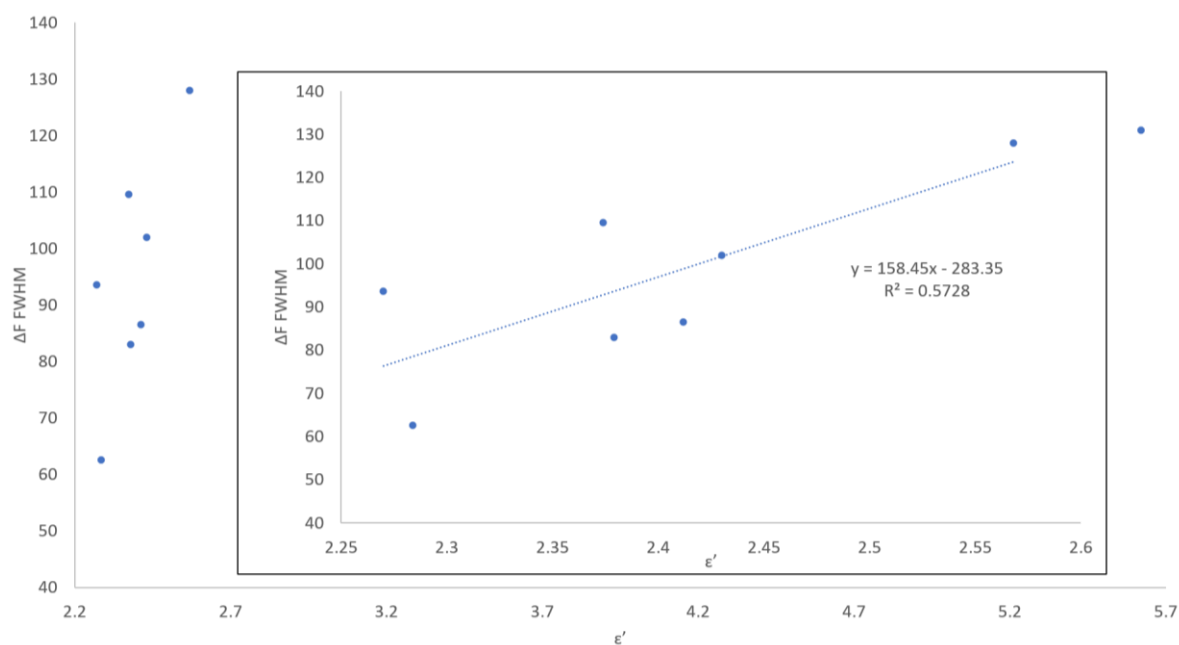


Figure 110 Plot of the  $\Delta F_{\text{zero}}$  time against the  $\epsilon'$  of each sample.  $\text{NMR}_{\text{zero}}$  is not plotted as the NMR plots never reach 0% concentration. Inset has the chlorobenzene result removed and has a line of best fit.

The FWHM in HPLC is often used to describe the resolution of a peak. The trend corresponding to the FWHM for each curve is the following: benzene < toluene < ethylbenzene < *p*-xylene < styrene < *m*-xylene < chlorobenzene < *o*-xylene. Toluene, ethylbenzene and *p*-xylene have very similar retention times consistent with literature reports.<sup>49,51</sup> The only inconsistency in this measurement is that *o*-xylene has a larger FWHM than chlorobenzene, when chlorobenzene is expected to have a much stronger interaction with the column than *o*-xylene. Furthermore, the  $\Delta F_{\max}$  value of *o*-xylene is significantly higher than the chlorobenzene sample, which is surprising based on the reported  $\epsilon'$  values (2.568 vs. 5.621, respectively). Normally we would consider this an anomalous result, except the experiments using *o*-xylene/*p*-xylene and *o*-xylene/*p*-xylene/*m*-xylene mixtures also report similar  $\Delta F_{\max}$  values. Therefore, this unexpectedly low value for chlorobenzene must be due to a difference in the way the xylenes interact with the MOF that has not been accounted for. The correlation between  $\epsilon'$  and the  $\Delta F$  FWHM is slightly weaker than the correlation between  $\Delta F_{\text{zero}}$  and permittivity (see Figure 111). The substantially weaker correlation between NMR FWHM and  $\epsilon'$  is likely due to the fact that we could not fit a curve to the NMR data, therefore the FWHM determined from the straight line point to point fittings will be imprecise.



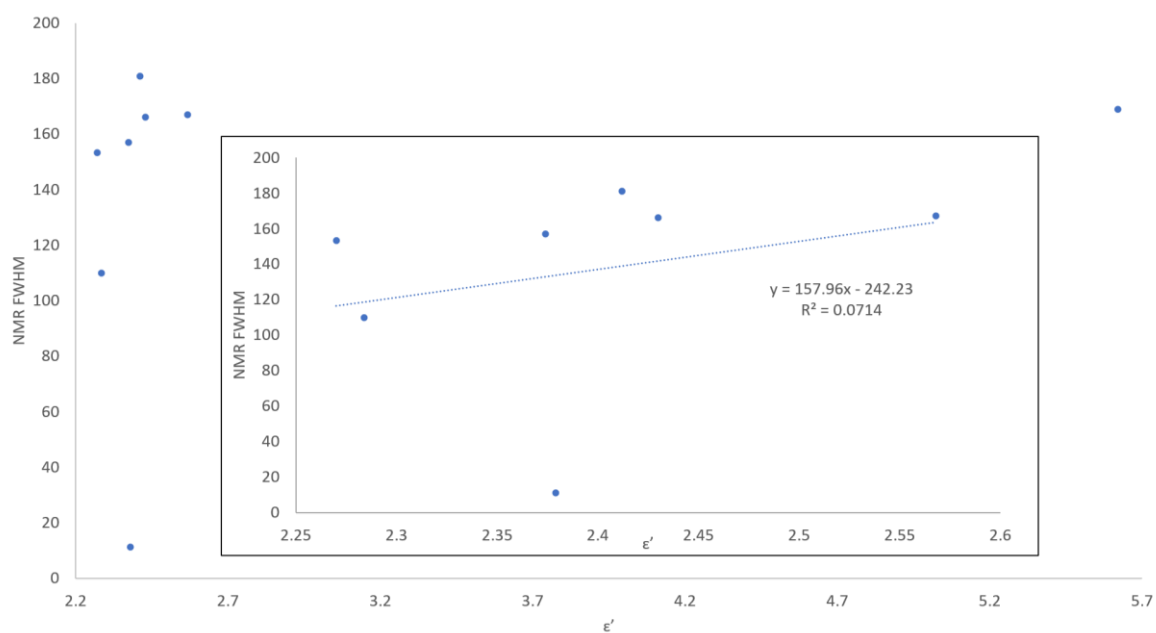


Figure 111 Plot of the  $\Delta F$  FWHM against the  $\epsilon'$  of each sample (top) and NMR FWHM against  $\epsilon'$  of each sample (bottom). Insets have the chlorobenzene results removed and have lines of best fit.

It would appear that the best parameter for comparing the selectivity of this framework is FWHM, despite the known experimental errors. Although the  $\Delta F_{\text{zero}}$  seems to have a more positive correlation and also the trend in the data is more in line with what is reported in the literature, the key issue is that we cannot validate it with a comparison to the NMR data.

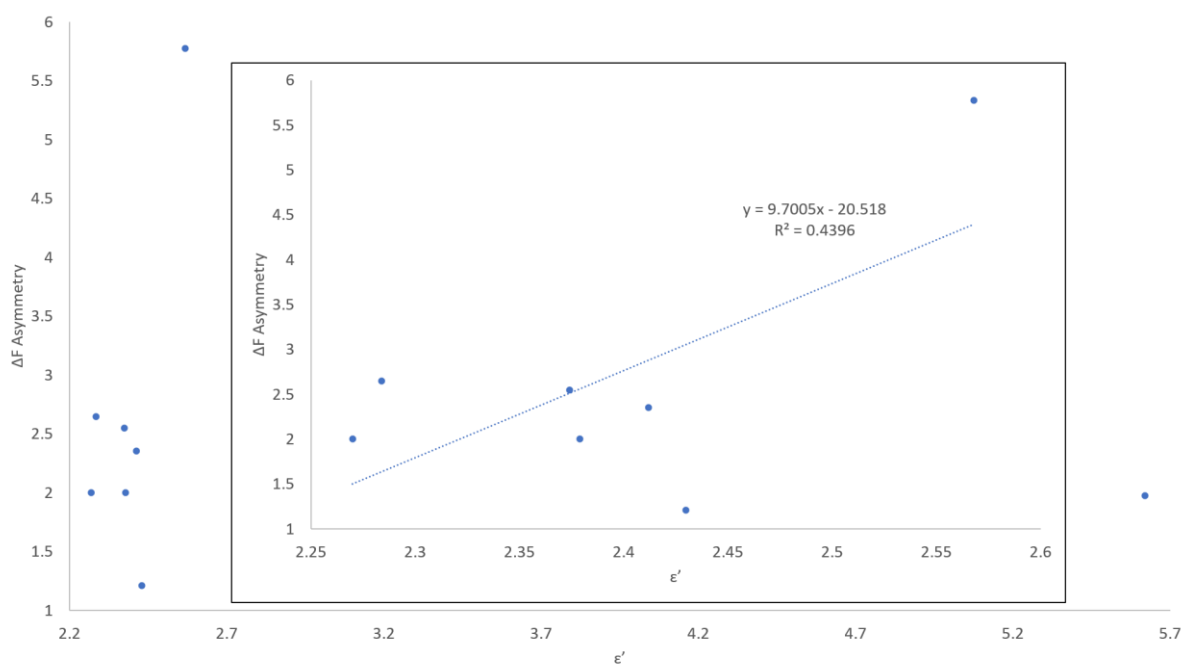
Next, we address the problem with the NMR quantification of analyte in the hexane carrier solvent. The calculated concentration of analyte coming off the column varies by an order of magnitude for different analyte mixtures. For example, in experimental runs **a)** and **b)** shown in Figure 107, *o*-xylene reaches peak concentrations of  $\approx 6$  mol% in hexane (just *o*-xylene) and  $\approx 0.4$  mol% in hexane (*o*-xylene/*m*-xylene mixture) respectively. It is quite clear that the integration of the two curves are not equal. This suggests either; our NMR measurements have some undetermined systematic error, or some *o*-xylene has been retained by the MOF and therefore would not show up in the run off. Since the  $\Delta F$  values return to zero in the microwave measurement, there is little to no *o*-xylene left in the system. Furthermore, instances where results are in conflict with the literature (such as ethylbenzene), we need to determine whether our analytical method is faulty or if the result is genuine. In order to investigate any systematic inaccuracies, a series of known concentration solutions of *o*-xylene in hexane were made up and measured by NMR (Table 28).

Concentration of <i>o</i> -xylene (mol% in hexane)	Concentration measured by NMR (mol% in hexane)	Error (% error)
10.7	11.3	0.60 (6%)

4.29	4.33	0.04 (1%)
2.11	1.83	0.28 (13%)
1.43	1.66	0.23 (16%)
1.05	1.00	0.05 (5%)
0.54	0.50	0.04 (7%)
0.42	0.47	0.05 (12%)
0.21	0.26	0.05 (24%)
0.16	0.14	0.02 (13%)
0.11	0.11	0.00
		Average = 0.136 (9.7%)

Table 28 Comparison of concentrations measured by NMR to the actual value. Mixtures of *o*-xylene made up using serial dilution and hamilton syringes.

Even taking into account human error and the very small instrumental errors, the percentage error does not seem to increase/decrease according to magnitude. The NMR technique has some inherent imprecision which could be due to a variety of reasons, e.g. hydrogen deuterium exchange. This 10% discrepancy still does not account the variation observed in Figure 107 and Figure 108. Although we are unable to determine the precise cause of this issue, the shapes of the curves are the key feature in these measurements and the curves obtained for mixed isomer runs are self-consistent and allow for comparison. With that in mind, we move on to comparing parameters that are more related to the shape of the curve rather than apparent concentration measured by NMR.



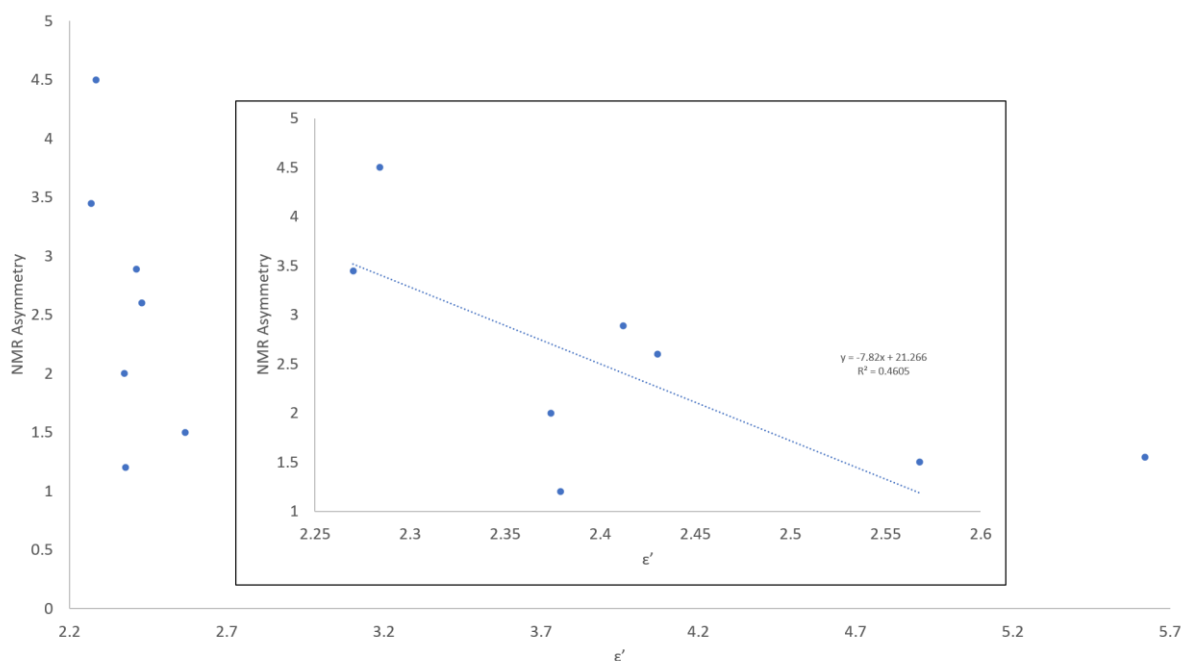


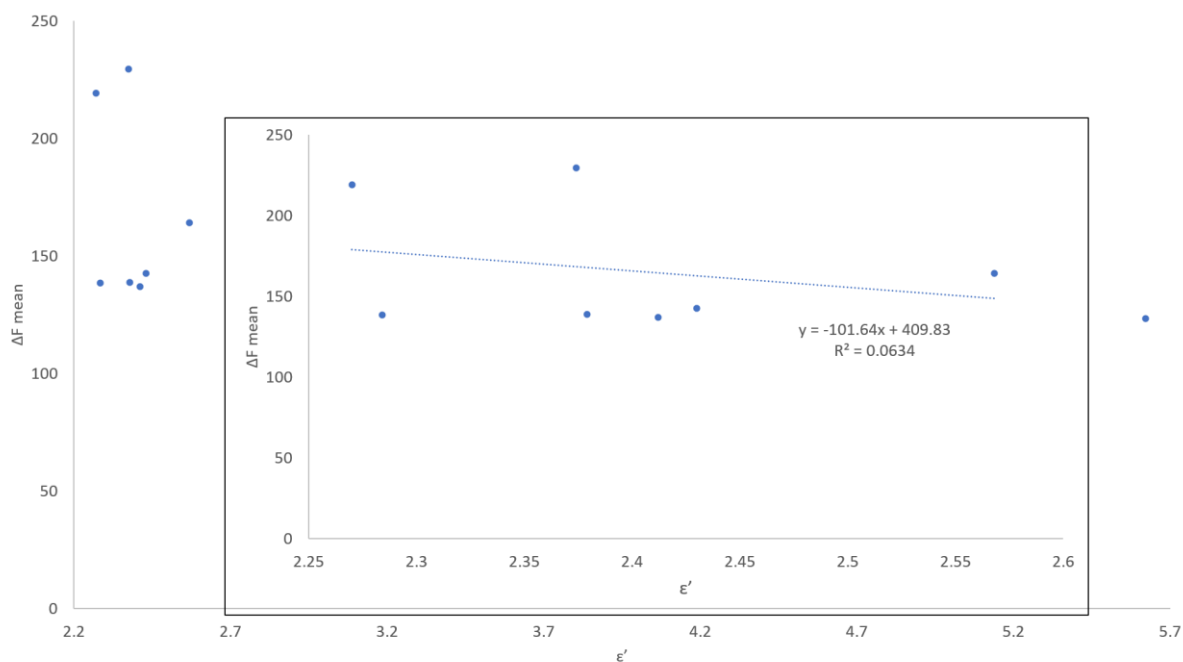
Figure 112 Plot of the  $\Delta F$  asymmetry against the  $\epsilon'$  of each sample (top) and NMR asymmetry against  $\epsilon'$  of each sample (bottom). Insets have the chlorobenzene results removed and have lines of best fit.

One feature of the NMR and  $\Delta F$  curve shapes that seems consistent in all the runs is that the left-hand side of the curve is significantly steeper than the right-hand side of the curve. This is obviously due to the fact that all the material going into the column of MOF particulate is going to come out at different rates depending on the strength of interactions present. Previously, when we looked at FWHM, a major disadvantage was the NMR data could not distinguish between the various analytes. Looking at the asymmetry of the curves, we can better observe the trends in the data, there is a clear negative correlation between the NMR asymmetry and  $\epsilon'$ . This means that low  $\epsilon'$  materials pass through quite quickly, while higher  $\epsilon'$  seem to be impeded more and therefore the analyte has a more symmetrical distribution throughout the column, which is what we would expect (e.g. *ortho*-xylene and chlorobenzene should take longer to travel through column than *para*-xylene and benzene). Conversely, the microwave perturbation method shows a strong positive correlation between asymmetry and the  $\epsilon'$  value. We believe that this demonstrates the difference between *in-situ* analysis and *ex-situ* analysis. The NMR analysis is simply collecting the runoff at the end of the column; therefore, we are only seeing the end result of the separation where the analytes have undergone through the full process of separation. The microwave method is recording over approximately 75% of the length of the column; therefore, it is detecting early and late in the separation at the same time. We know from the NMR curves **b), d), f), g)** (Figure 107) that there is significant overlap of each of the analytes, indicating poor separation throughout the column, as such it is likely that the microwave method is simply observing this.

Mixture	Asymmetry $\Delta F$	Asymmetry NMR oX	Asymmetry NMR mX	Asymmetry NMR pX
<i>ortho/para</i>	5.3	3.0	-	2.5
<i>ortho/meta</i>	2.4	4.0	5.3*	-
<i>meta/para</i>	3.8	-	1.5	1.5
<i>ortho/meta/para</i>	4.3	1.5	2.3	2.3
<i>ortho</i>	5.8	1.5	-	-
<i>meta</i>	2.5	-	2.0	-
<i>para</i>	2	-	-	3.4

Table 29 Displaying asymmetry values for the curves of data acquired when using 33% concentration of xylene isomers and mixtures. \*meta-xylene NMR is anomalous and is likely inaccurate.

The NMR method provides us with individual data sets for each component of the xylene mixtures while the microwave cavity perturbation method presents a curve that should be the sum of both components. In each case the asymmetry of the  $\Delta F$  curve is larger than each of the individual components, except in the case of the *ortho/meta*-xylene mixture (see Table 29).



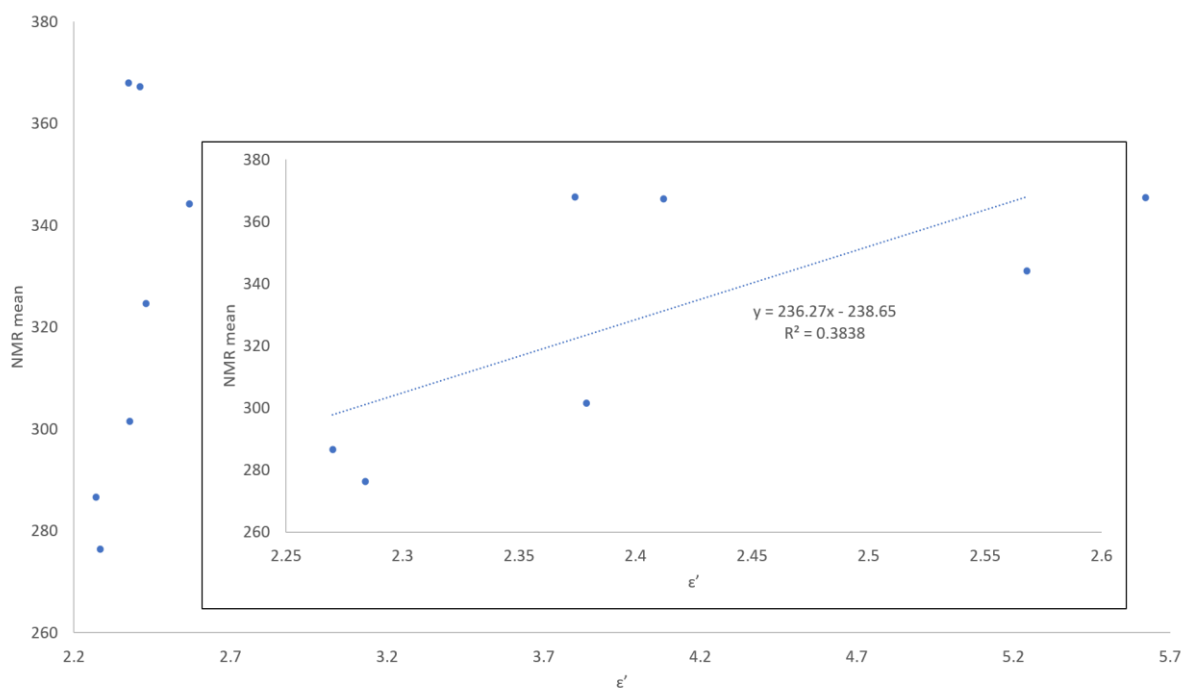


Figure 113 Plot of the  $\Delta F$  mean against the  $\epsilon'$  of each sample (top) and NMR mean against  $\epsilon'$  of each sample (bottom). Insets have the chlorobenzene results removed and have lines of best fit.

Another parameter we investigated was the mean time for both  $\Delta F$  and NMR curves. This provides information on the average transit time of analytes through the framework/column. As with all the time dependent parameters already discussed, this depends on flow rate, but after the initial experiments on flow rates, all flow rates were kept constant throughout. In the comparison of the mean values, we see a weak positive correlation with permittivity for the NMR means but almost no correlation for the  $\Delta F$  means. The positive correlation indicates analytes with larger  $\epsilon'$  values have a longer average transit time in the column, which is what we would expect. The lack of correlation between  $\Delta F$  and  $\epsilon'$  suggest that the analytes are not well separated in the measurement region.

Mixture	$\Delta F$ mean	oX NMR mean	mX NMR mean	pX NMR mean
<i>ortho/para</i>	156.4	401.9	-	351.4
<i>ortho/meta</i>	170.0	417.9	340.7	-
<i>meta/para</i>	141.7	-	281.4*	273.2
<i>ortho/meta/para</i>	172.7	317.1	266.6	261.2
<i>ortho</i>	164.1	344.2	-	-
<i>meta</i>	229.4	-	367.0	-
<i>para</i>	219.2	-	-	286.5

Table 30 Displaying mean values calculated for the curves of data acquired when using 33% concentration of xylene isomers and mixtures. \*meta-xylene NMR is anomalous and is likely inaccurate.

One feature of using the mean is that it depends on the variable of time. The microwave cavity perturbation method measures in real time while the NMR measures at the end of the column. As such there is a  $\approx 200$  second lag time for the NMR means compared to the  $\Delta F$  means in any given experiment. We also observe that when *para*- or *meta*- xylene is present at the same time as *ortho*-xylene, the NMR mean time is lower than the values calculated for the individual components. This indicates competition for interaction sites in the framework: *o*-xylene is probably competing with the *p/m*-xylene for pore space, causing the *p/m*-xylene components transit to be accelerated. The  $\Delta F$  mean values also indirectly indicate this as the  $\Delta F$  values for the mixtures are lower than the individual components (e.g.,  $\Delta F$  mean o/p-xylene: 156 s, o-xylene: 164 s, p-xylene: 219 s).

We can observe some meaningful data acquired with the microwave cavity perturbation method, but the separation of xylene components is poor. The framework pores have a maximum capacity for material to travel through while the rest will simply be forced through the interstitial voids between MOF particles, largely unaffected by the separative properties of the MOF. This is primarily a concentration issue. By reducing the concentration of analyte injected by diluting with hexane (which we have already shown to be a very poor competitor for pore space) we can exaggerate the interaction the analyte has with the pores which in turn will exaggerate the difference in curve shape. This will report more directly on the analyte:pore interactions. The difference in curve shape from analyte to analyte demonstrated by NMR will directly affect the difficulty in deconvoluting the raw  $\Delta F$  data into separate curves for each component. A balance must be obtained however, as we have seen with the more microwave insensitive materials (e.g. *m*-xylene, *p*-xylene) the  $\Delta F$  is much smaller and at lower concentrations may be too weak to reliably interpret. To test this, we repeated two of the experiments, but reduced the concentration by a factor of ten. Concentrations of 3% were attempted with p-xylene and a o/p-xylene mixture (Figure 114).

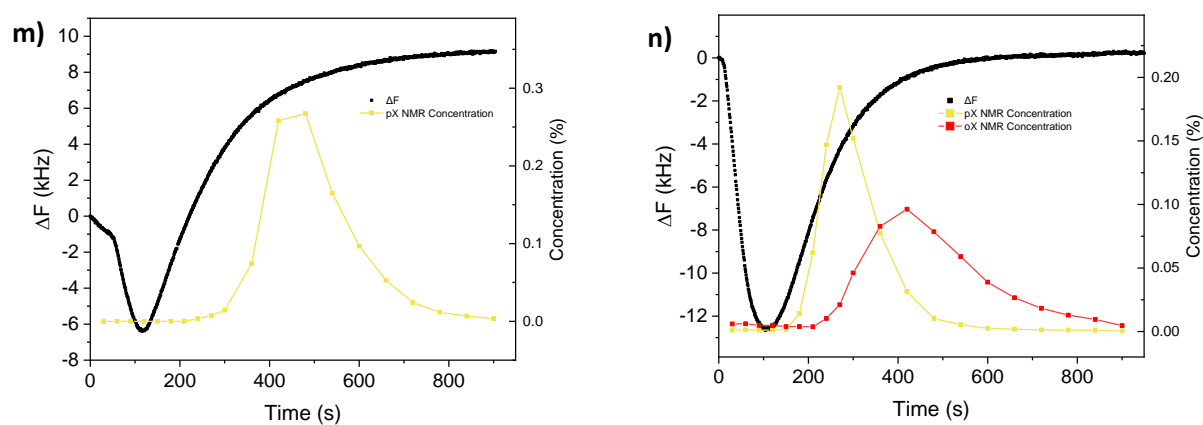


Figure 114  $\Delta F$  over time as well as the % concentration determined by NMR: left) p-xylene right) p/o-xylene mixture. Y axis is scaled individually to help show the information present. Analytes injected were 3% concentration mixtures of 0.1 mL aliquots.



As seen by **n)** the separation between curves determined by NMR of the *o/p*-xylene mixture is much more distinct, compared to the curves shown by **d)**. **n)** also demonstrates a 100 second difference between the peak concentration of *p*-xylene and *o*-xylene as opposed to the 10 second difference shown in **d)**. This is reflected in the  $\Delta F$  curve as the curve is significantly broader. We observe in graph **n)** that the NMR data indicates the passage of *o*-xylene was mostly complete after  $\approx 700$  seconds. The microwave cavity shows the point at which  $\Delta F = 0$  is 643 seconds. The  $\Delta F_{\max}$  has been reduced from 170 to 12 kHz which is quite a drastic reduction in sensitivity of the measurement. This is surprisingly not observed when comparing **m)** and **e)**, as the  $\Delta F_{\max}$  has remained  $\approx 6$  kHz. The baseline drift present in **e)** is even more significant in **m)** which is dramatically lowering the accuracy at which we can reliably determine the end point.

Mixture	$\Delta F$ mean	<i>o</i> X NMR mean	<i>p</i> X NMR mean	$\Delta F$ asymmetry	<i>o</i> X NMR asymmetry	<i>p</i> X NMR asymmetry
<i>ortho/para</i>	226.3	469.4	307.0	2.0	1.25	1.45
<i>para</i>	197.8	-	496.4	1.4	-	0.9

Table 31 Displaying mean and asymmetry values for the curves of data acquired when using 3% concentration aliquots of *p*-xylene and *p/o*-xylene mixture.

Comparison of the mean values again demonstrates that the addition of *o*-xylene accelerates the transit of *p*-xylene through the column. This is most strikingly observed in the NMR peak maximum for *p*-xylene when comparing **m)** and **n)** in Figure 114. The asymmetry values also show the curves becoming more symmetrical (closer to 1), which suggests the majority of the material is interacting with the framework as opposed to simply flowing through the interstitial voids. Unfortunately, the large baseline drift is likely affecting the calculated values for the  $\Delta F$  mean and asymmetry of the  $\Delta F$  curves, especially in the case of the *p*-xylene. This suggests that at this concentration we cannot reliably track *p*-xylene. If we could correct for the baseline drift then it is quite possible we would be able to use these concentrations or perhaps go even lower, but at this stage we do not have the resources or the knowledge to do so.

It is evident from these results that the separation would be more effective at a lower concentration than used previously but higher than the concentration used here, to try and improve the reliability of the determined end point. Another challenge with this technique is the packing of the narrow quartz tube with powder. It is not currently possible to replicate the size and arrangement of particles in the tube, therefore for experiments to be quantitatively comparable they need to be performed in sequence on the same sample, same quartz tube and in the same set up. This creates issues of time and resources, as once the apparatus has been set up it cannot be taken down until all the data has

been collected. As the equipment used belonged to Cardiff University Engineering Department, I could not use it indefinitely. There are practical alternatives that would improve these measurements (e.g. larger columns) that were not available at this time. To accommodate the practical limitations of the equipment available, we focused on the xylene isomers and stopped investigating the rest of the materials involved in the styrene separation. The concentration of the aliquots was dropped to 10% by volume, but the experiments were ran for 1200 seconds instead of 800 seconds to ensure that these experiments had reached completion. Also in order to maximise the sensitivity of the measurement the following parameters were changed: IF Bandwidth (Hz) 10 kHz -> 1 kHz, data points 301 -> 101. The reduction in IF Bandwidth increased the number of acquisitions, increasing the sensitivity of the measurement but lengthening acquisition time. To compensate for the increase in acquisition time the number of data points acquired per acquisition was reduced.

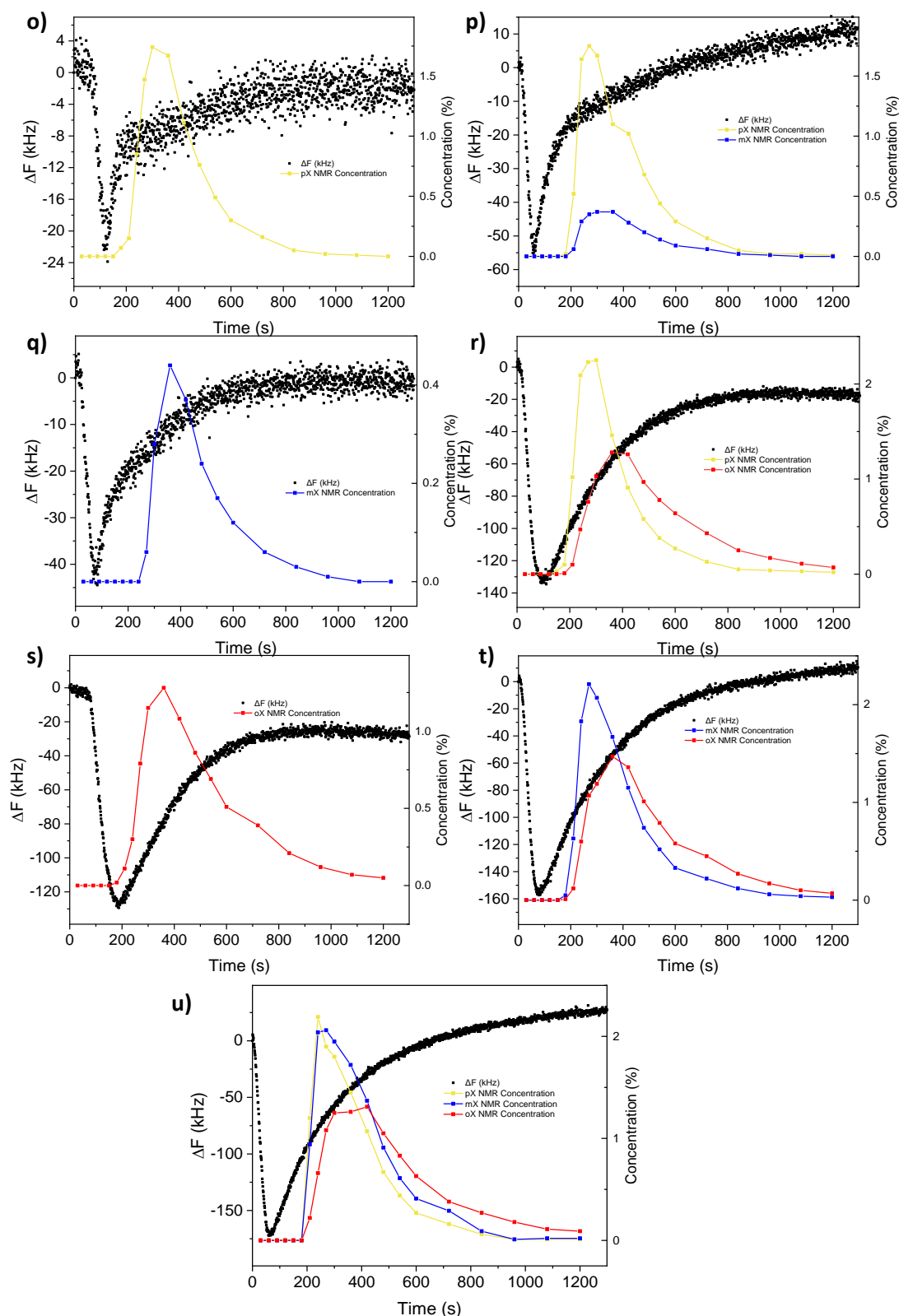


Figure 115  $\Delta F$  over time as well as the % concentration determined by NMR: o) p-xylene p) m-xylene q) o-xylene r) p/m-xylene s) p/o-xylene t) m/o-xylene u) p/m/o-xylene. Y axis is scaled individually to help show the information present.

Analytes injected were 10% volume concentration mixtures of 0.1 mL aliquots.

The change in “parameters” resulted in a boost in sensitivity despite the reduction in concentration (e.g. *p*-xylene  $\Delta F_{max} = 24\text{kHz}$ , an increase from 6kHz) however there is more noise in the measurements which is very apparent for graph **o**). The baseline drift is more significant now, even present in measurements containing *o*-xylene. As before with our previous experiments we can clearly see UiO-66 has a strong preference for *o*-xylene.

Analyte	$\Delta F$ mean	oX NMR mean	mX NMR mean	pX NMR mean
<i>ortho/para</i>	401.9	523.1	-	374.3
<i>ortho/meta</i>	320.0	509.4	407.3	-
<i>meta/para</i>	388.0	-	421.3	393.9
<i>ortho/meta/para</i>	314.6	511.1	402.6	376.5
<i>ortho</i>	477.6	505.2	-	-
<i>meta</i>	393.9	-	465.2	-
<i>para</i>	510.9	-	-	405.5

Table 32 Displaying mean values calculated for the curves of data acquired when using 10% concentration of xylene isomers and mixtures.

Before we observed an  $\approx 200\text{s}$  lag time between the microwave and NMR measurement, as we have changed the concentration we should see a change in the lag time. In the cases of single component mixtures, the lag between  $\Delta F$  means and NMR means are significantly less than 200s, or in the case of *p*-xylene the  $\Delta F$  mean is greater than the NMR mean (see Table 32). The accuracy of these values have likely suffered due to the lack of sensitivity and the greater influence of a shifting baseline. Furthermore, due to *o*-xylene producing a stronger signal, the weighting *o*-xylene will have a bigger weighting in the mixtures and therefore the mean calculations will likely reflect that.

Mixture	Asymmetry $\Delta F$	Asymmetry NMR oX	Asymmetry NMR mX	Asymmetry NMR pX
<i>ortho/para</i>	2.9	2.3	-	1.1
<i>ortho/meta</i>	4.5	1.8	3.3	-
<i>meta/para</i>	3.2	-	1.5	3.0
<i>ortho/meta/para</i>	3.8	1.0	3.8	6.0
<i>ortho</i>	2.9	2.1	-	-
<i>meta</i>	3.3	-	1.4	-
<i>para</i>	1.3	-	-	2.7

Table 33 Displaying asymmetry values for the curves of data acquired when using 10% concentration of xylene isomers and mixtures.

As we said earlier the  $\Delta F$  asymmetry value might be expected to be summative of the individual NMR components asymmetry value (accounting for the error in the NMR values). *ortho/para*-xylene and *ortho/meta* and *ortho* xylene mixtures seem to follow this expectation, however in the case of *meta/para* and *ortho/meta/para*, *meta* and *para* xylene mixtures they do not seem to obey this expectation. In the case where *o*-xylene is not present, the  $\Delta F$  curves are significantly noisier as we can see from Figure 115, this will manifest as error in the asymmetry values.

It would seem that, although we have improved the separation of the xylene isomers with lower concentrations, the microwave cavity perturbation method is struggling to provide accurate data regarding the isomers with weaker signals (*p*- and *m*-xylene). The method seems to have very little issue detecting the *o*-xylene component at these concentrations, it is likely that the *o*-xylene has some polarising effect on the overall framework to account for the significant difference to the *m*- and *p*-xylene isomers.

#### 4.4 Summary and Conclusions

We have designed a flow system that can detect the passage of materials through UiO-66 via an *in-situ* dielectric measurement. It can effectively detect the affinity of an analyte for this framework as well as competition effects.

A consistent problem in samples that produced weaker signals (lower  $\epsilon'$  values and/or lower concentration) was the presence of a significant baseline drift. It is unclear what the cause is of this baseline drift; it could be that the chemical makeup of the column is being changed gradually or it could simply be a physical artifact of the measurement technique. For example, there could be a temperature change over time inside the column itself, (perhaps from the enthalpy of analyte binding, or perhaps from temperature changes in the solvent medium) which the TM310 correction would not account for. Without having established what the cause is we cannot remove the issue with a simple baseline distraction. The baseline drift was more apparent at lower concentrations, while in some cases at higher concentrations it was negligible when compared to  $\Delta F$  therefore another valid strategy would be to improve the sensitivity of the measurement (i.e., reliably detect lower concentrations) or conversely, we increase the volume of the sample (and hence the column), so a bigger signal is generated by the analytes. These measures would also mitigate any noise in the data present in the samples with weaker signals (i.e. mixtures without *o*-xylene).

It would seem that the boosted signal strength exhibited by *o*-xylene is unique, as the static measurements showed that the  $\Delta F$  values for the xylene isomers without UiO-66 present were broadly similar. Although UiO-66 was chosen for its rigidity, there is still rotational degrees of freedom for the aromatic rings of the BDC linkers. It has been reported that these aromatic rings do rotate to

accommodate the analytes present in the framework, and it is entirely possible that the alignment of the aromatic rings in UiO-66 is in a particularly polarising conformation when *o*-xylene is present compared to the other analytes.<sup>61,62</sup>

The next step in this research would be to try and deconvolute the  $\Delta F$  curves to be able to identify the separate components present in the mixture. While this is possible with the data we have, specific experimental modifications would make this a much easier process: i) a narrower cavity measuring a smaller region of the column; ii) a wider bore column to contain more material; iii) optimised concentration to maximise signal without overloading the column, and iv) multiple cavity measurements along the column to demonstrate the separation process as it occurs.

## 4.5 Experimental

### 4.5.1 Microwave Cavity measurements

In the following experiments, the quartz capillary (L = 10 mm, ID = 2.0 mm, OD = 2.4 mm, CMSscientific) was filled up to 8 cm with the desired MOF. The T-pieces and PFA tubing (1/8" x 0.62" x 5 ft) were bought from Kinesis. The syringe pump was a Chemyx Fusion 100 Dual Infusion Pump and the Kalrez O-rings (2.90 mm x 1.78 mm) were purchased from EAP International Ltd. The hexane used was HPLC grade bought from Fisher Scientific. The microwave cavity resonator (MCR) was made from two aluminium blocks joined together to form a hollow, cylindrical cavity. The dimensions were chosen so that the cavity could be excited in the TM<sub>010</sub> mode at 2.5 GHz. The MCR was 80 mm high and the actual cavity (the measurement area) was 60 mm high. The diameter of the holes where the sample is inserted was 10 mm. To ensure the sample insertion was consistent, plastic spacers were laser printed to hold the sample in place and ensure a snug fit.

### 4.5.2 Static Experiments

The desired MOF was packed into a quartz capillary while sealing one of the ends with epoxy resin (except nitrobenzene to which the capillary was sealed via melting nylon around the ends).

For analytes that were liquid at room temp, the capillary was left to soak overnight in the desired analyte and then the other end was sealed. For analytes that were solid at room temperature (4,4' biphenyl and 2,2' bipyridine), the analyte (1.25 g) was mixed with the framework (1 g) in a conical flask and heated to 75°C for 2 days. The mixture was allowed to cool then the powder was spread evenly over a filter paper. The filter paper was then heated to 75°C, allowing any excess analyte to wick onto the filter paper, leaving behind the MOF loaded with analyte. The presence of the analyte was confirmed via TGA (see Appendix S3).

The sample was then placed in the microwave cavity and readings were taken using the TM010 and TM310 modes over a period of thirty seconds. The corrected values were then calculated via Equation 10 and an average of the readings was taken as the absolute value recorded.

The transmission ( $S_{21}$ ) measurements were obtained using Keysight Technologies Vector Network Analyser (PNA-L N5232A) with RF cables from Huber+Suhner. The VNA was connected to a PC running an in-house measurement acquisition program built with LabVIEW.

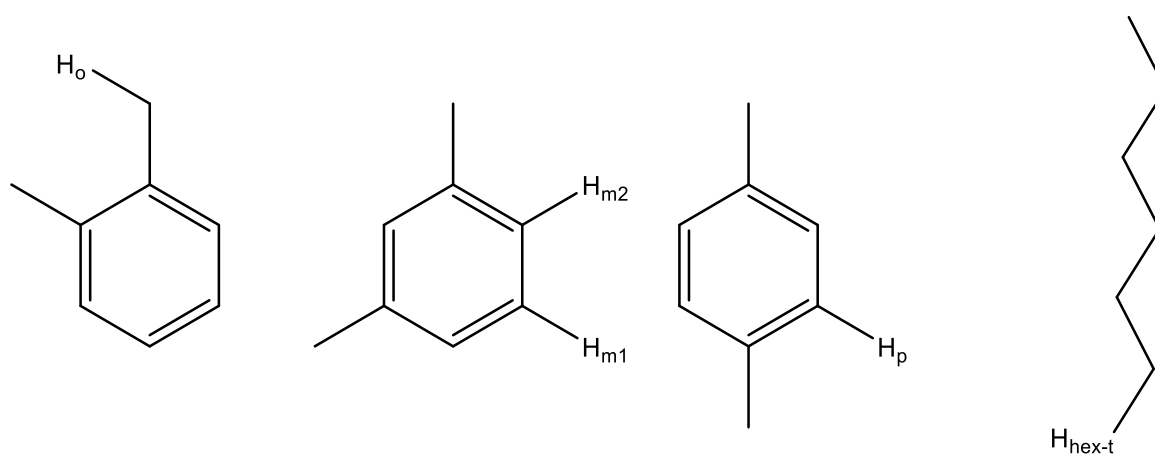
#### 4.5.2.1 Flow experiments

The desired MOF was packed into the quartz capillary and plugged with cotton wool at both ends to prevent the loss of framework material and then placed inside the microwave cavity. Two stainless steel Swagelok tube fittings (union, 1/8 in. tube OD) were affixed either side, with Kalrez® O-rings. The PFA tubing was connected to the fittings leading to a T-piece, allowing for the release of air bubbles, which was itself connected to a syringe pump. At the other end a piece of tubing was connected leading into a waste bottle.

These experiments, as well as the experiments described below, could not be done safely in the engineering department and required the use of a fumehood. The VNA used previously was replaced by the portable Copper Mountain S5085 VNA and done in the chemistry department.

#### Aliquot experiments

The setup was the same as the flow experiments except there was a second T piece allowing for the injection of a second material, placed just before the T-piece that allows air bubbles to escape. The injection region was measured to hold a total volume of  $0.1 \text{ cm}^3$ . Between experiments, this injection region was flushed thoroughly with air followed by hexane to ensure there was no remaining residual material. The runoff was collected in sample vials. These samples were then diluted with  $\text{CDCl}_3$  before being run on a 400 or 500 MHz NMR spectrometer.



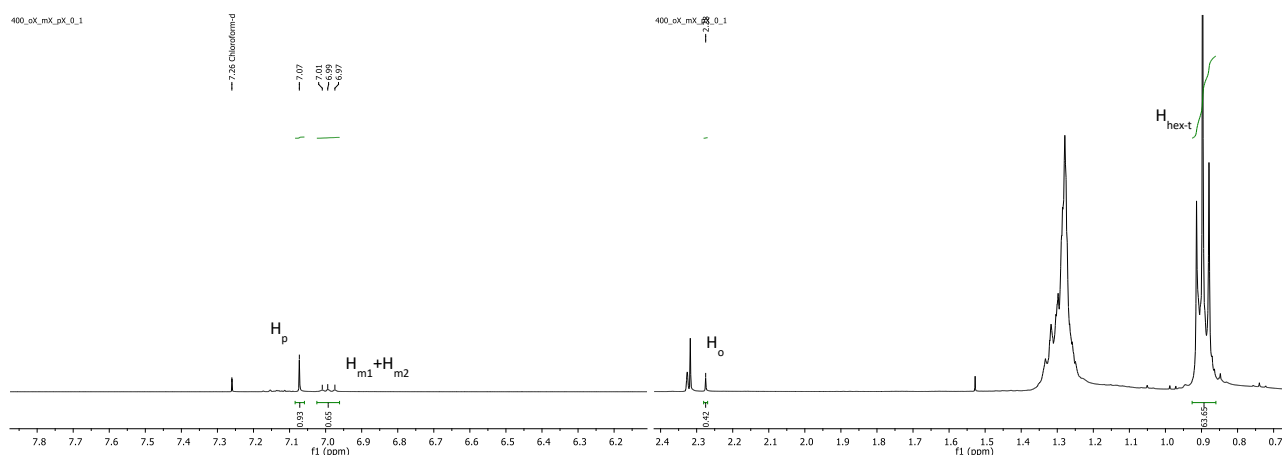


Figure 116 Proton environments for each of the xylene isomers and hexane (top). Example of NMR peak integration, annotated with corresponding proton environments. (Taken from *o/m/p*-xylene mixture at 10% volume concentration, time = 240 seconds).

For all acquired spectra, a baseline polynomial correction was applied. Peaks corresponding to each of the analytes were chosen so there was minimal overlap between peaks (i.e. the CH<sub>3</sub> peaks at 2.32 and 2.33 which correspond to *p*-xylene and *m*-xylene, respectively, were not used due to overlap but the CH<sub>3</sub> peak at 2.28 corresponding to *o*-xylene was suitable). The determined integrals for the xylene isomers use the hexane as an internal reference standard to determine a %concentration, after accounting for the number of protons.

$$\text{para xylene content} = \frac{0.93}{4} = 0.2325$$

$$\text{hexane content} = \frac{63.65}{6} = 10.6083$$

$$\text{para xylene \%concentration} = \frac{0.2325}{10.6083} \times 100\% = 2.19\%$$

Figure 117 Worked example of calculating *p*-xylene %concentration from Figure 116.

#### 4.5.2.1.1 Aliquot experiments – curve fitting

There was difficulty with fitting curves to the NMR data produced from this experiment. Chromatographic curve fits that were attempted: Chesler-Cram peak function, Edgeworth-Cramer peak function and the Gram-Charlier peak function. While our data could be fitted to these curves, small changes in initial parameters resulted in large changes in outputs and hence further consideration is required before using these chromatographic methods. The parameters presented (mean, asymmetry, FWHM) were estimated from straight line fits between the points. Mean and asymmetry are defined as follows.



$$\text{mean} = \frac{\int xy}{\int y}$$

Equation 11 showing how the mean is calculated for both the  $\Delta F$  and NMR data.

$$\text{Asymmetry} = \frac{\text{RHS}}{\text{LHS}}$$

Equation 12 showing how the value is obtained for asymmetry. The right hand side (RHS) represents the peak maximum to the half maximum right of the peak. The left hand side (LHS) is the peak maximum to the half maximum, left of the peak maximum.

#### 4.5.3 UiO-66 Synthesis

Synthesis of UiO-66 is based on the method reported by Schaate et al.<sup>63</sup> ZrCl<sub>4</sub> (2 g) and TPA (1.5 g) were fully dissolved in a mixture of DMF (500 mL) and acetic acid (15.45 g). The solution was then heated to 120°C for 48 hours. The mixture was then filtered and washed with hot DMF. The precipitate was then dispersed in methanol and left to soak for 3 hours, the mixture was then centrifuged to recover the precipitate. This process was repeated three more times. The white precipitate was then heated under air at 285°C for 1 hour, and then heated at 150°C for 24 hours.

## 4.6 References

- 1 S. Kulprathipanja, R. B. James, S. Kulprathipanja, S. J. Frey, S. W. Sohn, S. R. Dunne, J. O'Brien-Abraham and J. Y. S. Lin, *Zeolites Ind. Sep. Catal.*, 2010, 173–202.
- 2 S. Shevlin, *Nat. Mater.*, 2020, **19**, 1038–1039.
- 3 P. Z. Moghadam, A. Li, S. B. Wiggin, A. Tao, A. G. P. Maloney, P. A. Wood, S. C. Ward and D. Fairen-Jimenez, *Chem. Mater.*, 2017, **29**, 2618–2625.
- 4 D. S. Sholl and R. P. Lively, *Nature*, 2016, **532**, 435+.
- 5 W.-G. Cui, T.-L. Hu and X.-H. Bu, *Adv. Mater.*, 2020, **32**, 1806445.
- 6 M. Carboni, C. W. Abney, S. Liu and W. Lin, *Chem. Sci.*, 2013, **4**, 2396–2402.
- 7 M. Kadhom and B. Deng, *Appl. Mater. Today*, 2018, **11**, 219–230.
- 8 Z. Zhang, Y. Zhao, Q. Gong, Z. Li and J. Li, *Chem. Commun.*, 2013, **49**, 653–661.
- 9 M. I. Gonzalez, M. T. Kapelewski, E. D. Bloch, P. J. Milner, D. A. Reed, M. R. Hudson, J. A. Mason, G. Barin, C. M. Brown and J. R. Long, *J. Am. Chem. Soc.*, 2018, **140**, 3412–3422.

- 10 S. Mukherjee, B. Manna, A. V Desai, Y. Yin, R. Krishna, R. Babarao and S. K. Ghosh, *Chem. Commun.*, 2016, **52**, 8215–8218.
- 11 J. Jiang and O. M. Yaghi, *Chem. Rev.*, 2015, **115**, 6966–6997.
- 12 I. Ahmed and S. H. Jung, *Chem. Eng. J.*, 2017, **310**, 197–215.
- 13 X.-J. Wang, P.-Z. Li, Y. Chen, Q. Zhang, H. Zhang, X. X. Chan, R. Ganguly, Y. Li, J. Jiang and Y. Zhao, *Sci. Rep.*, 2013, **3**, 1149.
- 14 B. Wang, P. Wang, L.-H. Xie, R.-B. Lin, J. Lv, J.-R. Li and B. Chen, *Nat. Commun.*, 2019, **10**, 3861.
- 15 J. L. C. Rowsell, E. C. Spencer, J. Eckert, J. A. K. Howard and O. M. Yaghi, *Science (80-. )*, 2005, **309**, 1350 LP – 1354.
- 16 Y. T. A. Wong, V. Martins, B. E. G. Lucier and Y. Huang, *Chem. – A Eur. J.*, 2019, **25**, 1848–1853.
- 17 H. S. Cho, J. Yang, X. Gong, Y.-B. Zhang, K. Momma, B. M. Weckhuysen, H. Deng, J. K. Kang, O. M. Yaghi and O. Terasaki, *Nat. Chem.*, 2019, **11**, 562–570.
- 18 A. Greenaway, B. Gonzalez-Santiago, P. M. Donaldson, M. D. Frogley, G. Cinque, J. Sotelo, S. Moggach, E. Shiko, S. Brandani, R. F. Howe and P. A. Wright, *Angew. Chemie Int. Ed.*, 2014, **53**, 13483–13487.
- 19 G. Pagès, V. Gilard, R. Martino and M. Malet-Martino, *Analyst*, 2017, **142**, 3771–3796.
- 20 R. Clarke, A. Gregory, D. Cannell, M. Patrick, S. Wylie, I. Youngs and G. Hill, 2003.
- 21 D. M. Pozar, *Microwave engineering*, Fourth edition. Hoboken, NJ : Wiley, [2012] ©2012.
- 22 E. G. Spencer, R. C. LeCraw and L. A. Ault, *J. Appl. Phys.*, 1957, **28**, 130–132.
- 23 A. Porch, D. Odili and P. Childs, *Nanoscale Res. Lett.*, 2012, **7**, 429.
- 24 J. A. Cuenca, E. Thomas, S. Mandal, O. Williams and A. Porch, *IEEE Trans. Microw. Theory Tech.*, 2015, **63**, 4110–4118.
- 25 B. Riddle, J. Baker-Jarvis and J. Krupka, *Microw. Theory Tech. IEEE Trans.*, 2003, **51**, 727–733.
- 26 A. L. Higginbotham Duque, W. L. Perry and C. M. Anderson-Cook, *Propellants, Explos. Pyrotech.*, 2014, **39**, 275–283.
- 27 J. Hartley, A. Porch and M. Jones, *Sensors Actuators B Chem.*, 2015, **210**, 726–730.

- 28 M. Barter, J. Hartley, F.-J. Yazigi, R. J. Marshall, R. S. Forgan, A. Porch and M. O. Jones, *Phys. Chem. Chem. Phys.*, 2018, **20**, 10460–10469.
- 29 K. T. Mathew and U. Raveendranath, *Sensors Updat.*, 2000, **7**, 185–210.
- 30 M. Barter, S. Partridge, D. Slocombe and A. Porch, *IEEE Trans. Microw. Theory Tech.*, 2018, **PP**, 1–6.
- 31 J. Cuenca, D. Slocombe and A. Porch, *IEEE Trans. Microw. Theory Tech.*, 2017, **PP**, 1–9.
- 32 J. Winarta, B. Shan, S. M. McIntyre, L. Ye, C. Wang, J. Liu and B. Mu, *Cryst. Growth Des.*, 2020, **20**, 1347–1362.
- 33 C. Janiak and J. K. Vieth, *New J. Chem.*, 2010, **34**, 2366–2388.
- 34 D. V Patil, P. B. S. Rallapalli, G. P. Dangi, R. J. Tayade, R. S. Somani and H. C. Bajaj, *Ind. Eng. Chem. Res.*, 2011, **50**, 10516–10524.
- 35 B. Van de Voorde, B. Bueken, J. Denayer and D. De Vos, *Chem. Soc. Rev.*, 2014, **43**, 5766–5788.
- 36 C. Duan, Y. Yu, J. Xiao, X. Zhang, L. Li, P. Yang, J. Wu and H. Xi, *Sci. CHINA Mater.*, 2020, **63**, 667–685.
- 37 J. Hajek, C. Caratelli, R. Demuyne, K. De Wispelaere, L. Vanduyfhuys, M. Waroquier and V. Van Speybroeck, *Chem. Sci.*, 2018, **9**, 2723–2732.
- 38 T. Duerinck, R. Bueno-Perez, F. Vermoortele, D. E. De Vos, S. Calero, G. V Baron and J. F. M. Denayer, *J. Phys. Chem. C*, 2013, **117**, 12567–12578.
- 39 N. Prasetya and B. P. Ladewig, *J. Mater. Chem. A*, 2019, **7**, 15164–15172.
- 40 X. Liu, *Front. Chem. Sci. Eng.*, 2020, **14**, 216–232.
- 41 C. Wang, X. Liu, N. Keser Demir, J. P. Chen and K. Li, *Chem. Soc. Rev.*, 2016, **45**, 5107–5134.
- 42 W. Zhao, C. Zhang, Z. Yan, Y. Zhou, J. Li, Y. Xie, L. Bai, L. Jiang and F. Li, *PLoS One*, , DOI:10.1371/journal.pone.0178513.
- 43 T. G. Grissom, C. H. Sharp, P. M. Usov, D. Troya, A. J. Morris and J. R. Morris, *J. Phys. Chem. C*, 2018, **122**, 16060–16069.
- 44 Y. Weng, S. Qiu, L. Ma, Q. Liu, M. Ding, Q. Zhang, Q. Zhang and T. Wang, *Catal.* , 2015, **5**.
- 45 C. D. Baertsch, H. H. Funke, J. L. Falconer and R. D. Noble, *J. Phys. Chem.*, 1996, **100**, 7676–

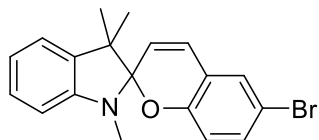
- 7679.
- 46 A. Perea-Cachero, J. Sánchez-Laínez, B. Zornoza, E. Romero-Pascual, C. Téllez and J. Coronas, *Dalt. Trans.*, 2019, **48**, 3392–3403.
- 47 T. Loiseau, C. Serre, C. Huguenard, G. Fink, F. Taulelle, M. Henry, T. Bataille and G. Férey, *Chem. – A Eur. J.*, 2004, **10**, 1373–1382.
- 48 W. Lu, Z. Wei, Z.-Y. Gu, T.-F. Liu, J. Park, J. Park, J. Tian, M. Zhang, Q. Zhang, T. Gentle III, M. Bosch and H.-C. Zhou, *Chem. Soc. Rev.*, 2014, **43**, 5561–5593.
- 49 Z. Yan, J. Zheng, J. Chen, P. Tong, M. Lu, Z. Lin and L. Zhang, *J. Chromatogr. A*, 2014, **1366**, 45–53.
- 50 J. A. Cuenca, Cardiff, 2015.
- 51 A. Peristy, P. N. Nesterenko, A. Das, D. M. D’Alessandro, E. F. Hilder and R. D. Arrua, *Chem. Commun.*, 2016, **52**, 5301–5304.
- 52 H. Liu, J. W. Finch and J. C. Gebler, *Anal. Chem.*, 2007, **79**, 2961–2964.
- 53 H. Hu, J. Zhu, F. Yang, Z. Chen, M. Deng, L. Weng, Y. Ling and Y. Zhou, *Chem. Commun.*, 2019, **55**, 6495–6498.
- 54 K. J. Hartlieb, J. M. Holcroft, P. Z. Moghadam, N. A. Vermeulen, M. M. Algaradah, M. S. Nassar, Y. Y. Botros, R. Q. Snurr and J. F. Stoddart, *J. Am. Chem. Soc.*, 2016, **138**, 2292–2301.
- 55 A. A. Maryott and E. R. Smith, *Table of dielectric constants of pure liquids*, U.S. Gov. Print. Office, Washington, D.C., 1951.
- 56 K. NAGY and K. VÉKEY, eds. K. Vékey, A. Telekes and A. B. T.-M. A. of M. S. Vertes, Elsevier, Amsterdam, 2008, pp. 61–92.
- 57 M. Maes, F. Vermoortele, L. Alaerts, S. Couck, C. E. A. Kirschhock, J. F. M. Denayer and D. E. De Vos, *J. Am. Chem. Soc.*, 2010, **132**, 15277–15285.
- 58 W.-W. Zhao, C.-Y. Zhang, Z.-G. Yan, L.-P. Bai, X. Wang, H. Huang, Y.-Y. Zhou, Y. Xie, F.-S. Li and J.-R. Li, *J. Chromatogr. A*, 2014, **1370**, 121–128.
- 59 C. Caratelli, J. Hajek, F. G. Cirujano, M. Waroquier, F. X. Llabrés i Xamena and V. Van Speybroeck, *J. Catal.*, 2017, **352**, 401–414.
- 60 R. Navarro, L. Cirre, M. Carboni and D. Meyer, *J. Environ. Manage.*, 2018, **214**, 17.

- 61 M. A. Granato, V. D. Martins, A. F. P. Ferreira and A. E. Rodrigues, *Microporous Mesoporous Mater.*, 2014, **190**, 165–170.
- 62 W. Morris, R. E. Taylor, C. Dybowski, O. M. Yaghi and M. A. Garcia-Garibay, *J. Mol. Struct.*, 2011, **1004**, 94–101.
- 63 A. Schaate, P. Roy, A. Godt, J. Lippke, F. Waltz, M. Wiebcke and P. Behrens, *Chem. – A Eur. J.*, 2011, **17**, 6643–6651.

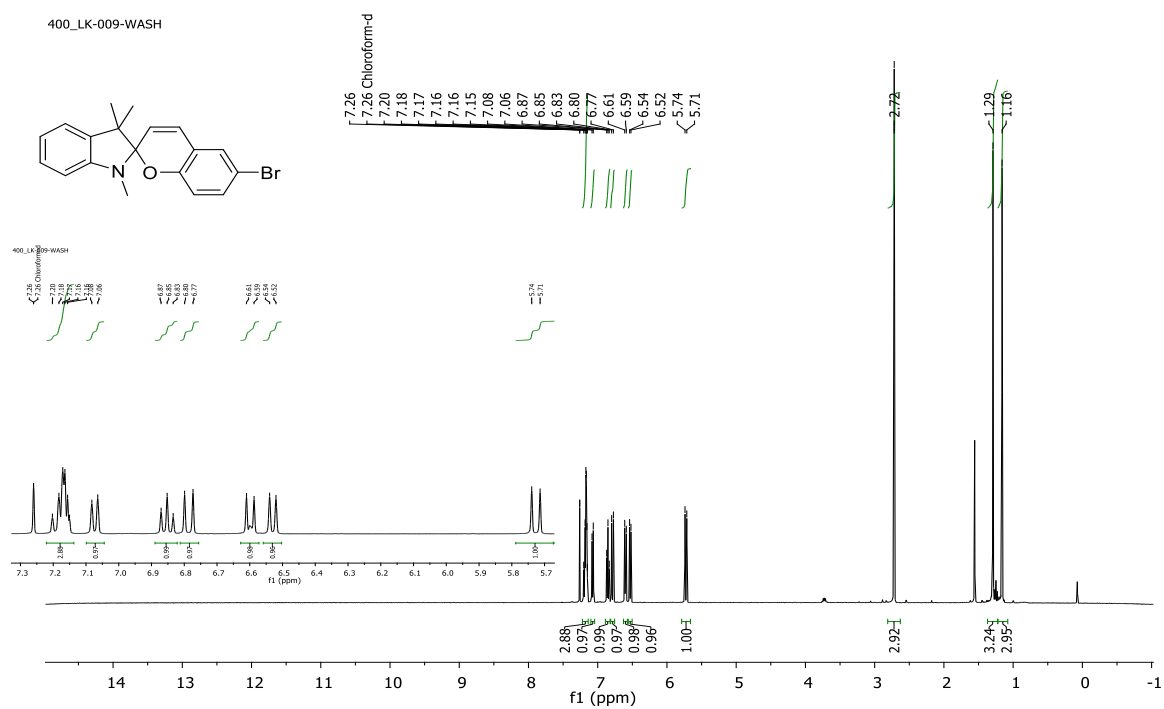
# Appendix

S1

## 6-Bromo-1',3',3'-trimethylspiro[chromene-2,2'-indoline] (1)



$^1\text{H}$

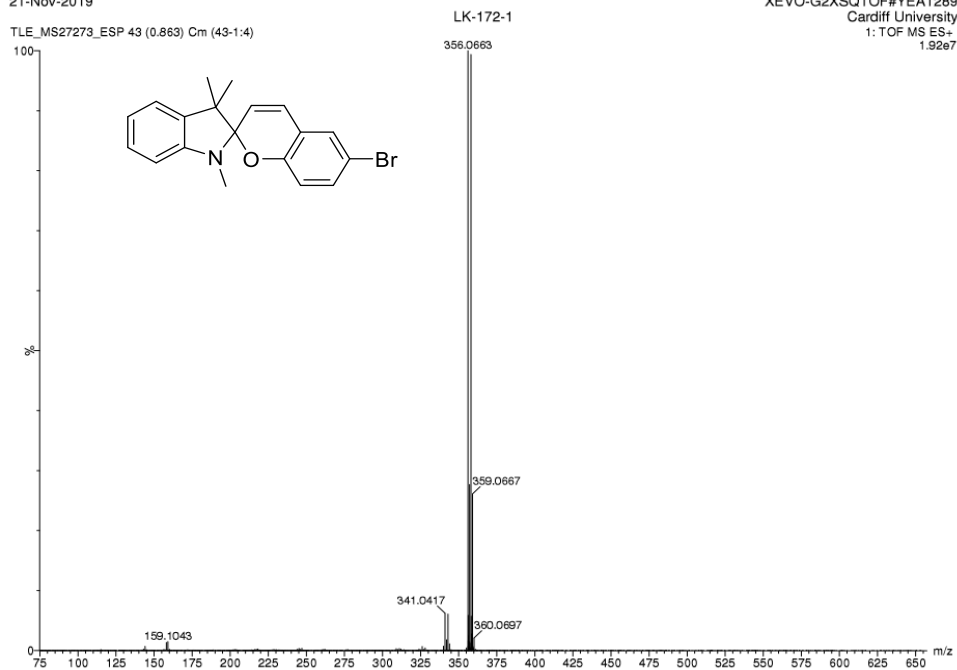


MS

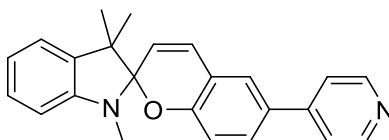
21-Nov-2019

TLE\_MS27273\_ESP 43 (0.883) Cm (43-1-4)

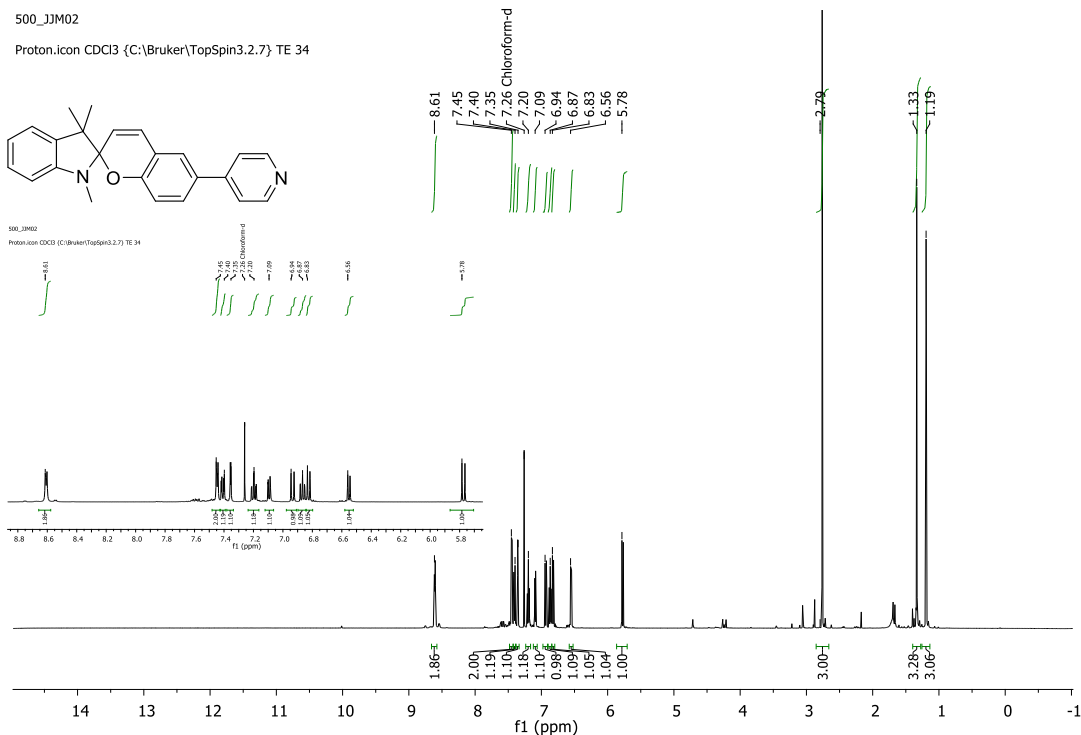
XEVO-G2XSQTOF#YEA1289  
Cardiff University  
1: TOF MS ES+  
1.92e7



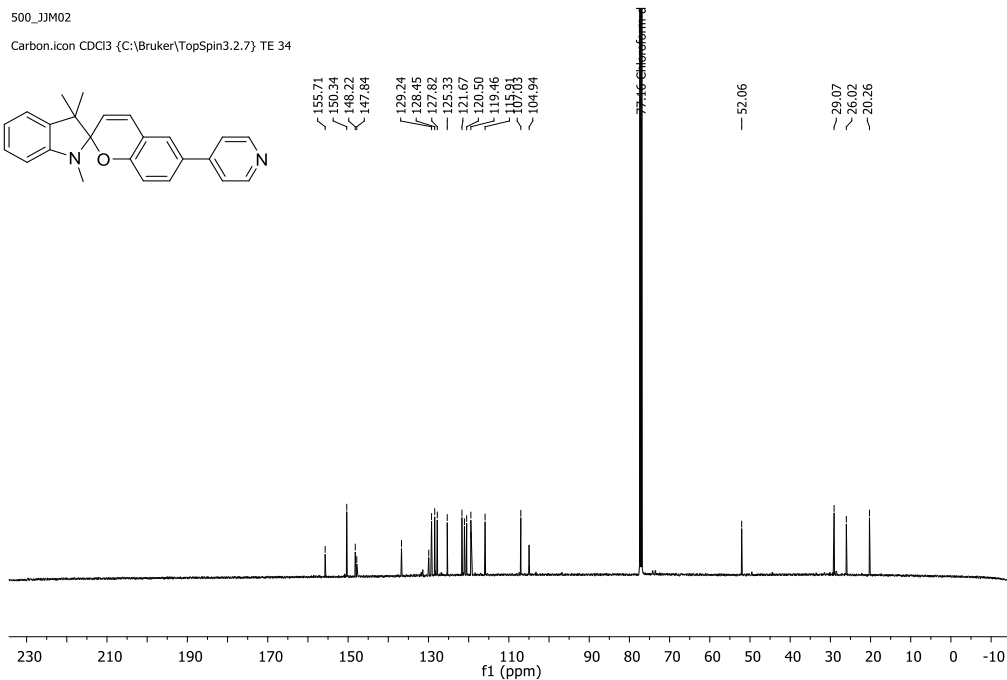
### 1',3',3'-trimethyl-6-(pyridin-4-yl)spiro[chromene-2,2'-indoline] (4a)



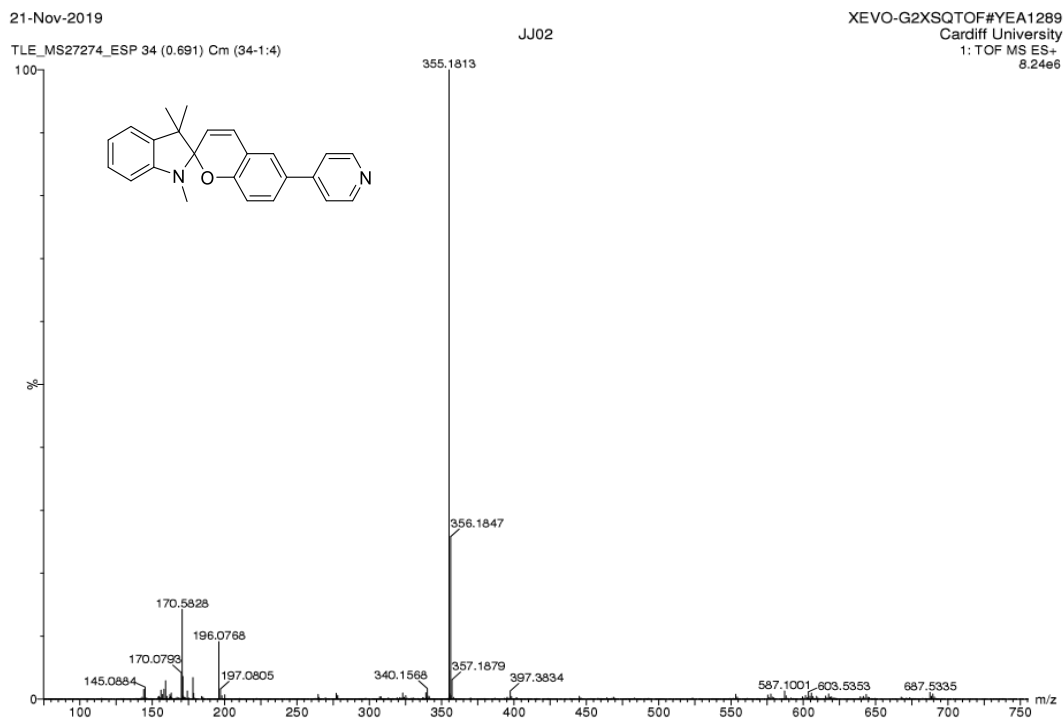
<sup>1</sup>H



<sup>13</sup>C

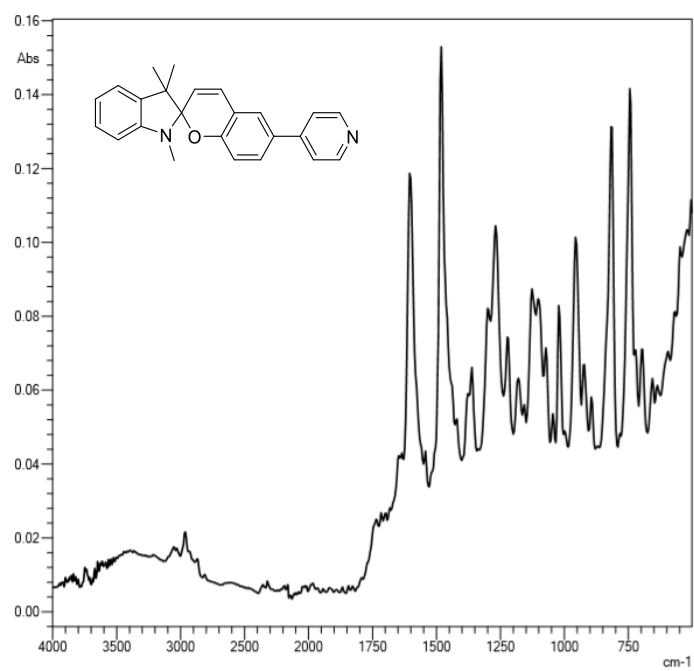


## MS

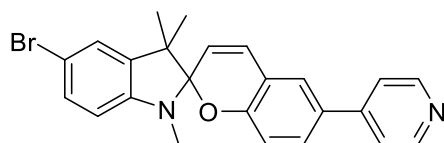


## IR





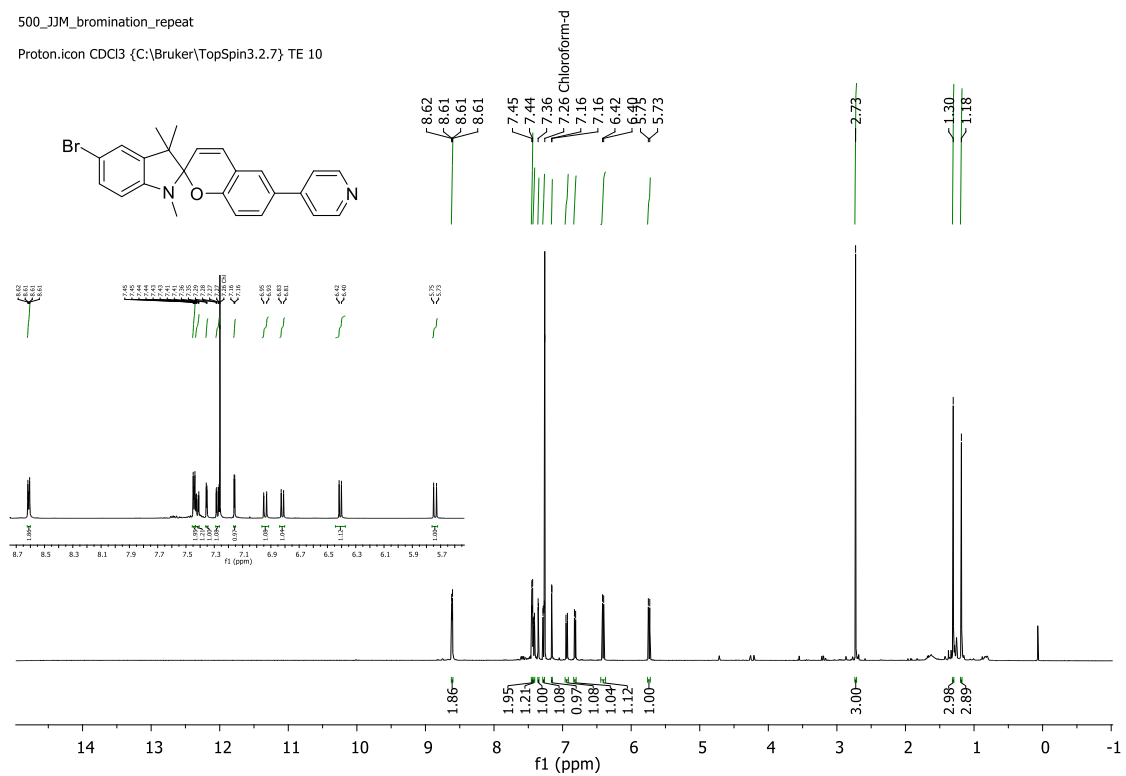
**5'-bromo-1',3',3'-trimethyl-6-(pyridine-4-yl)spiro[chromene-2,2'-indoline] (5a)**



**<sup>1</sup>H**

500\_JJM\_bromination\_repeat

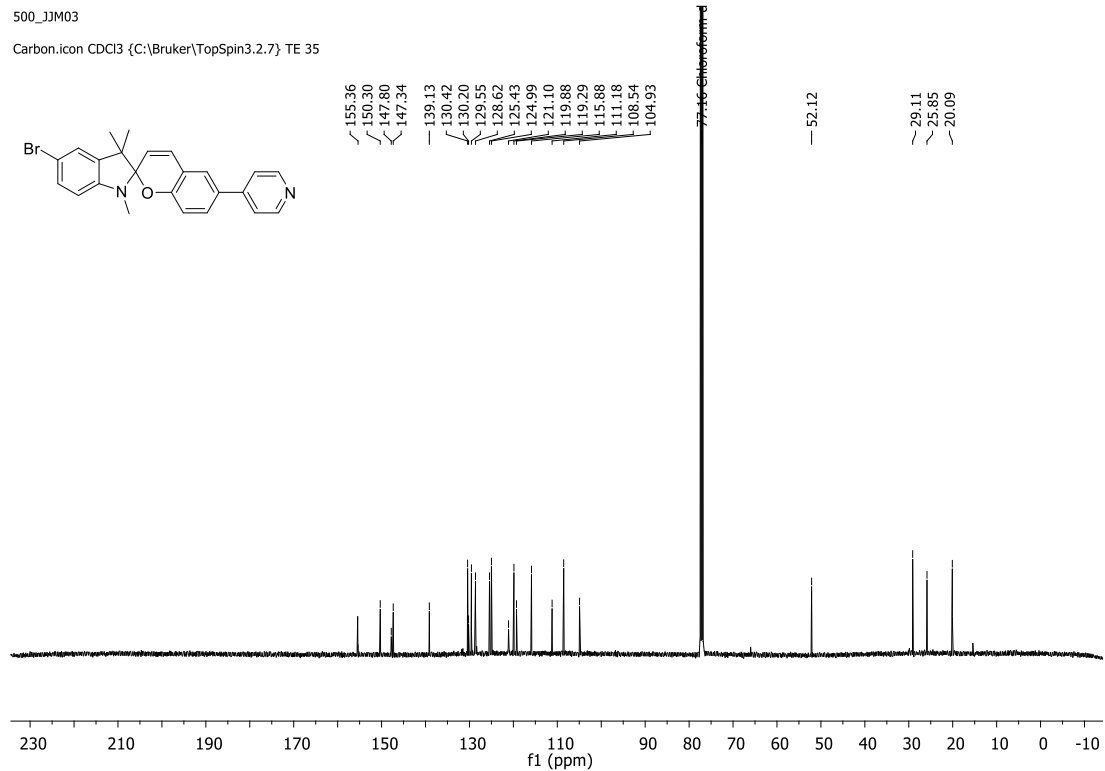
Proton.icon CDCl3 {C:\Bruker\TopSpin3.2.7} TE 10



### <sup>13</sup>C

500\_JJM03

Carbon.icon CDCl3 {C:\Bruker\TopSpin3.2.7} TE 35



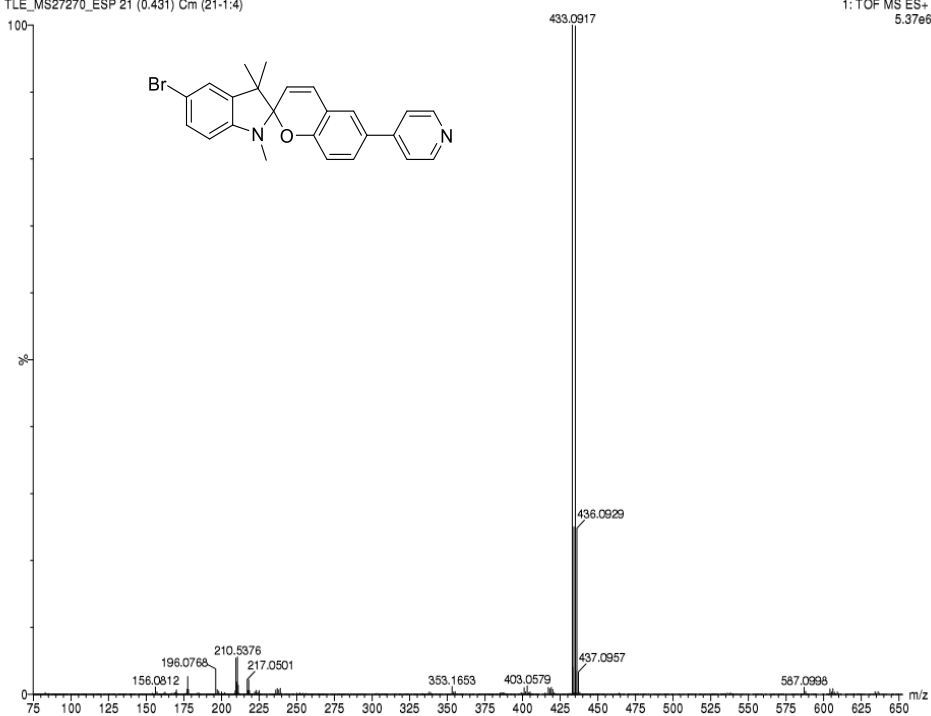
### MS

21-Nov-2019

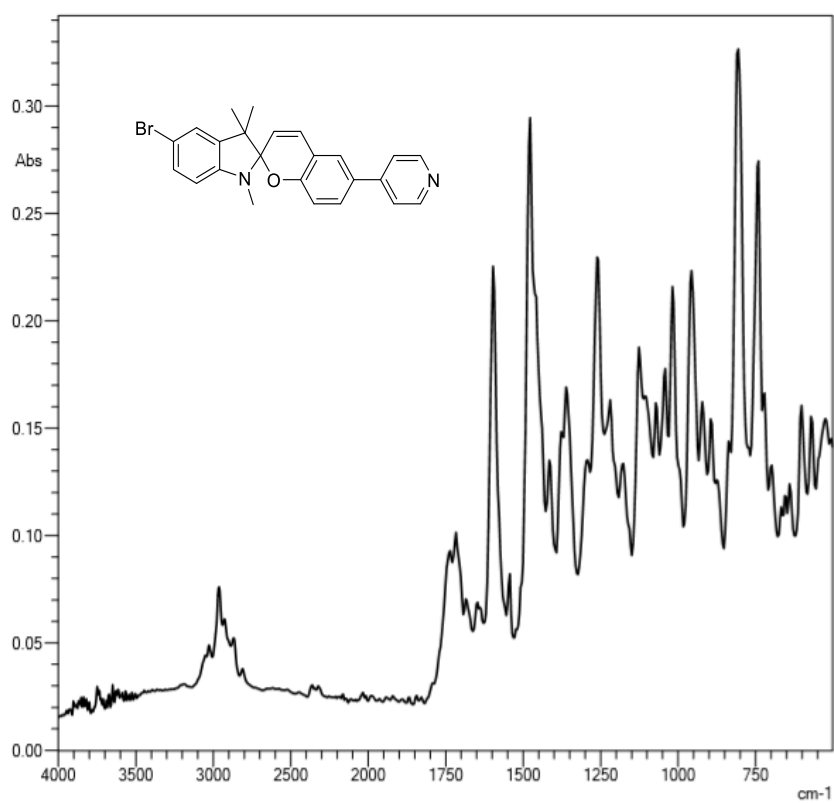
TLE\_MS27270\_ESP 21 (0.431) Cm (21-1:4)

JJM03

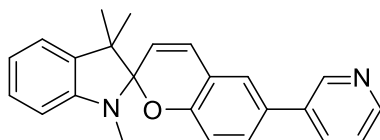
XEVO-G2XSQTOF#YEA1289  
Cardiff University  
1: TOF MS ES+  
5.37e6



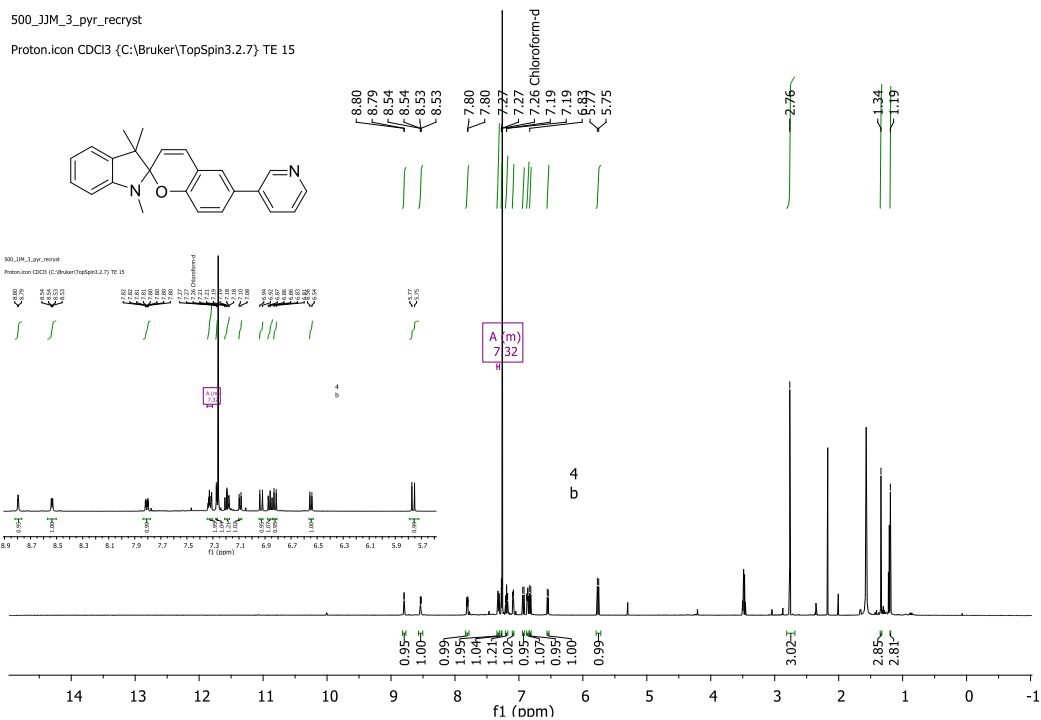
IR



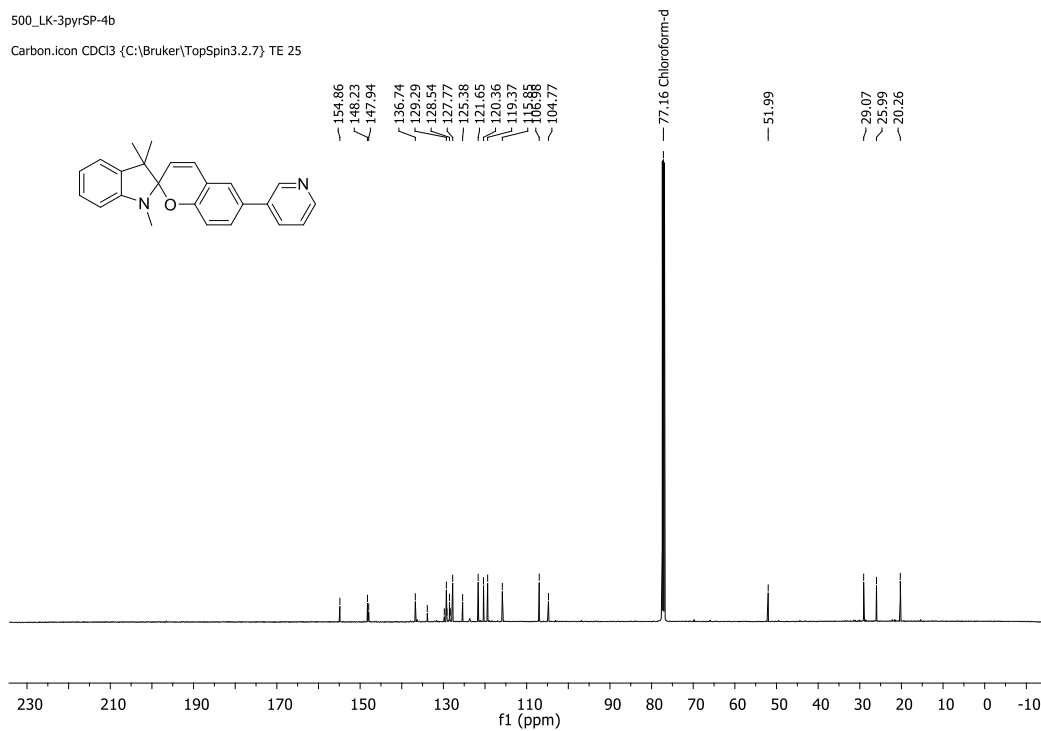
**1',3',3'-trimethyl-6-(pyridine-3-yl)spiro[chromene-2,2'-indoline] (4b)**



**<sup>1</sup>H**



**<sup>13</sup>C**



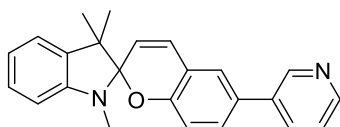
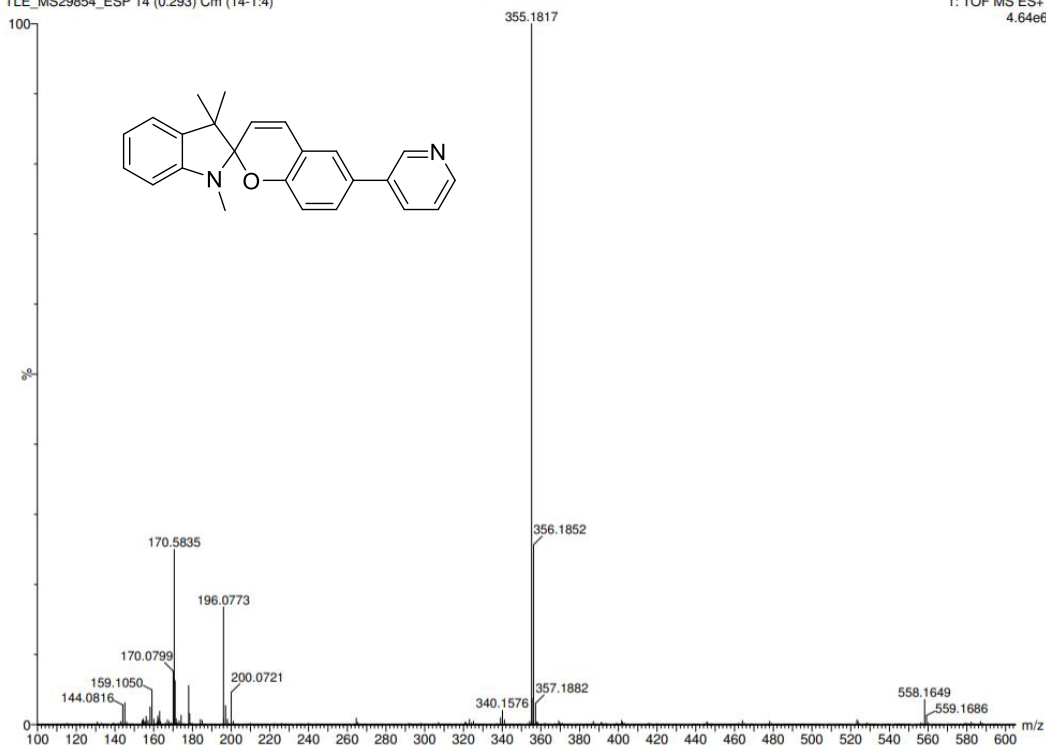
**MS**

20-Feb-2020

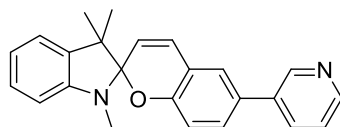
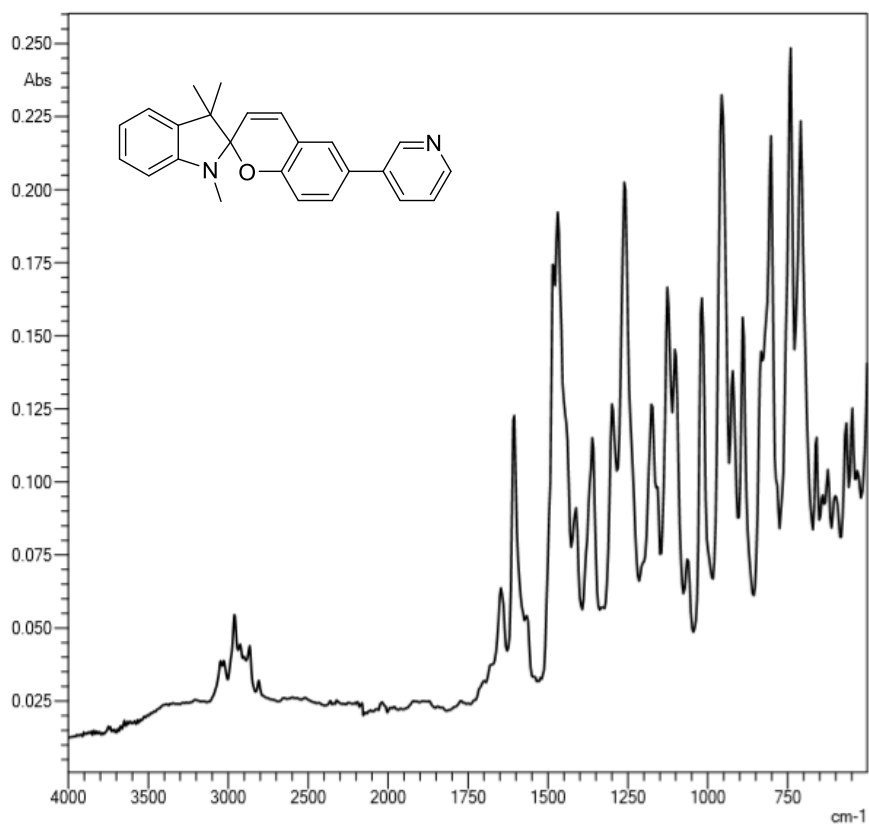
XEVO-G2XSQTOF#YEA1289  
Cardiff University  
1: TOF MS ES+  
4.64e6

TLE\_MS29854\_ESP 14 (0.293) Cm (14:1:4)

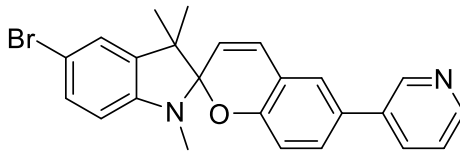
JJM3PYRR



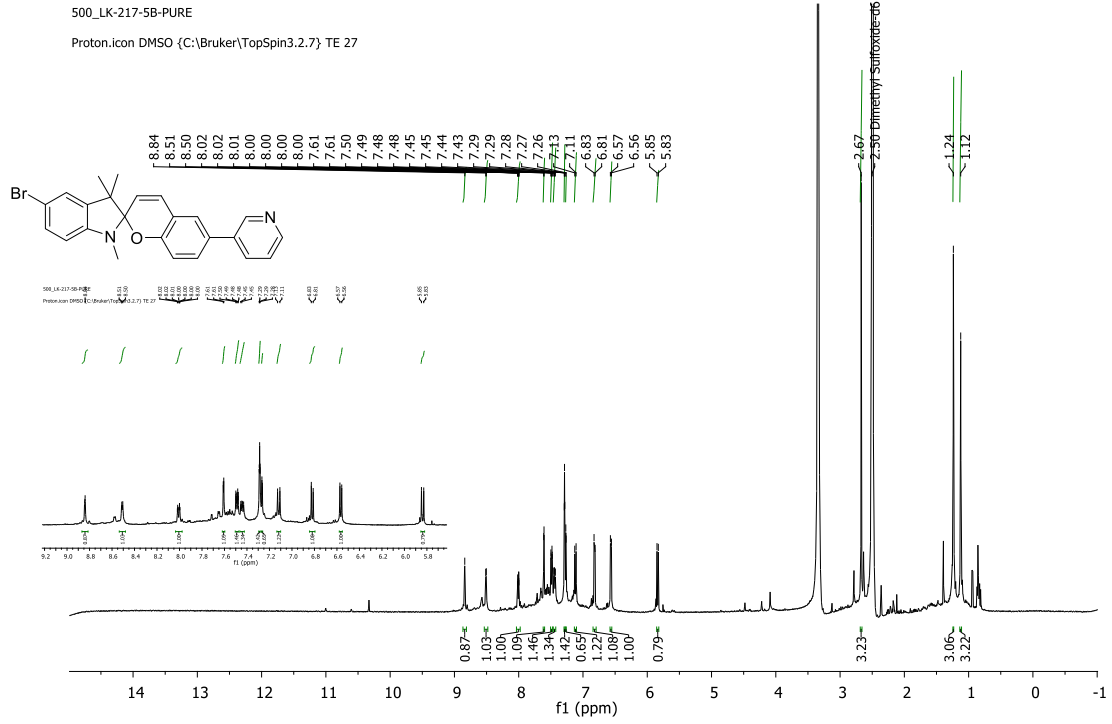
IR



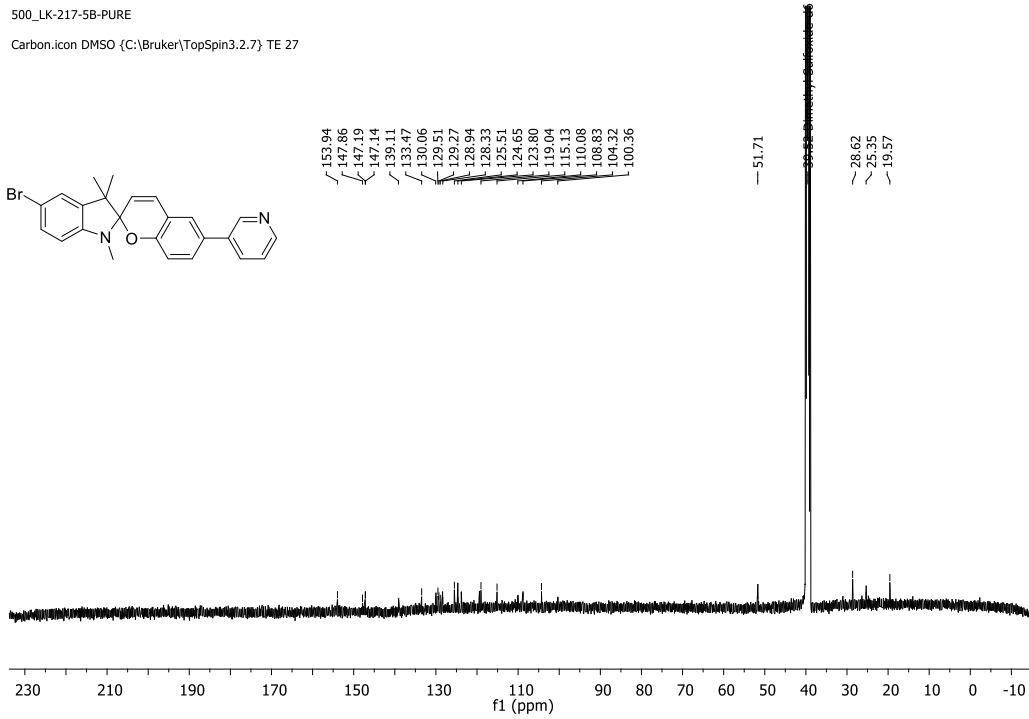
**5'-bromo-1',3',3'-trimethyl-6-(pyridin-3-yl)spiro[chromene-2,2'-indoline] (5b)**



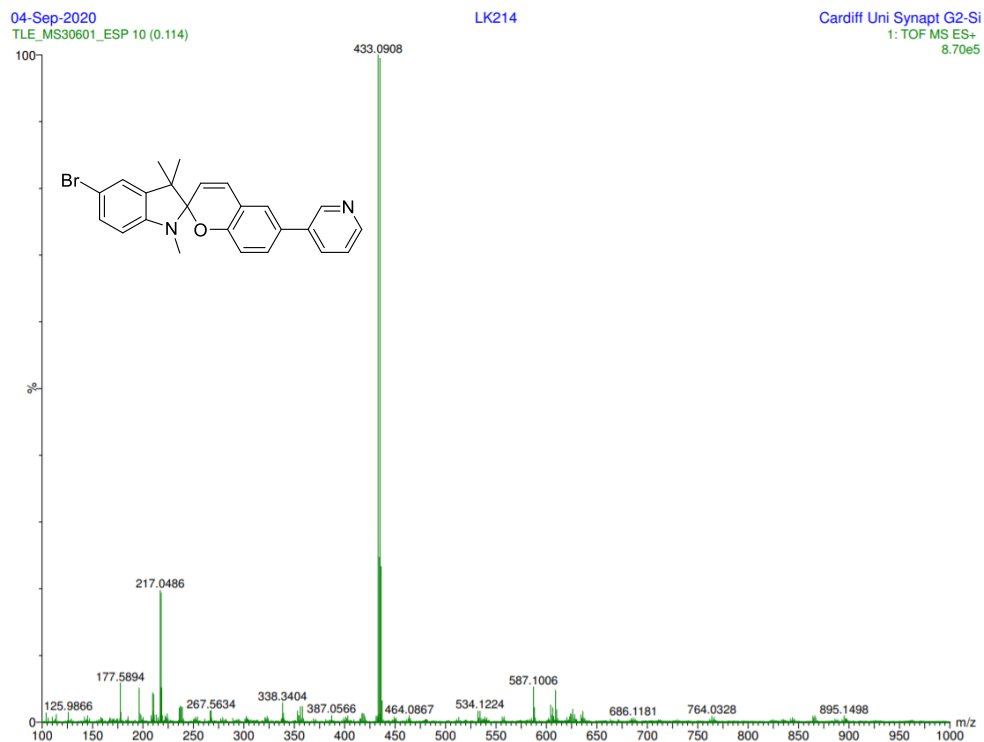
**<sup>1</sup>H**



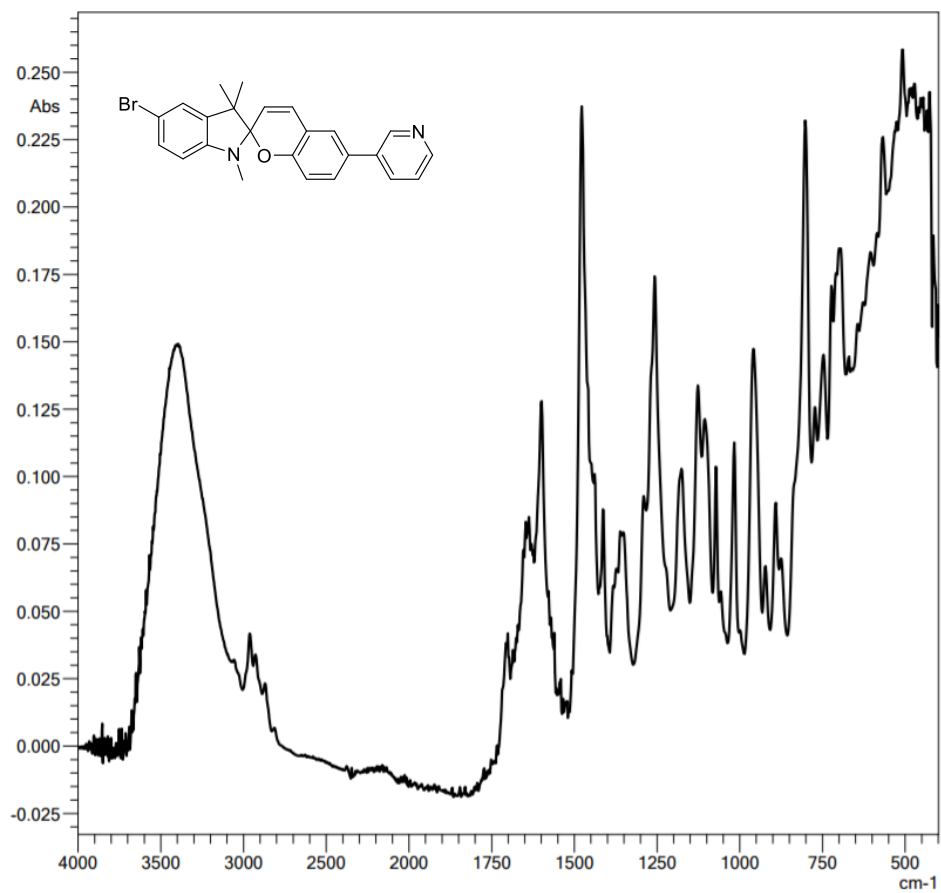
**<sup>13</sup>C**



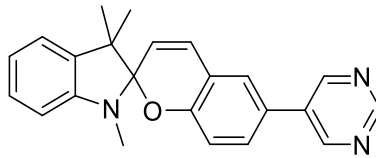
**MS**



## IR



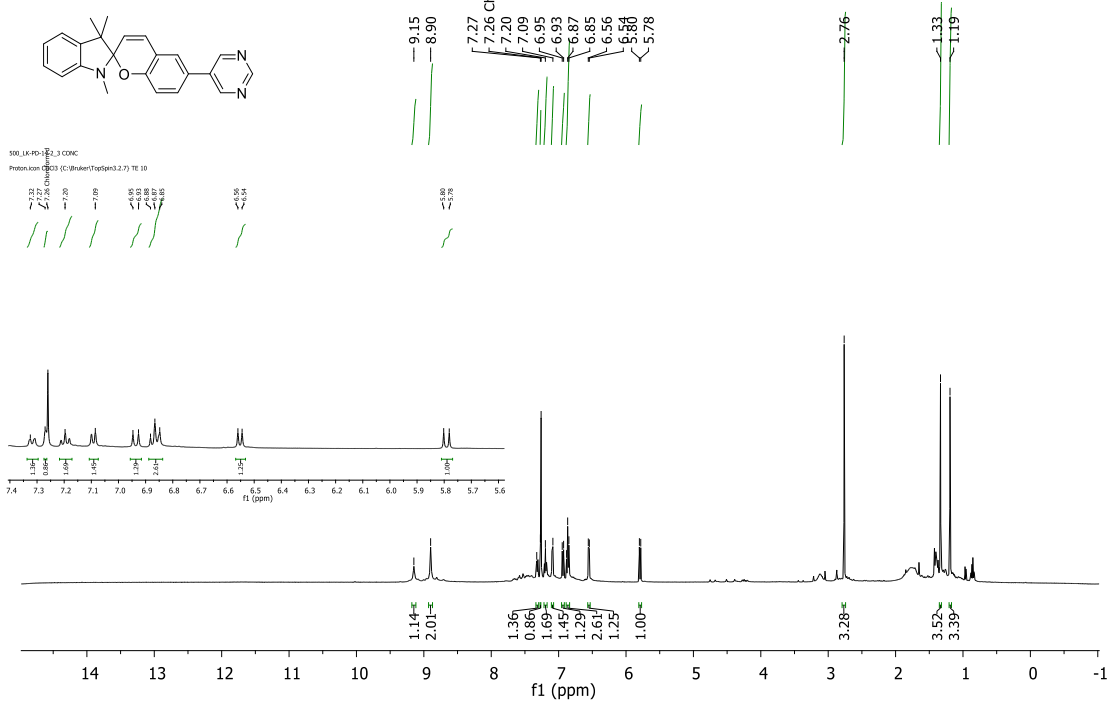
**1',3',3'-trimethyl-6-(pyrimidin-5-yl)spiro[chromene-2,2'-indoline] (4c)**



### <sup>1</sup>H

500\_LK-PD-14-2\_3 CONC

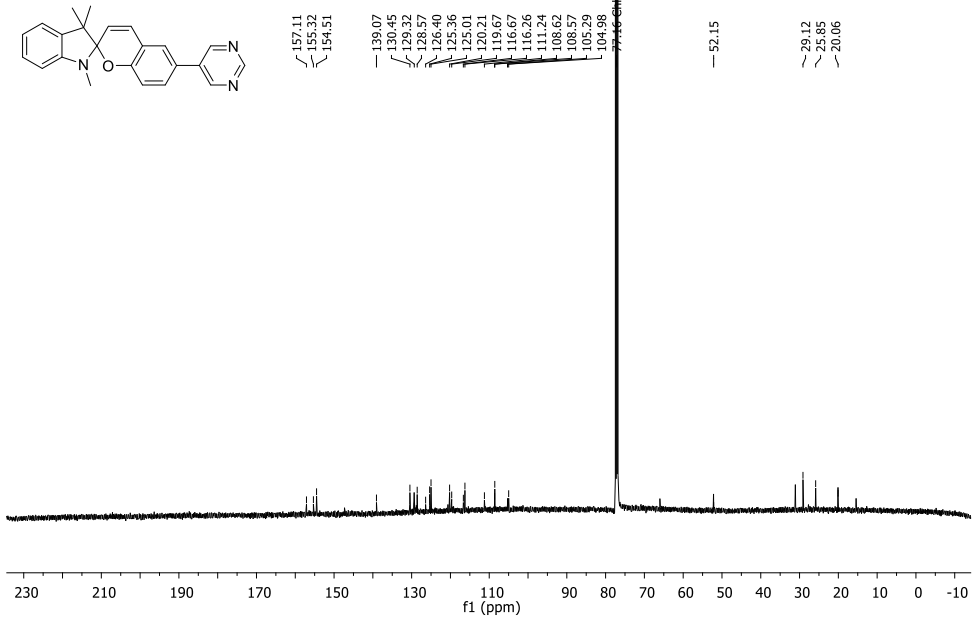
Proton.icon CDCl3 {C:\Bruker\TopSpin3.2.7} TE 10



### <sup>13</sup>C

500\_JJM\_pym\_recryst

Carbon.icon CDCl3 {C:\Bruker\TopSpin3.2.7} TE 40



### MS

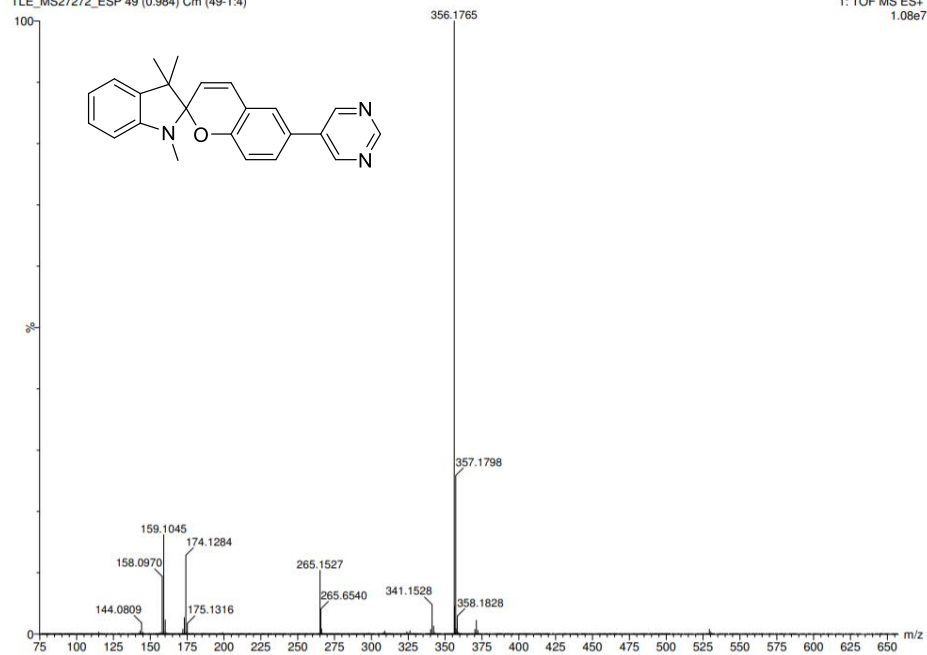


21-Nov-2019

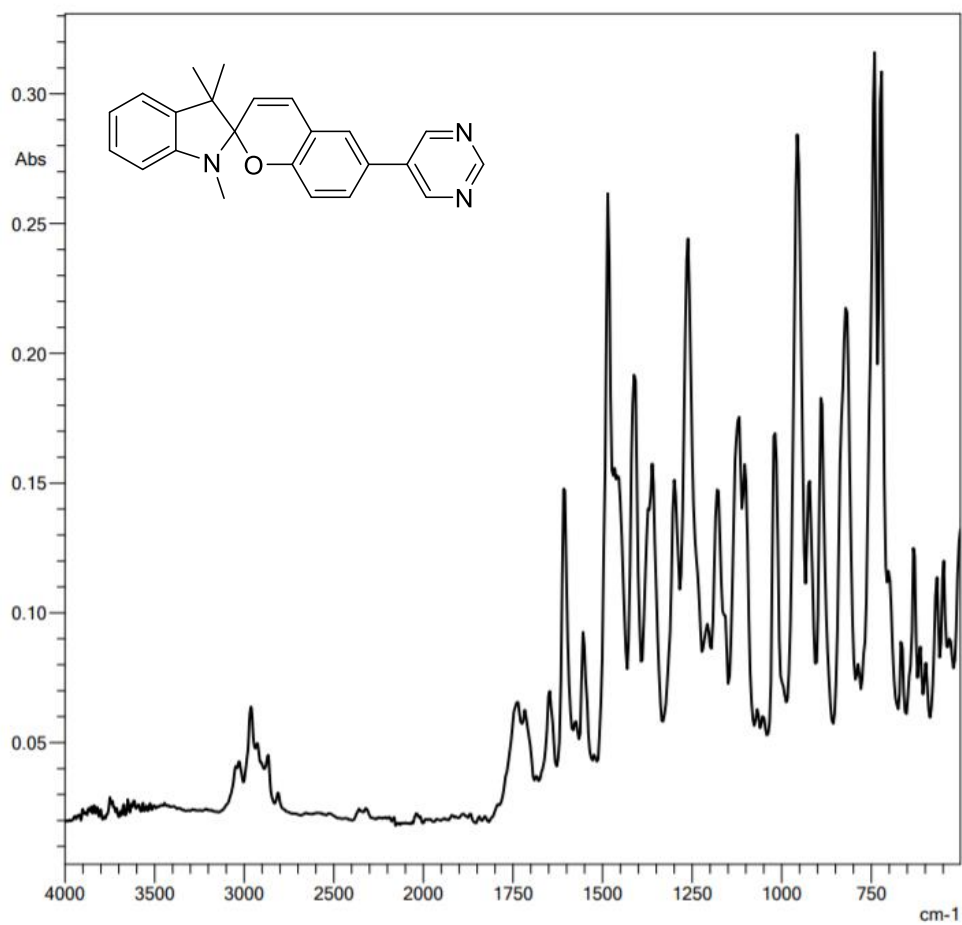
TLE\_MS27272\_ESP 49 (0.984) Cm (49-1:4)

PD-14-213

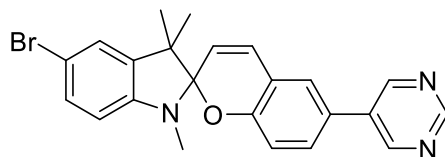
XEVO-G2XSQTOF#YEA1289  
Cardiff University  
1: TOF MS ES+  
1.08e7



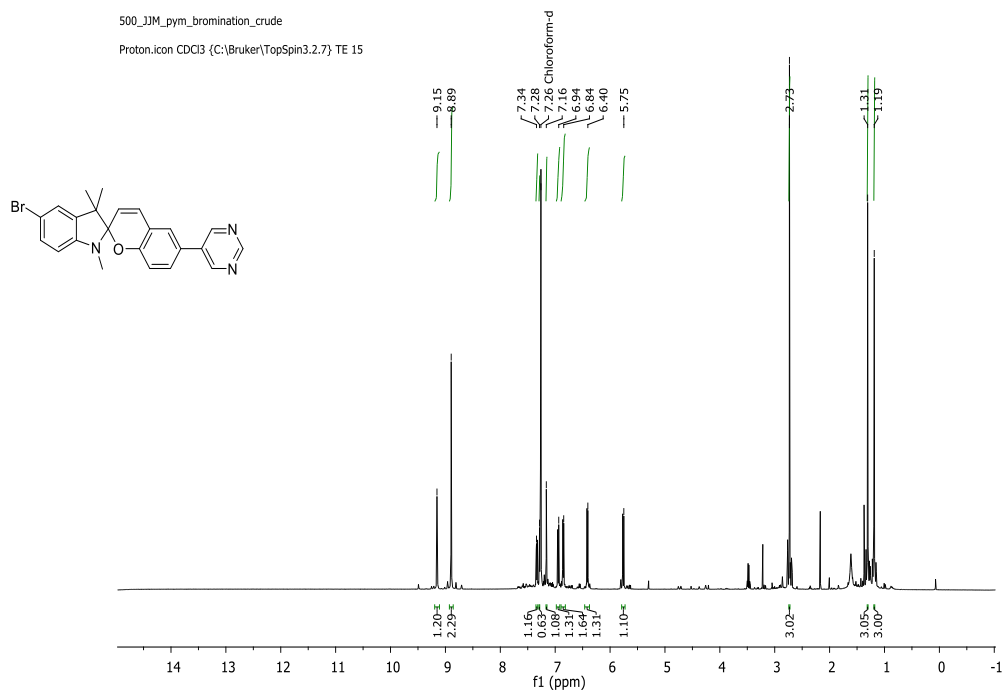
## IR



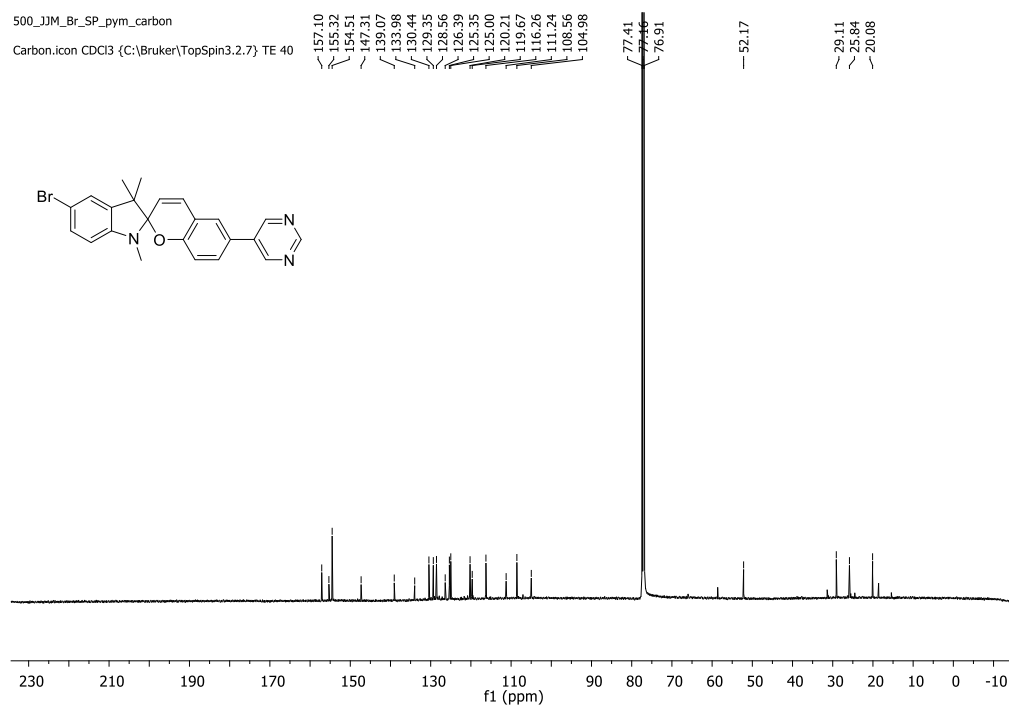
**5'-bromo-1',3',3'-trimethyl-6-(pyrimidin-5-yl)spiro[chromene-2,2'-indoline] (5c)**



<sup>1</sup>H



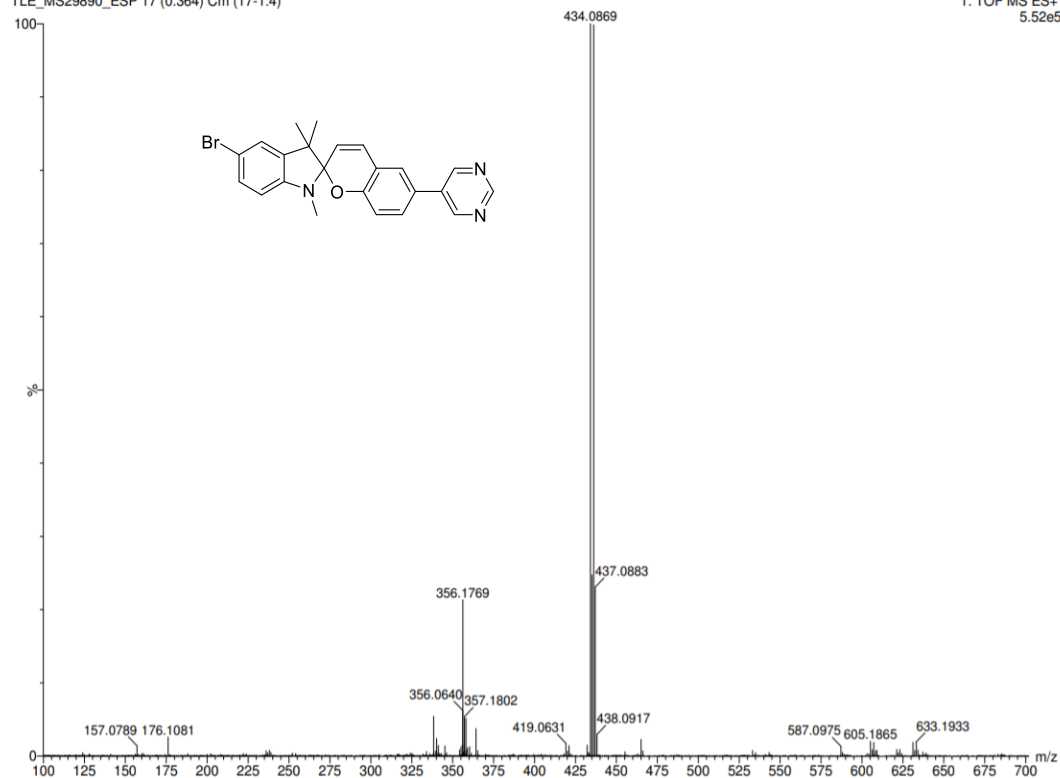
<sup>13</sup>C



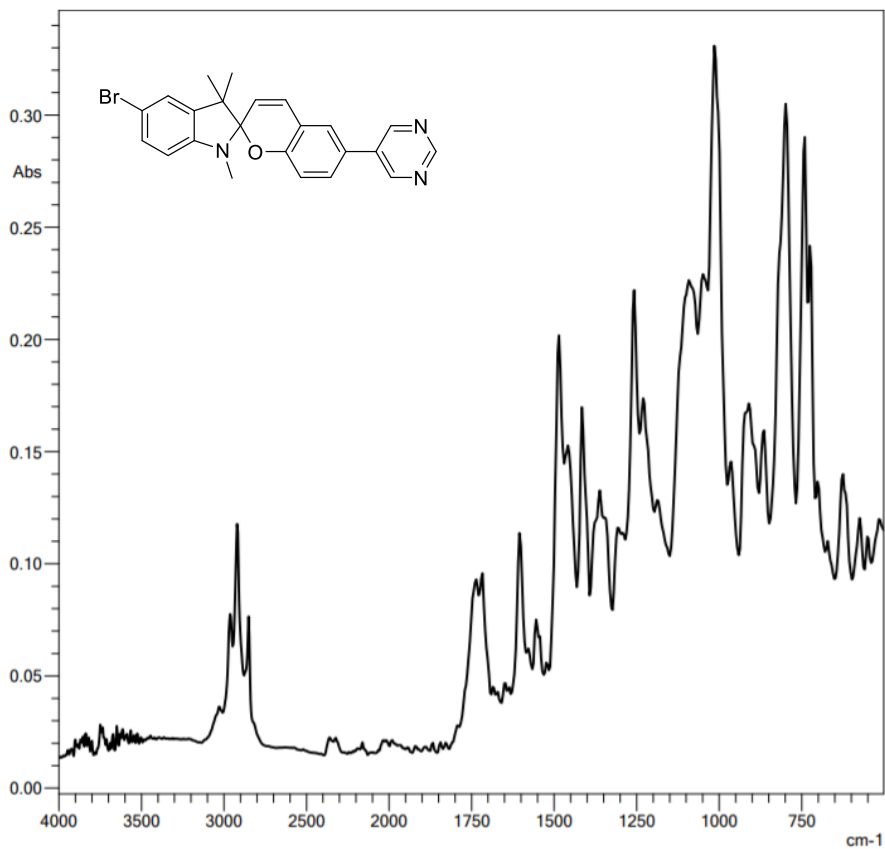
MS

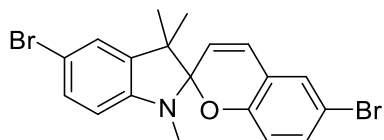
TLE\_MS29890\_ESP 17 (0.364) Cm (17:1:4)

JJMBRPYM

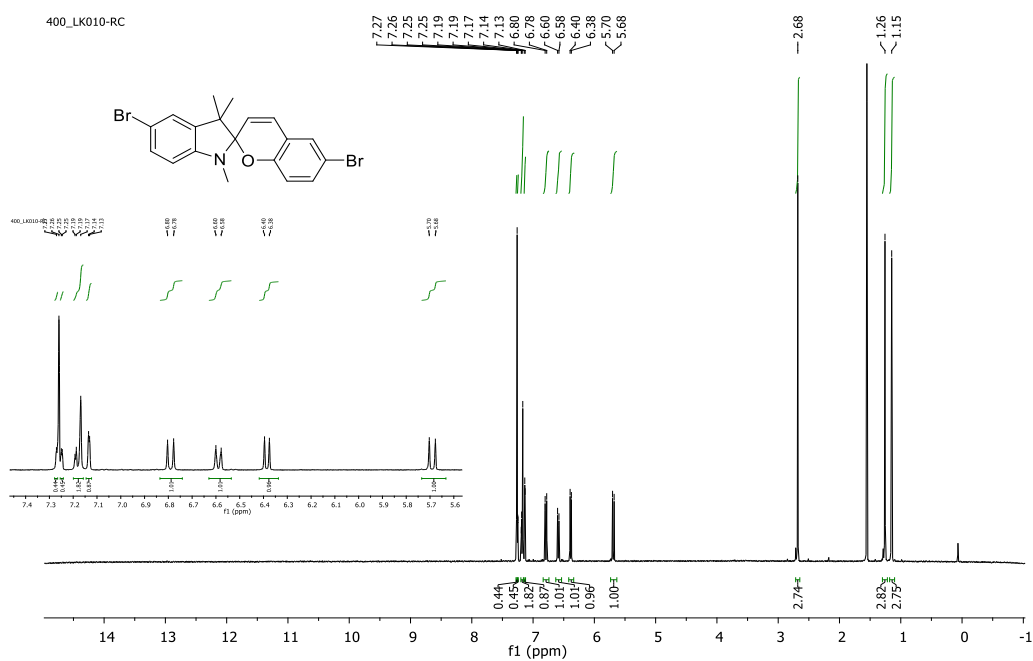


IR

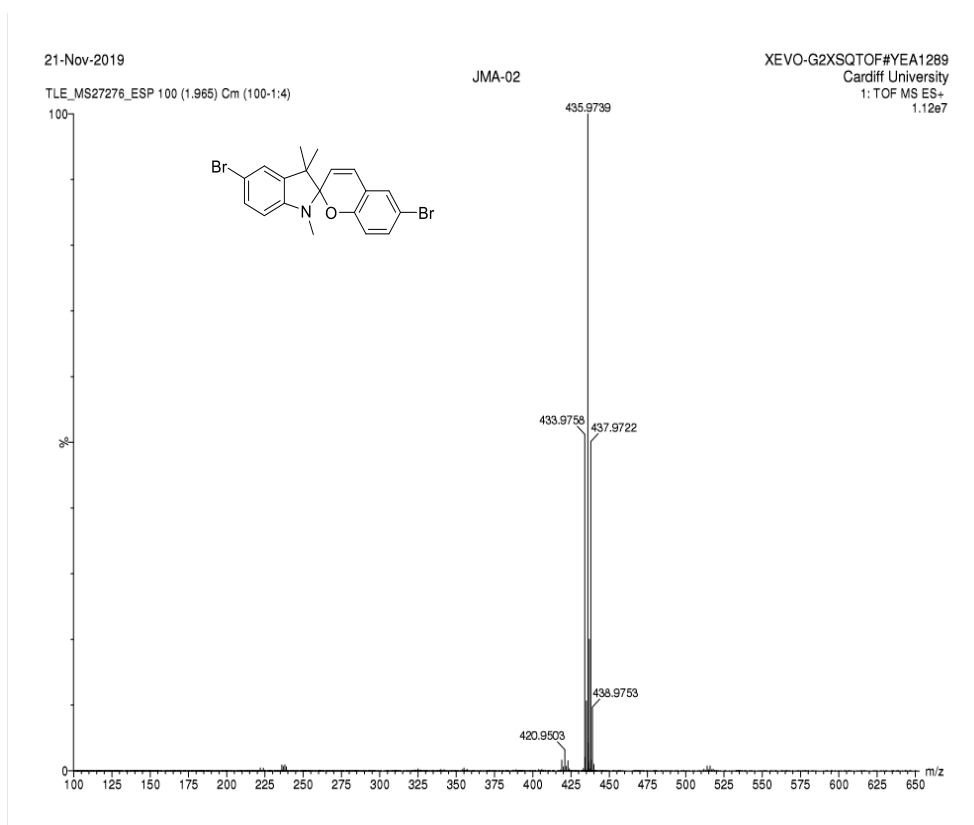
**5',6-dibromo-1',3',3'-trimethylspiro[chromene-2,2'-indoline] (2)**



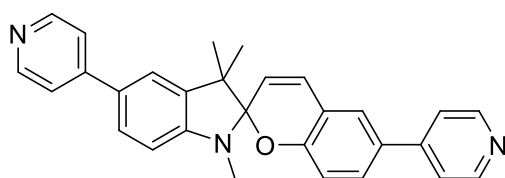
**<sup>1</sup>H**



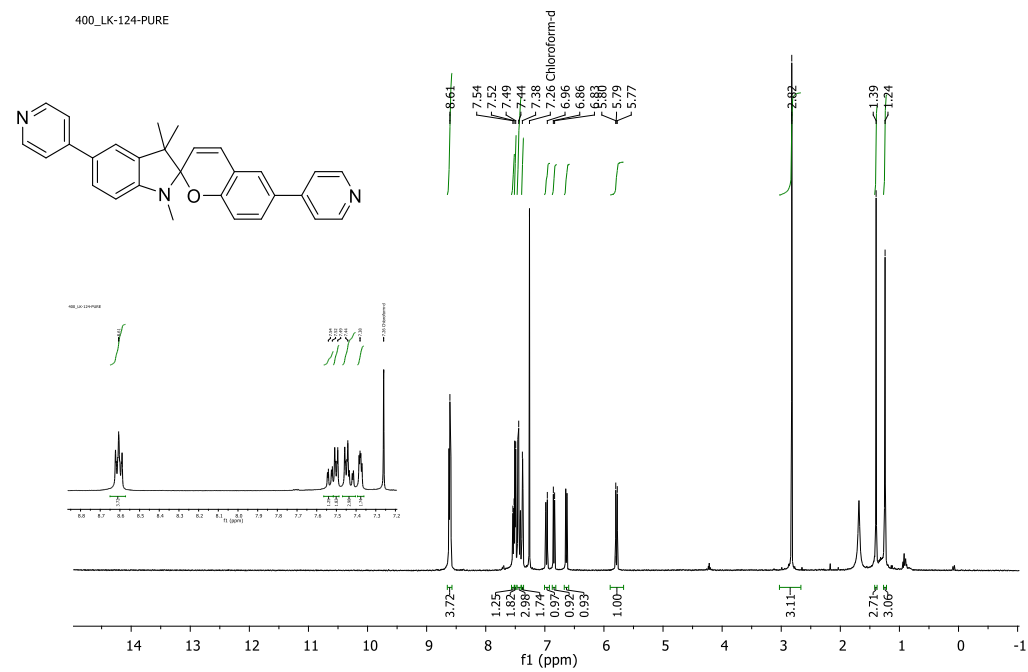
**MS**



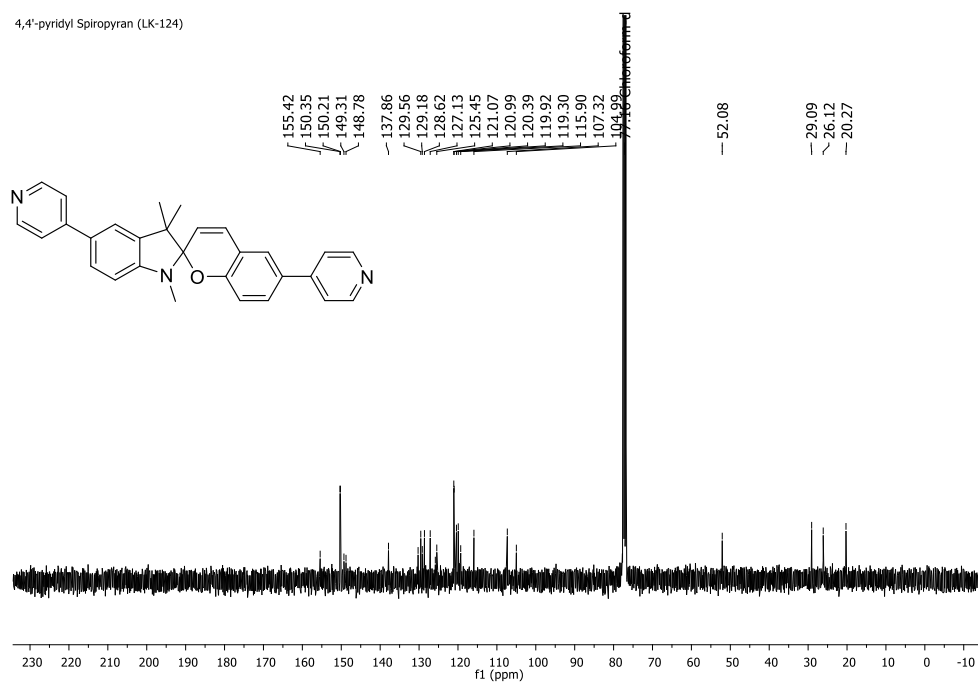
**1',3',3'-trimethyl-5',6-di(pyridin-4-yl)spiro[chromene-2,2'-indoline] (3a)**



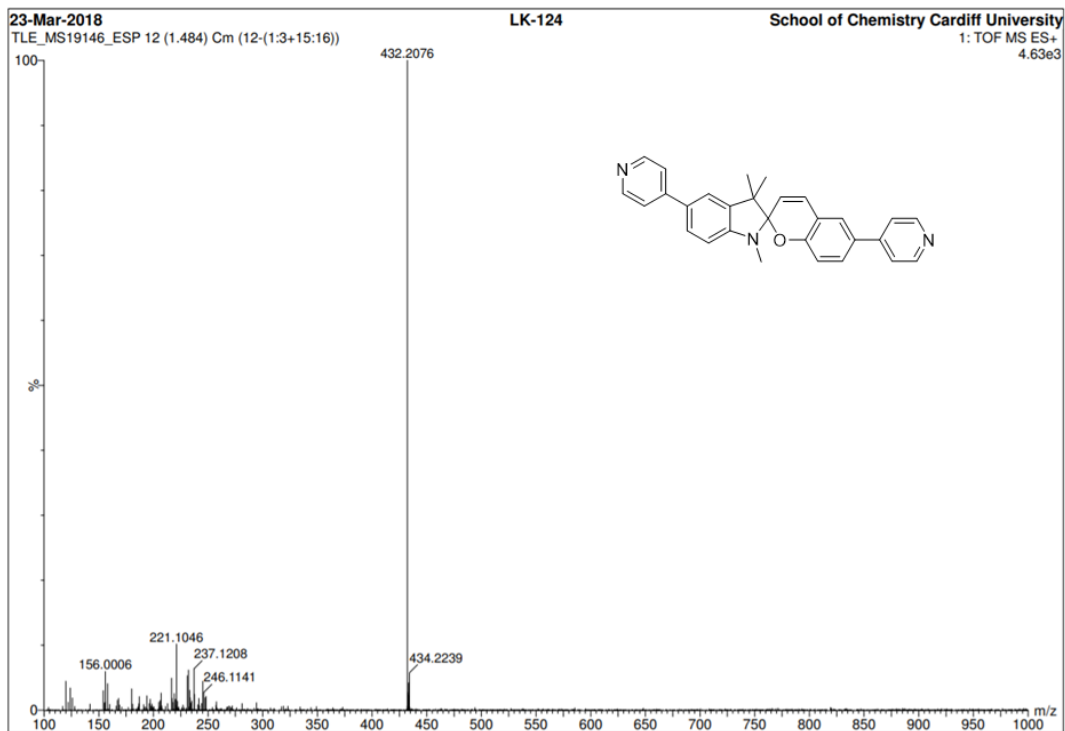
**<sup>1</sup>H**



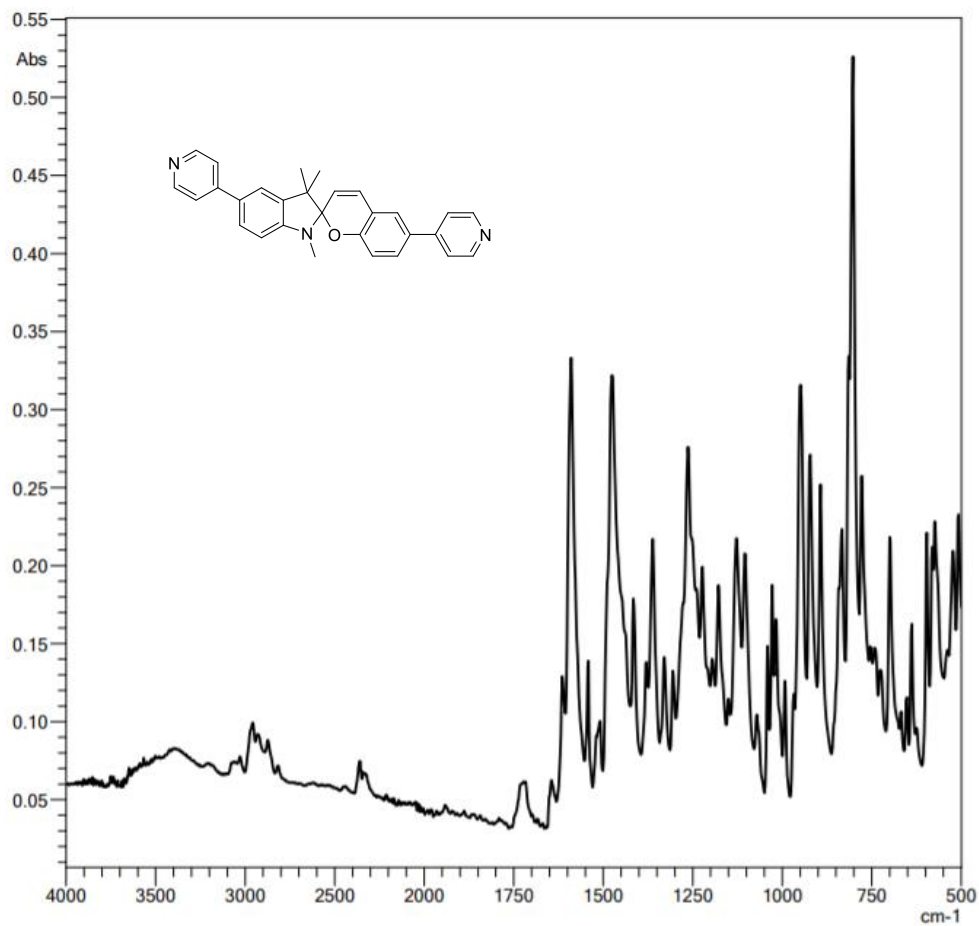
**<sup>13</sup>C**



**MS**



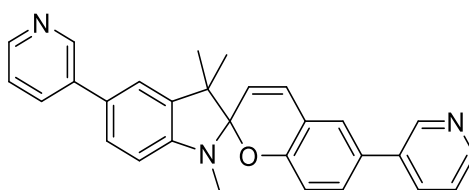
IR



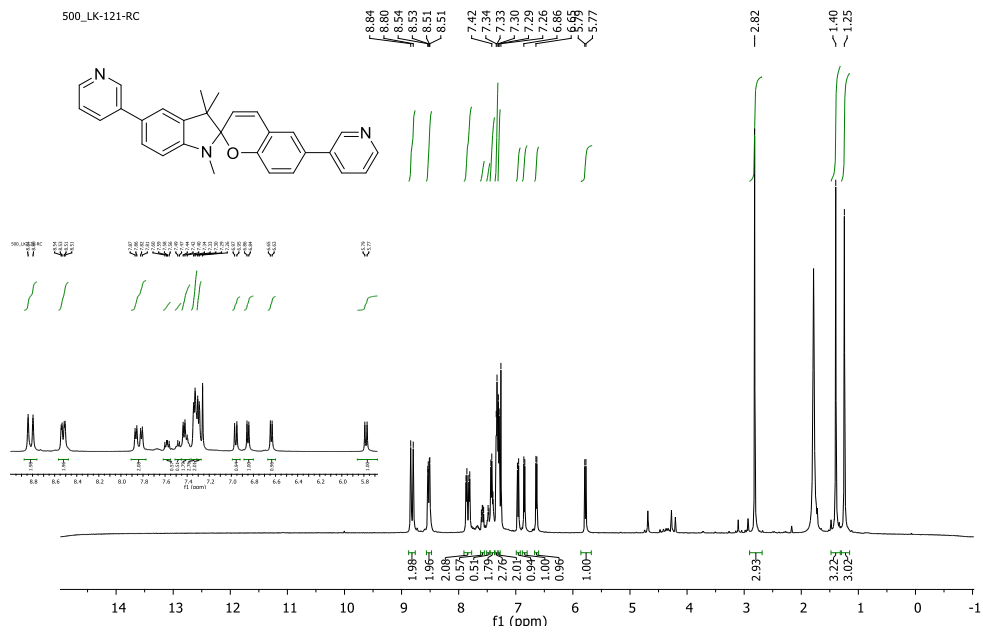
SCXRD

Identification code	<b>3a</b>
Empirical formula	C <sub>23.2</sub> H <sub>22</sub> N <sub>2.4</sub> O <sub>1.4</sub>
Formula weight	356.83
Temperature/K	122(4)
Crystal system	monoclinic
Space group	P2 <sub>1</sub> /c
a/Å	10.3318(18)
b/Å	10.3776(12)
c/Å	22.1756(18)
α/°	90
β/°	99.110(12)
γ/°	90
Volume/Å <sup>3</sup>	2347.7(5)
Z	5
ρ <sub>calc</sub> /cm <sup>3</sup>	1.262
μ/mm <sup>-1</sup>	0.079
F(000)	946.0
Crystal size/mm <sup>3</sup>	0.469 × 0.301 × 0.260
Radiation	MoKα (λ = 0.71073)
2θ range for data collection/°	6.098 to 60.454
Index ranges	-14 ≤ h ≤ 14, -14 ≤ k ≤ 13, -29 ≤ l ≤ 27
Reflections collected	37198
Independent reflections	6210 [R <sub>int</sub> = 0.1434, R <sub>sigma</sub> = 0.1234]
Data/restraints/parameters	6210/229/474
Goodness-of-fit on F <sup>2</sup>	1.476
Final R indexes [I ≥ 2σ (I)]	R <sub>1</sub> = 0.1694, wR <sub>2</sub> = 0.4565
Final R indexes [all data]	R <sub>1</sub> = 0.2656, wR <sub>2</sub> = 0.5030
Largest diff. peak/hole / e Å <sup>-3</sup>	0.44/-0.43

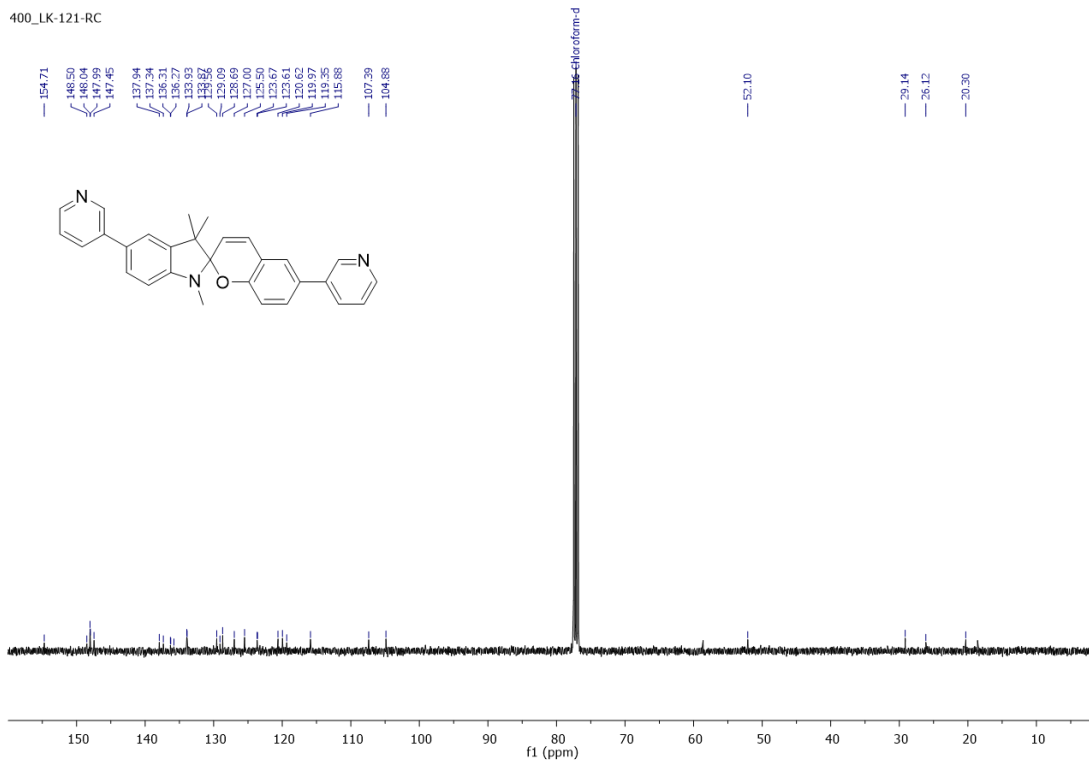
**1',3',3'-trimethyl-5',6-di(pyridin-3-yl)spiro[chromene-2,2'-indoline] (3b)**



<sup>1</sup>H

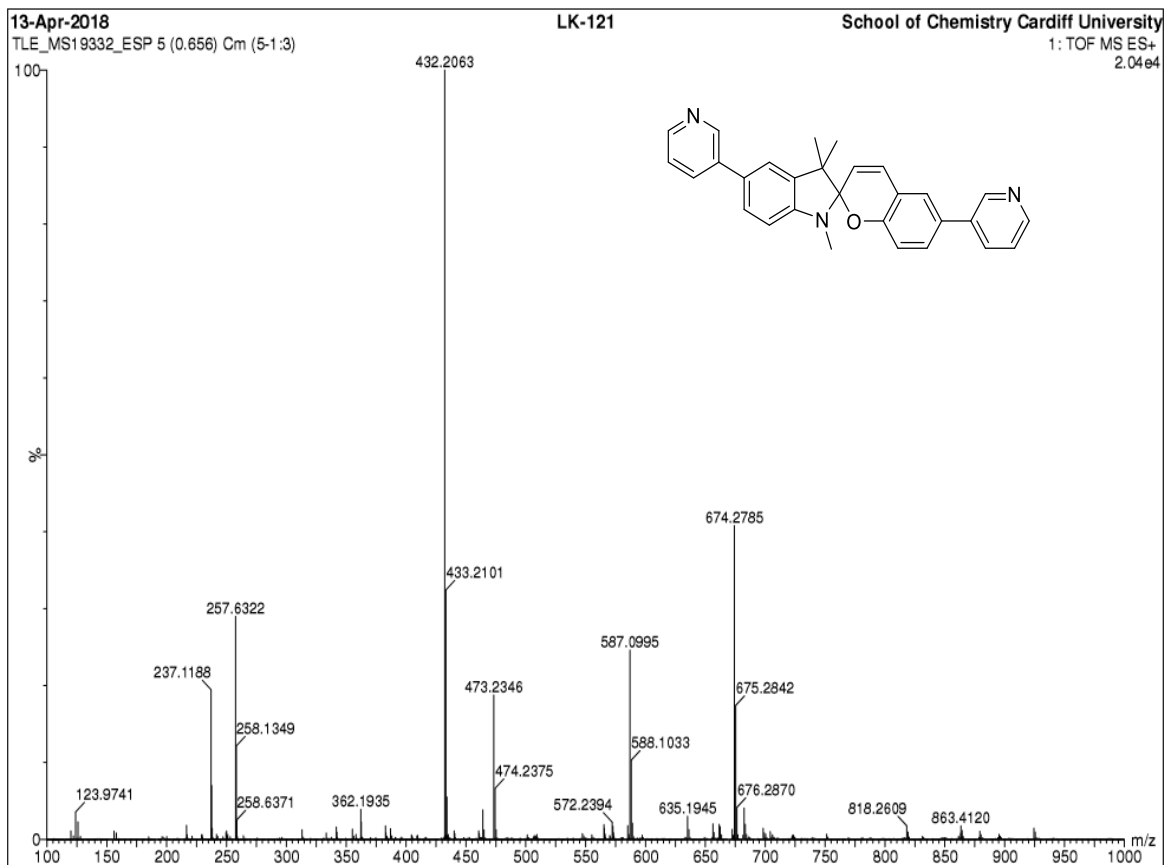


**<sup>13</sup>C**

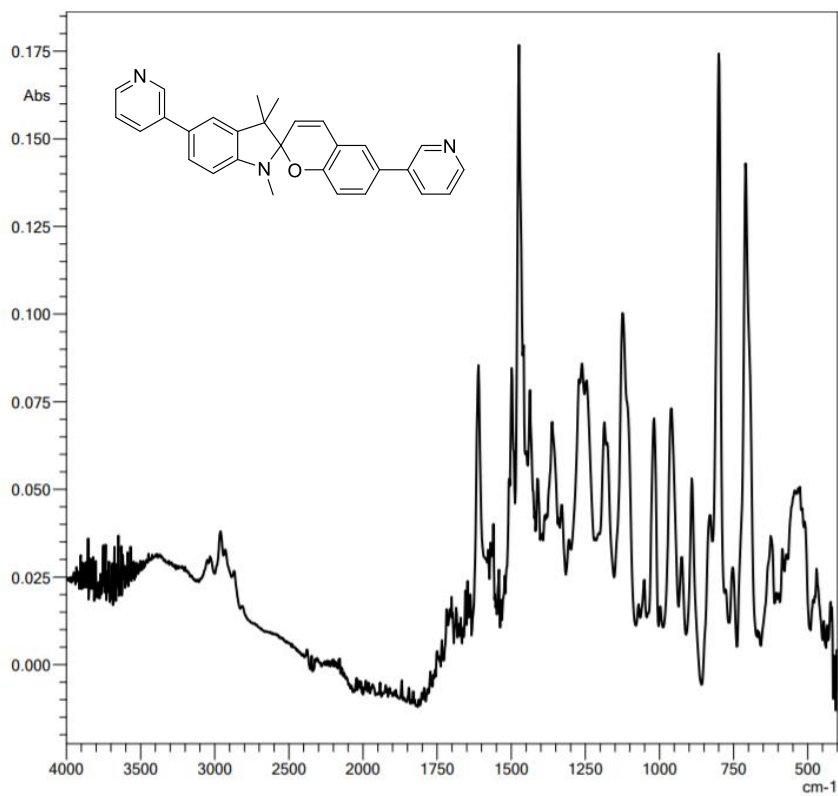


**MS**

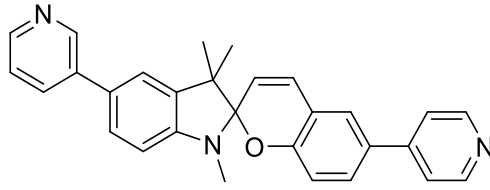




IR



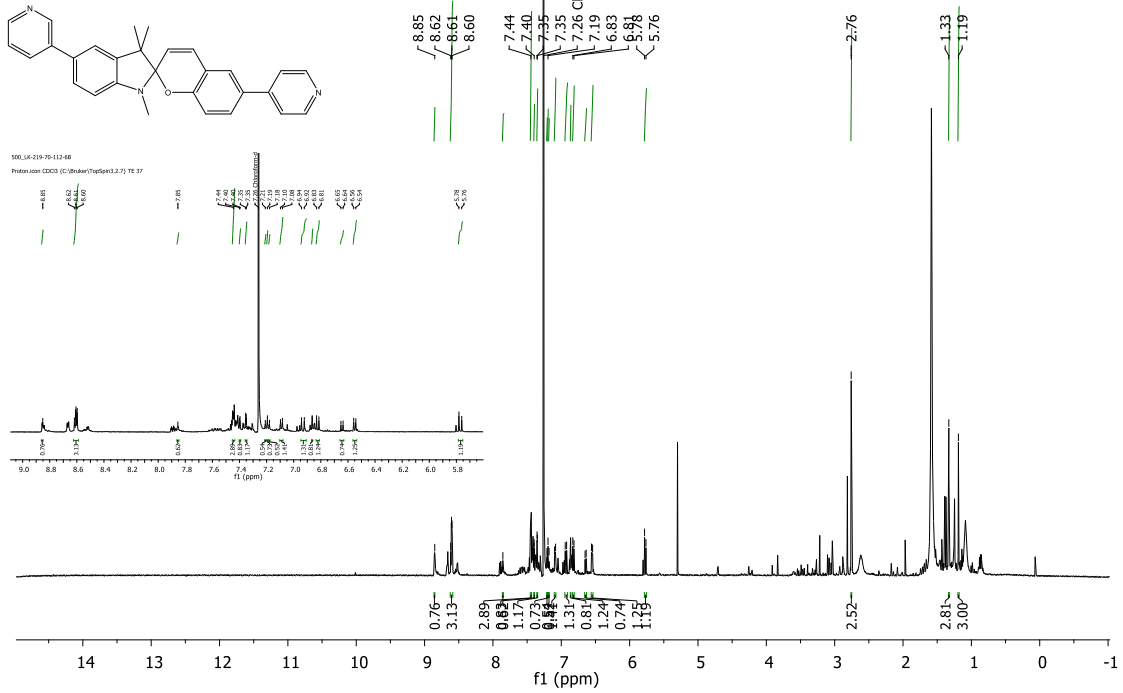
1,3,3'-trimethyl-5'-(pyridin-3-yl)-6-(pyridin-4-yl)spiro[chromene-2,2'-indoline] (6b)



**<sup>1</sup>H**

500\_LK-219-70-112-6B

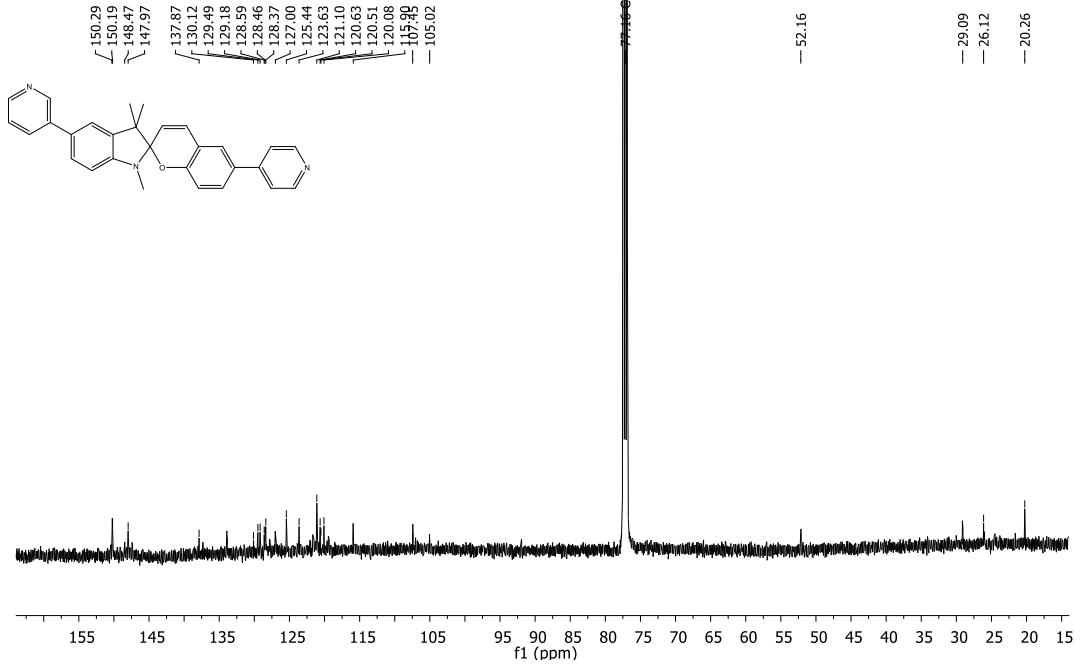
Proton.icon CDCl3 {C:\Bruker\TopSpin3.2.7} TE 37



**<sup>13</sup>C**

500\_lk-34pyrSP-6b

Carbon.icon CDCl3 {C:\Bruker\TopSpin3.2.7} TE 26



**MS**

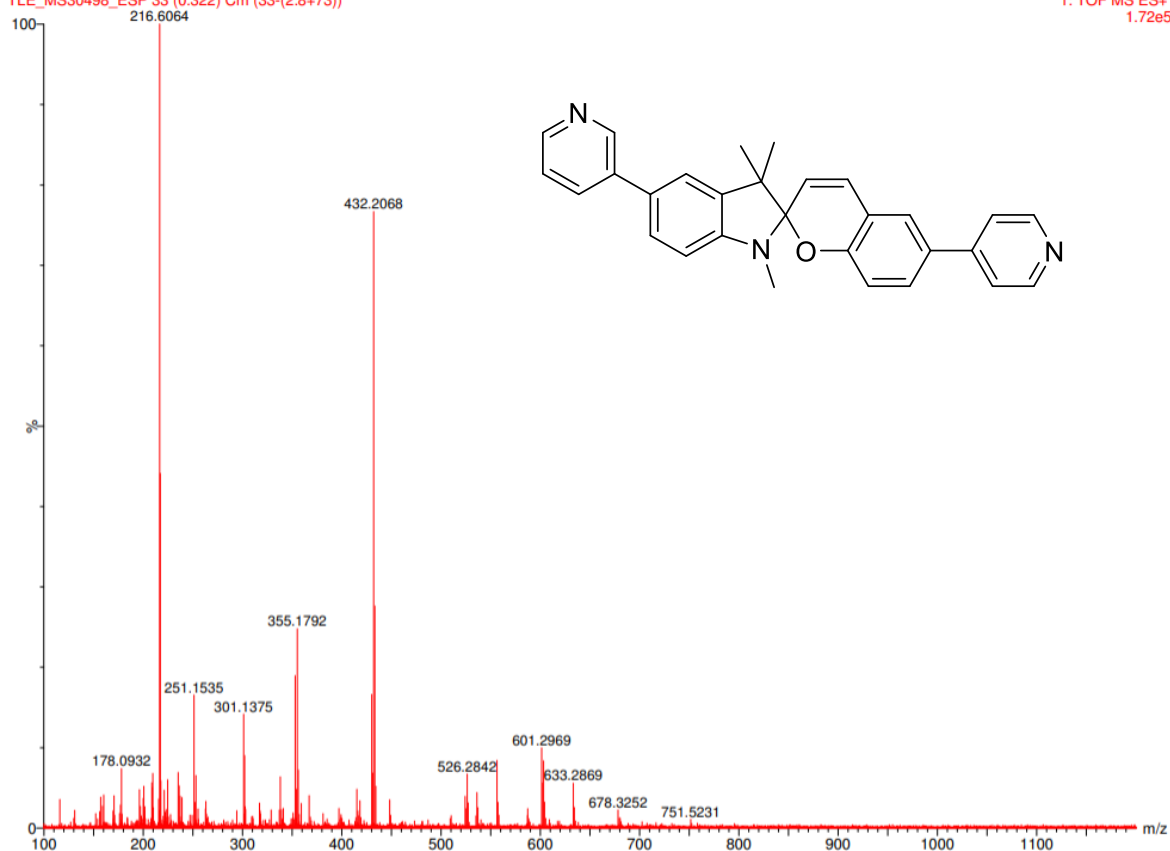
19-Aug-2020

TLE\_MS30498\_ESP 33 (0.322) Cm (33-(2:8+73))

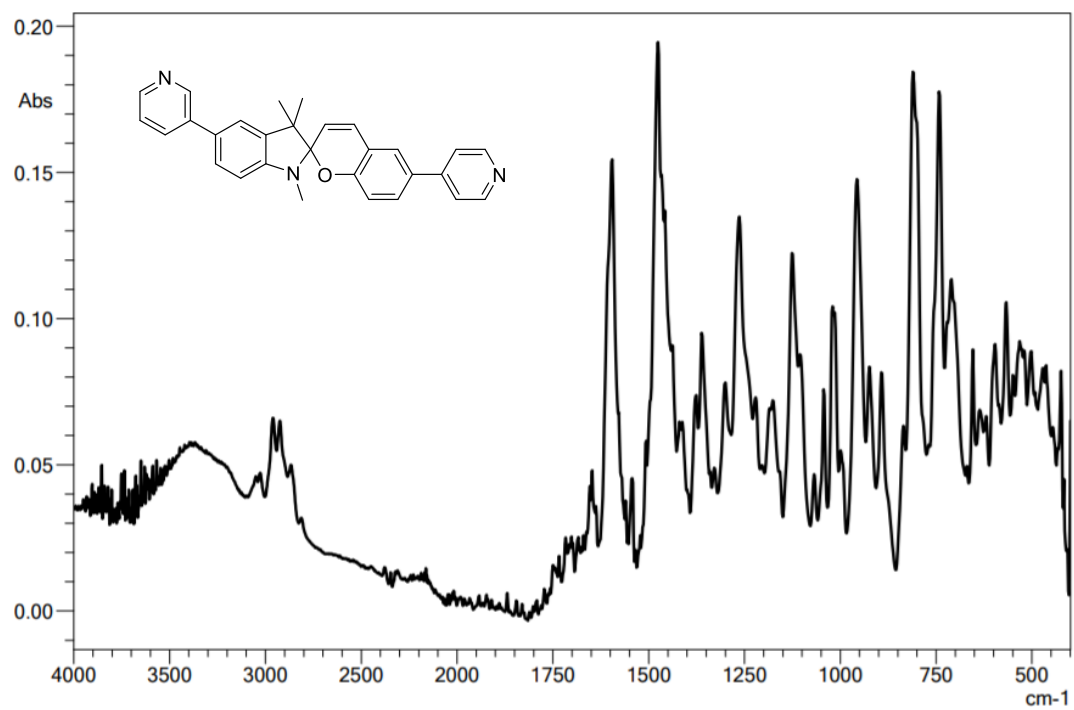
GG31-6b

Cardiff Uni Synapt G2-Si

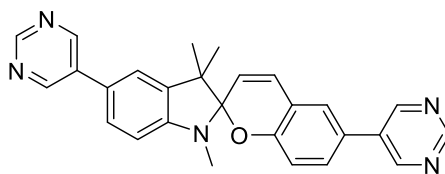
1: TOF MS ES+  
1.72e5



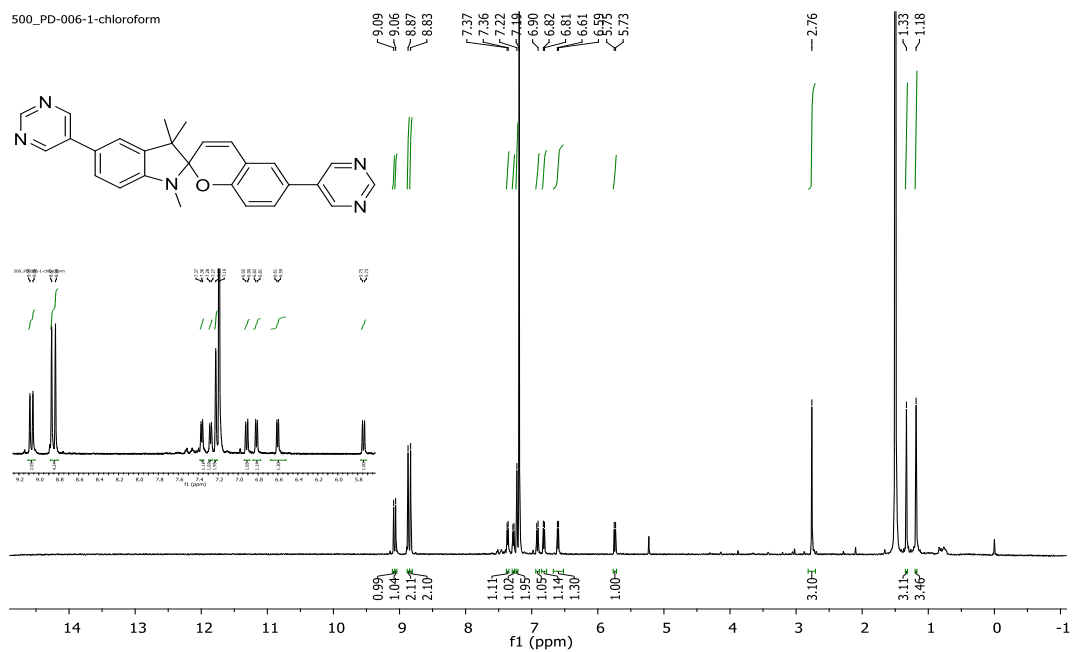
IR



# 1',3',3'-trimethyl-5',6-di(pyrimidin-5-yl)spiro[chromene-2,2'-indoline] (3c)



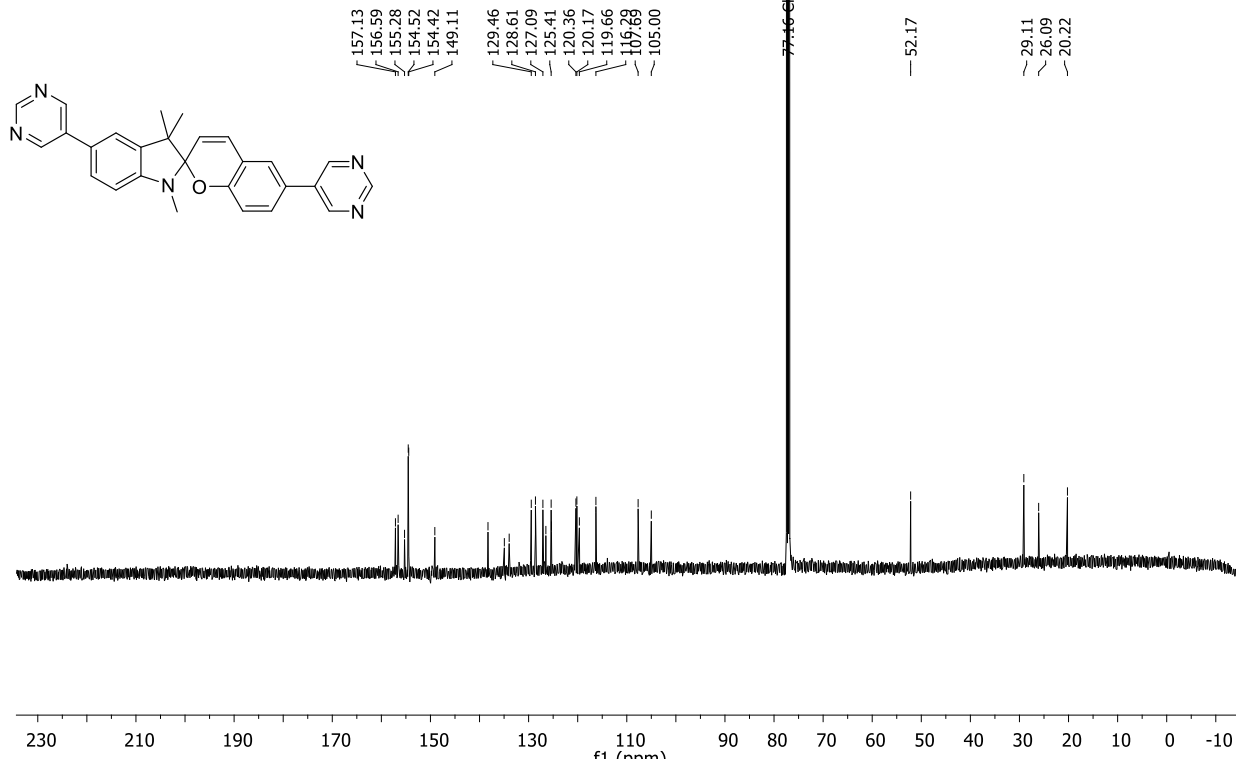
<sup>1</sup>H



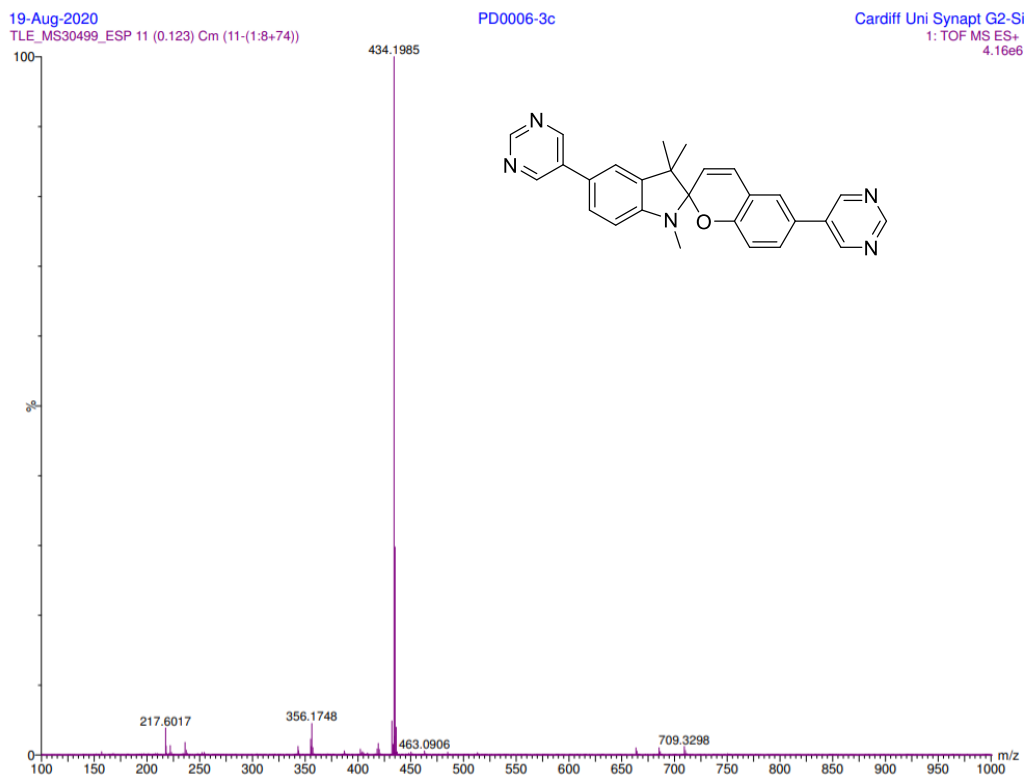
<sup>13</sup>C

500\_LK-PD006-3C

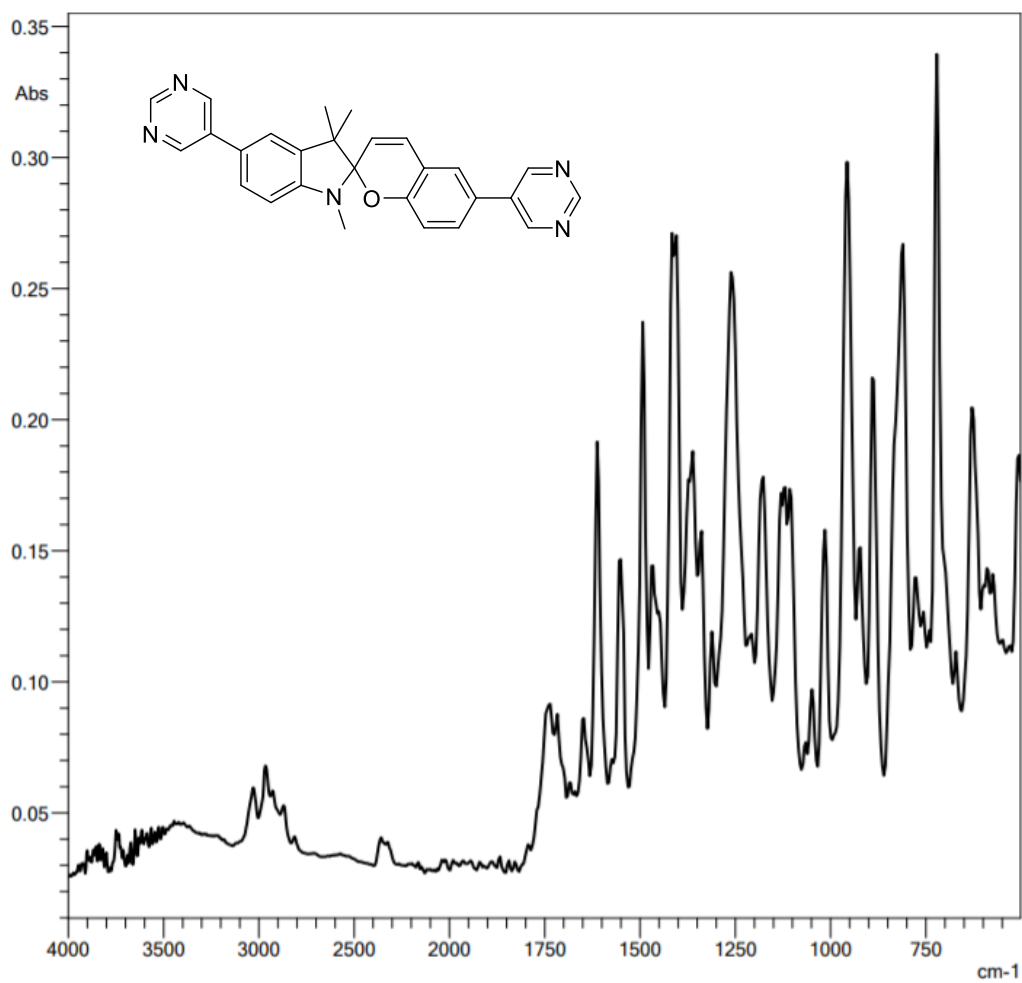
Carbon.1con CDCl3 {C:\Bruker\TopSpin3.2.7} TE 3



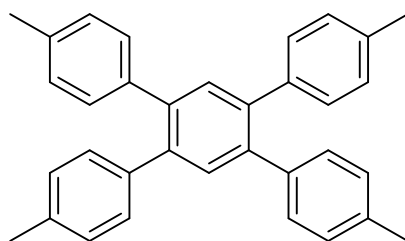
## MS



## IR



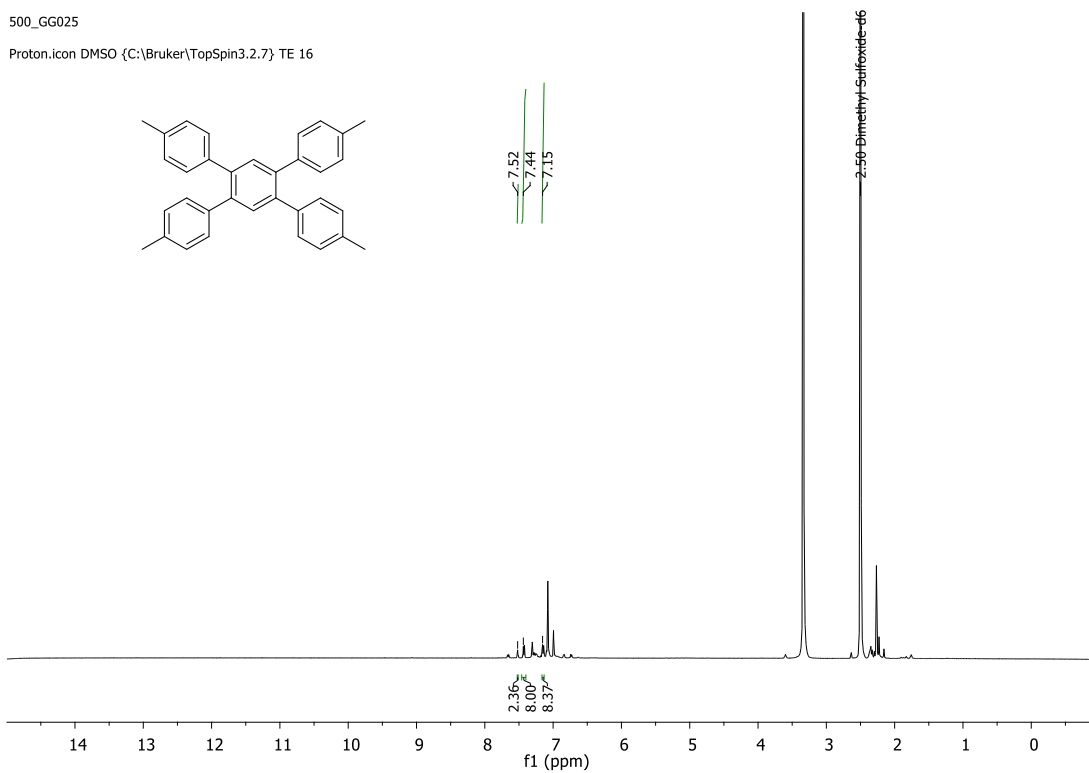
**4,4''-dimethyl-4',5'-di-p-tolyl-1,1':2',1''-terphenyl (7a)**



<sup>1</sup>H

500\_GG025

Proton.icon DMSO {C:\Bruker\TopSpin3.2.7} TE 16



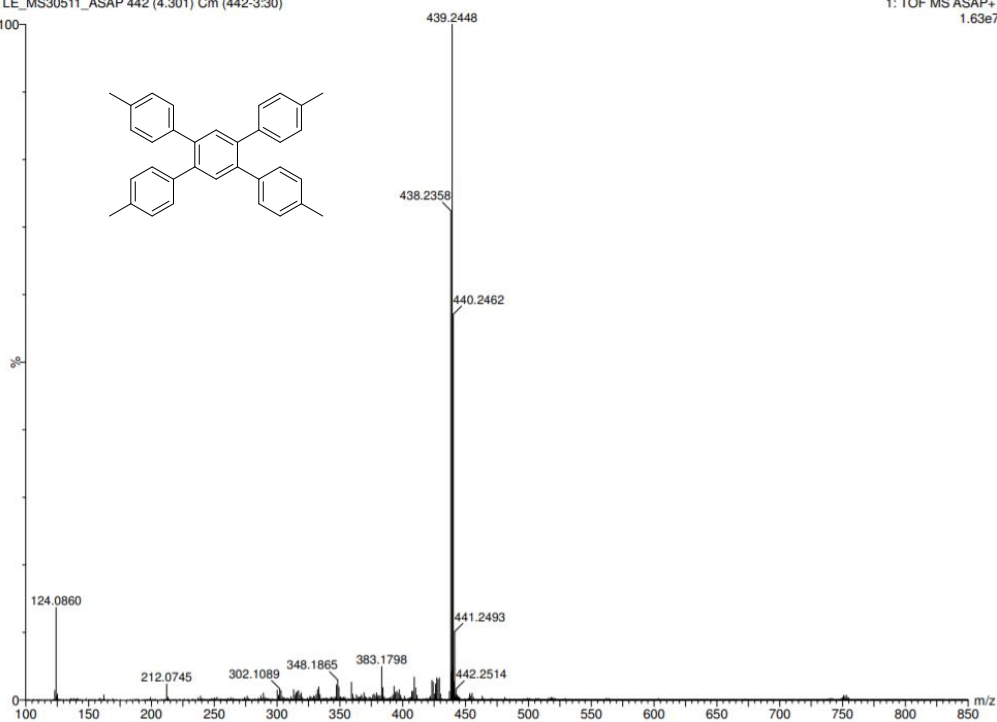
## MS

25-Aug-2020

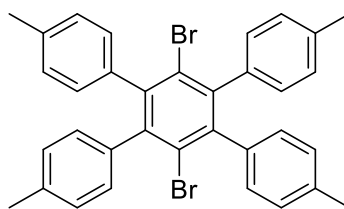
TLE\_MS30511\_ASAP 442 (4.301) Cm (442:3:30)

GG025-7a

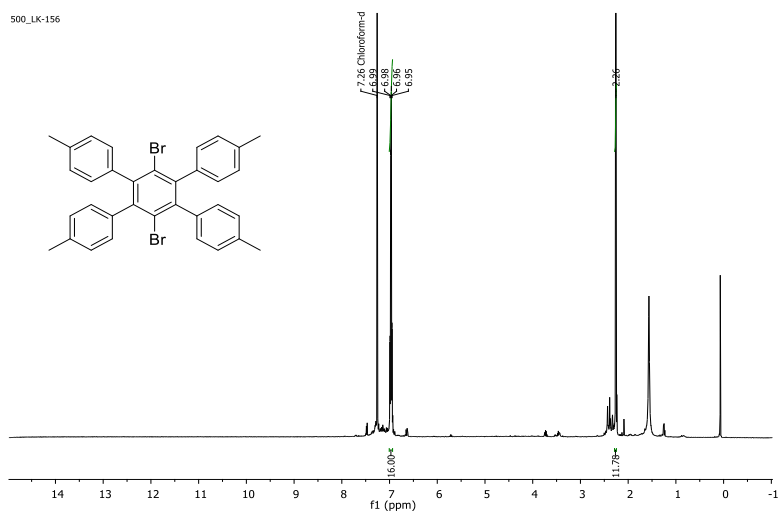
XEVO-G2XSQTOF#YEA1289  
Cardiff University  
1: TOF MS ASAP+  
1.63e7



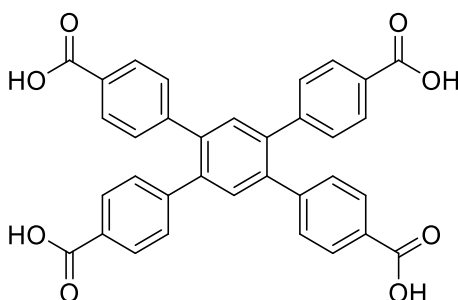
## 3',6'-dibromo-4,4''-dimethyl-4',5'-di-p-tolyl-1,1':2',1''-terphenyl (7b)



$^1\text{H}$



**4',5'-bis(4-carboxyphenyl)-[1,1':2',1''-terphenyl]-4,4''-dicarboxylic acid (8a)**

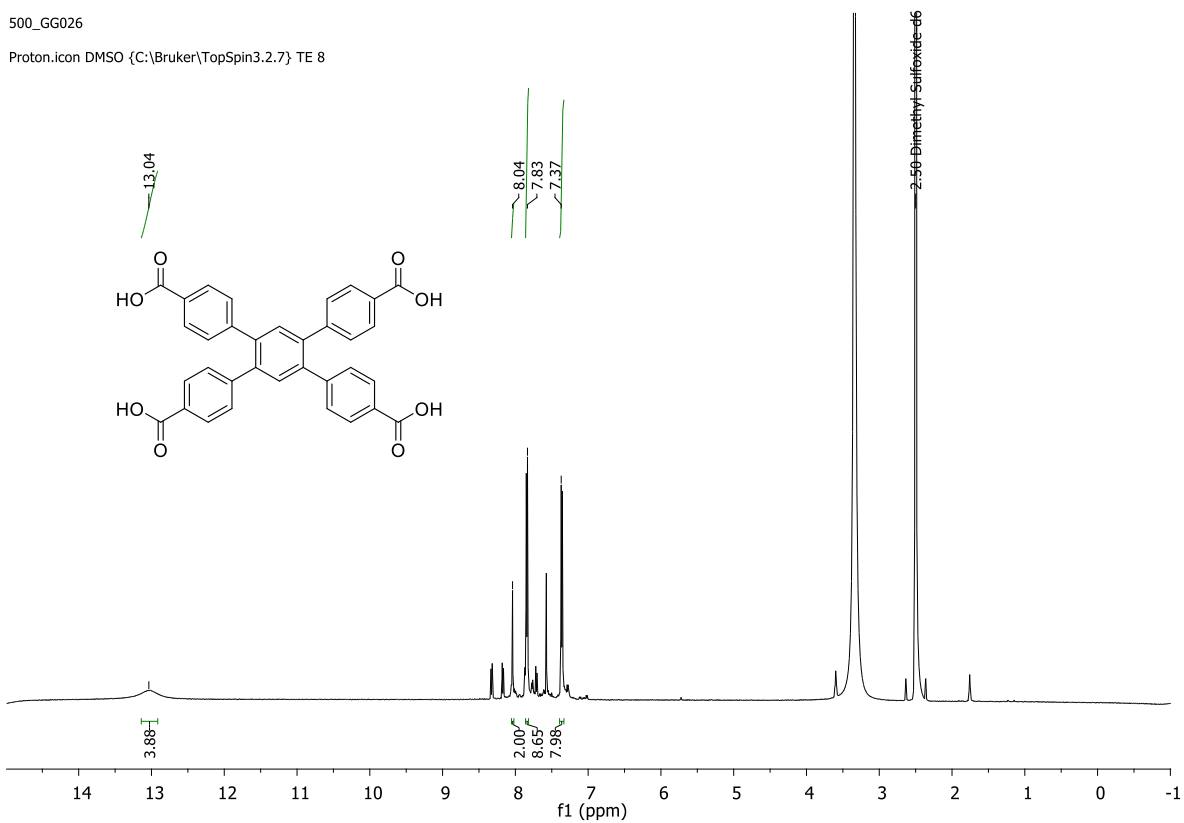


$^1\text{H}$

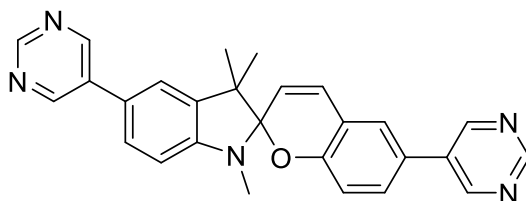


500\_GG026

Proton.icon DMSO {C:\Bruker\TopSpin3.2.7} TE 8

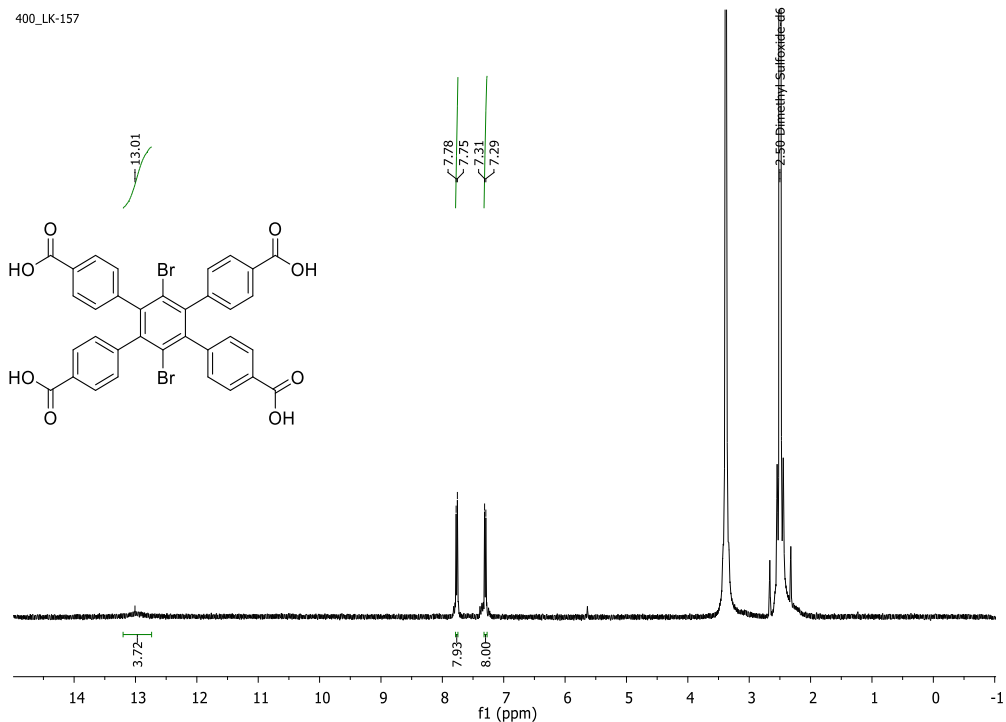


**3',6'-dibromo-4',5'-bis(4-carboxyphenyl)-[1,1':2,1''-terphenyl]-4,4''-dicarboxylic acid (8b)**



<sup>1</sup>H

400\_LK-157



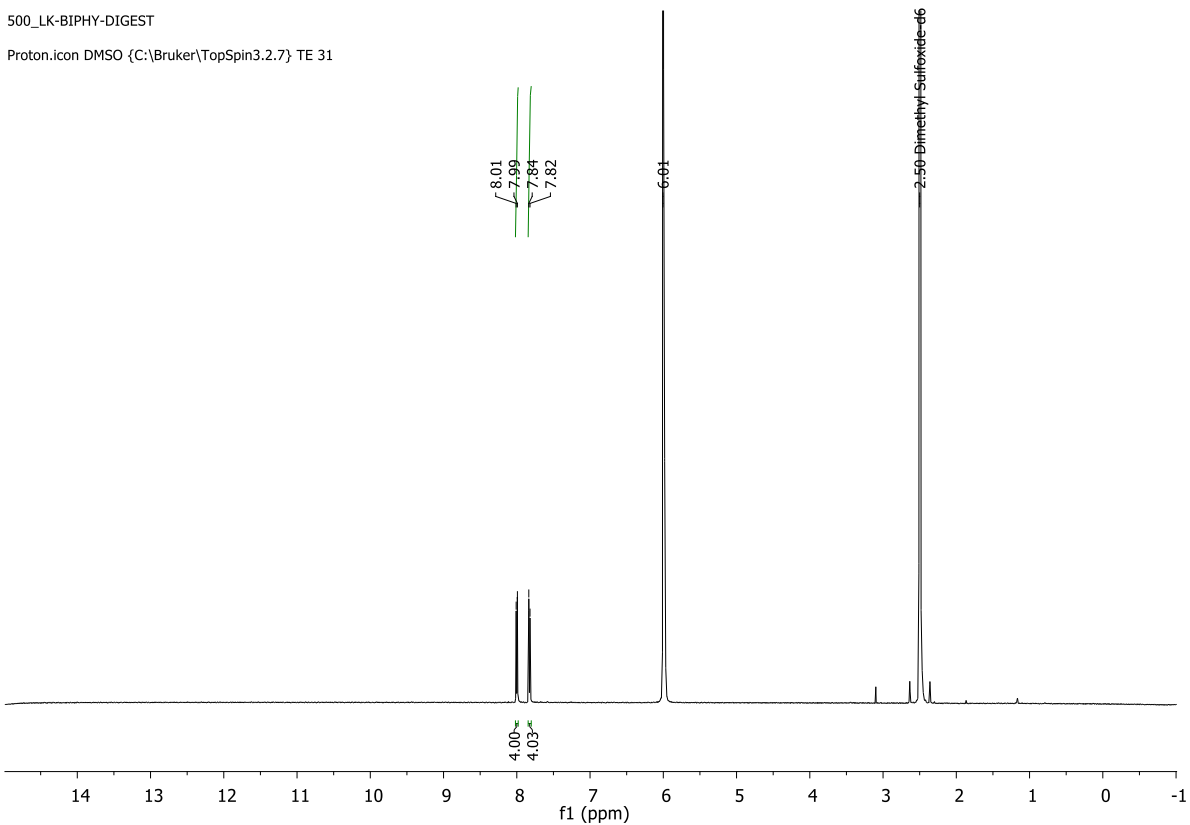
S2

## NMR Digests

### BPDC

500\_LK-BIPHY-DIGEST

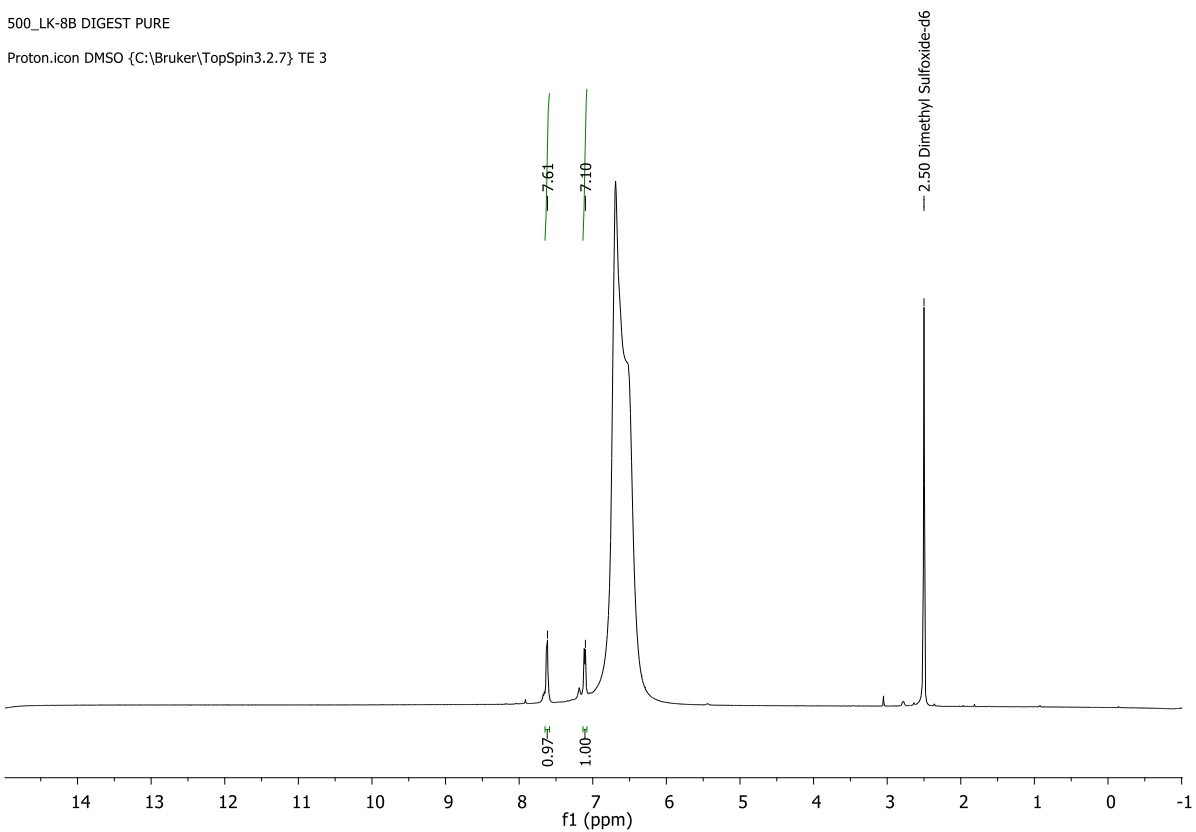
Proton.icon DMSO {C:\Bruker\TopSpin3.2.7} TE 31



### DBTD

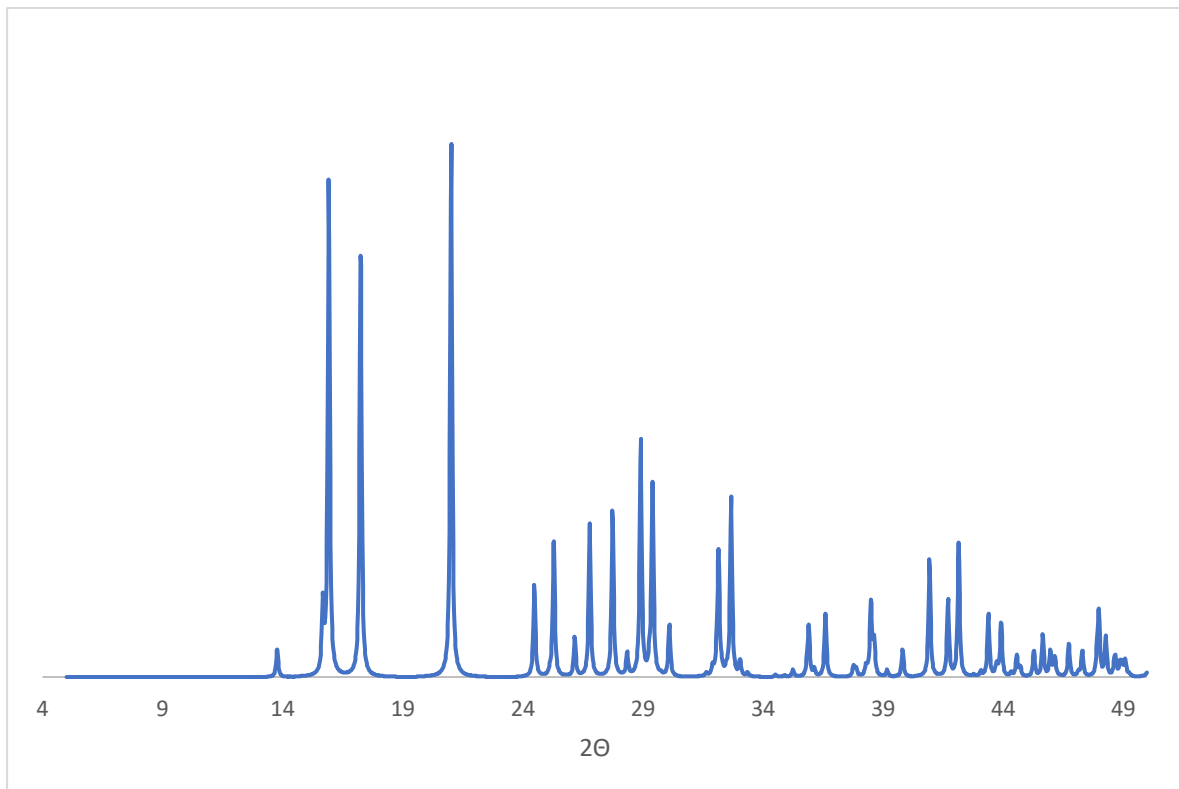
500\_LK-8B DIGEST PURE

Proton.icon DMSO {C:\Bruker\TopSpin3.2.7} TE 3



### PXRD

#### Zinc Nitrate Hexahydrate simulated pattern



**SCXRD**

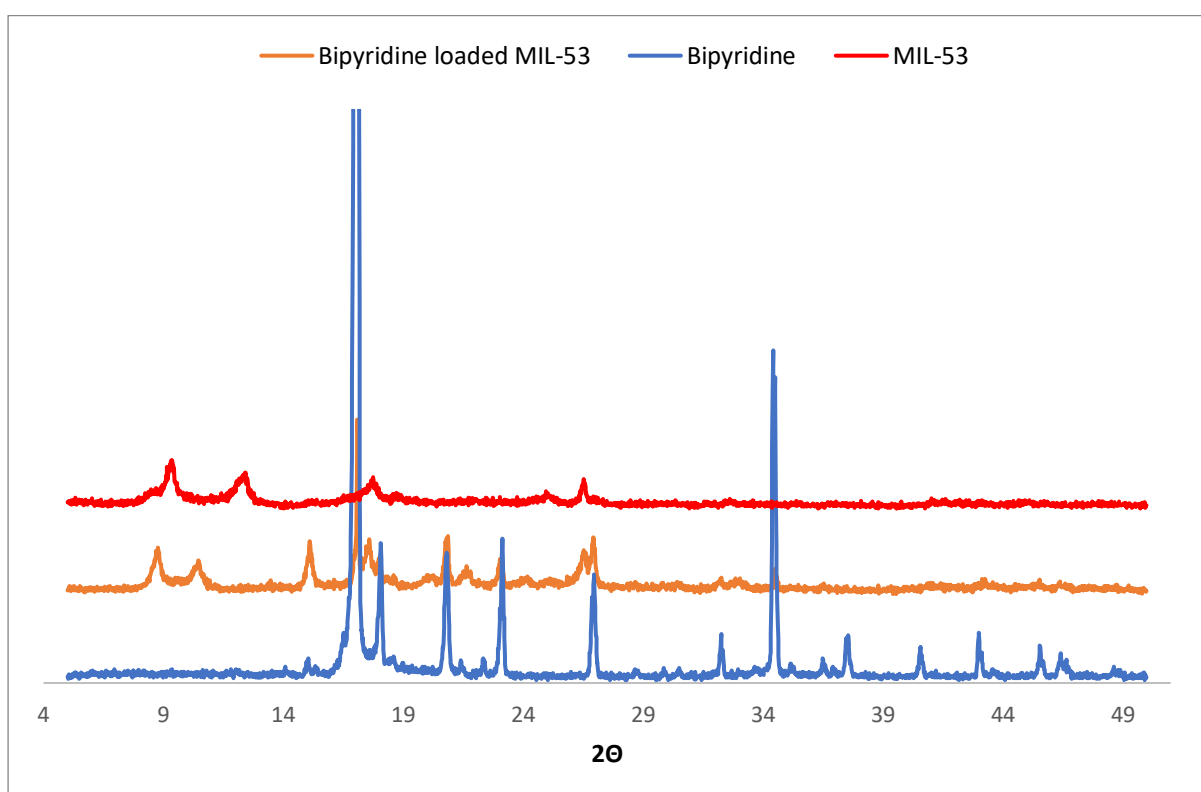
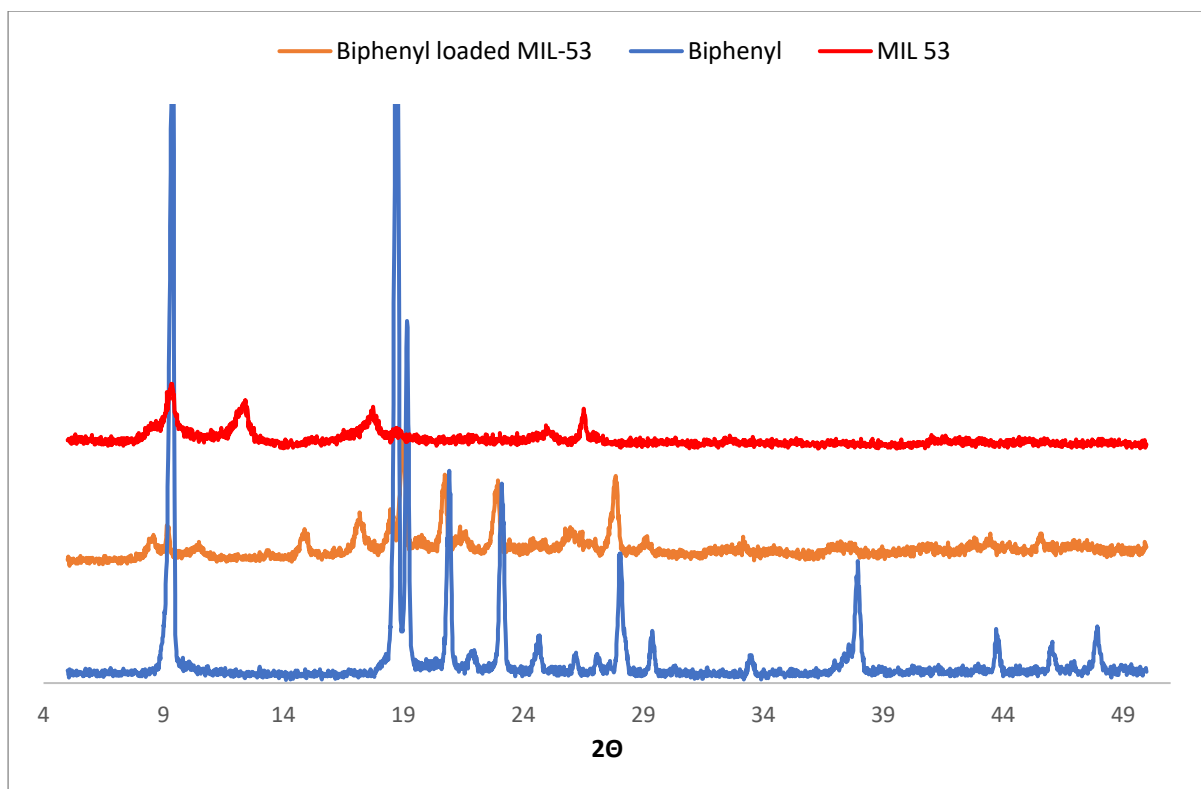
Identification code	LK-1	LK-2	GG-1	GG-32
Empirical formula	$C_{13.29}N_{0.71}O_{2.53}Zn_{0.59}H_{0.01}$	$C_{37}H_{29.5}N_2O_7Zn_{1.5}$	$C_{50}H_{50}NO_9ZnBr_2$	$C_{50}H_{50}N_6O_{12}ZnBr$
Formula weight	248.49	712.18	1034.10	1072.24
Temperature/K	150.0(3)	150.0(3)	150.0(3)	190.0(3)
Crystal system	orthorhombic	monoclinic	orthorhombic	triclinic
Space group	$C222_1$	$C2/c$	$Pmmm$	$P-1$
a/Å	34.021(5)	61.237(4)	11.1343(13)	8.602(6)
b/Å	37.146(6)	14.6895(6)	15.897(2)	9.816(6)
c/Å	42.043(9)	24.3658(13)	23.866(19)	15.790(10)
$\alpha/^\circ$	90	90	90	80.39(5)
$\beta/^\circ$	90	113.839(7)	90	79.06(6)
$\gamma/^\circ$	90	90	90	76.03(5)
Volume/Å <sup>3</sup>	53131(16)	20048(2)	4224(3)	1260.1(14)
Z	68	16	4	1
$\rho_{calc}/cm^3$	0.528	0.944	1.626	1.413
$\mu/mm^{-1}$	0.473	0.758	3.534	1.347
F(000)	8337.0	5864.0	2116.0	553.0
Crystal size/mm <sup>3</sup>	0.2 × 0.2 × 0.1*	0.258 × 0.215 × 0.075	0.24 × 0.07 × 0.015	0.138 × 0.136 × 0.044
Radiation	MoK $\alpha$ ( $\lambda = 0.71073$ )	MoK $\alpha$ ( $\lambda = 0.71073$ )	CuK $\alpha$ ( $\lambda = 1.54178$ )	MoK $\alpha$ ( $\lambda = 0.71073$ )
2 $\theta$ range for data collection/ $^\circ$	6.746 to 27.402	6.836 to 59.88	5.56 to 133.168	6.914 to 59.18
Index ranges	-22 ≤ h ≤ 22, -24 ≤ k ≤ 23, -28 ≤ l ≤ 25	-63 ≤ h ≤ 84, -15 ≤ k ≤ 20, -33 ≤ l ≤ 26	-13 ≤ h ≤ 12, -18 ≤ k ≤ 18, -28 ≤ l ≤ 28	-11 ≤ h ≤ 9, -11 ≤ k ≤ 12, -21 ≤ l ≤ 19
Reflections collected	14991	51867	19135	8687
Independent reflections	7396 [ $R_{int} = 0.2068$ , $R_{sigma} = 0.3045$ ]	23860 [ $R_{int} = 0.0375$ , $R_{sigma} = 0.0663$ ]	4193 [ $R_{int} = 0.1118$ , $R_{sigma} = 0.0682$ ]	5723 [ $R_{int} = 0.1924$ , $R_{sigma} = 0.6156$ ]
Data/restraints/parameters	7396/3292/1312	23860/96/883	4193/66/93	5723/4/77
Goodness-of-fit on $F^2$	1.343	1.325	1.820	1.965
Final R indexes [ $I > 2\sigma(I)$ ]	$R_1 = 0.1681$ , $wR_2 = 0.4159$	$R_1 = 0.1115$ , $wR_2 = 0.3463$	$R_1 = 0.2422$ , $wR_2 = 0.5391$	$R_1 = 0.4365$ , $wR_2 = 0.7035$
Final R indexes [all data]	$R_1 = 0.2433$ , $wR_2 = 0.4814$	$R_1 = 0.1657$ , $wR_2 = 0.3927$	$R_1 = 0.3486$ , $wR_2 = 0.6141$	$R_1 = 0.6244$ , $wR_2 = 0.7725$
Largest diff. peak/hole / e Å <sup>-3</sup>	0.59/-0.38	1.34/-0.84	14.60/-6.94	10.36/-2.90

\*Approximate value for crystal dimensions.

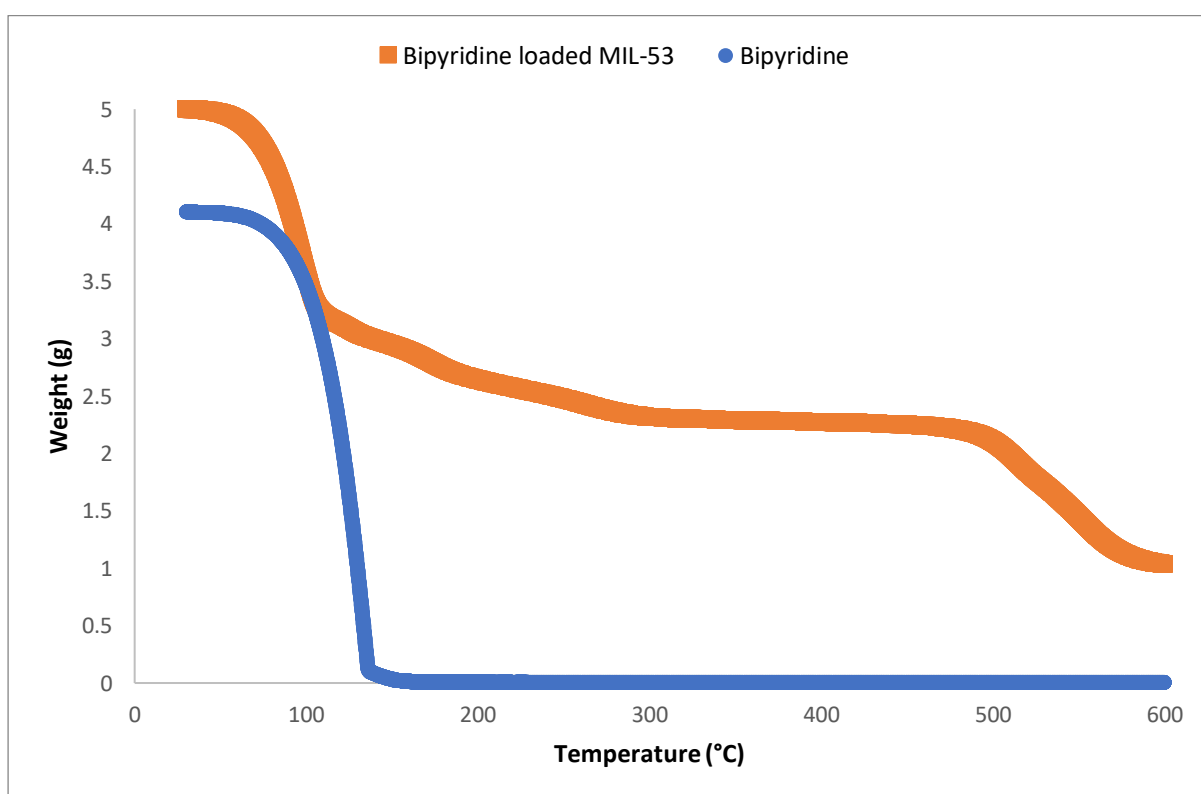
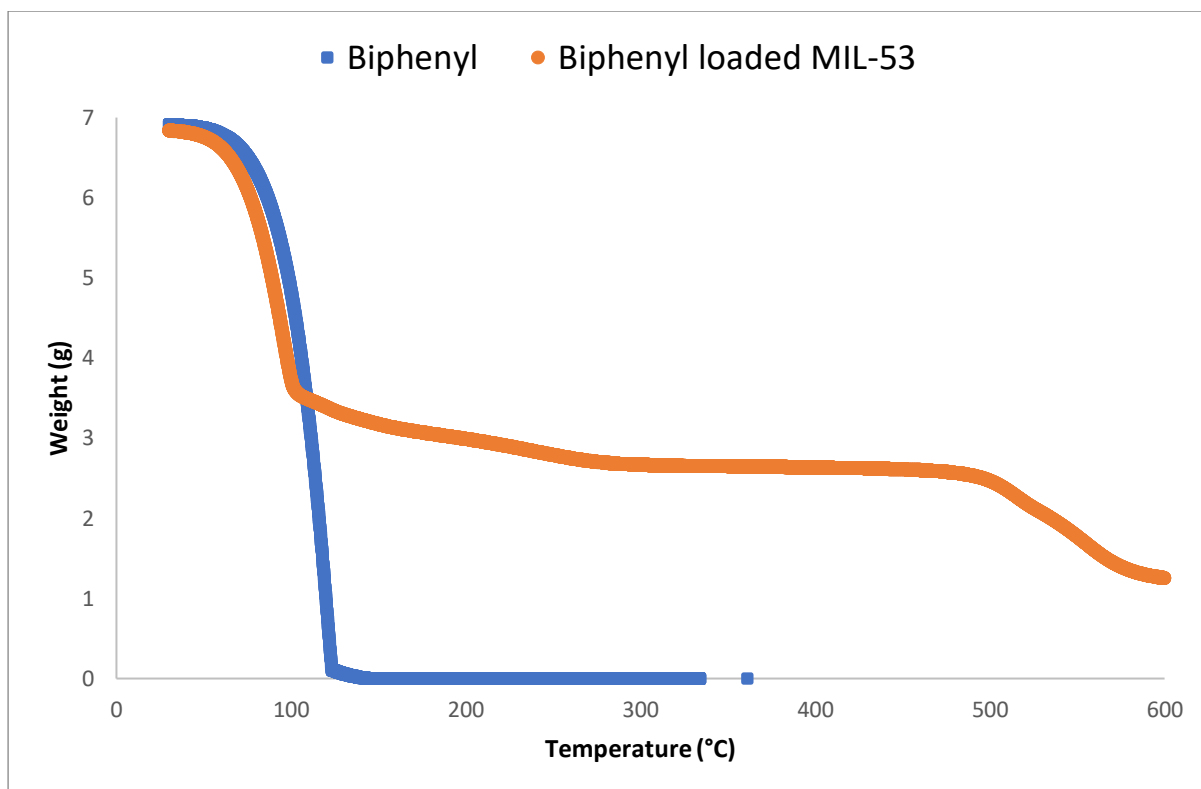
S3

**MIL-53**

**PXRD**



TGA



UiO-66

PXRD

